

The Dissertation Committee for Angela Sue Chambers Certifies that this is the approved version of the following dissertation:

A Comparison of Nuclide Production and Depletion using MCNPX and ORIGEN-ARP Reactor Models and a Sensitivity Study of Reactor Design Parameters Using MCNPX for Nuclear Forensics Purposes

Committee:

Steven R. Biegalski, Supervisor

William S. Charlton

Kendra M. Foltz Biegalski

Sheldon Landsberger

Erich A. Schneider

**A Comparison of Nuclide Production and Depletion using MCNPX and
ORIGEN-ARP Reactor Models and a Sensitivity Study of Reactor
Design Parameters Using MCNPX for Nuclear Forensics Purposes**

by

Angela Sue Chambers, BS, MS

Dissertation

Presented to the Faculty of the Graduate School of
The University of Texas at Austin
in Partial Fulfillment
of the Requirements
for the Degree of

Doctor of Philosophy

The University of Texas at Austin

May 2010

Dedication

For my family, for putting up with me, and especially for my husband, Terrel, and our children, Tonja, Hillary, Kara, Trinity and Tristan, who I live for.

Acknowledgements

I would like to thank my dissertation committee for taking the time to review this dissertation. I would especially like to thank Dr. Sheldon Landsberger for introducing me to UT's nuclear engineering program and my advisor, Dr. Steven Biegalski, for not giving up on me through the years (and for making Laplace transforms seem "easy").

I would like to acknowledge the Los Alamos National Laboratory, my former supervisors, Lee Anderson and Wayne Lunsford, the National Nuclear Security Administration, and my current supervisor, D. Ronald Baca for allowing me to complete this dissertation while I was employed by them.

I would also like to thank my parents, John and Janet Brown, grandparents, Don and Darlene Brown, and sister, Kimberly Brown, for supporting me, emotionally, spiritually, and financially, through more than 30 years of education: Kindergarten to PhD.

A Comparison of Nuclide Production and Depletion using MCNPX and ORIGEN-ARP Reactor Models and a Sensitivity Study of Reactor Design Parameters Using MCNPX for Nuclear Forensics Purposes

Publication No. _____

Angela Sue Chambers, PhD

The University of Texas at Austin, 2010

Supervisor: Steven Biegalski

The Oak Ridge Isotope Generation and Depletion – Automatic Rapid Processing (ORIGEN-ARP) deterministic code has been extensively utilized for determining nuclide concentrations at various specific burnup values for a variety of nuclear reactor designs. Given nuclide concentrations or ratios, such calculations can be used in nuclear forensics nuclear non-proliferation applications to reverse-calculate the type of reactor and specific burnup of the fuel from which the nuclides originated.

Recently, Los Alamos National Laboratory has released a version of its probabilistic radiation transport code, MCNPX 2.6.0, which incorporates a fuel burnup feature which can also determine, via the probabilistic Monte Carlo method, nuclide concentrations as a function of fuel burnup.

This dissertation compares the concentrations of 46 nuclides significant to nuclear forensics analyses for different reactor types using results from the ORIGEN-ARP and the MCNPX 2.6.0 codes. Three reactor types were chosen: the Westinghouse 17x17

Pressurized Water Reactor (PWR), the GE 8x8-4 Boiling Water Reactor (BWR), and the Canadian Deuterium Uranium, CANDU-37, reactor.

Additionally, a sensitivity study of the different reactor parameters within the MCNPX Westinghouse 17x17 PWR model was performed. This study analyzed the different nuclide concentrations resulting from minor perturbations of the following parameters: assembly rod pitch, initial moderator boron concentration, fuel pin cladding thickness, moderator density, and fuel temperature.

Table of Contents

List of Tables	ix
List of Figures	xi
Chapter 1: Introduction	1
1.1 Background Information	1
1.2 The Use of Reactor Transmuted Species as Nuclear Forensic Indicators	3
1.3 Theory and Mathematics.....	11
1.3.1 Why Do We Measure Burnup?.....	11
1.3.2 Nuclides Useful as Spent Fuel Monitors	13
1.3.3 Dissertation Objectives	28
Chapter 2: Computational Methods for Determining Nuclide Concentrations	30
2.1 Actinide Production in Reactors	30
2.2 Fission Fragment Production in Reactors	35
2.3 Actinide and Fission Fragment Depletion and Production in Nuclear Reactors using ORIGEN-ARP	37
2.4 Actinide and Fission Fragment Depletion and Production in Nuclear Reactors using MCNPX.....	42
2.5 ORIGEN-ARP versus MCNPX.....	44
Chapter 3: The BWR Reactor Model.....	55
3.1 The Model.....	55
3.2 The Results.....	66
3.3 Sources of Error	89
Chapter 4: The PWR Reactor Model	93
4.1 The Model.....	93
4.2 The Results.....	99
4.3 Sources of Error	114
Chapter 5: The CANDU-37 Reactor Model	116
5.1 The Model.....	116
5.2 The Results.....	130

5.3	Sources of Error	151
Chapter 6:	Sensitivity Study	152
6.1	Reactor Design and Operating Parameters	153
6.1.1	Fuel Assembly Rod Pitch.....	160
6.1.2	Boron Concentration in the Moderator	162
6.1.3	Cladding Thickness.....	165
6.1.4	Moderator/Coolant Density	168
6.1.5	Fuel Temperature	168
6.2	Sensitivity Study Results and Conclusions.....	170
6.2.1	Fuel Assembly Rod Pitch.....	170
6.2.2	Boron Concentration in the Moderator	177
6.2.3	Different Cladding Thicknesses.....	181
6.2.4	Different Moderator Densities	184
6.2.5	Different Fuel Temperatures.....	187
Chapter 7:	Conclusions and Recommendations	194
7.1	Conclusions for ORIGEN-ARP and MCNPX Comparisons.....	194
7.2	Conclusions for MCNPX Sensitivity Study	196
7.3	Recommendations for Future Work.....	196
Appendix A:	The MCNPX BWR Model.....	198
Appendix B:	The MCNPX PWR Model	203
Appendix C:	The MCNPX CANDU Model.....	206
Appendix D:	BWR Plots of 46 Nuclides of Interest.....	212
Appendix E:	PWR Plots of 46 Nuclides of Interest.....	236
Appendix F:	CANDU-37 Plots of 46 Nuclides of Interest	260
Appendix G:	PWR Sensitivity Study Plots of 46 Nuclides of Interest.....	284
Appendix H:	ARP Cross Section Extraction Input and Output Files	405
References	412
Vita	415

List of Tables

Table 1: Nuclides generated from the BWR case with $R_c > 1000$ and $T_{1/2} > 200$ years .	22
Table 2: Actinide Fission Yield Data Sets Available in ORIGEN-S ⁵ and MCNPX ³⁰	48
Table 3: MCNPX and ORIGEN-S ²³⁵ U Fission Product Yields for Several Nuclides ...	54
Table 4: BWR Design and Operating Data for MCNPX Model	57
Table 5: BWR Design and Operating Data for ORIGEN-ARP Model	58
Table 6: Nuclides Analyzed in the Comparison of the Two Models.....	67
Table 7: BWR Fission Product Differences at Maximum Burnup Values	82
Table 8: ²³⁵ U Fission Rates for the ORIGEN and MCNPX GE 8x8-4 BWR Models.....	86
Table 9: ²³⁸ U Fission Rates for the ORIGEN and MCNPX GE 8x8-4 BWR Models.....	86
Table 10: ²³⁹ Pu Fission Rates for the ORIGEN and MCNPX GE 8x8-4 BWR Models .	87
Table 11: ²⁴¹ Pu Fission Rates for the ORIGEN and MCNPX GE 8x8-4 BWR Models .	87
Table 12: MCNPX PWR Model	95
Table 13: PWR Design and Operating Data for ORIGEN-ARP Model.....	96
Table 14: PWR Fission Product Differences at Maximum Burnup Values	106
Table 15: ²³⁵ U Fission Rates for the ORIGEN and MCNPX W 17x17 PWR Models..	109
Table 16: ²³⁸ U Fission Rates for the ORIGEN and MCNPX W 17x17 PWR Models..	109
Table 17: ²³⁹ Pu Fission Rates for the ORIGEN and MCNPX W 17x17 PWR Models.	110
Table 18: ²⁴¹ Pu Fission Rates for the ORIGEN and MCNPX W 17x17 PWR Models.	110
Table 19: CANDU-37 MCNPX Model Fuel Assembly Parameters	124
Table 20: CANDU Design and Operating Data for ORIGEN-ARP Model	125
Table 21: CANDU Fission Product Differences at Maximum Burnup Values.....	139

Table 22: ^{235}U Fission Rates for the ORIGEN and MCNPX CANDU-37 Models.....	144
Table 23: ^{238}U Fission Rates for the ORIGEN and MCNPX CANDU-37 Models.....	144
Table 24: ^{239}Pu Fission Rates for the ORIGEN and MCNPX CANDU-37 Models	145
Table 25: ^{241}Pu Fission Rates for the ORIGEN and MCNPX CANDU-37 Models	145
Table 26: Reactor Design and Operating Parameters for Sensitivity Study.....	154
Table 27: MCNPX PWR Case 1 Model	155
Table 28: Key Nuclides Analyzed in the Sensitivity Study.....	159
Table 29: Zircaloy-2 and Zircaloy-4 Alloy Constituents ¹⁴	165
Table 30: Natural Zirconium Atom Percent Abundances.....	167

List of Figures

Figure 1: ORIGEN Calculation of ^{241}Am Production in a MAGNOX Reactor	6
Figure 2: ^{241}Am Production in a PWR.....	7
Figure 3: ^{243}Am Production as a Function of Burn-up at Different Reactor Powers.....	8
Figure 4: Power Dependence of the Burn-up Monitors Suggested in Scott (2005) ²	9
Figure 5: ORIGEN-ARP Production Calculation for Four Different Fission Products ..	10
Figure 6: Plutonium Isotopic Ratios Used in Nuclear Forensics	15
Figure 7: Surface Plot of the BWR Long to Short Cycle Ratio of Nuclides	20
Figure 8: Different Americium Ratios for Long and Short Irradiation Cases	24
Figure 9: Americium Ratios as a Function of Burn-up in a BWR.....	25
Figure 10: Americium Ratio Burn-up Plots for Four Different Reactors	26
Figure 11: $^{243}\text{Am}/^{246}\text{Cm}$ Ratio as a Function of Burn-up for Five Different Reactor Types	27
Figure 12: Fission Product Yield Distribution.....	36
Figure 13: ORIGEN-ARP Flow ⁵	38
Figure 14: ORIGEN-ARP Effective Neutron Absorption Cross Sections	41
Figure 15: ORIGEN-ARP Effective Fission Cross Sections.....	42
Figure 16: Illustration of an Acceptable (left) and an Unacceptable (right) Time Step ..	45
Figure 17: ^{235}U Fission Product Yield for Different Energy Incident Neutrons.....	49
Figure 18: ^{238}U Fission Product Yield for Different Energy Incident Neutrons.....	50
Figure 19: Thermal Neutron Fission Product Yield for Two Different Nuclides.....	51
Figure 20: Plot of ^{155}Gd Depletion in BWR Models	60
Figure 21: Plot of ^{157}Gd Depletion in BWR Models	60

Figure 22: Plot of Radiative Capture Cross Sections for ^{155}Gd and ^{157}Gd (ENDF-B/VII)	61
.....	
Figure 23: VisEd Plot of BWR Fuel Assembly	62
Figure 24: Single Fuel Lattice Element for the BWR Model	63
Figure 25: ^{235}U Enrichment Loading of BWR Fuel Assembly for MCNPX Model	65
Figure 26: ^{235}U Depletion in BWR Models	68
Figure 27: ^{235}U Radiative Capture and Fission Cross Sections	70
Figure 28: ^{238}U Depletion in BWR Models	71
Figure 29: ^{239}Pu Production in BWR Models	72
Figure 30: ^{238}U Radiative Capture Cross Sections	73
Figure 31: ^{235}U Fission Cross Sections and ^{238}U Fission and Radiative Capture Cross Sections	74
.....	
Figure 32: ^{240}Pu Production in BWR Models	76
Figure 33: ^{238}Np Production in BWR Models	77
Figure 34: ^{243}Am Production in BWR Models	78
Figure 35: ^{245}Cm Production in BWR Models	79
Figure 36: ^{91}Y Production in BWR Models	80
Figure 37: ^{131}Xe Production in BWR Models	81
Figure 38: BWR Nuclide Chart of Actinides at Final Burnup (M=MCNPX, O=ORIGEN)	83
.....	
Figure 39: Fission Rates for the GE 8x8-4 BWR Model	88
Figure 40: Plot of Computed One-energy Group Flux Values in BWR	89
Figure 41: Zirconium Production in the BWR Models	92

Figure 42: MCNPX Model of W 17x17 Pressurized Water Reactor	97
Figure 43: Cross Sectional View of PWR Model.....	98
Figure 44: Plot of ²³⁵ U Depletion for the PWR Models	100
Figure 45: ²³⁸ U Depletion in PWR Models.....	100
Figure 46: Plot of ²³⁹ Pu Production for the PWR Models	101
Figure 47: Plot of ²⁴³ Am Production for the PWR Models	102
Figure 48: Plot of ²⁴⁵ Cm Production for the PWR Models.....	102
Figure 49: Plot of ²⁴⁶ Cm Production for the PWR Models.....	103
Figure 50: Plot of ¹³⁷ Cs Production for the PWR Models	104
Figure 51: Plot of ⁹¹ Y Production for the PWR Models	105
Figure 52: Plot of ¹³⁸ Ba Production for the PWR Models	105
Figure 53: Plot of Computed One-energy Group Flux Values in PWR	107
Figure 54: Fission Rates for the W 17x17 PWR Model	111
Figure 55: PWR Nuclide Chart of Computed Actinide Values at Final Burnup.....	112
Figure 56: Fission Product Yields for the MCNPX and ORIGEN-ARP PWR Models	113
Figure 57: CANDU Nuclear Reactor Schematic and Calandria Photo ¹⁰	117
Figure 58: Two-dimensional Rendering of the CANDU-37 Model Cross Section.....	119
Figure 59: Picture of a CANDU-37 fuel assembly ¹⁰	120
Figure 60: Fuel Rod Dimensions for the MCNPX CANDU-37 Model	121
Figure 61: CANDU-37 MCNPX Model with Surrounding D ₂ O Moderator.....	122
Figure 62: Side Cross Sectional View of the CANDU-37 MCNPX Model.....	123
Figure 63: Two Spheres – D ₂ O and H ₂ O each with 1 neutron particle track	126
Figure 64: Hydrogen and Deuterium Neutron Absorption Cross Sections	128

Figure 65: CANDU-37 Results for ^{235}U Depletion	130
Figure 66: ^{235}U Reaction Rates for the CANDU-37 MCNPX Model	131
Figure 67: CANDU-37 Results for ^{238}U Depletion	132
Figure 68: CANDU-37 Results for ^{239}Pu Production	133
Figure 69: ^{245}Cm Production in CANDU-37 Reactor Model	134
Figure 70: CANDU Nuclide Chart of Computed Actinide Values at Final Burnup	135
Figure 71: MCNPX, ORIGEN-S, and NNDC Cross Sections for $^{243}\text{Pu}(n,\gamma)$ Reaction.	136
Figure 72: ^{136}Xe Production in CANDU-37 Reactor.....	137
Figure 73: Fission Rates Calculated by MCNPX for the CANDU-37 Model.....	140
Figure 74: Fission Rates Derived from ORIGEN-ARP CANDU-37 Model.....	142
Figure 75: MCNPX versus ORIGEN Fission Rate Comparison	143
Figure 76: Plot of Computed One-energy Group Flux Values in CANDU.....	146
Figure 77: Fission Product Yields for the MCNPX and ORIGEN-ARP CANDU Models	147
Figure 78: Fission Yields for the Thermal Fission of ^{235}U and ^{239}Pu	149
Figure 79: ARP Effective Fission Cross Sections for the CANDU-37 Reactor.....	150
Figure 80: VisEd Plot of PWR Kcode Source Particles	156
Figure 81: Particle Track Plot of the PWR MCNPX Model	157
Figure 82: ^{235}U Fission Cross Section Plot	161
Figure 83: ^{238}U Radiative Capture Cross Section Plot.....	162
Figure 84: Plot Illustrating the ^{10}B Neutron Absorption Cross Sections	164
Figure 85: ^{10}B (n, α) Reaction Cross Sections	164
Figure 86: ^{90}Zr Radiative Capture Cross Sections	166

Figure 87: Doppler Broadening of the (n, γ) cross section for ^{240}Pu . The temperatures are 0 K(solid), 30,000 K(dotted), and 300,000 K (dash-dot) ¹⁵	169
Figure 88: ^{235}U Depletion at Different Rod Pitch Values	171
Figure 89: ^{235}U Depletion at Different Rod Pitch Values (Expanded View)	172
Figure 90: ^{239}Pu Production in the PWR Model at Different Rod Pitch Values.....	173
Figure 91: ^{241}Am Production in the PWR Model at Different Rod Pitch Values.....	174
Figure 92: ^{148}Nd Production in the PWR Model at Different Rod Pitch Values.....	175
Figure 93: ^{135}Xe Production in the PWR Model at Different Rod Pitch Values	176
Figure 94: ^{135}Xe Decay at the Termination of Reactor Irradiation	176
Figure 95: ^{235}U Depletion in PWR for Different Boron Concentrations	177
Figure 96: ^{239}Pu Production in PWR for Different Boron Concentrations	178
Figure 97: ^{241}Am Production in PWR for Different Boron Concentrations	179
Figure 98: ^{245}Cm Production in PWR for Different Boron Concentrations	179
Figure 99: ^{241}Am Production in PWR for Different Boron Concentrations	180
Figure 100: ^{91}Y Production in PWR for Different Boron Concentrations.....	181
Figure 101: ^{235}U Depletion in PWR for Different Cladding Thicknesses	182
Figure 102: ^{239}Pu Production in PWR for Different Cladding Thicknesses	183
Figure 103: ^{142}Ce Production in PWR for Different Cladding Thicknesses.....	183
Figure 104: ^{137}Cs Production in PWR for Different Cladding Thicknesses	184
Figure 105: ^{235}U Depletion in the PWR for the Different Water Densities.....	185
Figure 106: ^{239}Pu Production in the PWR for the Different Water Densities.....	186
Figure 107: ^{161}Dy Production in the PWR for the Different Water Densities.....	187
Figure 108: ^{235}U Depletion in the PWR for the Different Fuel Temperatures	188

Figure 109:	^{239}Pu Production in the PWR for the Different Fuel Temperatures	189
Figure 110:	^{242}Pu Production in the PWR for the Different Fuel Temperatures	190
Figure 111:	^{100}Mo Production in the PWR for the Different Fuel Temperatures	191
Figure 112:	^{91}Y Production in the PWR for the Different Fuel Temperatures	192
Figure 113:	^{149}Sm Production in the PWR for the Different Fuel Temperatures	193
Figure 114:	^{234}U Depletion in GE 8x8-4 BWR Model	213
Figure 115:	^{235}U Depletion in GE 8x8-4 BWR Model	213
Figure 116:	^{236}U Production in GE 8x8-4 BWR Model	214
Figure 117:	^{238}U Depletion in GE 8x8-4 BWR Model	214
Figure 118:	^{239}U Production in GE 8x8-4 BWR Model	215
Figure 119:	^{237}Np Production in GE 8x8-4 BWR Model	215
Figure 120:	^{238}Np Production in GE 8x8-4 BWR Model	216
Figure 121:	^{239}Np Production in GE 8x8-4 BWR Model	216
Figure 122:	^{238}Pu Production in GE 8x8-4 BWR Model	217
Figure 123:	^{239}Pu Production in GE 8x8-4 BWR Model	217
Figure 124:	^{240}Pu Production in GE 8x8-4 BWR Model	218
Figure 125:	^{241}Pu Production in GE 8x8-4 BWR Model	218
Figure 126:	^{242}Pu Production in GE 8x8-4 BWR Model	219
Figure 127:	^{241}Am Production in GE 8x8-4 BWR Model	219
Figure 128:	^{243}Am Production in GE 8x8-4 BWR Model	220
Figure 129:	^{242}Cm Production in GE 8x8-4 BWR Model	220
Figure 130:	^{245}Cm Production in GE 8x8-4 BWR Model	221
Figure 131:	^{246}Cm Production in GE 8x8-4 BWR Model	221

Figure 132: ^{97}Mo Production in GE 8x8-4 BWR Model.....	222
Figure 133: ^{98}Mo Production in GE 8x8-4 BWR Model.....	222
Figure 134: ^{100}Mo Production in GE 8x8-4 BWR Model.....	223
Figure 135: ^{138}Ba Production in GE 8x8-4 BWR Model.....	223
Figure 136: ^{140}Ce Production in GE 8x8-4 BWR Model.....	224
Figure 137: ^{142}Ce Production in GE 8x8-4 BWR Model.....	224
Figure 138: ^{148}Nd Production in GE 8x8-4 BWR Model	225
Figure 139: ^{72}Ge Production in GE 8x8-4 BWR Model.....	225
Figure 140: ^{90}Sr Production in GE 8x8-4 BWR Model.....	226
Figure 141: ^{91}Y Production in GE 8x8-4 BWR Model.....	226
Figure 142: ^{91}Zr Production in GE 8x8-4 BWR Model.....	227
Figure 143: ^{92}Zr Production in GE 8x8-4 BWR Model.....	227
Figure 144: ^{93}Zr Production in GE 8x8-4 BWR Model.....	228
Figure 145: ^{94}Zr Production in GE 8x8-4 BWR Model.....	228
Figure 146: ^{95}Zr Production in GE 8x8-4 BWR Model.....	229
Figure 147: ^{130}Te Production in GE 8x8-4 BWR Model.....	229
Figure 148: ^{131}I Production in GE 8x8-4 BWR Model.....	230
Figure 149: ^{135}I Production in GE 8x8-4 BWR Model.....	230
Figure 150: ^{131}Xe Production in GE 8x8-4 BWR Model	231
Figure 151: ^{132}Xe Production in GE 8x8-4 BWR Model	231
Figure 152: ^{134}Xe Production in GE 8x8-4 BWR Model	232
Figure 153: ^{135}Xe Production in GE 8x8-4 BWR Model	232
Figure 154: ^{136}Xe Production in GE 8x8-4 BWR Model	233

Figure 155: ^{134}Cs Production in GE 8x8-4 BWR Model.....	233
Figure 156: ^{137}Cs Production in GE 8x8-4 BWR Model.....	234
Figure 157: ^{139}La Production in GE 8x8-4 BWR Model.....	234
Figure 158: ^{149}Sm Production in GE 8x8-4 BWR Model.....	235
Figure 159: ^{161}Dy Production in GE 8x8-4 BWR Model	235
Figure 160: ^{234}U Depletion in W 17x17 PWR Model	237
Figure 161: ^{235}U Depletion in W 17x17 PWR Model	237
Figure 162: ^{236}U Production in W 17x17 PWR Model.....	238
Figure 163: ^{238}U Depletion in W 17x17 PWR Model	238
Figure 164: ^{239}U Production in W 17x17 PWR Model.....	239
Figure 165: ^{237}Np Production in W 17x17 PWR Model.....	239
Figure 166: ^{238}Np Production in W 17x17 PWR Model.....	240
Figure 167: ^{239}Np Production in W 17x17 PWR Model.....	240
Figure 168: ^{238}Pu Production in W 17x17 PWR Model	241
Figure 169: ^{239}Pu Production in W 17x17 PWR Model	241
Figure 170: ^{240}Pu Production in W 17x17 PWR Model	242
Figure 171: ^{241}Pu Production in W 17x17 PWR Model	242
Figure 172: ^{242}Pu Production in W 17x17 PWR Model	243
Figure 173: ^{241}Am Production in W 17x17 PWR Model	243
Figure 174: ^{243}Am Production in W 17x17 PWR Model	244
Figure 175: ^{242}Cm Production in W 17x17 PWR Model.....	244
Figure 176: ^{245}Cm Production in W 17x17 PWR Model.....	245
Figure 177: ^{246}Cm Production in W 17x17 PWR Model.....	245

Figure 178:	^{97}Mo Production in W 17x17 PWR Model	246
Figure 179:	^{98}Mo Production in W 17x17 PWR Model	246
Figure 180:	^{100}Mo Production in W 17x17 PWR Model.....	247
Figure 181:	^{138}Ba Production in W 17x17 PWR Model.....	247
Figure 182:	^{140}Ce Production in W 17x17 PWR Model.....	248
Figure 183:	^{142}Ce Production in W 17x17 PWR Model.....	248
Figure 184:	^{148}Nd Production in W 17x17 PWR Model.....	249
Figure 185:	^{72}Ge Production in W 17x17 PWR Model	249
Figure 186:	^{90}Sr Production in W 17x17 PWR Model	250
Figure 187:	^{91}Y Production in W 17x17 PWR Model.....	250
Figure 188:	^{91}Zr Production in W 17x17 PWR Model.....	251
Figure 189:	^{92}Zr Production in W 17x17 PWR Model.....	251
Figure 190:	^{93}Zr Production in W 17x17 PWR Model.....	252
Figure 191:	^{94}Zr Production in W 17x17 PWR Model.....	252
Figure 192:	^{95}Zr Production in W 17x17 PWR Model.....	253
Figure 193:	^{130}Te Production in W 17x17 PWR Model	253
Figure 194:	^{131}I Production in W 17x17 PWR Model	254
Figure 195:	^{135}I Production in W 17x17 PWR Model	254
Figure 196:	^{131}Xe Production in W 17x17 PWR Model.....	255
Figure 197:	^{132}Xe Production in W 17x17 PWR Model.....	255
Figure 198:	^{134}Xe Production in W 17x17 PWR Model.....	256
Figure 199:	^{135}Xe Production in W 17x17 PWR Model.....	256
Figure 200:	^{136}Xe Production in W 17x17 PWR Model.....	257

Figure 201: ^{134}Cs Production in W 17x17 PWR Model	257
Figure 202: ^{137}Cs Production in W 17x17 PWR Model	258
Figure 203: ^{139}La Production in W 17x17 PWR Model	258
Figure 204: ^{149}Sm Production in W 17x17 PWR Model	259
Figure 205: ^{161}Dy Production in W 17x17 PWR Model.....	259
Figure 206: ^{234}U Depletion in CANDU-37 Model	261
Figure 207: ^{235}U Depletion in CANDU-37 Model	261
Figure 208: ^{236}U Production in CANDU-37 Model	262
Figure 209: ^{238}U Depletion in CANDU-37 Model	262
Figure 210: ^{239}U Production in CANDU-37 Model	263
Figure 211: ^{237}Np Production in CANDU-37 Model	263
Figure 212: ^{238}Np Production in CANDU-37 Model	264
Figure 213: ^{239}Np Production in CANDU-37 Model	264
Figure 214: ^{238}Pu Production in CANDU-37 Model	265
Figure 215: ^{239}Pu Production in CANDU-37 Model	265
Figure 216: ^{240}Pu Production in CANDU-37 Model	266
Figure 217: ^{241}Pu Production in CANDU-37 Model	266
Figure 218: ^{242}Pu Production in CANDU-37 Model	267
Figure 219: ^{241}Am Production in CANDU-37 Model	267
Figure 220: ^{243}Am Production in CANDU-37 Model	268
Figure 221: ^{242}Cm Production in CANDU-37 Model.....	268
Figure 222: ^{245}Cm Production in CANDU-37 Model.....	269
Figure 223: ^{246}Cm Production in CANDU-37 Model.....	269

Figure 224: ^{97}Mo Production in CANDU-37 Model	270
Figure 225: ^{98}Mo Production in CANDU-37 Model	270
Figure 226: ^{100}Mo Production in CANDU-37 Model.....	271
Figure 227: ^{138}Ba Production in CANDU-37 Model.....	271
Figure 228: ^{140}Ce Production in CANDU-37 Model.....	272
Figure 229: ^{142}Ce Production in CANDU-37 Model.....	272
Figure 230: ^{148}Nd Production in CANDU-37 Model	273
Figure 231: ^{72}Ge Production in CANDU-37 Model.....	273
Figure 232: ^{90}Sr Production in CANDU-37 Model	274
Figure 233: ^{91}Y Production in CANDU-37 Model.....	274
Figure 234: ^{91}Zr Production in CANDU-37 Model.....	275
Figure 235: ^{92}Zr Production in CANDU-37 Model.....	275
Figure 236: ^{93}Zr Production in CANDU-37 Model.....	276
Figure 237: ^{94}Zr Production in CANDU-37 Model.....	276
Figure 238: ^{95}Zr Production in CANDU-37 Model.....	277
Figure 239: ^{130}Te Production in CANDU-37 Model	277
Figure 240: ^{131}I Production in CANDU-37 Model.....	278
Figure 241: ^{135}I Production in CANDU-37 Model.....	278
Figure 242: ^{131}Xe Production in CANDU-37 Model.....	279
Figure 243: ^{132}Xe Production in CANDU-37 Model.....	279
Figure 244: ^{134}Xe Production in CANDU-37 Model.....	280
Figure 245: ^{135}Xe Production in CANDU-37 Model.....	280
Figure 246: ^{136}Xe Production in CANDU-37 Model.....	281

Figure 247:	^{134}Cs Production in CANDU-37 Model	281
Figure 248:	^{137}Cs Production in CANDU-37 Model	282
Figure 249:	^{139}La Production in CANDU-37 Model	282
Figure 250:	^{149}Sm Production in CANDU-37 Model	283
Figure 251:	^{161}Dy Production in CANDU-37 Model	283
Figure 252:	^{234}U Depletion in the PWR Model for Different Rod Pitch Values	286
Figure 253:	^{235}U Depletion in the PWR Model for Different Rod Pitch Values	286
Figure 254:	^{236}U Production in the PWR Model for Different Rod Pitch Values	287
Figure 255:	^{238}U Depletion in the PWR Model for Different Rod Pitch Values	287
Figure 256:	^{239}U Production in the PWR Model for Different Rod Pitch Values	288
Figure 257:	^{237}Np Production in the PWR Model for Different Rod Pitch Values	288
Figure 258:	^{238}Np Production in the PWR Model for Different Rod Pitch Values	289
Figure 259:	^{239}Np Production in the PWR Model for Different Rod Pitch Values	289
Figure 260:	^{238}Pu Production in the PWR Model for Different Rod Pitch Values	290
Figure 261:	^{239}Pu Production in the PWR Model for Different Rod Pitch Values	290
Figure 262:	^{240}Pu Production in the PWR Model for Different Rod Pitch Values	291
Figure 263:	^{241}Pu Production in the PWR Model for Different Rod Pitch Values	291
Figure 264:	^{242}Pu Production in the PWR Model for Different Rod Pitch Values	292
Figure 265:	^{241}Am Production in the PWR Model for Different Rod Pitch Values	292
Figure 266:	^{243}Am Production in the PWR Model for Different Rod Pitch Values	293
Figure 267:	^{242}Cm Production in the PWR Model for Different Rod Pitch Values	293
Figure 268:	^{245}Cm Production in the PWR Model for Different Rod Pitch Values	294
Figure 269:	^{246}Cm Production in the PWR Model for Different Rod Pitch Values	294

Figure 270:	^{97}Mo Production in the PWR Model for Different Rod Pitch Values.....	295
Figure 271:	^{98}Mo Production in the PWR Model for Different Rod Pitch Values.....	295
Figure 272:	^{100}Mo Production in the PWR Model for Different Rod Pitch Values	296
Figure 273:	^{138}Ba Production in the PWR Model for Different Rod Pitch Values.....	296
Figure 274:	^{140}Ce Production in the PWR Model for Different Rod Pitch Values.....	297
Figure 275:	^{142}Ce Production in the PWR Model for Different Rod Pitch Values.....	297
Figure 276:	^{148}Nd Production in the PWR Model for Different Rod Pitch Values	298
Figure 277:	^{72}Ge Production in the PWR Model for Different Rod Pitch Values.....	298
Figure 278:	^{90}Sr Production in the PWR Model for Different Rod Pitch Values.....	299
Figure 279:	^{91}Y Production in the PWR Model for Different Rod Pitch Values	299
Figure 280:	^{91}Zr Production in the PWR Model for Different Rod Pitch Values.....	300
Figure 281:	^{92}Zr Production in the PWR Model for Different Rod Pitch Values.....	300
Figure 282:	^{93}Zr Production in the PWR Model for Different Rod Pitch Values.....	301
Figure 283:	^{94}Zr Production in the PWR Model for Different Rod Pitch Values.....	301
Figure 284:	^{95}Zr Production in the PWR Model for Different Rod Pitch Values.....	302
Figure 285:	^{130}Te Production in the PWR Model for Different Rod Pitch Values.....	302
Figure 286:	^{131}I Production in the PWR Model for Different Rod Pitch Values.....	303
Figure 287:	^{135}I Production in the PWR Model for Different Rod Pitch Values.....	303
Figure 288:	^{131}Xe Production in the PWR Model for Different Rod Pitch Values	304
Figure 289:	^{132}Xe Production in the PWR Model for Different Rod Pitch Values	304
Figure 290:	^{134}Xe Production in the PWR Model for Different Rod Pitch Values	305
Figure 291:	^{135}Xe Production in the PWR Model for Different Rod Pitch Values	305
Figure 292:	^{136}Xe Production in the PWR Model for Different Rod Pitch Values	306

Figure 293:	^{137}Cs Production in the PWR Model for Different Rod Pitch Values.....	306
Figure 294:	^{137}Cs Production in the PWR Model for Different Rod Pitch Values.....	307
Figure 295:	^{139}La Production in the PWR Model for Different Rod Pitch Values.....	307
Figure 296:	^{150}Sm Production in the PWR Model for Different Rod Pitch Values.....	308
Figure 297:	^{161}Dy Production in the PWR Model for Different Rod Pitch Values	308
Figure 298:	^{234}U Depletion in the PWR Model for Different Boron Concentrations.....	310
Figure 299:	^{235}U Depletion in the PWR Model for Different Boron Concentrations.....	310
Figure 300:	^{236}U Production in the PWR Model for Different Boron Concentrations...	311
Figure 301:	^{238}U Depletion in the PWR Model for Different Boron Concentrations.....	311
Figure 302:	^{239}U Production in the PWR Model for Different Boron Concentrations...	312
Figure 303:	^{237}Np Production in the PWR Model for Different Boron Concentrations..	312
Figure 304:	^{238}Np Production in the PWR Model for Different Boron Concentrations..	313
Figure 305:	^{239}Np Production in the PWR Model for Different Boron Concentrations..	313
Figure 306:	^{238}Pu Production in the PWR Model for Different Boron Concentrations..	314
Figure 307:	^{239}Pu Production in the PWR Model for Different Boron Concentrations..	314
Figure 308:	^{240}Pu Production in the PWR Model for Different Boron Concentrations..	315
Figure 309:	^{241}Pu Production in the PWR Model for Different Boron Concentrations..	315
Figure 310:	^{242}Pu Production in the PWR Model for Different Boron Concentrations..	316
Figure 311:	^{241}Am Production in the PWR Model for Different Boron Concentrations	316
Figure 312:	^{243}Am Production in the PWR Model for Different Boron Concentrations	317
Figure 313:	^{242}Cm Production in the PWR Model for Different Boron Concentrations	317
Figure 314:	^{245}Cm Production in the PWR Model for Different Boron Concentrations	318
Figure 315:	^{246}Cm Production in the PWR Model for Different Boron Concentrations	318

Figure 316:	^{97}Mo Production in the PWR Model for Different Boron Concentrations..	319
Figure 317:	^{98}Mo Production in the PWR Model for Different Boron Concentrations..	319
Figure 318:	^{100}Mo Production in the PWR Model for Different Boron Concentrations	320
Figure 319:	^{138}Ba Production in the PWR Model for Different Boron Concentrations .	320
Figure 320:	^{140}Ce Production in the PWR Model for Different Boron Concentrations .	321
Figure 321:	^{142}Ce Production in the PWR Model for Different Boron Concentrations .	321
Figure 322:	^{148}Nd Production in the PWR Model for Different Boron Concentrations .	322
Figure 323:	^{72}Ge Production in the PWR Model for Different Boron Concentrations ..	322
Figure 324:	^{90}Sr Production in the PWR Model for Different Boron Concentrations....	323
Figure 325:	^{91}Y Production in the PWR Model for Different Boron Concentrations	323
Figure 326:	^{91}Zr Production in the PWR Model for Different Boron Concentrations ...	324
Figure 327:	^{92}Zr Production in the PWR Model for Different Boron Concentrations ...	324
Figure 328:	^{93}Zr Production in the PWR Model for Different Boron Concentrations ...	325
Figure 329:	^{94}Zr Production in the PWR Model for Different Boron Concentrations ...	325
Figure 330:	^{95}Zr Production in the PWR Model for Different Boron Concentrations ...	326
Figure 331:	^{130}Te Production in the PWR Model for Different Boron Concentrations..	326
Figure 332:	^{131}I Production in the PWR Model for Different Boron Concentrations	327
Figure 333:	^{135}I Production in the PWR Model for Different Boron Concentrations	327
Figure 334:	^{131}Xe Production in the PWR Model for Different Boron Concentrations .	328
Figure 335:	^{132}Xe Production in the PWR Model for Different Boron Concentrations .	328
Figure 336:	^{134}Xe Production in the PWR Model for Different Boron Concentrations .	329
Figure 337:	^{135}Xe Production in the PWR Model for Different Boron Concentrations .	329
Figure 338:	^{135}Xe Production in the PWR Model for Different Boron Concentrations .	330

Figure 339:	^{134}Cs Production in the PWR Model for Different Boron Concentrations..	330
Figure 340:	^{137}Cs Production in the PWR Model for Different Boron Concentrations..	331
Figure 341:	^{139}La Production in the PWR Model for Different Boron Concentrations..	331
Figure 342:	^{149}Sm Production in the PWR Model for Different Boron Concentrations	332
Figure 343:	^{161}Dy Production in the PWR Model for Different Boron Concentrations.	332
Figure 344:	^{234}U Depletion in the PWR Model for Different Cladding Thicknesses.....	334
Figure 345:	^{235}U Depletion in the PWR Model for Different Cladding Thicknesses.....	334
Figure 346:	^{236}U Production in the PWR Model for Different Cladding Thicknesses ...	335
Figure 347:	^{2386}U Depletion in the PWR Model for Different Cladding Thicknesses ...	335
Figure 348:	^{239}U Production in the PWR Model for Different Cladding Thicknesses ...	336
Figure 349:	^{237}Np Production in the PWR Model for Different Cladding Thicknesses.	336
Figure 350:	^{236}U Production in the PWR Model for Different Cladding Thicknesses ...	337
Figure 351:	^{236}U Production in the PWR Model for Different Cladding Thicknesses ...	337
Figure 352:	^{238}Pu Production in the PWR Model for Different Cladding Thicknesses .	338
Figure 353:	^{239}Pu Production in the PWR Model for Different Cladding Thicknesses .	338
Figure 354:	^{240}Pu Production in the PWR Model for Different Cladding Thicknesses .	339
Figure 355:	^{241}Pu Production in the PWR Model for Different Cladding Thicknesses .	339
Figure 356:	^{242}Pu Production in the PWR Model for Different Cladding Thicknesses .	340
Figure 357:	^{241}Am Production in the PWR Model for Different Cladding Thicknesses	340
Figure 358:	^{243}Am Production in the PWR Model for Different Cladding Thicknesses	341
Figure 359:	^{242}Cm Production in the PWR Model for Different Cladding Thicknesses	341
Figure 360:	^{245}Cm Production in the PWR Model for Different Cladding Thicknesses	342
Figure 361:	^{246}Cm Production in the PWR Model for Different Cladding Thicknesses	342

Figure 362:	^{97}Mo Production in the PWR Model for Different Cladding Thicknesses .	343
Figure 363:	^{98}Mo Production in the PWR Model for Different Cladding Thicknesses .	343
Figure 364:	^{100}Mo Production in the PWR Model for Different Cladding Thicknesses	344
Figure 365:	^{138}Ba Production in the PWR Model for Different Cladding Thicknesses .	344
Figure 366:	^{140}Ce Production in the PWR Model for Different Cladding Thicknesses .	345
Figure 367:	^{142}Ce Production in the PWR Model for Different Cladding Thicknesses .	345
Figure 368:	^{148}Nd Production in the PWR Model for Different Cladding Thicknesses.	346
Figure 369:	^{72}Ge Production in the PWR Model for Different Cladding Thicknesses ..	346
Figure 370:	^{90}Sr Production in the PWR Model for Different Cladding Thicknesses....	347
Figure 371:	^{91}Y Production in the PWR Model for Different Cladding Thicknesses	347
Figure 372:	^{91}Zr Production in the PWR Model for Different Cladding Thicknesses ...	348
Figure 373:	^{92}Zr Production in the PWR Model for Different Cladding Thicknesses ...	348
Figure 374:	^{92}Zr Production in the PWR Model for Different Cladding Thicknesses ...	349
Figure 375:	^{94}Zr Production in the PWR Model for Different Cladding Thicknesses ...	349
Figure 376:	^{95}Zr Production in the PWR Model for Different Cladding Thicknesses ...	350
Figure 377:	^{130}Te Production in the PWR Model for Different Cladding Thicknesses .	350
Figure 378:	^{131}I Production in the PWR Model for Different Cladding Thicknesses	351
Figure 379:	^{135}I Production in the PWR Model for Different Cladding Thicknesses	351
Figure 380:	^{131}Xe Production in the PWR Model for Different Cladding Thicknesses .	352
Figure 381:	^{132}Xe Production in the PWR Model for Different Cladding Thicknesses .	352
Figure 382:	^{134}Xe Production in the PWR Model for Different Cladding Thicknesses .	353
Figure 383:	^{135}Xe Production in the PWR Model for Different Cladding Thicknesses .	353
Figure 384:	^{136}Xe Production in the PWR Model for Different Cladding Thicknesses .	354

Figure 385:	^{134}Cs Production in the PWR Model for Different Cladding Thicknesses .	354
Figure 386:	^{137}Cs Production in the PWR Model for Different Cladding Thicknesses .	355
Figure 387:	^{139}La Production in the PWR Model for Different Cladding Thicknesses .	355
Figure 388:	^{149}Sm Production in the PWR Model for Different Cladding Thicknesses	356
Figure 389:	^{161}Dy Production in the PWR Model for Different Cladding Thicknesses.	356
Figure 390:	^{234}U Depletion in the PWR Model for Different Water Densities	358
Figure 391:	^{235}U Depletion in the PWR Model for Different Water Densities	358
Figure 392:	^{236}U Production in the PWR Model for Different Water Densities	359
Figure 393:	^{238}U Depletion in the PWR Model for Different Water Densities	359
Figure 394:	^{239}U Production in the PWR Model for Different Water Densities	360
Figure 395:	^{237}Np Production in the PWR Model for Different Water Densities	360
Figure 396:	^{238}Np Production in the PWR Model for Different Water Densities	361
Figure 397:	^{239}Np Production in the PWR Model for Different Water Densities	361
Figure 398:	^{238}Pu Production in the PWR Model for Different Water Densities	362
Figure 399:	^{239}Pu Production in the PWR Model for Different Water Densities	362
Figure 400:	^{240}Pu Production in the PWR Model for Different Water Densities	363
Figure 401:	^{241}Pu Production in the PWR Model for Different Water Densities	363
Figure 402:	^{242}Pu Production in the PWR Model for Different Water Densities	364
Figure 403:	^{241}Am Production in the PWR Model for Different Water Densities	364
Figure 404:	^{243}Am Production in the PWR Model for Different Water Densities	365
Figure 405:	^{242}Cm Production in the PWR Model for Different Water Densities.....	365
Figure 406:	^{245}Cm Production in the PWR Model for Different Water Densities.....	366
Figure 407:	^{246}Cm Production in the PWR Model for Different Water Densities.....	366

Figure 408:	^{97}Mo Production in the PWR Model for Different Water Densities	367
Figure 409:	^{98}Mo Production in the PWR Model for Different Water Densities	367
Figure 410:	^{100}Mo Production in the PWR Model for Different Water Densities.....	368
Figure 411:	^{138}Ba Production in the PWR Model for Different Water Densities.....	368
Figure 412:	^{140}Ce Production in the PWR Model for Different Water Densities.....	369
Figure 413:	^{142}Ce Production in the PWR Model for Different Water Densities.....	369
Figure 414:	^{148}Nd Production in the PWR Model for Different Water Densities	370
Figure 415:	^{72}Ge Production in the PWR Model for Different Water Densities	370
Figure 416:	^{90}Sr Production in the PWR Model for Different Water Densities	371
Figure 417:	^{91}Y Production in the PWR Model for Different Water Densities.....	371
Figure 418:	^{91}Zr Production in the PWR Model for Different Water Densities.....	372
Figure 419:	^{92}Zr Production in the PWR Model for Different Water Densities.....	372
Figure 420:	^{93}Zr Production in the PWR Model for Different Water Densities.....	373
Figure 421:	^{94}Zr Production in the PWR Model for Different Water Densities.....	373
Figure 422:	^{95}Zr Production in the PWR Model for Different Water Densities.....	374
Figure 423:	^{130}Te Production in the PWR Model for Different Water Densities	374
Figure 424:	^{131}I Production in the PWR Model for Different Water Densities	375
Figure 425:	^{135}I Production in the PWR Model for Different Water Densities	375
Figure 426:	^{131}Xe Production in the PWR Model for Different Water Densities.....	376
Figure 427:	^{132}Xe Production in the PWR Model for Different Water Densities.....	376
Figure 428:	^{134}Xe Production in the PWR Model for Different Water Densities.....	377
Figure 429:	^{135}Xe Production in the PWR Model for Different Water Densities.....	377
Figure 430:	^{136}Xe Production in the PWR Model for Different Water Densities.....	378

Figure 431:	^{134}Cs Production in the PWR Model for Different Water Densities	378
Figure 432:	^{137}Cs Production in the PWR Model for Different Water Densities	379
Figure 433:	^{139}La Production in the PWR Model for Different Water Densities	379
Figure 434:	^{149}Sm Production in the PWR Model for Different Water Densities	380
Figure 435:	^{161}Dy Production in the PWR Model for Different Water Densities	380
Figure 436:	^{234}U Depletion in the PWR Model for Different Fuel Temperatures	382
Figure 437:	^{235}U Depletion in the PWR Model for Different Fuel Temperatures	382
Figure 438:	^{236}U Production in the PWR Model for Different Fuel Temperatures	383
Figure 439:	^{238}U Depletion in the PWR Model for Different Fuel Temperatures	383
Figure 440:	^{239}U Production in the PWR Model for Different Fuel Temperatures	384
Figure 441:	^{237}Np Production in the PWR Model for Different Fuel Temperatures	384
Figure 442:	^{238}Np Production in the PWR Model for Different Fuel Temperatures	385
Figure 443:	^{239}Np Production in the PWR Model for Different Fuel Temperatures	385
Figure 444:	^{238}Pu Production in the PWR Model for Different Fuel Temperatures	386
Figure 445:	^{239}Pu Production in the PWR Model for Different Fuel Temperatures	386
Figure 446:	^{240}Pu Production in the PWR Model for Different Fuel Temperatures	387
Figure 447:	^{241}Pu Production in the PWR Model for Different Fuel Temperatures	387
Figure 448:	^{242}Pu Production in the PWR Model for Different Fuel Temperatures	388
Figure 449:	^{241}Am Production in the PWR Model for Different Fuel Temperatures	388
Figure 450:	^{243}Am Production in the PWR Model for Different Fuel Temperatures	389
Figure 451:	^{242}Cm Production in the PWR Model for Different Fuel Temperatures	389
Figure 452:	^{245}Cm Production in the PWR Model for Different Fuel Temperatures	390
Figure 453:	^{246}Cm Production in the PWR Model for Different Fuel Temperatures	390

Figure 454:	^{97}Mo Production in the PWR Model for Different Fuel Temperatures.....	391
Figure 455:	^{98}Mo Production in the PWR Model for Different Fuel Temperatures.....	391
Figure 456:	^{100}Mo Production in the PWR Model for Different Fuel Temperatures	392
Figure 457:	^{138}Ba Production in the PWR Model for Different Fuel Temperatures	392
Figure 458:	^{140}Ce Production in the PWR Model for Different Fuel Temperatures	393
Figure 459:	^{142}Ce Production in the PWR Model for Different Fuel Temperatures	393
Figure 460:	^{148}Nd Production in the PWR Model for Different Fuel Temperatures	394
Figure 461:	^{72}Ge Production in the PWR Model for Different Fuel Temperatures.....	394
Figure 462:	^{90}Sr Production in the PWR Model for Different Fuel Temperatures.....	395
Figure 463:	^{91}Y Production in the PWR Model for Different Fuel Temperatures	395
Figure 464:	^{91}Zr Production in the PWR Model for Different Fuel Temperatures	396
Figure 465:	^{92}Zr Production in the PWR Model for Different Fuel Temperatures	396
Figure 466:	^{93}Zr Production in the PWR Model for Different Fuel Temperatures	397
Figure 467:	^{94}Zr Production in the PWR Model for Different Fuel Temperatures	397
Figure 468:	^{95}Zr Production in the PWR Model for Different Fuel Temperatures	398
Figure 469:	^{130}Te Production in the PWR Model for Different Fuel Temperatures.....	398
Figure 470:	^{131}I Production in the PWR Model for Different Fuel Temperatures.....	399
Figure 471:	^{131}I Production in the PWR Model for Different Fuel Temperatures.....	399
Figure 472:	^{131}Xe Production in the PWR Model for Different Fuel Temperatures	400
Figure 473:	^{132}Xe Production in the PWR Model for Different Fuel Temperatures	400
Figure 474:	^{134}Xe Production in the PWR Model for Different Fuel Temperatures	401
Figure 475:	^{135}Xe Production in the PWR Model for Different Fuel Temperatures	401
Figure 476:	^{136}Xe Production in the PWR Model for Different Fuel Temperatures	402

Figure 477: ^{137}Cs Production in the PWR Model for Different Fuel Temperatures.....	402
Figure 478: ^{137}Cs Production in the PWR Model for Different Fuel Temperatures.....	403
Figure 479: ^{139}La Production in the PWR Model for Different Fuel Temperatures.....	403
Figure 480: ^{149}Sm Production in the PWR Model for Different Fuel Temperatures.....	404
Figure 481: ^{161}Dy Production in the PWR Model for Different Fuel Temperatures	404

Chapter 1: Introduction

1.1 BACKGROUND INFORMATION

Commercial U.S. reactors use UO_2 , slightly enriched in the ^{235}U isotope, as the nuclear fuel in the core. Commercial reactors outside the U.S. use a variety of different fuels including UO_2 (*e.g.* Boiling Water Reactors (BWRs) and Pressurized Water Reactors (PWRs)), uranium metal (*e.g.* Magnesium Non-oxidizing Reactors (MAGNOX)), and mixed-oxide (MOX) (*e.g.* Liquid Metal Fast Breeder Reactors (LMFBRs), MOX BWRs, MOX PWRs) which is a combination of UO_2 and PuO_2 . The chemical composition of fresh, un-irradiated UO_2 fuel is typically uranium and oxygen with only trace amounts of other elements. The composition of fresh, un-irradiated MOX fuel includes plutonium, uranium, oxygen, and americium from plutonium decay.

Fuel that has been irradiated in a nuclear reactor may easily be distinguished from fresh fuel by the depletion of the original fissile material and by the great number of additional nuclides that are produced during the irradiation period. These additional nuclides result from a variety of nuclear processes occurring within the reactor. The three dominant processes are 1) the neutron-induced fission process, 2) the neutron absorption process, and 3) the radioactive decay process.

Two key reactor attributes account for radionuclide production and depletion in a reactor: initial core composition and the total reactor neutron flux that the material is exposed to. The flux of a reactor is dependent on a vast number of variables and is time-dependent as well as energy dependent.

Factors that affect the total reactor neutron flux that the reactor fuel is exposed to include:

1. Initial fuel make-up: uranium isotopic enrichment, presence/absence of Pu (*e.g.* MOX), presence of other fissile or fertile nuclides (*e.g.* ^{233}U , ^{232}Th)
2. Fuel Burnup: power of reactor, fuel dwell time in reactor
3. Moderator composition
4. Moderator density
5. Reactor operating temperature

There are several computer codes available to calculate nuclide generation and depletion. One such code is the Oak Ridge National Laboratory's (ORNL's) Standardized Computer Analyses for Licensing Evaluation (SCALE). This code package includes the Oak Ridge Isotope Generation and Depletion (ORIGEN) sequence. ORIGEN has a set of libraries for various reactor types that account for the changes in neutron flux based upon the above parameters.

The Oak Ridge Isotope Generation and Depletion – Automatic Rapid Processing (ORIGEN-ARP) deterministic code has been extensively utilized for determining nuclide concentrations at various specific burnup values for a variety of nuclear reactor designs.^{1,3,4,8} Given nuclide concentrations or ratios, such calculations can be used in nuclear forensics and nuclear non-proliferation applications to reverse-calculate the type of reactor and specific burnup of the fuel from which the nuclides originated.

Recently, Los Alamos National Laboratory has released a version of its probabilistic radiation transport code, MCNPX 2.6.0, which incorporates a fuel burnup feature which can also determine, via the probabilistic Monte Carlo method, nuclide concentrations as a function of fuel burnup.⁵

This dissertation compares the concentrations of 46 nuclides significant to nuclear forensics analyses for different reactor types using results from the ORIGEN-ARP and the MCNPX 2.6.0 codes. Three reactor types were chosen: the Westinghouse 17x17 Pressurized Water Reactor (PWR), the GE 8x8-4 Boiling Water Reactor (BWR), and the Canadian Deuterium Uranium, CANDU-37, reactor.

Additionally, a sensitivity study of the different reactor parameters within the MCNPX Westinghouse 17x17 PWR model was performed. This study analyzed the different nuclide concentrations resulting from minor perturbations of the following parameters: assembly rod pitch, initial moderator boron concentration, fuel pin cladding thickness, moderator density, and fuel temperature.

1.2 THE USE OF REACTOR TRANSMUTATED SPECIES AS NUCLEAR FORENSIC INDICATORS

Nuclear forensics analysis may be used to determine the origin of nuclear or radiological materials. Knowledge obtained from such analysis may lead to the identities of the perpetrators of a terrorist attack, lead to the origin of smuggled special nuclear materials, or indicate that commercial nuclear power plants are being used for nuclear proliferation purposes.

In some instances, nuclear forensic analysts are faced with the burden of characterizing a sample of nuclear fuel from an unknown reactor type of unknown initial fuel enrichment, of unknown irradiation time, and of unknown reactor power profile. In the event of a terrorist act releasing radioactive materials, such as a radiological dispersal device (RDD), the investigation to determine the perpetrators of the act would begin immediately by collecting residual radiological evidence. An RDD using spent nuclear

fuel would most likely be the worst case scenario for an RDD event and could potentially expose a large population to very high radiation doses; therefore, real-time analysis and results typical to what may be obtained from an ORIGEN-ARP calculation could be decidedly useful to emergency responders and investigators attempting to characterize and respond to the event.

One method for determining the origin of spent nuclear fuel is to determine the quantities of a number of nuclides found in the fuel and compare the ratios of those nuclides to the same nuclide ratios from known reactors. One of the main characteristics that can affect nuclide ratios is reactor type. Other factors that also have significant effect on nuclide ratios are those parameters listed above in Section 1.1.

While there is a finite number of reactor types in the world, and it is not outside the realm of possibility that a nuclide analysis could be completed on fuel assemblies from each reactor type, the data derived from such analysis would only give results for the fuel assemblies analyzed and the specific power profile that it underwent. The number of permutations of different power profiles, fuel enrichments, burnup times, as well as other design and operating parameters, can be limitless. For example, the nuclide ratios for a BWR using 3% enriched uranium fuel can vary drastically from the results obtained by using MOX fuel in that same BWR reactor.

Computational code calculations can be completed to perform forward calculations of the various reactor design and operating parameters to determine nuclide quantities in order to fill in the gaps left by the empirical data obtained from actual spent nuclear fuel samples.

In the past, nuclear forensics has relied primarily on the nuclides found in high concentrations of spent nuclear fuel such as uranium and plutonium isotopes. These isotopes can be quantified through measurements made by radiation detection instrumentation. Advances in mass spectrometry have resulted in nuclides found even in the minute quantities being able to be detected and accurately quantified.³ This, in turn, has greatly increased the number of nuclides which can be used for nuclear forensics purposes. Ideally, each reactor would produce a different set of nuclide quantities for the different operational parameters that it might experience.

For the purposes of nuclear forensic analysis, it is preferred to limit the number of variables to apply to a system for analysis. Additionally, trying to unfold the many permutations of potential power profiles is a daunting task. For these reasons, nuclear forensic analysts desire to choose nuclides which are not dependent (or only mildly dependent) on reactor power.

For example, in the field of non-proliferation, the burn-up for a particular fuel is often a key indicator for determining whether weapons grade plutonium was produced. Assuming that the plutonium is unavailable for direct inspection because it was extracted from the fuel for reprocessing or for more “nefarious” proliferation purposes, the nuclear forensic analyst must determine the burn-up of the fuel from other nuclide burn-up indicators. Assuming the reactor power profile is unknown or subject to question, the analyst will desire to use nuclides which provide a unique burn-up signature. In order to provide a unique burn-up signature, the production quantity of a particular nuclide should not vary significantly with reactor power. Figure 1 shows the results from an ORIGEN

calculation to determine the quantity of ^{241}Am produced in a MAGNOX reactor as a function of fuel burn-up for three different reactor powers.

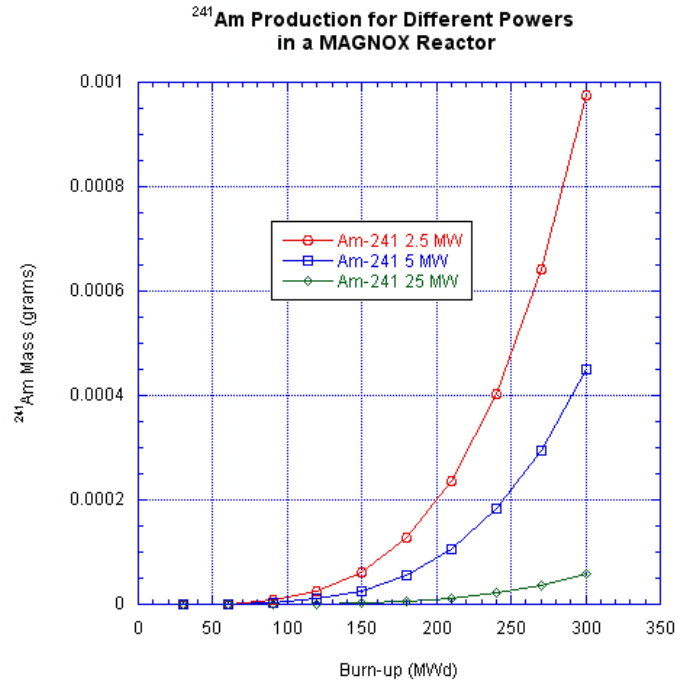


Figure 1: ORIGEN Calculation of ^{241}Am Production in a MAGNOX Reactor

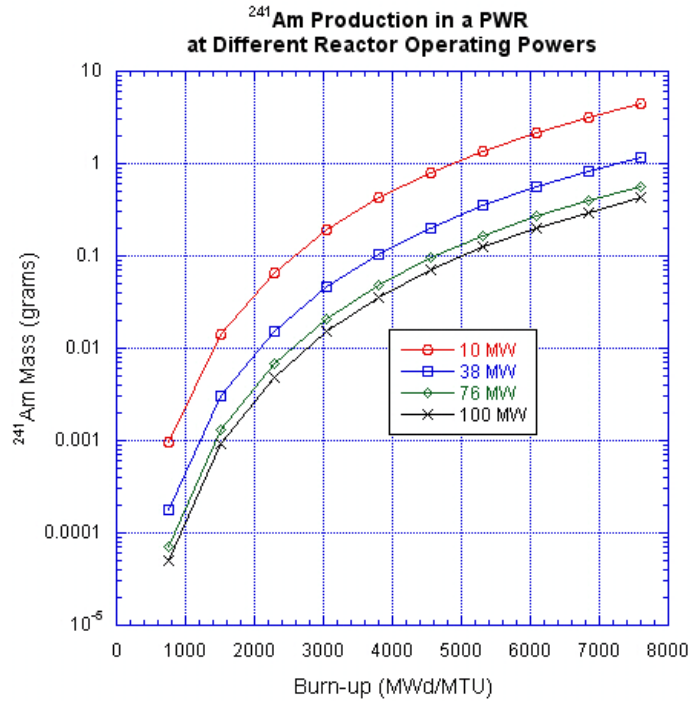


Figure 2: ²⁴¹Am Production in a PWR

Figure 2 is a plot of ²⁴¹Am build-up in a PWR at different reactor operating powers. The mass of ²⁴¹Am, as a function of fuel burn-up, varies significantly at different reactor operating powers. In this case, a specific ²⁴¹Am concentration or nuclide ratio does not lead to a unique burn-up value. Moody, *et al.*, (2005) describes this phenomenon by explaining that ²⁴¹Am primarily originates from the decay of ²⁴¹Pu ($T_{1/2}=14.4$ years). For a specific fuel burn-up, short irradiation periods (at higher powers) result in less accumulated ²⁴¹Am from ²⁴¹Pu decay than in long irradiation periods (at lower powers). Note that two different ²⁴¹Am quantities, for a single reactor design, can track back to the same burn-up value. For this reason, ²⁴¹Am and its subsequently produced nuclides (*e.g.* ^{242m}Am and ²⁴²Cm) make poor burn-up indicators assuming that the reactor operating power is not known.

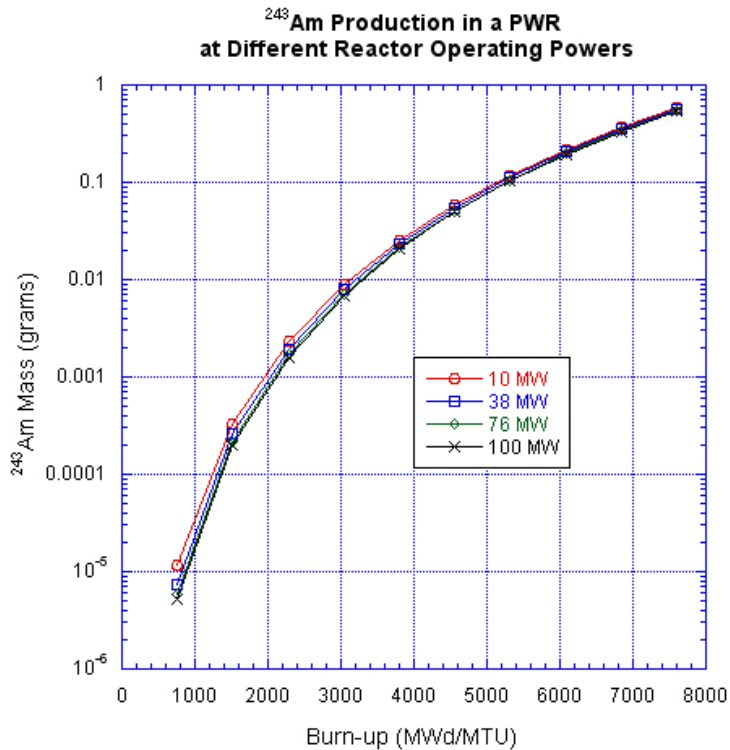


Figure 3: ^{243}Am Production as a Function of Burn-up at Different Reactor Powers

Figure 3 shows that ^{243}Am production, unlike ^{241}Am production, is largely independent of reactor power. This independence arises from the fact that ^{243}Am is produced from the decay of ^{243}Pu which has a half-life of approximately 5 hours, which is much shorter than the 14.4 year half-life of ^{241}Pu .

Mark R. Scott² presents the following nuclides as potential indicators to be used in determining burn-up of various reactor fuels: ^{138}Ba , ^{140}Ce , ^{142}Cd , ^{100}Mo , ^{97}Mo , ^{98}Mo , and ^{148}Nd .

Figure 4 below shows that the production of these nuclides in a PWR for a specific burn-up is constant with various reactor powers, with one exception: ^{140}Ce . As

can be seen in the figure, ^{140}Ce production is significantly less at higher reactor powers than it is for lower reactor powers at the same burn-up value.

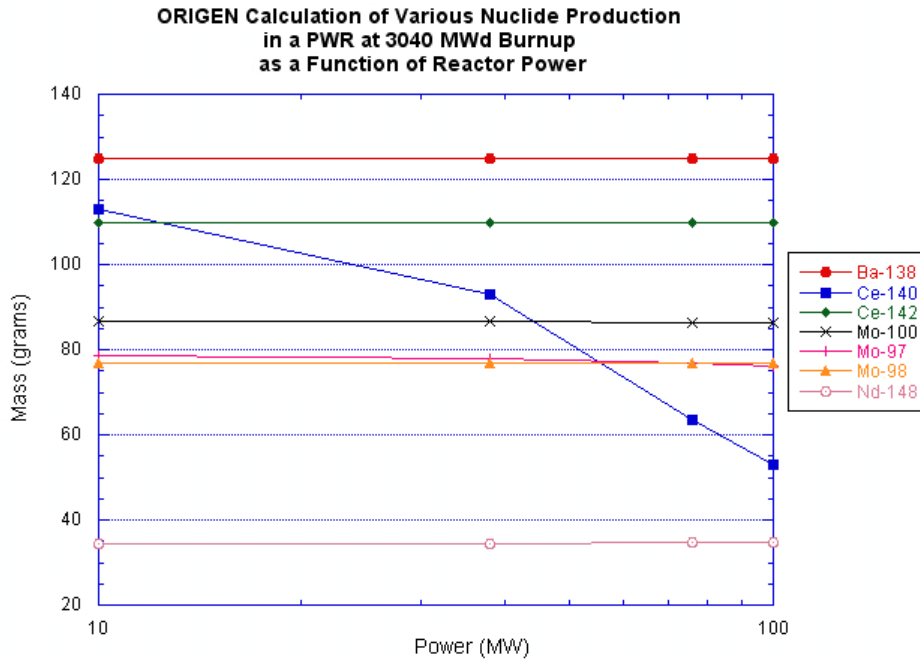


Figure 4: Power Dependence of the Burn-up Monitors Suggested in Scott (2005)²

Plotting nuclide production as a function of fuel burn-up for different powers (Figure 5) reveals that for a specific ^{140}Ce nuclide production value, there exists more than one possible value for the burn-up of the fuel. Plots of the other nuclides show that nuclide production as a function of burn-up is independent of reactor power. This independence indicates that these nuclides have a unique concentration for each burn-up value, and hence (added to the fact that they are stable nuclides) lend themselves well to be used as burn-up indicators even years after the fuel has been removed from the reactor.

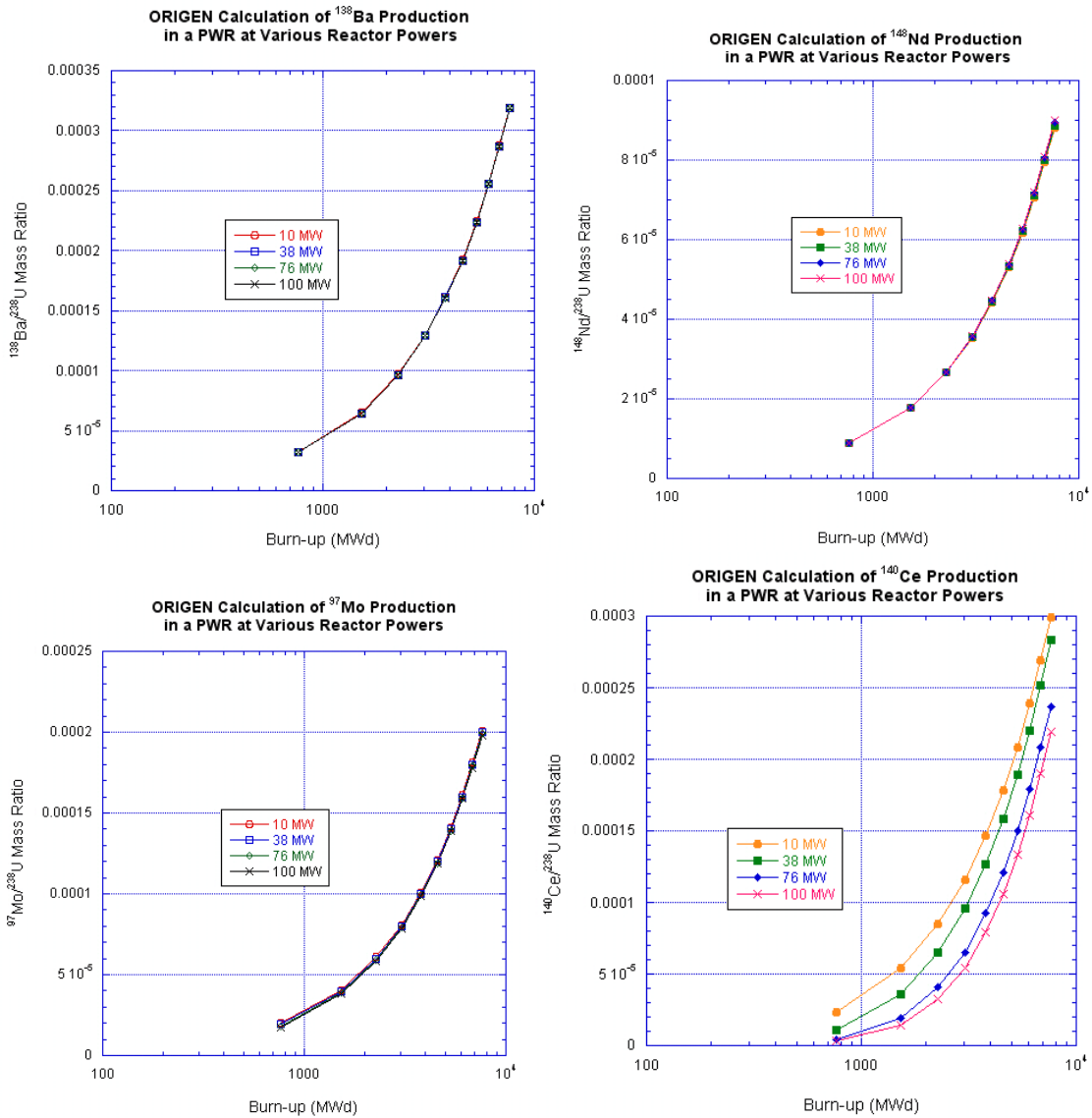


Figure 5: ORIGEN-ARP Production Calculation for Four Different Fission Products

Figure 5 is an ORIGEN calculation of the production of four different fission products as a function of fuel burn-up and reactor power. Notice that ¹⁴⁰Ce has more than one potential burn-up value for a specific ¹⁴⁰Ce production value.

Physically, this phenomenon may be explained by the fact that for a specific burn-up at high power and short irradiation time, there is less ^{140}Ce produced than for a low power long irradiation time resulting in the same fuel burn-up. This fact, in turn, can be explained by understanding how ^{140}Ce is produced in a reactor. ^{140}Ce is produced primarily via fission product production and by beta-minus decay of the fission product ^{140}La ($T_{1/2}=1.68$ days). ^{140}La is also produced by beta-minus decay of the fission product ^{140}Ba ($T_{1/2}=12.75$ days). In high power, short irradiation-time burn-ups, much of the ^{140}La and ^{140}Ba produced via fission has not had enough time to decay into stable ^{140}Ce . Therefore, similar to the ^{241}Am case described above, for short irradiation periods, there is less ^{140}Ce accumulation from radioactive decay than for longer irradiation periods. However, after approximately ten ^{140}Ba half-lives, the quantities of ^{140}Ce begin to merge for the four different powers.

1.3 THEORY AND MATHEMATICS

1.3.1 Why Do We Measure Burnup?

The goal of nuclear proliferators is the production of fissile material for use in a nuclear explosive. ^{233}U , ^{235}U , and ^{239}Pu all readily fission after thermal neutron absorption and are thus categorized as fissile material. ^{235}U is found in naturally occurring uranium with an abundance of 0.711 weight percent. In order to attain weapons grade weight percentages ($>20\%$ $^{235}\text{U}^1$), uranium must undergo an enrichment process. Enrichment processes consume great quantities of electricity and require massive facilities which are difficult to conceal from regulatory inspections if the proliferators intend to remain covert. ^{233}U is not found in significant quantities in nature

and must be produced in a reactor from fertile ^{232}Th . Though a feasible option, past fuel cycles have rarely used ^{233}U due to the readily available fertile ^{238}U and the fact that the ^{238}U to ^{239}Pu conversion process technology and methods have been in existence since the early 1940's. ^{233}U fuel cycles are most economic to countries such as India which has very small uranium reserves, but is a world leader in thorium reserves.

With a half-life of 2.41×10^4 years and a thermal fission cross section of 750 barns, ^{239}Pu makes an attractive material for nuclear proliferators. However, like ^{233}U , ^{239}Pu is not found in significant quantities in nature and must be artificially produced in a nuclear reactor from fertile ^{238}U . Commercial nuclear reactors operate with natural uranium or with slightly enriched ($\sim 3\text{-}5\%$ ^{235}U) uranium fuel. As such, a large portion of the fuel composition is the fertile ^{238}U isotope. As a by-product of a ^{235}U fission reactor, ^{239}Pu production processes can readily be masked by a nation's commercial nuclear energy production fuel cycle.

As ^{239}Pu is produced, a reactor will produce additional plutonium isotopes from neutron capture reactions and beta decay. These additional plutonium isotopes do not preclude the plutonium from being recycled and reused as reactor fuel. However, in the context of nuclear proliferation, these additional plutonium isotopes act as contaminants in the fissile material. Though several chemical processes capable of separating the plutonium and uranium from the spent reactor fuel exist, there is no large-scale process available for isotopic plutonium separation. Weapons grade plutonium is defined as less than 7% ^{240}Pu ¹. For a given reactor thermal power, the longer the reactor fuel is irradiated in the reactor, the more ^{239}Pu is produced. However, the ratio of ^{240}Pu to ^{239}Pu

also increases with increasing irradiation time. Therefore, if the plutonium material is intended for a nuclear explosive, the irradiation time should be short.

The term burn-up is defined as the thermal operating power of a reactor multiplied by the number of days of operation and is usually given in the terms of megawatt days (MWd). Specific burn-up is defined as the burn-up of fuel per unit mass of the reactor fuel and is usually given in terms of MWd per metric ton of uranium or heavy metal (MWd/MTU). Burn-up is an indicator of how much of the fissile material in the core has undergone fission, or “burned”. For power production purposes, it is desirable to burn as much of the fissile material as possible, while continuing to meet electrical demands, before changing out the nuclear fuel. In the context of nuclear proliferation, low fuel burn-up values are associated with weapons production.

1.3.2 Nuclides Useful as Spent Fuel Monitors

When analyzing spent fuel, the nuclear forensic analyst is interested in knowing where the spent fuel came from and what it was used for (e.g. ^{239}Pu production). Key parameters that can assist in fuel identification are: reactor type, fuel burn-up, fuel ^{235}U enrichment, and elapsed time since fuel discharge. The goal of the analyst is to identify which nuclides found in the spent fuel best characterize these parameters. Since plutonium is one of the main by-products of spent fuel, it is obviously one of the choices available for evaluation.

Figure 6 show plutonium ratios as a function of burnup. The plot was created using the ORIGEN-ARP computer code and shows the ratios of three different plutonium isotopes generated in a BWR using the ORIGEN-ARP computer code. A similar plot can

be found in Moody *et al.* (2005)¹ and was produced using the ORIGEN 2 code. The plot was produced here using ORIGEN-ARP to determine that similar results could be obtained using the ORIGEN-ARP code. The ratio of ²⁴⁰Pu and ²⁴²Pu to ²³⁹Pu varies directly with burn-up. In this manner, the burn-up of a fuel can be “back-calculated” if the ratios of these nuclides are known. The ratio of ²⁴¹Pu to ²³⁹Pu also varies with burn-up, but because ²⁴¹Pu has a “moderately low” half-life of 14.4 years, the amount of ²⁴¹Pu present in the fuel begins to diminish significantly once the fuel has been removed from the reactor. However, ²⁴¹Pu can still be a useful isotope for nuclear forensics. Once the fuel burn-up is determined (using the other plutonium isotopes), the amount of ²⁴¹Pu that was present when the fuel was removed from the reactor can be determined. A comparison of the amount of ²⁴¹Pu remaining in the fuel to that of what was determined to be in the fuel at discharge can determine the time elapsed since the fuel was removed from the reactor.

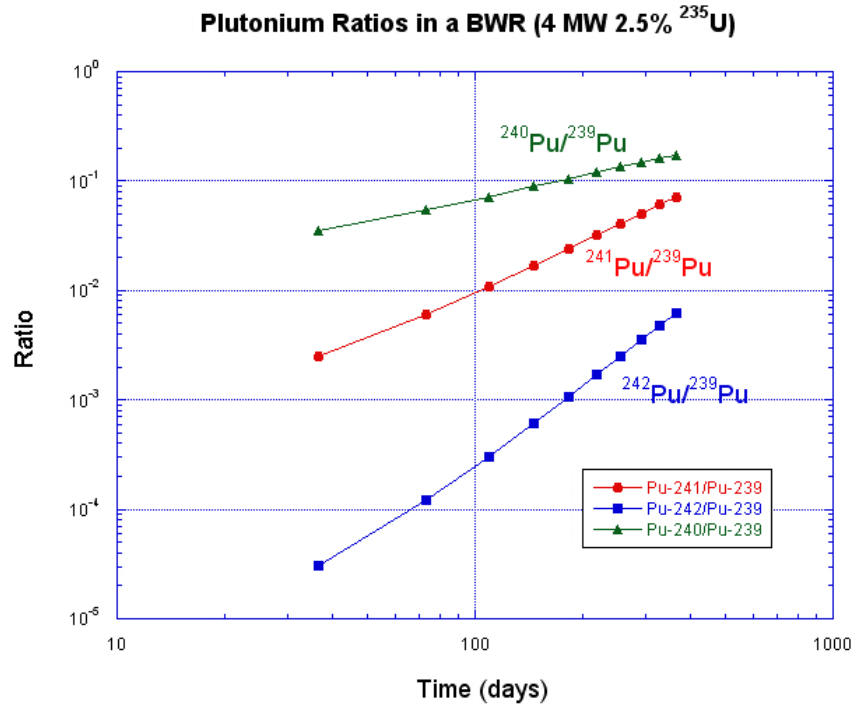


Figure 6: Plutonium Isotopic Ratios Used in Nuclear Forensics

Uranium and plutonium isotopes make excellent proliferation monitors. However, assuming that the plutonium and uranium are extracted from the fuel, the nuclear forensic analyst must rely on other nuclides to determine the key parameters for unfolding the spent fuel's origin and purpose. These nuclides are categorized into two groups: actinides and non-actinides (e.g. fission products). Fission products can be direct or indirect. Direct fission products are produced directly from fission, and indirect are produced from the decay of fission products. Also, fission products may undergo neutron absorption reactions (e.g. n,γ) and be transformed into other nuclides.

Part of the preliminary work of this dissertation was to determine which nuclides may be of significant interest for nuclear forensics applications. Scott (2005)² contains a table of approximately 40 suggested monitor nuclides for performing reverse calculations of spent nuclear fuel in order to determine fuel burnup, fuel enrichment, reactor type, fuel age, and time since discharge.

In the past, the primary means of measuring different isotopic species in spent nuclear fuel was the use of radiation detection equipment. This detection equipment is best utilized when significant quantities of the isotope being measured are present. Also, the isotope would have to be radioactive in order for the equipment to be able to detect it.

Due to advances in mass spectrometry, nuclides that were previously disregarded because they were only found in trace quantities of spent nuclear fuel, now lend themselves to nuclear forensics analysis use. For example, we can compare the quantity of a particular nuclide produced at a low burnup value to the quantity of the same nuclide at a high burnup value. If the ratio of the two quantities is significantly large (or small), then that nuclide may be useful as a forensic burnup indicator. Ideally, we would want to compare ratios of nuclides to normalize power differences, initial fuel quantities, etc. For example, if we found that ^{245}Cm was a good burnup indicator, then we could compare the ratios of $^{245}\text{Cm}/^{238}\text{U}$ for the low and high burnup results.

The first step to determine which nuclides would be useful for forensic monitors was to develop and run a reactor model using ORIGEN-ARP. The first case was a BWR. The long burn-up run was chosen for an irradiation period of 1461 days (~3 years) because one-third of a BWR's fuel is changed out annually. The irradiation period for the short burn-up was chosen as 110 days. This is approximately the burn-up (when running at full reactor power) that the ratio of ^{240}Pu to ^{239}Pu begins to increase above 7%. 110 days was selected as the irradiation period for the short burn-up for all reactor types. Both the long and short irradiation periods were followed by a 365 day fuel cooling period.

The cutoff for ORIGEN-ARP to report isotopes was 1×10^{-14} grams of a nuclide. This is the first screening criteria. Even with this cutoff, ORIGEN-ARP generated over 1000 nuclides.

The next step was to screen out nuclides based on their lowest detectable limits. Lower level detection limits vary with the detection method. The lower level detection limits were determined using the method detailed in Whitney *et al.* (2007)³ which assumes a mass spectrometry system.

This method assumes an LLD of 10^9 atoms. Using that assumption, the minimum mass of spent nuclear fuel necessary to generate a mass of nuclide, N, above the LLD is determined as follows:

$$M_N = \frac{(10^9 \text{ atoms})(MW)}{N_A}$$

$$\frac{M_s}{M_N} = \frac{M_T}{M_E} \quad (\text{Equation 1})$$

$$\Rightarrow M_s = M_N \left(\frac{M_T}{M_E} \right)$$

where,

M_T = total mass of spent fuel from reactor cycle in ORIGEN calculation

M_E = total output mass of isotope from simulated reactor cycle in ORIGEN calculation

M_N = mass needed for 10^9 atoms of the isotope

MW = molecular weight in g/mol

N_A = Avogadro's number.

Assuming that the largest sample size of spent nuclear fuel available to draw the sample size from was 10^5 grams, the author was able to narrow down the number of nuclides requiring additional evaluation to 300.

The primary goal of the preliminary analysis was to develop a method for determining which nuclide pairs (ratios) generated in a reactor are most useful for determining burn-up values and reactor type. Whitney *et al.* (2007)³ assumes that the “isotopic pairs that are most informative...are those pairs that show the most dramatic differences in production with respect to the short or long cycle.”

The use of ratios allows certain variables, such as initial fuel quantities, to be factored out of the results.

Whitney *et al.* (2007)³ derives a term called, R_c , which is defined as the cycle ratio and is given by the following equation:

$$R_c = \frac{\left(\begin{smallmatrix} A \\ Z \end{smallmatrix} X\right)_{short} / \left(\begin{smallmatrix} A-i \\ Z \end{smallmatrix} X\right)_{short}}{\left(\begin{smallmatrix} A \\ Z \end{smallmatrix} X\right)_{long} / \left(\begin{smallmatrix} A-i \\ Z \end{smallmatrix} X\right)_{long}} \quad (\text{Equation 2})$$

As the equation implies, Whitney *et al.* (2007)³ used different isotopes of the same element to perform the ratio determinations. For this work, that constraint is removed. Ratios of all nuclides to all other nuclides are determined once the initial mass screening methods described above are complete.

$$R_c = \frac{\left(\begin{smallmatrix} A_1 \\ Z_1 \end{smallmatrix} X \right)_{short}}{\left(\begin{smallmatrix} A_1 \\ Z_1 \end{smallmatrix} X \right)_{long}} \bigg/ \frac{\left(\begin{smallmatrix} A_2 \\ Z_2 \end{smallmatrix} X \right)_{short}}{\left(\begin{smallmatrix} A_2 \\ Z_2 \end{smallmatrix} X \right)_{long}} \quad (\text{Equation 3})$$

As mentioned previously, the BWR case resulted in 300 nuclides that required further evaluation after the mass screening. The ORIGEN-produced concentration values of the 300 nuclides for both the long and short cycles were then loaded into MATLAB. A MATLAB program was written to take the ratios of every nuclide to every other nuclide, and then to take that ratio for the short cycle and divide it by that same ratio for the long cycle. The result is a 300 by 300 matrix of R_c values. These values were imported back into MS Excel so they could be further evaluated. Figure 10 is a surface plot of a portion of the matrix of R_c values.

The next screening value applied to reduce the number of nuclides for further evaluation was the value of R_c . R_c values that were less than 10^3 (or alternatively, greater than 10^{-3}) were eliminated from further consideration.

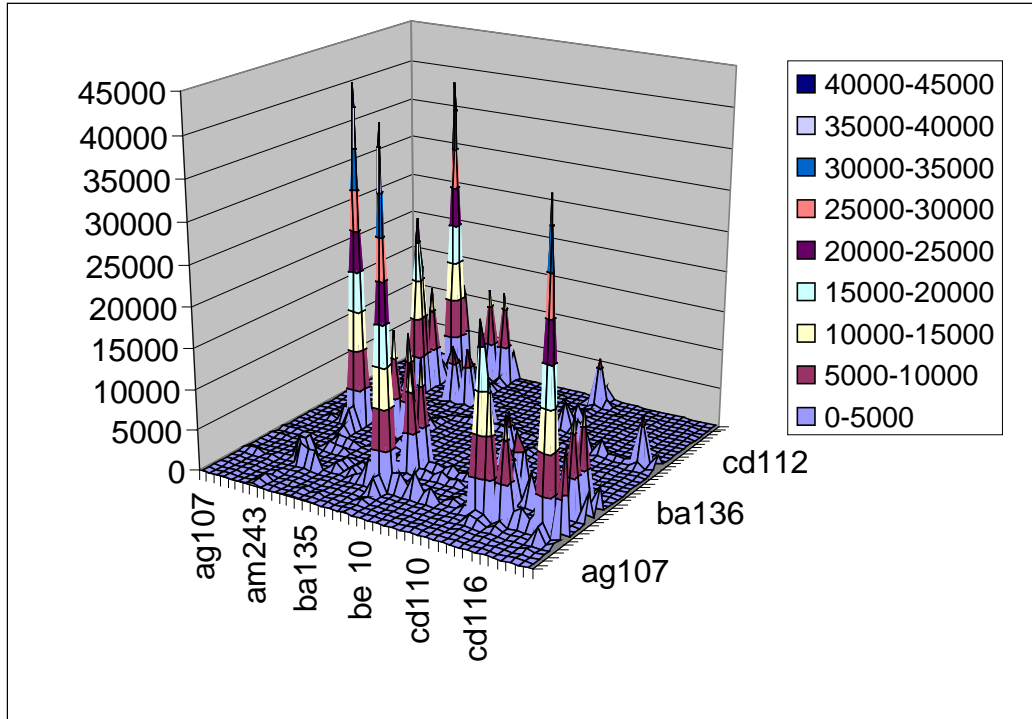


Figure 7: Surface Plot of the BWR Long to Short Cycle Ratio of Nuclides

As can be seen in Figure 7, many of the peaks are in line with other peaks. This indicates that that nuclide not only has a ratio of greater than 1000 with a specific nuclide, it also has a ratio of greater than 1000 with most of the nuclides evaluated. For example, the curium nuclide values had the highest ratios ($>10^8$). There were four different curium isotopes (^{243}Cm , ^{244}Cm , ^{245}Cm , and ^{246}Cm) which had acceptable ratios for most of the nuclides evaluated. Obviously, these nuclides should be considered as potential cycle length (burn-up) monitors.

All together, for the BWR long vs. short cycle case, there were thousands of nuclide ratios with acceptable values ($R_c > 1000$). In an effort to narrow down the number of nuclides to undergo further evaluation, only those nuclides that had multiple

acceptable ratios (*e.g.* the “lines” in Figure 10) and half-lives greater than 200 years were selected. Table 2 lists the selected nuclides and their associated half-life.

Even though these nuclides had acceptable ratios with most of the other nuclides, some of them did not have acceptable ratios with each other. For example, ^{243}Am and ^{245}Cm both had multiple occurrences of acceptable ratios with other nuclides. However, the ratio of ^{243}Am to ^{245}Cm was less than 1000. Table 1 lists which nuclides had acceptable ratios with each other.

Because chemical purification processes can preferentially remove some elements but not others, it is desirable to compare ratios of nuclides in the same elemental species. Table 1 lists four sets of isotopes of the same elements (curium, molybdenum, plutonium, and uranium). However, none of these isotopes had acceptable ratios when compared to the other isotope of that element. When comparing ratios of the other nuclides, it must be assumed that chemical processes that result in the preferential depletion of the other nuclides have not occurred. Also, as stated previously, it is probable that the plutonium and/or uranium have been extracted from the spent nuclear fuel. In that case, these nuclides cannot be expected to give reliable results.

Table 2: Nuclides generated from the BWR case with $R_c > 1000$ and $T_{1/2} > 200$ years

$T_{1/2}$ (years)	N	^{243}Am	^{135}Ba	^{245}Cm	^{246}Cm	^{157}Gd	^{94}Mo	^{96}Mo	^{242}Pu	^{244}Pu	^{149}Sm	^{123}Te	^{234}U	^{235}U	^{89}Y
7.37×10^3	^{243}Am	No	No	No	Yes	Yes	No	No	No	No	Yes	Yes	Yes	Yes	Yes
Stable	^{135}Ba	No	No	No	Yes	Yes	No	No	No	No	Yes	No	Yes	Yes	Yes
8.5×10^3	^{245}Cm	No	No	No	No	Yes	Yes	Yes	Yes	No	Yes	Yes	Yes	Yes	Yes
4.76×10^3	^{246}Cm	Yes	Yes	No	No	Yes	Yes	Yes	Yes	Yes	Yes	Yes	Yes	Yes	Yes
Stable	^{157}Gd	Yes	Yes	Yes	Yes	No	No	Yes	Yes	Yes	No	Yes	No	No	No
Stable	^{94}Mo	No	No	Yes	Yes	No	No	No	No	No	No	No	No	Yes	No
Stable	^{96}Mo	No	No	Yes	Yes	Yes	No	No	No	No	No	No	Yes	Yes	No
3.75×10^5	^{242}Pu	No	No	Yes	Yes	Yes	No	No	No	No	Yes	No	Yes	Yes	No
8.0×10^7	^{244}Pu	No	No	No	Yes	Yes	No	No	No	No	Yes	No	Yes	Yes	Yes
Stable	^{149}Sm	Yes	Yes	Yes	Yes	No	No	No	Yes	Yes	No	Yes	No	No	No
Stable*	^{123}Te	Yes	No	Yes	Yes	Yes	No	No	No	No	Yes	No	Yes	Yes	No
2.46×10^5	^{234}U	Yes	Yes	Yes	Yes	No	No	Yes	Yes	Yes	No	Yes	No	No	No
7.04×10^8	^{235}U	Yes	Yes	Yes	Yes	No	Yes	Yes	Yes	Yes	No	Yes	No	No	No
Stable	^{89}Y	Yes	Yes	Yes	Yes	No	No	No	No	Yes	No	No	No	No	No

* $T_{1/2} > 10^{14}$ years

Table 1: Nuclides generated from the BWR case with $R_c > 1000$ and $T_{1/2} > 200$ years

For ^{243}Am , the nuclides that were evaluated were ^{246}Cm , ^{157}Gd , ^{149}Sm , ^{123}Te , and ^{89}Y . ^{234}U and ^{235}U were eliminated because it is assumed that they will be chemically extracted from the spent nuclear fuel. ^{123}Te was also eliminated. Upon evaluation of the $^{243}\text{Am} / ^{123}\text{Te}$ plot, it was discovered that in-growth decay of ^{123}Te from the decay of $^{123\text{m}}\text{Te}$ ($T_{1/2} = 119.7$ days) leads to a noticeable decrease in the $^{243}\text{Am} / ^{123}\text{Te}$ over time.

For the purpose presenting the preliminary results, only the americium ratios are presented here. Figure 8 is a plot of the four different ^{243}Am ratios for the long and short irradiation cases. As mentioned previously, a long irradiation for the BWR is 1461 days (3 years). A short cycle is 110 days which is the approximate cycle length that the ^{240}Pu to ^{239}Pu ratio begins to exceed 7% (weapons grade). Both irradiation cases are followed by a 365 day cooling period to allow the fission products with extremely short half-lives time to decay.

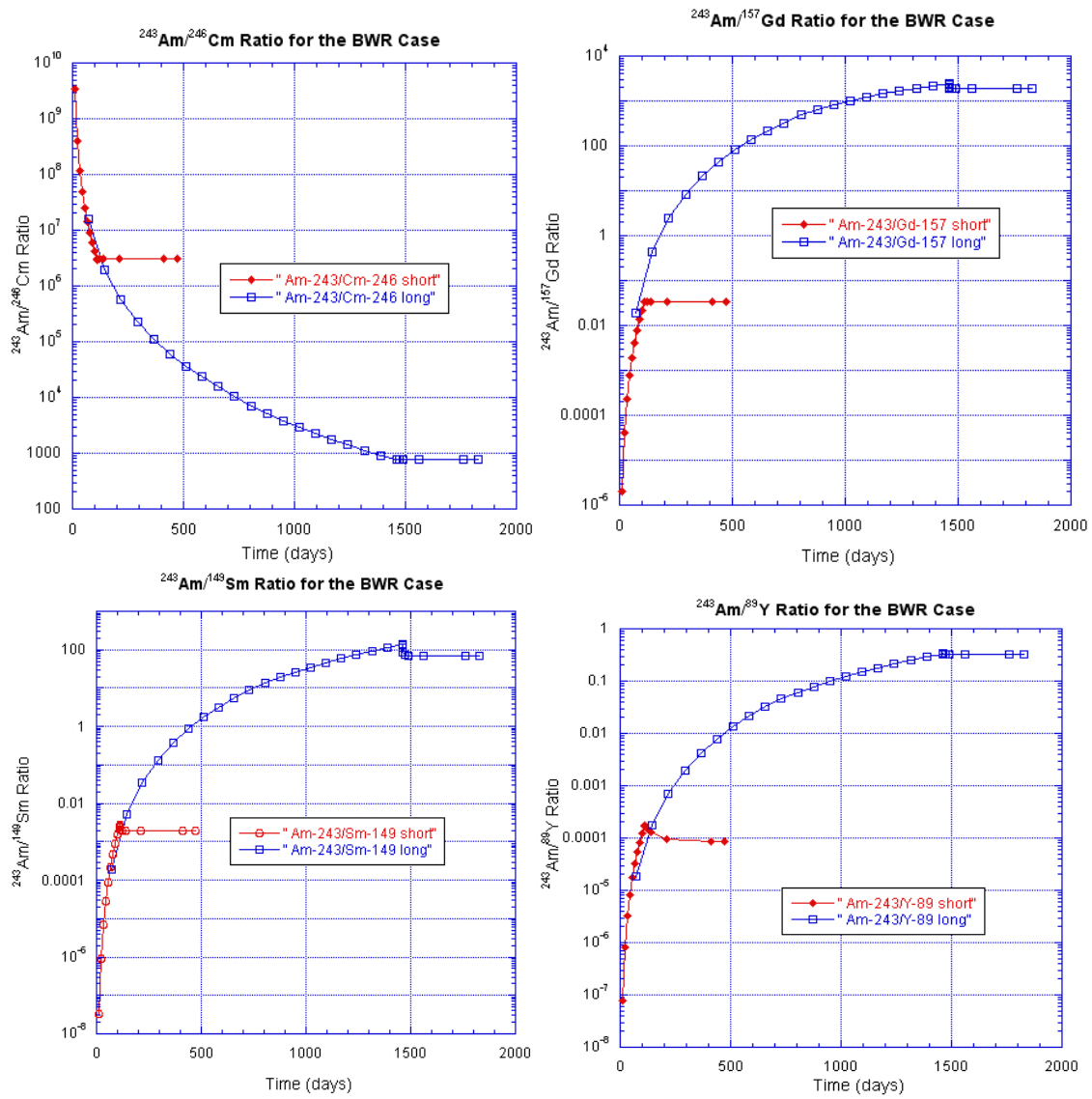


Figure 8: Different Americium Ratios for Long and Short Irradiation Cases

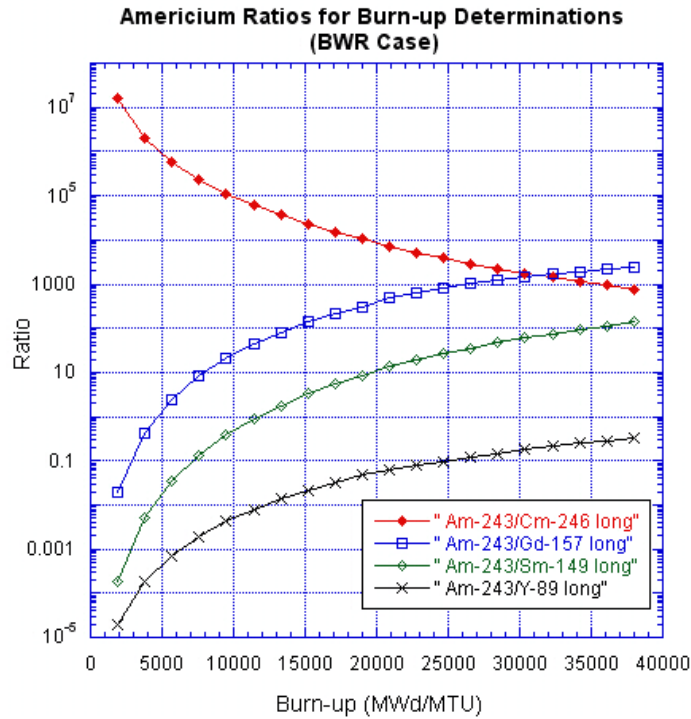


Figure 9: Americium Ratios as a Function of Burn-up in a BWR

Figure 9 is a plot of the four americium ratios versus burn-up for a BWR. The advantage of these particular ratios is that the difference between the ratio at typical low burn-ups and that at typical high burn-ups differs by approximately two to three orders of magnitude thereby reducing the effects of errors associated with the measurement of the nuclide masses.

Figure 10 is a plot of the same ratio values for four additional reactor types. These plots allow burn-up values to be determined from these ratios provided that the reactor type is known.

Figure 11 is a comparison of the $^{243}\text{Am}/^{246}\text{Cm}$ ratios for the different reactor types. The results for the PWR, BWR, and AGR agree well. The CANDU and

MAGNOX results do not. Even for power production purposes, burn-up values are typically low for the CANDU and MAGNOX reactors. Both reactors undergo continuous refueling operations and typically have low fuel burn-up values and are thus intrinsically capable of producing material for nuclear explosives.

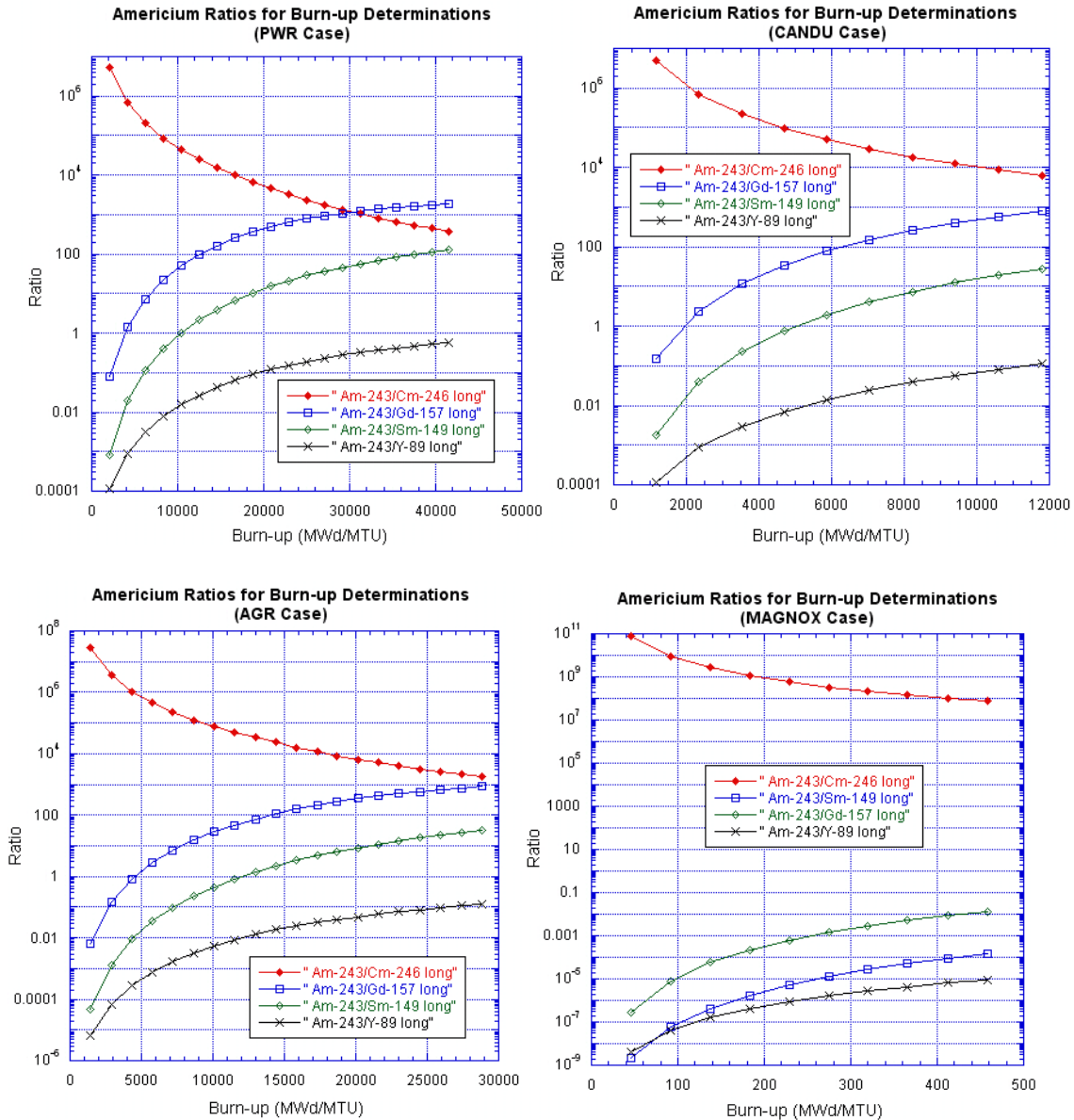


Figure 10: Americium Ratio Burn-up Plots for Four Different Reactors

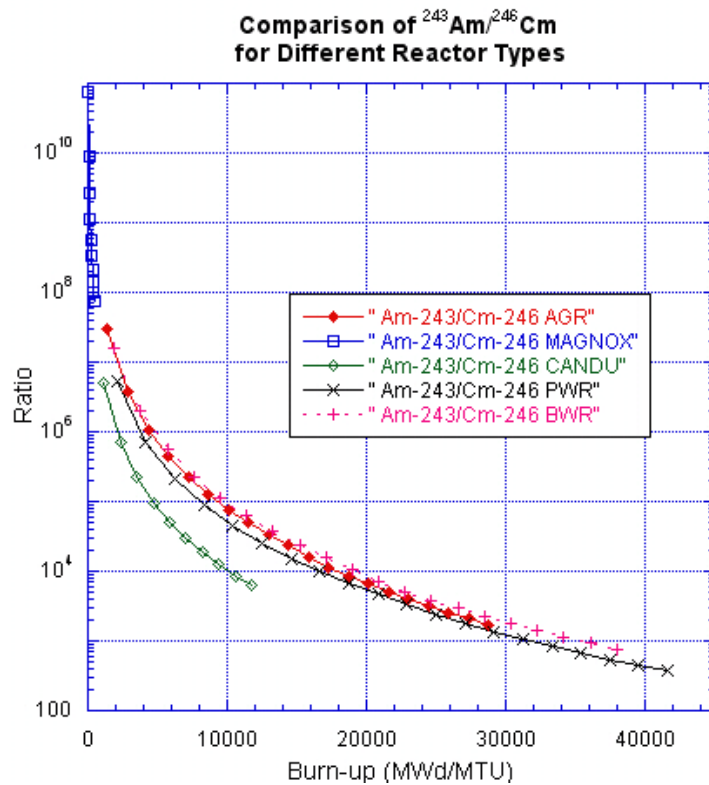


Figure 11: $^{243}\text{Am}/^{246}\text{Cm}$ Ratio as a Function of Burn-up for Five Different Reactor Types

Even with the applied screening criteria, hundreds of ratios remain to be further investigated. As mentioned previously, ^{243}Am production is independent of reactor operating power. It would be beneficial to evaluate the power variance of the other potential monitor nuclides identified in this work.

The 46 nuclides chosen for analysis in this study were based upon those recommended by previous studies found in the reference section, those having very large (or very small) ration values for different cycle times, and those which produced

significant quantities in the ORIGEN-ARP results. Also, a fission product at the lower end of the fission product distribution curve (^{72}Ge) and one at the upper end of the curve (^{161}Dy) were also chosen for analysis. The complete list of nuclides analyzed in this study can be found in Chapter 3.

Weaver *et al.* (2009)⁴ provides additional information on using nuclide ratios for nuclear forensics purposes.

1.3.3 Dissertation Objectives

The 46 nuclides listed in Chapter 3 will be analyzed for three different reactor types in Chapters 3, 4, and 5. The three most common commercial reactor types in North America are the Boiling Water Reactor (BWR), the Pressurized Water Reactor (PWR) and the Canadian Deuterium Uranium Reactor (CANDU). Significant work has been conducted to validate these reactor types against ORIGEN results. Once reactor types were chosen, reactor design and operating parameters had to be determined for the ORIGEN-ARP and MCNPX models. These parameters were derived from various sources in the reference section, but primarily from the ORIGEN-ARP manual⁵.

Because the ORIGEN-ARP models were relatively easy to develop and the code calculations could be completed in very little time, the ORIGEN-ARP models will be completed prior to the MCNPX models. Once the MCNPX models are developed and the calculations were completed, the results of the two codes were compared. Finally, an analysis of the results and the codes will be completed to explain the differences between the results.

As mentioned previously, the ORIGEN code has been used extensively to complete nuclide depletion calculations. Though ORIGEN has been validated, those validation results are limited in scope. As detection technologies become more advanced, the number of nuclides available for analysis increases. A comparison of the two codes (ORIGEN-ARP and MCNPX) and their results may reveal advantages in one code over the other for completing particular calculations or determining quantities of certain nuclides.

This dissertation will:

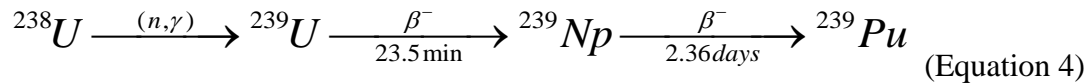
1. Develop MCNPX and ORIGEN-ARP single fuel assembly models for BWR, PWR, and CANDU reactors.
2. For each reactor type, compare the nuclide generation and depletion results of the two different models for 46 different nuclides.
3. Attempt to explain any difference in results between the two codes by investigating differences in the operating algorithms of the two codes.
4. Perform a sensitivity study of the MCNPX PWR fuel assembly model by performing small variances of five different reactor design and operating parameters (rod pitch, initial boron concentration, cladding thickness, water density, and fuel temperature).

Chapter 2: Computational Methods for Determining Nuclide Concentrations

2.1 ACTINIDE PRODUCTION IN REACTORS

Actinide materials in reactors are typically formed by a series of neutron capture reactions and subsequent radioactive decays.

^{239}Pu is produced in reactors via the following process:



Loss rates of ^{239}Pu in reactors can be attributed to neutron-induced fission and non-fission neutron absorption, such as radiative capture which produces ^{240}Pu .



For the isotopes involved in converting ^{238}U in reactor fuel into fissile ^{239}Pu , the following are the equations of time rate of change:

Generically, the time rate of change is equal to:

$$\frac{dN}{dt} = \text{rate of production} - \text{rate of loss} \quad (\text{Equation 6})$$

Assume (n, γ) is the only significant ^{239}U production reaction mechanism and there is no significant ^{238}U production reactions.

$$\frac{dN_{^{239}\text{U}}}{dt} = \underbrace{\varphi\sigma_{(n,\gamma)}^{^{238}\text{U}} N_{^{238}\text{U}}}_{\text{production from radioactive capture}} - \underbrace{\lambda^{^{239}\text{U}} N_{^{239}\text{U}}}_{\text{decay loss}} - \underbrace{\varphi\sigma_a^{^{239}\text{U}} N_{^{239}\text{U}}}_{\text{neutron absorption loss (including fission)}} \quad (\text{Equation 7})$$

Solving using Laplace transforms....

$$sN_{^{239}\text{U}}(s) - N_{^{239}\text{U}}(t=0) = \varphi\sigma_{(n,\gamma)}^{^{238}\text{U}} N_{^{238}\text{U}}(s) - \lambda^{^{239}\text{U}} N_{^{239}\text{U}}(s) - \varphi\sigma_a^{^{239}\text{U}} N_{^{239}\text{U}}(s) \quad (\text{Equation 8})$$

We need to solve for $N_{^{238}\text{U}}(s)$

$$\text{Assume } N_{^{238}\text{U}}(\text{at } t=0) \equiv N_0^{^{238}\text{U}}$$

$$\frac{dN_{^{238}\text{U}}}{dt} = -\lambda^{^{238}\text{U}} N_{^{238}\text{U}} - \varphi\sigma_a^{^{238}\text{U}} N_{^{238}\text{U}}$$

$$sN_{^{238}\text{U}}(s) - N_{^{238}\text{U}}(t=0) = -\lambda^{^{238}\text{U}} N_{^{238}\text{U}}(s) - \varphi\sigma_a^{^{238}\text{U}} N_{^{238}\text{U}}(s)$$

$$sN_{^{238}\text{U}}(s) + \lambda^{^{238}\text{U}} N_{^{238}\text{U}}(s) + \varphi\sigma_a^{^{238}\text{U}} N_{^{238}\text{U}}(s) = N_0^{^{238}\text{U}}$$

$$N_{^{238}\text{U}}(s)(s + \lambda^{^{238}\text{U}} + \varphi\sigma_a^{^{238}\text{U}}) = N_0^{^{238}\text{U}}$$

$$N_{^{238}\text{U}}(s) = \frac{N_0^{^{238}\text{U}}}{(s + \lambda^{^{238}\text{U}} + \varphi\sigma_a^{^{238}\text{U}})}$$

Solving for $N_{^{238}\text{U}}(t)$

$$\boxed{N_{^{238}\text{U}}(t) = N_0^{^{238}\text{U}} e^{-\left(\lambda^{^{238}\text{U}} + \varphi\sigma_a^{^{238}\text{U}}\right)t}} \quad (\text{Equation 9})$$

$$sN^{239U}(s) - N^{239U}(t=0) = \varphi\sigma_{(n,\gamma)}^{238U} N^{238U}(s) - \lambda^{239U} N^{239U}(s) - \varphi\sigma_a^{239U} N^{239U}(s) \quad (\text{Equation 10})$$

Assume $N^{239U}(t=0) = 0$

Substitute in $N^{238U}(s)$

$$sN^{239U}(s) = \varphi\sigma_{(n,\gamma)}^{238U} \left(\frac{N_0^{238U}}{s + \lambda^{238U} + \varphi\sigma_a^{238U}} \right) - \lambda^{239U} N^{239U}(s) - \varphi\sigma_a^{239U} N^{239U}(s)$$

$$sN^{239U}(s) + \lambda^{239U} N^{239U}(s) + \varphi\sigma_a^{239U} N^{239U}(s) = \frac{\varphi\sigma_{(n,\gamma)}^{238U} N_0^{238U}}{s + \lambda^{238U} + \varphi\sigma_a^{238U}}$$

$$N^{239U}(s) (s + \lambda^{239U} + \varphi\sigma_a^{239U}) = \frac{\varphi\sigma_{(n,\gamma)}^{238U} N_0^{238U}}{s + \lambda^{238U} + \varphi\sigma_a^{238U}}$$

$$N^{239U}(s) = \frac{\varphi\sigma_{(n,\gamma)}^{238U} N_0^{238U}}{(s + \lambda^{239U} + \varphi\sigma_a^{239U})(s + \lambda^{238U} + \varphi\sigma_a^{238U})} \quad (\text{Equation 11})$$

The subsequent time rate of change equations may be solved using the same method. Those equations and their solutions are listed below:

$$\frac{dN_{239Np}}{dt} = \lambda^{239U} N^{239U} - \lambda^{239Np} N^{239Np} - \varphi\sigma_a^{239Np} N^{239Np} \quad (\text{Equation 12})$$

$$N^{239Np}(t) = \lambda^{239U} \varphi\sigma_{(n,\gamma)}^{238U} N_0^{238U} * \left(\begin{array}{l} \frac{e^{-(\lambda^{239Np} - \varphi\sigma_a^{239Np})t}}{(\lambda^{239Np} + \varphi\sigma_a^{239Np} - \lambda^{239U} - \varphi\sigma_a^{239U})(\lambda^{239Np} + \varphi\sigma_a^{239Np} - \lambda^{238U} - \varphi\sigma_a^{238U})} \\ - \frac{e^{-(\lambda^{239U} + \varphi\sigma_a^{239U})t}}{(\lambda^{239Np} + \varphi\sigma_a^{239Np} - \lambda^{239U} - \varphi\sigma_a^{239U})(\lambda^{239U} + \varphi\sigma_a^{239U} - \lambda^{238U} - \varphi\sigma_a^{238U})} \\ + \frac{e^{-(\lambda^{238U} + \varphi\sigma_a^{238U})t}}{(\lambda^{239Np} + \varphi\sigma_a^{239Np} - \lambda^{238U} - \varphi\sigma_a^{238U})(\lambda^{239U} + \varphi\sigma_a^{239U} - \lambda^{238U} - \varphi\sigma_a^{238U})} \end{array} \right) \quad (\text{Equation 13})$$

$$\frac{dN_{^{239}\text{Pu}}}{dt} = \lambda^{^{239}\text{Np}} N^{^{239}\text{Np}} - \lambda^{^{239}\text{Pu}} N^{^{239}\text{Pu}} - \varphi\sigma_a^{^{239}\text{Pu}} N^{^{239}\text{Pu}} \quad (\text{Equation 14})$$

$$N^{^{239}\text{Pu}}(t) = \lambda^{^{238}\text{U}} \frac{^{238}\text{U}}{\varphi\sigma_a^{(n,\gamma)}} N^{^{238}\text{U}} *$$

$$\left(\begin{array}{l} \frac{-e^{-(\lambda^{^{239}\text{Pu}} + \varphi\sigma_a^{^{239}\text{Pu}})t}}{(\lambda^{^{239}\text{Pu}} + \varphi\sigma_a^{^{239}\text{Pu}} - \lambda^{^{239}\text{Np}} - \varphi\sigma_a^{^{239}\text{Np}})(\lambda^{^{239}\text{Pu}} + \varphi\sigma_a^{^{239}\text{Pu}} - \lambda^{^{239}\text{U}} - \varphi\sigma_a^{^{239}\text{U}})(\lambda^{^{239}\text{Pu}} + \varphi\sigma_a^{^{239}\text{Pu}} - \lambda^{^{238}\text{U}} - \varphi\sigma_a^{^{238}\text{U}})} \\ + \frac{e^{-(\lambda^{^{239}\text{Np}} + \varphi\sigma_a^{^{239}\text{Np}})t}}{(\lambda^{^{239}\text{Pu}} + \varphi\sigma_a^{^{239}\text{Pu}} - \lambda^{^{239}\text{Np}} - \varphi\sigma_a^{^{239}\text{Np}})(\lambda^{^{239}\text{Np}} + \varphi\sigma_a^{^{239}\text{Np}} - \lambda^{^{239}\text{U}} - \varphi\sigma_a^{^{239}\text{U}})(\lambda^{^{239}\text{Np}} + \varphi\sigma_a^{^{239}\text{Np}} - \lambda^{^{238}\text{U}} - \varphi\sigma_a^{^{238}\text{U}})} \\ + \frac{e^{-(\lambda^{^{239}\text{U}} + \varphi\sigma_a^{^{239}\text{U}})t}}{(\lambda^{^{239}\text{Pu}} + \varphi\sigma_a^{^{239}\text{Pu}} - \lambda^{^{239}\text{U}} - \varphi\sigma_a^{^{239}\text{U}})(\lambda^{^{239}\text{U}} + \varphi\sigma_a^{^{239}\text{U}} - \lambda^{^{239}\text{Np}} - \varphi\sigma_a^{^{239}\text{Np}})(\lambda^{^{239}\text{U}} + \varphi\sigma_a^{^{239}\text{U}} - \lambda^{^{238}\text{U}} - \varphi\sigma_a^{^{238}\text{U}})} \\ + \frac{e^{-(\lambda^{^{238}\text{U}} + \varphi\sigma_a^{^{238}\text{U}})t}}{(\lambda^{^{239}\text{Pu}} + \varphi\sigma_a^{^{239}\text{Pu}} - \lambda^{^{238}\text{U}} - \varphi\sigma_a^{^{238}\text{U}})(\lambda^{^{238}\text{U}} + \varphi\sigma_a^{^{238}\text{U}} - \lambda^{^{239}\text{Np}} - \varphi\sigma_a^{^{239}\text{Np}})(\lambda^{^{238}\text{U}} + \varphi\sigma_a^{^{238}\text{U}} - \lambda^{^{239}\text{U}} - \varphi\sigma_a^{^{239}\text{U}})} \end{array} \right)$$

$$(\text{Equation 15})$$

Each subsequent reaction results in additional terms to the solution. Solving such equations manually is a tedious process. ORIGEN computationally solves these differential equations using input parameters such as initial fuel loading (including composition and enrichment), reactor type, reactor power, irradiation time, and decay time based upon an internal set of decay libraries and predetermined absorption and fission cross section libraries which are a function of reactor type. In this manner, ORIGEN accounts for the different reactor design parameters such as moderator composition, moderator density, etc.

It should be noted that the above method also applies to light element production in a reactor. Such calculations are pertinent when the analyst requires an understanding of nuclide concentrations in the cladding and other reactor materials (*e.g.* the moderator, the reflector). ORIGEN will also calculate these nuclide concentrations when these materials are added to the input deck. However, in this work, the only concern is the fuel itself, so the light materials (*e.g.* cladding, moderator, reflector, etc.) are not included in the computational model.

2.2 FISSION FRAGMENT PRODUCTION IN REACTORS

Fission fragments, or fission products, are produced directly from fission or indirectly via radioactive decay (primarily beta minus decay) of other fission products. Figure 12 is a plot of fission fragment production yield as a function of atomic mass number. The plot illustrates that fission products are most likely to be produced with mass numbers around 95 and 140. The shape of the plot varies somewhat with fissile species and with neutron energy. This data is from a MAGNOX reactor which utilizes ^{235}U , as the fissile species, and thermal energy neutrons.

Because this plot is produced from ORIGEN-ARP results for a reactor design (*i.e.* Magnox), the plot includes both direct and indirect fission products as well as neutron activated nuclides.

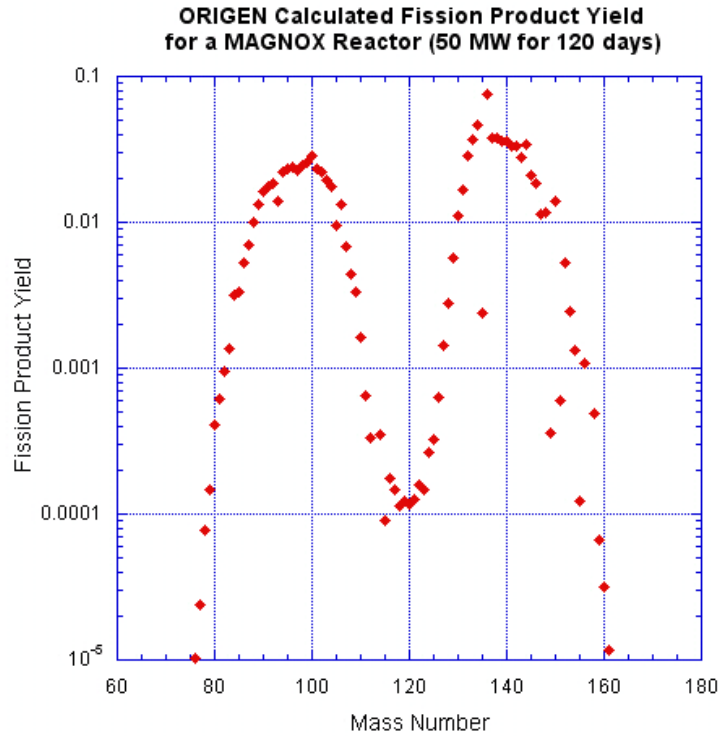


Figure 12: Fission Product Yield Distribution

The analytical solution for fission product nuclide concentrations can be determined by a manner similar to that used for actinide nuclide concentrations. ^{135}I and ^{135}Xe are both fission products which are produced from the fission of ^{235}U . However, ^{135}Xe is also produced from the beta-minus decay of ^{135}I . The time rate of change equations for the nuclide concentrations of ^{135}I and ^{135}Xe are derived below. ^{135}I and ^{135}Xe both have decay loss terms. ^{135}Xe also has a loss term from neutron absorption. For the equations below, the term “I” refers to the ^{135}I nuclide, and the term “Xe” refers to the ^{135}Xe nuclide. The term χ refers to the fission yield production of the corresponding fission product nuclide and is specific to the nuclide undergoing fission

(e.g. ^{235}U). Σ_f is the macroscopic fission cross section of the nuclide undergoing fission

(e.g. ^{235}U).

$$\frac{dN_I(t)}{dt} = \chi_I \phi \Sigma_f - \lambda_I N_I(t) \quad (\text{Equation 16})$$

$$N_I(t) = \frac{\chi_I \phi \Sigma_f}{\lambda_I} (1 - e^{-\lambda_I t}) \quad (\text{Equation 17})$$

$$\frac{dN_{Xe}(t)}{dt} = \chi_{Xe} \phi \Sigma_f + \lambda_I N_I(t) - \lambda_{Xe} N_{Xe}(t) - \phi \sigma_a^{Xe} N_{Xe}(t) \quad (\text{Equation 18})$$

$$N_{Xe}(t) = \frac{\chi_{Xe} \phi \Sigma_f}{\lambda_{Xe} + \phi \sigma_a^{Xe}} \left(1 - e^{-(\lambda_{Xe} + \phi \sigma_a^{Xe})t} \right) + \lambda_I \chi_I \phi \Sigma_f \left(\frac{1}{(\lambda_{Xe} + \phi \sigma_a^{Xe}) \lambda_I} + \frac{e^{-(\lambda_{Xe} + \phi \sigma_a^{Xe})t}}{(\lambda_{Xe} + \phi \sigma_a^{Xe})(\lambda_{Xe} + \phi \sigma_a^{Xe} - \lambda_I)} \right) + \frac{e^{-\lambda_I t}}{\lambda_I (\lambda_I - (\lambda_{Xe} + \phi \sigma_a^{Xe}))} \quad (\text{Equation 19})$$

2.3 ACTINIDE AND FISSION FRAGMENT DEPLETION AND PRODUCTION IN NUCLEAR REACTORS USING ORIGEN-ARP

The ORIGEN-ARP Sequence within the Standardized Computer Analyses for Licensing Evaluation (SCALE) code allows the user to determine nuclide depletion and production as a function of fuel burnup for a series of predefined reactor types.

ORIGEN-ARP utilized a graphical user interface to greatly simplify the generation of the ORIGEN input file. Figure 13 below illustrates the ORIGEN-ARP Sequence.

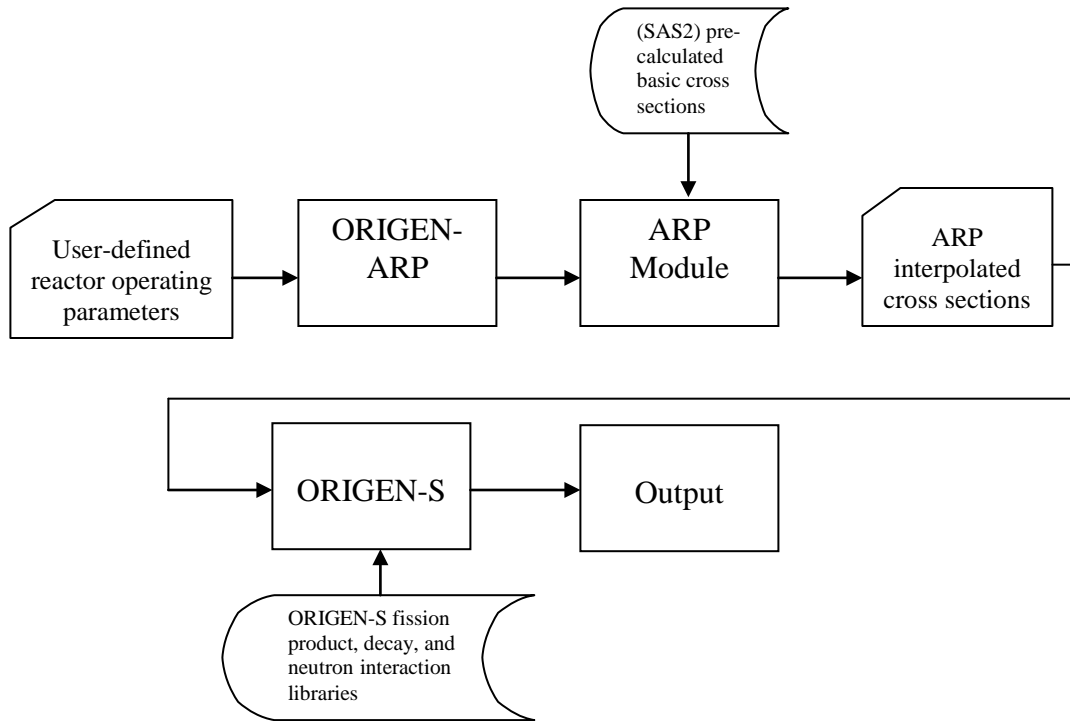


Figure 13: ORIGEN-ARP Flow⁵

Using the graphical interface, the user enters applicable reactor operating parameters: reactor type, reactor operating power profile (using time steps), enrichment, moderator density, and initial fuel composition. ORIGEN-ARP uses the fuel quantity and reactor operating power profile to determine the specific burnup range for the calculation. ORIGEN-ARP converts the user input into an ORIGEN formatted input deck. The SCALE code then executes the ARP module which takes the user defined burnup, enrichment, and moderator densities and develops an interpolated library of ARP

effective absorption and fission cross sections. The ARP module interpolates between pre-calculated (using the SAS2 code) ARP effective absorption and fission cross sections based upon reactor type. For example, if the desired calculation is for a GE 8x8-4 BWR reactor with 3.5 weight percent enrichment, the ARP module will take the existing cross section libraries for a GE 8x8-4 BWR with 3 weight percent enrichment and for a GE 8x8-4 BWR with 4 weight percent enrichment and interpolate between the two in order to develop a GE 8x8-4 BWR with 3.5 weight percent enrichment cross section library.

The SCALE code then, using the ORIGEN-ARP prepared input deck, executes the ORIGEN-S module. ORIGEN-S is the version of ORIGEN incorporated into the SCALE code. The ORIGEN-S program uses the ARP effective cross sections to generate the radiation source term which provides the neutron flux values for each time step.

At each time step, the calculated flux, along with the ORIGEN-S fission product libraries, decay libraries, and neutron reaction libraries are input into the time rate of change equation (See Equation 20 below) to determine the nuclide concentration at the end of that time interval.

The ORIGEN-S neutron reaction cross section libraries are binned into 3 energy groups. The three neutron energy groups are thermal (1×10^{-11} to 6.25×10^{-7} MeV), resonance (6.25×10^{-7} to 1 MeV), and fast (1 to 20 MeV). The three energy groups are combined into an “effective” one-group cross section by using flux weighting factors. This process is described further in Section M6.2.7 of the SCALE Manual⁵.

ORIGEN combines the actinide (and light element) production and fission product production time rate of change equations into one equation. The following

equation and definitions are taken directly from the ORIGEN-ARP manual contained with the SCALE 5.1 manual⁵.

The time rate of change of the concentration for a particular nuclide, N_i , is:

$$\frac{dN_i}{dt} = \sum_j \gamma_{ji} \sigma_{ff} N_j \phi + \sigma_{c,i-1} N_{i-1} \phi + \lambda_i' N_i' - \sigma_{f,i} N_i \phi - \sigma_{c,i} N_i \phi - \lambda_i N_i \quad (\text{Equation 20})^5$$

where ($I = 1, \dots, I$), and

- $\sum_j \gamma_{ji} \sigma_{ff} N_j \phi$ is the yield rate of N_i due to the fission of all nuclides N_j ;
- $\sigma_{c,i-1} N_{i-1} \phi$ is the rate of transmutation into N_i due to radiative neutron capture by nuclide N_{i-1} ;
- $\lambda_i' N_i'$ is the rate of formation of N_i due to the radioactive decay of nuclides N_i' ;
- $\sigma_{f,i} N_i \phi$ is the destruction rate of N_i due to fission;
- $\sigma_{c,i} N_i \phi$ is the destruction rate of N_i due to all forms of neutron absorption other than fission (n, γ , n, α , n, p , $n, 2n$, $n, 3n$);
- $\lambda_i N_i$ is the radioactive decay rate of N_i .

As mentioned previously, for generating the radiation source term for ORIGEN-S, ORIGEN-ARP has a pre-determined set of neutron absorption and fission cross sections as a function of fuel burn-up for a finite set of reactor designs. Additional ORIGEN-ARP cross sections libraries for reactor types not available with the distributed ORIGEN-ARP code may be generated by the user from other computational codes within the SCALE 5.1 software package. Figures 14 and 15 are plots of the effective fission and absorption

cross sections as function of reactor fuel burn-up generated for a 3% ^{235}U enriched 17x17 PWR from the ORIGEN-ARP libraries.

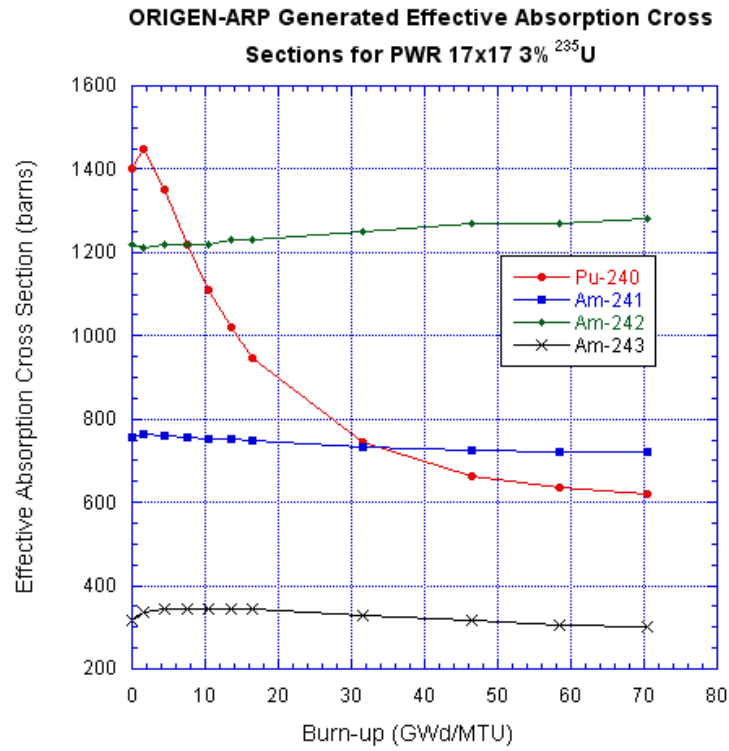


Figure 14: ORIGEN-ARP Effective Neutron Absorption Cross Sections

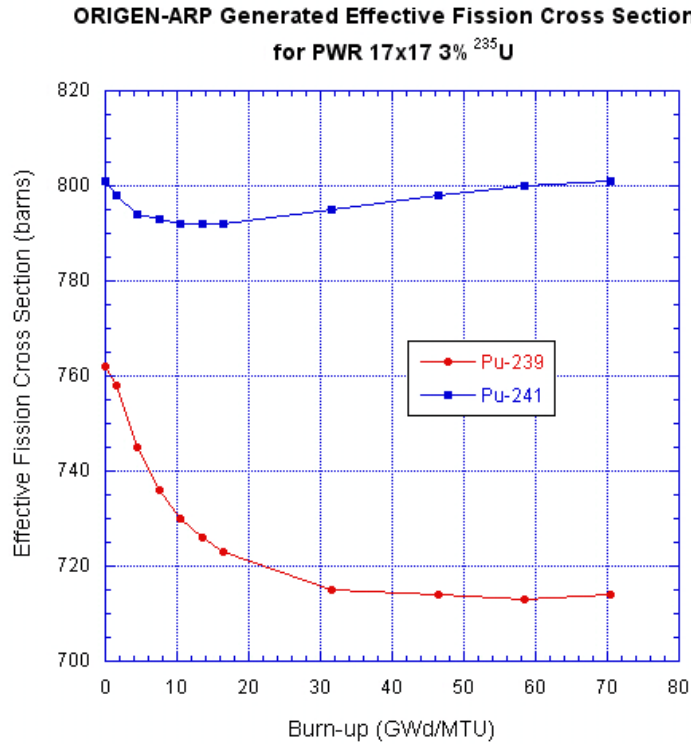


Figure 15: ORIGEN-ARP Effective Fission Cross Sections

2.4 ACTINIDE AND FISSION FRAGMENT DEPLETION AND PRODUCTION IN NUCLEAR REACTORS USING MCNPX

MCNPX is a radiation transport code which utilizes the Monte Carlo method for determining the probabilistic behavior of a number of particles. The probabilities of different particle interactions are given by particle cross sections. For each interaction, random numbers are generated to determine what energy a particle is “born” at, what direction it travels in, whether or not an interaction occurs, what type of interaction occurs, how much energy is absorbed by the reaction, what direction the resulting

particle(s) travel in, etc. By running a statistically significant number of particle “histories” it is possible to determine the average behavior of the group of particles⁶.

The MCNPX (Version 2.6.0) Code has incorporated the CINDER90 deterministic code to perform the nuclide production and depletion part of the calculation. Using the transport cross sections available within MCNPX, MCNPX can determine the time-step neutron flux and nuclide reaction rates. For those nuclides that do not have transport cross sections, MCNPX generates a 63 (energy)-group neutron flux at each time step. MCNPX sends this 63-group flux to CINDER90 which then determines the nuclide reaction rates for those nuclides⁷.

In order to utilize the “Burn” feature within MCNPX, the MCNPX input deck must be set up in the KCODE criticality mode. In this mode, the user defines a number of neutron source locations within the nuclear fuel. The code then generates (virtual) neutrons at these locations and runs particle histories for each particle generated. For fission reactions, it follows the histories of each of the neutrons through the user-defined number of cycles (or neutron generations). From this probabilistic neutron transport calculation, the calculated neutron flux can then be determined. This calculated neutron flux must then be multiplied by the flux normalization parameters (e.g. power level) in order to determine the “true” time-step neutron flux which then is used with CINDER90 to determine the nuclide reaction rates.

Along with the nuclear decay libraries, MCNPX can then determine the nuclide concentrations at each time step in the problem.

2.5 ORIGEN-ARP VERSUS MCNPX

The primary difference between ORIGEN-ARP and MCNPX is that ORIGEN-ARP is a deterministic computational method whereas MCNPX is a probabilistic computational method. However, as noted previously, CINDER90 is a deterministic code; therefore, MCNPX depletion calculations have both a probabilistic and a deterministic aspect to them. Deterministic calculations provide an exact solution but often must make approximations (e.g. energy groups, first order differential equation assumptions) in order to complete a calculation. Probabilistic calculations often do not need to make such approximations but are otherwise limited by the probabilistic nature of the solution (i.e. confidence levels).

Both ORIGEN and MCNPX determine a time-step-averaged neutron flux which is then used (along with the additional input, including reactor power) to perform the depletion (and generation) calculation for that time step. Results (i.e. nuclide quantities) from the depletion calculation are then used to determine the next time-step-averaged flux. This continues for each time step listed in the input file. Both programs rely on the assumption that the time-step-averaged neutron flux changes little during the time step.

As shown in Figure 16, an acceptable time step is one where the flux has little variation. An unacceptable time step is one where the flux has great variation.

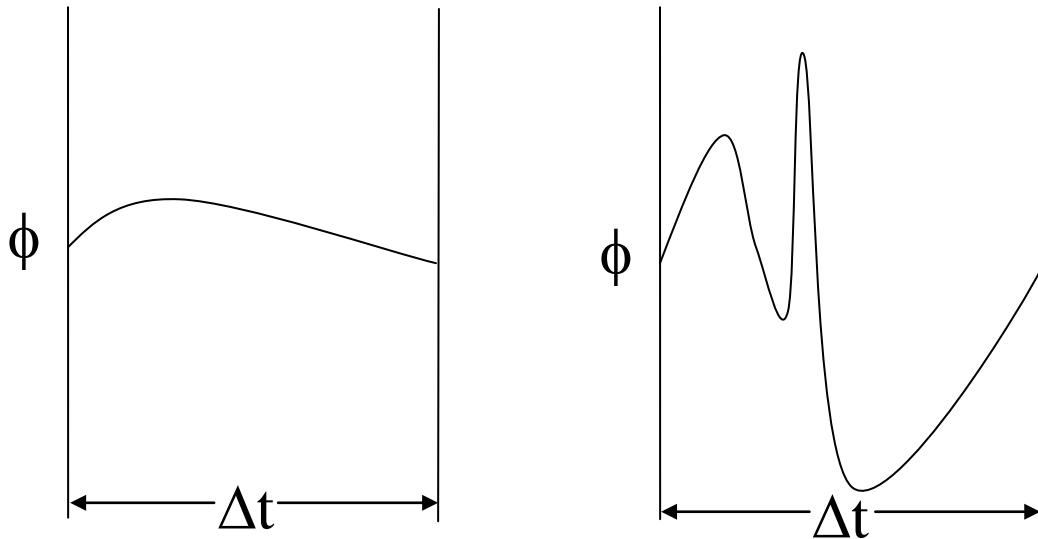


Figure 16: Illustration of an Acceptable (left) and an Unacceptable (right) Time Step

Both codes perform a predictor-corrector calculation. In this calculation, the initial nuclide concentrations at the start of the time step are used to calculate the starting flux. This flux is then used to do a depletion calculation for the nuclide concentrations at the end of the time step (the predictor calculation). The nuclide concentration from the predictor calculation is then used to determine the end-of-time-step flux. The end flux is averaged with the initial flux, and this average flux is then used to do the depletion calculation for the time step (the corrector calculation). Clearly, if the average flux

differs greatly from the initial flux, the probability of error in the calculation is great. For the ORIGEN code, if the average flux differs from the initial flux by more than 20%, a warning message is generated notifying the user that the time steps are too large⁵.

As mentioned previously, ORIGEN-ARP interpolates the cross sections in the available libraries to fit the enrichment and water density of each reactor type so that it matches that of the user input. These available libraries have been generated from the SAS2 or TRITON control modules in SCALE. There are three ORIGEN-ARP models used in this study: a BWR, a PWR, and a CANDU reactor type. The BWR and PWR ORIGEN-ARP libraries were pre-generated using TRITON (from a 2-D lattice code). The CANDU libraries were obtained from the RSICC code package DLC-210, contributed by Atomic Energy of Canada Limited⁵. Because MCNPX is a three-dimension code, it is expected that the source term generated would be of a higher fidelity because it incorporates the axial dimension not included in a 2-D calculation. The ORIGEN-ARP results in this study are based upon the pre-generated cross section libraries that are packaged with SCALE 5.1 code. A user could use TRITON and a 3-D lattice code (e.g. KENO) to generate libraries for the BWR and PWR models. This was not done for this study.

There is some difference in the computation of fission product yield between ORIGEN-S and MCNPX. Both programs only track fission products for actinides that have explicit fission yields defined in the codes. However, ORIGEN-S has 30 actinides with explicit fission yields defined, whereas MCNPX has 36 actinides with explicit fission yields. Also, ORIGEN-S has only one fission energy yield set per each of those

30 actinides. The fission yield set for each actinide is based on either a thermal or a fast incident neutron energy dependent on the predominant source of fission (either fast or thermal neutrons) for that actinide. MCNPX has a total of 60 fission yield sets for the 36 actinides. Each of the 36 actinides has one or more fission yield sets. Fission yield sets include thermal, fast, high energy, and spontaneous fission yield data. Table 2, below, lists the actinides and the fission sets included for ORIGEN-S and MCNPX.

Figures 17 and 18 are plots illustrating the different fission yield probabilities for different energy incident neutrons for ^{235}U and ^{238}U . As shown by the plots, there are significant differences in fission yield for different energy impinging neutrons. This difference is most evident in the trough area between the two peaks on the charts.

Figure 19 is a plot of the ^{235}U thermal neutron fission yield probability compared to the ^{241}Am thermal neutron fission yield probability. As shown, there is significant difference in the fission yields between the two different actinide species.

<i>Actinide</i>	<i>ORIGEN-S (Scale 5.1)</i>	<i>MCNPX (v 2.6.0)</i>
<i>Undergoing Fission</i>		
²²⁷ <i>Th</i>	Thermal	Thermal
²²⁹ <i>Th</i>	Thermal	Thermal
²³² <i>Th</i>	Fast	Fast, High Energy
²³¹ <i>Pa</i>	Thermal	Thermal
²³² <i>U</i>	Thermal	Thermal
²³³ <i>U</i>	Thermal	Thermal, Fast, High Energy
²³⁴ <i>U</i>	Fast	Fast, High Energy
²³⁵ <i>U</i>	Thermal	Thermal, Fast, High Energy
²³⁶ <i>U</i>	Fast	Fast, High Energy
²³⁷ <i>U</i>	Fast	Fast
²³⁸ <i>U</i>	Fast	Spontaneous, Fast, High Energy
²³⁷ <i>Np</i>	Thermal	Thermal, Fast, High Energy
²³⁸ <i>Np</i>	Fast	Fast
²³⁸ <i>Pu</i>	Fast	Fast
²³⁹ <i>Pu</i>	Thermal	Thermal, Fast, High Energy
²⁴⁰ <i>Pu</i>	Thermal	Thermal, Fast, High Energy
²⁴¹ <i>Pu</i>	Thermal	Thermal, Fast
²⁴² <i>Pu</i>	Thermal	Thermal, Fast, High Energy
²⁴¹ <i>Am</i>	Thermal	Thermal, Fast, High Energy
^{242m} <i>Am</i>	Thermal	Thermal
²⁴³ <i>Am</i>	Fast	Fast
²⁴² <i>Cm</i>	Fast	Fast
²⁴³ <i>Cm</i>	Thermal	Thermal, Fast
²⁴⁴ <i>Cm</i>	Fast	Spontaneous, Fast
²⁴⁵ <i>Cm</i>	Thermal	Thermal
²⁴⁶ <i>Cm</i>	Fast	Spontaneous, Fast
²⁴⁸ <i>Cm</i>	Fast	Spontaneous, Fast
²⁴⁹ <i>Cf</i>	Thermal	Thermal
²⁵⁰ <i>Cf</i>	NONE	Spontaneous
²⁵¹ <i>Cf</i>	Thermal	Thermal
²⁵² <i>Cf</i>	NONE	Spontaneous
²⁵³ <i>Es</i>	NONE	Spontaneous
²⁵⁴ <i>Es</i>	Thermal	Thermal
²⁵⁴ <i>Fm</i>	NONE	Spontaneous
²⁵⁵ <i>Fm</i>	NONE	Thermal
²⁵⁶ <i>Fm</i>	NONE	Spontaneous

Table 2: Actinide Fission Yield Data Sets Available in ORIGEN-S⁵ and MCNPX³⁰

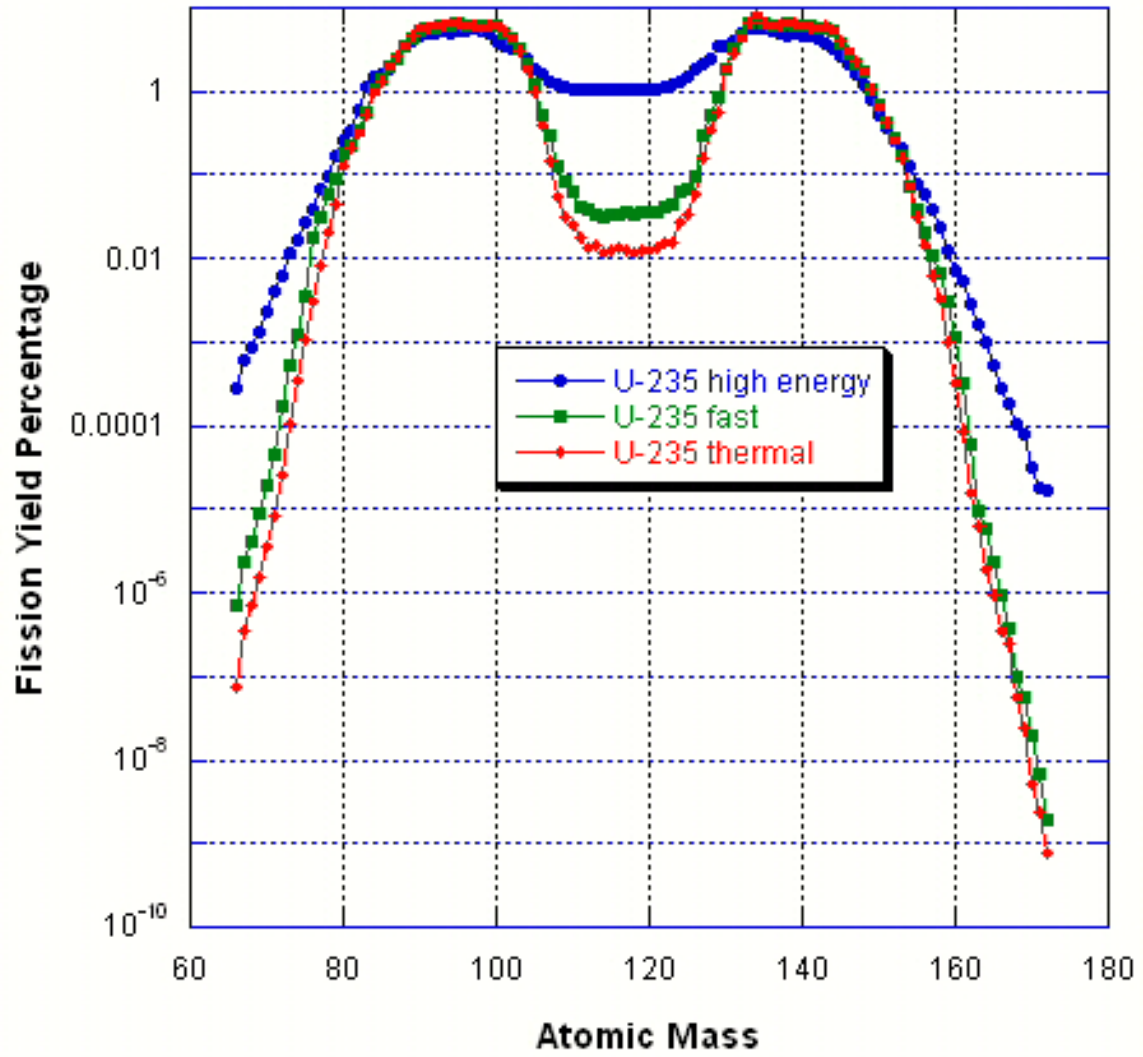


Figure 17: ²³⁵U Fission Product Yield for Different Energy Incident Neutrons

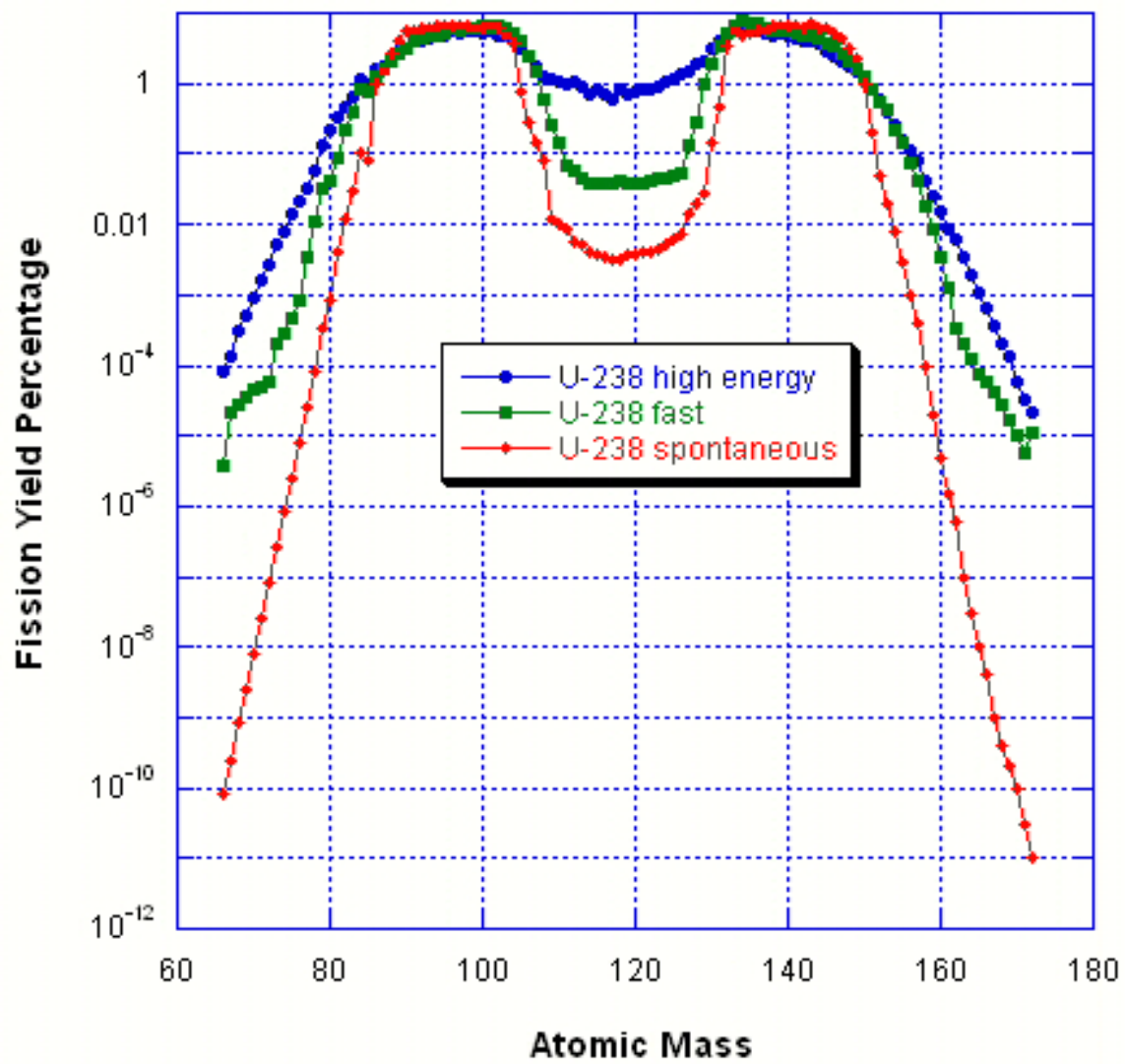


Figure 18: ^{238}U Fission Product Yield for Different Energy Incident Neutrons

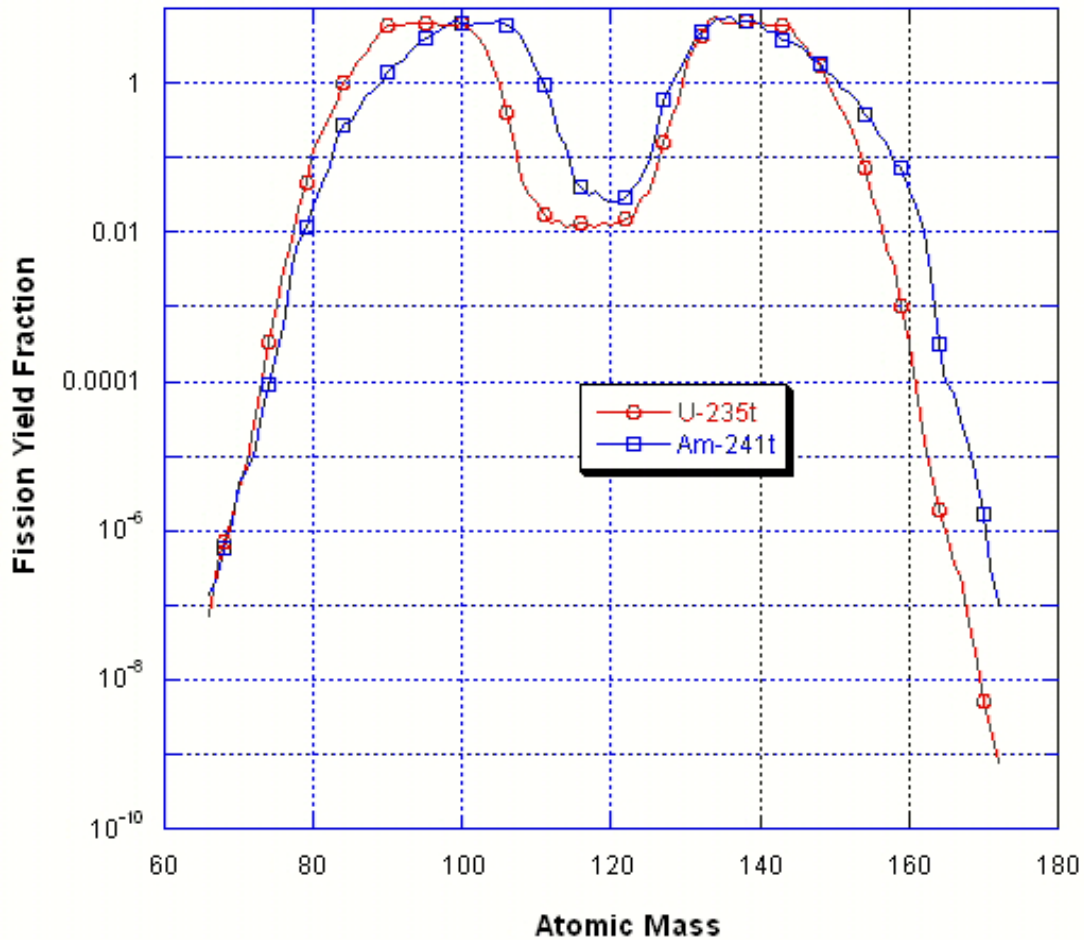


Figure 19: Thermal Neutron Fission Product Yield for Two Different Nuclides

Based upon Table 2, MCNPX has more fission yield sets than ORIGEN-S. However, the thermal reactor models being evaluated in this study will not generate any significant quantity of high energy neutrons; therefore it may be assumed that the 11 high energy fission yield sets within MCNPX do not provide appreciable value to this study. However, the occurrence of spontaneous fission and fast neutrons is expected in the reactors modeled in this study. For many of the actinides which have only thermal fission yield sets in ORIGEN-S, MCNPX contains both thermal and fast fission yield

sets. For the purposes of this study, these additional fission yield sets within MCNPX should result in a more realistic model of the actual fission product production than the ORIGEN-S model.

The ORIGEN-S *origen.rev02.pwrlib* file and MCNPX *cinder.dat* file contain the fission yield sets listed in Table 3 for each respective program. As noted previously, MCNPX has 60 fission yield sets for 36 actinide species. ORIGEN-S only has 30 fission yield sets, one for each actinide species. For ^{235}U , ORIGEN-S uses only the thermal neutron fission yield set. MCNPX contains thermal, fast, and high energy neutron fission yield sets for ^{235}U . For the fission products analyzed in this dissertation, the table below lists both the thermal and fast fission yield sets for MCNPX and the only ^{235}U fission yield set for ORIGEN-S. According to the program documentation, both programs use ENDF/B-VI fission yield sets. However, on close examination of several common fission products in both files, there exist some small differences between the ORIGEN-S fission yield set and the MCNPX thermal yield set. See Table 3 below. The author assumes that these differences are due to rounding for the ORIGEN set.

Though the differences in the ^{235}U thermal neutron fission yield fractions for the two codes are quite small (and therefore unlikely to generate large differences in results for the reactors modeled in this study), Table 3 also lists the ^{235}U fast neutron fission yield fractions, and many of these are quite different from the thermal neutron values. For example, the fast fission yields for the zirconium isotopes are quite different from the thermal neutron values, particularly for ^{92}Zr . Based upon this table, we would expect, for

any reactor model that had a significant fast neutron component to the neutron flux, that the ORIGEN-S code would over predict the quantity of ^{92}Zr .

<i>Fission Product</i>	<i>Origen.rev02.pwrlib 235U Fission Yield Fraction</i>	<i>Cinder.dat 235U Thermal Fission Yield Fraction</i>	<i>Cinder.dat 235U Fast Fission Yield Fraction</i>
⁹⁷ Mo	2.4900x10 ⁻⁸	2.48982x10 ⁻⁸	9.93991x10 ⁻⁹
⁹⁸ Mo	9.5790x10 ⁻⁷	9.57932x10 ⁻⁷	4.22996x10 ⁻⁷
¹⁰⁰ Mo	7.2950x10 ⁻⁴	7.29498x10 ⁻⁴	1.07399x10 ⁻⁴
¹³⁸ Ba	4.1160x10 ⁻⁵	4.11571x10 ⁻⁵	2.12998x10 ⁻⁵
¹⁴⁰ Ce	1.1500x10 ⁻⁹	1.14992x10 ⁻⁹	3.56997x10 ⁻¹⁰
¹⁴² Ce	1.7600x10 ⁻⁶	1.75988x10 ⁻⁶	7.11994x10 ⁻⁷
¹⁴⁸ Nd	9.9290x10 ⁻⁶	9.92930x10 ⁻⁶	5.17996x10 ⁻⁶
⁷² Ge	3.6400x10 ⁻¹³	3.63974x10 ⁻¹³	1.35999x10 ⁻¹²
⁹⁰ Sr	7.3710x10 ⁻⁴	7.37128x10 ⁻⁴	3.43157x10 ⁻⁴
⁹¹ Y	1.6500x10 ⁻⁶	1.64988x10 ⁻⁶	8.59993x10 ⁻⁷
⁹¹ Zr	4.4200x10 ⁻¹⁰	4.41969x10 ⁻¹⁰	2.00998x10 ⁻¹⁰
⁹² Zr	1.1900x10 ⁻⁴	1.18982x10 ⁻⁴	1.66999x10 ⁻⁸
⁹³ Zr	1.3700x10 ⁻⁶	1.36990x10 ⁻⁶	4.92996x10 ⁻⁷
⁹⁴ Zr	1.9490x10 ⁻⁴	1.94946x10 ⁻⁴	1.29099x10 ⁻⁵
⁹⁵ Zr	1.2720x10 ⁻³	1.27244x10 ⁻³	1.47749x10 ⁻⁴
¹³⁰ Te	5.7870x10 ⁻⁴	5.78719x10 ⁻⁴	2.40188x10 ⁻⁴
¹³¹ I	3.9160x10 ⁻⁵	3.91572x10 ⁻⁵	1.08099x10 ⁻⁵
¹³⁵ I	2.9270x10 ⁻²	2.92737x10 ⁻²	3.60323x10 ⁻²
¹³¹ Xe	1.4200x10 ⁻⁹	1.41990x10 ⁻⁹	8.45993x10 ⁻¹⁰
¹³² Xe	4.2200x10 ⁻⁷	4.21970x10 ⁻⁷	1.70999x10 ⁻⁷
¹³⁴ Xe	1.0550x10 ⁻⁴	1.05483x10 ⁻⁴	5.06096x10 ⁻⁵
¹³⁵ Xe	7.8510x10 ⁻⁴	7.85125x10 ⁻⁴	1.19610x10 ⁻³
¹³⁶ Xe	2.1920x10 ⁻²	2.19242x10 ⁻²	1.71223x10 ⁻²
¹³⁴ Cs	3.8550x10 ⁻⁸	3.85473x10 ⁻⁸	2.51998x10 ⁻⁸
¹³⁷ Cs	6.0000x10 ⁻⁴	5.99988x10 ⁻⁴	2.28352x10 ⁻³
¹³⁹ La	2.2700x10 ⁻⁷	2.26984x10 ⁻⁷	8.91992x10 ⁻⁸
¹⁴⁹ Sm	1.7100x10 ⁻¹²	1.70988x10 ⁻¹²	5.71995x10 ⁻¹³
¹⁶¹ Dy	2.5100x10 ⁻¹³	2.50982x10 ⁻¹³	2.14998x10 ⁻¹³

Table 3: MCNPX and ORIGEN-S 235U Fission Product Yields for Several Nuclides

Chapter 3: The BWR Reactor Model

3.1 THE MODEL

The BWR model was developed using two primary references: 1) the Scale 5.1 Manual⁵ and 2) ORNL/TM-1999/193, *Investigation of Burnup Credit Modeling Issues Associated with BWR Fuel*⁸.

Table 4 lists the design and operating parameters used for the MCNPX BWR model. Reactor design parameters in Table 4 were found in the literature^{5,8}. The uranium mass in the model was determined by MCNPX based upon the given density, composition, and dimensions of the fuel. Typically, one third of a US commercial nuclear reactor's fuel is changed out every year. Each fuel assembly typically has a dwell time of 3 years. The burnup for the BWR and PWR fuel assemblies in this study were taken to 42 GWd/MTU which is a typical maximum burnup value for BWR commercial reactor fuel. However, the burnup in the model is accelerated achieving the maximum burnup value in less than one year. This power profiles for the MCNPX and ORIGEN-ARP files are identical; therefore, this accelerated burnup does not adversely affect the comparison of results between the two codes. Appendix A contains the MCNPX input deck used for this study. Table 5 below lists the ORIGEN-ARP input parameters.

The BWR model is a GE 8x8-4 type reactor with 60 UO₂ fuel rods of various enrichments and one large water rod located at the center of the fuel assembly. Nine of the fuel rods contain 2.6% natural gadolinium, used as a burnable neutron poison, mixed in with the fuel. The presence of the gadolinium, specifically ¹⁵⁵Gd and ¹⁵⁷Gd which

have extremely large thermal neutron absorption cross sections, in a BWR design results in a more uniform power generation rate over the life of the fuel assembly. When the fuel is fresh, the gadolinium absorbs neutrons resulting in lower power generation in those rods. As the gadolinium content in the fuel rods is depleted through neutron absorptions, positive reactivity is generated due to the increase in thermal neutron flux. This positive reactivity will balance out the negative reactivity created by the decrease in the ^{235}U -content in the non-gadolinium containing fuel rods as the fuel burns.

Reactor Design and Operating Data for MCNPX BWR Model	
Fuel Assembly Type	GE 8x8-4 BWR
Fuel Type	UO ₂ pellet
Fuel Density	9.863 g/cm ³
Fuel Temperature	1128 K
Fuel Diameter	10.566 mm
Fuel Enrichment	1.8 to 3.9 % ²³⁵ U
Fuel Height	381 cm
Fuel Rod Pitch	1.6256 cm
Number of Fuel Rods per Assembly	60 fuel rods with 1 water hole
Cladding	Zircaloy-4
Cladding Thickness	0.0813 cm
Cladding Temperature	560 K
Cladding Density	6.52 g/cm ³
Moderator/Coolant	H ₂ O
Moderator Density	0.6 g/cm ³
Moderator Temperature	553 K
Gadolinium Content	2.6% in 9 fuel rods
Total Uranium Mass	173,557 g (0.173557 MTU)
Reactor Operating Power	30.9 MW
Reactor Operating Time	240 Days
Total Fuel Burnup	43 GWd/MTU

Table 4: BWR Design and Operating Data for MCNPX Model

<i>Reactor Design and Operating Data for ORIGEN-ARP Model</i>	
<i>Fuel Assembly Type</i>	GE 8x8-4 BWR
<i>Fuel Type</i>	UO ₂
<i>Fuel Enrichment (average)</i>	3.23 w/o
<i>²³⁴U Initial Mass</i>	49.92 g
<i>²³⁵U Initial Mass</i>	5,607 g
<i>²³⁸U Initial Mass</i>	167,900 g
<i>Total Uranium Mass</i>	173,557 g (0.173557 MTU)
<i>Reactor Operating Power</i>	30.9 MW
<i>Reactor Operating Time</i>	240 Days
<i>Total Fuel Burnup</i>	43 GWd/MTU

Table 5: BWR Design and Operating Data for ORIGEN-ARP Model

The MCNPX model is a much higher fidelity model than the ORIGEN-ARP model in terms of the input deck. MCNPX allows the specific reactor assembly geometry, multiple fuel enrichments, and masses of non-actinide materials (including the burnable poisons and moderator for the BWR fuel assembly) to explicitly be defined in the model. The neutron fluxes are actually calculated at each time step based upon neutron interactions using the Monte Carlo method. Materials in the model, including any burnable poisons, such as gadolinium, directly affect the neutron flux calculations.

The ORIGEN-ARP model requires only the initial actinides present in the fuel to be input into the input deck. Gadolinium quantities were added to the ORIGEN-ARP

model only to track their depletion. The addition of gadolinium (or any non-actinide material) to the ORIGEN-ARP model does not affect the results in the same manner as does the addition of gadolinium to the MCNPX model. This is because the ARP effective cross sections, which are a function of burnup, have the various reactor parameters, including the presence of burnable poisons and moderator material, factored into them. Neutron fluxes at each time step are calculated based upon the neutron fluxes of the previous time step.

For example, Figures 20 and 21 illustrate the depletion of the ^{155}Gd and ^{157}Gd content in the BWR assembly fuel in the MCNPX model. The quantities of ^{155}Gd and ^{157}Gd are essentially depleted (having been converted to the ^{156}Gd and ^{158}Gd , respectively through neutron capture) at a Burnup of 10 GWd/MTU.

The results of ORIGEN-ARP indicate a much quicker decrease in the ^{155}Gd and ^{157}Gd content.

Figure 22 is a plot of the ENDF-B/VII radiative capture cross section for ^{155}Gd and ^{157}Gd . This plot illustrates why these isotopes are such effective neutron poisons for thermal reactors.

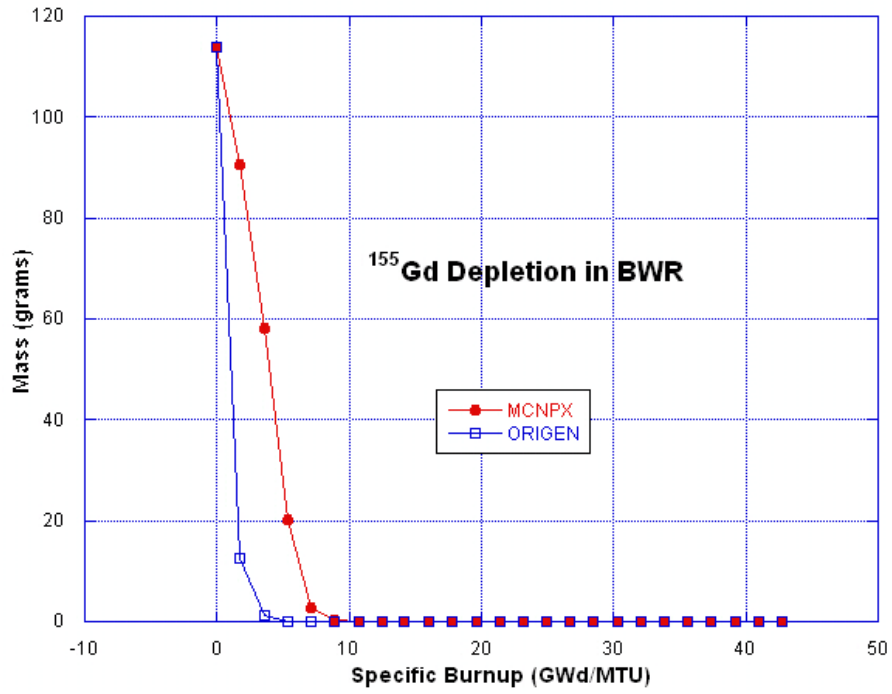


Figure 20: Plot of ¹⁵⁵Gd Depletion in BWR Models

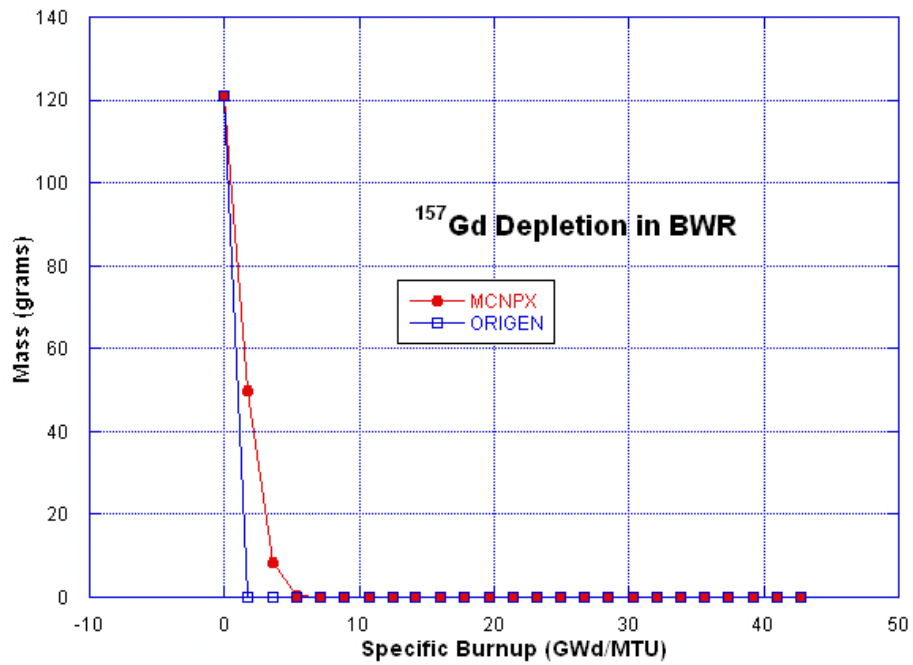


Figure 21: Plot of ¹⁵⁷Gd Depletion in BWR Models

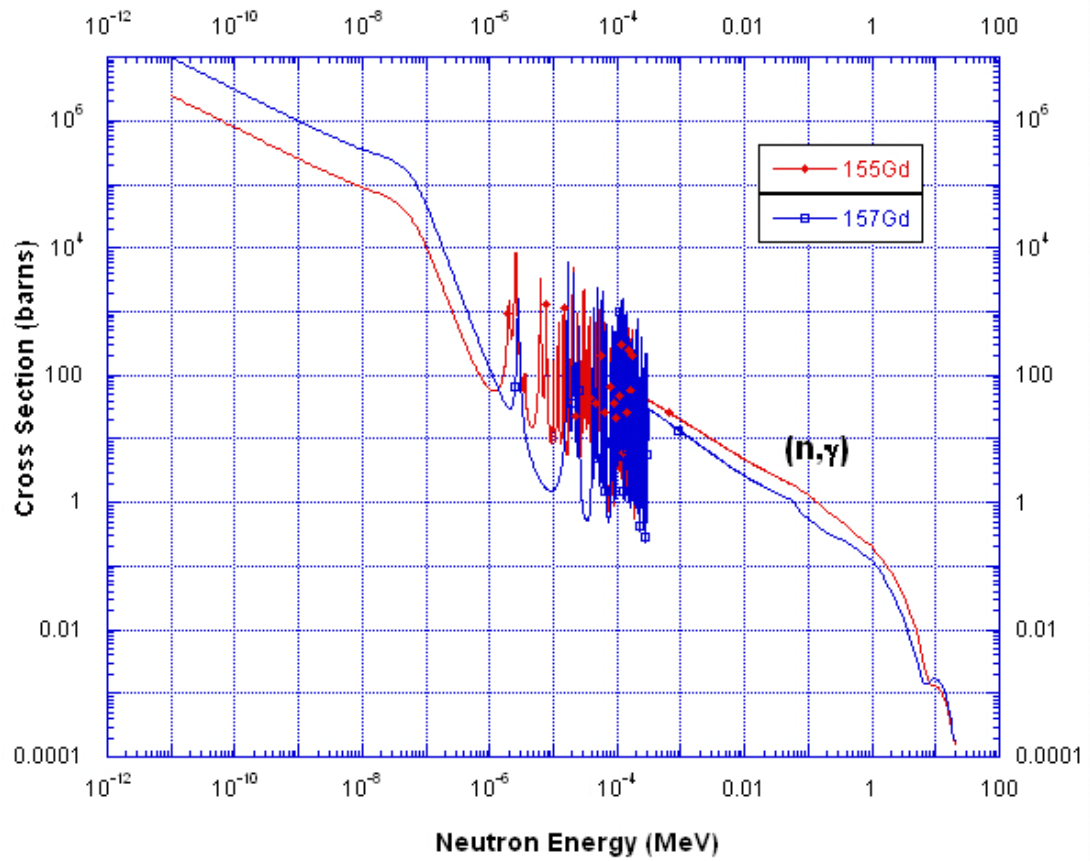


Figure 22: Plot of Radiative Capture Cross Sections for ^{155}Gd and ^{157}Gd (ENDF-B/VII)

Figure 23 is a VisEd plot of a two-dimensional view of the MCNPX model of the BWR reactor fuel assembly showing the UO_2 fuel rods in red and the gadolinium-loaded fuel rods in green.

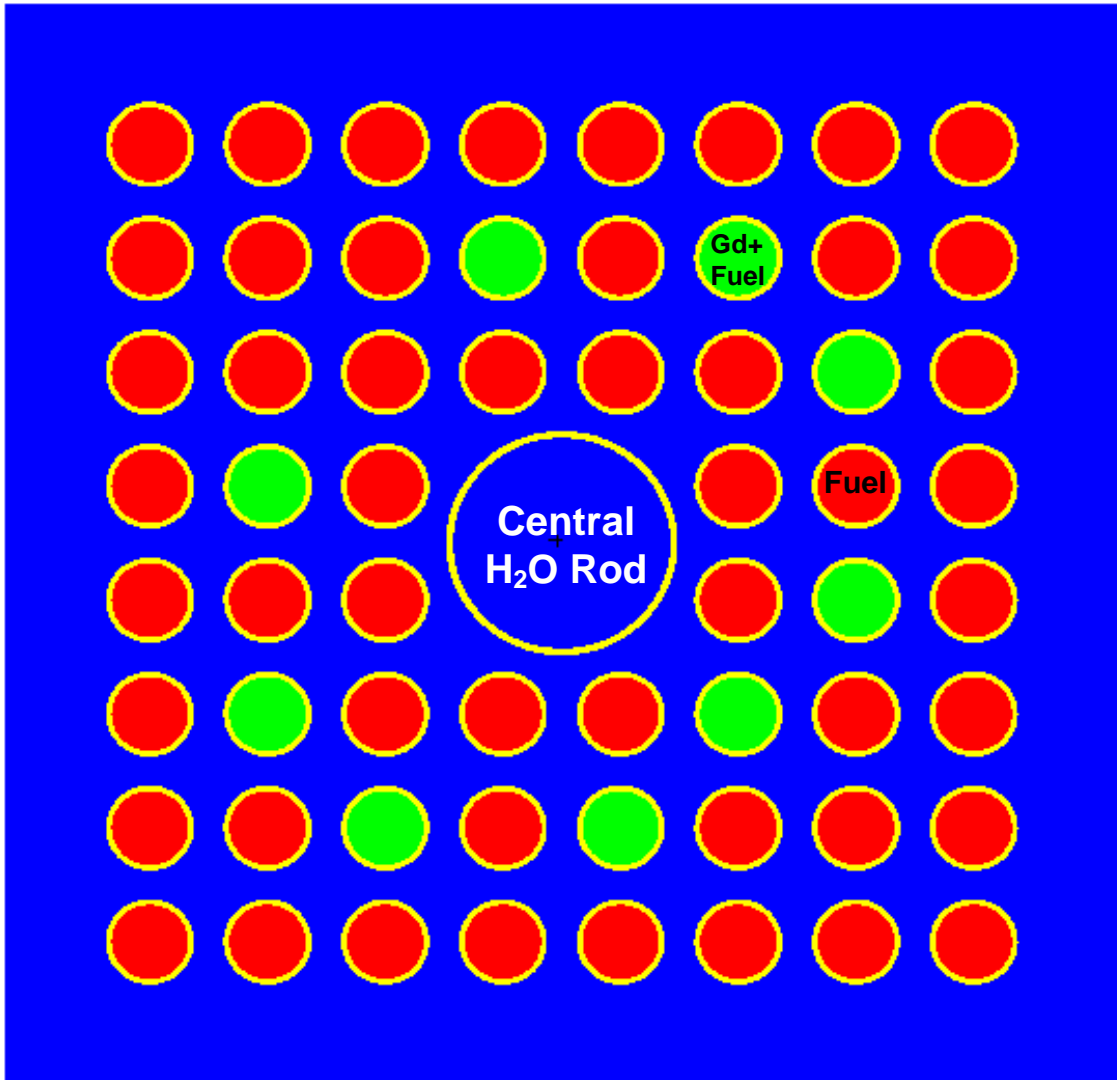


Figure 23: VisEd Plot of BWR Fuel Assembly

Figure 24 is a VisEd plot of a two-dimensional view of a single fuel rod cell of the MCNPX BWR model illustrating fuel radius, cladding thickness, air gap thickness, and rod pitch. The cladding is 0.0813 cm thick and is composed of Zircaloy-4 material.

An air gap of 0.0038 cm was placed into the MCNPX model. However, the author performed runs of the model with and without the air gap. The difference between the results of the two models was insignificant for the generated isotopes of interest in this study.

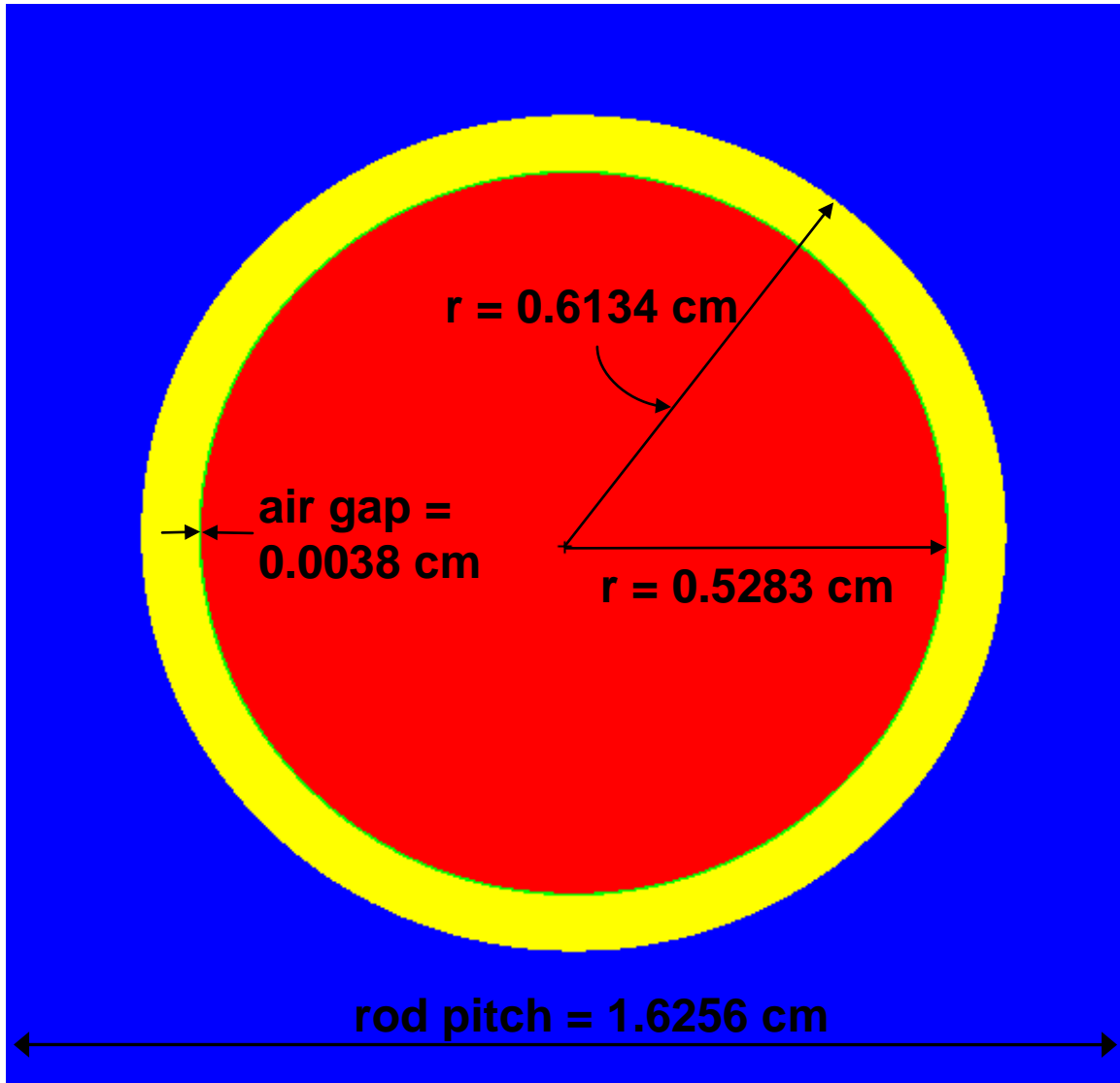


Figure 24: Single Fuel Lattice Element for the BWR Model

Figure 25 is a VisEd plot of a two-dimensional view of the MCNPX BWR model illustrating the ^{235}U enrichment loading of the fuel assembly. The gadolinium-loaded fuel rods contain fuel enriched to 3.2 weight percent ^{235}U . The fuel assembly loading is per ORNL/TM-1999/193, *Investigation of Burnup Credit Modeling Issues Associated with BWR Fuel*⁸.

Fuel enrichment within the fuel assembly varies from 1.8% to 3.9% ^{235}U . MCNPX gives the user the freedom to model individual fuel rod enrichments and burnable poison rods. In contrast, ORIGEN-ARP uses pre-generated reactor specific cross sections that are a function of fuel burnup. According to the ORIGEN-ARP Manual⁵, the cross sections for the BWR fuels have been generated using the two-dimensional lattice physics code NEWT as applied in the TRITON depletion analysis module. In contrast, MCNPX models a three-dimensional system.

With the built-in GUI, ORIGEN-ARP provides a greater ease of setting up the calculation than does MCNPX. Also, ORIGEN-ARP completes the calculation much more quickly. The MCNPX BWR model in this study takes approximately 5 days to run on a Windows XP format PC. The ORIGEN-ARP model runs in about a minute on the same PC.

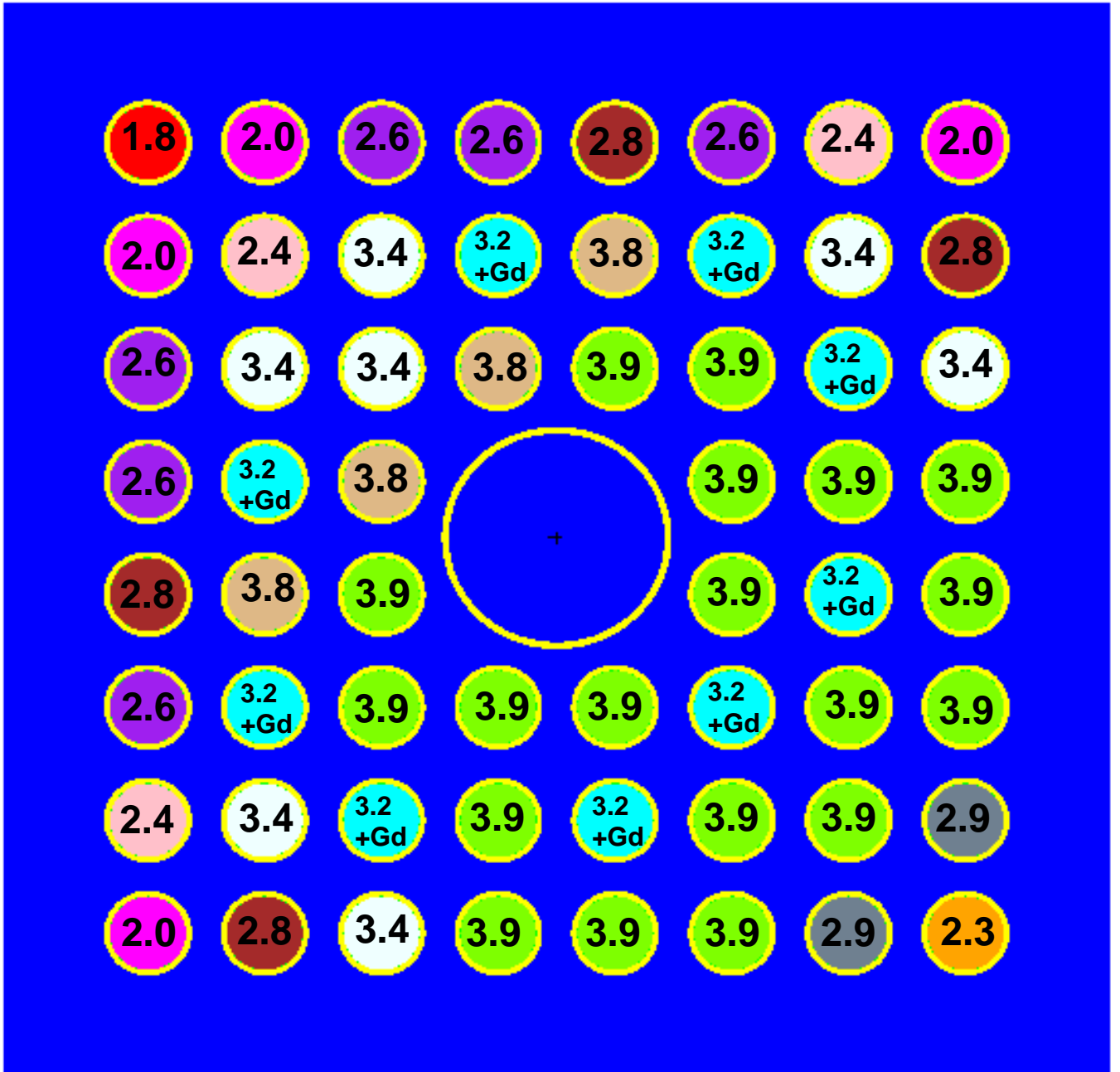


Figure 25: ^{235}U Enrichment Loading of BWR Fuel Assembly for MCNPX Model

3.2 THE RESULTS

Table 6 lists the 46 nuclides analyzed in this study. The actinides listed are some of the more abundant actinides found in spent UO_2 fuel, were identified by one of the references as a fission product of nuclear forensics interest, and/or produced a significant R_c ratio as described in Chapter 1. The burnup indicator nuclides² are common fission product nuclides used to determine the burnup values of fuels. As shown in Appendices D, E, and F, the quantity of these burnup indicators increase linearly as a function of fuel burnup and are generally independent of reactor power for a given burnup value. These nuclides are not radioactive (i.e. stable) and have relatively small thermal neutron absorption cross section. So in terms of nuclide quantities produced by fission, “what you get is what you see” for these burnup indicators. However, it should be noted that these are not “shielded” nuclides. It is possible for quantities of these nuclides to be produced from in-decay and from absorption reactions of other nuclides. The other fission products of interest are other commonly produced fission products of thermal ^{235}U fission in UO_2 fuel.

<i>Actinides</i>	<i>Burn Up Indicators</i>	<i>Other Fission Products of Interest</i>
^{234}U	^{97}Mo	^{90}Sr
^{235}U	^{98}Mo	^{91}Y
^{236}U	^{100}Mo	^{91}Zr
^{238}U	^{138}Ba	^{92}Zr
^{239}U	^{140}Ce	^{93}Zr
^{237}Np	^{142}Ce	^{94}Zr
^{238}Np	^{148}Nd	^{95}Zr
^{239}Np		^{130}Te
^{238}Pu		^{131}I
^{239}Pu		^{135}I
^{240}Pu		^{131}Xe
^{241}Pu		^{132}Xe
^{242}Pu		^{134}Xe
^{241}Am		^{135}Xe
^{243}Am		^{136}Xe
^{242}Cm		^{134}Cs
^{245}Cm		^{137}Cs
^{246}Cm		^{139}La
		^{149}Sm
		^{161}Dy
		^{72}Ge

Table 6: Nuclides Analyzed in the Comparison of the Two Models

The results of the comparisons of all 46 nuclides of interest can be found in Appendix D. Figure 26 is a plot of ^{235}U depletion. Depletion occurs primarily due to

thermal fission, although some loss occurs from radiative capture. The plot shows good agreement between the MCNPX and the ORIGEN-ARP models. At the higher burnup values, the ORIGEN-ARP model has a higher ^{235}U value than does the MCNPX model. This suggests that more ^{235}U is depleted in the MCNPX model.

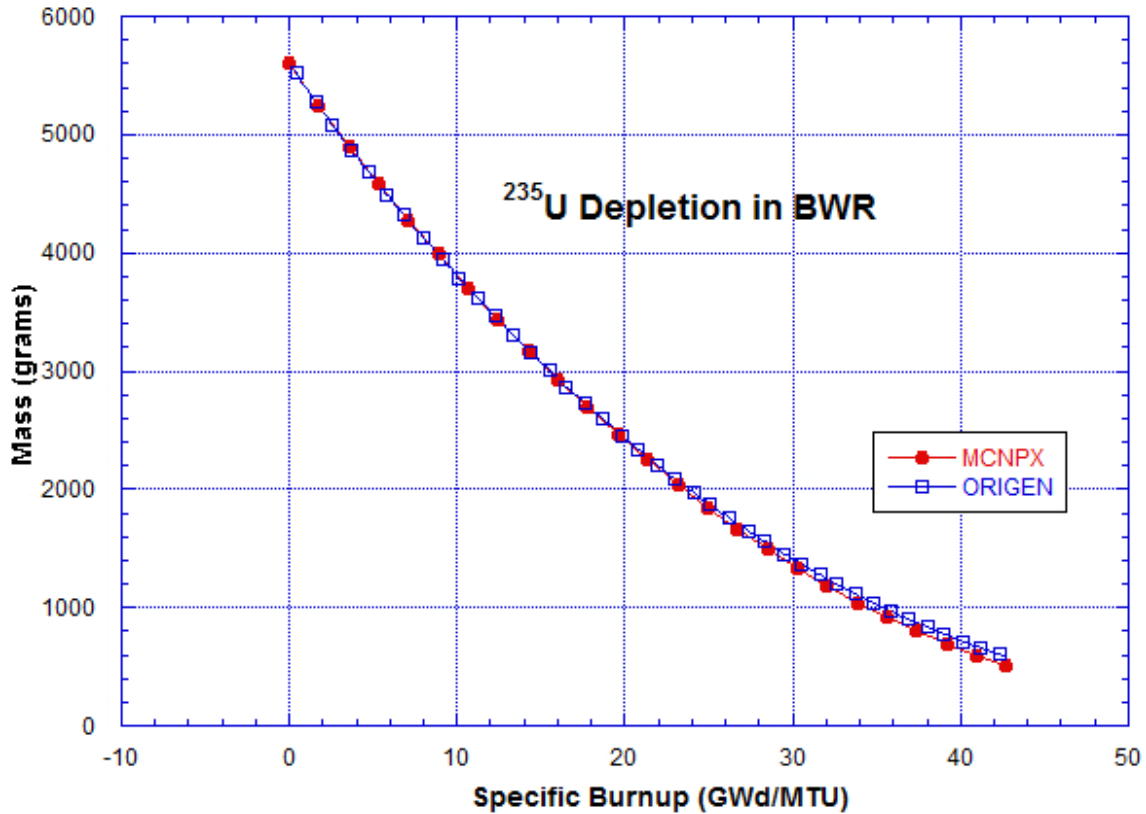


Figure 26: ^{235}U Depletion in BWR Models

Both models begin with identical quantities of uranium fuel, and both models experience the same power profile. However, the models generate different results because the two models generate the source terms in two different ways (one model is probabilistic and the other deterministic), the time-dependent neutron spectra will differ

for each model. If the parameters and approximations going into both models are correct, the results should agree reasonably well with each other. Though it is not possible to unfold the time- and energy- dependent neutron spectra of the two models by comparing the nuclide quantities of a few nuclides, the differences can tell us a little about total flux and qualitative flux shape. Again, the purpose of this study was to generate the two models using available data, and compare the results. Available fuel design and operating data for the ORIGEN-ARP reactor type was used in the MCNPX model. Also, data entered explicitly into the ORIGEN-ARP GUI (e.g. operating parameters in Table 5) was also entered into the MCNPX model. It should be noted that the author was able to generate similar results by increasing the moderator density in the ORIGEN-ARP model.

Loss of ^{235}U occurs primarily due to 1) fission, 2) radiative capture, and 3) radioactive decay. Because ^{235}U is fissile, it fissions with neutrons of any energy, including thermal neutrons. The half-life of ^{235}U is 7.04×10^8 years; therefore, ^{235}U decay during the irradiation time period in this study is negligible. Figure 27 is a plot of ENDF/B-VII.0 cross sections for radiative capture and fission cross section for ^{235}U . Fission of ^{235}U dominates over radiative capture. Therefore, one may conclude that the primary loss mechanism for ^{235}U in a BWR thermal nuclear reactor is through neutron-induced fission. Because there is more ^{235}U loss in the MCNPX model, it appears as if the total flux in the MCNPX model is greater than the total flux in the ORIGEN-ARP model, or the MCNPX model has a larger thermal flux component, or both.

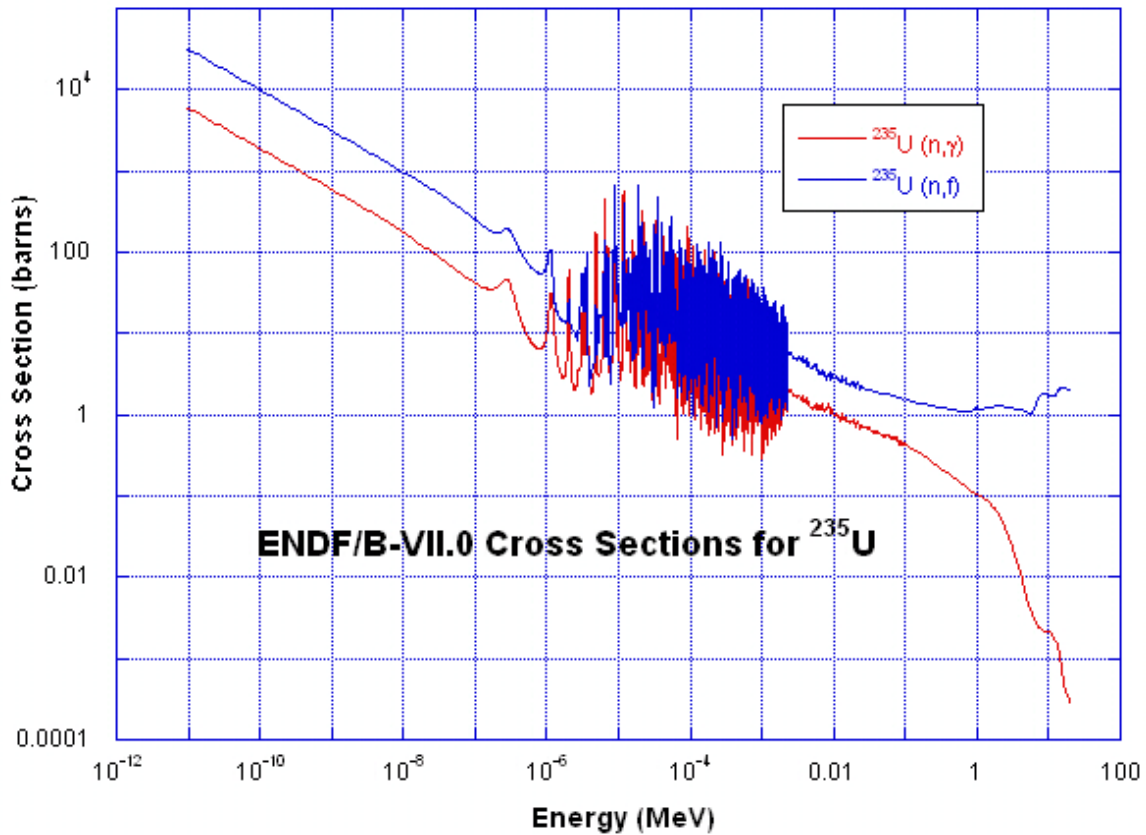


Figure 27: ^{235}U Radiative Capture and Fission Cross Sections

The ^{238}U depletion calculations for both models are in very good agreement (See Figure 28 below). However, the quantity of ^{238}U is very large compared to the ^{239}Pu produced. There is about a 400 g difference in ^{238}U depletion calculations at 42.7 GWd/MTU; therefore, the ORIGEN-ARP model is losing ^{238}U at a faster rate than the MCNPX model. There are three primary loss mechanisms for ^{238}U : 1) radioactive decay, 2) radiative capture and 3) fission. The half-life of ^{238}U is 4.47×10^9 years. Again, ^{238}U decay during the irradiation time period in this study is negligible. Radiative capture of

^{238}U generates ^{239}U which then undergoes two successive β^- decays transforming into ^{239}Pu .

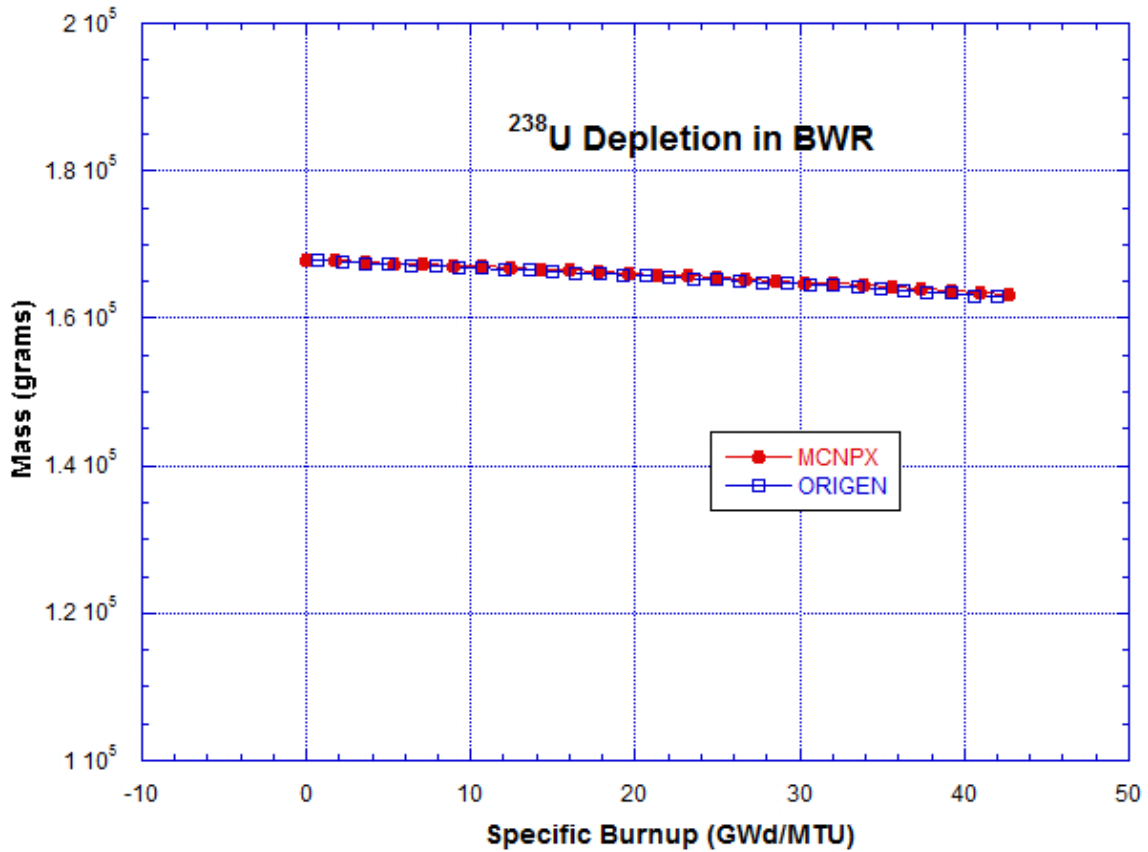


Figure 28: ^{238}U Depletion in BWR Models

Figure 29 is a plot of the ^{239}Pu production in BWR models. There is a significant difference (~17 percent) in the quantities of ^{239}Pu produced in the two models. The ORIGEN-ARP model produces about 150 grams more ^{239}Pu than the MCNPX model (at 42.7 GWd/MTU burnup). As mentioned previously, ^{239}Pu is produced primarily through

radiative capture by ^{238}U followed by two successive β^- decays. Therefore, the conversion of ^{238}U to ^{239}Pu is occurring more frequently in the ORIGEN-ARP model than in the MCNPX model.

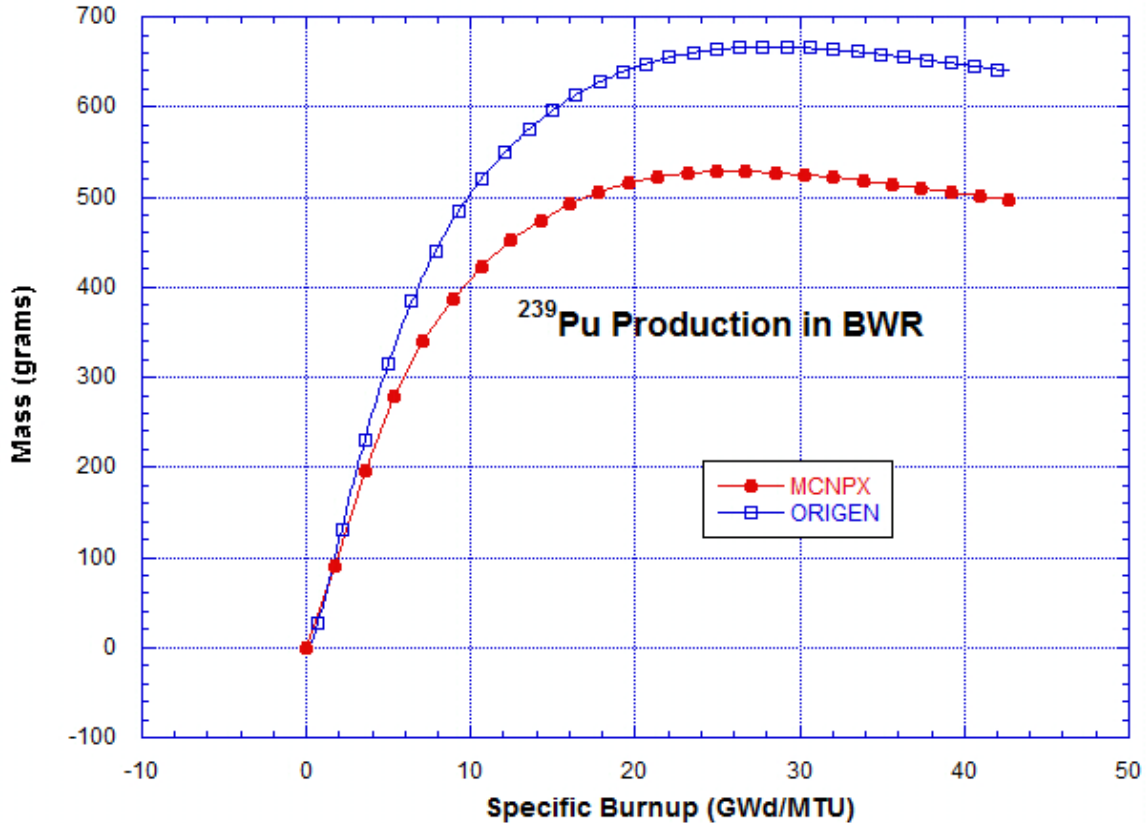


Figure 29: ^{239}Pu Production in BWR Models

Figure 30 is a plot of the ^{238}U radiative capture cross sections including 1) the ENDF/B-VII.0 “continuous” cross sections, 2) the 63-group MCNPX cross sections found in the *cinder.dat* file, and 3) the 3-group ORIGEN-S cross sections. This plot suggests that if the generated neutron flux had predominance in the 100 keV to 1 MeV range, then it is possible that the ORIGEN-ARP code might overestimate the ^{238}U

radiative cross section reactions. However, it is more probable that the source term for the MCNPX model differs somewhat significantly than that of the ORIGEN-ARP model.

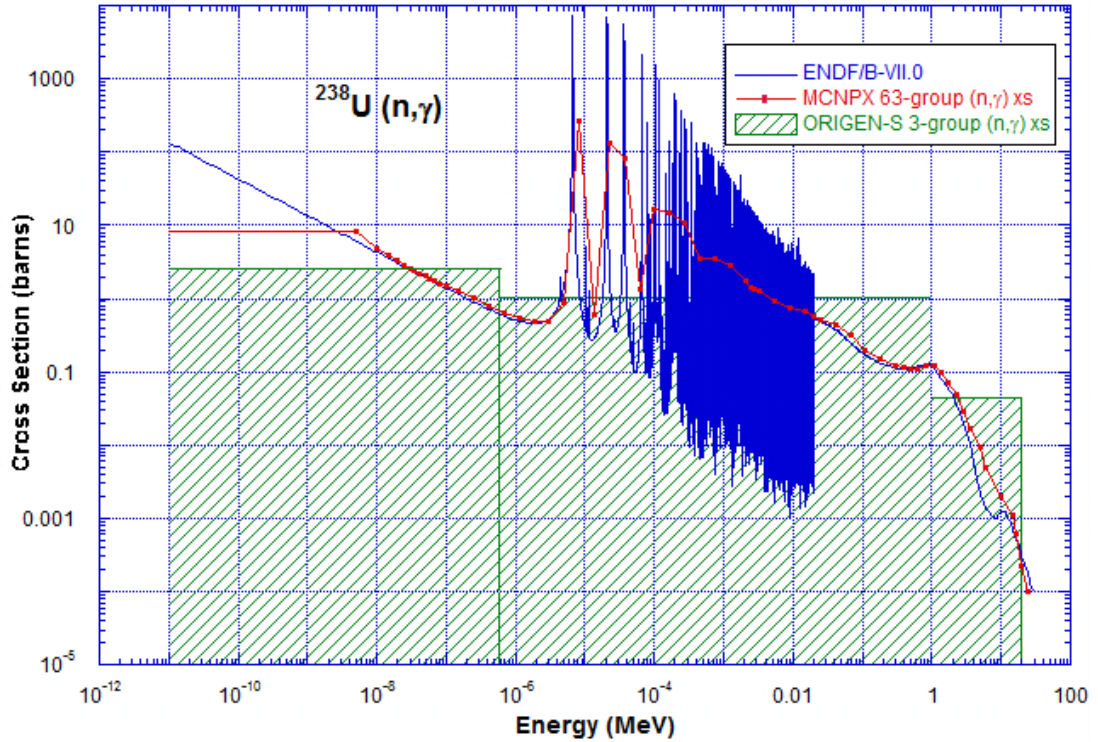


Figure 30: ^{238}U Radiative Capture Cross Sections

Figure 31 below is a plot of the ENDF/B-VII.0 ^{235}U fission cross sections and ^{238}U fission and radiative capture cross sections. The fission cross sections for ^{235}U are greater than the fission cross sections for ^{238}U at all neutron energies. The radiative capture cross section of ^{238}U is higher than the fission cross section of ^{238}U until approximately 1 MeV when the ^{238}U cross sections approaches values similar to those for ^{235}U fission. Table 8 below is a table of the calculated ^{238}U fission rates for the

ORIGEN-ARP and the MCNPX models. The MCNPX model has a greater ^{238}U fission rate than the ORIGEN-ARP model. Of course, the fission rate is proportional to the quantity of material, but the ^{238}U fission rate per gram of ^{238}U , also, is greater in the MCNPX model.

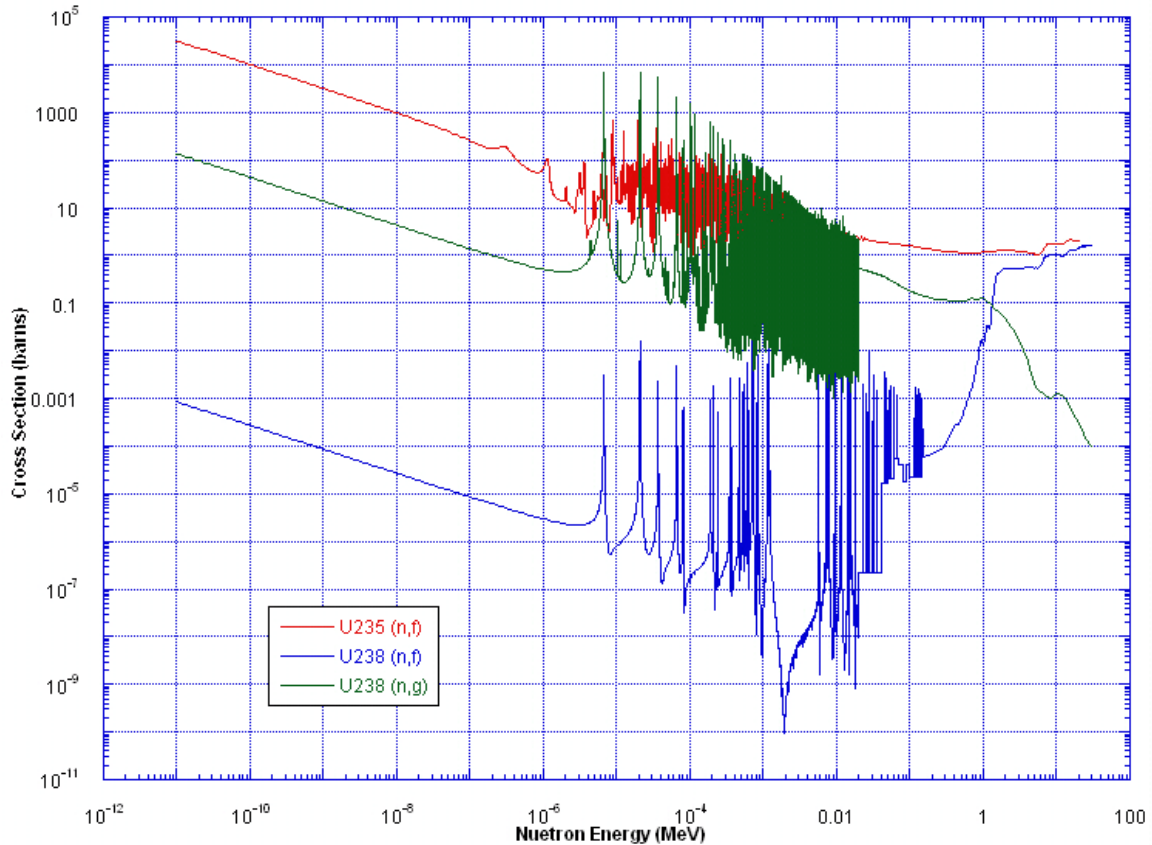


Figure 31: ^{235}U Fission Cross Sections and ^{238}U Fission and Radiative Capture Cross Sections

Because the rate of ^{238}U radiative capture is greater in the ORIGEN-ARP model and the rate of ^{238}U fission is greater in the MCNPX model, one may conclude that the ORIGEN-ARP neutron flux has a greater thermal component (or alternatively, lesser fast component) than the MCNPX model. Combined with the fact that more ^{235}U fission is

occurring in the MCNPX model suggests that the total (one energy group) neutron flux in the MCNPX model is greater than the total neutron flux in the ORIGEN-ARP model. Also, as shown in Figures 20 and 21 above, the ^{155}Gd and ^{157}Gd quantities decrease much more quickly (due to (n,γ) reactions) in the ORIGEN-ARP model than in the MCNPX model. This also points to the ORIGEN-ARP model having a greater relative thermal neutron flux than the MCNPX model.

Figure 32 is a plot of the ^{240}Pu production in the BWR models. The quantity of ^{240}Pu is slightly greater in the ORIGEN-ARP model than the MCNPX model. Because ^{240}Pu is produced primarily from radiative capture of ^{239}Pu , it is expected that the ORIGEN-ARP model (which generates more ^{239}Pu for a given burnup value) to have larger quantities of ^{240}Pu .

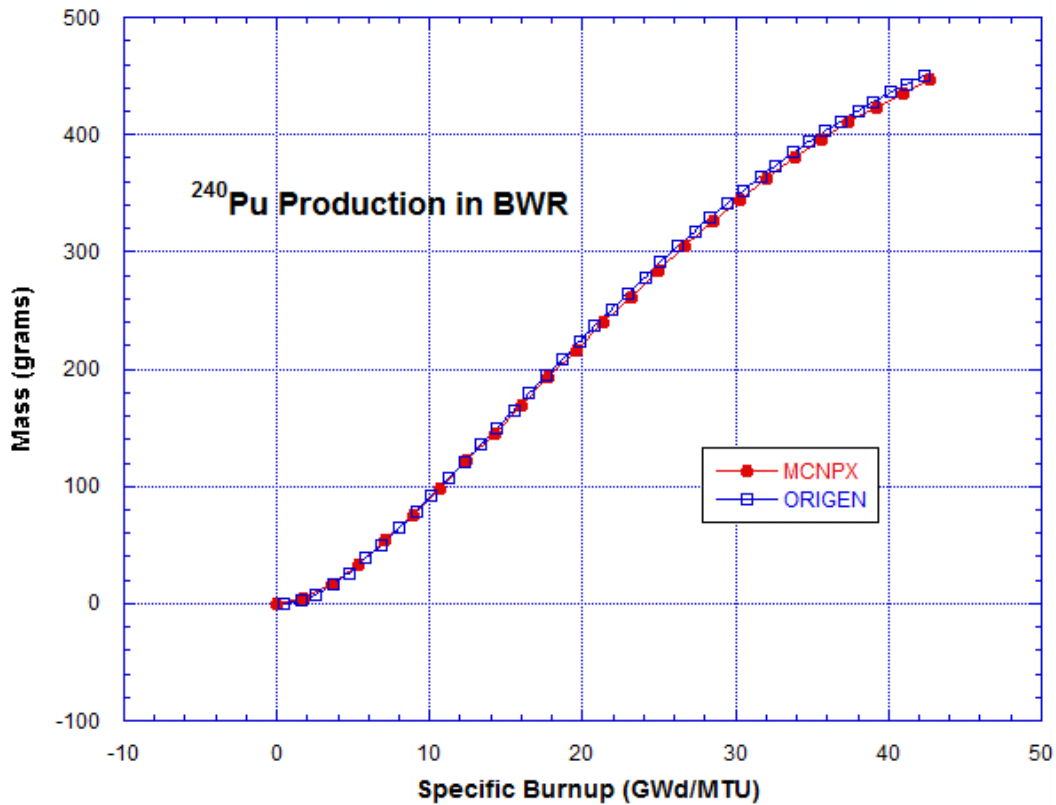


Figure 32: ^{240}Pu Production in BWR Models

Figure 33 is a plot of ^{238}Np production in the models. ^{238}Np is produced primarily from radiative capture reactions in ^{237}Np . ^{238}Np loss is primarily due to β^- decay into ^{238}Pu and radiative capture reactions which produce ^{239}Np . The agreement between the models is good with an approximate 8 percent maximum difference between the results.

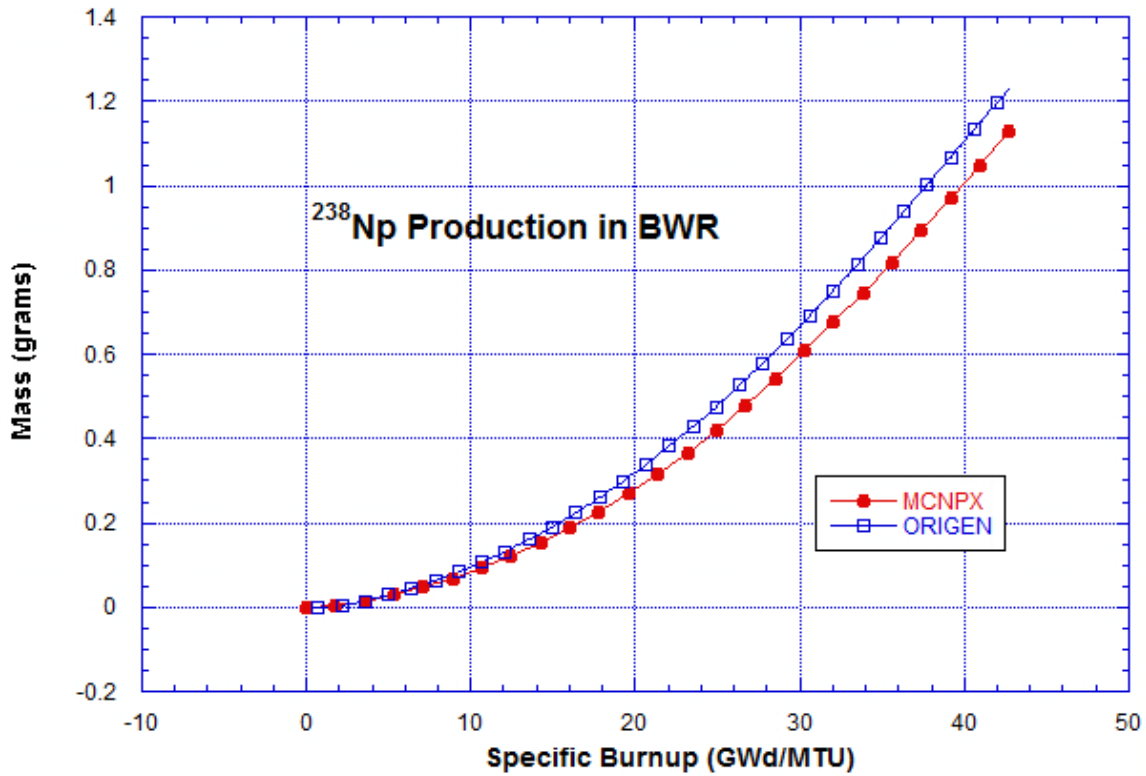


Figure 33: ^{238}Np Production in BWR Models

Figure 34 is a plot of ^{243}Am production in the BWR models. The quantity of ^{243}Am produced in the ORIGEN-ARP model is greater than 20% more than the MCNPX model. ^{243}Am is produced primarily from β^- decay of ^{243}Pu or radiative capture by ^{242}Am . Both processes trace back to the quantity of ^{239}Pu produced. Because the ORIGEN-ARP model has more ^{239}Pu , the ORIGEN-ARP model will also have more ^{243}Am .

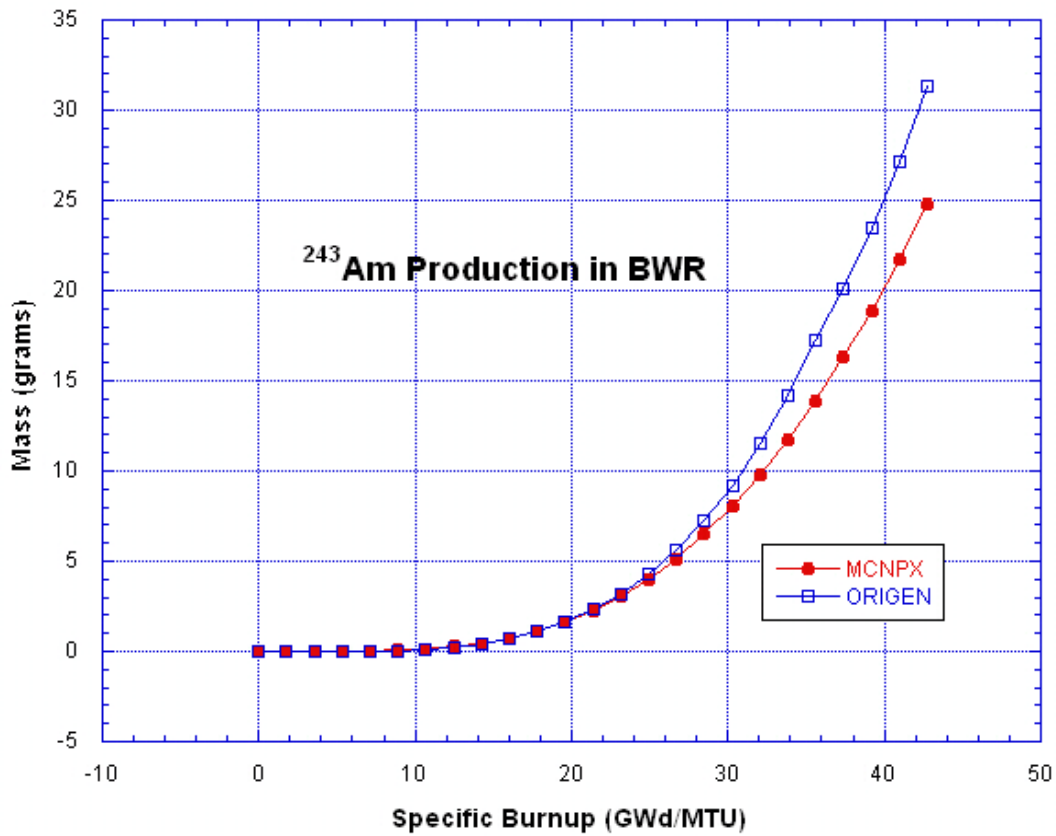


Figure 34: ²⁴³Am Production in BWR Models

Figure 35 is a plot of ²⁴⁵Cm production in the BWR models. Unlike many of the other actinide plots, this plot shows a greater quantity produced in the MCNPX model than in the ORIGEN-ARP model. This may be due to the fact that to produce the higher actinides, multiple n,γ reactions are necessary. This is best achieved in a high flux environment. Assuming that the MCNPX model has a significantly higher total flux would explain the greater quantities of curium isotopes in the MCNPX model.

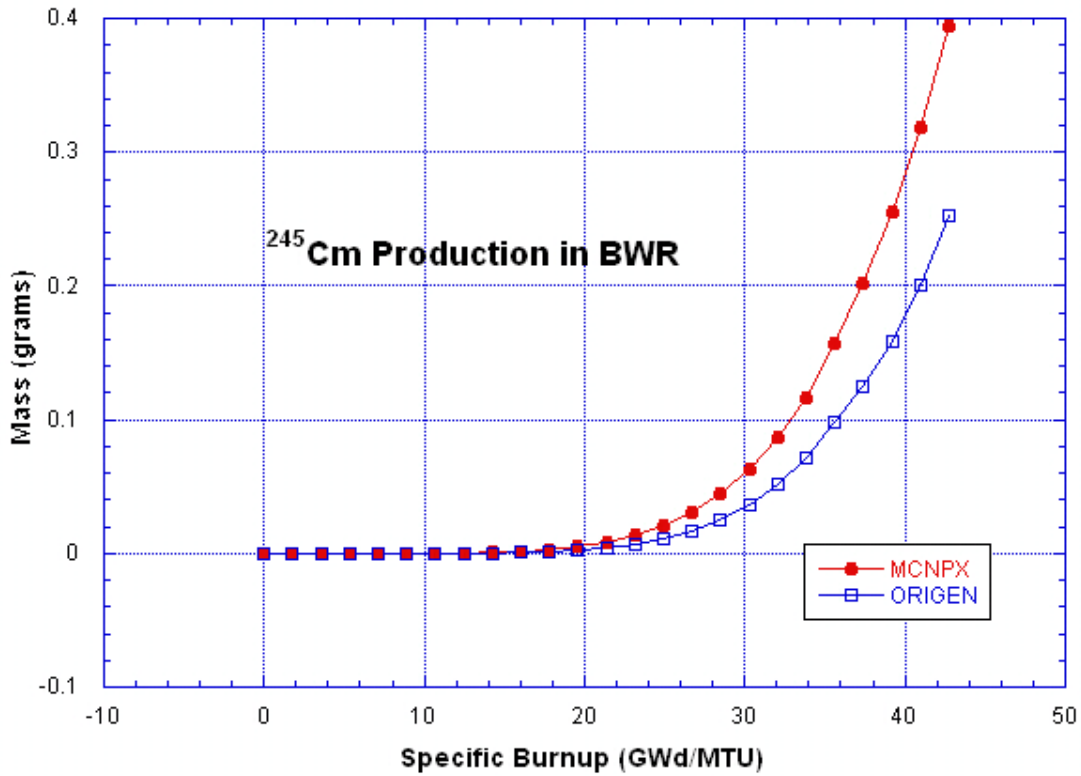


Figure 35: ^{245}Cm Production in BWR Models

Figure 36 is a plot of ^{91}Y production in the BWR models. ^{91}Y is a fission product and is produced primarily (in these models) via the fission of ^{235}U and ^{239}Pu . The ORIGEN-ARP total production of ^{91}Y is slightly larger than that of the MCNPX model. This is due to the greater quantity of ^{239}Pu produced in the ORIGEN-ARP model. At low burnups, the plot is linear. As the burnup value increases, the plot turns over. This is due to the radioactive decay of the ^{91}Y which has a half-life of 58.5 days.

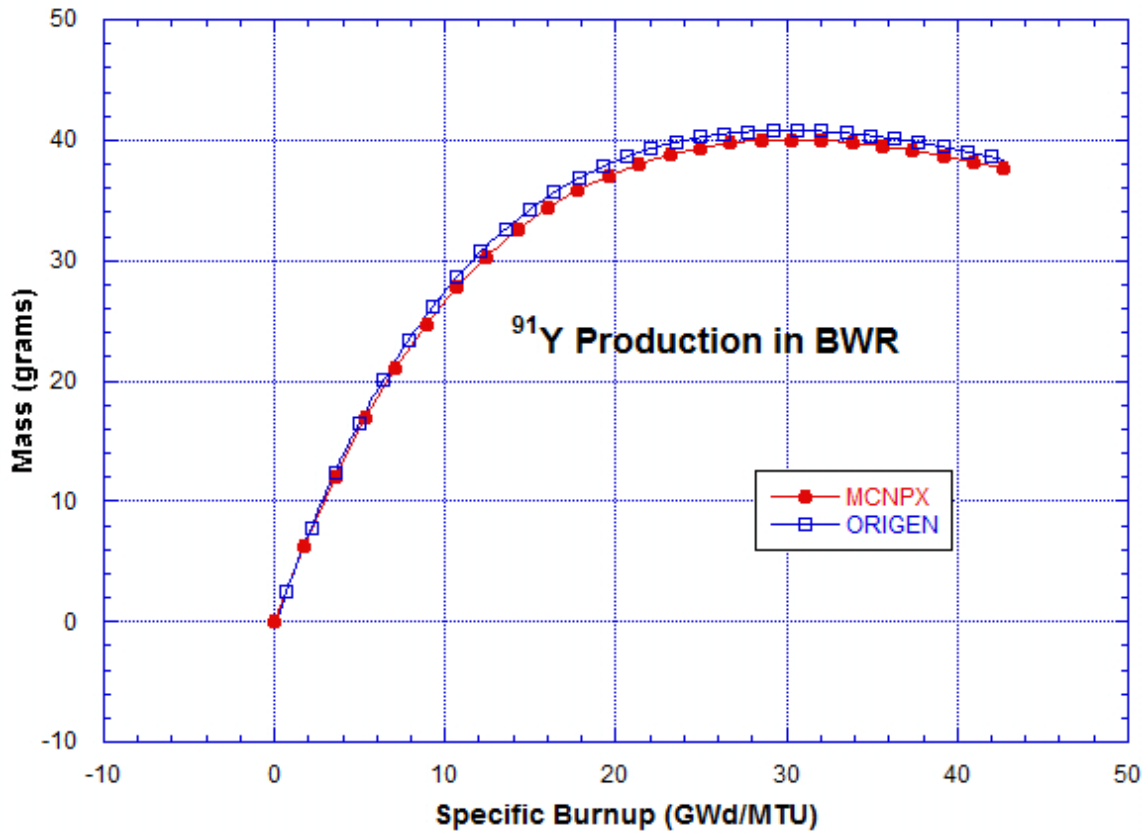


Figure 36: ⁹¹Y Production in BWR Models

Figure 37 is a plot of the ¹³¹Xe production in the BWR models. Again, this nuclide is a fission product, and the ORIGEN-ARP value is slightly higher due to the greater quantity of ²³⁹Pu undergoing fission in the ORIGEN-ARP model.

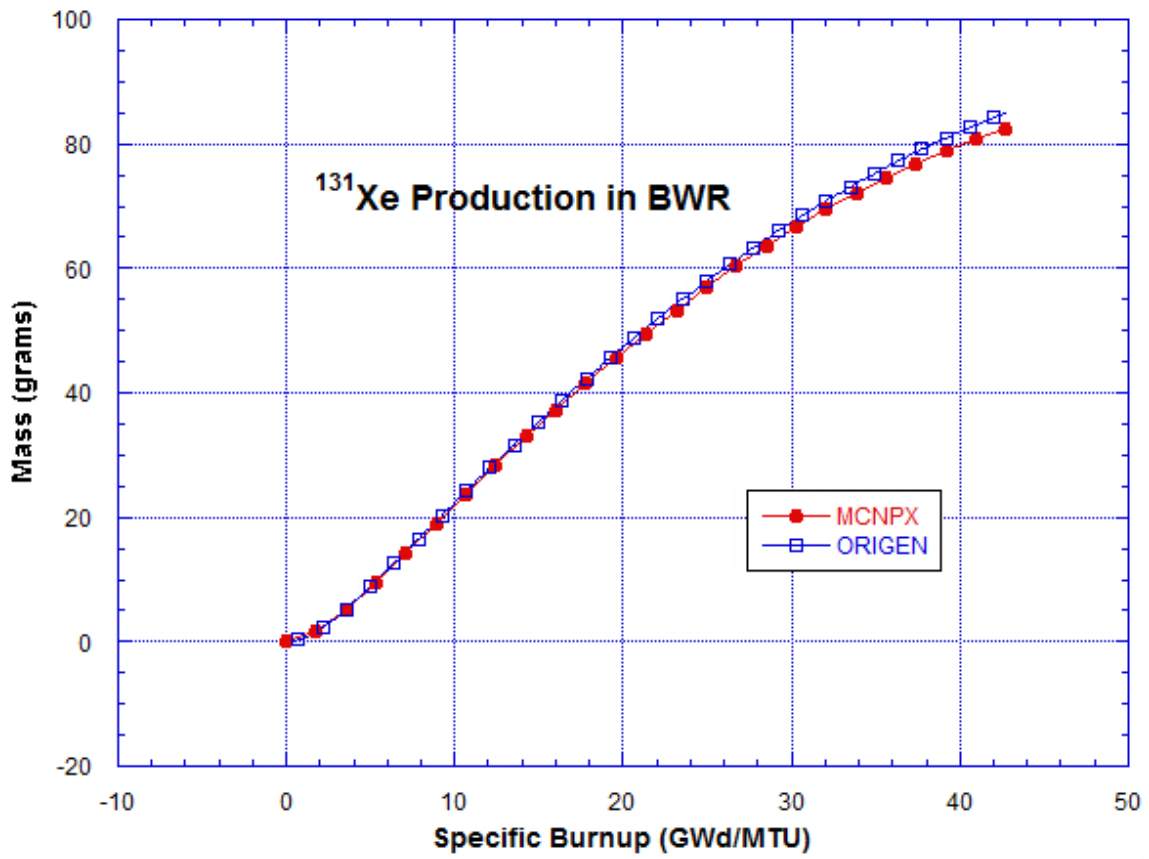


Figure 37: ^{131}Xe Production in BWR Models

Table 7 is a table comparing the fission product results for the two models at the maximum burnup value.

<i>Fission Product</i>	<i>Percent Difference (%) (Negative value indicates MCNPX value is greater)</i>
⁹⁷ Mo	4.13
⁹⁸ Mo	2.85
¹⁰⁰ Mo	3.20
¹³⁸ Ba	0.90
¹⁴⁰ Ce	0.32
¹⁴² Ce	1.19
¹⁴⁸ Nd	0.09
⁷² Ge	10.41
⁹⁰ Sr	-0.66
⁹¹ Y	0.16
⁹¹ Zr	1.22
⁹² Zr	4.67
⁹³ Zr	1.87
⁹⁴ Zr	0.41
⁹⁵ Zr	1.32
¹³⁰ Te	0.37
¹³¹ I	-0.87
¹³⁵ I	3.86
¹³¹ Xe	0.03
¹³² Xe	1.35
¹³⁴ Xe	0.75
¹³⁵ Xe	13.07
¹³⁶ Xe	0.80
¹³⁴ Cs	-12.0
¹³⁷ Cs	1.18
¹³⁹ La	1.78
¹⁴⁹ Sm	20.15
¹⁶¹ Dy	8.53

Table 7: BWR Fission Product Differences at Maximum Burnup Values

Figure 38 is a nuclide chart of actinides present in the BWR models at the maximum calculated burnup of 42.7 GWd/MTU. Values next to the “M” represent the MCNPX calculated values, and values next to the “O” represent the ORIGEN-ARP calculated values.

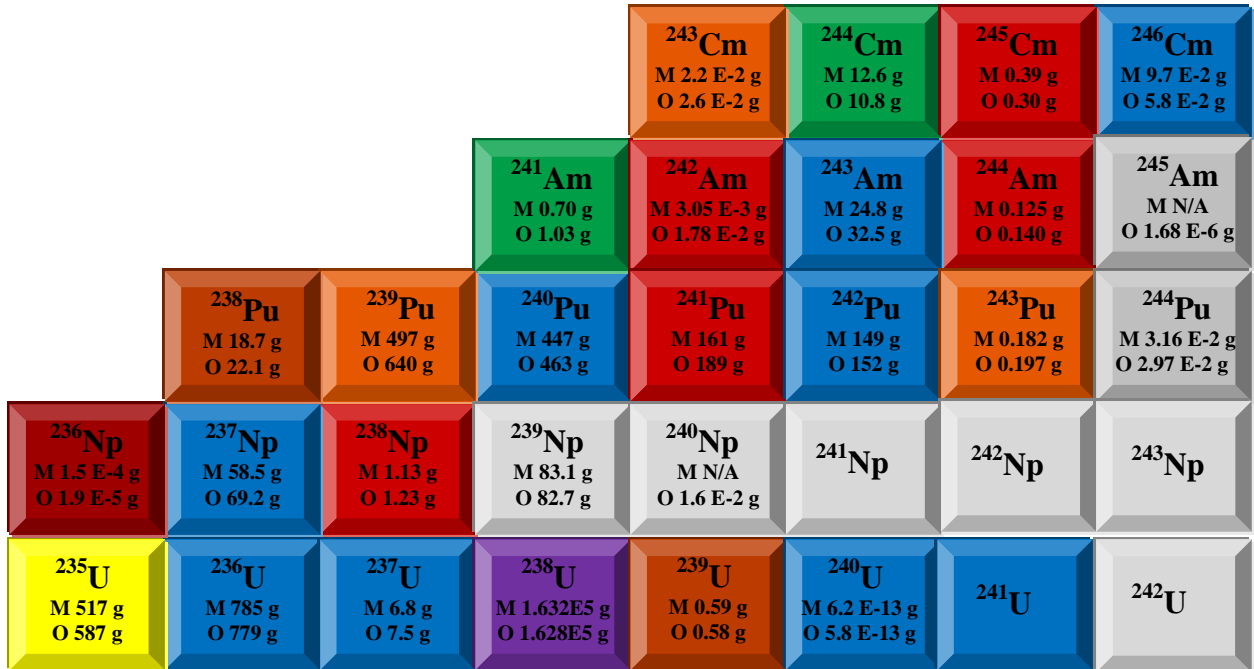


Figure 38: BWR Nuclide Chart of Actinides at Final Burnup (M=MCNPX, O=ORIGEN)

In order to understand the differences between the ORIGEN and MCNPX results, it is necessary to understand the differences in how the two codes perform the burnup calculations.

The MCNPX output files contain the calculated fission rates and neutron absorption rates as a function of fuel burnup for more than 280 different nuclides. Both MCNPX and ORIGEN account for the following neutron absorption reactions: (n,γ),

(n,2n), (n,3n), (n, α), (n,p), and (n,fission). The (n, γ) and (n,fission) reactions are the dominant reactions for the actinides. Due to the reaction high energy threshold, (n, α) and (n,p) reactions are negligible for the actinides. Figure 39 is a plot of the fission rates of the dominant actinides undergoing fission in the BWR reactor models. As shown in the figure, ^{235}U fission dominates at the lower burnups, but at higher burnups, where the ^{235}U quantity in the fuel has been significantly depleted and ^{238}U neutron absorption has led to the production of a significant quantity of ^{239}Pu , ^{239}Pu fission begins to dominate. This switch in fission species domination occurs at a fuel burnup of approximately 30 GWd/MTU.

In order to understand how closely the MCNPX model matches the ORIGEN model, we can compare the fission and absorption reaction rates of the two models.

Though the ORIGEN-ARP output file does not contain these rates, they can be calculated from the given flux, isotopic mass, and the ARP effective cross sections. The flux and isotopic mass, as a function of burnup, are contained in the ORIGEN-ARP output file. However, the ARP effective cross sections are contained in binary format in the library files of the SCALE code. These cross sections can be extracted by using the *xseclist* command within the SCALE code. Appendix H is an example of the SCALE 5.1 input deck for extracting the ORIGEN-ARP cross sections from the CANDU-37 libraries.

There are two ARP effective cross sections for each of the nuclides in the ORIGEN-S library (approximately 1400 nuclides): fission and absorption. The absorption cross section is the sum of the cross sections for (n, γ), (n,2n), (n,3n), (n, α), (n,p), and (n,fission) reactions.

The ORIGEN fission rate for each actinide can be calculated using the following equation:

$$Fission\ Rate = \phi \left(\frac{n}{cm^2 s} \right) * \sigma (cm^2) * N \quad (\text{Equation 21})$$

where

ϕ is the ORIGEN-determined neutron flux,

σ is the ARP effective fission cross section for the actinide, and

N is the number of atoms of the actinide.

Each term of the above equation is time- (fuel burnup-) dependent.

Tables 8-11 show a comparison of the calculated ORIGEN-ARP fission rates versus the listed MCNPX output file fission rates of the highest four fission rate actinides for the BWR model: ^{235}U , ^{238}U , ^{239}Pu , and ^{241}Pu .

Figure 39 is a plot of the MCNPX vs. ORIGEN-ARP fission rates. At approximately 30 GWd/MTU, due to depletion of ^{235}U quantities, ^{239}Pu fission begins to dominate over ^{235}U fission. Also, at the higher burnup values (e.g. 43 GWd/MTU), ^{241}Pu fission begins to compete with ^{235}U fission. Changes in the dominant fission actinide will result in different neutron energy spectra as well as differences in the average amount of energy and average number of neutrons released per fission.

<i>Burnup (GWd/MTU)</i>	<i>ORIGEN Flux (n/cm²s)</i>	<i>ARP Effective Fission Cross Section (barns)</i>	<i>ORIGEN Mass (grams)</i>	<i>ORIGEN Fission Rate (fissions/s)</i>	<i>MCNPX Fission Rate (fissions/s)</i>
0.00	0.00E+00	2.46E+02	5.61E+03	0.00E+00	0.00E+00
3.56	2.64E+14	2.44E+02	4.91E+03	8.10E+17	8.31E+17
10.68	2.87E+14	2.53E+02	3.71E+03	6.90E+17	6.96E+17
14.24	3.02E+14	2.60E+02	3.18E+03	6.40E+17	6.40E+17
21.36	3.34E+14	2.75E+02	2.25E+03	5.30E+17	5.36E+17
24.93	3.63E+14	2.77E+02	1.85E+03	4.77E+17	4.84E+17
30.27	4.07E+14	2.79E+02	1.33E+03	3.87E+17	4.03E+17
35.61	4.49E+14	2.85E+02	9.15E+02	3.00E+17	3.19E+17
39.17	4.80E+14	2.86E+02	6.93E+02	2.44E+17	2.65E+17
42.73	5.14E+14	2.85E+02	5.13E+02	1.93E+17	2.14E+17

Table 8: ²³⁵U Fission Rates for the ORIGEN and MCNPX GE 8x8-4 BWR Models

<i>Burnup (GWd/MTU)</i>	<i>ORIGEN Flux (n/cm²s)</i>	<i>ARP Effective Fission Cross Section (barns)</i>	<i>ORIGEN Mass (grams)</i>	<i>ORIGEN Fission Rate (fissions/s)</i>	<i>MCNPX Fission Rate (fissions/s)</i>
0.00	0.00E+00	3.76E-01	1.679E+05	0.00E+00	0.00E+00
3.56	2.64E+14	3.86E-01	1.676E+05	4.32E+16	4.77E+16
10.68	2.87E+14	3.68E-01	1.669E+05	4.46E+16	4.90E+16
14.24	3.02E+14	3.33E-01	1.666E+05	4.24E+16	5.10E+16
21.36	3.34E+14	3.29E-01	1.658E+05	4.61E+16	5.62E+16
24.93	3.63E+14	3.26E-01	1.654E+05	4.96E+16	5.92E+16
30.27	4.07E+14	3.23E-01	1.648E+05	5.48E+16	6.38E+16
35.61	4.49E+14	3.08E-01	1.640E+05	5.74E+16	6.87E+16
39.17	4.80E+14	3.09E-01	1.635E+05	6.13E+16	7.23E+16
42.73	5.14E+14	3.15E-01	1.630E+05	6.67E+16	7.58E+16

Table 9: ²³⁸U Fission Rates for the ORIGEN and MCNPX GE 8x8-4 BWR Models

<i>Burnup (GWd/MTU)</i>	<i>ORIGEN Flux (n/cm²s)</i>	<i>ARP Effective Fission Cross Section (barns)</i>	<i>ORIGEN Mass (grams)</i>	<i>ORIGEN Fission Rate (fissions/s)</i>	<i>MCNPX Fission Rate (fissions/s)</i>
0.00	0.00E+00	7.01E+02	0.000E+00	0.00E+00	0.00E+00
3.56	2.64E+14	6.97E+02	1.893E+02	7.76E+16	6.97E+16
10.68	2.87E+14	6.90E+02	4.715E+02	2.09E+17	1.91E+17
14.24	3.02E+14	6.85E+02	5.453E+02	2.57E+17	2.30E+17
21.36	3.34E+14	6.82E+02	6.099E+02	3.17E+17	2.97E+17
24.93	3.63E+14	6.79E+02	6.169E+02	3.48E+17	3.28E+17
30.27	4.07E+14	6.78E+02	6.217E+02	3.94E+17	3.73E+17
35.61	4.49E+14	6.82E+02	6.230E+02	4.38E+17	4.15E+17
39.17	4.80E+14	6.79E+02	6.080E+02	4.58E+17	4.36E+17
42.73	5.14E+14	6.78E+02	5.982E+02	4.82E+17	4.72E+17

Table 10: ²³⁹Pu Fission Rates for the ORIGEN and MCNPX GE 8x8-4 BWR Models

<i>Burnup (GWd/MTU)</i>	<i>ORIGEN Flux (n/cm²s)</i>	<i>ARP Effective Fission Cross Section (barns)</i>	<i>ORIGEN Mass (grams)</i>	<i>ORIGEN Fission Rate (fissions/s)</i>	<i>MCNPX Fission Rate (fissions/s)</i>
0.00	0.00E+00	6.50E+02	0.000E+00	0.00E+00	0.00E+00
3.56	2.64E+14	7.03E+02	1.198E+00	5.56E+14	5.95E+14
10.68	2.87E+14	6.98E+02	2.686E+01	1.34E+16	1.30E+16
14.24	3.02E+14	7.07E+02	5.236E+01	2.79E+16	2.40E+16
21.36	3.34E+14	7.09E+02	9.133E+01	5.40E+16	5.34E+16
24.93	3.63E+14	7.10E+02	1.085E+02	6.99E+16	7.02E+16
30.27	4.07E+14	7.12E+02	1.397E+02	1.01E+17	9.80E+16
35.61	4.49E+14	7.22E+02	1.681E+02	1.36E+17	1.27E+17
39.17	4.80E+14	7.24E+02	1.690E+02	1.47E+17	1.47E+17
42.73	5.14E+14	7.23E+02	1.763E+02	1.64E+17	1.66E+17

Table 11: ²⁴¹Pu Fission Rates for the ORIGEN and MCNPX GE 8x8-4 BWR Models

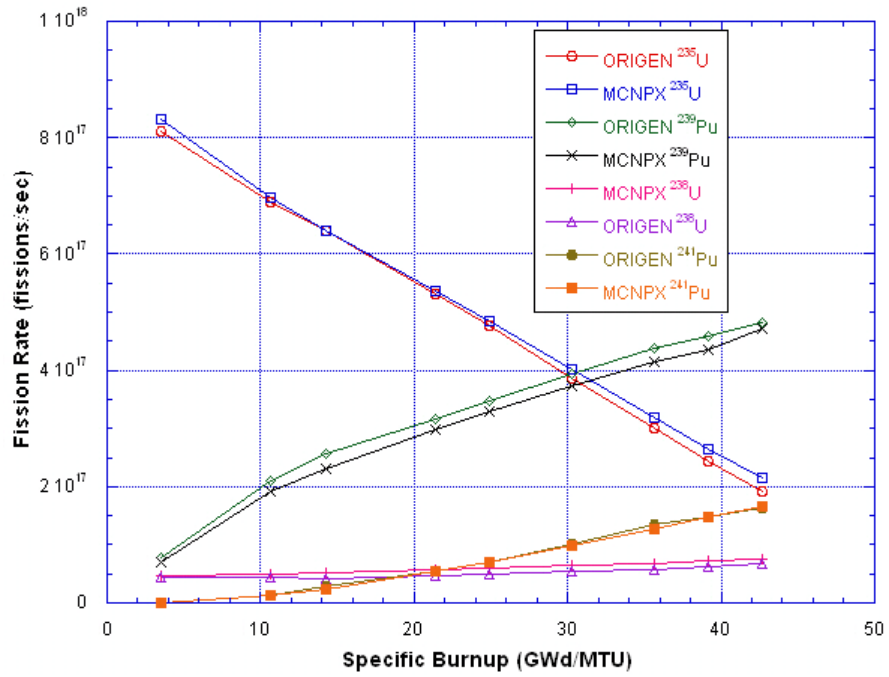


Figure 39: Fission Rates for the GE 8x8-4 BWR Model

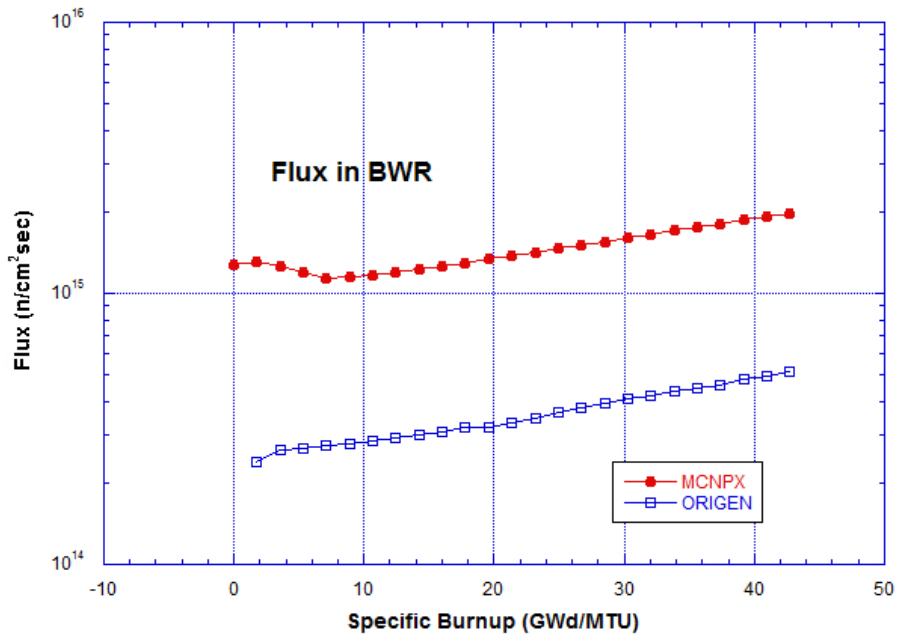


Figure 40: Plot of Computed One-energy Group Flux Values in BWR

3.3 SOURCES OF ERROR

There are numerous possible sources for error in the models. The MCNPX model is the model of a single fuel assembly rather than a whole reactor. The single fuel assembly takes less time to model and significantly less time to run a complete calculation on than would be the case for a complete reactor. Because there is only one fuel assembly, the leakage of neutrons into the fuel assembly from other fuel assemblies in the reactor must be simulated. This can be accomplished by setting up a reflecting boundary around the MCNPX model fuel assembly. This reflecting boundary approximates the neutron influx from surrounding fuel assemblies and was used for all three reactor types in this study. The single fuel assembly also does not take into account radial flux variation within the reactor or other localized effects such as proximity to

control rods, reflectors, or reactor boundaries. The model also assumes fuel homogeneity for the UO₂ fuel (e.g. uniform density) as well as the moderator (e.g. no bubbles) and other materials used in the model. There is the potential for error within the nuclear data files (e.g. neutron interaction cross sections, decay values, and fission product yields), but given the fidelity of evaluated nuclear data files for the nuclides investigated in this study seems unlikely.

MCNPX uses a 63-group energy structure whereas ORIGEN-S uses a 3-group energy structure (which actually becomes a weighted 1-group energy structure). This approximation by ORIGEN-S results in decreased computational time but may result in errors in the results.

The ARP-specific cross sections are generated from two-dimensional models. The lack of the axial direction may reduce the fidelity of the model. Also, the MCNPX model explicitly models the fuel loading with different fuel enrichments for different fuel rods. If the models used to develop the ARP-specific cross sections used homogenized fuel and gadolinium content, it may account for differing results. As mentioned previously, gadolinium is a burnable poison placed in some of the fuel rods to level out reactor power over the life of the fuel. Its presence can drastically alter the neutron spectrum; therefore, any differences in gadolinium content, or in the manner that the gadolinium is depleted over time, between the two models could result in significant differences.

Also, as mentioned previously, MCNPX has a total of 60 fission yield sets for 36 different actinides whereas ORIGEN-ARP has only 30 fission yield sets as shown in

Table 2. Table 2 also shows, for ^{235}U fission, ORIGEN contains only the thermal fission yield set. MCNPX contains the thermal, fast, and high energy fission yield sets for ^{235}U fission. As shown in Table 3, the MCNPX thermal fission yield is significantly different from the fast fission yield for some nuclides (e.g. ^{92}Zr).

Figure 41 below shows the plots of ^{91}Zr through ^{94}Zr for the BWR model. There is excellent agreement between the ORIGEN-ARP and the MCNPX results for each isotope; however, the ^{92}Zr MCNPX plot shows a slightly smaller mass produced at the higher burnup values than the ORIGEN plot. As shown in Table 3, the ^{235}U fast fission yield for ^{92}Zr is significantly smaller than the thermal fission yield. Because ORIGEN only uses the thermal fission yield, this would suggest (assuming that there is a fast component to the neutron flux) that the MCNPX results for ^{92}Zr may be less than the ORIGEN results.

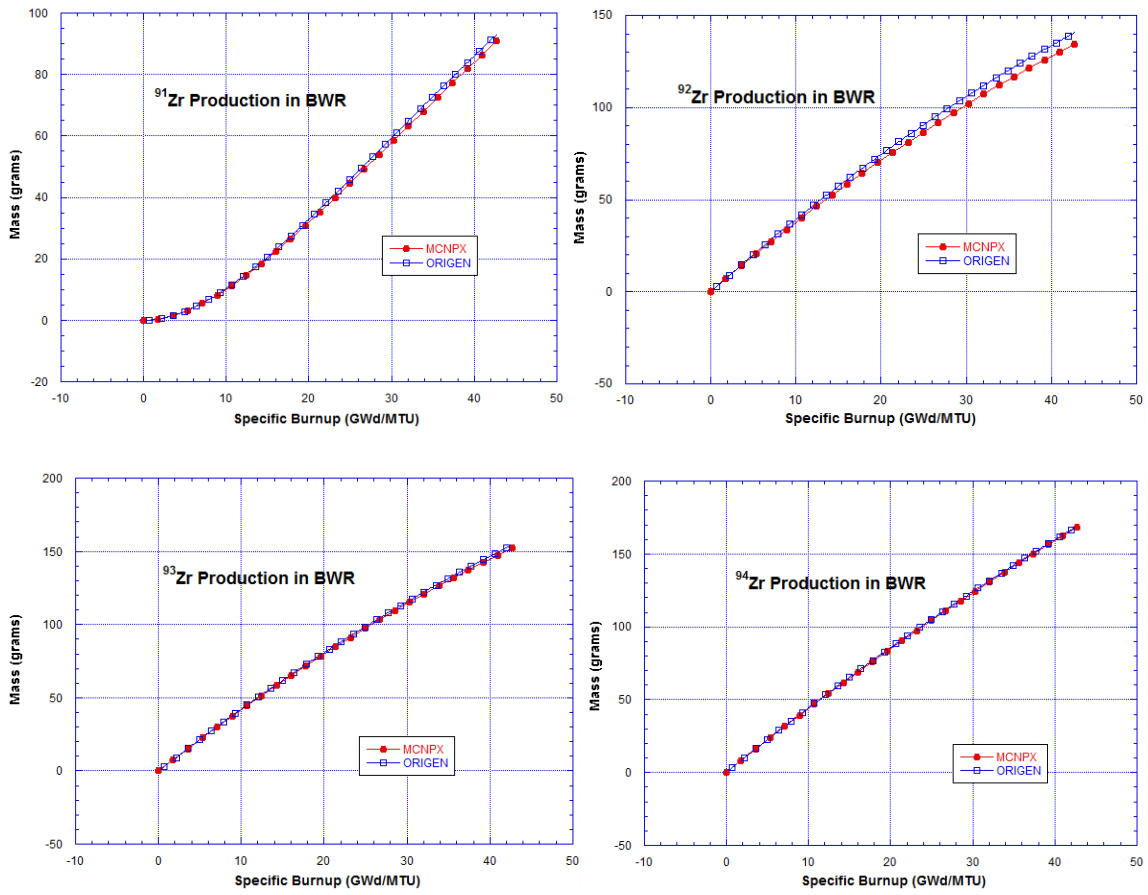


Figure 41: Zirconium Production in the BWR Models

Chapter 4: The PWR Reactor Model

4.1 THE MODEL

The PWR Model was developed from information contained in the Scale 5.1 Manual⁵ and the 2007 World Nuclear Industry Handbook⁹. Table 12 contains the reactor design and operating parameters for the MCNPX model. Again, the uranium mass was determined by the MCNPX model based upon the density, composition, and volume of the fuel. A Westinghouse 17x17 PWR fuel assembly was modeled. The model consists of UO₂ pellets of 10.41 g/cm³ density enriched to 4.5 weight percent ²³⁵U. The fuel diameter is 8.05 mm, and the fuel assembly is 365 cm in height. The fuel rod pitch is 1.26 cm. The assembly contains 264 fuel rods and 25 water holes as shown in Figure 42. The cladding consists of Zircaloy-4 with a thickness of 0.0571 cm. The fuel assembly is cooled and moderated with light water at a density of 0.723 g/cm³. The fuel temperature is modeled at 900 K with a cladding temperature of 622 K and a moderator temperature of 576 K. The total uranium mass in the fuel assembly is 450,030 grams. The reactor operating profile is a constant 54 MW for 360 days resulting in a 43 GWd/MTU final fuel specific burnup.

Appendix B contains the MCNPX input deck for the Westinghouse 17x17 PWR model.

During the MCNPX model development stage, it was noticed that even moderate changes (a couple of hundred ppm) to initial boron concentration in the reactor resulted in significant changes to the depletion/production quantities of ²³⁸U and ²³⁹Pu, as well as

other nuclides. This phenomenon is discussed further in the sensitivity analysis found later in this dissertation.

A similar PWR reactor model was developed by Fensin *et. al.* (2009)^{31,32} and, similarly, MCNPX results were compared to ORIGEN-ARP results. Reactor operating and design parameters are slightly different in this study.

Reactor Design and Operating Data	
Fuel Assembly Type	Westinghouse 17x17 PWR
Fuel Type	UO ₂ pellet
Fuel Density	10.41 g/cm ³
Fuel Temperature	900 K
Fuel Diameter	8.05 mm
Fuel Enrichment	4.5 weight percent ²³⁵ U
Fuel Height	365 cm
Fuel Rod Pitch	1.26 cm
Number of Fuel Rods per Assembly	264 fuel rods with 25 water holes
Cladding	Zircaloy-4
Cladding Thickness	0.0571 cm
Cladding Temperature	622 K
Cladding Density	6.52 g/cm ³
Moderator/Coolant	H ₂ O
Moderator Density	0.723 g/cm ³
Moderator Temperature	576 K
Boron Concentration	850 ppm
Total Uranium Mass	450,030 g (0.450030 MTU)
Reactor Operating Power	54 MW
Reactor Operating Time	360 Days
Total Fuel Burnup	43 GWd/MTU

Table 12: MCNPX PWR Model

Table 13 below contains the ORIGEN-ARP GUI input reactor design and operating data.

<i>Reactor Design and Operating Data for ORIGEN-ARP Model</i>	
<i>Fuel Assembly Type</i>	Westinghouse 17x17 PWR
<i>Fuel Type</i>	UO ₂
<i>Fuel Enrichment</i>	4.5 weight percent ²³⁵ U
<i>²³⁴U Initial Mass</i>	180.2 g
<i>²³⁵U Initial Mass</i>	20,250 g
<i>²³⁸U Initial Mass</i>	429,600 g
<i>Total Uranium Mass</i>	450,030 g (0.450030 MTU)
<i>Reactor Operating Power</i>	54 MW
<i>Reactor Operating Time</i>	360 Days
<i>Total Fuel Burnup</i>	43 GWd/MTU

Table 13: PWR Design and Operating Data for ORIGEN-ARP Model

Figure 42 below is a VISEd plot of the MCNPX model of the 17x17 array. There are 264 identical fuel rods and 24 guide tube holes and one instrumentation hole.

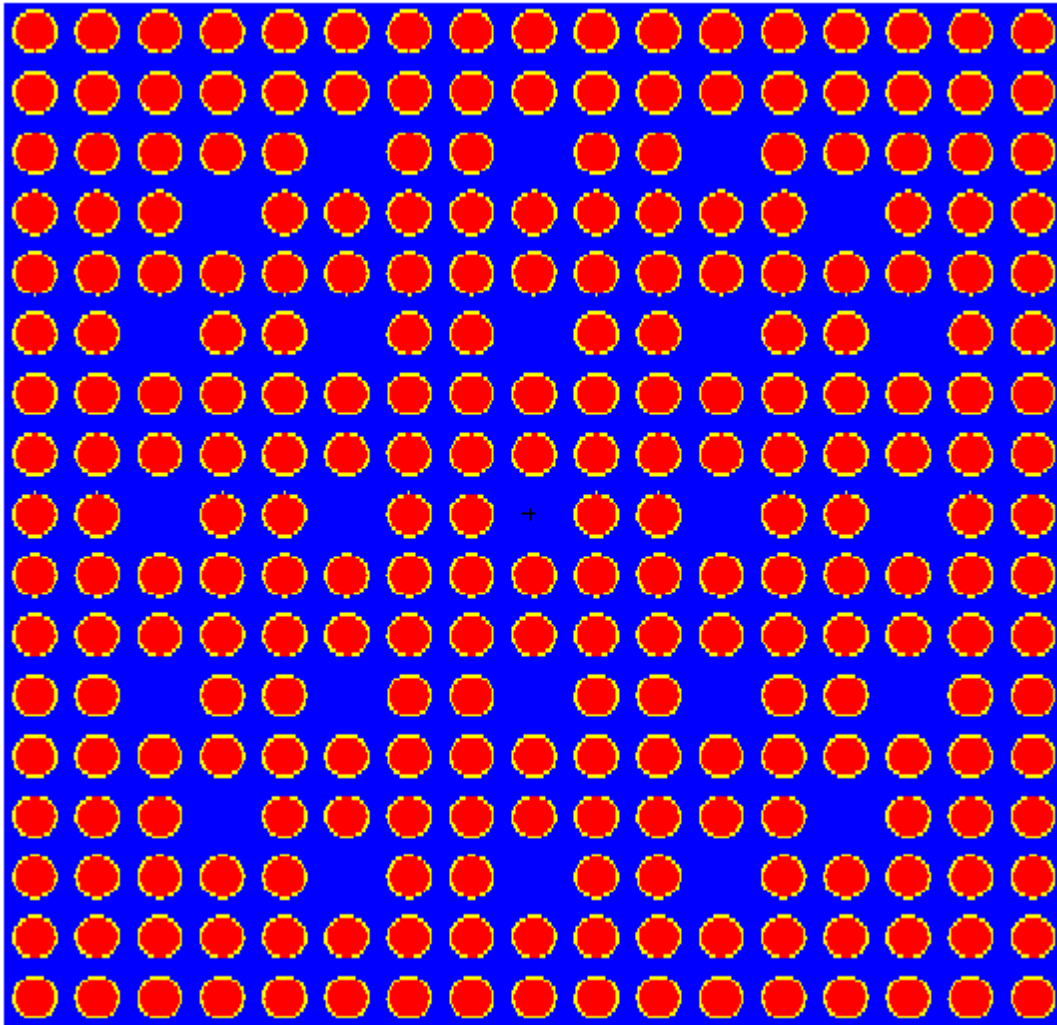


Figure 42: MCNPX Model of W 17x17 Pressurized Water Reactor

Figure 43 below is a VISEd plot of a portion of the cross sectional view. Because the length of the fuel assembly is much greater than the width, only a portion of the cross section view is shown. The top and bottom of the fuel assembly are not shown.

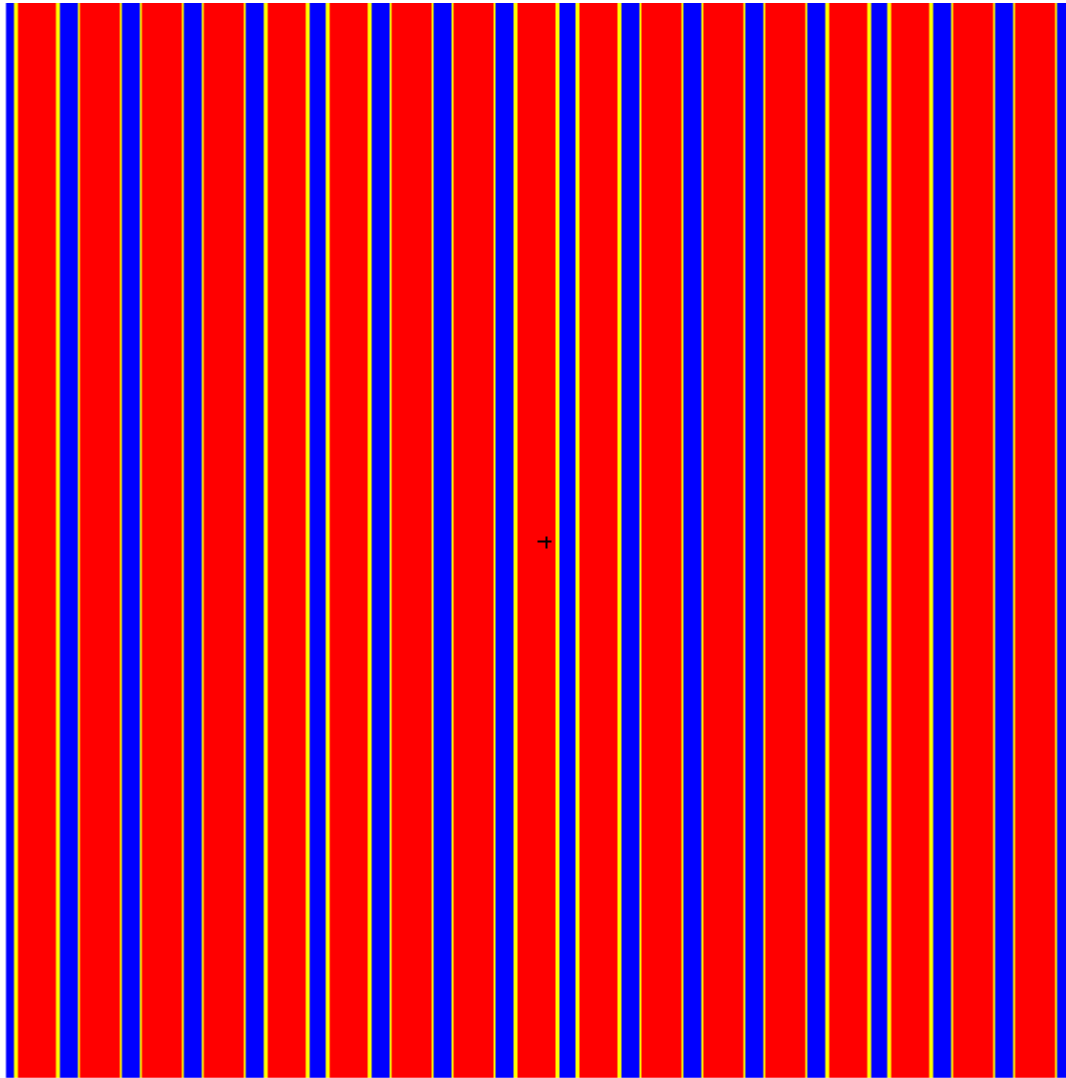


Figure 43: Cross Sectional View of PWR Model

4.2 THE RESULTS

Figures 44-52 show the comparison of the depletion calculations performed by MCNPX and ORIGEN-ARP for several different nuclides. The plots of all 46 nuclide comparisons can be found in Appendix E. The agreement between the MCNPX and ORIGEN-ARP models is quite good for ^{239}Pu , ^{235}U , and ^{238}U as well as for the fission productions. However, some of the higher actinides on the neutron-rich side of the stability line (e.g. ^{244}Pu , ^{245}Cm , and ^{246}Cm) have significant differences. In these nuclides, the MCNPX values are significantly greater than the ORIGEN values. This may be attributed to the higher flux values found in the MCNPX model. Figure 53 is a plot of the commutated (one-energy group) flux values for the MCNPX and ORIGEN-ARP models. Despite the fact that both models used the same power profile (power, time step width, and irradiation time), the MCNPX model flux values are approximately an order of magnitude greater than the ORIGEN-ARP model. This difference in flux may cause the differences in the computed values of the higher neutron-rich actinides.

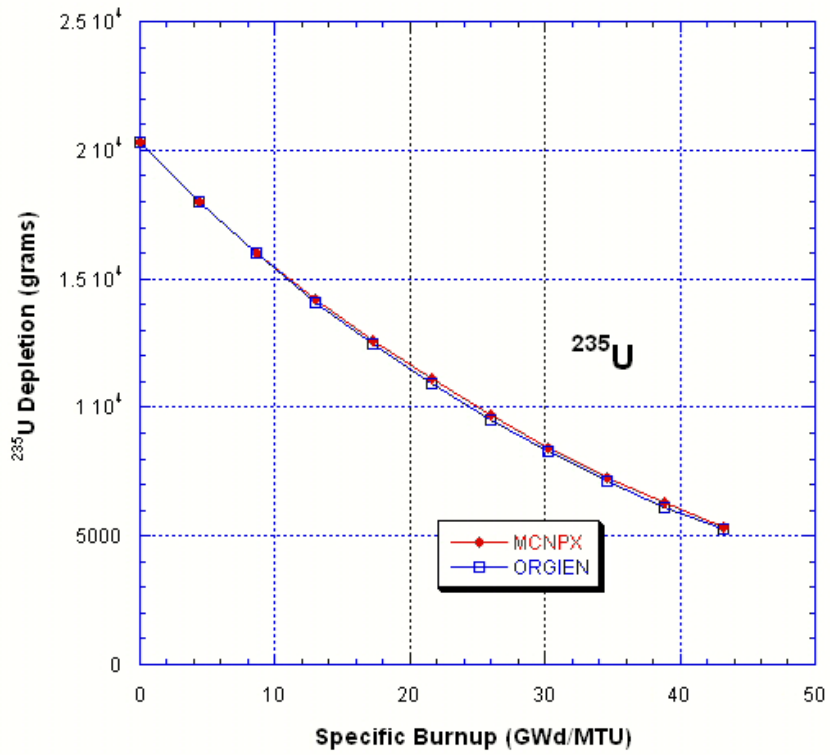


Figure 44: Plot of ^{235}U Depletion for the PWR Models

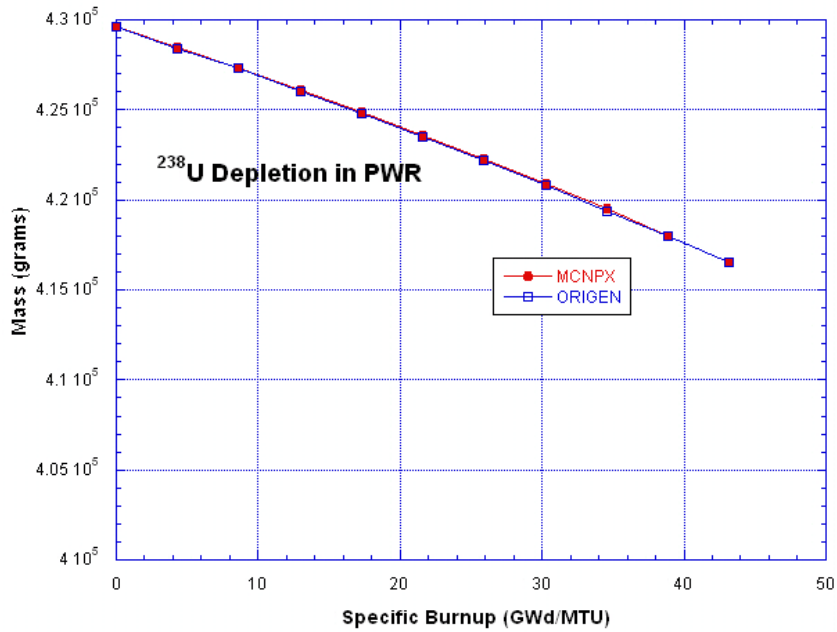


Figure 45: ^{238}U Depletion in PWR Models

Figure 46 is the plot of ^{239}Pu production in the PWR models. The plot shows that the ORIGEN-ARP model produces slightly more ^{239}Pu than the MCNPX model until the higher burnup values where the ORIGEN-ARP turns over slightly more than the MCNPX model. ^{239}Pu production occurs primarily due to radiative capture of ^{238}U . Loss of ^{239}Pu occurs primarily due to fission. As can be seen in Figure 54 below, the fission rate of ^{239}Pu in the ORIGEN-ARP model is slightly greater than that in the MCNPX model which may explain the downward turn in the ORIGEN-ARP ^{239}Pu plot at the higher burnup values.

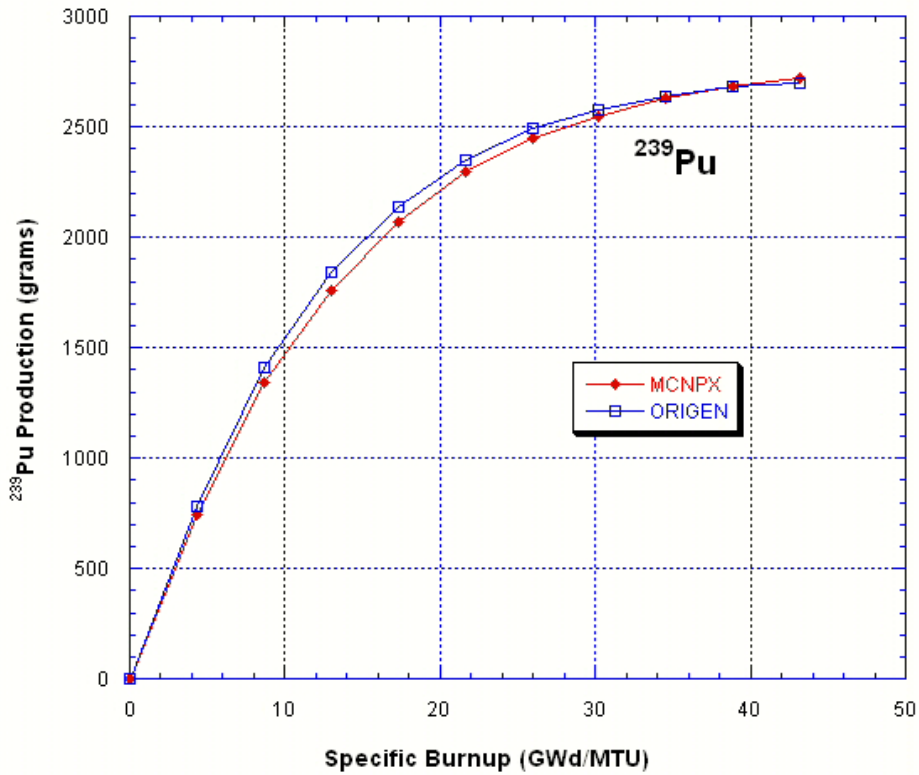


Figure 46: Plot of ^{239}Pu Production for the PWR Models

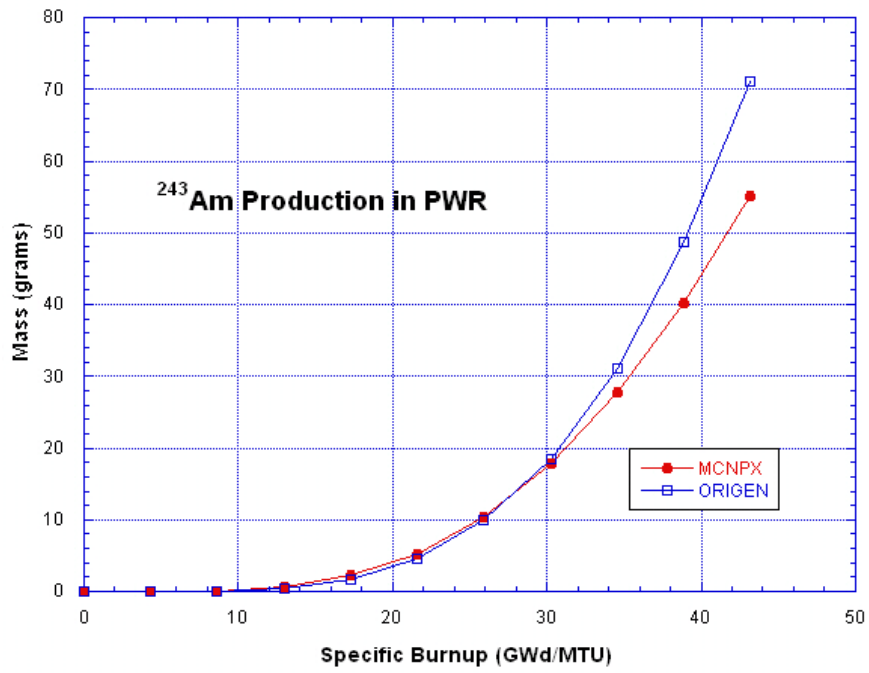


Figure 47: Plot of ²⁴³Am Production for the PWR Models

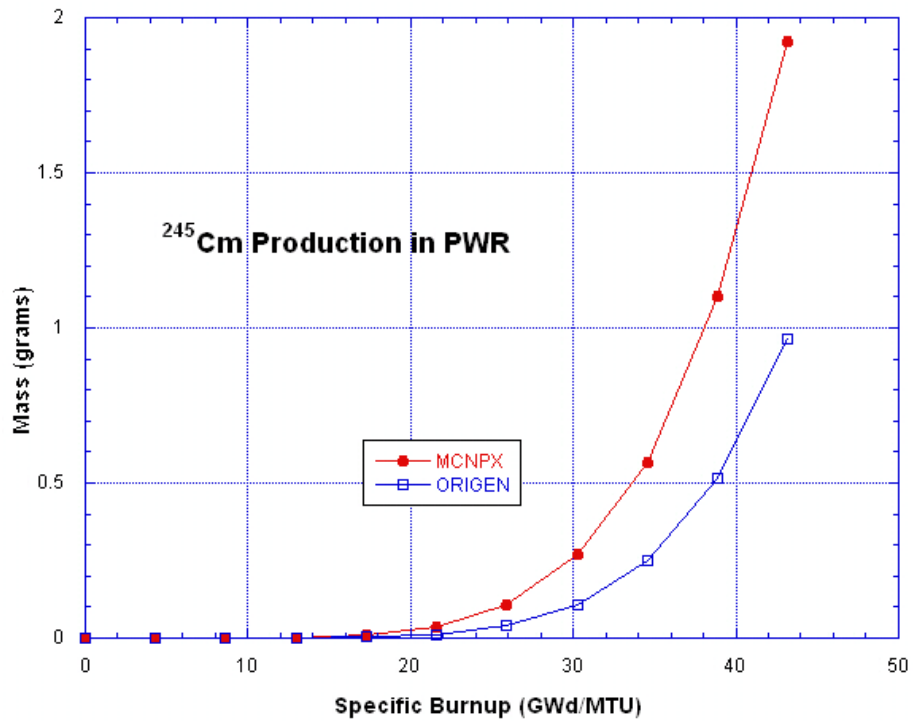


Figure 48: Plot of ²⁴⁵Cm Production for the PWR Models

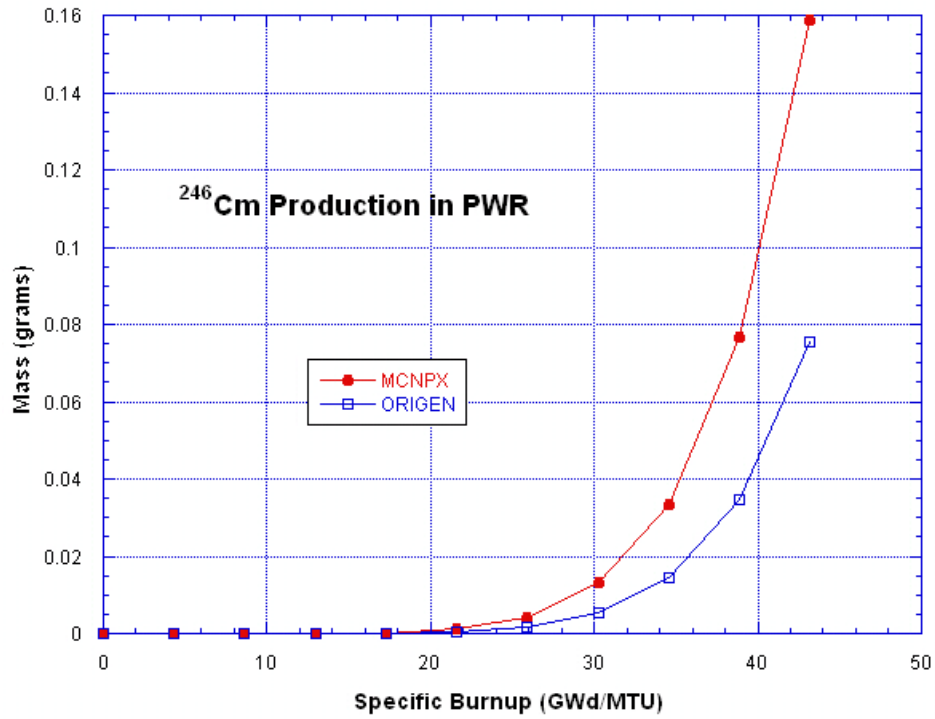


Figure 49: Plot of ^{246}Cm Production for the PWR Models

The fission product masses determined by the two codes agree well for most of the fission products, though most have a greater quantity for the ORIGEN-ARP values (See Figures 50-52 below). Table 14 lists the percent differences for the fission products.

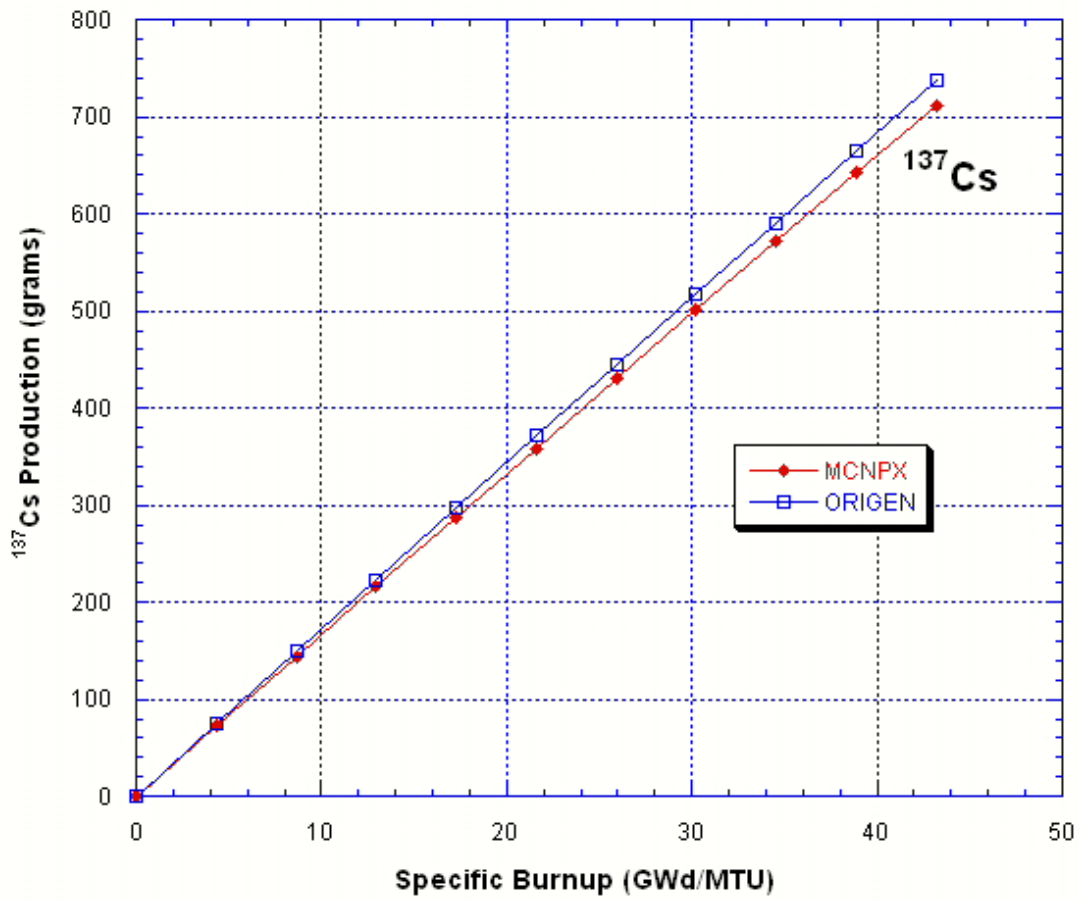


Figure 50: Plot of ^{137}Cs Production for the PWR Models

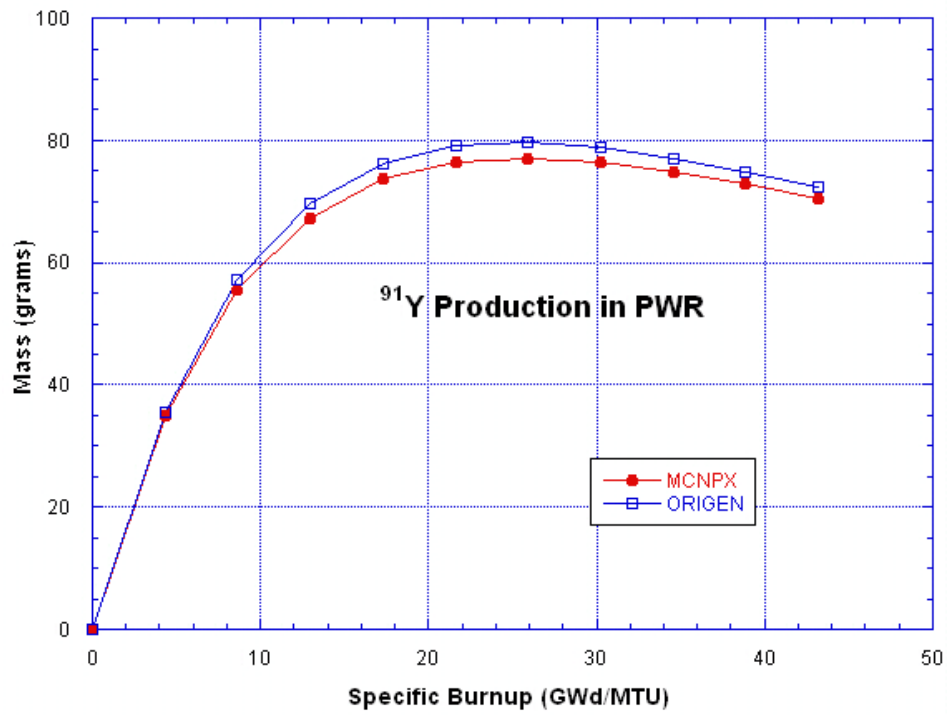


Figure 51: Plot of ⁹¹Y Production for the PWR Models

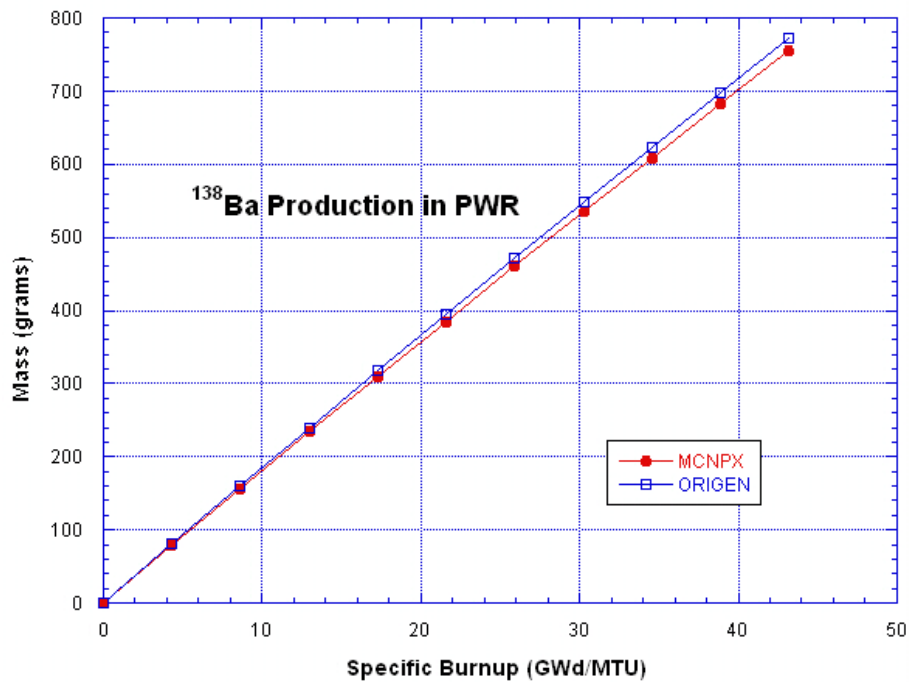


Figure 52: Plot of ¹³⁸Ba Production for the PWR Models

<i>Fission Product</i>	<i>Percent Difference (%) (Negative value indicates MCNPX value is greater)</i>
⁹⁷ Mo	9.78
⁹⁸ Mo	6.76
¹⁰⁰ Mo	7.15
¹³⁸ Ba	2.28
¹⁴⁰ Ce	6.92
¹⁴² Ce	2.90
¹⁴⁸ Nd	1.31
⁷² Ge	9.95
⁹⁰ Sr	0.27
⁹¹ Y	2.59
⁹¹ Zr	3.78
⁹² Zr	4.23
⁹³ Zr	5.33
⁹⁴ Zr	1.76
⁹⁵ Zr	4.38
¹³⁰ Te	1.23
¹³¹ I	-0.51
¹³⁵ I	5.51
¹³¹ Xe	3.97
¹³² Xe	1.43
¹³⁴ Xe	2.04
¹³⁵ Xe	2.29
¹³⁶ Xe	3.38
¹³⁴ Cs	-19.14
¹³⁷ Cs	3.39
¹³⁹ La	3.35
¹⁴⁹ Sm	13.32
¹⁶¹ Dy	9.78

Table 14: PWR Fission Product Differences at Maximum Burnup Values

Figure 53 is a plot of the computed one-energy group flux values for the PWR models. The MCNPX values are approximately one order of magnitude greater than the ORIGEN-ARP values.

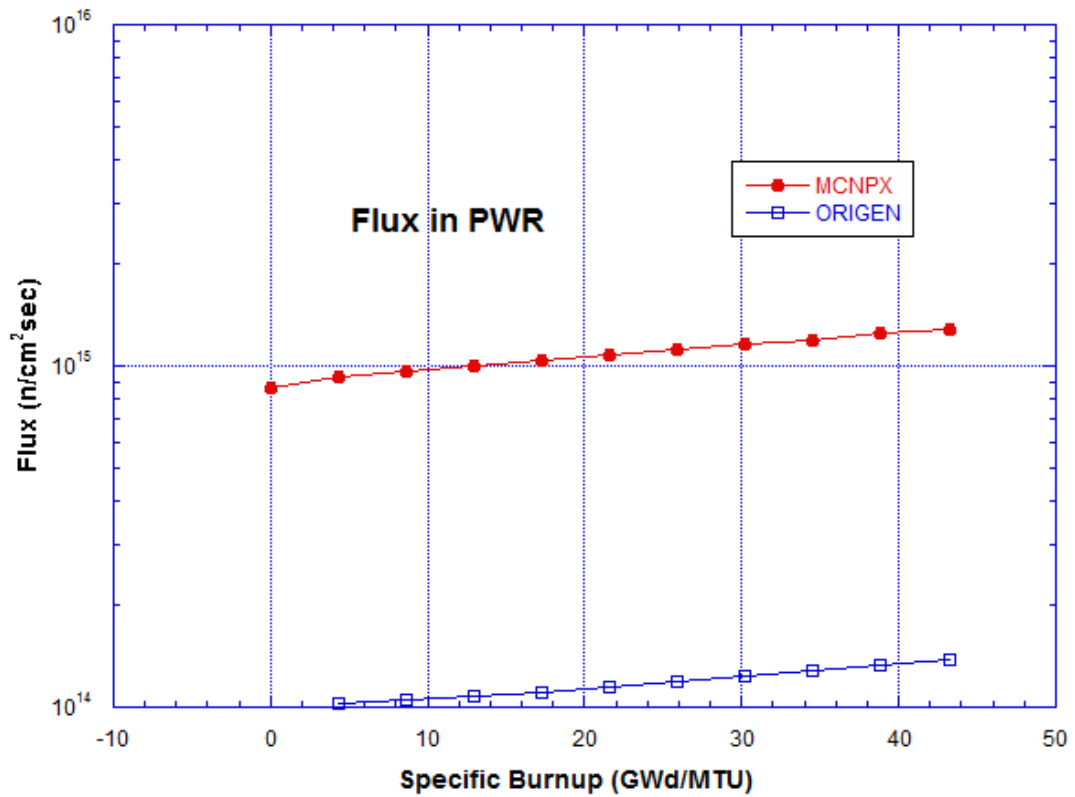


Figure 53: Plot of Computed One-energy Group Flux Values in PWR

As was done for the BWR case, the PWR fission rates were calculated for ORIGEN-ARP and extracted from the MCNPX output file to create the tables below (Tables 15-18) for the four actinides with the highest fission rates. These results are

plotted in Figure 54.

<i>Burnup (GWd/MTU)</i>	<i>ORIGEN Flux (n/cm²s)</i>	<i>ARP Effective Fission Cross Section (barns)</i>	<i>ORIGEN Mass (grams)</i>	<i>ORIGEN Fission Rate (fissions/s)</i>	<i>MCNPX Fission Rate (fissions/s)</i>
4.32	1.03E+14	2.8606E+02	1.80E+04	1.36E+18	1.50E+18
8.64	1.05E+14	2.8573E+02	1.59E+04	1.22E+18	1.33E+18
12.96	1.07E+14	2.8791E+02	1.41E+04	1.11E+18	1.21E+18
17.28	1.10E+14	2.8997E+02	1.24E+04	1.01E+18	1.10E+18
21.60	1.14E+14	2.9188E+02	1.09E+04	9.29E+17	9.97E+17
25.92	1.18E+14	2.9364E+02	9.49E+03	8.43E+17	9.12E+17
30.24	1.23E+14	2.9528E+02	8.24E+03	7.67E+17	8.35E+17
34.56	1.28E+14	3.0205E+02	7.11E+03	7.04E+17	7.55E+17
38.88	1.33E+14	3.0723E+02	6.11E+03	6.40E+17	6.79E+17
43.20	1.38E+14	3.1040E+02	5.22E+03	5.73E+17	6.07E+17

Table 15: ²³⁵U Fission Rates for the ORIGEN and MCNPX W 17x17 PWR Models

<i>Burnup (GWd/MTU)</i>	<i>ORIGEN Flux (n/cm²s)</i>	<i>ARP Effective Fission Cross Section (barns)</i>	<i>ORIGEN Mass (grams)</i>	<i>ORIGEN Fission Rate (fissions/s)</i>	<i>MCNPX Fission Rate (fissions/s)</i>
4.32	1.03E+14	8.3323E-01	4.284E+05	9.30E+16	1.07E+17
8.64	1.05E+14	8.7559E-01	4.273E+05	9.94E+16	1.11E+17
12.96	1.07E+14	9.0805E-01	4.260E+05	1.05E+17	1.14E+17
17.28	1.10E+14	9.3305E-01	4.248E+05	1.10E+17	1.18E+17
21.60	1.14E+14	9.5198E-01	4.235E+05	1.16E+17	1.25E+17
25.92	1.18E+14	9.6576E-01	4.222E+05	1.22E+17	1.28E+17
30.24	1.23E+14	9.7528E-01	4.208E+05	1.28E+17	1.32E+17
34.56	1.28E+14	9.8024E-01	4.194E+05	1.33E+17	1.36E+17
38.88	1.33E+14	9.5040E-01	4.180E+05	1.34E+17	1.41E+17
43.20	1.38E+14	9.2054E-01	4.165E+05	1.34E+17	1.44E+17

Table 16: ²³⁸U Fission Rates for the ORIGEN and MCNPX W 17x17 PWR Models

<i>Burnup (GWd/MTU)</i>	<i>ORIGEN Flux (n/cm²s)</i>	<i>ARP Effective Fission Cross Section (barns)</i>	<i>ORIGEN Mass (grams)</i>	<i>ORIGEN Fission Rate (fissions/s)</i>	<i>MCNPX Fission Rate (fissions/s)</i>
4.32	1.03E+14	7.6945E+02	7.856E+02	1.57E+17	7.53E+16
8.64	1.05E+14	7.6600E+02	1.406E+03	2.85E+17	2.19E+17
12.96	1.07E+14	7.5372E+02	1.841E+03	3.74E+17	3.20E+17
17.28	1.10E+14	7.4465E+02	2.143E+03	4.42E+17	4.00E+17
21.60	1.14E+14	7.3767E+02	2.350E+03	4.98E+17	4.62E+17
25.92	1.18E+14	7.3218E+02	2.490E+03	5.42E+17	5.21E+17
30.24	1.23E+14	7.2780E+02	2.582E+03	5.82E+17	5.70E+17
34.56	1.28E+14	7.1582E+02	2.640E+03	6.09E+17	6.08E+17
38.88	1.33E+14	7.1211E+02	2.675E+03	6.38E+17	6.48E+17
43.20	1.38E+14	7.1156E+02	2.695E+03	6.67E+17	6.81E+17

Table 17: ²³⁹Pu Fission Rates for the ORIGEN and MCNPX W 17x17 PWR Models

<i>Burnup (GWd/MTU)</i>	<i>ORIGEN Flux (n/cm²s)</i>	<i>ARP Effective Fission Cross Section (barns)</i>	<i>ORIGEN Mass (grams)</i>	<i>ORIGEN Fission Rate (fissions/s)</i>	<i>MCNPX Fission Rate (fissions/s)</i>
4.32	1.03E+14	7.8697E+02	6.051E+00	1.23E+15	2.55E+14
8.64	1.05E+14	7.8421E+02	3.801E+01	7.82E+15	6.15E+15
12.96	1.07E+14	7.8158E+02	1.022E+02	2.14E+16	1.93E+16
17.28	1.10E+14	7.8027E+02	1.939E+02	4.16E+16	3.79E+16
21.60	1.14E+14	7.7964E+02	3.040E+02	6.75E+16	6.07E+16
25.92	1.18E+14	7.7943E+02	4.223E+02	9.71E+16	8.49E+16
30.24	1.23E+14	7.7950E+02	5.396E+02	1.29E+17	1.11E+17
34.56	1.28E+14	7.8225E+02	6.489E+02	1.62E+17	1.37E+17
38.88	1.33E+14	7.8691E+02	7.457E+02	1.95E+17	1.64E+17
43.20	1.38E+14	7.9073E+02	8.275E+02	2.26E+17	1.91E+17

Table 18: ²⁴¹Pu Fission Rates for the ORIGEN and MCNPX W 17x17 PWR Models

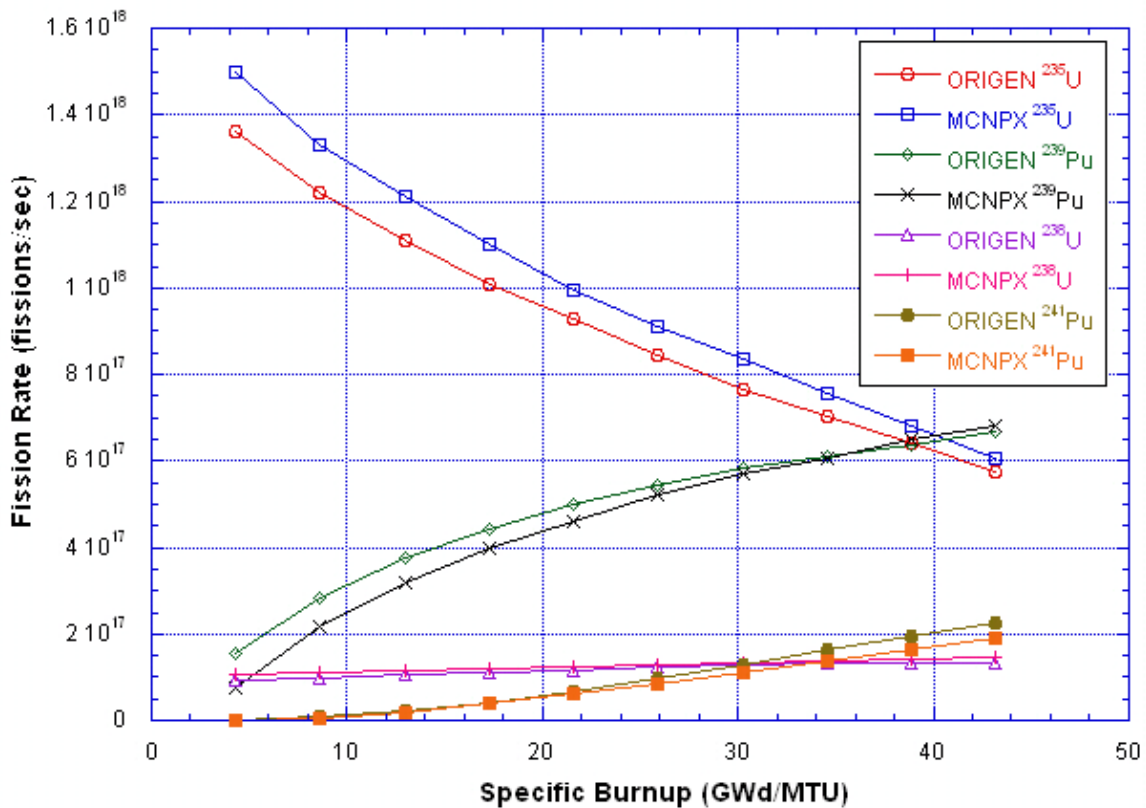


Figure 54: Fission Rates for the W 17x17 PWR Model

As can be seen in Figure 54, unlike in the BWR model, the ²³⁹Pu fission rate does not dominate until a much higher burnup value (~39 GWd/MTU).

Figure 55 below is a nuclide chart layout of several of the computed actinide values at final burnup. Again, the higher MCNPX values for the greater actinides (e.g. curium) are indicative of a higher flux value.

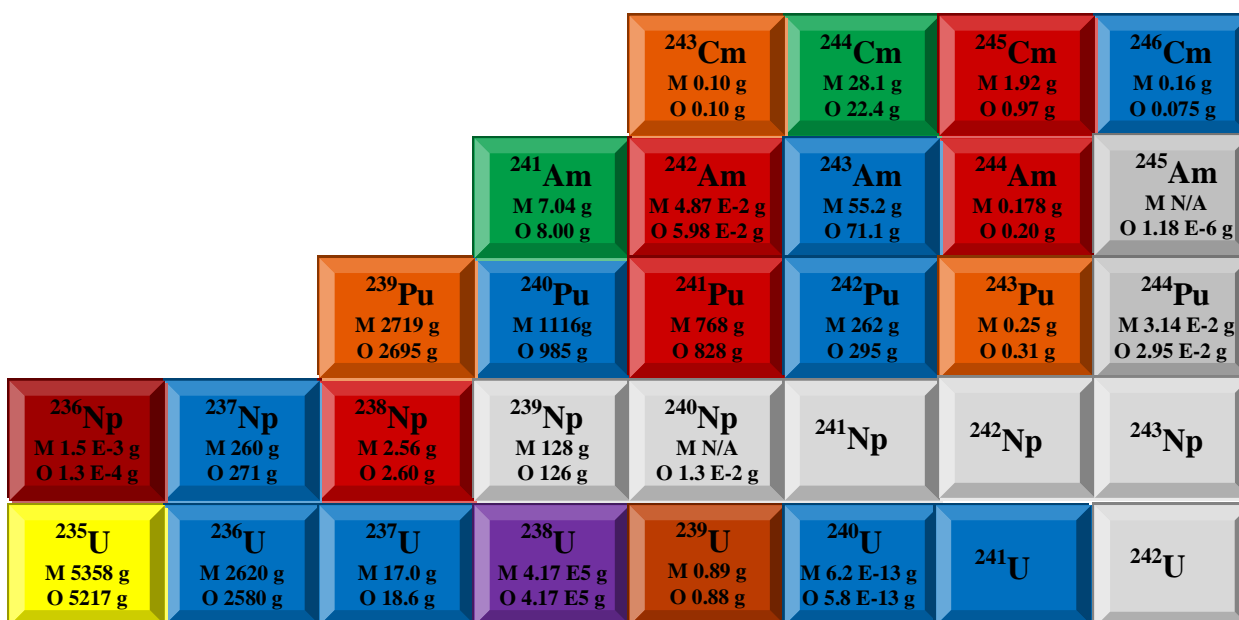


Figure 55: PWR Nuclide Chart of Computed Actinide Values at Final Burnup

Figure 56 is a plot of the fission yield of the two PWR models. Mass quantities used are for the final burnup value. The majority of the data points match very closely for the two models. For some data points (e.g. Mass Number 113) the MCNPX value is lower than the ORIGEN-ARP values because one or more nuclides of that mass number were generated by ORIGEN-ARP but not MCNPX. For example, ORIGEN-ARP had nuclide quantities for ten elements with mass number 13. MCNPX had only three. This does not mean that the MCNPX model is not able to generate these values, only that the user-defined input deck did not specifically request that these values be included in the output file. Using the highest available input tier for nuclide output values in MCNPX only generates about 300 nuclides. If output values are required for nuclides in addition

to these nuclides, then each additional nuclide must be entered into the input deck.

ORIGEN-ARP automatically generates output for approximately 1100 nuclides.

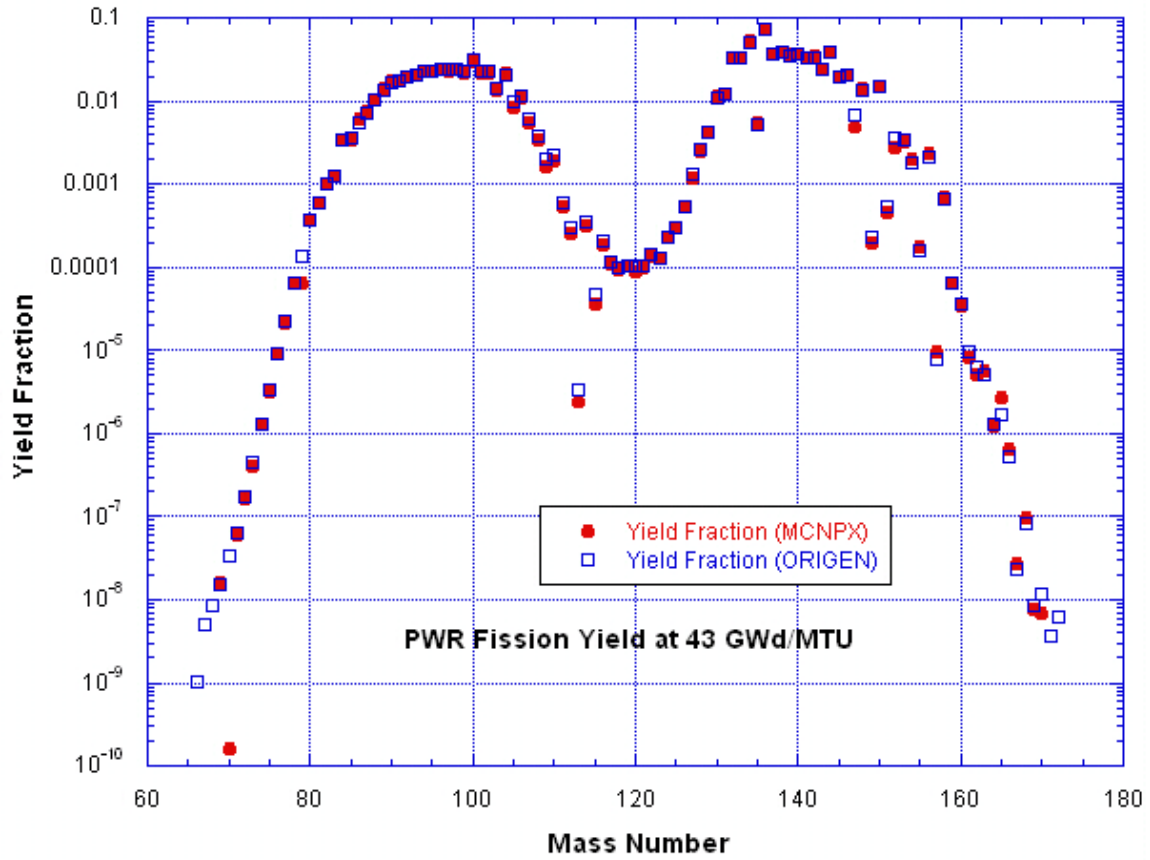


Figure 56: Fission Product Yields for the MCNPX and ORIGEN-ARP PWR Models

4.3 SOURCES OF ERROR

With the exception of the gadolinium content, the sources of error from the previous BWR section apply here to the PWR model as well. As mentioned in the previous section, MCNPX contains 60 fission yield sets whereas ORIGEN-ARP contains only 30. Therefore, even if both calculations predicted an identical number of ^{235}U fissions, the fission product results would still vary due to the fact that MCNPX has a fast fission yield set that it would apply to any ^{235}U fissions resulting from an incident neutron in the fast energy range.

Also, according to the ORIGEN-ARP manual⁵, the basis model (e.g. NEWT, TRITON) used to develop the ARP specific cross sections used an “average” boron concentration. In the MCNPX model, an explicit “initial” boron concentration is defined in the input deck, and this quantity of boron is depleted as a function of fuel burnup. The presence of boron in the model has a significant effect on the results. If the ARP basis model assumes a constant, “average” boron concentration, this would give a different neutron flux profile than the MCNPX model which has an initial boron concentration that is depleted as the fuel burns. Also, the method used to convert ppm to a weight percent (or atom percent) value which is the required input format for MCNPX may have varied from the method used in the development of the ARP specific cross sections. For example, if you use the standard method of conversion, you would use one milligram of ^{10}B per one kilogram of H_2O . Other methods include one atom of ^{10}B to one molecule of

H₂O or one milligram of boric acid to one kilogram of H₂O. These three methods each result in a slightly different ¹⁰B weight fraction.

Chapter 5: The CANDU-37 Reactor Model

5.1 THE MODEL

The reactor parameters for the MCNPX CANDU-37 model in this study were derived from three primary references: 1) the CANTeach website¹⁰, 2) the Scale 5.1 Manual⁵, and 3) AECL report, RC-1429, *Verification and Validation of the ORIGEN-S Code and Nuclear Data Libraries*¹¹.

CANDU is an acronym for CANadian Deuterium Uranium. A CANDU reactor uses natural uranium (~0.711 weight percent ²³⁵U) as its fuel. In order for the natural uranium to maintain criticality, deuterium, in the form of heavy water, is used for both the neutron moderator and the coolant for the reactor. The CANDU reactor consists of a large horizontal cylinder referred to as the Calandria which contains hundreds of horizontal fuel channels. Each fuel channel contains pressurized heavy water coolant and approximately 12 fuel assemblies. Each CANDU-37 fuel assembly contains 37 fuel rods. The large number of fuel channels allows the Calandria to contain thousands of fuel assemblies. The pressurized heavy water coolant cycles through heat exchangers for energy production. Each pressurized fuel channel is surrounded by insulating CO₂ gas within a Calandria tube. The Calandria is filled with heavy water moderator which remains at a lower temperature than the heavy water coolant. The heavy water moderator surrounds each Calandria tube. The insulating CO₂ gas keeps the moderator at a much lower temperature than the coolant eliminating the need for a large pressure vessel

around the Calandria. The unique design of the CANDU reactor allows continuous reactor refueling without shutting the reactor down. Fuel is simply loaded at one end of the reactor and removed from the other end once the fuel reaches its burnup limit. Figure 57 is a schematic of a CANDU¹⁰. The Calandria is item number 2 in the figure. Item number 4 shows the horizontal fuel channels.

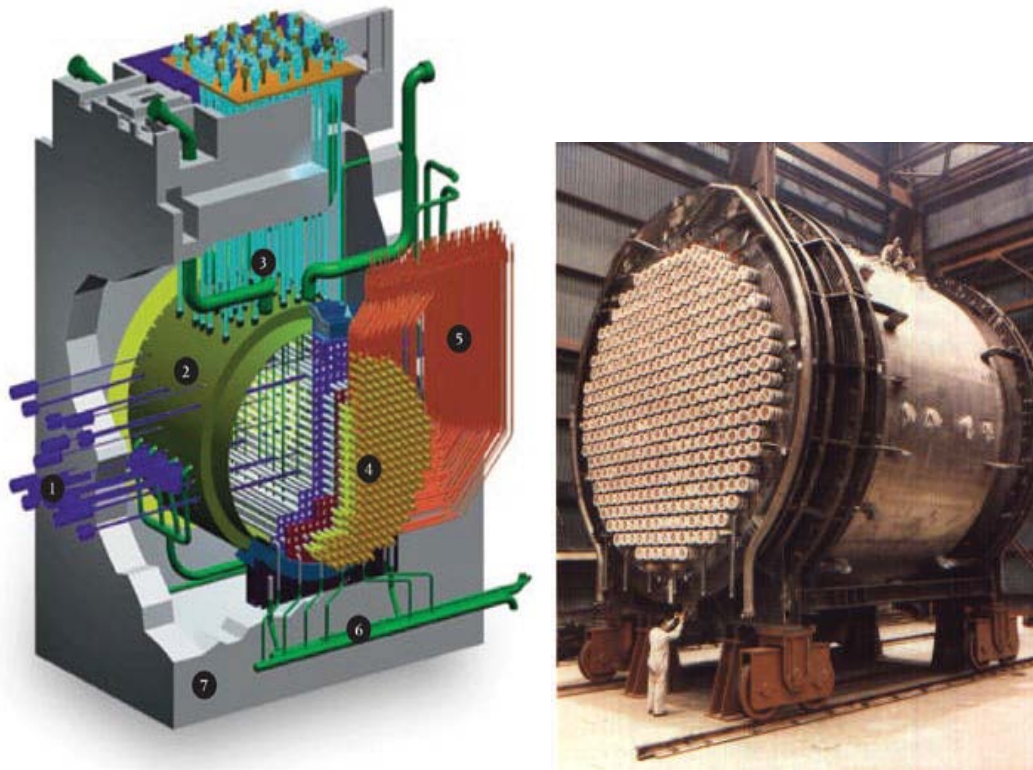


Figure 57: CANDU Nuclear Reactor Schematic and Calandria Photo¹⁰

The high concentration of ^{238}U , the ability to refuel online, and the low fuel burnup make the CANDU reactor highly attractive to nuclear proliferators seeking ^{239}Pu .

Figure 58 is a two-dimension cross sectional view of the fuel assembly model. According to the ORIGEN-ARP Manual⁵, the average rod pitch of a CANDU-37 fuel rod

bundle is 1.46 cm. MCNPX has two lattice structure options available for repeated structures: square lattice and hexagonal lattice. Neither of these lattices provided an accurate representation of the concentric ring geometry in a true CANDU model (See Figure 59¹⁰). Therefore, the MCNPX repeated structure option was abandoned for this model. Instead, the fuel assembly geometry is approximated with right circular cylinders in a concentric pattern with a central fuel rod, surrounded by 3 rings of six, twelve, and eighteen fuel rods resulting in a total of 37 fuel rods per fuel assembly. The rod pitch for the model is 1.46 cm. The natural uranium fuel consists of 1.215 cm diameter UO₂ pellets with a density of 10.59 g/cm³ and 49.53 cm in height (See Figure 62). The fuel temperature for the model is 1155 K. The fuel is surrounded by 0.0465 cm thick Zircaloy-4 cladding (See Figure 60) with a density of 6.52 g/cm³ and at a temperature of 599 K.

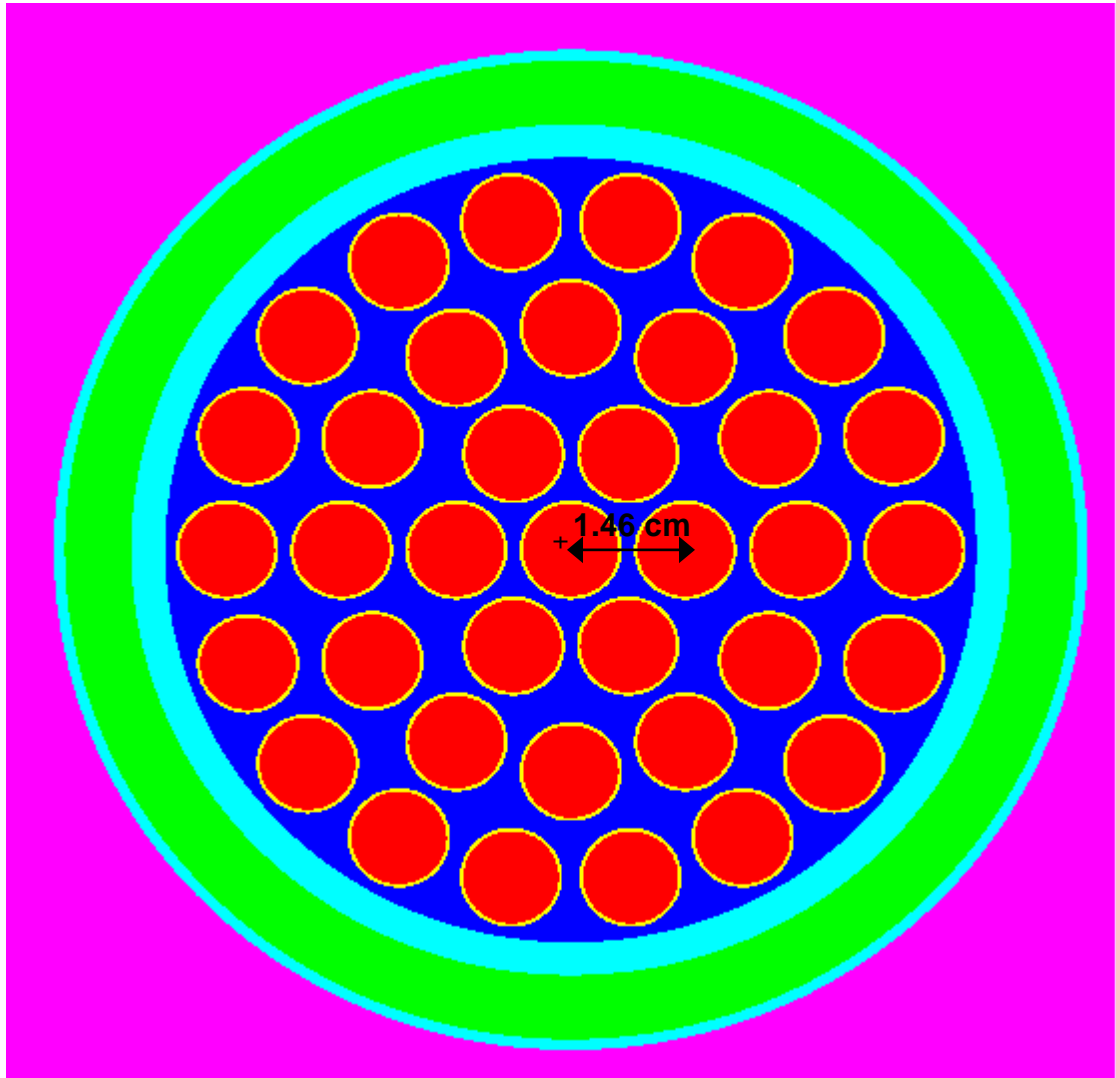


Figure 58: Two-dimensional Rendering of the CANDU-37 Model Cross Section



Figure 59: Picture of a CANDU-37 fuel assembly¹⁰

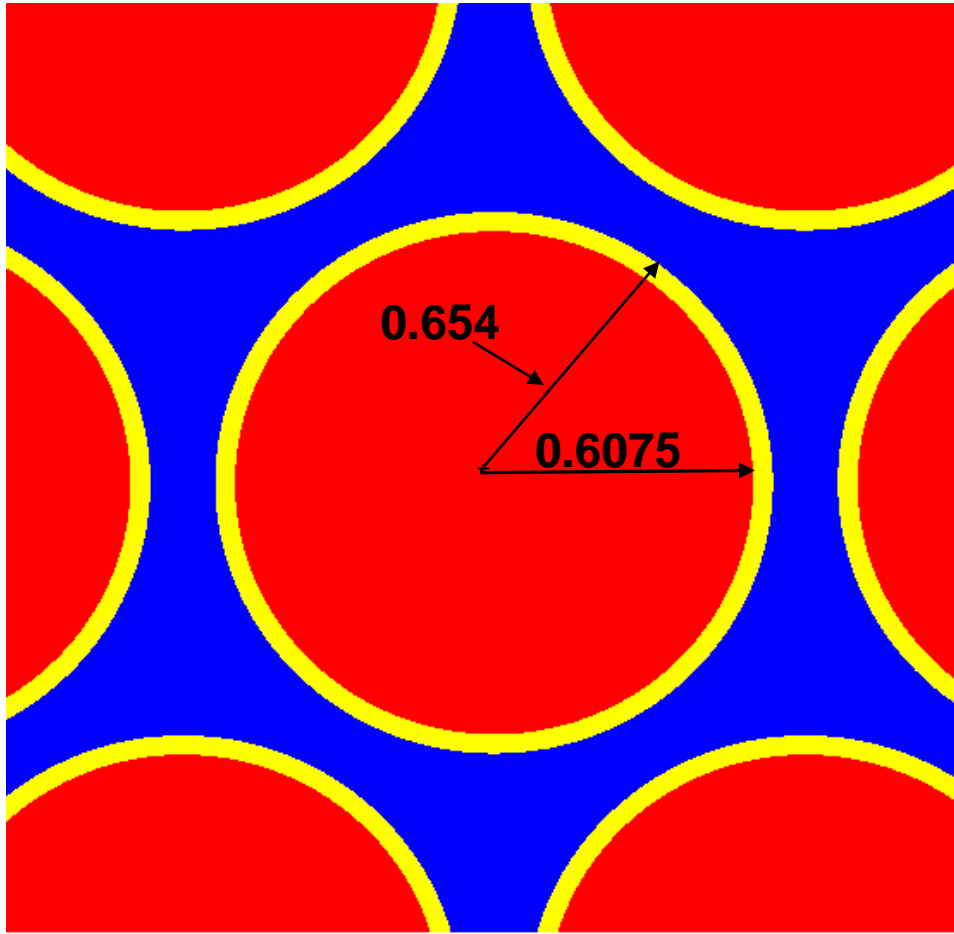


Figure 60: Fuel Rod Dimensions for the MCNPX CANDU-37 Model

The 37-rod fuel assembly is within a Zircaloy-2 pressure tube 0.4343 cm thick which contains pressurized heavy water (D_2O) coolant at a density of 0.836 g/cm^3 and temperature of 583 K (See Figure 61). The Calandria tube, constructed of 0.1397 cm thick Zircaloy-2, contains the pressure tube. An insulating layer (0.8446 cm thick) of CO_2 surrounds the pressure tube within the Calandria tube. The Calandria tube is surrounded by the heavy water moderator which is at a density of 1.0829 g/cm^3 and a temperature of only 343 K. The CO_2 insulator surrounding the pressurized heavy water coolant tubes

keeps the D₂O moderator at a relatively low temperature. Figure 62 is a side view of the MCNPX CANDU model.

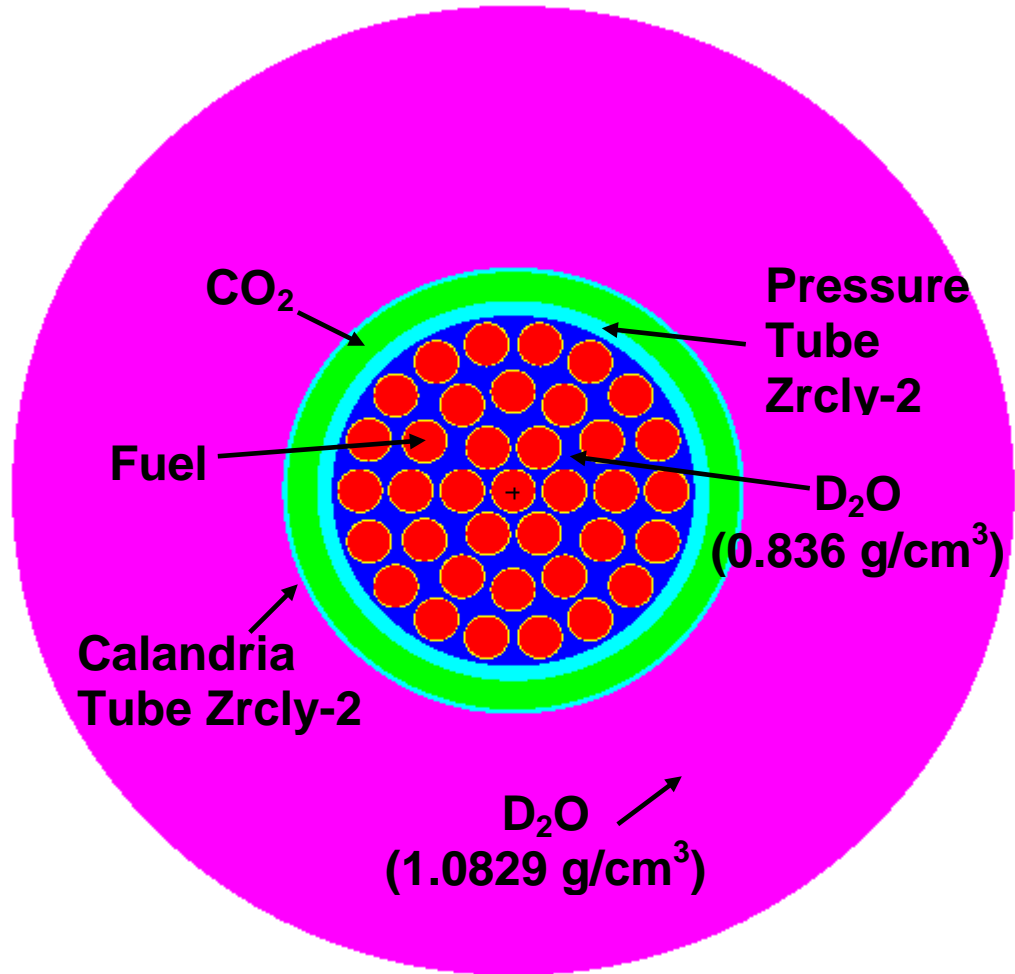


Figure 61: CANDU-37 MCNPX Model with Surrounding D₂O Moderator

Appendix C contains the MCNPX CANDU-37 reactor. The reactor design and operating data for the MCNPX model of the CANDU-37 reactor are contained in Table 19.



Figure 62: Side Cross Sectional View of the CANDU-37 MCNPX Model

Reactor Design and Operating Data	
<i>Fuel Assembly Type</i>	CANDU 37
<i>Fuel Type</i>	UO ₂ pellet
<i>Fuel Density</i>	10.59 g/cm ³
<i>Fuel Temperature</i>	1155 K
<i>Fuel Diameter</i>	12.15 mm
<i>Fuel Enrichment</i>	Natural Uranium
<i>Fuel Height</i>	49.53 cm
<i>Fuel Rod Pitch</i>	1.46 cm
<i>Number of Fuel Rods</i>	37 fuel rods
<i>Cladding</i>	Zircaloy-4
<i>Cladding Thickness</i>	0.0465 cm
<i>Cladding Temperature</i>	599 K
<i>Cladding Density</i>	6.52 g/cm ³
<i>Coolant/Moderator</i>	D ₂ O
<i>Coolant Density</i>	0.836 g/cm ³
<i>Coolant Temperature</i>	583 K
<i>Moderator Density</i>	1.0829 g/cm ³
<i>Moderator Temperature</i>	343 K
<i>CO₂ Layer Thickness</i>	0.8446 cm
<i>Total Uranium Mass</i>	19,832 g (0.019832 MTU)
<i>Reactor Operating Power</i>	0.5 MW
<i>Reactor Operating Time</i>	360 Days
<i>Total Fuel Burnup</i>	9 GWd/MTU

Table 19: CANDU-37 MCNPX Model Fuel Assembly Parameters

Table 20 lists the reactor design and operating data entered into the ORIGEN-ARP GUI for the CANDU-37 model.

<i>Reactor Design and Operating Data for ORIGEN-ARP Model</i>	
<i>Fuel Assembly Type</i>	CANDU-37
<i>Fuel Type</i>	UO ₂
<i>Fuel Enrichment</i>	Natural Uranium
<i>Moderator Density</i>	1.0829 g/cm ³
<i>²³⁴U Initial Mass</i>	1.071 g
<i>²³⁵U Initial Mass</i>	141 g
<i>²³⁸U Initial Mass</i>	19,690 g
<i>Total Uranium Mass</i>	19,832 g (0.019832 MTU)
<i>Reactor Operating Power</i>	0.5 MW
<i>Reactor Operating Time</i>	360 Days
<i>Total Fuel Burnup</i>	9 GWd/MTU

Table 20: CANDU Design and Operating Data for ORIGEN-ARP Model

During the development of the MCNPX CANDU-37 model, the author noted an extreme sensitivity of the results (e.g. actinide production rate) to changes in the radius of the surrounding D₂O moderator. To understand this sensitivity, it is first necessary to understand how D₂O works as a moderator. Figure 63 below is an illustration of the properties of D₂O and H₂O as moderators. The figure shows two spheres of the same dimensions (100 cm radius), each with an identical source at the center of the sphere.

Each sphere has a reflective boundary. The yellow sphere on the left contains D_2O , and the blue sphere on the right contains H_2O . The author used MCNPX and VISEd to model and illustrate the spheres with one neutron particle track in each sphere.

In the H_2O sphere on the right side of Figure 63, one neutron originates from the source material at the center of the light water sphere. The particle is then tracked through each collision until it is absorbed. As shown, the neutron only travels a short distance before each collision and is absorbed after a relatively few number of collisions.

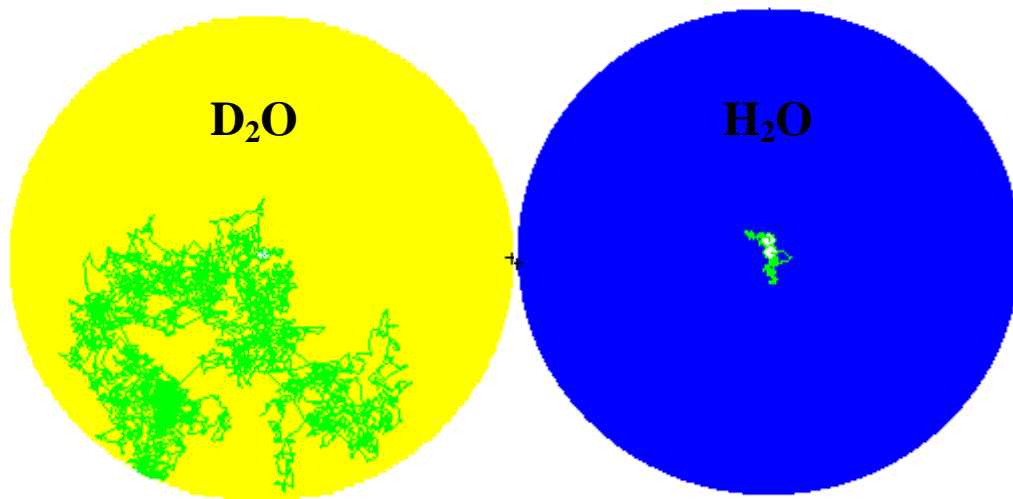


Figure 63: Two Spheres – D_2O and H_2O each with 1 neutron particle track

In contrast, in the D_2O sphere of the left side of Figure 63, one neutron is also started at the center of the heavy water sphere. This neutron, however, undergoes a much larger number of collisions and travels a much greater distance prior to being absorbed. This can be explained by the fact that a hydrogen nuclide in light water has approximately the same mass as the neutron traveling through the light water; therefore, when the neutron collides with the hydrogen nuclide, it loses much of its energy. Conversely, a deuterium nuclide is about twice as massive as a neutron and, consequently, results in the colliding neutron losing less energy per collision than it would in a hydrogen nuclide collision. This can be explained by understanding the concept of diffusion lengths. The diffusion length of a material characterizes the distance a neutron can travel in that material before being absorbed.

According to Lamarsh¹², the thermal neutron diffusion length of H_2O is 2.85 cm, and the thermal neutron diffusion length of D_2O is 97 cm. The greater the diffusion length value, the further the neutron will travel before reaching thermal energies and subsequently being absorbed. For this reason, heavy water is not as efficient as light water is at slowing down neutrons to thermal energies, but heavy water also absorbs fewer neutrons than light water. Figure 64 is a graph of the absorption cross section of hydrogen and deuterium as a function of incident neutron energy. This figure was generated using ENDF/B-VII.0 data published on Brookhaven National Laboratory's National Nuclear Data Center's web site.

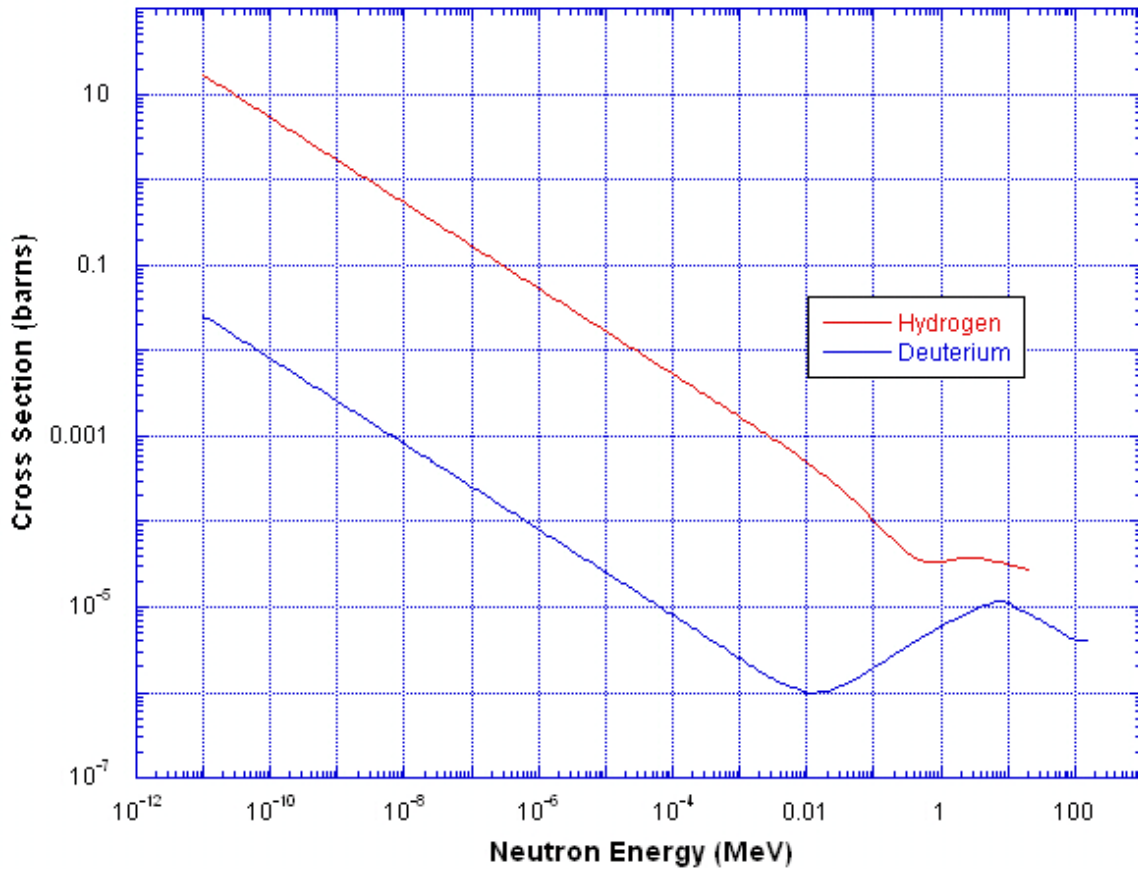


Figure 64: Hydrogen and Deuterium Neutron Absorption Cross Sections

This property of absorbing fewer neutrons than light water allows heavy water to be used as both a coolant and moderator in certain reactor designs. However, because heavy water has a greater diffusion length, the fuel assembly must be surrounded by a large amount of heavy water in which the neutrons can thermalize prior to being absorbed by the fuel.

In the CANDU-37 MCNPX model in this study, the author discovered that the radius of the outer fuel assembly cylinder (containing the D₂O) moderator had a dramatic effect on the actinide production as well as the k-effective value calculated by MCNPX.

If the cylinder radius was too small (e.g. 10 cm), the k-effective fell below 1.0 and the actinide agreement with ORIGEN-ARP values was very poor. Good agreement with the ORIGEN-ARP values was obtained when increasing the radius of the outer cylinder to 14.29 cm (28.58 cm diameter) which corresponds to the fuel channel pitch (28.575 cm) listed in Gauld *et al.* (1995)¹¹.

5.2 THE RESULTS

In general, the CANDU results, using the final CANDU-37 model in Appendix C, were in good agreement with the ORIGEN-ARP results.

Figures 65, 67-69, and 72 are plots of the MCNPX CANDU-37 model and ORIGEN-ARP model results for several of the nuclides of interest in this study. The remaining nuclide production plots for the CANDU-37 models are found in Appendix F.

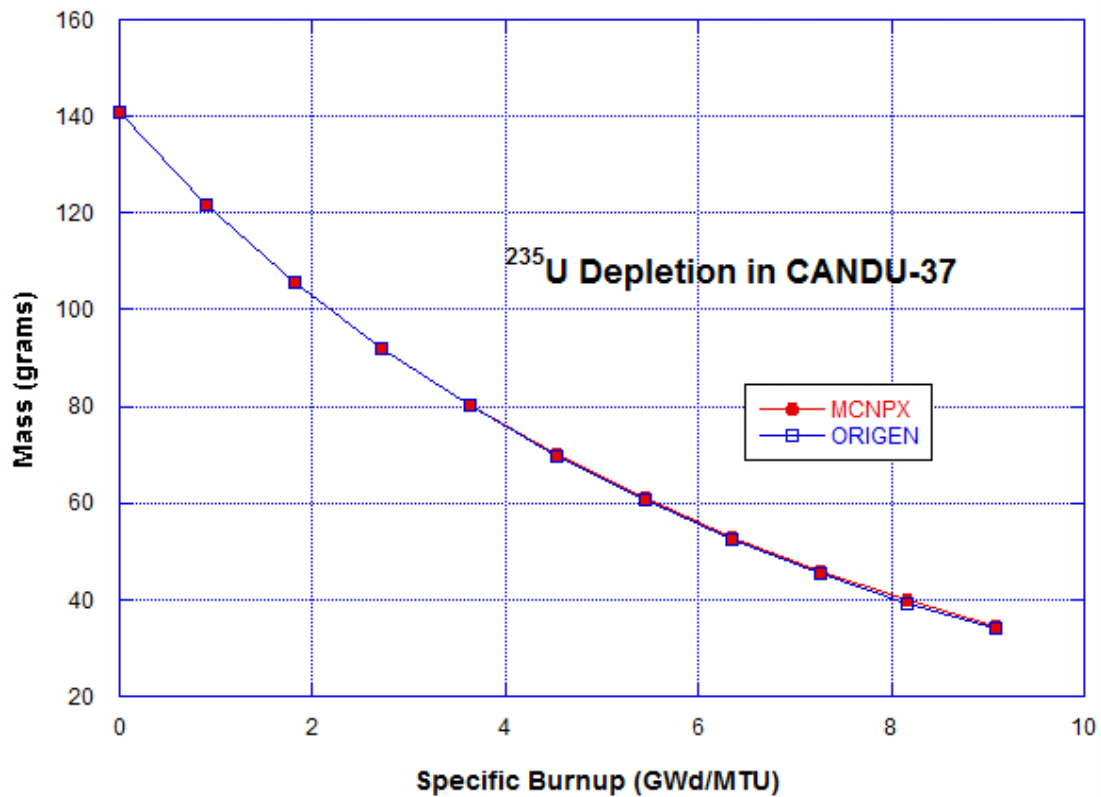


Figure 65: CANDU-37 Results for ²³⁵U Depletion

At very low burnup values, the ^{235}U depletion appears linear. ^{235}U nuclide loss is due primarily to thermal neutron fission, but also occurs due to radiative capture. Figure 66 is a plot of the different neutron absorption reaction rates for ^{235}U as calculated by MCNPX for the CANDU-37 reactor model in this study. As shown by the plot, thermal neutron fission reactions dominate neutron reaction rate of ^{235}U and therefore, are the primary contributors to the shape of the ^{235}U depletion curve.

At higher burnup values, the rate of ^{235}U depletion slows as the ^{235}U fission rate decreases with less available ^{235}U to fission. There is no significant difference between the MCNPX and ORIGEN-ARP ^{235}U values for the CANDU-37 models.

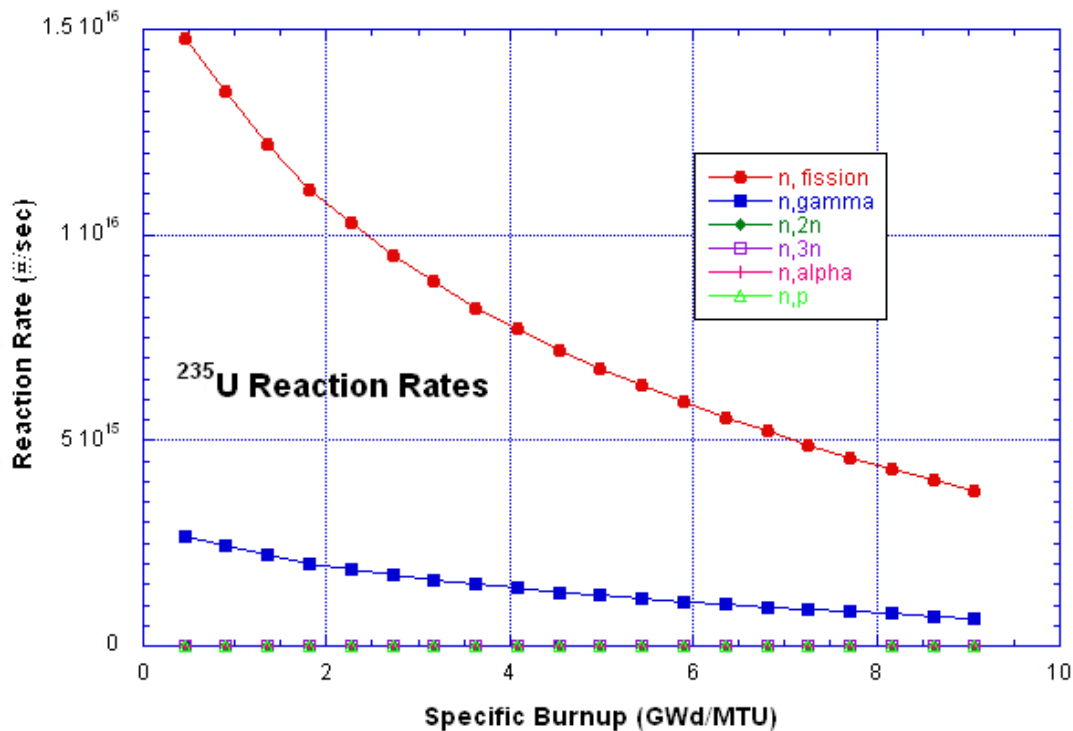


Figure 66: ^{235}U Reaction Rates for the CANDU-37 MCNPX Model

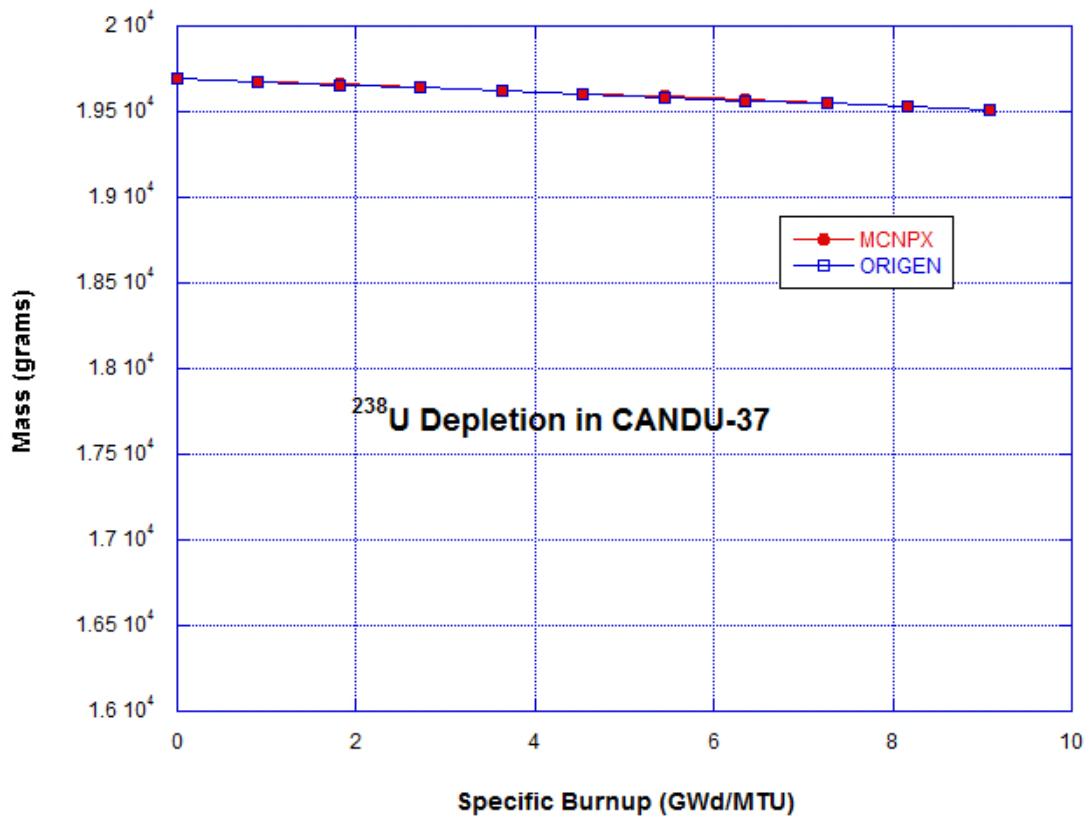
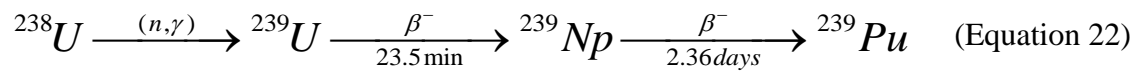


Figure 67: CANDU-37 Results for ^{238}U Depletion

Figure 67 is a plot of the ^{238}U depletion in the CANDU-37 reactor models. The depletion is roughly linear as a function of fuel burnup. Radiative capture (n,γ) reactions are the dominant loss mechanism for ^{238}U in the CANDU-37 reactor model. ^{238}U radiative capture results in the production of ^{239}Pu as shown below:



There is no significant difference in the quantity of ^{235}U produced between the MCNPX and ORIGEN-ARP models.

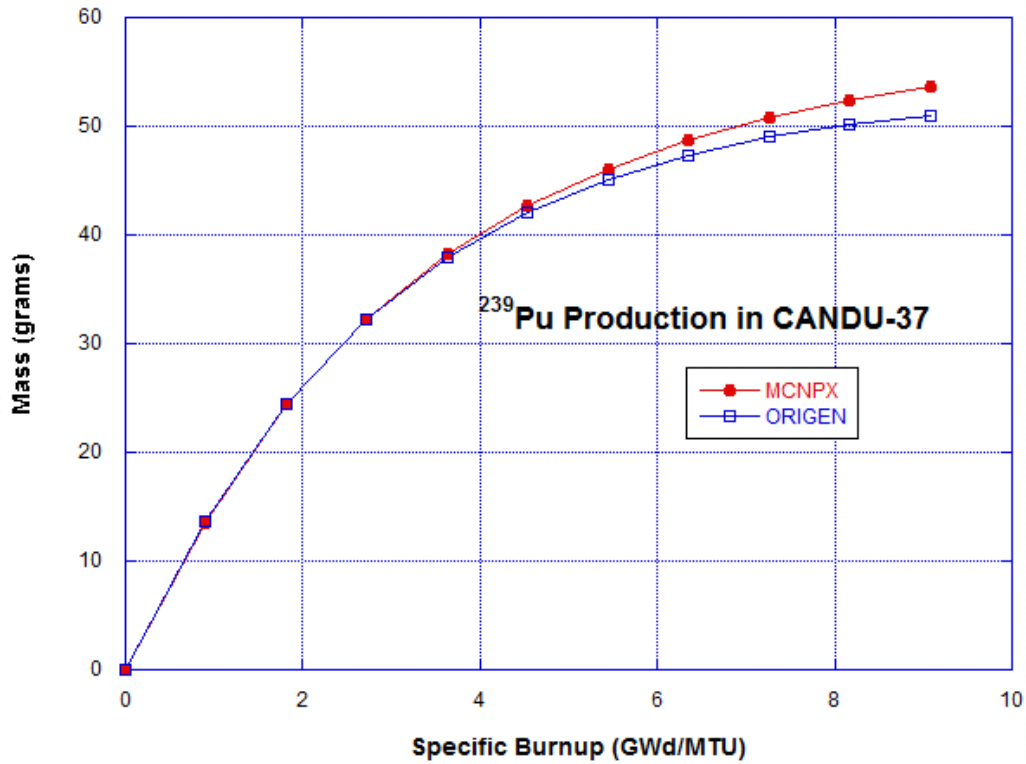


Figure 68: CANDU-37 Results for ^{239}Pu Production

As shown in Figure 68, the ^{239}Pu growth rate appears linear at low burnup values. At higher burnup values, in both the MCNPX and the ORIGEN-ARP models, the ^{239}Pu growth rate slows due to the competing loss from neutron absorption reactions, primarily fission (n, f) and radiative capture (n, γ).

The ^{239}Pu production rates for the MCNPX and the ORIGEN-ARP models agree well at low fuel burnup values. At higher burnup values, the MCNPX model indicates a greater production of ^{239}Pu than the ORIGEN-ARP model.

Figure 69 shows the ^{245}Cm production in the CANDU-37 reactor models. Again, as in the BWR and PWR models, the ^{245}Cm quantities are greater. This can be attributed to the larger total neutron flux value in the MCNPX model.

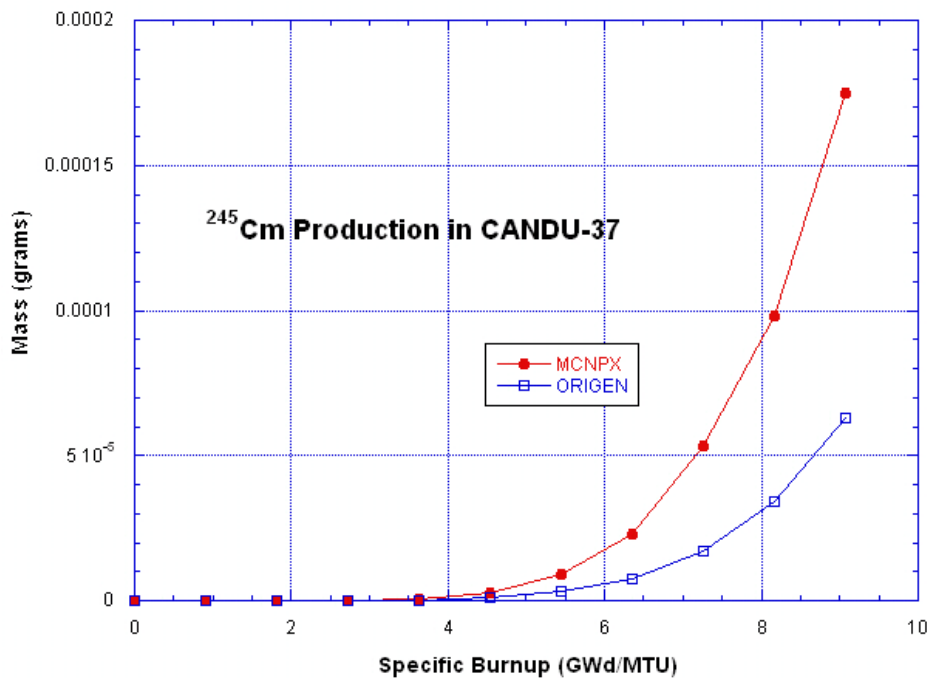


Figure 69: ^{245}Cm Production in CANDU-37 Reactor Model

Figure 70 is a nuclide chart of computed actinide values at final burnup. Again, the greater values for higher actinides are indicative of a higher total neutron flux in the MCNPX model.

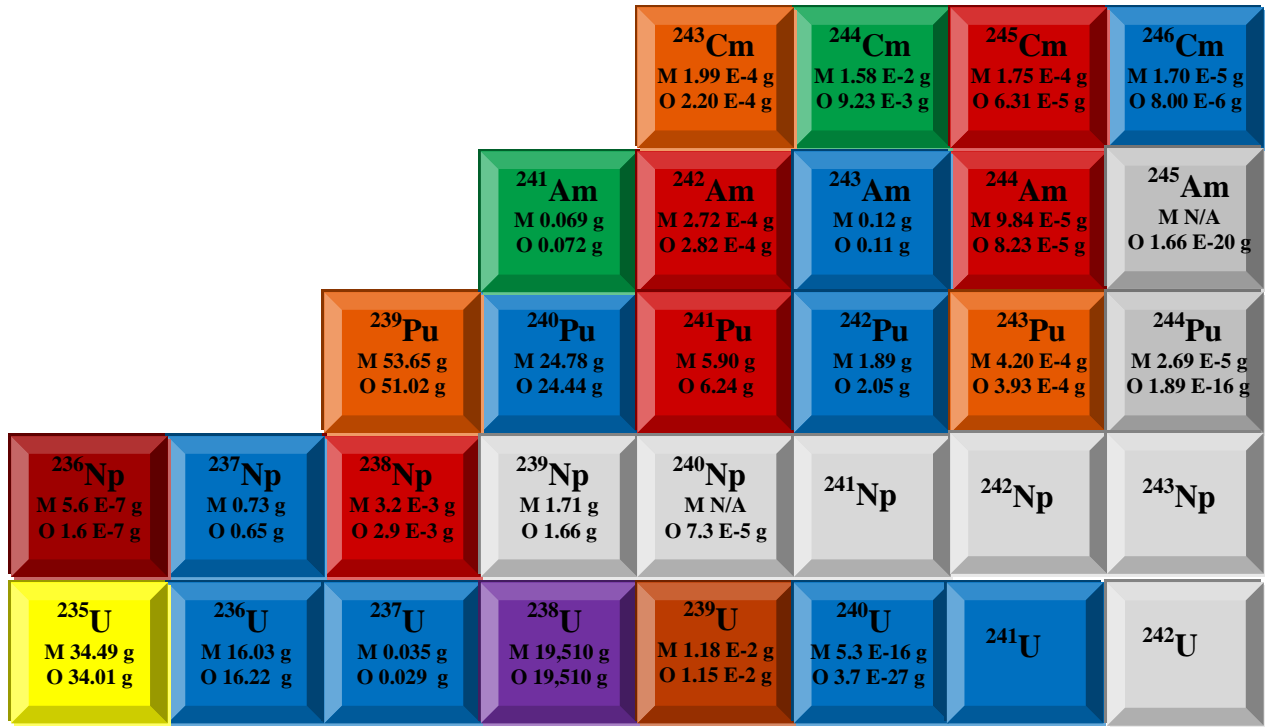


Figure 70: CANDU Nuclide Chart of Computed Actinide Values at Final Burnup

As Figure 70 shows, there is a large variance in the ²⁴⁴Pu results for the two models. The MCNPX value is much greater than the ORIGEN-ARP values. Again, a higher flux in the MCNPX model can cause greater values for the higher actinides.

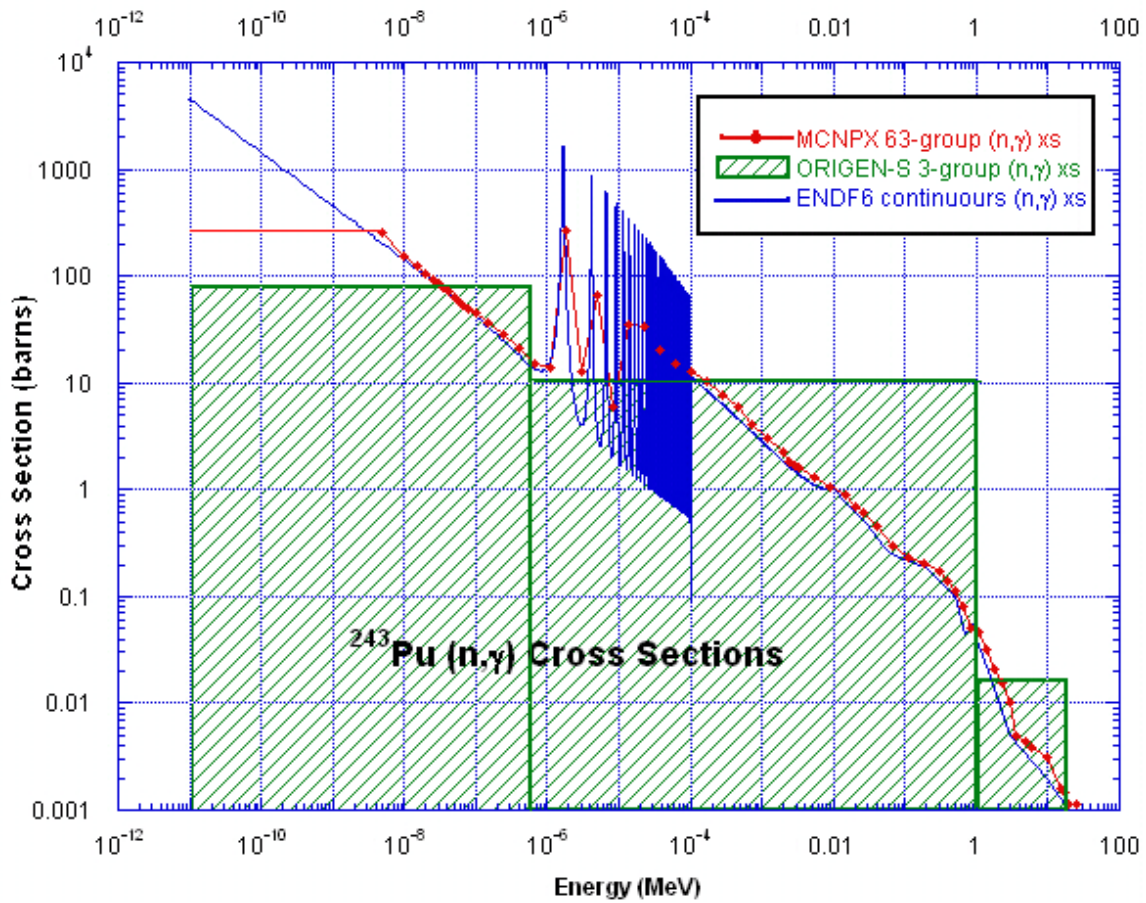


Figure 71: MCNPX, ORIGEN-S, and NNDC Cross Sections for $^{243}\text{Pu}(n,\gamma)$ Reaction

Figure 71 shows the radiative capture cross sections from ENDF/B-VII.0¹³, the *cinder.dat* file used by MCNPX, and the ORIGEN-S libraries. ORIGEN-S uses a three-energy group structure, whereas MCNPX uses a 63-energy group structure which more closely resembles the ENDF/B-VII.0 “continuous” spectrum.

Figure 72 is a plot of ^{136}Xe for the two models. As with the majority of the fission products analyzed, the agreement between the two models is good.

Table 21 shows the percent differences between the two models for the fission products analyzed in this study.

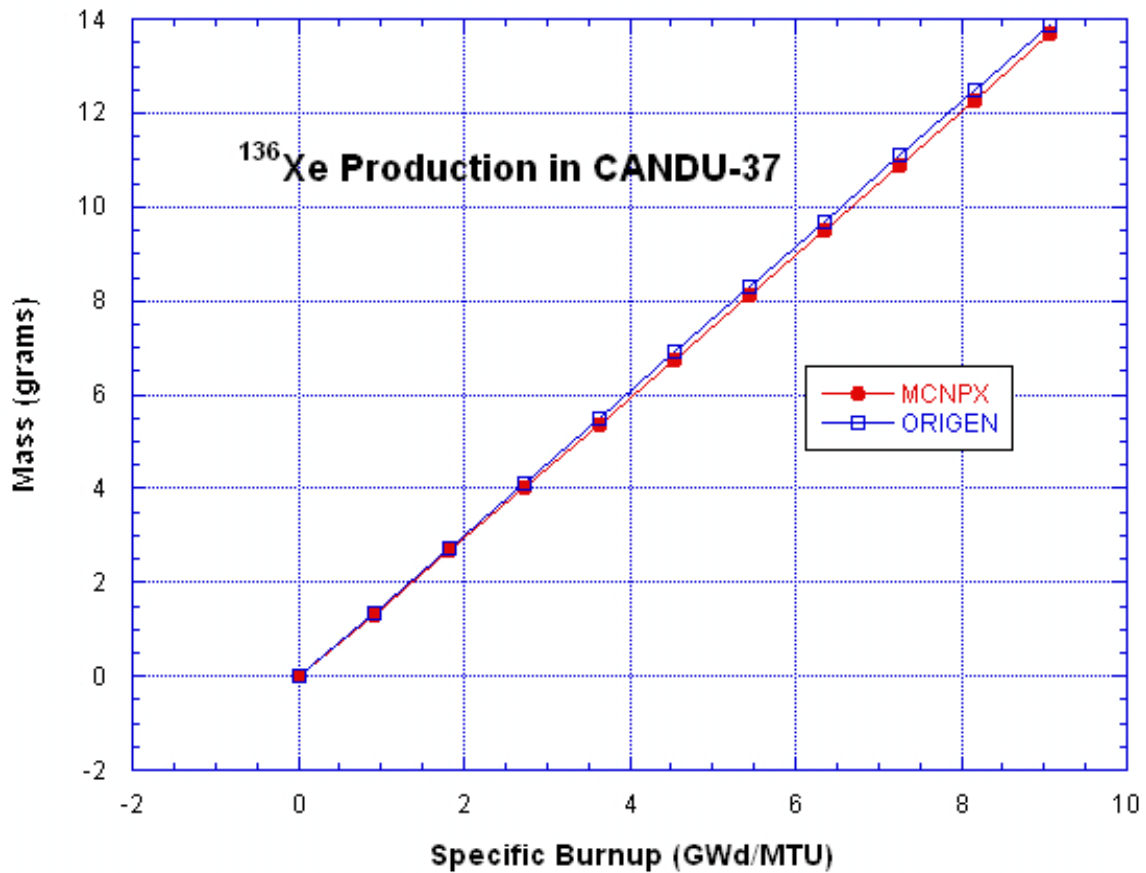


Figure 72: ¹³⁶Xe Production in CANDU-37 Reactor

In order to understand the differences between the ORIGEN and MCNPX results, it is necessary to understand the differences in how the two codes perform the burnup calculations.

The MCNPX output files contain the calculated fission rates and neutron absorption rates as a function of fuel burnup for more than 280 different nuclides. Both MCNPX and ORIGEN account for the following neutron absorption reactions: (n, γ), (n,2n), (n,3n), (n, α), (n,p), and (n,fission). The (n, γ) and (n,fission) reactions are the

dominant reactions for the actinides. Due to the reaction high energy threshold, (n, α) and (n,p) reactions are negligible for the actinides. Figure 73 is a plot of the fission rates of the dominant actinides undergoing fission in the CANDU-37 reactor model. As shown in the figure, ^{235}U fission dominates at the lower burnups, but at higher burnups, where the ^{235}U quantity in the fuel has been significantly depleted and ^{238}U neutron absorption has led to the production of a significant quantity of ^{239}Pu , ^{239}Pu fission begins to dominate. This switch in fission species domination occurs at a fuel burnup of approximately 4.75 GWd/MTU.

<i>Fission Product</i>	<i>Percent Difference (%) (Negative value indicates MCNPX value is greater)</i>
⁹⁷ Mo	5.37
⁹⁸ Mo	8.97
¹⁰⁰ Mo	8.45
¹³⁸ Ba	1.15
¹⁴⁰ Ce	9.36
¹⁴² Ce	4.17
¹⁴⁸ Nd	5.31
⁷² Ge	-10.99
⁹⁰ Sr	3.77
⁹¹ Y	4.50
⁹¹ Zr	5.26
⁹² Zr	4.76
⁹³ Zr	-39.99
⁹⁴ Zr	2.82
⁹⁵ Zr	5.97
¹³⁰ Te	-1.66
¹³¹ I	-2.12
¹³⁵ I	4.61
¹³¹ Xe	1.26
¹³² Xe	2.26
¹³⁴ Xe	1.05
¹³⁵ Xe	0.94
¹³⁶ Xe	1.51
¹³⁴ Cs	-14.40
¹³⁷ Cs	5.38
¹³⁹ La	1.15
¹⁴⁹ Sm	5.73
¹⁶¹ Dy	8.98

Table 21: CANDU Fission Product Differences at Maximum Burnup Values

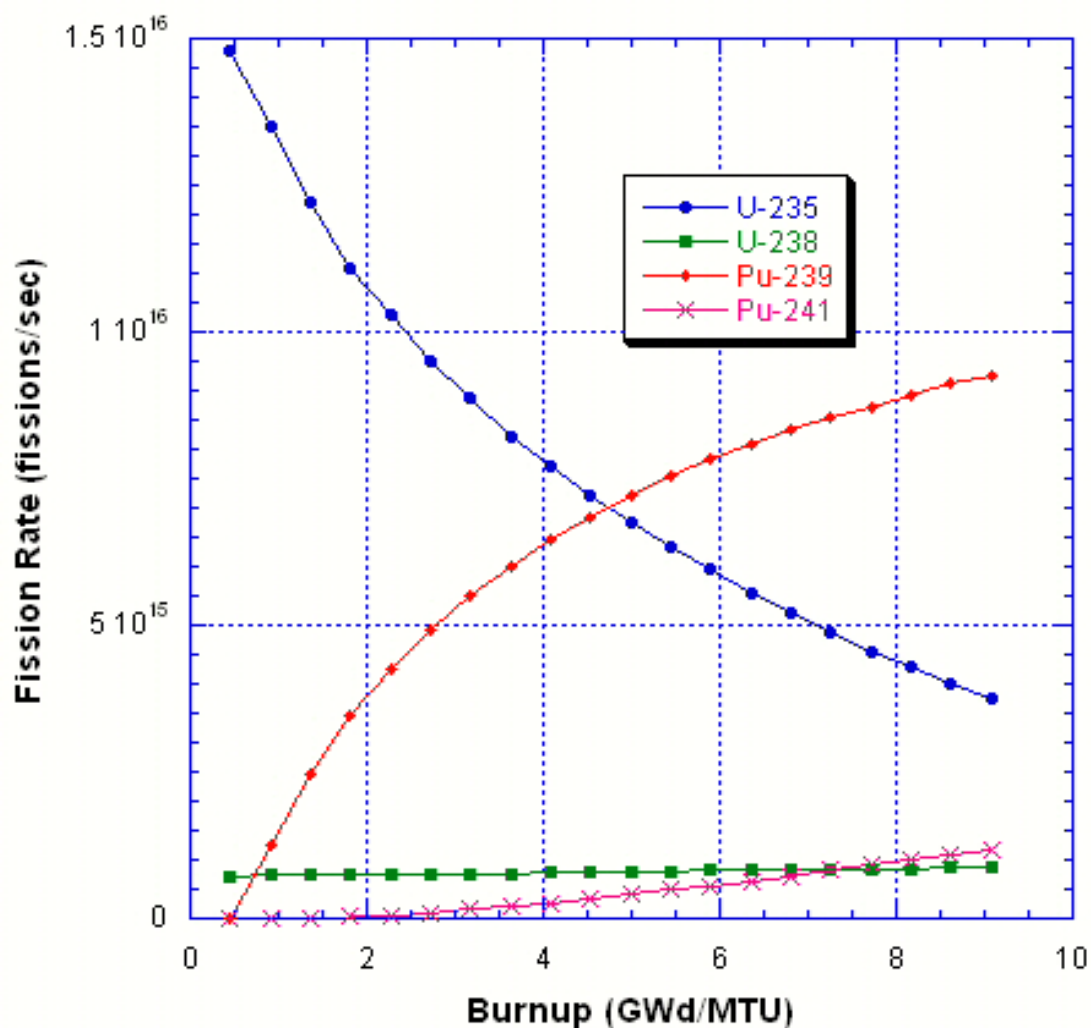


Figure 73: Fission Rates Calculated by MCNPX for the CANDU-37 Model

In order to understand how closely the MCNPX model matches the ORIGEN model, we can compare the fission and absorption reaction rates of the two models.

Though the ORIGEN-ARP output file does not contain these rates, they can be calculated from the given flux, isotopic mass, and the ARP effective cross sections. The flux and isotopic mass, as a function of burnup, are contained in the ORIGEN-ARP

output file. However, the ARP effective cross sections are contained in binary format in the library files of the SCALE code. These cross sections can be extracted by using the *xseclist* command within the SCALE code. Appendix H is an example of the SCALE 5.1 input deck for extracting the ORIGEN-ARP cross sections from the ORIGEN-ARP libraries.

There are two ARP effective cross sections for each of the nuclides in the ORIGEN-S library (approximately 1400 nuclides): fission and absorption. The absorption cross section is the sum of the cross sections for (n, γ), (n,2n), (n,3n), (n, α), (n,p), and (n,fission) reactions.

The ORIGEN fission rate for each actinide can be calculated using the following equation:

$$Fission\ Rate = \phi \left(\frac{n}{cm^2 s} \right) * \sigma (cm^2) * N \quad (Equation\ 23)$$

where

ϕ is the ORIGEN-determined neutron flux,

σ is the ARP effective fission cross section for the actinide, and

N is the number of atoms of the actinide.

Each term of the above equation is time- (fuel burnup-) dependent.

Tables 22-25 show a comparison of the calculated ORIGEN-ARP fission rates versus the listed MCNPX output file fission rates of the highest four fission rate actinides for the CANDU-37 model: ^{235}U , ^{238}U , ^{239}Pu , and ^{241}Pu . Figure 74 is a plot of the ORIGEN-ARP fission rates.

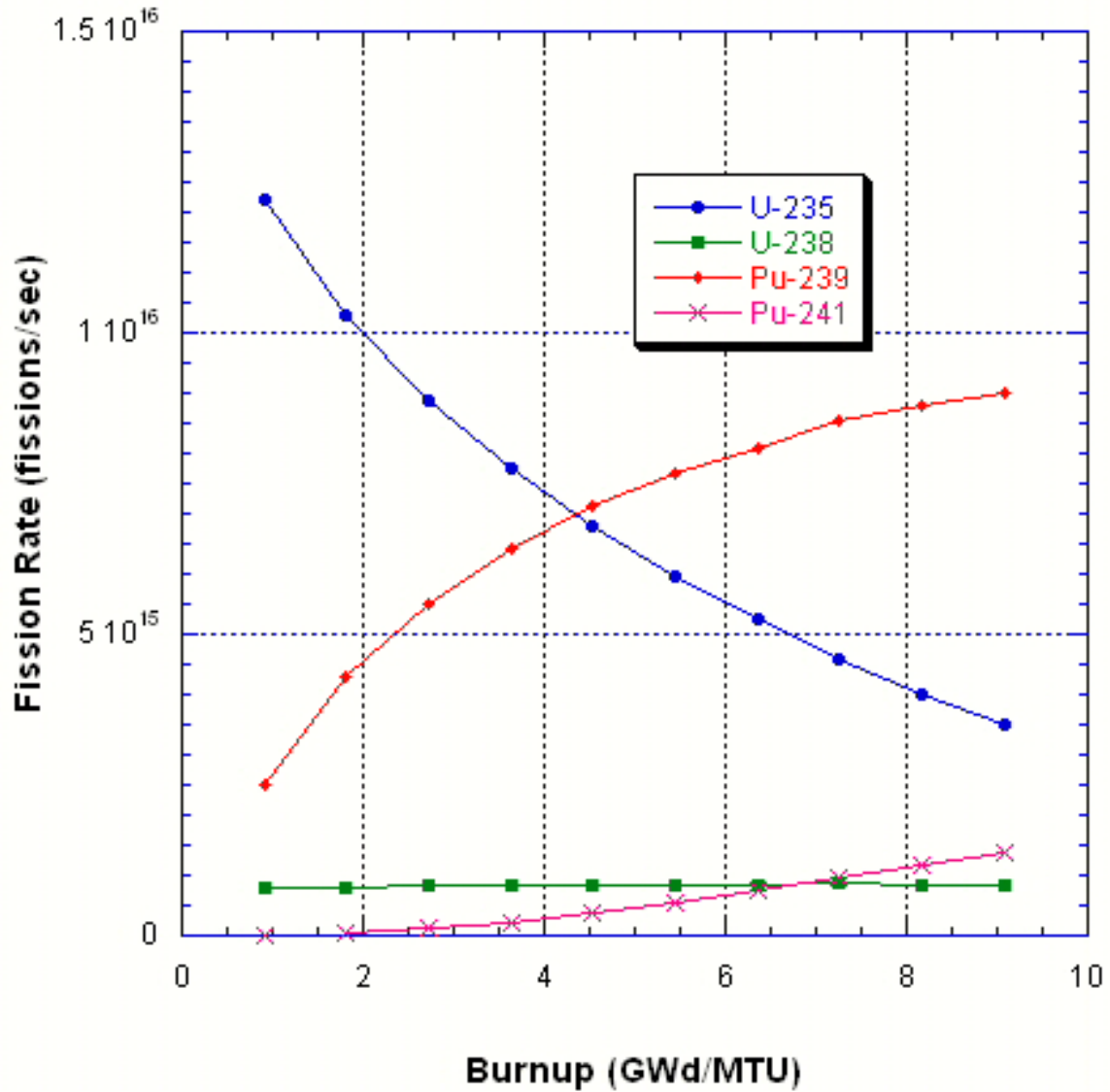


Figure 74: Fission Rates Derived from ORIGEN-ARP CANDU-37 Model

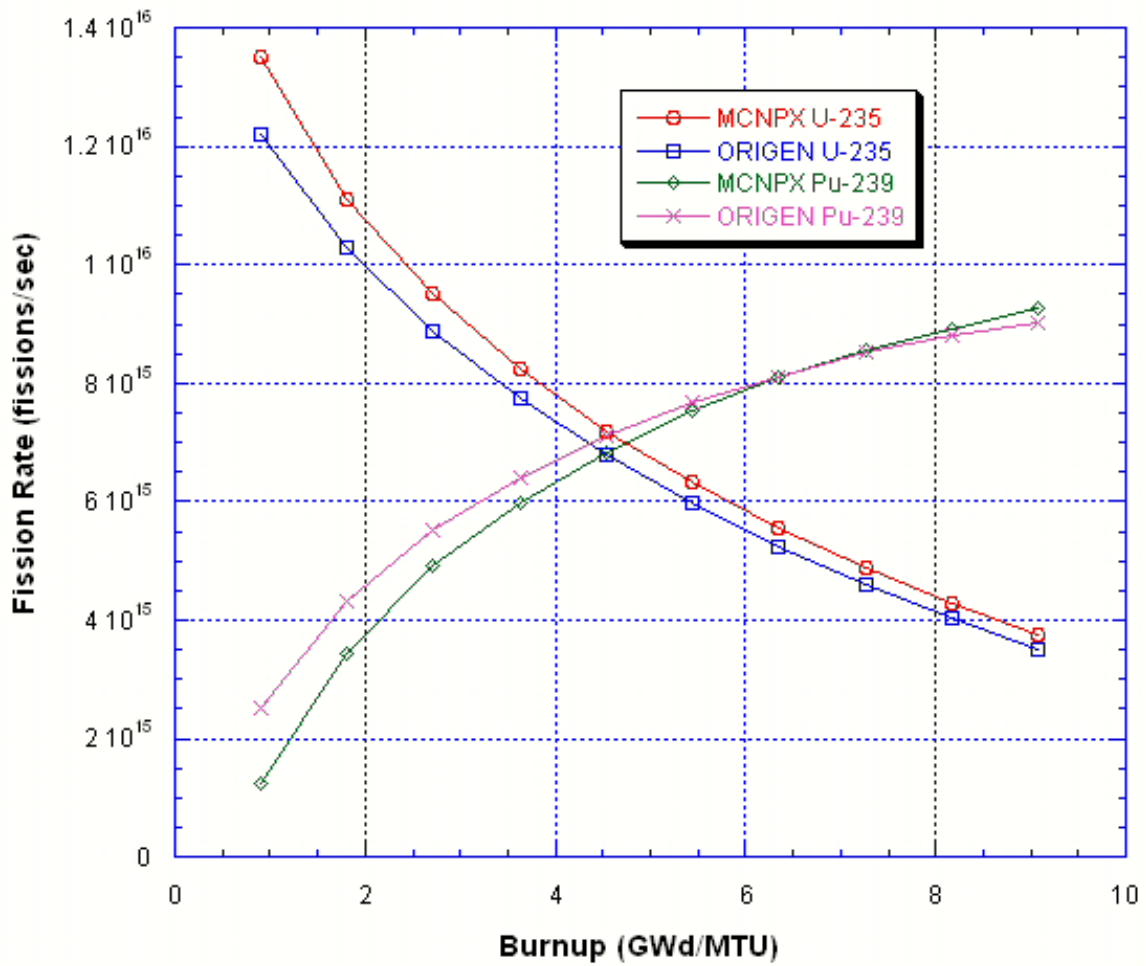


Figure 75: MCNPX versus ORIGEN Fission Rate Comparison

Figure 75 is a plot of the ²³⁵U and ²³⁹Pu fission rates for the CANDU-37 model for both codes. The MCNPX model ²³⁵U fission rate is higher than the ORIGEN-ARP model of ²³⁵U fission rate.

<i>Burnup (GWd/MTU)</i>	<i>ORIGEN Flux (n/cm²s)</i>	<i>ARP Effective Fission Cross Section (barns)</i>	<i>ORIGEN Mass (grams)</i>	<i>ORIGEN Fission Rate (fissions/s)</i>	<i>MCNPX Fission Rate (fissions/s)</i>
0.91	1.03E+14	3.78E+02	1.22E+02	1.22E+16	1.35E+16
1.81	9.99E+13	3.81E+02	1.06E+02	1.03E+16	1.11E+16
2.72	9.82E+13	3.84E+02	9.20E+01	8.89E+15	9.52E+15
3.63	9.79E+13	3.86E+02	8.01E+01	7.76E+15	8.23E+15
4.54	9.83E+13	3.88E+02	6.97E+01	6.80E+15	7.19E+15
5.44	9.92E+13	3.89E+02	6.05E+01	5.98E+15	6.33E+15
6.35	1.00E+14	3.89E+02	5.25E+01	5.25E+15	5.56E+15
7.26	1.01E+14	3.88E+02	4.55E+01	4.59E+15	4.89E+15
8.17	1.03E+14	3.89E+02	3.94E+01	4.02E+15	4.29E+15
9.07	1.04E+14	3.89E+02	3.40E+01	3.51E+15	3.76E+15

Table 22: ²³⁵U Fission Rates for the ORIGEN and MCNPX CANDU-37 Models

<i>Burnup (GWd/MTU)</i>	<i>ORIGEN Flux (n/cm²s)</i>	<i>ARP Effective Fission Cross Section (barns)</i>	<i>ORIGEN Mass (grams)</i>	<i>ORIGEN Fission Rate (fissions/s)</i>	<i>MCNPX Fission Rate (fissions/s)</i>
0.91	1.03E+14	1.56E-01	1.97E+04	8.00E+14	7.32E+14
1.81	9.99E+13	1.63E-01	1.97E+04	8.12E+14	7.50E+14
2.72	9.82E+13	1.71E-01	1.96E+04	8.35E+14	7.55E+14
3.63	9.79E+13	1.74E-01	1.96E+04	8.44E+14	7.72E+14
4.54	9.83E+13	1.72E-01	1.96E+04	8.39E+14	7.93E+14
5.44	9.92E+13	1.69E-01	1.96E+04	8.30E+14	8.08E+14
6.35	1.00E+14	1.66E-01	1.96E+04	8.23E+14	8.30E+14
7.26	1.01E+14	1.72E-01	1.96E+04	8.63E+14	8.45E+14
8.17	1.03E+14	1.69E-01	1.95E+04	8.56E+14	8.52E+14
9.07	1.04E+14	1.66E-01	1.95E+04	8.49E+14	8.75E+14

Table 23: ²³⁸U Fission Rates for the ORIGEN and MCNPX CANDU-37 Models

<i>Burnup (GWd/MTU)</i>	<i>ORIGEN Flux (n/cm²s)</i>	<i>ARP Effective Fission Cross Section (barns)</i>	<i>ORIGEN Mass (grams)</i>	<i>ORIGEN Fission Rate (fissions/s)</i>	<i>MCNPX Fission Rate (fissions/s)</i>
0.91	1.03E+14	7.01E+02	1.37E+01	2.50E+15	1.25E+15
1.81	9.99E+13	6.97E+02	2.45E+01	4.30E+15	3.44E+15
2.72	9.82E+13	6.90E+02	3.23E+01	5.52E+15	4.92E+15
3.63	9.79E+13	6.85E+02	3.79E+01	6.41E+15	5.99E+15
4.54	9.83E+13	6.82E+02	4.21E+01	7.11E+15	6.82E+15
5.44	9.92E+13	6.79E+02	4.51E+01	7.66E+15	7.54E+15
6.35	1.00E+14	6.78E+02	4.74E+01	8.10E+15	8.09E+15
7.26	1.01E+14	6.82E+02	4.90E+01	8.53E+15	8.55E+15
8.17	1.03E+14	6.79E+02	5.02E+01	8.80E+15	8.92E+15
9.07	1.04E+14	6.78E+02	5.10E+01	9.02E+15	9.26E+15

Table 24: ²³⁹Pu Fission Rates for the ORIGEN and MCNPX CANDU-37 Models

<i>Burnup (GWd/MTU)</i>	<i>ORIGEN Flux (n/cm²s)</i>	<i>ARP Effective Fission Cross Section (barns)</i>	<i>ORIGEN Mass (grams)</i>	<i>ORIGEN Fission Rate (fissions/s)</i>	<i>MCNPX Fission Rate (fissions/s)</i>
0.91	1.03E+14	8.56E+02	3.27E-02	7.23E+12	1.28E+12
1.81	9.99E+13	8.55E+02	2.07E-01	4.41E+13	3.05E+13
2.72	9.82E+13	8.55E+02	5.64E-01	1.18E+14	1.01E+14
3.63	9.79E+13	8.55E+02	1.10E+00	2.29E+14	2.09E+14
4.54	9.83E+13	8.54E+02	1.78E+00	3.73E+14	3.37E+14
5.44	9.92E+13	8.53E+02	2.58E+00	5.45E+14	4.89E+14
6.35	1.00E+14	8.53E+02	3.46E+00	7.38E+14	6.47E+14
7.26	1.01E+14	8.54E+02	4.38E+00	9.47E+14	8.19E+14
8.17	1.03E+14	8.53E+02	5.31E+00	1.16E+15	9.96E+14
9.07	1.04E+14	8.53E+02	6.24E+00	1.38E+15	1.17E+15

Table 25: ²⁴¹Pu Fission Rates for the ORIGEN and MCNPX CANDU-37 Models

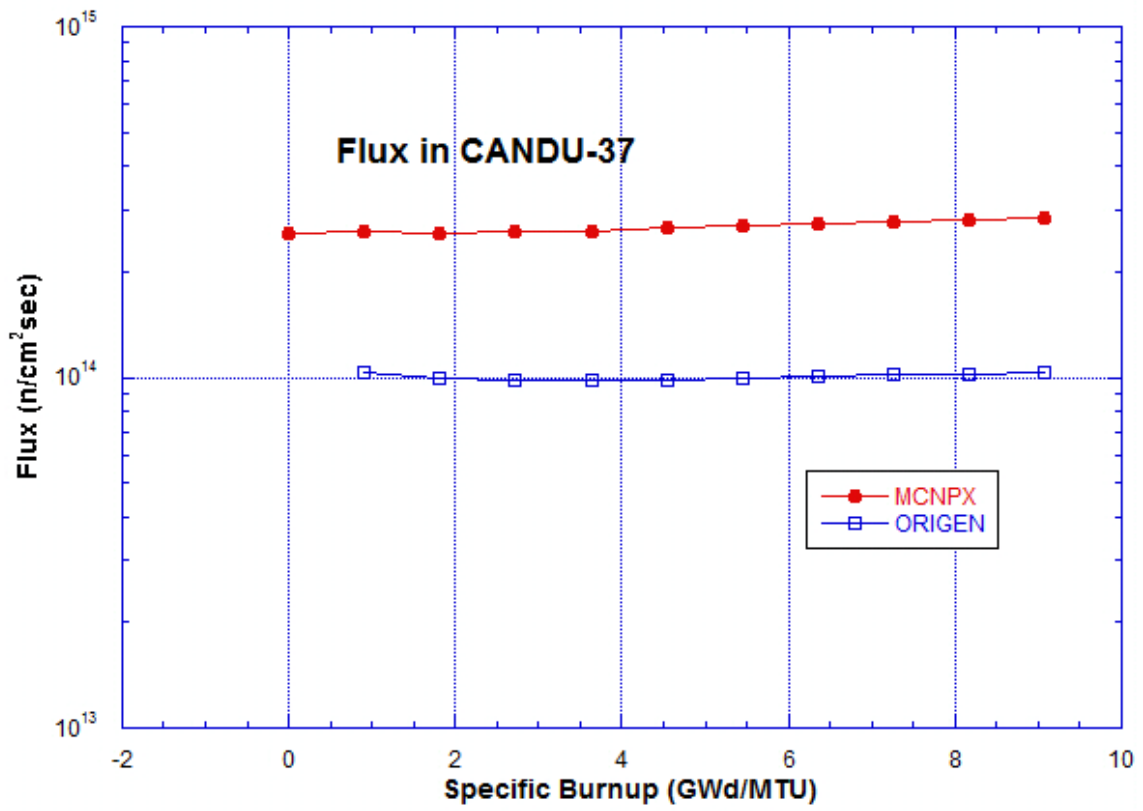


Figure 76: Plot of Computed One-energy Group Flux Values in CANDU

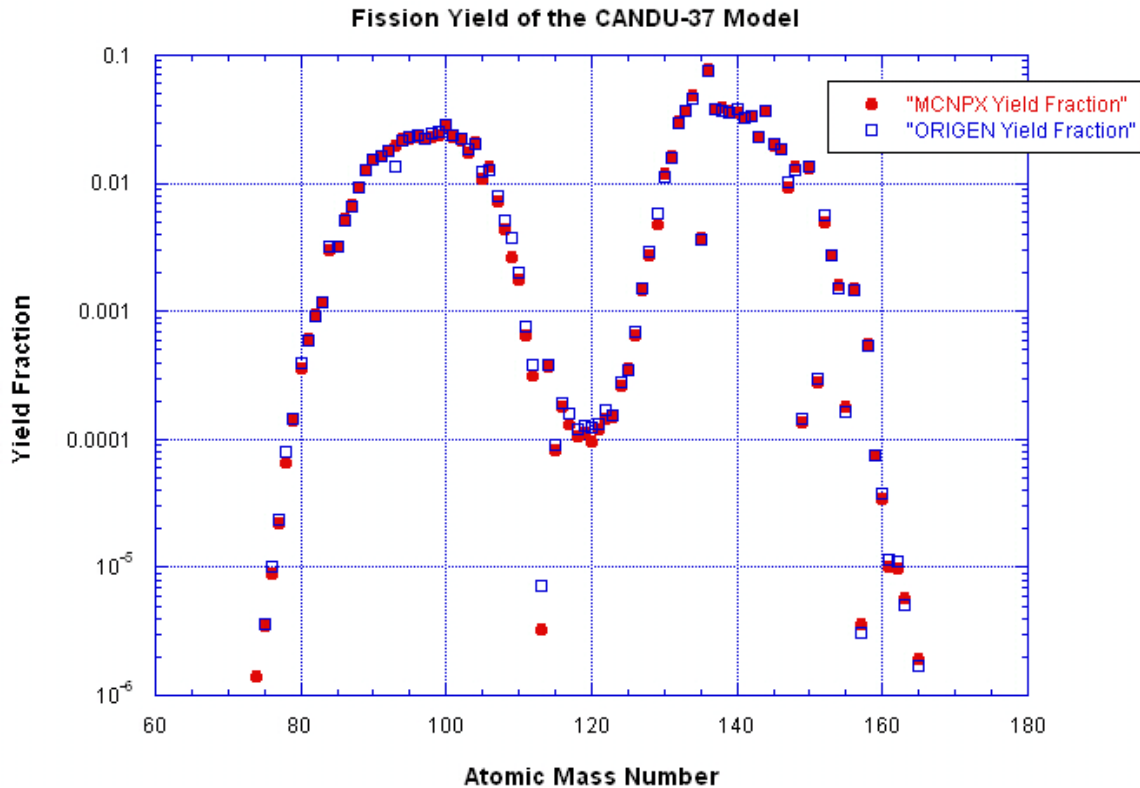


Figure 77: Fission Product Yields for the MCNPX and ORIGEN-ARP CANDU Models

Figure 77 is a plot of the fission product yields for the CANDU-37 models. The ORIGEN-ARP results include a greater number of nuclides than the MCNPX results. Therefore, it is expected that some of the ORIGEN-ARP data points to have a higher yield fraction than the MCNPX data. Additionally, there are primarily four actinides (^{235}U , ^{239}Pu , ^{238}U , and ^{241}Pu) undergoing fission and contributing to the fission product yield. Each of these actinides has a slightly different fission product yield curve, and those curves are different for different energy neutrons. See Figure 78 below, which shows the difference between fission product yields for thermal neutron induced fission in ^{235}U and ^{239}Pu . It should also be noted that the CANDU-37 fission product yield in

Figure 77 above includes both direct and indirect fission products as well as fission products that have been exposed to a high neutron flux environment. Figure 78 below only includes direct fission yield. For example, in Figure 77 above, there are a number of data points that do not follow the natural curve of the plot (e.g. Mass Numbers 135 and 136). Mass Number 136 is shown to be unexpectedly high, whereas Mass Number 135 is too low. This is due to indirect fission product yield and neutron irradiation. ^{135}I , which is a direct fission product, decays into ^{135}Xe . ^{135}Xe has a very high radiative capture cross section ($\sim 2.6 \times 10^6$ barns). The radiative capture of a neutron by ^{135}Xe generates ^{136}Xe which is stable. This, in turn, causes Mass Number 135 to be lower and 136 to be higher than the fission product yield curve.

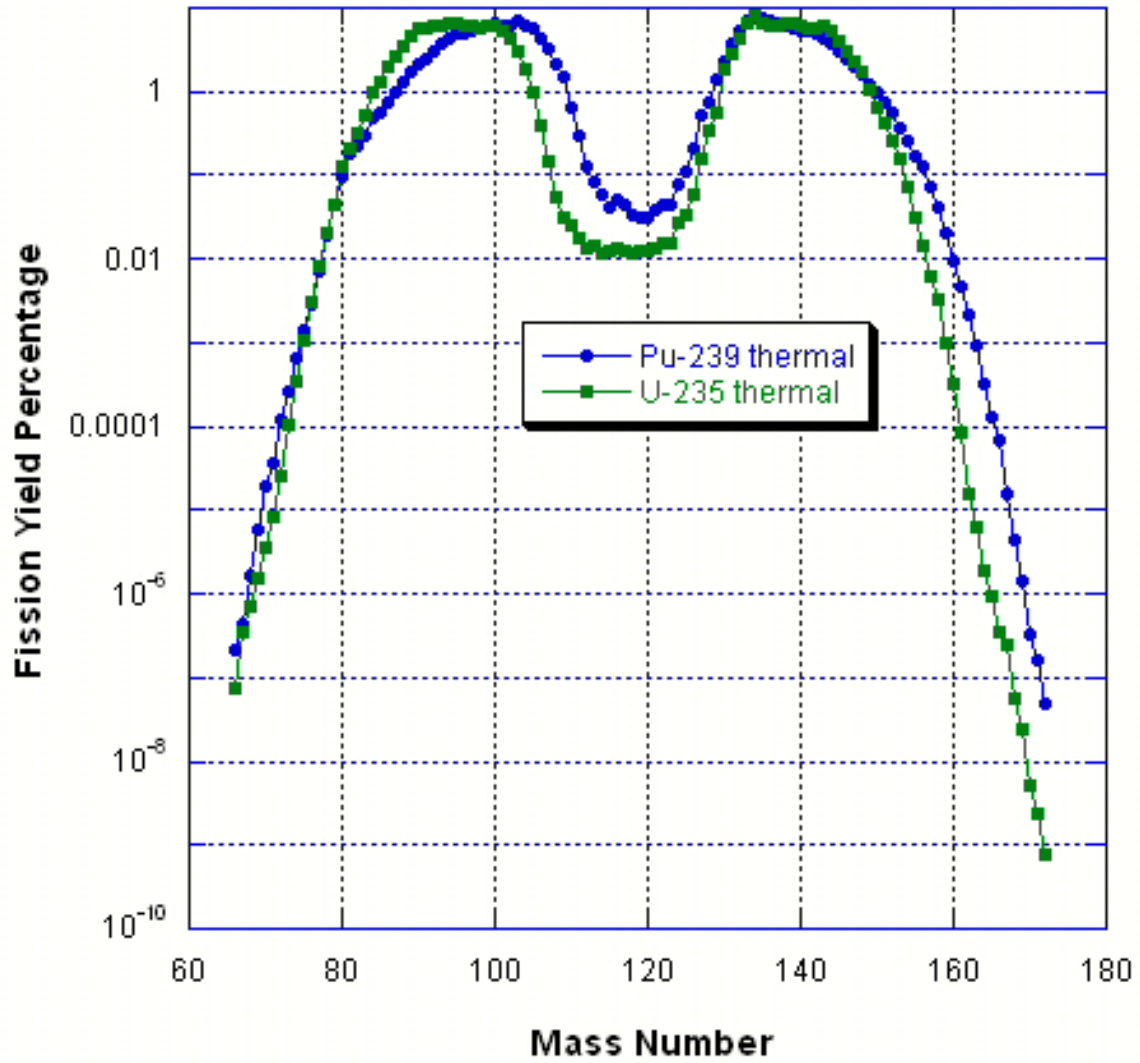


Figure 78: Fission Yields for the Thermal Fission of ^{235}U and ^{239}Pu

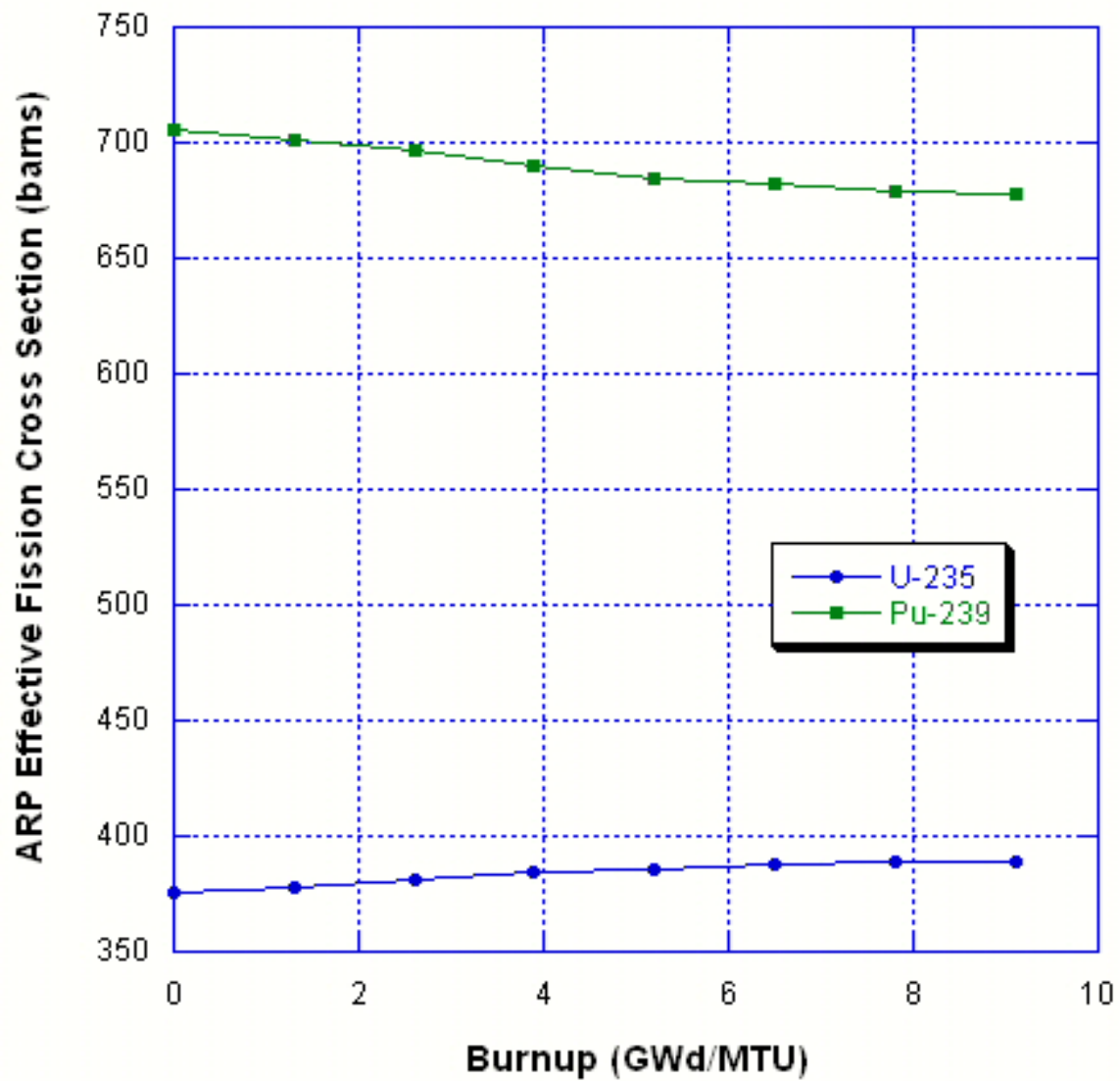


Figure 79: ARP Effective Fission Cross Sections for the CANDU-37 Reactor

5.3 SOURCES OF ERROR

With the exception of the gadolinium and boron content, the sources of error from the previous BWR section apply here to the PWR model as well. The results of the 46 nuclide comparison for the CANDU-37 reactor match even more closely than the BWR and PWR model comparisons do. Strong influences in the behavior of the MCNPX model include: assembly pitch (i.e. how much D₂O surrounded the assembly), moderator and coolant density, and rod pitch. Some minor adjustments to these values may have achieved even closer agreement between these models. Additionally, the power profile in the MCNPX model could have been adjusted to achieve flux matching between the models which would be expected to further drive the results to better agreement. However, such methods would negate the purpose of the study which was to model three different reactors using MCNPX and compare the results to the ORIGEN-ARP results for those same three reactors.

Chapter 6: Sensitivity Study

The fission and absorption cross sections for ORIGEN-ARP are a function of fuel burnup, enrichment, and moderator density and are developed using a very specific set of reactor design parameters. For example, the ORIGEN-ARP code requires, as part of the fuel composition data, that a “fuel type” be chosen from a pull down list of available choices in the code. One available choice is “w17x17” which is a Westinghouse-designed 17x17 PWR fuel assembly. Each “fuel type” assumes a specific type of fuel (e.g. UO₂, U metal), fuel assembly rod pitch, fuel temperature, and moderator temperature. Several reactor design parameters can result in major deviations in the signature of actinide and non-actinide nuclides produced by a reactor. Variation in reactor operating and design parameters, such as ²³⁵U fuel enrichment, irradiation time, reactor power, and reactor type (e.g. PWR vs. CANDU) result in dramatic variation of nuclide production. For this reason, these parameters must be specified in ORIGEN-ARP.

However, other reactor design and operating parameters, such as water density, cladding thickness, and rod pitch would be expected to have a less dramatic variation in nuclide production provided the values of such parameters were kept within the bounds expected to be encountered during normal reactor operation. However, to the nuclear forensic analyst who is attempting to characterize reactor material origin, such variations in reactor design and operating parameters may have the potential to introduce a variation in nuclide production great enough to invalidate his analysis.

For example, if a nuclear forensic analyst is performing a burnup determination on a sample of spent nuclear fuel from a known reactor type (e.g. W-17x17) and known reactor enrichment (e.g. 3.5 weight percent ^{235}U), a series of basic ORIGEN-ARP calculations could be used to reverse-determine the fuel burnup based upon the quantities of certain nuclide quantities which are indicative of fuel burnup values. However, if reactor parameters such as moderator boron concentration or reactor rod pitch are different from the values intrinsic to the ORIGEN-ARP cross section libraries, then the potential exists for the ORIGEN-ARP calculation to give incorrect results. If the reactor design parameters do not match those that went into the ORIGEN-ARP model, then you would have use other methods (e.g. radiation transport modules within the SCALE code) to develop the reactor-specific ORIGEN-ARP cross sections. For an MCNPX model, the source term is derived the exact reactor model which is explicitly defined in the input deck.

This chapter is focused on a MCNPX PWR model sensitivity study which will examine the effects of varying five different reactor design or reactor operating parameters on nuclide production. The five parameters are: fuel assembly rod pitch, moderator boron concentration, cladding thickness, moderator/coolant density, and fuel temperature.

6.1 REACTOR DESIGN AND OPERATING PARAMETERS

Table 26 lists the values of the reactor design and operating parameters analyzed in this sensitivity study.

<i>Case</i>	<i>Boron</i>					
	<i>Rod pitch (cm)</i>	<i>Concentration in Moderator (ppm)</i>	<i>Cladding Thickness (cm)</i>	<i>Water Density (g/cm³)</i>	<i>Fuel Temp (K)</i>	<i>H/U Ratio</i>
<i>1</i>	1.26	850	0.0571	0.723	900	4.394
<i>2</i>	1.285	850	0.0571	0.723	900	4.680
<i>3</i>	1.412	850	0.0571	0.723	900	6.212
<i>4</i>	1.43	850	0.0571	0.723	900	6.441
<i>5</i>	1.26	1000	0.0571	0.723	900	4.393
<i>*</i>	1.26	850	0.0571	0.723	900	4.394
<i>6</i>	1.26	300	0.0571	0.723	900	4.396
<i>7</i>	1.26	0	0.0571	0.723	900	4.397
<i>*</i>	1.26	850	0.0571	0.723	900	4.394
<i>8</i>	1.26	850	0.06175	0.723	900	4.338
<i>9</i>	1.26	850	0.0653	0.723	900	4.296
<i>10</i>	1.26	850	0.0665	0.723	900	4.282
<i>11</i>	1.26	850	0.0571	0.7264	900	4.414
<i>*</i>	1.26	850	0.0571	0.723	900	4.394
<i>12</i>	1.26	850	0.0571	0.7135	900	4.336
<i>13</i>	1.26	850	0.0571	0.710	900	4.315
<i>14</i>	1.26	850	0.0571	0.723	700	4.394
<i>*</i>	1.26	850	0.0571	0.723	900	4.394
<i>15</i>	1.26	850	0.0571	0.723	1100	4.394
<i>16</i>	1.26	850	0.0571	0.723	1300	4.394

*identical to Case 1

Table 26: Reactor Design and Operating Parameters for Sensitivity Study

The MCNPX PWR Model was discussed in depth in Chapter 4 of this dissertation. A copy of the MCNPX input deck (Case 1) is included in Appendix B. Table 27 lists the design/operating parameters of the baseline model which is referred to as “Case 1” in this sensitivity study.

Reactor Design and Operating Data	
Fuel Assembly Type	Westinghouse 17x17 PWR
Fuel Type	UO ₂ pellet
Fuel Density	10.41 g/cm ³
Fuel Temperature*	900 K
Fuel Diameter	8.05 mm
Fuel Enrichment	4.5 weight percent ²³⁵ U
Fuel Height	365 cm
Fuel Rod Pitch*	1.26 cm
Number of Fuel Rods per Assembly	264 fuel rods with 25 water holes
Cladding	Zircaloy-4
Cladding Thickness*	0.0571 cm
Cladding Temperature	622 K
Cladding Density	6.52 g/cm ³
Moderator/Coolant	H ₂ O
Moderator Density*	0.723 g/cm ³
Moderator Temperature	576 K
Boron Concentration*	850 ppm
Total Uranium Mass	450,030 g (0.450030 MTU)
Reactor Operating Power	54 MW
Reactor Operating Time	360 Days
Total Fuel Burnup	43 GWd/MTU

*parameter varied for sensitivity study

Table 27: MCNPX PWR Case 1 Model

Figure 80 is a two dimensional plot of the PWR 17x17 MCNPX model using the Visual Editor Software. The uranium fuel is colored red, the cladding is yellow, and the water is blue. A kcode source particle run was completed using the VISED software. The white dots on each fuel rod illustrate a number of the source particles generated for the kcode MCNPX run.

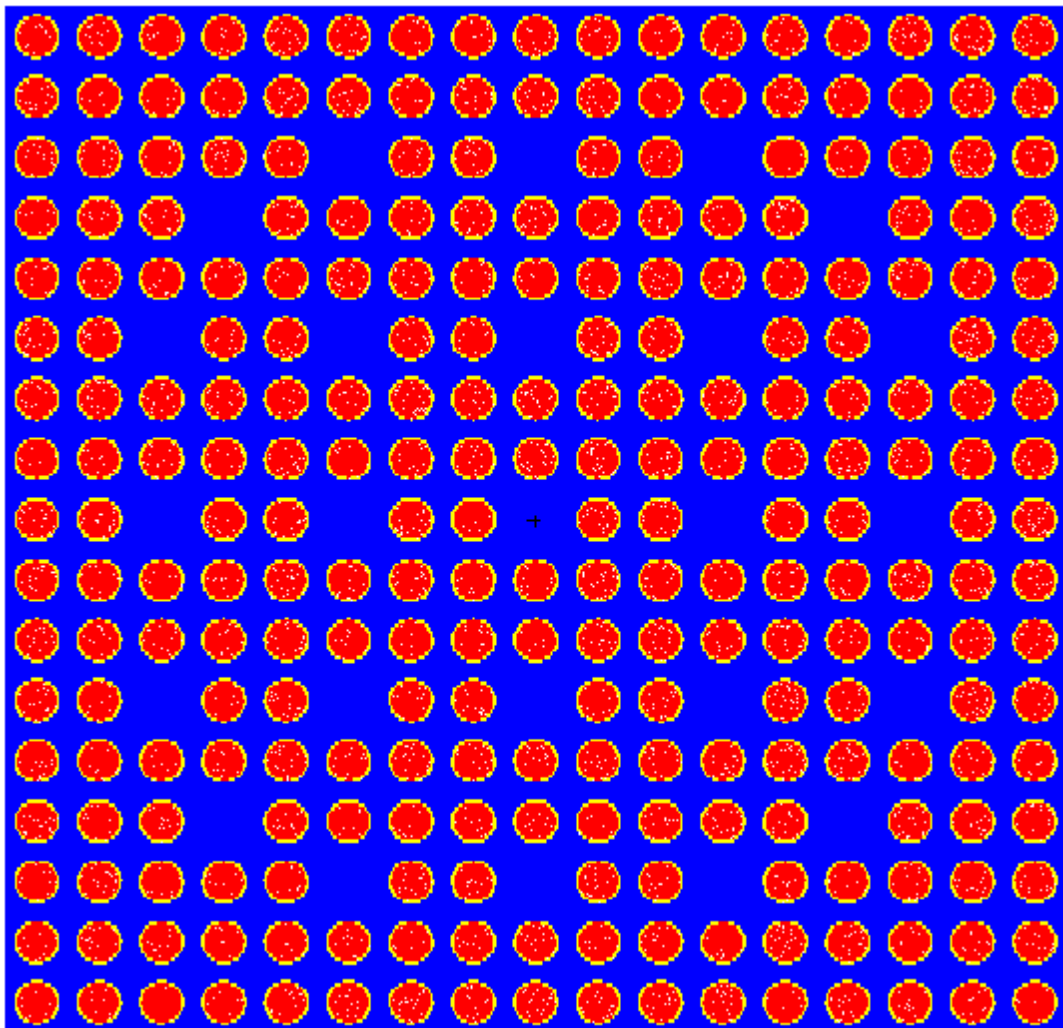


Figure 80: VisEd Plot of PWR Kcode Source Particles

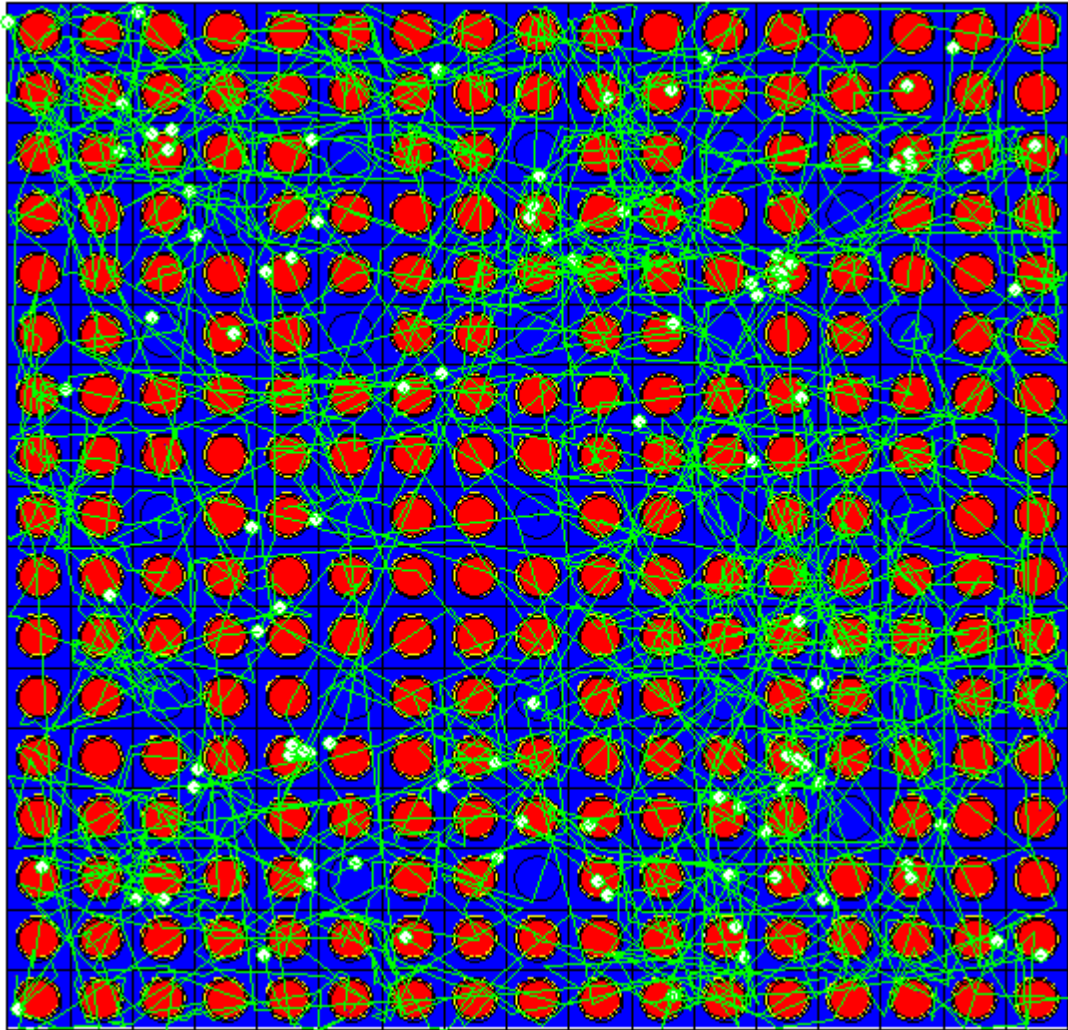


Figure 81: Particle Track Plot of the PWR MCNPX Model

Figure 81 is a VISED particle track plot of the PWR model showing the tracks of 100 neutrons generated for the plot. The green dots are the neutron absorption points. Notice that no neutrons leak from the fuel assembly. This is due to the reflector surface boundary card which reflects the neutrons back into the fuel assembly in order to simulate a reactor with multiple fuel assemblies.

Nuclides of interest were determined based upon traditional burnup indicators, actinides of interest, and fission products which produced relatively significant quantities of materials for the burnup values in this study. Additionally one fission product from the lower atomic mass end (^{72}Ge) of the fission product yield distribution and one fission product from the upper end (^{161}Dy) of the fission product yield distribution were chosen to be analyzed. Table 25 lists the key actinides and fission products analyzed in this study.

<i>Actinides</i>	<i>Burn Up Indicators</i>	<i>Other Fission Products of Interest</i>
^{234}U	^{97}Mo	^{90}Sr
^{235}U	^{98}Mo	^{91}Y
^{236}U	^{100}Mo	^{91}Zr
^{238}U	^{138}Ba	^{92}Zr
^{239}U	^{140}Ce	^{93}Zr
^{237}Np	^{142}Ce	^{94}Zr
^{238}Np	^{148}Nd	^{95}Zr
^{239}Np		^{130}Te
^{238}Pu		^{131}I
^{239}Pu		^{135}I
^{240}Pu		^{131}Xe
^{241}Pu		^{132}Xe
^{242}Pu		^{134}Xe
^{241}Am		^{135}Xe
^{243}Am		^{136}Xe
^{242}Cm		^{134}Cs
^{245}Cm		^{137}Cs
^{246}Cm		^{139}La
		^{149}Sm
		^{161}Dy
		^{72}Ge

Table 28: Key Nuclides Analyzed in the Sensitivity Study

6.1.1 Fuel Assembly Rod Pitch

Fuel assembly rod pitch values, varying from 1.26 to 1.43 cm, were chosen from PWR rod pitch values listed in Table D1.A.2 of the ORIGEN-ARP Manual⁵. Also, the *2007 World Nuclear Industry Handbook*⁹, lists five different values of reactor rod pitches for 17x17 PWRs: 1.26, 1.27, 1.275, 1.3 and 2.95 cm. A rod pitch of 1.26 cm was the baseline rod pitch for the ORIGEN-ARP w17x17 reactor ARP-effective cross sections, and therefore, that value was used in the MCNPX baseline model of the PWR that is compared to the ORIGEN-ARP results.

Increasing the fuel assembly rod pitch results in more moderator (light water) between each fuel rod. This increase in the moderator to fuel ratio should result in a softer (less energetic) neutron spectrum. Figures 82 and 83 are plots of the ²³⁵U fission cross sections and the ²³⁸U radiative capture cross sections, respectively. As you can see in Figure 82, the probability of thermal neutron fission is much greater than fission at higher neutron energies. In Figure 83, the probability of a (n,γ) reaction in ²³⁸U is only around 10 barns at thermal neutron energies. The resonance region has significantly higher cross section values than the thermal region. Because the production of ²³⁹Pu is dependent on neutron absorption by ²³⁸U, a low energy neutron spectrum should result in less ²³⁹Pu (and subsequent ²⁴⁰Pu, ²⁴¹Pu, and ²⁴²Pu) production.

As mentioned in the previous paragraph, a softer neutron spectrum should result in: 1) more thermal neutron fission reactions in ²³⁵U and 2) less actinide production through fast (resonance) energy neutron interactions such as radiative capture (n,γ).

Therefore, with increasing reactor rod pitch, we would expect to see smaller quantities of ^{239}Pu and ^{240}Pu due to less radiative capture and smaller quantities of ^{235}U due to a greater number of thermal fissions occurring. However, if the rod pitch is increased too much, then the reactor will become subcritical thus dramatically reducing the neutron flux.

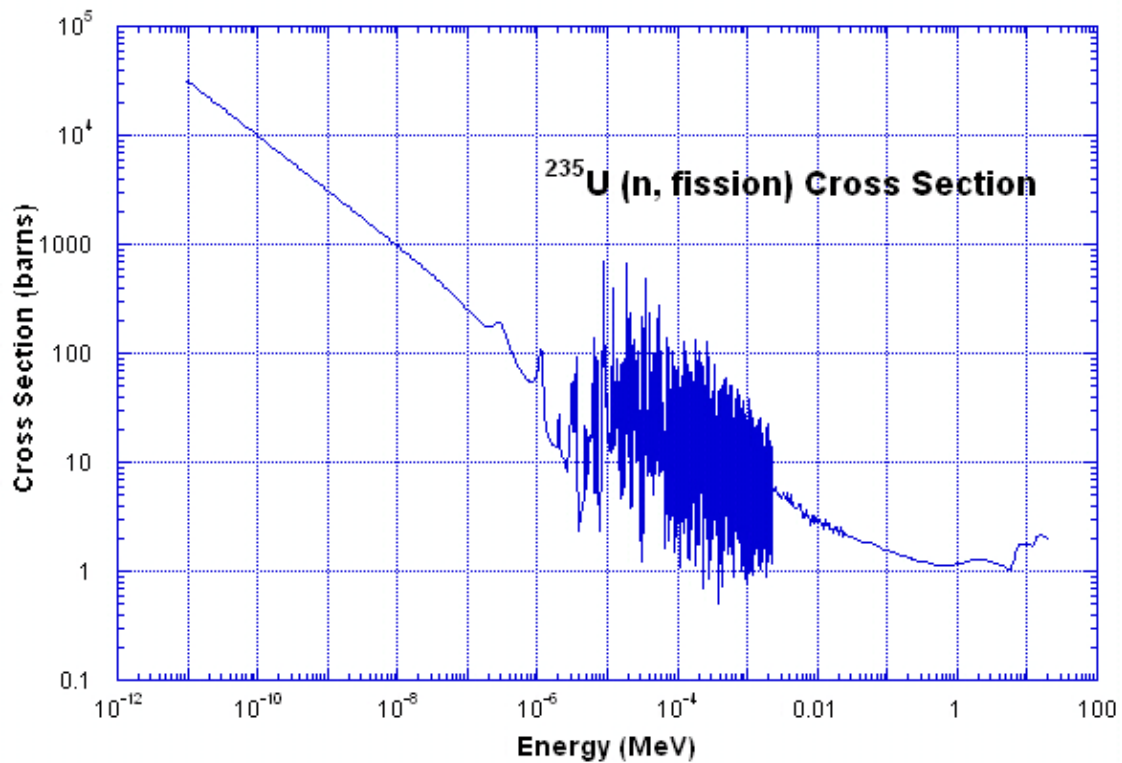


Figure 82: ^{235}U Fission Cross Section Plot

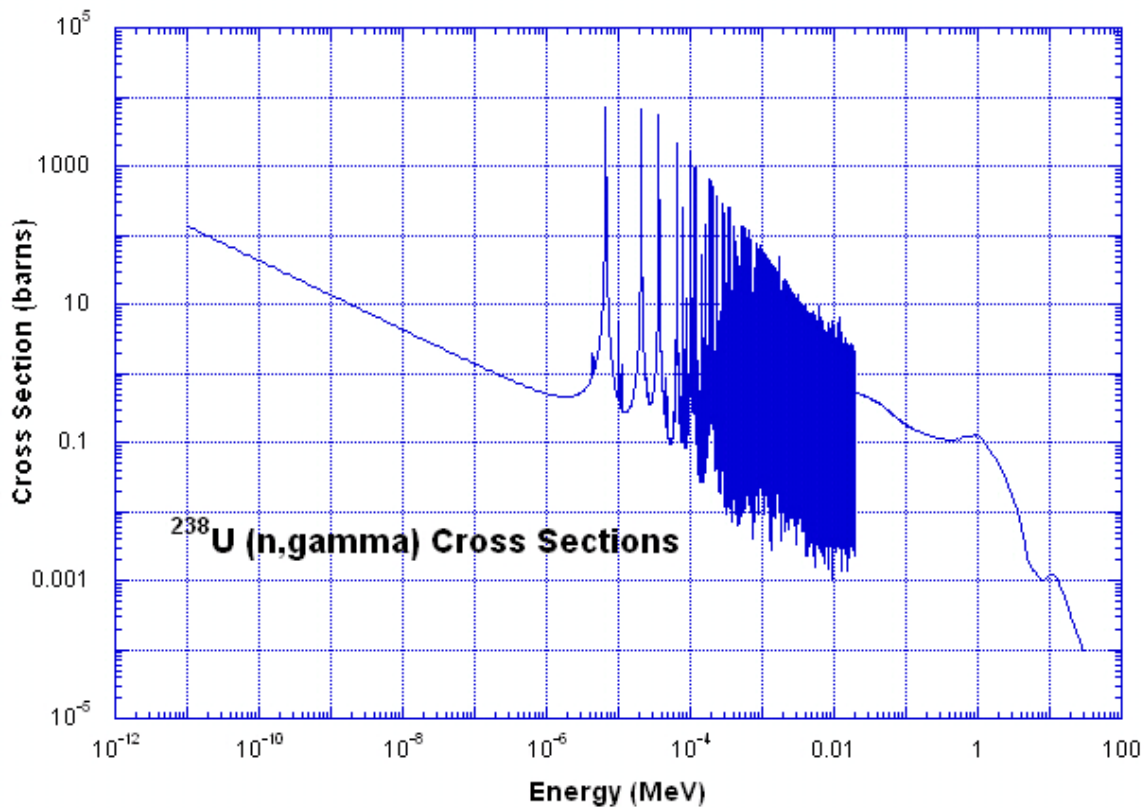


Figure 83: ^{238}U Radiative Capture Cross Section Plot

6.1.2 Boron Concentration in the Moderator

In order to reduce excess reactivity in PWRs, soluble boron (boric acid) is added to the moderator. The boron is normally enriched in the isotope ^{10}B because this isotope has a very large cross section for absorbing thermal neutrons. See Figure 84 below. As the burnup of the fuel increases, the amount of ^{235}U decreases and the amount of fission product poisons such as ^{135}Xe increases. This leads to a decrease in reactivity. To counteract this decrease in reactivity, the amount of boron in the water is reduced. This results in a flatter power profile over the lifetime of the fuel. Also, use of boric acid helps provide a flatter power profile radially across the reactor than the power profile resulting

from the use of control rods which would result in decreased areas of power around the control rod locations. Typical values of boron concentration start at around 1200 ppm boron for new fuel and go down to 0 ppm for fuel reaching its end of cycle life. Average fuel cycle boron concentrations tend to be around 600 ppm. For this sensitivity study, boron concentration values of 1000, 850, 300, and 0 ppm were used. This difference is most likely attributed to the method used to convert ppm to a weight percent (or atom percent) value which is the required input format for MCNPX. For example, if you use the standard method of conversion, you would use one milligram of ^{10}B per one kilogram of H_2O . Other methods include one atom of ^{10}B to one molecule of H_2O or one milligram of boric acid to one kilogram of H_2O . These three methods each result in a slightly different ^{10}B weight fraction.

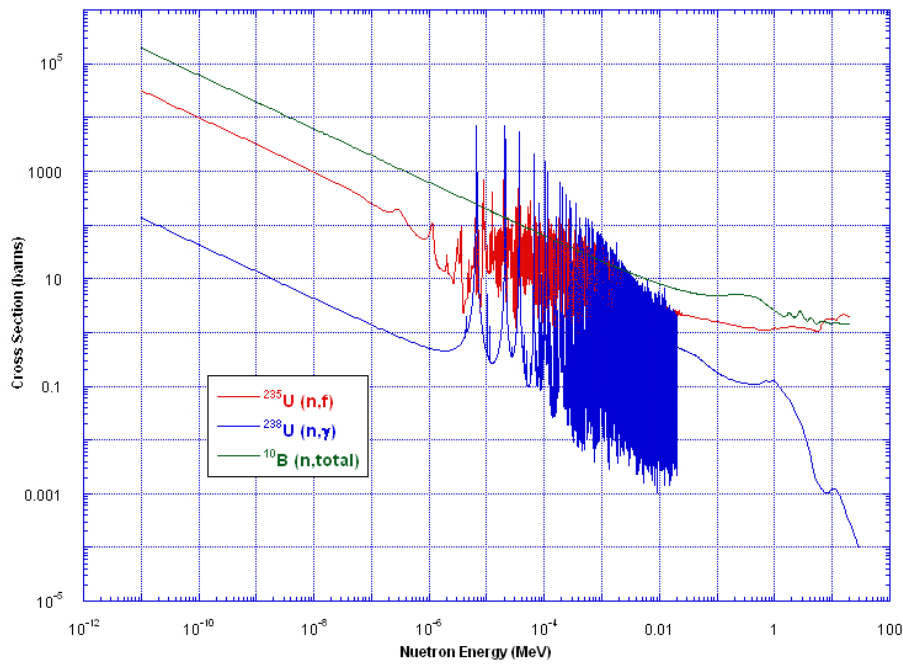


Figure 84: Plot Illustrating the ^{10}B Neutron Absorption Cross Sections

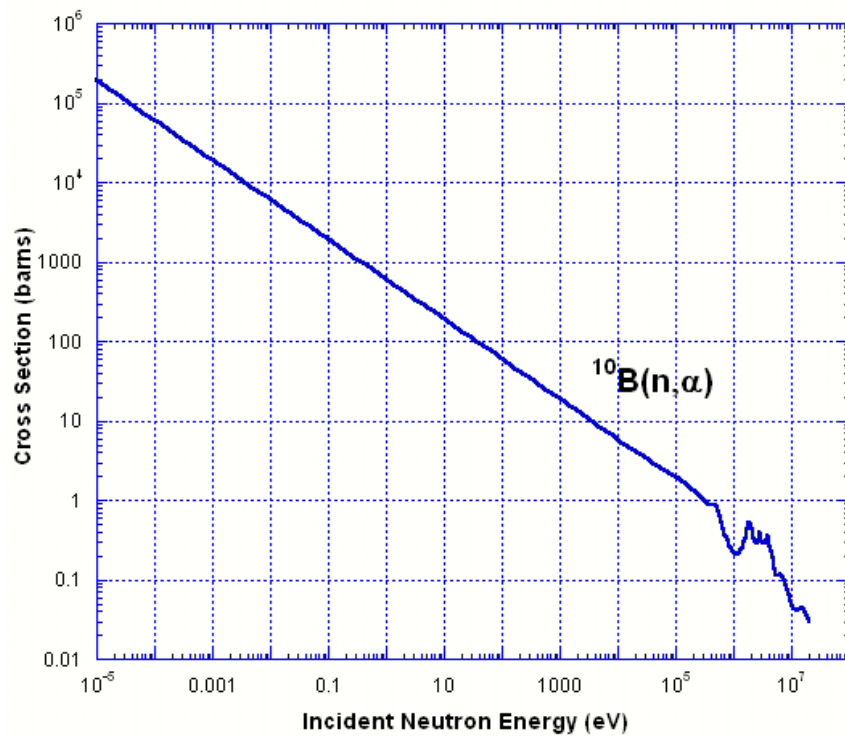


Figure 85: $^{10}\text{B}(n,\alpha)$ Reaction Cross Sections

Figure 85 is a plot of the (n, α) reaction cross section for ^{10}B (Reference 13). The (n, α) reaction is the primary neutron interaction at thermal neutron energies. The plot shows that the probability of neutrons of thermal energies being absorbed by ^{10}B is much greater than the probability at higher neutron energies. Therefore, the presence of ^{10}B in the moderator should result in a harder (higher energy) neutron spectrum. This should decrease the rate of thermal fission reactions and increase the amount of actinide production from fast neutrons. Therefore, for a particular burnup value, one would expect to see both a higher amount of ^{235}U and ^{239}Pu (as well as ^{240}Pu , ^{241}Pu , and ^{242}Pu) in the fuel when boric acid is added to the fuel.

6.1.3 Cladding Thickness

PWR and BWR fuel pin cladding is typically made of zircaloy which is a zirconium alloy. There are two main types of zircaloy used in PWRs and BWRs: Zircaloy-2 and Zircaloy-4. Based upon information in Neeb (1997)¹⁴, the constituents (in addition to zirconium) of each alloy are listed in Table 29.

<i>Element</i>	<i>Zircaloy-2</i>	<i>Zircaloy-4</i>
<i>Tin</i>	1.20-1.70 %	1.20-1.70 %
<i>Iron</i>	0.07-0.20 %	0.18-0.24 %
<i>Chromium</i>	0.05-0.15 %	0.07-0.13 %
<i>Nickel</i>	0.03-0.08 %	----
<i>Oxygen</i>	0.07-0.15 %	0.10-0.16 %

Table 29: Zircaloy-2 and Zircaloy-4 Alloy Constituents¹⁴

Relative to many metals, zirconium has a low neutron absorption cross section for thermal neutrons. See Figure 86 for a plot of the radiative capture cross section for ^{90}Zr . When zirconium is combined with small amounts of the elements listed in Table 23 to form Zircaloy-2 or Zircaloy-4, it is resistant to corrosion. These two characteristics make Zircaloy-2 and Zircaloy-4 attractive materials for nuclear fuel cladding. A review of the 2007 World Nuclear Industry Handbook⁹ revealed that Zircaloy-4 is the most commonly used zircaloy in PWRs around the world; therefore, Zircaloy-4 was used for the MCNPX PWR model in this dissertation.

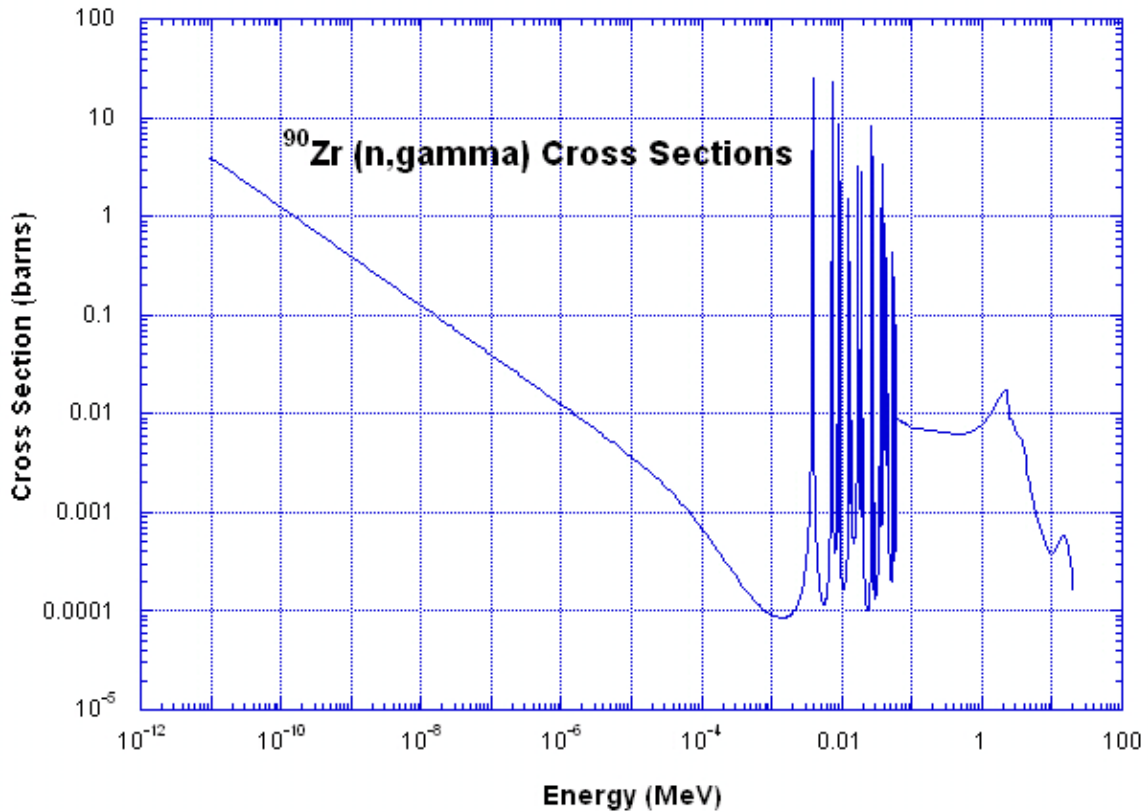


Figure 86: ^{90}Zr Radiative Capture Cross Sections

For a specified rod pitch, the thicker the cladding, the less water moderator is present due to the cladding taking up space that would otherwise be occupied by water. Therefore, with thicker cladding, a harder neutron spectrum is expected. This harder neutron spectrum would result in a lower thermal fission rate and a higher production rate of actinides. Therefore, similar to a higher concentration of ^{10}B in the water, for a particular burnup value, one would expect to see both a higher amount of ^{235}U and ^{239}Pu (as well as ^{240}Pu , ^{241}Pu , and ^{242}Pu) in the fuel with thicker cladding.

Natural zirconium consists of the following isotopes listed in Table 30.

<i>Isotope</i>	<i>Natural Atom Percent Abundance</i>
^{90}Zr	51.45
^{91}Zr	11.22
^{92}Zr	17.15
^{94}Zr	17.38
^{96}Zr	2.8

Table 30: Natural Zirconium Atom Percent Abundances

Because natural zirconium consists of several different isotopes, it is important to either use natural zirconium in the material card or use each of the different isotopes according to natural atom percent abundance for the MCNPX model. Natural zirconium was used in the model for this dissertation. It should also be noted the typical

commercial zirconium has a small amount of hafnium present. Hafnium is a strong neutron absorber. Therefore, zirconium that is normally used to make zircaloy for nuclear fuel cladding has had the hafnium removed.

The *2007 World Nuclear Industry Handbook*⁹, contains a number of cladding thicknesses for PWRs varying from 0.057 cm to 0.07 cm. A thickness of 0.0571 cm was used for the cladding thickness in this MCNP model. The four cladding thickness values chosen for this sensitivity study were 0.0571, 0.06175, 0.0653, and 0.0665 cm.

6.1.4 Moderator/Coolant Density

In a PWR, light water is used as both the moderator and coolant. The density of the water will vary with the pressure and temperature of the water in the reactor core. As density of the water increases, the neutron interaction rate with the atoms in the water molecules will increase resulting in more neutrons slowing down. This will result in a softer neutron spectrum in the reactor. A more thermal neutron spectrum will give rise to more thermal fission reactions decreasing the amount of ^{235}U present in the fuel for a given fuel burnup value. Also, with the softer spectrum, we should expect less actinide generation.

6.1.5 Fuel Temperature

With increasing temperatures, Doppler Broadening occurs. Doppler Broadening results in an increase in the widths of the cross section peaks in the resonance region of the cross section plot. This can result in more neutrons being absorbed by the fuel before

the neutrons can be slowed to thermal energies. Fewer thermal neutrons results in a smaller thermal fission rate and less reactor power. This can also in a higher production of actinides for a given fuel burnup value.

Figure 87 illustrates Doppler Broadening.

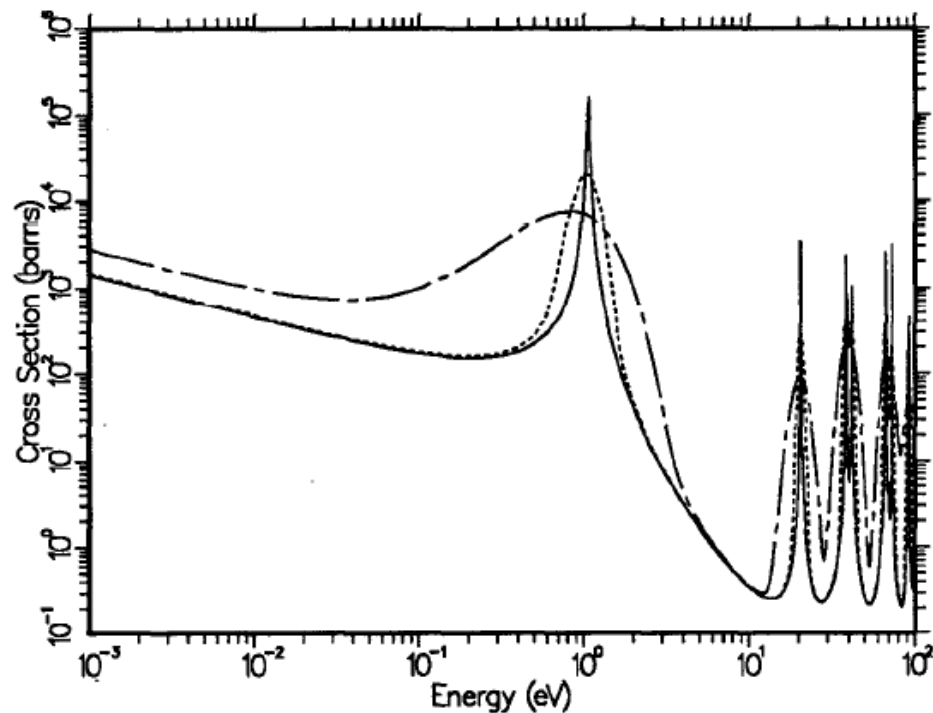


Figure 87: Doppler Broadening of the (n, γ) cross section for ^{240}Pu . The temperatures are 0 K(solid), 30,000 K(dotted), and 300,000 K (dash-dot)¹⁵.

The w17x17 model in the ORIGEN-ARP has a fuel temperature of 900 K as a baseline. Therefore, 900 K was used as the baseline temperature for the PWR in this study. Four fuel temperatures were used in this study: 700, 900, 1100, and 1300 K. However, for this study, only the MCNPX “TMP” card was used to adjust the

temperature of the fuel, cladding, and water necessary for the free-gas thermal treatment of low-energy neutron transport. Neither the absorption cross sections nor the densities were changed for the fuel or cladding materials.

6.2 SENSITIVITY STUDY RESULTS AND CONCLUSIONS

6.2.1 Fuel Assembly Rod Pitch

As mentioned previously, we would expect that as we increase fuel assembly rod pitch, we create a softer neutron spectrum in the reactor decreasing the amount of certain actinides produced from neutron absorption reactions and increasing the amount of thermal neutron fission. This increase in thermal neutron fission would then result in a greater decrease in the amount of ^{235}U . Figures 88 and 89 are plots of ^{235}U depletion at different fuel assembly rod pitches. As predicted, ^{235}U depletion is greater in the higher rod pitch values due to the higher ^{235}U fission rate.

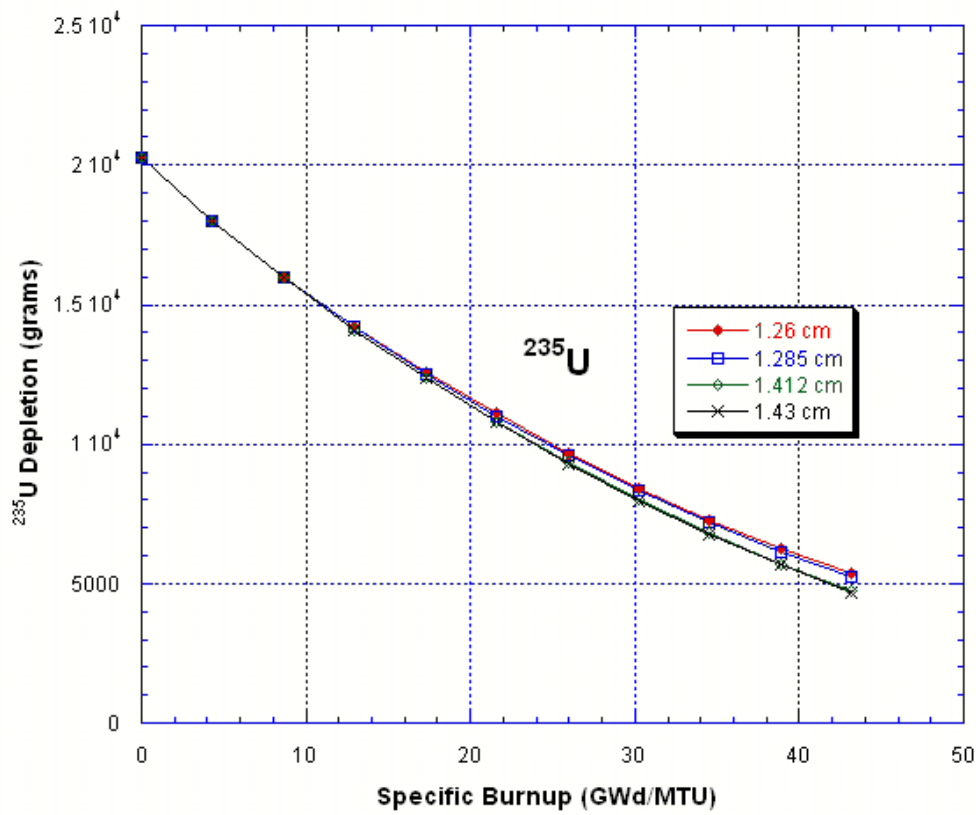


Figure 88: ^{235}U Depletion at Different Rod Pitch Values

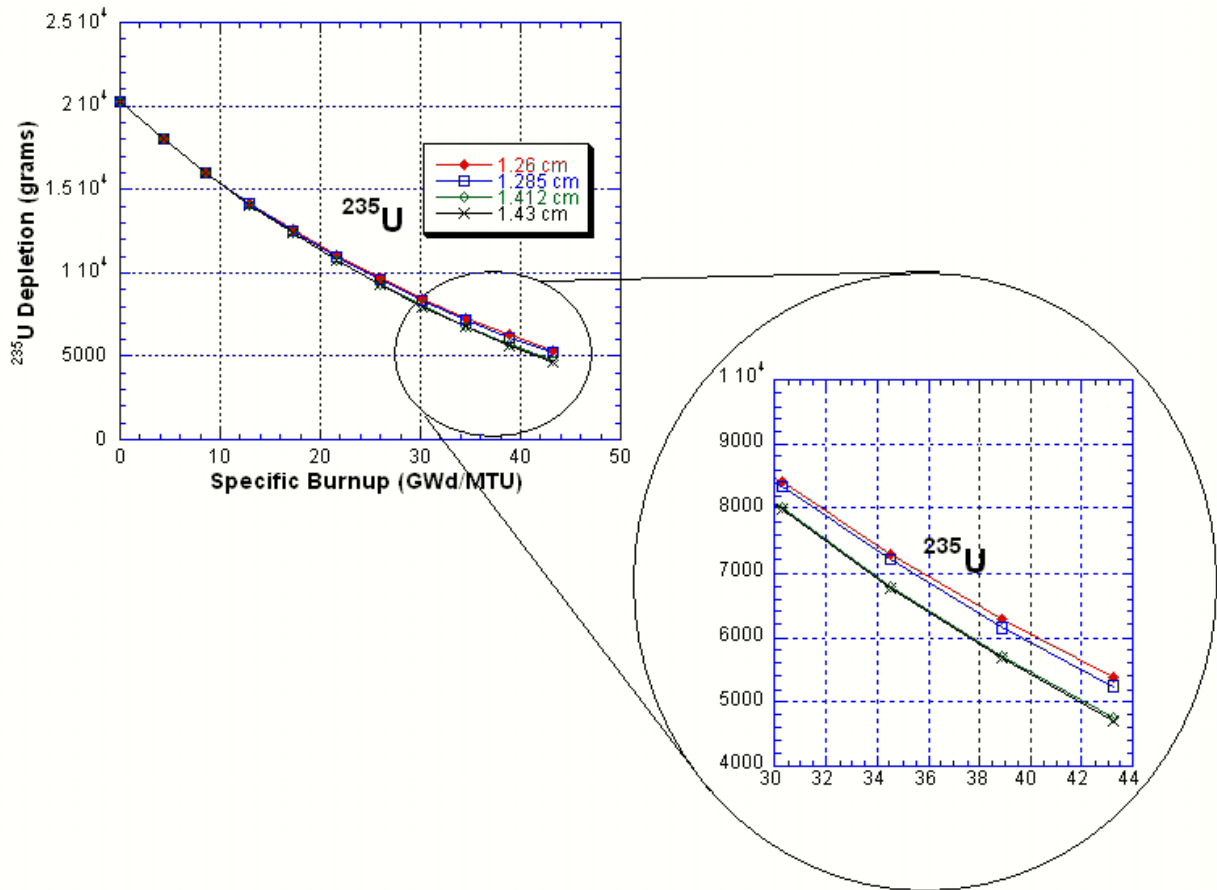


Figure 89: ^{235}U Depletion at Different Rod Pitch Values (Expanded View)

Figure 90 is a plot of ^{239}Pu production in the PWR model at four different rod pitches. As expected, the increased rod pitch resulted in a decrease in ^{239}Pu production. A similar effect is seen in the other actinides that result from ^{235}U and ^{238}U neutron absorption reactions. Figure 91 is a plot of ^{241}Am production. The other actinide plots are in Appendix G.

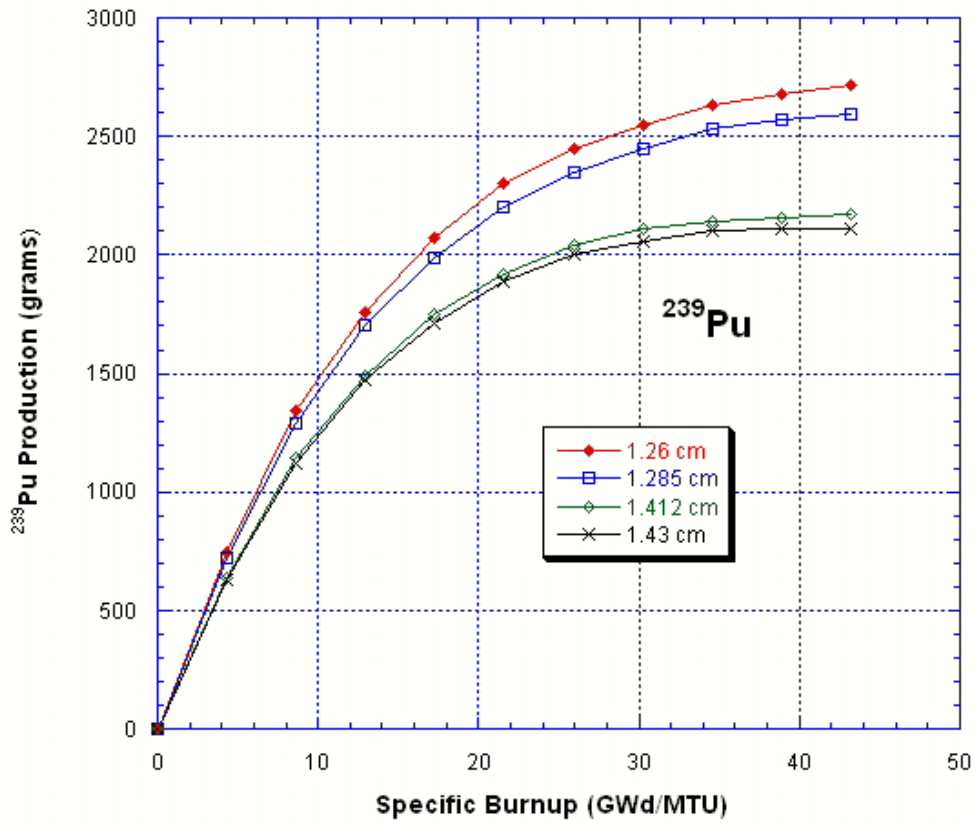


Figure 90: ^{239}Pu Production in the PWR Model at Different Rod Pitch Values

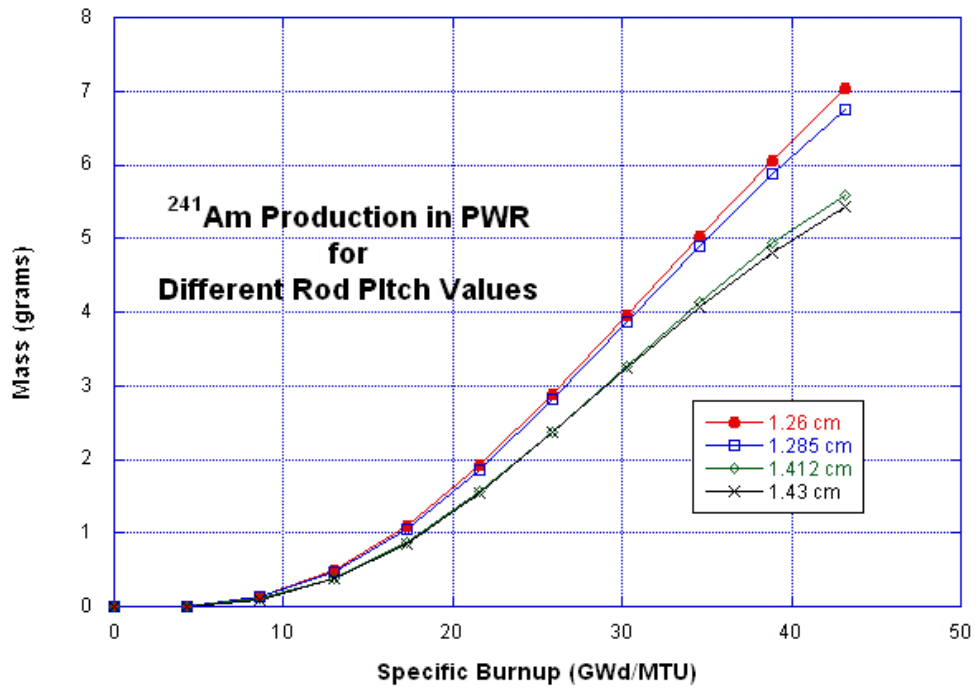


Figure 91: ²⁴¹Am Production in the PWR Model at Different Rod Pitch Values

Figure 92 is a plot of ¹⁴⁸Nd production in the PWR for different rod pitch values. Like the other burnup indicator nuclides, this nuclide shows very little variance to the small changes in reactor pitch values.

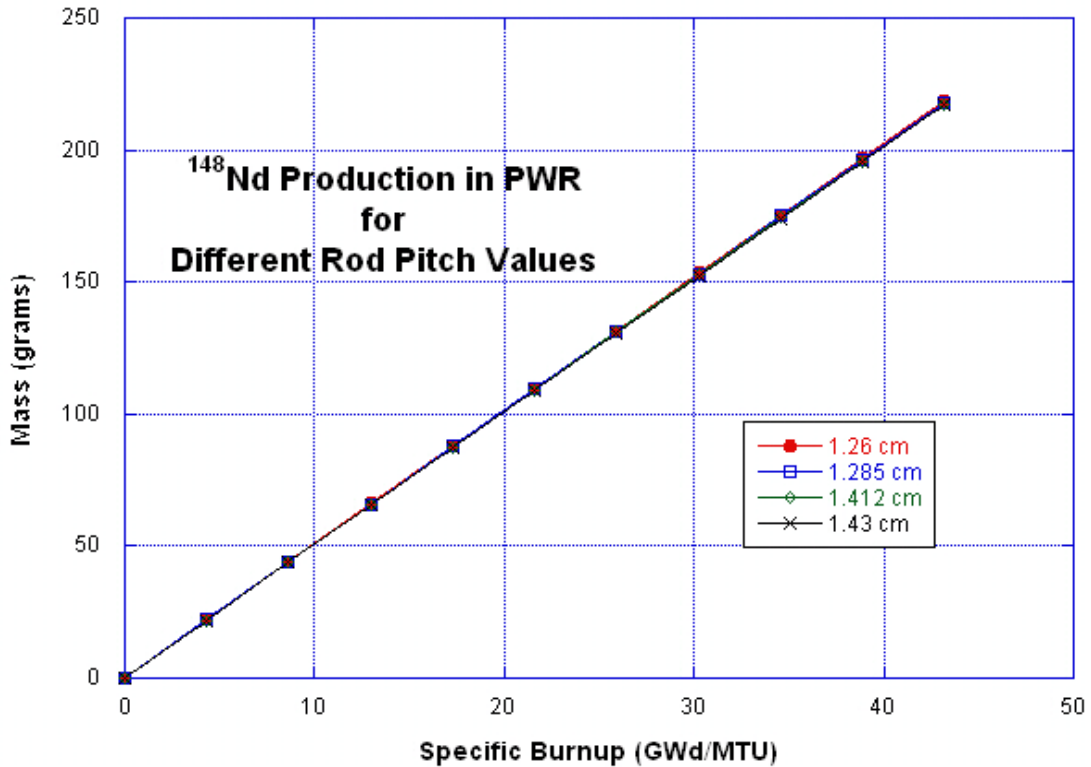


Figure 92: ¹⁴⁸Nd Production in the PWR Model at Different Rod Pitch Values

The remaining fission product nuclides in this study show some variance dependence with varying rod pitch values. One of the nuclides that shows a greater variance is ¹³⁵Xe. Figure 93 is a plot of the ¹³⁵Xe production. As can be seen, the greater rod pitch values result in less ¹³⁵Xe production. However, it may not be practical to rely on such a measurement for forensics purposes because ¹³⁵I β⁻ decays into ¹³⁵Xe with a half-life of approximately 6 hours, and ¹³⁵Xe also β⁻ decays into ¹³⁵Cs with an approximate 9 hour half-life. Figure 94 shows that after approximately 4 days, the ¹³⁵Xe has all effectively decayed away.

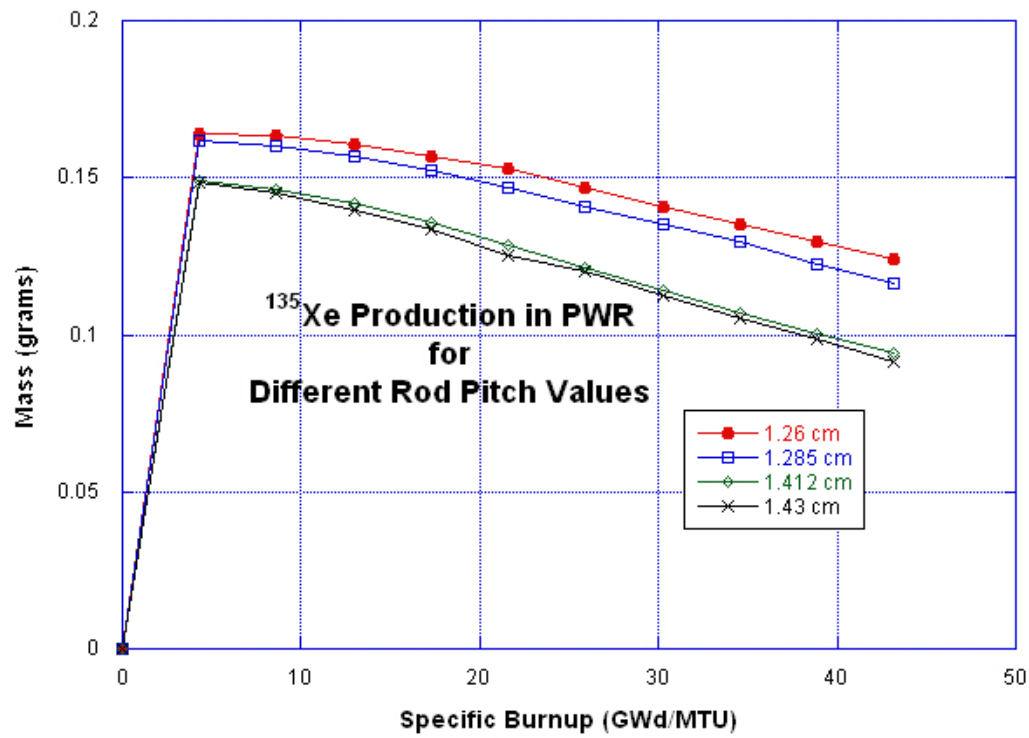


Figure 93: ¹³⁵Xe Production in the PWR Model at Different Rod Pitch Values

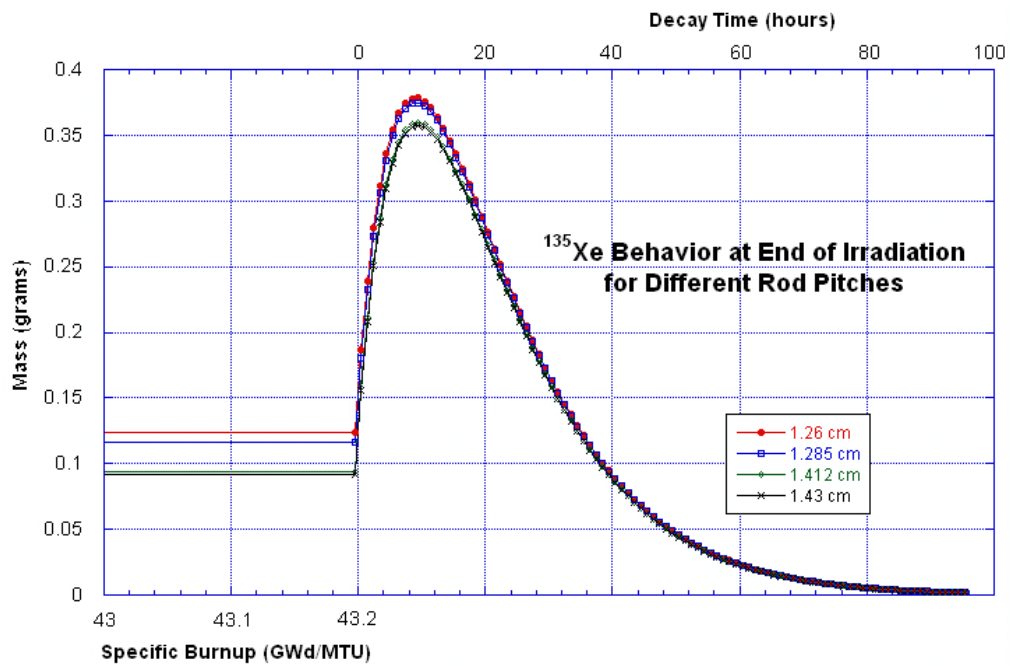


Figure 94: ¹³⁵Xe Decay at the Termination of Reactor Irradiation

6.2.2 Boron Concentration in the Moderator

As mentioned previously, with increased moderator boron concentration, we expect to see a harder neutron spectrum with less ^{235}U fission and more actinide production from neutron absorption reactions. Figure 95 illustrates the higher values of ^{235}U in the higher boron concentration cases (i.e. There are fewer fission reactions occurring in the case with more initial boron).

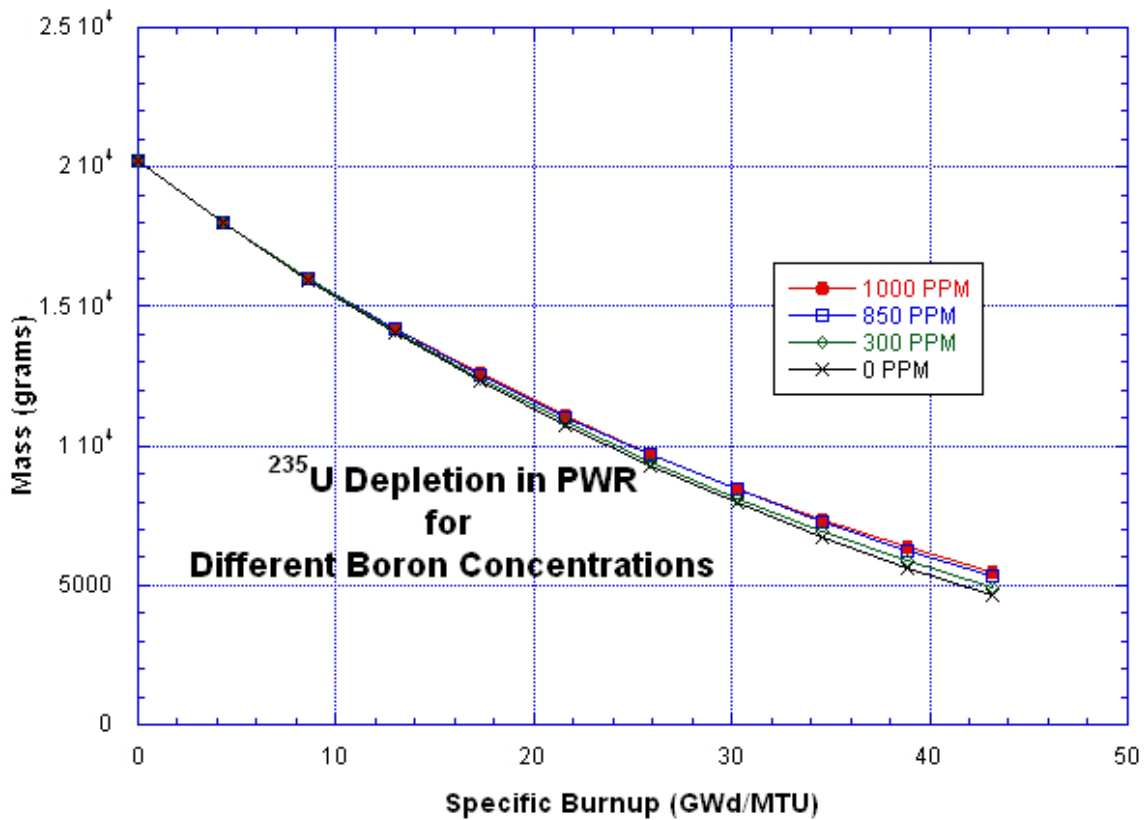


Figure 95: ^{235}U Depletion in PWR for Different Boron Concentrations

Figure 96 is a plot of ^{239}Pu production. As described previously, there is less plutonium production in the cases where there is less boron present in the moderator.

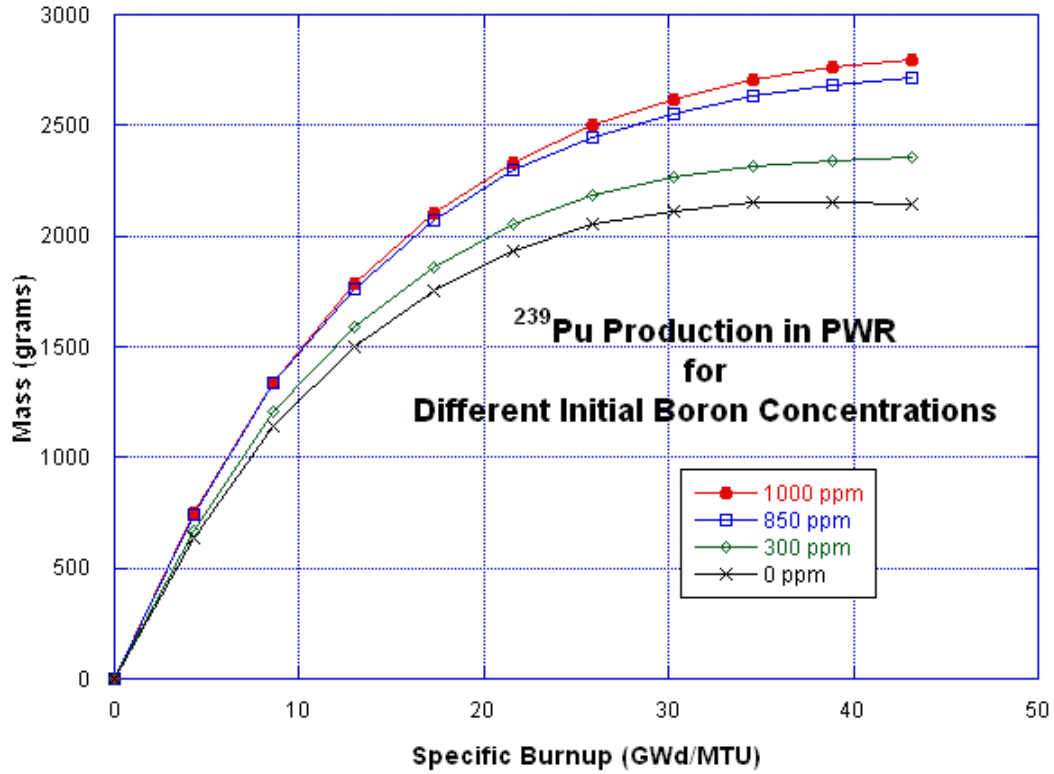


Figure 96: ^{239}Pu Production in PWR for Different Boron Concentrations

Less ^{239}Pu production can result in less production of the greater actinides. See the ^{241}Am and ^{245}Cm production plots (Figures 98 and 98) below.

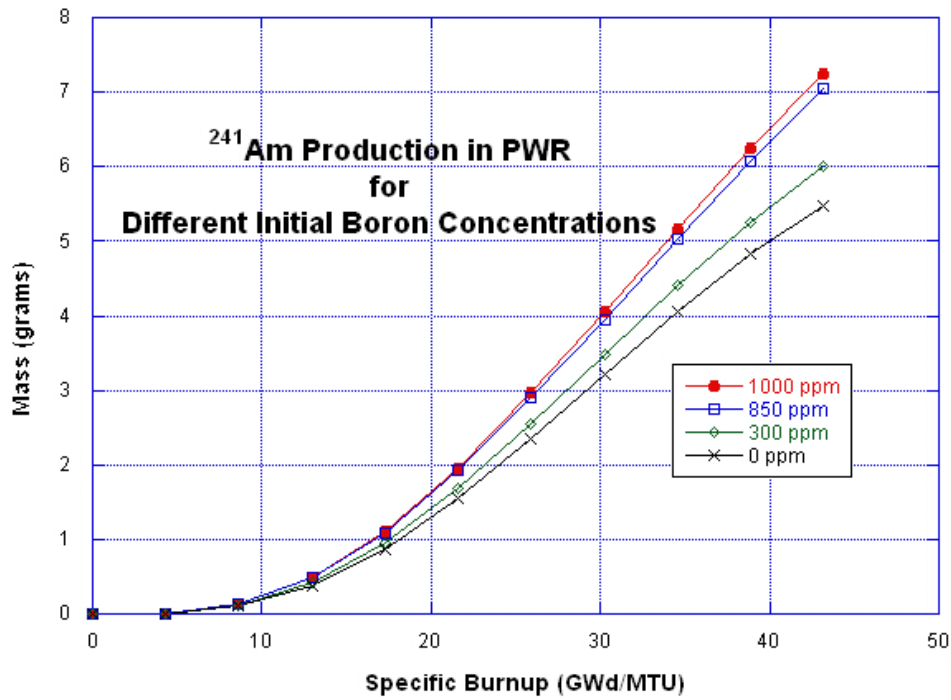


Figure 97: ²⁴¹Am Production in PWR for Different Boron Concentrations

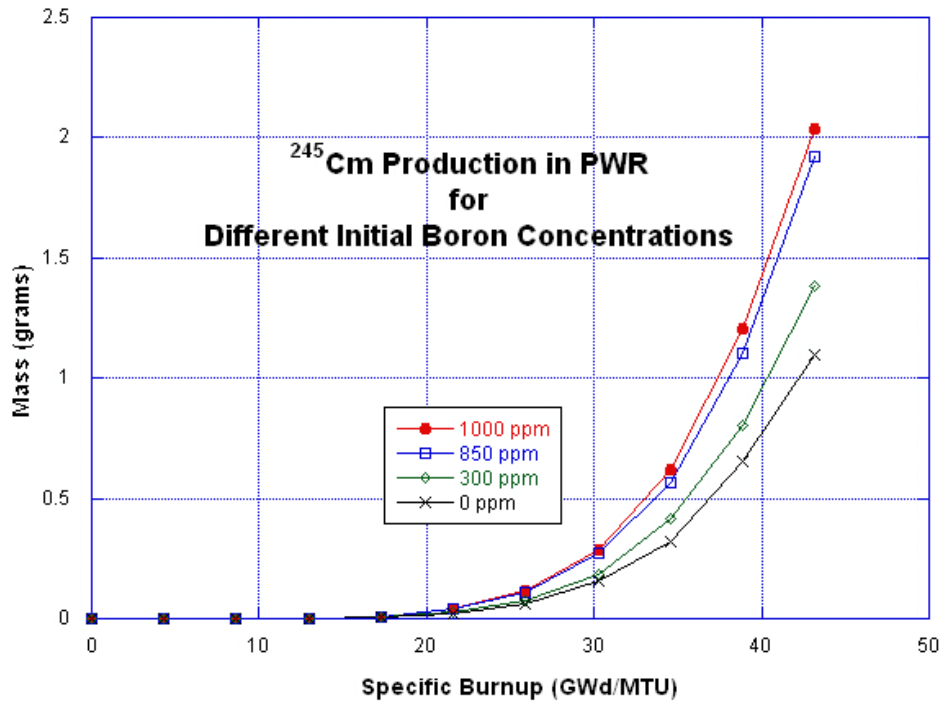


Figure 98: ²⁴⁵Cm Production in PWR for Different Boron Concentrations

Figure 99 below is a plot of the ^{138}Ba production in the PWR model for the four different initial boron concentration. Like the other burnup indicator nuclides, the ^{138}Ba also does not show any dependency on initial boron concentration.

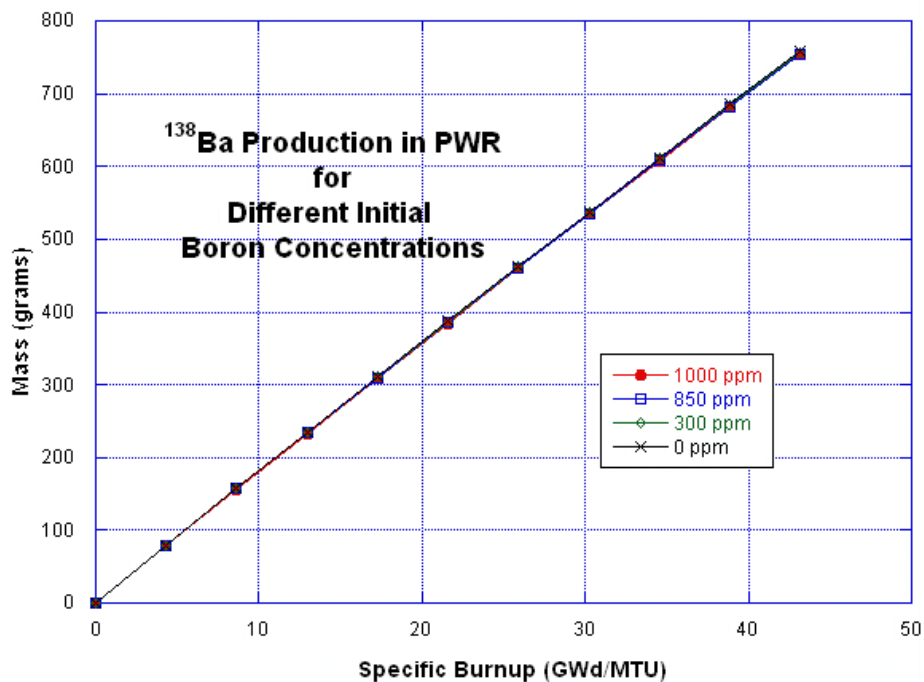


Figure 99: ^{241}Am Production in PWR for Different Boron Concentrations

Figure 100 below is a plot of ^{91}Y in the PWR MCNPX model for the different initial boron concentrations. For the lower boron concentration cases, where more ^{235}U fission is occurring, there is more ^{91}Y production.

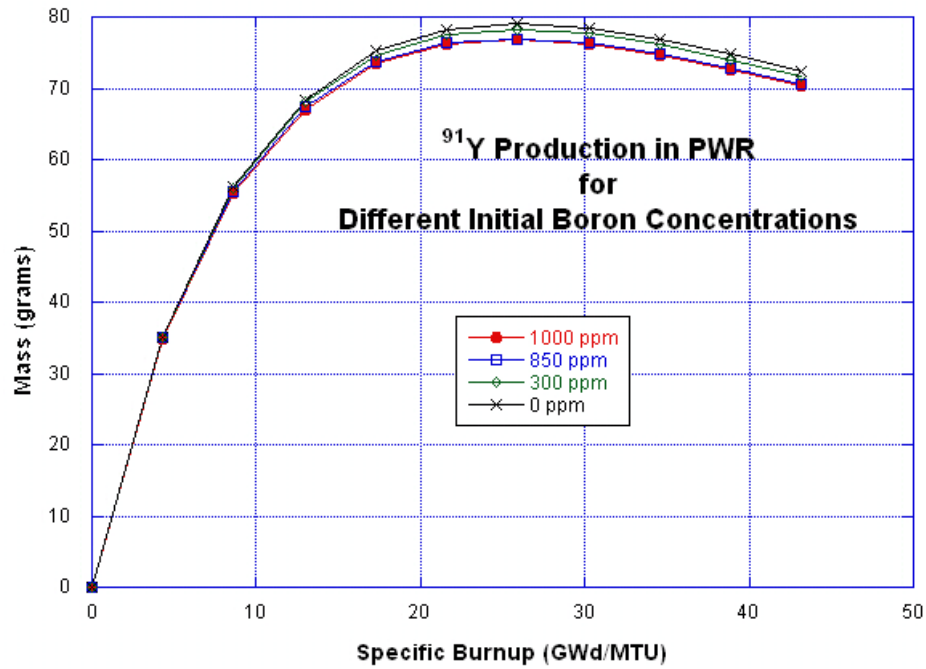


Figure 100: ⁹¹Y Production in PWR for Different Boron Concentrations

6.2.3 Different Cladding Thicknesses

As mentioned previously, with increased cladding thickness, which gives a lower moderator to fuel value, we expect to see less ²³⁵U fission and a harder neutron spectrum and more actinide production from neutron absorption reactions.

Figure 101 below is a plot of ²³⁵U depletion for the four different cladding thicknesses cases. The values of cladding thicknesses used did not generate a significant different in any of the cases.

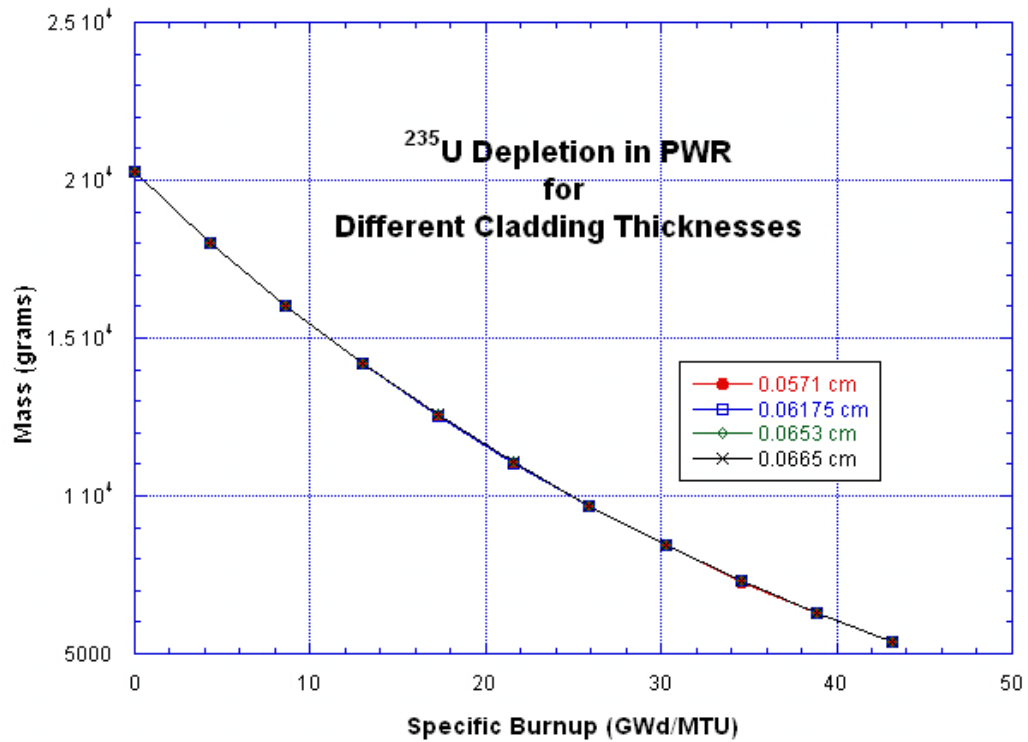


Figure 101: ²³⁵U Depletion in PWR for Different Cladding Thicknesses

However, Figure 102 is a plot of ²³⁹Pu production. As expected, for the higher cladding thickness cases, there is more ²³⁹Pu production than the lower cladding thickness cases.

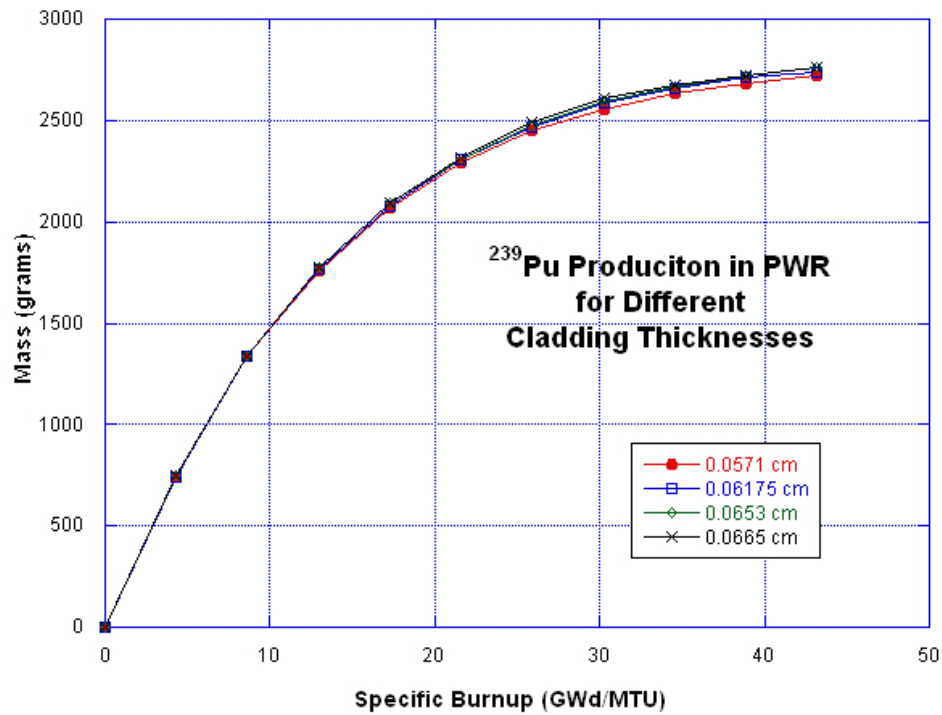


Figure 102: ²³⁹Pu Production in PWR for Different Cladding Thicknesses

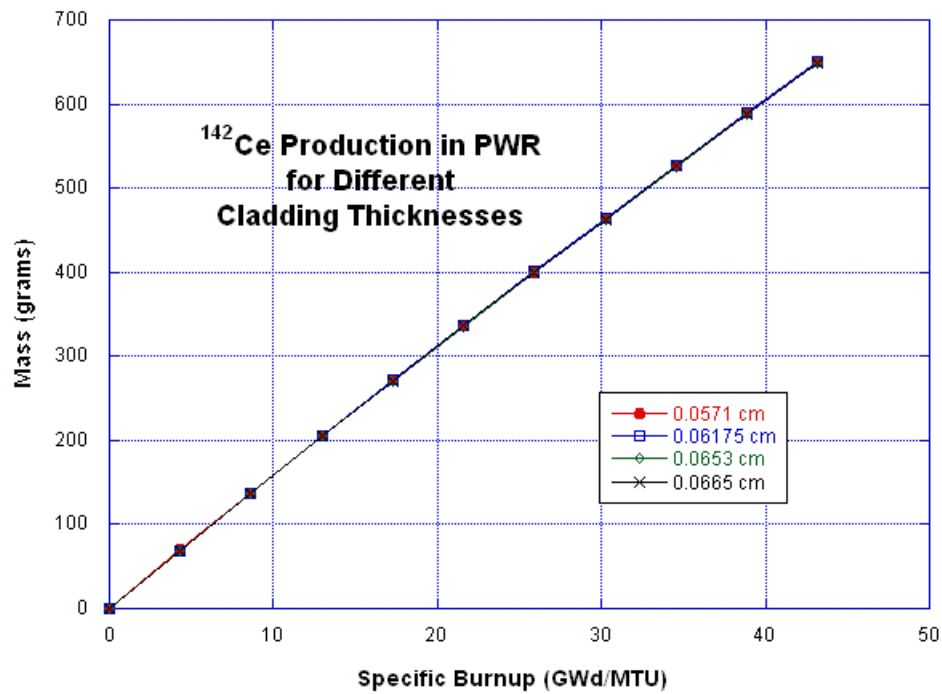


Figure 103: ¹⁴²Ce Production in PWR for Different Cladding Thicknesses

Figures 103 and 104 show the production of the burnup indicator ^{142}Ce and the fission production ^{137}Cs . For both plots, as well as most of the other fission products, there is no significant difference between the different cladding thickness cases.

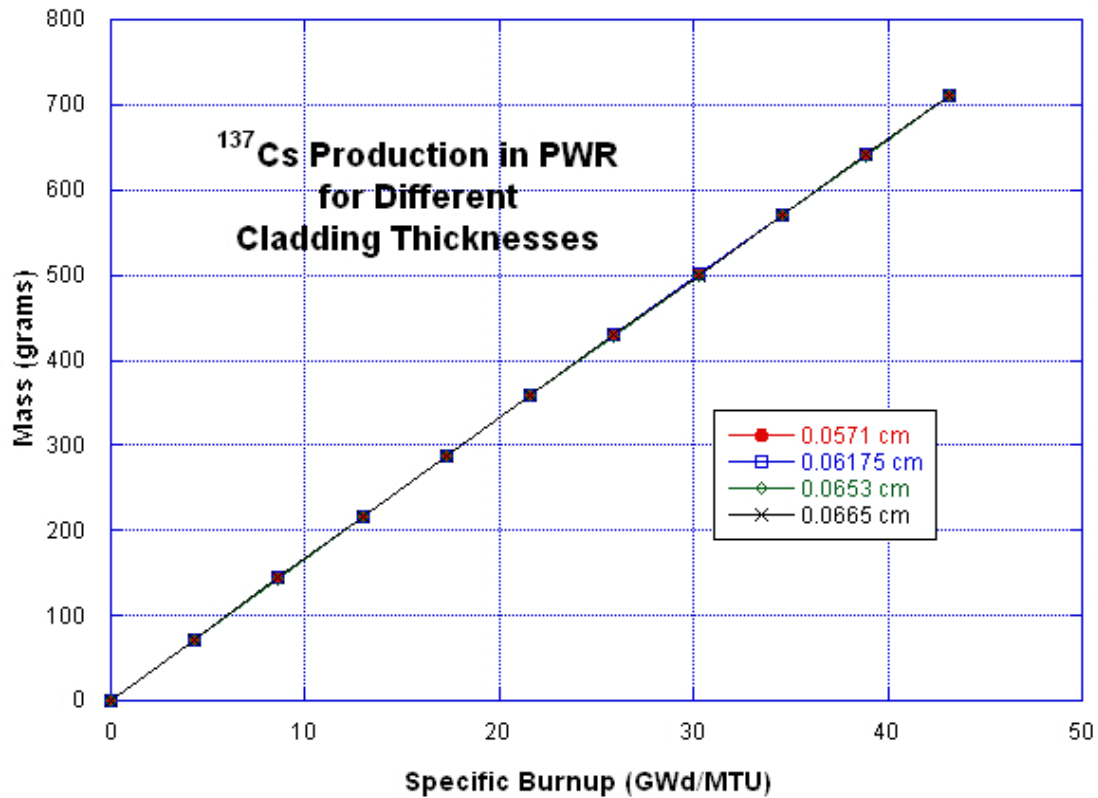


Figure 104: ^{137}Cs Production in PWR for Different Cladding Thicknesses

6.2.4 Different Moderator Densities

As mentioned previously, with decreased moderator density, which results in a lower moderator to fuel ratio, we expect to see less ^{235}U fission and a harder neutron spectrum and more actinide production from neutron absorption reactions.

Figure 105 is a plot of ^{235}U depletion for the different water density cases. There is no significant difference between the four cases shown on the plot.

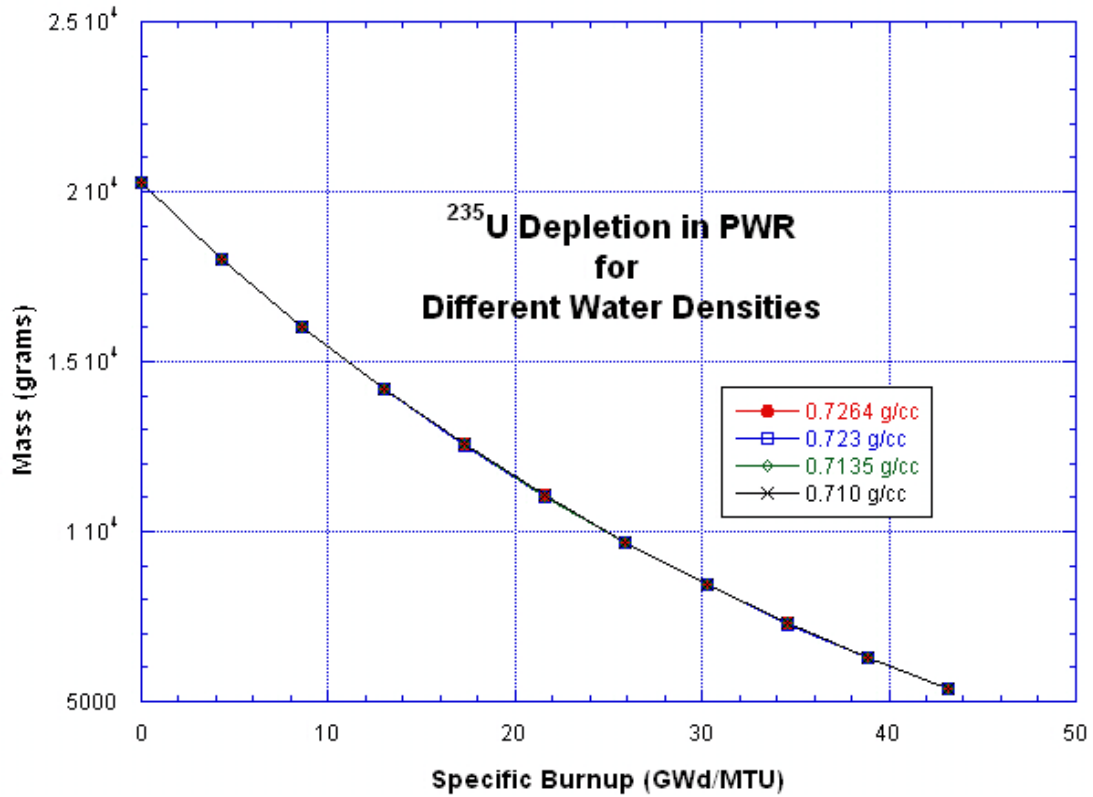


Figure 105: ^{235}U Depletion in the PWR for the Different Water Densities

Figure 106 is a plot of ^{239}Pu production for the four different water density cases. As expected, the lower density cases show a slight increase in the quantity of ^{239}Pu produced.

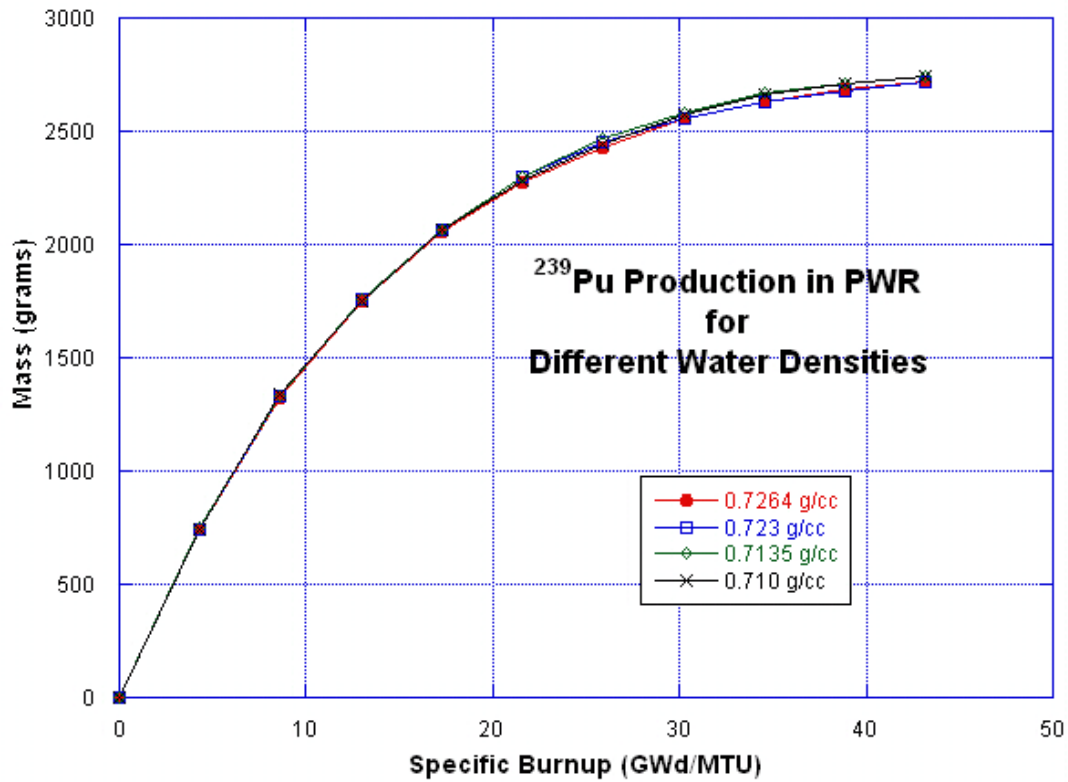


Figure 106: ²³⁹Pu Production in the PWR for the Different Water Densities

The burnup indicator nuclides and the fission product nuclides (See Figure 107 below) do now show any significant difference for the water density values used in the sensitivity study. Varying the water densities more drastically should show a greater difference in the results.

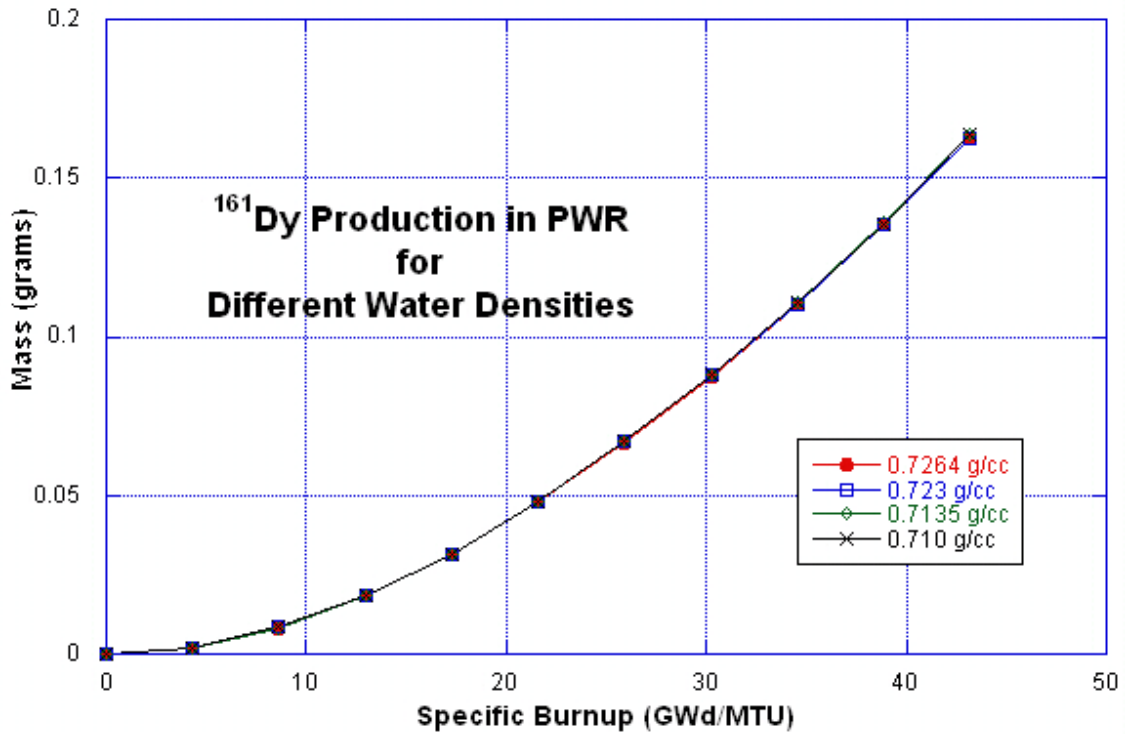


Figure 107: ¹⁶¹Dy Production in the PWR for the Different Water Densities

6.2.5 Different Fuel Temperatures

As mentioned previously, with increased fuel temperature, we expect to see the resonance peaks broaden. This broadening should result in additional neutron absorption reactions.

Figure 108 shows ²³⁵U depletion for the PWR model at different fuel temperatures. There is no significant between the 700, 900, 1100, and 1300 K cases.

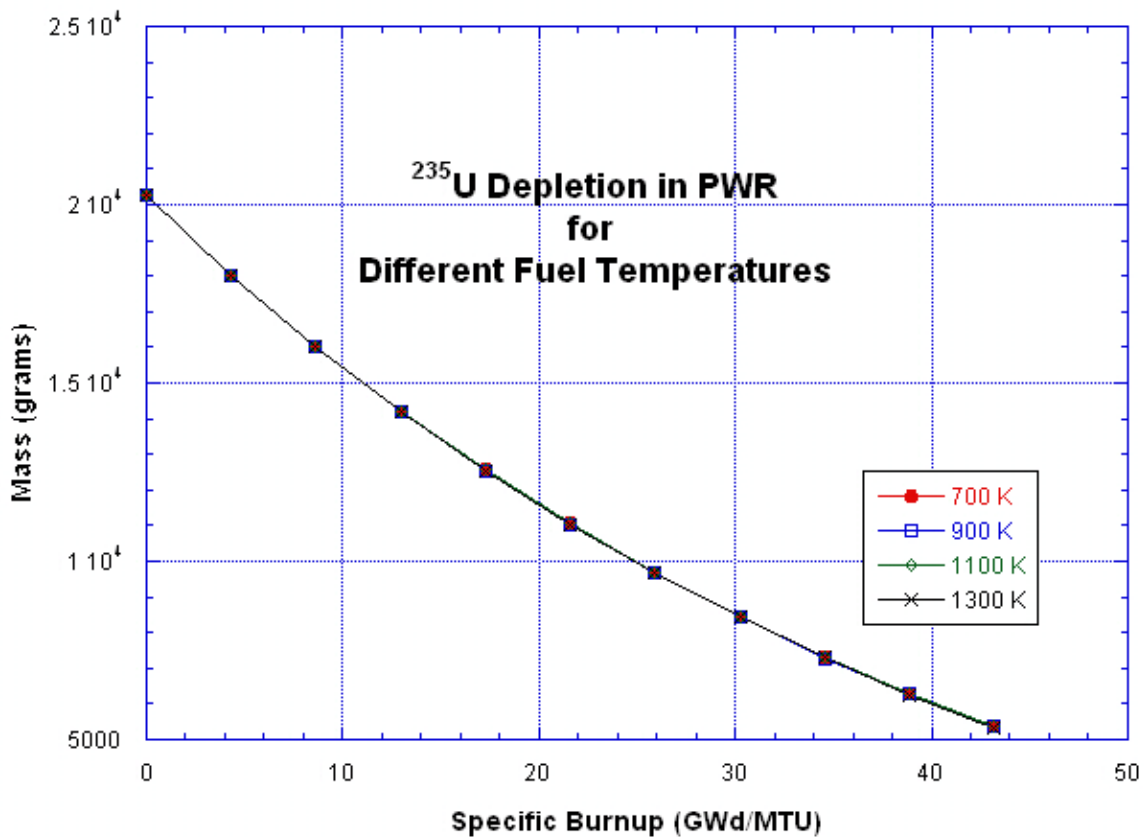


Figure 108: ²³⁵U Depletion in the PWR for the Different Fuel Temperatures

Figure 109 is a plot of ²³⁹Pu production. With the broader resonance peaks, we would expect there to be greater ²³⁹Pu production with greater temperature. However, this is less ²³⁹Pu production for the 1300 K case. However, the plot for ²⁴²Pu (See Figure 110) shows greater values for the 1300 K case. This may suggest that the increased resonance spectra widths are resulting in additional production of the greater actinides. Indeed, for many of the actinides in this study greater than ²⁴¹Pu, the 1300 K case shows more production of those actinides.

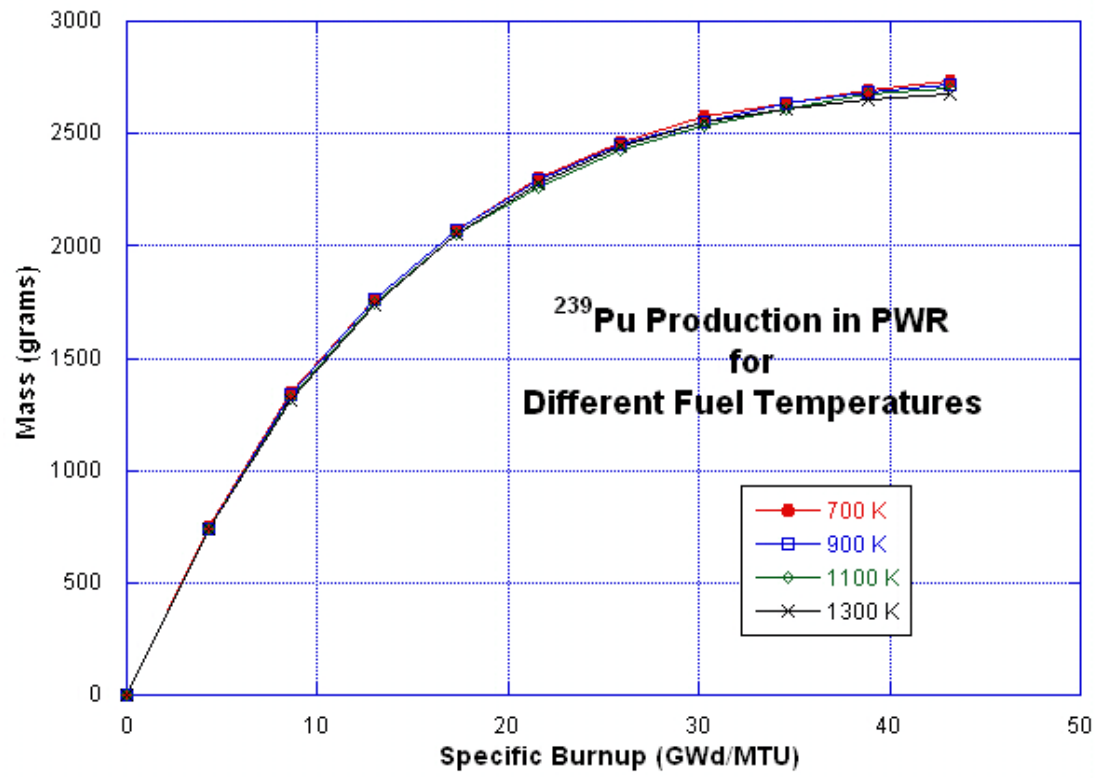


Figure 109: ²³⁹Pu Production in the PWR for the Different Fuel Temperatures

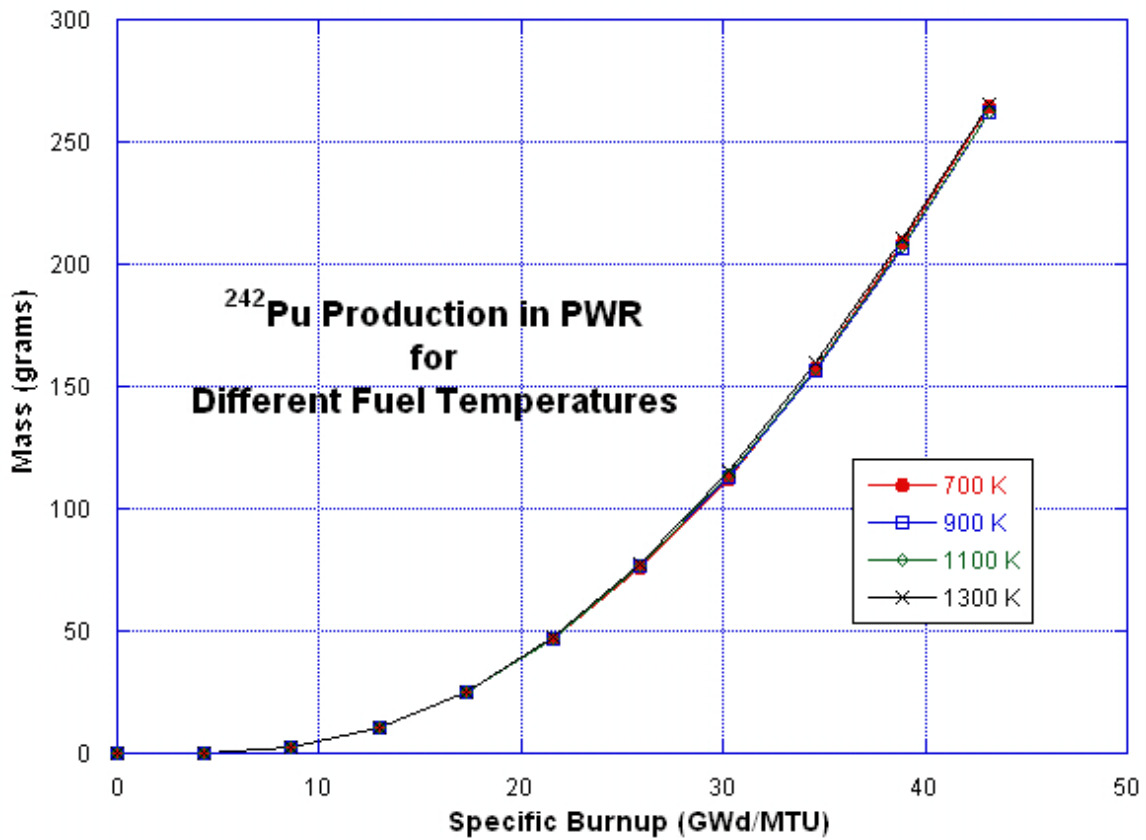


Figure 110: ²⁴²Pu Production in the PWR for the Different Fuel Temperatures

Figure 111 shows the ¹⁰⁰Mo production plot for the different temperature cases. Like the other burnup indicator nuclides, there is no significant difference between the different temperature cases.

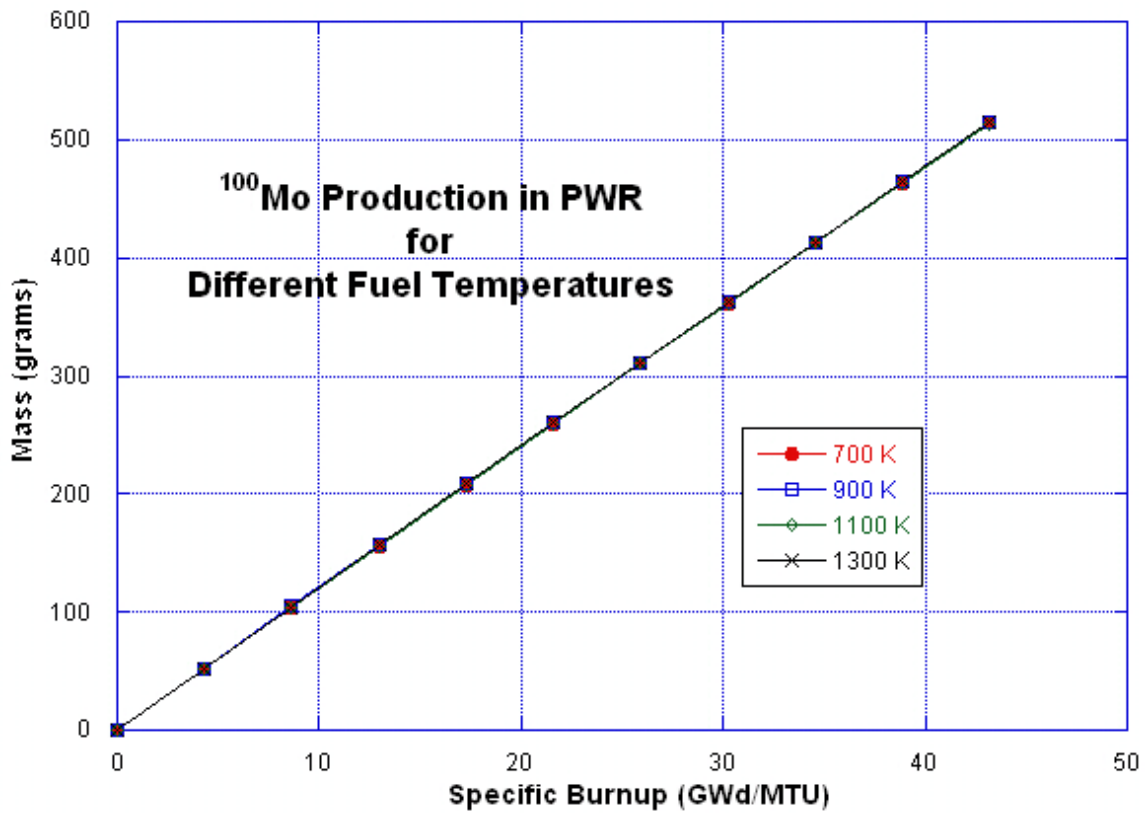


Figure 111: ¹⁰⁰Mo Production in the PWR for the Different Fuel Temperatures

Figure 112 is a plot of ⁹¹Y production for the different fuel temperature cases. As can be seen in the plot, there is less ⁹¹Y production for the 20,000 K case where less ²³⁵U fission is occurring.

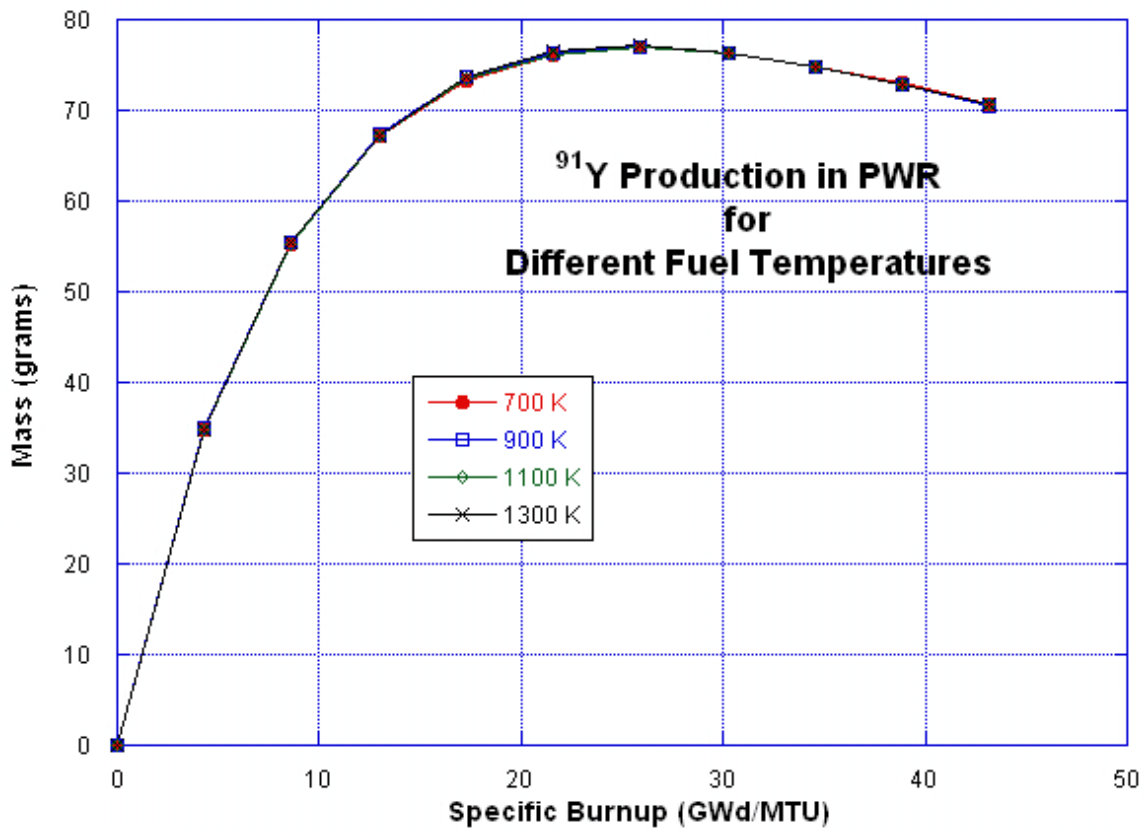


Figure 112: ^{91}Y Production in the PWR for the Different Fuel Temperatures

Figure 113 is a plot of ^{149}Sm production for the different fuel temperature cases. As can be seen in the plot, there is more ^{149}Sm production for the 20,000 K case.

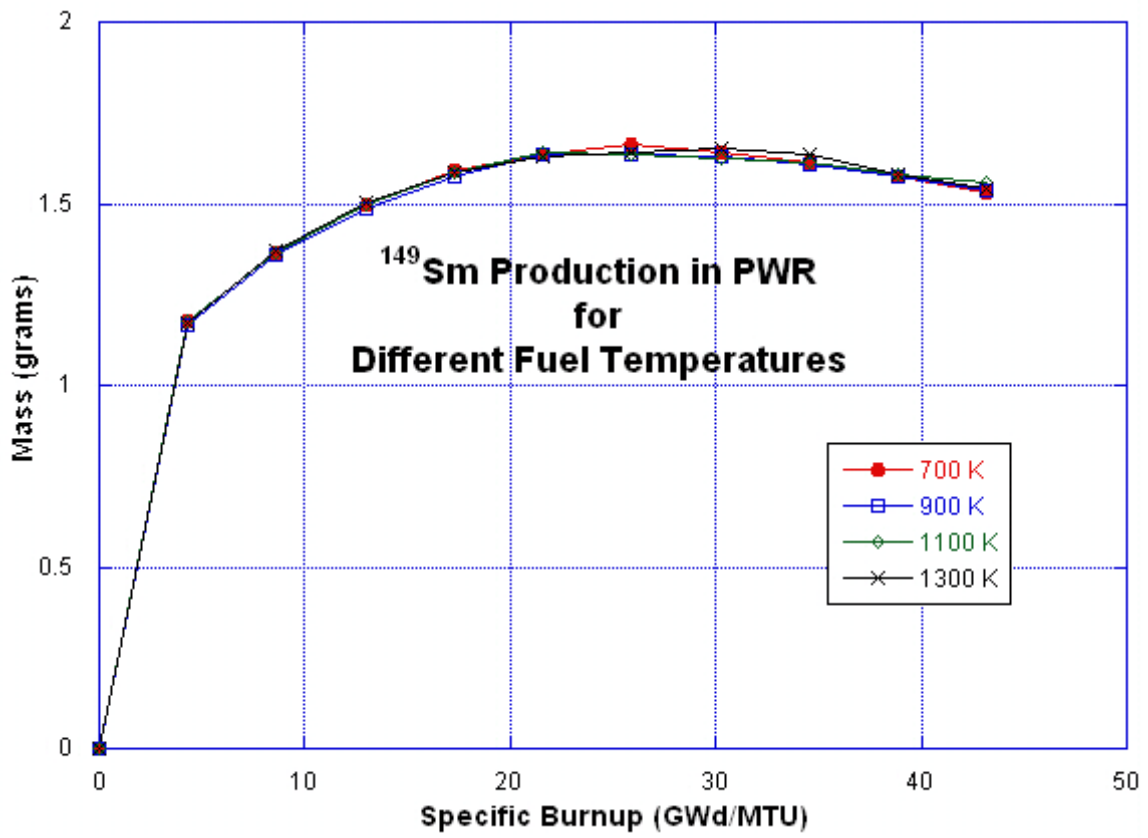


Figure 113: ¹⁴⁹Sm Production in the PWR for the Different Fuel Temperatures

Chapter 7: Conclusions and Recommendations

7.1 CONCLUSIONS FOR ORIGEN-ARP AND MCNPX COMPARISONS

This dissertation illustrates the variances that can be obtained in forward calculation models that serve as the comparisons for nuclear forensics analysis. While the advances in mass spectrometry allow the analysis of numerous more nuclides than previous capabilities did, the forward models which calculate these nuclides can generate significant differences based upon the calculation codes used and the reactor parameters input into the model.

This dissertation completed the four objectives found in Section 1.3.3. MCNPX and ORIGEN-ARP models were developed for BWR, PWR, and CANDU reactor types. For each reactor type, the results of the MCNPX calculation were compared to the results of the ORIGEN-ARP calculation. A comparison of the algorithms for each code was performed in order to explain differences in the results. Finally, a sensitivity study of the MCNPX PWR model was completed to investigate any differences in nuclide generation and depletion where five different reactor design or operating parameters were varied slightly.

The ORIGEN-ARP calculation package has many advantages, the main one being time. If you are using one of the pre-calculated reactor design types whose ARP-effective cross sections come packaged with the code, then ORIGEN-ARP can save the user countless hours of having to perform the radiation transport calculations to determine the initial ARP-effective cross sections. The user can perform dozens of calculations changing enrichment, moderator density, reactor power, and fuel quantities

in a single hour. Even if the user desires to perform calculations for a reactor type that is not pre-packaged with the code, then the user can use other modules contained within the SCALE code package to perform a one-time radiation transport calculation to determine the ARP-effective cross sections and then input those cross section libraries into the ORIGEN-ARP code allowing the user to perform calculations in a similar manner as if the reactor type came packaged with the code. In contrast, MCNPX must perform a radiation transport calculation every time any reactor design or operating parameter is changed. However, in this study, the author attempted to use MCNPX to model three different reactor types contained within the ORIGEN-ARP code using the available design and operating data in the SCALE manual, its references, and some standard industry sources. The MCNPX results were then compared to ORIGEN-ARP results for those three reactor types. Both models contained the same initial quantities of fuel and experienced identical power profiles. The two sets of results match well for most of the 46 nuclides analyzed for the three reactor types with notable exceptions being ^{239}Pu , ^{241}Pu , ^{241}Am , ^{243}Am , and ^{149}Sm for the BWR model, ^{149}Sm for the PWR model, ^{93}Zr for the CANDU model, and the curium isotopes for all three models. Primary sources of error include 1) discrepancies in how the reactor design and operating parameters are incorporated into each model (e.g. boron concentrations, gadolinium content, homogenization); 2) the fact that the ARP-effective cross sections originate from a two-dimensional radiation transport code rather than a three-dimension code such as MCNPX; and 3) differences in the methods used to determine nuclide generation and depletion rates, including the fact that MCNPX has 60 fission product yields compared to ORIGEN-S' 36 fission product yields, and ORIGEN-S' three-group neutron energy structure compared to MCNPX's 63-group neutron energy structure.

7.2 CONCLUSIONS FOR MCNPX SENSITIVITY STUDY

The actinides in this study are particularly sensitive to changes in the reactor parameters analyzed. The ten burnup indicators studied showed remarkably little variance for the reactor parameters analyzed. The other fission products, in general, showed variance directly related to the decrease or increase of the ^{235}U fission rate.

Reasonable variation in cladding thickness, water density, and fuel temperature did not result in significant differences in most of the nuclides analyzed. Water density was not varied drastically in this study. For a BWR, where water density within the reactor vessel may vary considerably, possibly resulting in significant differences in the production of the nuclides studied in this dissertation.

Changes in fuel assembly rod pitch and initial boron concentration, however, did result in significant difference for most of the nuclides studied (except for the burnup indicator nuclides).

Whether using the SCALE code or the MCNPX code to model any given reactor, correctly modeling these two variables may be essential for ensuring that the results are accurate.

7.3 RECOMMENDATIONS FOR FUTURE WORK

The ORIGEN-ARP libraries used in this dissertation came packaged with the SCALE 5.1 code, which were developed from two-dimension transport codes also found within the SCALE 5.1 package. A higher fidelity comparison of the results may be found

by using one of the three-dimensional codes to develop the ARP effective cross sections. This would “factor out” any differences resulting from approximations made during the initial reactor design setup for the model and would allow a better comparison of how the MCNPX algorithm for nuclide depletion varies when compared to that of ORIGEN-ARP. Nuclides in addition to the 46 examined here should also be analyzed with particular emphasis on nuclides which may be used for nuclear forensics analysis. Results from additional reactor types should also be compared.

Sensitivity studies may also be done for different reactor types using parameters in addition to those examined here. Though the slight variations in water density for this PWR model did not result in appreciable differences for most of the nuclides analyzed, a BWR has greater variation of water density throughout the reactor core which could be modeled to determine the effect of such variation.

As discussed in Chapter 1, numerous forward calculations of different reactor types and operating parameters could be completed to fill in the gaps left by the lack of empirical data for reactors not yet sampled and/or nuclides not yet quantified from existing samples.

Appendix A: The MCNPX BWR Model

GE 8X8-4 Fuel Assembly

1 1 -9.863 -1 u=1 imp:n=1 vol=334.07 tmp=9.71e-8 \$1.8 FUEL at 1128 K
10 4 -1.2e-3 1 -10 u=1 imp:n=1 tmp=4.819e-8 \$dry N gap
2 3 -6.52 10 -2 u=1 imp:n=1 tmp=4.819e-8 \$CLADDING at 560 Kelvin
3 2 -0.6 2 u=1 imp:n=1 tmp=4.7588e-8 \$T=553 Kelvin
31 2 -0.6 -2 u=2 imp:n=1 tmp=4.7588e-8 \$channel T=553 Kelvin
32 2 -0.6 2 u=2 imp:n=1 tmp=4.7588e-8 \$channel T=553 Kelvin
33 5 -9.863 -1 u=3 imp:n=1 vol=334.07 tmp=9.71e-8 \$3.0 Fuel with Gd
c poison
34 4 -1.2e-3 1 -10 u=3 imp:n=1 tmp=4.819e-8 \$dry N gap
35 3 -6.52 10 -2 u=3 imp:n=1 tmp=4.819e-8 \$CLADDING at 560 Kelvin
36 2 -0.6 2 u=3 imp:n=1 tmp=4.7588e-8 \$water around fuel
37 2 -0.6 -6 u=4 imp:n=1 tmp=4.7588e-8 \$water rod
38 3 -6.52 6 -7 u=4 imp:n=1 tmp=4.7588e-8 \$water rod
39 2 -0.6 7 u=4 imp:n=1 tmp=4.7588e-8 \$water rod
40 2 -0.6 -8 u=5 imp:n=1 tmp=4.7588e-8 \$water rod
41 3 -6.52 8 -9 u=5 imp:n=1 tmp=4.7588e-8 \$water rod
42 2 -0.6 9 u=5 imp:n=1 tmp=4.7588e-8 \$water rod
43 2 -0.6 -11 u=6 imp:n=1 tmp=4.7588e-8 \$water rod
44 3 -6.52 11 -12 u=6 imp:n=1 tmp=4.7588e-8 \$water rod
45 2 -0.6 12 u=6 imp:n=1 tmp=4.7588e-8 \$water rod
46 2 -0.6 -13 u=7 imp:n=1 tmp=4.7588e-8 \$water rod
47 3 -6.52 13 -14 u=7 imp:n=1 tmp=4.7588e-8 \$water rod
48 2 -0.6 14 u=7 imp:n=1 tmp=4.7588e-8 \$water rod
49 6 -9.863 -1 u=8 imp:n=1 vol=334.07 tmp=9.71e-8 \$2.0 FUEL at 1128 K
50 4 -1.2e-3 1 -10 u=8 imp:n=1 tmp=4.819e-8 \$dry N gap
51 3 -6.52 10 -2 u=8 imp:n=1 tmp=4.819e-8 \$CLADDING at 560 Kelvin
52 2 -0.6 2 u=8 imp:n=1 tmp=4.7588e-8 \$T=553 Kelvin
53 7 -9.863 -1 u=9 imp:n=1 vol=334.07 tmp=9.71e-8 \$2.3 FUEL at 1128 K
54 4 -1.2e-3 1 -10 u=9 imp:n=1 tmp=4.819e-8 \$dry N gap
55 3 -6.52 10 -2 u=9 imp:n=1 tmp=4.819e-8 \$CLADDING at 560 Kelvin
56 2 -0.6 2 u=9 imp:n=1 tmp=4.7588e-8 \$T=553 Kelvin
57 8 -9.863 -1 u=10 imp:n=1 vol=334.07 tmp=9.71e-8 \$2.4 FUEL at 1128K
58 4 -1.2e-3 1 -10 u=10 imp:n=1 tmp=4.819e-8 \$dry N gap
59 3 -6.52 10 -2 u=10 imp:n=1 tmp=4.819e-8 \$CLADDING at 560 Kelvin
60 2 -0.6 2 u=10 imp:n=1 tmp=4.7588e-8 \$T=553 Kelvin
61 9 -9.863 -1 u=11 imp:n=1 vol=334.07 tmp=9.71e-8 \$2.6 FUEL at 1128K
62 4 -1.2e-3 1 -10 u=11 imp:n=1 tmp=4.819e-8 \$dry N gap
63 3 -6.52 10 -2 u=11 imp:n=1 tmp=4.819e-8 \$CLADDING at 560 Kelvin
64 2 -0.6 2 u=11 imp:n=1 tmp=4.7588e-8 \$T=553 Kelvin
65 10 -9.863 -1 u=12 imp:n=1 vol=334.07 tmp=9.71e-8 \$2.8 FUEL at1128K
66 4 -1.2e-3 1 -10 u=12 imp:n=1 tmp=4.819e-8 \$dry N gap
67 3 -6.52 10 -2 u=12 imp:n=1 tmp=4.819e-8 \$CLADDING at 560 Kelvin
68 2 -0.6 2 u=12 imp:n=1 tmp=4.7588e-8 \$T=553 Kelvin
69 11 -9.863 -1 u=13 imp:n=1 vol=334.07 tmp=9.71e-8 \$2.9 FUEL at1128K
70 4 -1.2e-3 1 -10 u=13 imp:n=1 tmp=4.819e-8 \$dry N gap
71 3 -6.52 10 -2 u=13 imp:n=1 tmp=4.819e-8 \$CLADDING at 560 Kelvin
72 2 -0.6 2 u=13 imp:n=1 tmp=4.7588e-8 \$T=553 Kelvin
73 12 -9.863 -1 u=14 imp:n=1 vol=334.07 tmp=9.71e-8 \$3.4 FUEL at1128K
74 4 -1.2e-3 1 -10 u=14 imp:n=1 tmp=4.819e-8 \$dry N gap
75 3 -6.52 10 -2 u=14 imp:n=1 tmp=4.819e-8 \$CLADDING at 560 Kelvin

```

76 2 -0.6 2 u=14 imp:n=1 tmp=4.7588e-8 $T=553 Kelvin
77 13 -9.863 -1 u=15 imp:n=1 vol=334.07 tmp=9.71e-8 $3.8 FUEL at1128K
78 4 -1.2e-3 1 -10 u=15 imp:n=1 tmp=4.819e-8 $dry N gap
79 3 -6.52 10 -2 u=15 imp:n=1 tmp=4.819e-8 $CLADDING at 560 Kelvin
80 2 -0.6 2 u=15 imp:n=1 tmp=4.7588e-8 $T=553 Kelvin
81 14 -9.863 -1 u=16 imp:n=1 vol=334.07 tmp=9.71e-8 $3.9 FUEL at1128K
82 4 -1.2e-3 1 -10 u=16 imp:n=1 tmp=4.819e-8 $dry N gap
83 3 -6.52 10 -2 u=16 imp:n=1 tmp=4.819e-8 $CLADDING at 560 Kelvin
84 2 -0.6 2 u=16 imp:n=1 tmp=4.7588e-8 $T=553 Kelvin
4 0 -3 lat=1 u=17 imp:n=1 fill=-4:3 0:0 -4:3
    8 12 14 16 16 16 13 9
    10 14 3 16 3 16 16 13
    11 3 16 16 16 3 16 16
    12 15 16 4 5 16 3 16
    11 3 15 6 7 16 16 16
    11 14 14 15 16 16 3 14
    8 10 14 3 15 3 14 12
    1 8 11 11 12 11 10 8
5 0 -4 fill=17 imp:n=1 $window filled with lattice
6 2 -0.7396 4 -5 imp:n=1 tmp=4.7588e-8 $reflective box
800 0 5 -900 imp:n=1 $inside world
900 0 900 imp:n=0 $outside world

1 rcc 0 0 0 0 385 0 0.5283 $pellet is 10.566 mm diamter or 0.5283
c cm radius
10 rcc 0 0 0 0 385 0 0.5321 $dry nitrogen air gap 0.0038 cm thick
2 rcc 0 0 0 0 385 0 0.6134 $cladding is 0.0813 cm thick
3 box -0.8128 0 -0.8128 1.6256 0 0 0 381 0 0 0 1.6256
c individual box for each fuel element pitch is 1.6256 cm
4 rpp -7.3152 5.6896 0 381 -7.3152 5.6896 $ box for fuel assembly
*5 rpp -8.5152 6.8896 -1.2 382.2 -8.5152 6.8896 $reflective box
6 rcc 0.8128 0 0.8128 0 385 0 1.5
7 rcc 0.8128 0 0.8128 0 385 0 1.6
8 rcc -0.8128 0 0.8128 0 385 0 1.5
9 rcc -0.8128 0 0.8128 0 385 0 1.6
11 rcc 0.8128 0 -0.8128 0 385 0 1.5
12 rcc 0.8128 0 -0.8128 0 385 0 1.6
13 rcc -0.8128 0 -0.8128 0 385 0 1.5
14 rcc -0.8128 0 -0.8128 0 385 0 1.6
900 rcc 0 -50 0 0 510 0 50 $cylinder to define outside world

Burn Time=24,24,24,24,24,24,24,24,24,24
    PFRAC=1.0, 1.0, 1.0, 1.0, 1.0, 1.0, 1.0, 1.0, 1.0, 1.0, 1.0
    Power=30.9
    Mat=1 5 6 7 8 9 10 11 12 13 14
    MATVOL=334.07 3006.63 1336.28 334.07 1002.21 2004.42
        1336.28 668.14 2338.49 1336.28 6347.33
    AFMIN=1e-36
    BOPT=1.0 24 1
AWTAB 44105 104.0065424 49117 115.9002498 49116 114.9209546
    49118 116.8934824 49119 117.884388 49121 119.8691923
    54137 135.9
m1 92235 -0.015867 92238 -0.865502 8016 -0.11849 92234 -0.000141

```



```

          95241 -1e-36 95243 -1e-36 96245 -1e-36 96246 -1e-36
c      UO2 fuel at 1.8 percent enrichment
c      54137 -1e-36 49116 -1e-36 49117 -1e-36 49118 -1e-36 49119 -1e-36
$2.5 percent U-235 UO2 fuel
m2 1001 0.666667 8016 0.333333 $WATER
mt2 lwtr.62t $S(alpha, beta) for water (Temp 600 K)
m3 40000 -0.9845 50000 -0.012 26000 -0.0018 24000 -0.0007 8016 -0.001
$Zry-4 from Neeb
m4 7014 1 $dry nitrogen
m5 92235 -0.027475 92238 -0.830871 8016 -0.115409 92234 -0.000245
      64152 -0.000052 64154 -0.0005668 64155 -0.003848
      64156 -0.0053222
      64157 -0.004069 64158 -0.0064584 64160 -0.0056836
      95241 -1e-36 95243 -1e-36 96245 -1e-36 96246 -1e-36
c      UO2 fuel at 3.2% enrichment with 0.026 natural Gd
m6 92235 -0.01763 92238 -0.863723 8016 -0.11849 92234 -0.000157
      95241 -1e-36 95243 -1e-36 96245 -1e-36 96246 -1e-36
c      UO2 fuel at 2.0 percent enrichment
m7 92235 -0.020275 92238 -0.861055 8016 -0.11849 92234 -0.00018
      95241 -1e-36 95243 -1e-36 96245 -1e-36 96246 -1e-36
c      UO2 fuel at 2.3 percent enrichment
m8 92235 -0.021156 92238 -0.860166 8016 -0.11849 92234 -0.000188
      95241 -1e-36 95243 -1e-36 96245 -1e-36 96246 -1e-36
c      UO2 fuel at 2.4 percent enrichment
m9 92235 -0.022919 92238 -0.858387 8016 -0.11849 92234 -0.000204
      95241 -1e-36 95243 -1e-36 96245 -1e-36 96246 -1e-36
c      UO2 fuel at 2.6 percent enrichment
m10 92235 -0.024682 92238 -0.856608 8016 -0.11849 92234 -0.00022
      95241 -1e-36 95243 -1e-36 96245 -1e-36 96246 -1e-36
c      UO2 fuel at 2.8 percent enrichment
m11 92235 -0.025564 92238 -0.855719 8016 -0.11849 92234 -0.000227
      95241 -1e-36 95243 -1e-36 96245 -1e-36 96246 -1e-36
c      UO2 fuel at 2.9 percent enrichment
m12 92235 -0.029971 92238 -0.851272 8016 -0.11849 92234 -0.000267
      95241 -1e-36 95243 -1e-36 96245 -1e-36 96246 -1e-36
c      UO2 fuel at 3.4 percent enrichment
m13 92235 -0.033497 92238 -0.847715 8016 -0.11849 92234 -0.000298
      95241 -1e-36 95243 -1e-36 96245 -1e-36 96246 -1e-36
c      UO2 fuel at 3.8 percent enrichment
m14 92235 -0.034379 92238 -0.846825 8016 -0.11849 92234 -0.000306
      95241 -1e-36 95243 -1e-36 96245 -1e-36 96246 -1e-36
c      UO2 fuel at 3.9 percent enrichment
KCODE 3000 1.0 30 150
KSRC -6.5 192 4.8 -4.8 192 4.8 -3.3 100 4.8 -1.6 192 4.8 0 192 4.8
      1.6 192 4.8 3.3 192 4.8 4.8 192 4.8
      -6.5 192 3.3 -4.8 100 3.3 -3.3 300 3.3 -1.6 192 3.3 0 192 3.3
      1.6 100 3.3 3.3 192 3.3 4.8 192 3.3
      -6.5 192 1.6 -4.8 300 1.6 -3.3 100 1.6 -1.6 192 1.6 0 192 1.6
      1.6 300 1.6 3.3 192 1.6 4.8 192 1.6
      -6.5 192 0 -4.8 100 0 -3.3 300 0
      1.6 100 0 3.3 192 0 4.8 192 0
      -6.5 192 -1.6 -4.8 300 -1.6 -3.3 100 -1.6
      1.6 300 -1.6 3.3 192 -1.6 4.8 192 -1.6

```

```
-6.5 192 -3.3 -4.8 100 -3.3 -3.3 300 -3.3
-1.6 100 -3.3 0 192 -3.3
 1.6 192 -3.3 3.3 300 -3.3 4.8 192 -3.3
-6.5 300 -4.8 -4.8 192 -4.8 -3.3 100 -4.8
-1.6 192 -4.8 0 100 -4.8
 1.6 100 -4.8 3.3 192 -4.8 4.8 192 -4.8
-6.5 192 -6.5 -4.8 300 -6.5 -3.3 300 -6.5
-1.6 300 -6.5 0 192 -6.5
 1.6 192 -6.5 3.3 100 -6.5 4.8 192 -6.5
c sources in ALL elements
```

Appendix B: The MCNPX PWR Model

```

W 17x17 Fuel Assembly for PWR
1 1 -10.41 -1 u=1 imp:n=1 vol=49043.15866 tmp=7.74-8 $FUEL at
c 900 Kelvin
2 3 -6.52 1 -2 u=1 imp:n=1 tmp=5.353e-8 $CLADDING at 622 Kelvin
3 2 -0.723 2 u=1 imp:n=1 tmp=4.96e-8 $T=576 Kelvin
31 2 -0.723 -2 u=2 imp:n=1 tmp=4.96e-8 $channel T=576 Kelvin
32 2 -0.723 2 u=2 imp:n=1 tmp=4.96e-8 $channel T=576 Kelvin
4 0 -3 lat=1 u=3 imp:n=1 fill=-8:8 0:0 -8:8
    1 16r
    1 16r
    1 1 1 1 1 2 1 1 2 1 1 2 1 1 1 1 1
    1 1 1 2 1 1 1 1 1 1 1 1 1 1 2 1 1 1
    1 1 1 1 1 1 1 1 1 1 1 1 1 1 1 1 1
    1 1 2 1 1 2 1 1 2 1 1 2 1 1 2 1 1
    1 1 1 1 1 1 1 1 1 1 1 1 1 1 1 1 1
    1 1 1 1 1 1 1 1 1 1 1 1 1 1 1 1 1
    1 1 2 1 1 2 1 1 2 1 1 2 1 1 2 1 1
    1 1 1 1 1 1 1 1 1 1 1 1 1 1 1 1 1
    1 1 1 1 1 1 1 1 1 1 1 1 1 1 1 1 1
    1 1 2 1 1 2 1 1 2 1 1 2 1 1 2 1 1
    1 1 1 1 1 1 1 1 1 1 1 1 1 1 1 1 1
    1 1 1 2 1 1 1 1 1 1 1 1 1 2 1 1 1
    1 1 1 1 1 2 1 1 2 1 1 2 1 1 1 1 1
    1 16r
    1 16r
5 0 -4 fill=3 imp:n=1 $window filled with lattice
6 2 -0.723 4 -5 imp:n=1 tmp=4.96e-8 $reflective box T=576 Kelvin
800 0 5 -900 imp:n=1 $inside world
900 0 900 imp:n=0 $outside world

1 rcc 0 0 0 0 365 0 0.4025 $pellet is 8.05 mm diamter or 0.4025 cm
c radius
2 rcc 0 0 0 0 365 0 0.4596 $cladding is 0.0571 cm thick
3 box -0.63 0 -0.63 1.26 0 0 0 385 0 0 0 1.26 $individual box for
each fuel element pitch is 1.26 cm
4 rpp -10.71 10.71 0 365 -10.71 10.71 $ box for fuel assembly
*5 rpp -10.711 10.711 -0.001 365.001 -10.711 10.711 $reflective box
900 rcc 0 -50 0 0 510 0 50 $cylinder to define outside world

Burn Time=36, 36, 36, 36, 36, 36, 36, 36, 36, 36
    PFRAC=1.0, 1.0, 1.0, 1.0, 1.0, 1.0, 1.0, 1.0, 1.0, 1.0
    Power=54
    Mat=1
    AFMIN=1e-36
    BOPT=1.0 24 1
AWTAB 44105 104.0065424 49117 115.9002498 49116 114.9209546
    49118 116.8934824 49119 117.884388 49121 119.8691923
    54137 135.9
m1 92235 -0.039669 92238 -0.841515 8016 -0.118463 92234 -0.000353
    95241 -1e-36 95243 -1e-36 96245 -1e-36 96246 -1e-36 $ UO2
fuel at 4.5% enrichment
c 54137 -1e-36 49116 -1e-36 49117 -1e-36 49118 -1e-36 49119 -1e-36
c $3.5 percent U-235 UO2 fuel

```

```

m2 1001 0.66651 8016 0.3332 5010 0.00029 $WATER with B
c   at 850 ppm
mt2 lwtr.62t  $S(alpha, beta) for water (Temp 600 K)
m3 40000 -0.9845 50000 -0.012 26000 -0.0018 24000 -0.0007 8016 -0.001
c  $Zry-4 from Neeb
KCODE 1000 1.0 30 130
KSRC 7.56 192 7.56 7.56 192 -7.56 5.04 192 5.04 5.04 192 -5.04
      0 192 6.3 0 192 -6.3
      -7.56 192 7.56 -7.56 192 -7.56 -5.04 192 5.04 -5.04 192 -5.04
c  sources in elements (6,0,6) (6,0,-6) (4,0,2) (4,0,-2)
c                      (0,0,5)(0,0,-5)
c                      (-6,0,6) (-6,0,-6) (-4,0,2) (-4,0,-2)

```

Appendix C: The MCNPX CANDU Model

CANDU 37 Fuel Assembly Annular Bundle Geometry Rod Pitch=1.46 cm

1	1	-10.59	-1	imp:n=1	tmp=9.94e-8	vol=57.4263	\$FUEL	at 1155 Kelvin
2	1	-10.59	-2	imp:n=1	tmp=9.94e-8	vol=57.4263	\$FUEL	at 1155 Kelvin
3	1	-10.59	-3	imp:n=1	tmp=9.94e-8	vol=57.4263	\$FUEL	at 1155 Kelvin
4	1	-10.59	-4	imp:n=1	tmp=9.94e-8	vol=57.4263	\$FUEL	at 1155 Kelvin
5	1	-10.59	-5	imp:n=1	tmp=9.94e-8	vol=57.4263	\$FUEL	at 1155 Kelvin
6	1	-10.59	-6	imp:n=1	tmp=9.94e-8	vol=57.4263	\$FUEL	at 1155 Kelvin
7	1	-10.59	-7	imp:n=1	tmp=9.94e-8	vol=57.4263	\$FUEL	at 1155 Kelvin
8	1	-10.59	-8	imp:n=1	tmp=9.94e-8	vol=57.4263	\$FUEL	at 1155 Kelvin
9	1	-10.59	-9	imp:n=1	tmp=9.94e-8	vol=57.4263	\$FUEL	at 1155 Kelvin
10	1	-10.59	-10	imp:n=1	tmp=9.94e-8	vol=57.4263	\$FUEL	at 1155 Kelvin
11	1	-10.59	-11	imp:n=1	tmp=9.94e-8	vol=57.4263	\$FUEL	at 1155 Kelvin
12	1	-10.59	-12	imp:n=1	tmp=9.94e-8	vol=57.4263	\$FUEL	at 1155 Kelvin
13	1	-10.59	-13	imp:n=1	tmp=9.94e-8	vol=57.4263	\$FUEL	at 1155 Kelvin
14	1	-10.59	-14	imp:n=1	tmp=9.94e-8	vol=57.4263	\$FUEL	at 1155 Kelvin
15	1	-10.59	-15	imp:n=1	tmp=9.94e-8	vol=57.4263	\$FUEL	at 1155 Kelvin
16	1	-10.59	-16	imp:n=1	tmp=9.94e-8	vol=57.4263	\$FUEL	at 1155 Kelvin
17	1	-10.59	-17	imp:n=1	tmp=9.94e-8	vol=57.4263	\$FUEL	at 1155 Kelvin
18	1	-10.59	-18	imp:n=1	tmp=9.94e-8	vol=57.4263	\$FUEL	at 1155 Kelvin
19	1	-10.59	-19	imp:n=1	tmp=9.94e-8	vol=57.4263	\$FUEL	at 1155 Kelvin
20	1	-10.59	-20	imp:n=1	tmp=9.94e-8	vol=57.4263	\$FUEL	at 1155 Kelvin
21	1	-10.59	-21	imp:n=1	tmp=9.94e-8	vol=57.4263	\$FUEL	at 1155 Kelvin
22	1	-10.59	-22	imp:n=1	tmp=9.94e-8	vol=57.4263	\$FUEL	at 1155 Kelvin
23	1	-10.59	-23	imp:n=1	tmp=9.94e-8	vol=57.4263	\$FUEL	at 1155 Kelvin
24	1	-10.59	-24	imp:n=1	tmp=9.94e-8	vol=57.4263	\$FUEL	at 1155 Kelvin
25	1	-10.59	-25	imp:n=1	tmp=9.94e-8	vol=57.4263	\$FUEL	at 1155 Kelvin
26	1	-10.59	-26	imp:n=1	tmp=9.94e-8	vol=57.4263	\$FUEL	at 1155 Kelvin
27	1	-10.59	-27	imp:n=1	tmp=9.94e-8	vol=57.4263	\$FUEL	at 1155 Kelvin
28	1	-10.59	-28	imp:n=1	tmp=9.94e-8	vol=57.4263	\$FUEL	at 1155 Kelvin
29	1	-10.59	-29	imp:n=1	tmp=9.94e-8	vol=57.4263	\$FUEL	at 1155 Kelvin
30	1	-10.59	-30	imp:n=1	tmp=9.94e-8	vol=57.4263	\$FUEL	at 1155 Kelvin
31	1	-10.59	-31	imp:n=1	tmp=9.94e-8	vol=57.4263	\$FUEL	at 1155 Kelvin
32	1	-10.59	-32	imp:n=1	tmp=9.94e-8	vol=57.4263	\$FUEL	at 1155 Kelvin
33	1	-10.59	-33	imp:n=1	tmp=9.94e-8	vol=57.4263	\$FUEL	at 1155 Kelvin
34	1	-10.59	-34	imp:n=1	tmp=9.94e-8	vol=57.4263	\$FUEL	at 1155 Kelvin
35	1	-10.59	-35	imp:n=1	tmp=9.94e-8	vol=57.4263	\$FUEL	at 1155 Kelvin
36	1	-10.59	-36	imp:n=1	tmp=9.94e-8	vol=57.4263	\$FUEL	at 1155 Kelvin
37	1	-10.59	-37	imp:n=1	tmp=9.94e-8	vol=57.4263	\$FUEL	at 1155 Kelvin
61	3	-6.52	1	imp:n=1	tmp=5.155e-8		\$CLADDING	at 599 Kelvin
62	3	-6.52	2	imp:n=1	tmp=5.155e-8		\$CLADDING	at 599 Kelvin
63	3	-6.52	3	imp:n=1	tmp=5.155e-8		\$CLADDING	at 599 Kelvin
64	3	-6.52	4	imp:n=1	tmp=5.155e-8		\$CLADDING	at 599 Kelvin
65	3	-6.52	5	imp:n=1	tmp=5.155e-8		\$CLADDING	at 599 Kelvin
66	3	-6.52	6	imp:n=1	tmp=5.155e-8		\$CLADDING	at 599 Kelvin
67	3	-6.52	7	imp:n=1	tmp=5.155e-8		\$CLADDING	at 599 Kelvin
68	3	-6.52	8	imp:n=1	tmp=5.155e-8		\$CLADDING	at 599 Kelvin
69	3	-6.52	9	imp:n=1	tmp=5.155e-8		\$CLADDING	at 599 Kelvin
70	3	-6.52	10	imp:n=1	tmp=5.155e-8		\$CLADDING	at 599 Kelvin
71	3	-6.52	11	imp:n=1	tmp=5.155e-8		\$CLADDING	at 599 Kelvin
72	3	-6.52	12	imp:n=1	tmp=5.155e-8		\$CLADDING	at 599 Kelvin
73	3	-6.52	13	imp:n=1	tmp=5.155e-8		\$CLADDING	at 599 Kelvin
74	3	-6.52	14	imp:n=1	tmp=5.155e-8		\$CLADDING	at 599 Kelvin
75	3	-6.52	15	imp:n=1	tmp=5.155e-8		\$CLADDING	at 599 Kelvin

```

76 3 -6.52 16 -76 imp:n=1 tmp=5.155e-8 $CLADDING at 599 Kelvin
77 3 -6.52 17 -77 imp:n=1 tmp=5.155e-8 $CLADDING at 599 Kelvin
78 3 -6.52 18 -78 imp:n=1 tmp=5.155e-8 $CLADDING at 599 Kelvin
79 3 -6.52 19 -79 imp:n=1 tmp=5.155e-8 $CLADDING at 599 Kelvin
80 3 -6.52 20 -80 imp:n=1 tmp=5.155e-8 $CLADDING at 599 Kelvin
81 3 -6.52 21 -81 imp:n=1 tmp=5.155e-8 $CLADDING at 599 Kelvin
82 3 -6.52 22 -82 imp:n=1 tmp=5.155e-8 $CLADDING at 599 Kelvin
83 3 -6.52 23 -83 imp:n=1 tmp=5.155e-8 $CLADDING at 599 Kelvin
84 3 -6.52 24 -84 imp:n=1 tmp=5.155e-8 $CLADDING at 599 Kelvin
85 3 -6.52 25 -85 imp:n=1 tmp=5.155e-8 $CLADDING at 599 Kelvin
86 3 -6.52 26 -86 imp:n=1 tmp=5.155e-8 $CLADDING at 599 Kelvin
87 3 -6.52 27 -87 imp:n=1 tmp=5.155e-8 $CLADDING at 599 Kelvin
88 3 -6.52 28 -88 imp:n=1 tmp=5.155e-8 $CLADDING at 599 Kelvin
89 3 -6.52 29 -89 imp:n=1 tmp=5.155e-8 $CLADDING at 599 Kelvin
90 3 -6.52 30 -90 imp:n=1 tmp=5.155e-8 $CLADDING at 599 Kelvin
91 3 -6.52 31 -91 imp:n=1 tmp=5.155e-8 $CLADDING at 599 Kelvin
92 3 -6.52 32 -92 imp:n=1 tmp=5.155e-8 $CLADDING at 599 Kelvin
93 3 -6.52 33 -93 imp:n=1 tmp=5.155e-8 $CLADDING at 599 Kelvin
94 3 -6.52 34 -94 imp:n=1 tmp=5.155e-8 $CLADDING at 599 Kelvin
95 3 -6.52 35 -95 imp:n=1 tmp=5.155e-8 $CLADDING at 599 Kelvin
96 3 -6.52 36 -96 imp:n=1 tmp=5.155e-8 $CLADDING at 599 Kelvin
97 3 -6.52 37 -97 imp:n=1 tmp=5.155e-8 $CLADDING at 599 Kelvin
c Cell 50 is the coolant pressure tube which contains the fuel rods
c and the D2O coolant at 310 C and 10.5 MPa, rho from CANTEACH webpage
50 2 -0.8360 -38 61 62 63 64 65 66 67 68 69 70 71 72 73
    74 75 76 77 78 79 80 81 82 83 84 85 86 87
    88 89 90 91 92 93 94 95 96 97
    tmp=5.02e-8 vol=1694.83427 imp:n=1 $inner fuel assembly
cylinder 548 K
38 5 -6.52 38 -39 imp:n=1 tmp=4.72e-8 $Pressure tube
39 4 -0.00198 39 -40 imp:n=1 tmp=4.72e-8 $CO2 layer
40 5 -6.52 40 -41 imp:n=1 tmp=3.8e-8 $Calandria tube
41 6 -1.0829 41 -43 imp:n=1 tmp=2.95e-8 $outer assembly cylinder with
D2O moderator
c rho from CANTEACH webpage
60 6 -1.0829 43 -50 imp:n=1 tmp=2.95e-8 $reflective cylinder
800 0 50 -900 imp:n=1 $inside world
900 0 900 imp:n=0 $outside world

c Fuel rod surfaces
1 rcc 0.000 0.000 0 0 0 49.53 0.6075 $ Rod at Origin pitch is
1.46 cm
2 rcc 1.460 0.000 0 0 0 49.53 0.6075 $ 1st ring
3 rcc 0.730 1.264 0 0 0 49.53 0.6075 $ 1st ring
4 rcc -0.730 1.264 0 0 0 49.53 0.6075 $ 1st ring
5 rcc -1.460 0.000 0 0 0 49.53 0.6075 $ 1st ring
6 rcc -0.730 -1.264 0 0 0 49.53 0.6075 $ 1st ring
7 rcc 0.730 -1.264 0 0 0 49.53 0.6075 $ 1st ring
8 rcc 2.920 0.000 0 0 0 49.53 0.6075 $2nd ring
9 rcc 2.529 1.460 0 0 0 49.53 0.6075 $2nd ring
10 rcc 1.460 2.529 0 0 0 49.53 0.6075 $2nd ring
11 rcc 0.000 2.920 0 0 0 49.53 0.6075 $2nd ring
12 rcc -1.460 2.529 0 0 0 49.53 0.6075 $2nd ring

```


13	rcc	-2.529	1.460	0	0	0	49.53	0.6075	\$2nd ring
14	rcc	-2.920	0.000	0	0	0	49.53	0.6075	\$2nd ring
15	rcc	-2.529	-1.460	0	0	0	49.53	0.6075	\$2nd ring
16	rcc	-1.460	-2.529	0	0	0	49.53	0.6075	\$2nd ring
17	rcc	0.000	-2.920	0	0	0	49.53	0.6075	\$2nd ring
18	rcc	1.460	-2.529	0	0	0	49.53	0.6075	\$2nd ring
19	rcc	2.529	-1.460	0	0	0	49.53	0.6075	\$2nd ring
20	rcc	4.380	0.000	0	0	0	49.53	0.6075	\$3rd ring
21	rcc	4.116	1.498	0	0	0	49.53	0.6075	\$3rd ring
22	rcc	3.355	2.815	0	0	0	49.53	0.6075	\$3rd ring
23	rcc	2.190	3.793	0	0	0	49.53	0.6075	\$3rd ring
24	rcc	0.761	4.313	0	0	0	49.53	0.6075	\$3rd ring
25	rcc	-0.761	4.313	0	0	0	49.53	0.6075	\$3rd ring
26	rcc	-2.190	3.793	0	0	0	49.53	0.6075	\$3rd ring
27	rcc	-3.355	2.815	0	0	0	49.53	0.6075	\$3rd ring
28	rcc	-4.116	1.498	0	0	0	49.53	0.6075	\$3rd ring
29	rcc	-4.380	0.000	0	0	0	49.53	0.6075	\$3rd ring
30	rcc	-4.116	-1.498	0	0	0	49.53	0.6075	\$3rd ring
31	rcc	-3.355	-2.815	0	0	0	49.53	0.6075	\$3rd ring
32	rcc	-2.190	-3.793	0	0	0	49.53	0.6075	\$3rd ring
33	rcc	-0.761	-4.313	0	0	0	49.53	0.6075	\$3rd ring
34	rcc	0.761	-4.313	0	0	0	49.53	0.6075	\$3rd ring
35	rcc	2.190	-3.793	0	0	0	49.53	0.6075	\$3rd ring
36	rcc	3.355	-2.815	0	0	0	49.53	0.6075	\$3rd ring
37	rcc	4.116	-1.498	0	0	0	49.53	0.6075	\$3rd ring
c	Cladding Surfaces								
61	rcc	0.000	0.000	0	0	0	49.53	0.654	\$Cladding is 0.0465 cm thick
62	rcc	1.460	0.000	0	0	0	49.53	0.654	\$1st ring
63	rcc	0.730	1.264	0	0	0	49.53	0.654	\$1st ring
64	rcc	-0.730	1.264	0	0	0	49.53	0.654	\$1st ring
65	rcc	-1.460	0.000	0	0	0	49.53	0.654	\$1st ring
66	rcc	-0.730	-1.264	0	0	0	49.53	0.654	\$1st ring
67	rcc	0.730	-1.264	0	0	0	49.53	0.654	\$1st ring
68	rcc	2.920	0.000	0	0	0	49.53	0.654	\$2nd ring
69	rcc	2.529	1.460	0	0	0	49.53	0.654	\$2nd ring
70	rcc	1.460	2.529	0	0	0	49.53	0.654	\$2nd ring
71	rcc	0.000	2.920	0	0	0	49.53	0.654	\$2nd ring
72	rcc	-1.460	2.529	0	0	0	49.53	0.654	\$2nd ring
73	rcc	-2.529	1.460	0	0	0	49.53	0.654	\$2nd ring
74	rcc	-2.920	0.000	0	0	0	49.53	0.654	\$2nd ring
75	rcc	-2.529	-1.460	0	0	0	49.53	0.654	\$2nd ring
76	rcc	-1.460	-2.529	0	0	0	49.53	0.654	\$2nd ring
77	rcc	0.000	-2.920	0	0	0	49.53	0.654	\$2nd ring
78	rcc	1.460	-2.529	0	0	0	49.53	0.654	\$2nd ring
79	rcc	2.529	-1.460	0	0	0	49.53	0.654	\$2nd ring
80	rcc	4.380	0.000	0	0	0	49.53	0.654	\$3rd ring
81	rcc	4.116	1.498	0	0	0	49.53	0.654	\$3rd ring
82	rcc	3.355	2.815	0	0	0	49.53	0.654	\$3rd ring
83	rcc	2.190	3.793	0	0	0	49.53	0.654	\$3rd ring
84	rcc	0.761	4.313	0	0	0	49.53	0.654	\$3rd ring
85	rcc	-0.761	4.313	0	0	0	49.53	0.654	\$3rd ring
86	rcc	-2.190	3.793	0	0	0	49.53	0.654	\$3rd ring

```

87 rcc -3.355 2.815 0 0 0 49.53 0.654 $3rd ring
88 rcc -4.116 1.498 0 0 0 49.53 0.654 $3rd ring
89 rcc -4.380 0.000 0 0 0 49.53 0.654 $3rd ring
90 rcc -4.116 -1.498 0 0 0 49.53 0.654 $3rd ring
91 rcc -3.355 -2.815 0 0 0 49.53 0.654 $3rd ring
92 rcc -2.190 -3.793 0 0 0 49.53 0.654 $3rd ring
93 rcc -0.761 -4.313 0 0 0 49.53 0.654 $3rd ring
94 rcc 0.761 -4.313 0 0 0 49.53 0.654 $3rd ring
95 rcc 2.190 -3.793 0 0 0 49.53 0.654 $3rd ring
96 rcc 3.355 -2.815 0 0 0 49.53 0.654 $3rd ring
97 rcc 4.116 -1.498 0 0 0 49.53 0.654 $3rd ring
38 rcc 0 0 0 0 0 49.53 5.1689 $inner cylinder for pressure tube
39 rcc 0 0 0 0 0 49.53 5.6032 $outer cylinder for pressure tube
40 rcc 0 0 0 0 0 49.53 6.4478 $outer cylinder for CO2
41 rcc 0 0 0 0 0 49.53 6.5875 $outer cylinder for Calandria tube
43 rcc 0 0 0 0 0 49.53 14.29 $cylinder for fuel assembly
+50 rcc 0 0 -1.5 0 0 52.53 14.30 $white boundary cylinder
900 rcc 0 0 -50 0 0 150 50 $cylinder to define outside world

```

Burn Time=36, 36, 36, 36, 36, 36, 36, 36, 36, 36

PFRAC=1.0, 1.0, 1.0, 1.0, 1.0, 1.0, 1.0, 1.0, 1.0, 1.0

Power=0.5

Mat=1

AFMIN=1e-36

BOPT=1.0 24 1

MATVOL=2124.773

```

AWTAB 44105 104.0065424 49117 115.9002498 49116 114.9209546
      49118 116.8934824 49119 117.884388 49121 119.8691923
      54137 135.9

```

```

m1 92235 -0.0062675 92238 -0.8751887 92234 -0.0000476 8016 -0.1184962
      95241 -1e-36 95243 -1e-36 96245 -1e-36 96246 -1e-36

```

c \$Nat U UO2 fuel

m2 1001 0.00167 1002 0.665 8016 0.33333 \$Heavy WATER

mt2 hwtr.62t \$S(alpha, beta) for Heavy water (Temp 600 K)

m3 40000 -0.9845 50000 -0.012 26000 -0.0018 24000 -0.0007 8016 -0.001

\$Zry-4 from Neeb

m4 6000 0.33333 8016 0.66667 \$CO2 for annular gas

m5 40000 -0.9858 50000 -0.012 26000 -0.0007 24000 -0.0005 28000 -0.0003

8016 -0.0007 \$Zry-2 from Neeb

m6 1001 0.00167 1002 0.665 8016 0.33333 \$Heavy WATER

mt6 hwtr.60t \$S(alpha, beta) for Heavy water (Temp 294 K)

KCODE 1000 1.0 30 130

```

KSRC 0.000 0.000 25
      1.460 0.000 25
      0.730 1.264 25
      -0.730 1.264 25
      -1.460 0.000 25
      -0.730 -1.264 25
      0.730 -1.264 25
      2.920 0.000 25
      2.529 1.460 25
      1.460 2.529 25
      0.000 2.920 25

```

```
-1.460 2.529 25
-2.529 1.460 25
-2.920 0.000 25
-2.529 -1.460 25
-1.460 -2.529 25
 0.000 -2.920 25
 1.460 -2.529 25
 2.529 -1.460 25
 4.380 0.000 25
 4.116 1.498 25
 3.355 2.815 25
 2.190 3.793 25
 0.761 4.313 25
-0.761 4.313 25
-2.190 3.793 25
-3.355 2.815 25
-4.116 1.498 25
-4.380 0.000 25
-4.116 -1.498 25
-3.355 -2.815 25
-2.190 -3.793 25
-0.761 -4.313 25
 0.761 -4.313 25
 2.190 -3.793 25
 3.355 -2.815 25
 4.116 -1.498 25
c sources ALL elements
```

Appendix D: BWR Plots of 46 Nuclides of Interest

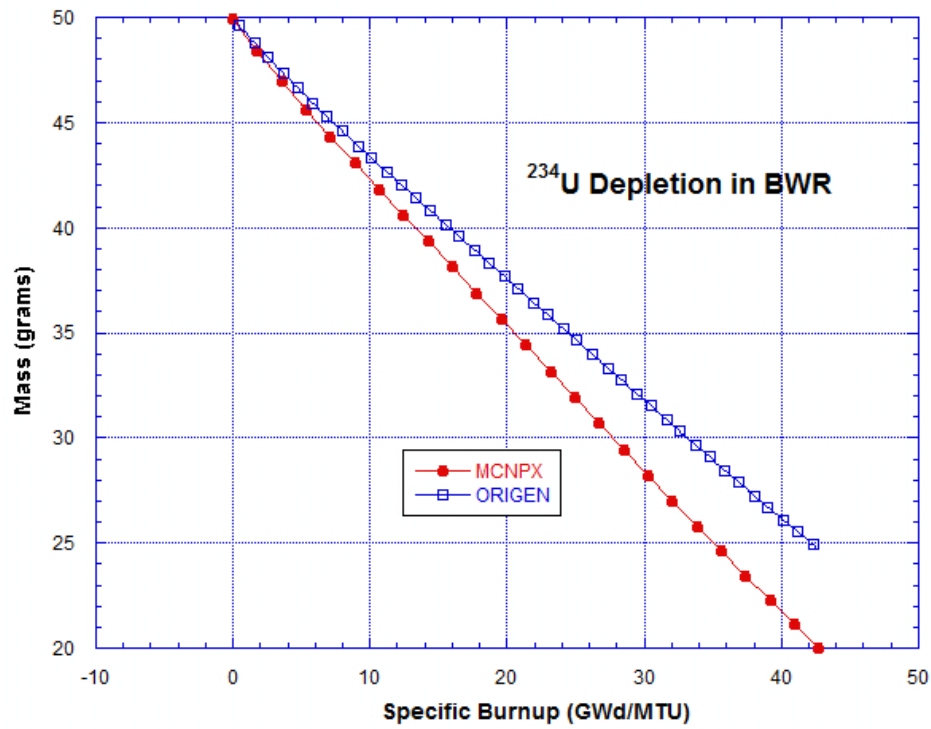


Figure 114: ^{234}U Depletion in GE 8x8-4 BWR Model

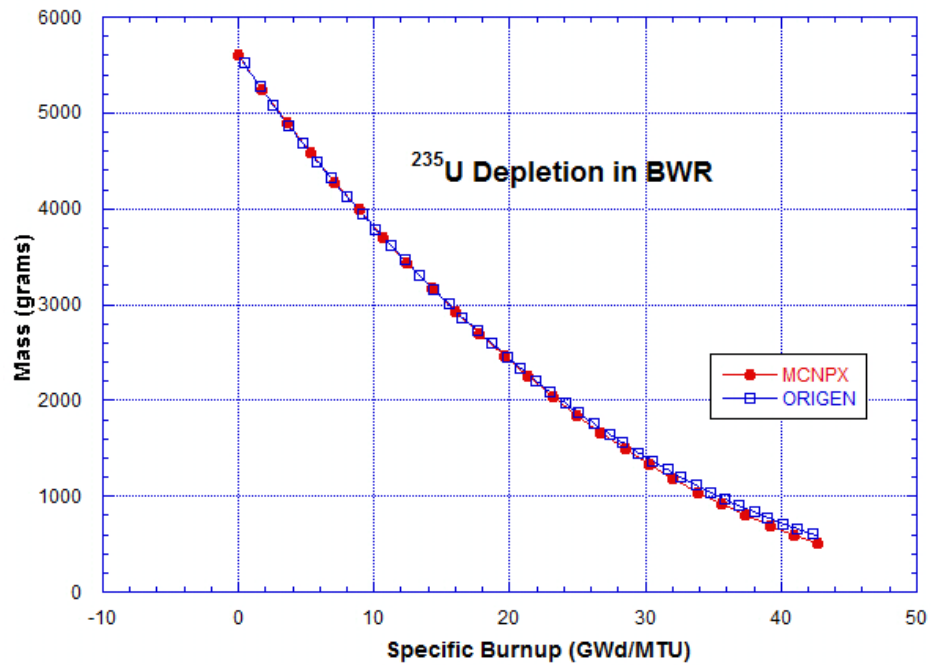


Figure 115: ^{235}U Depletion in GE 8x8-4 BWR Model

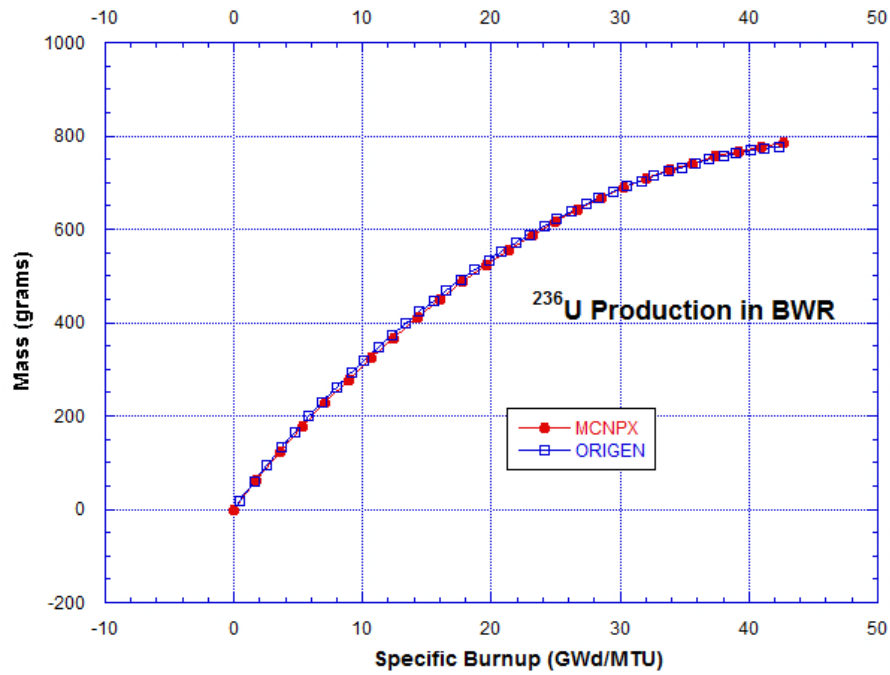


Figure 116: ^{236}U Production in GE 8x8-4 BWR Model

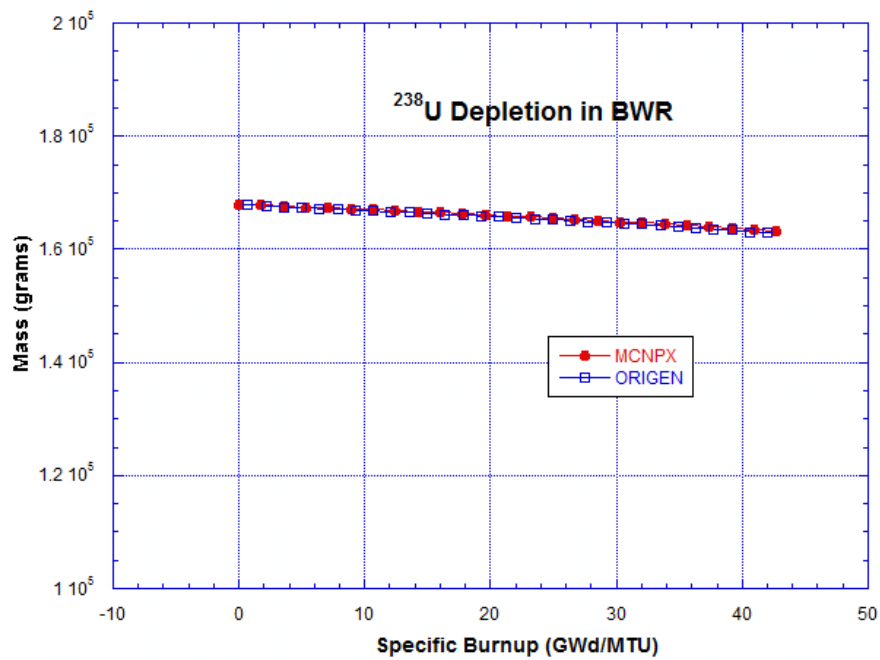


Figure 117: ^{238}U Depletion in GE 8x8-4 BWR Model

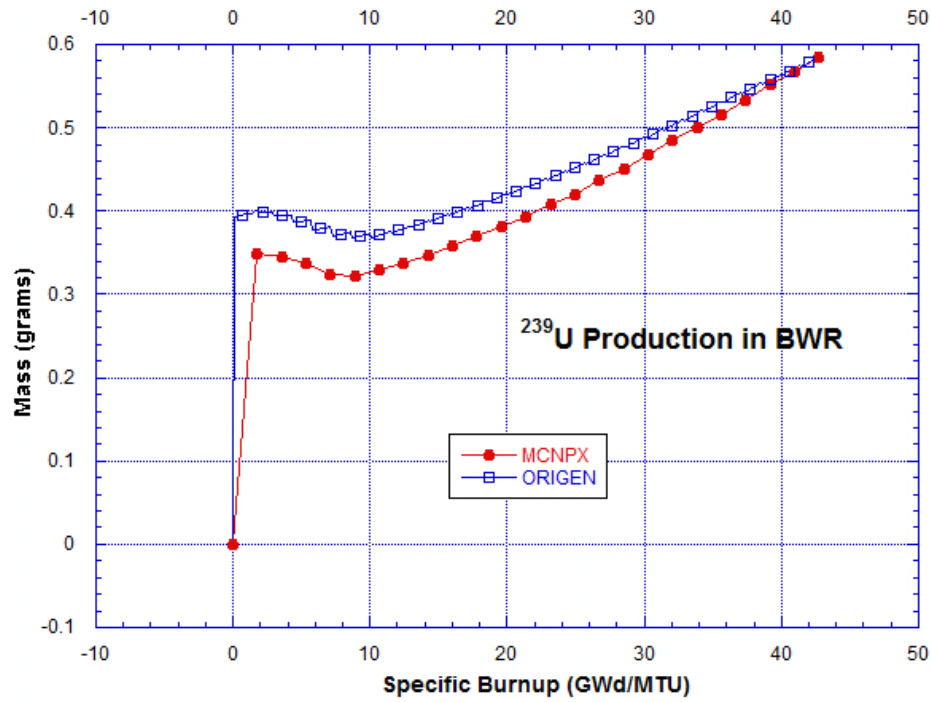


Figure 118: ²³⁹U Production in GE 8x8-4 BWR Model

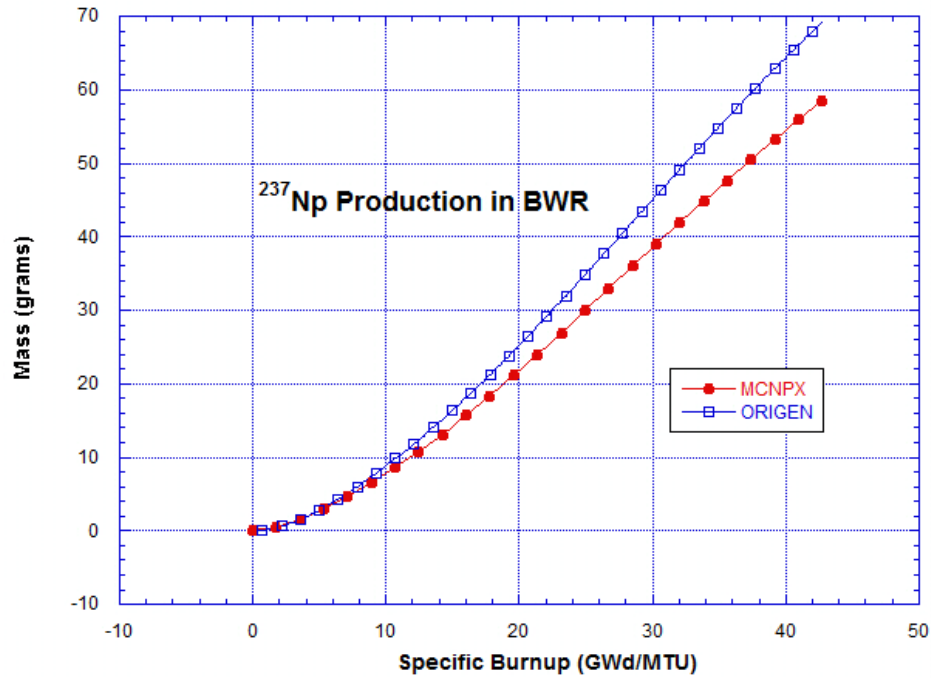


Figure 119: ²³⁷Np Production in GE 8x8-4 BWR Model

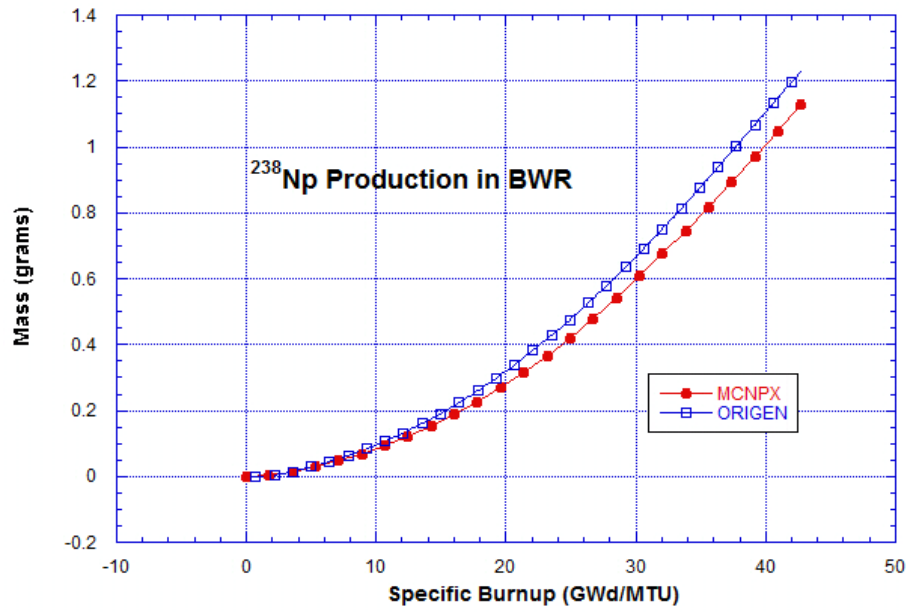


Figure 120: ²³⁸Np Production in GE 8x8-4 BWR Model

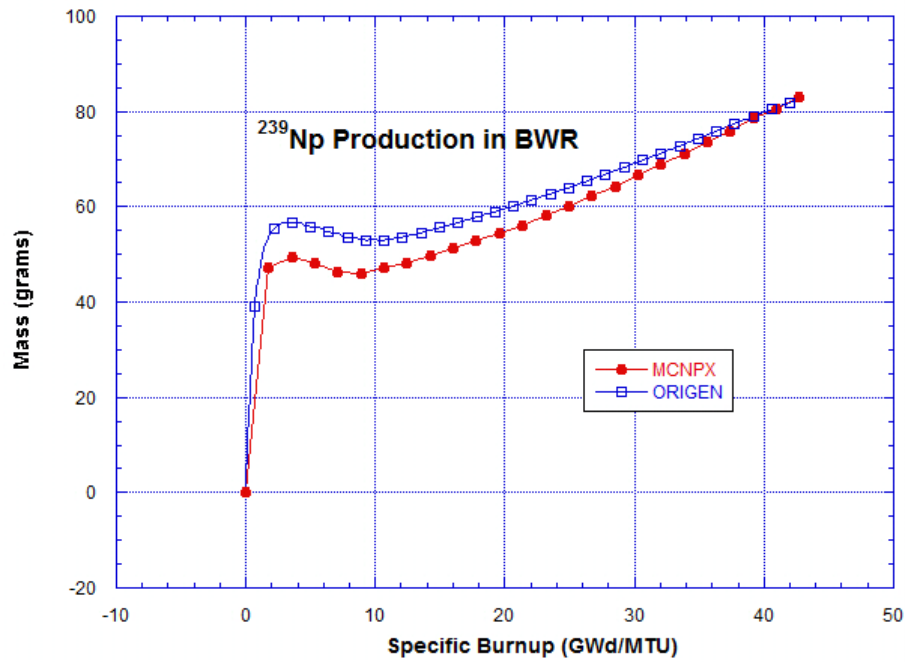


Figure 121: ²³⁹Np Production in GE 8x8-4 BWR Model

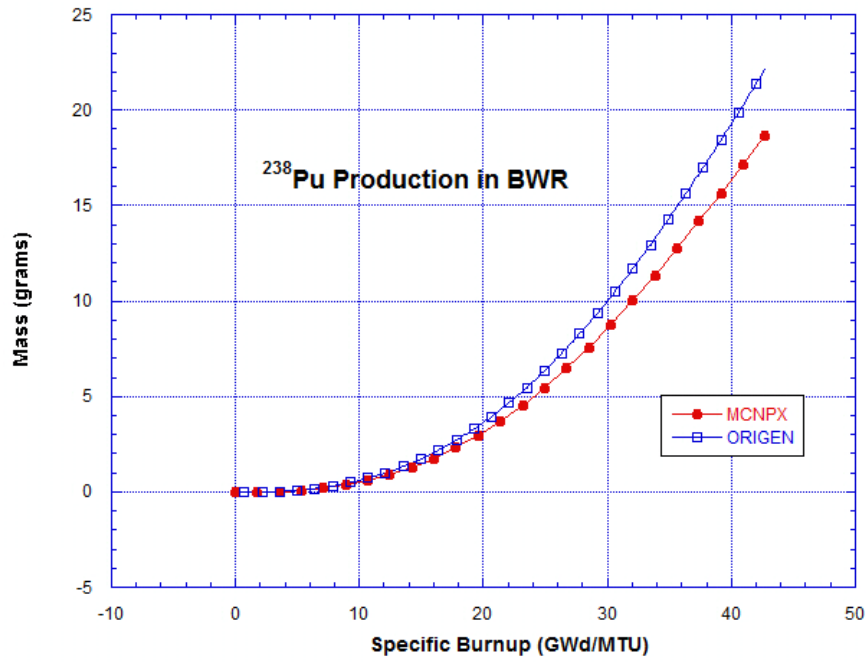


Figure 122: ²³⁸Pu Production in GE 8x8-4 BWR Model

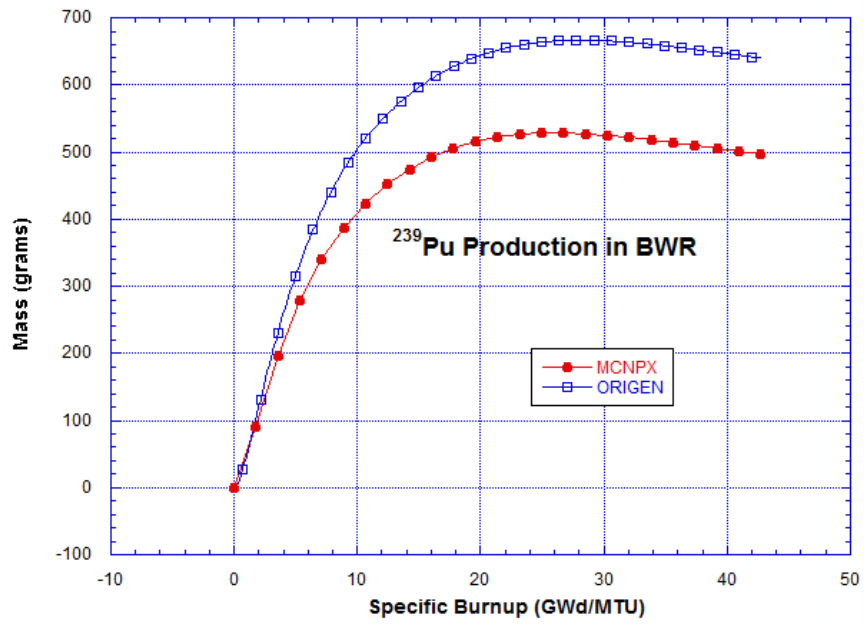


Figure 123: ²³⁹Pu Production in GE 8x8-4 BWR Model

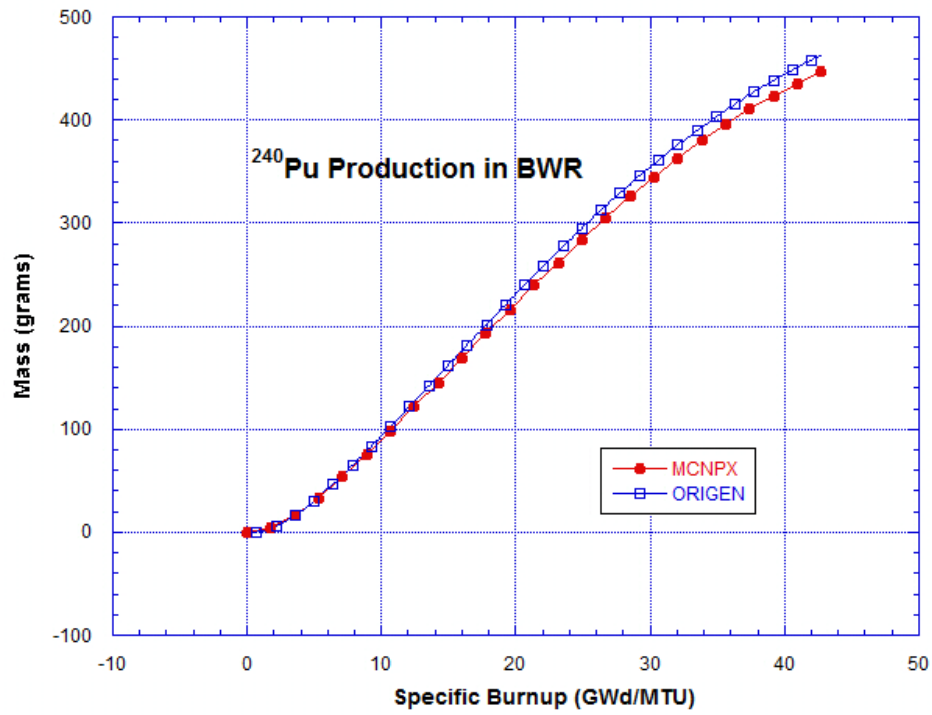


Figure 124: ²⁴⁰Pu Production in GE 8x8-4 BWR Model

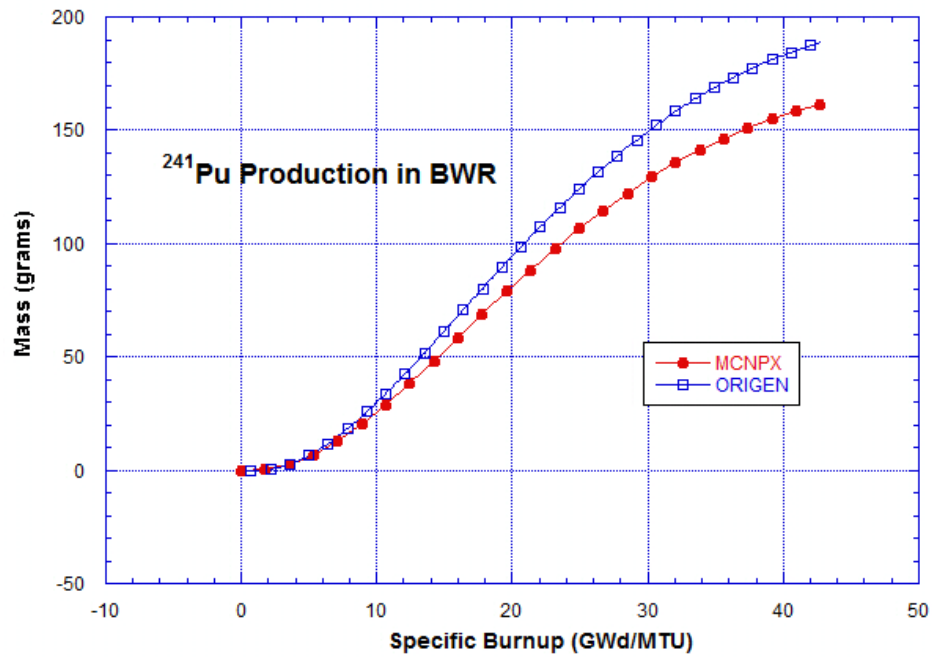


Figure 125: ²⁴¹Pu Production in GE 8x8-4 BWR Model

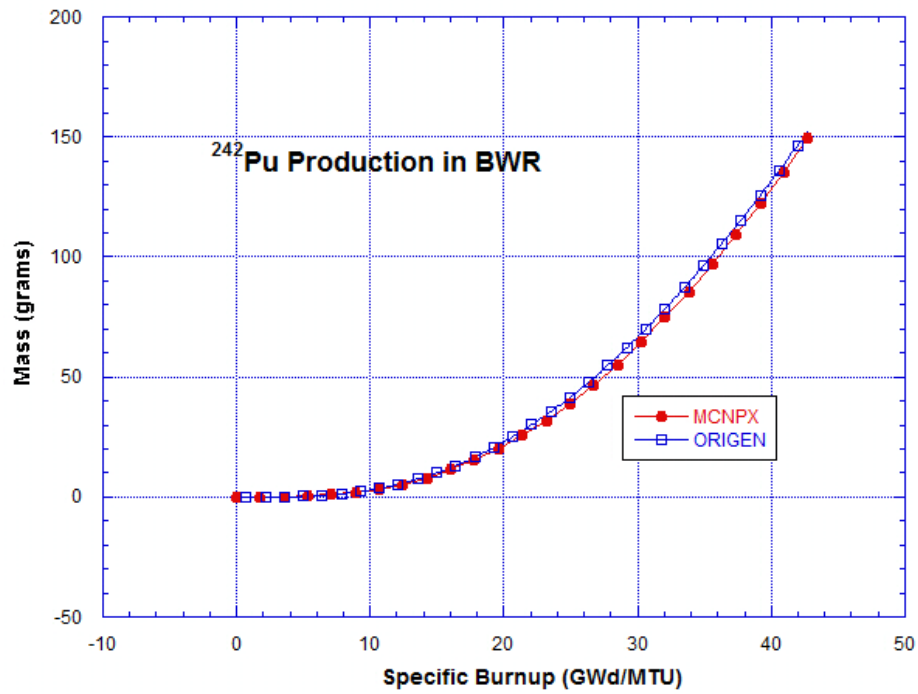


Figure 126: ²⁴²Pu Production in GE 8x8-4 BWR Model

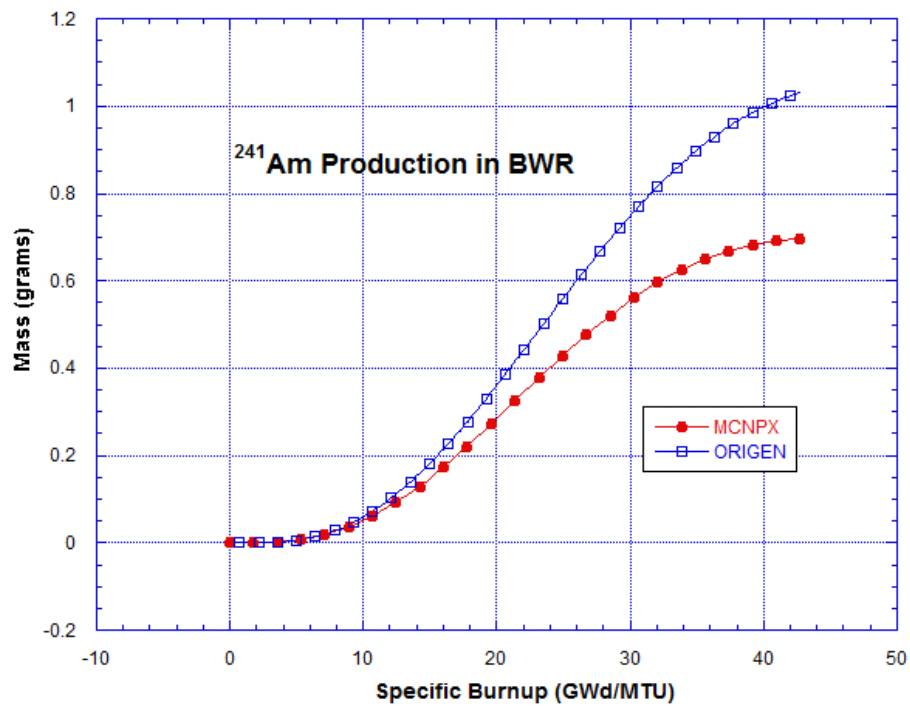


Figure 127: ²⁴¹Am Production in GE 8x8-4 BWR Model

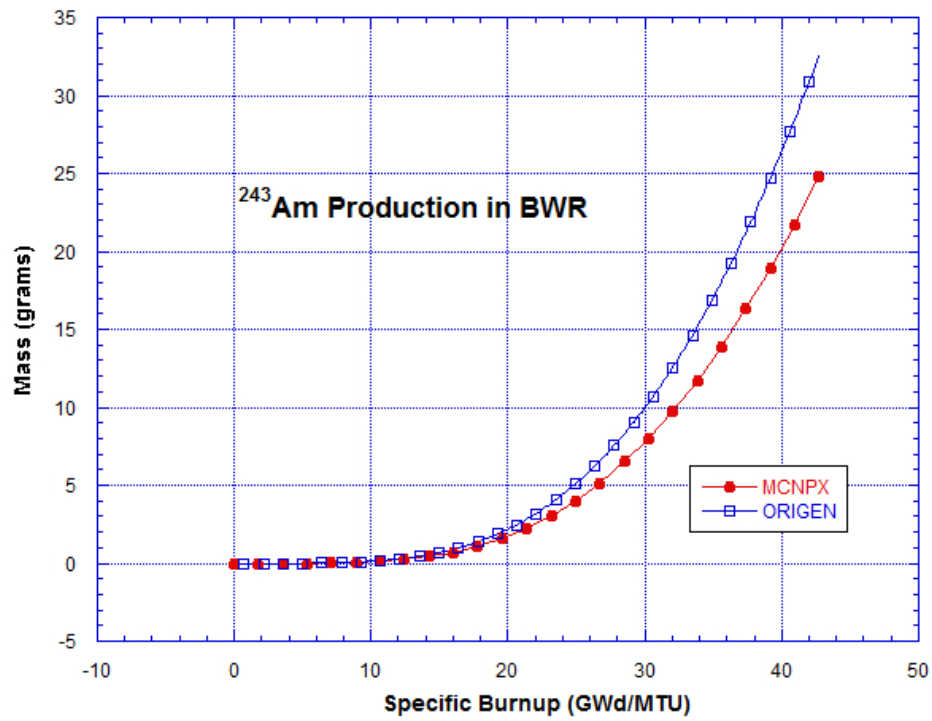


Figure 128: ²⁴³Am Production in GE 8x8-4 BWR Model

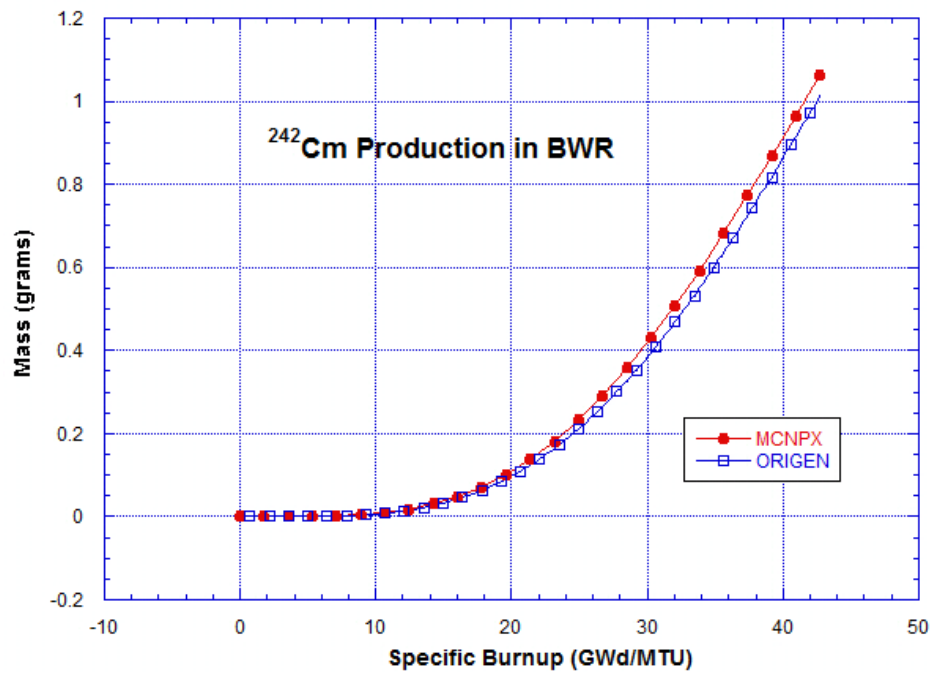


Figure 129: ²⁴²Cm Production in GE 8x8-4 BWR Model

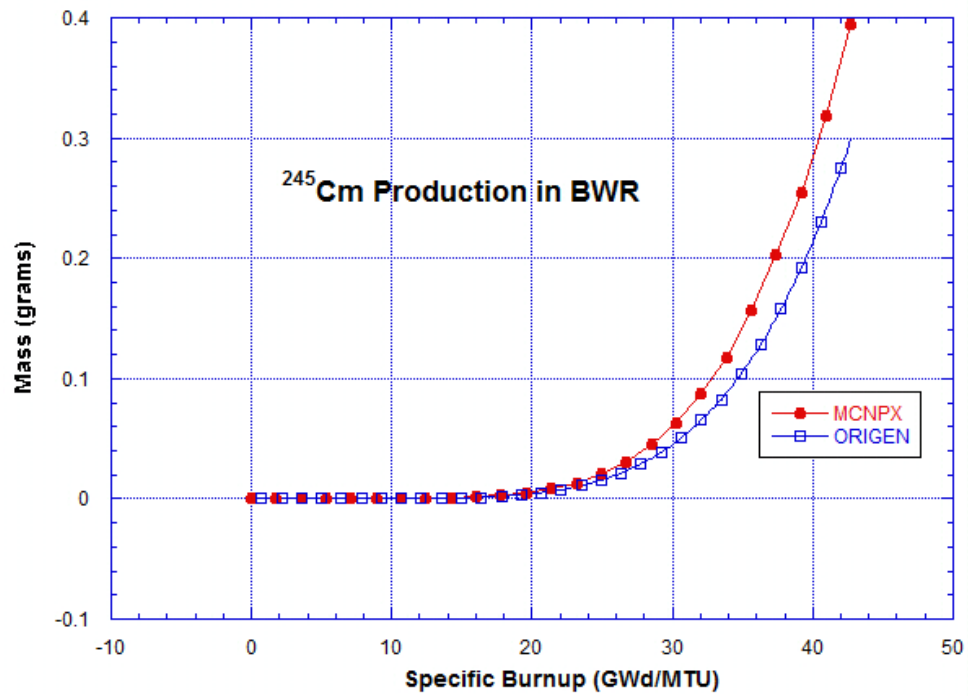


Figure 130: ²⁴⁵Cm Production in GE 8x8-4 BWR Model

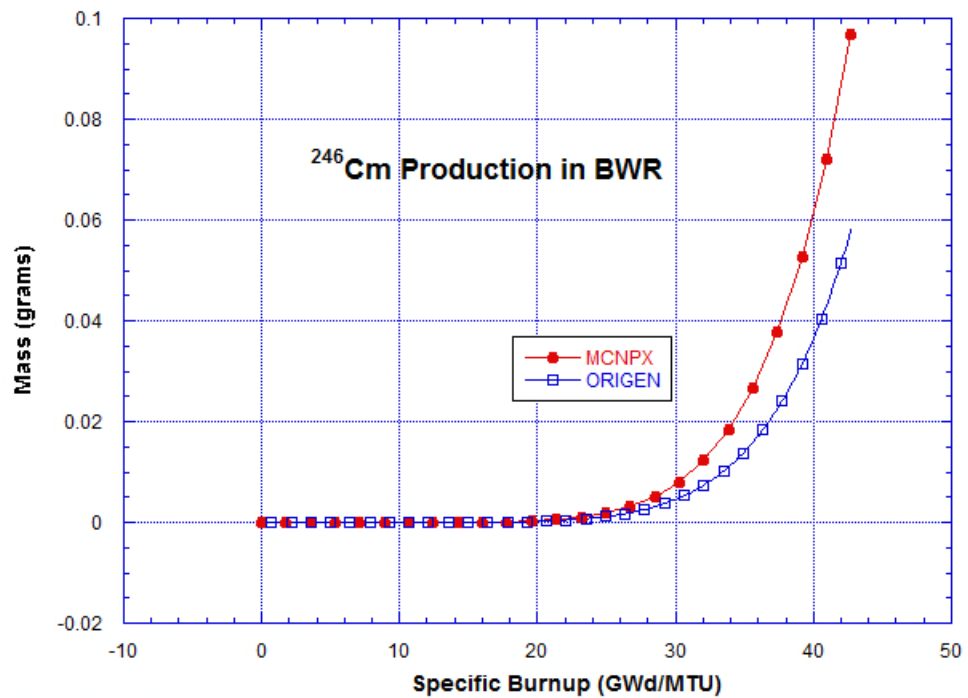


Figure 131: ²⁴⁶Cm Production in GE 8x8-4 BWR Model

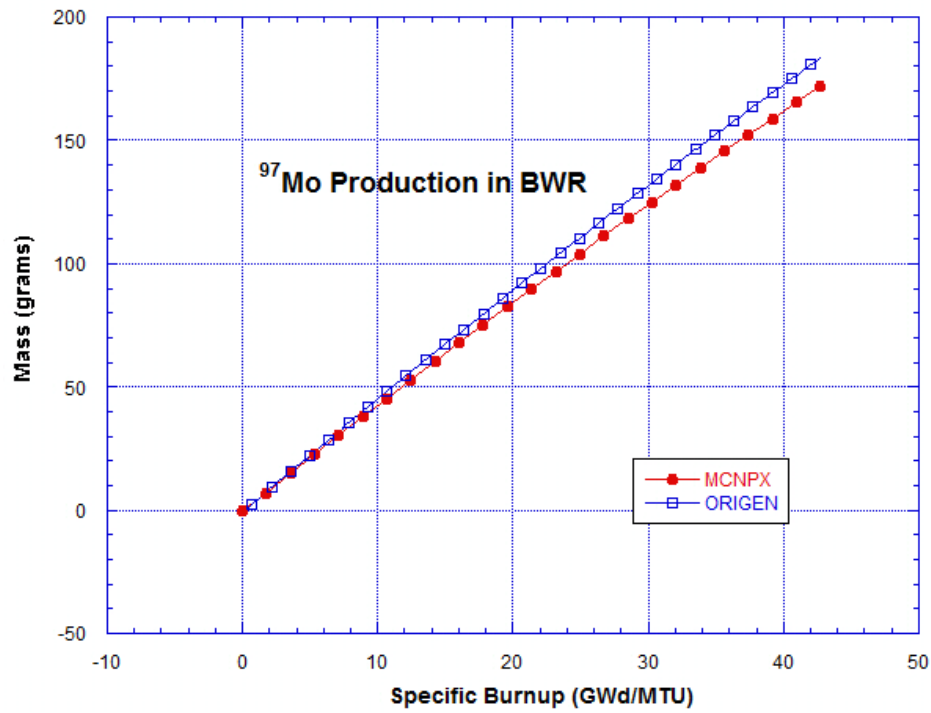


Figure 132: ⁹⁷Mo Production in GE 8x8-4 BWR Model

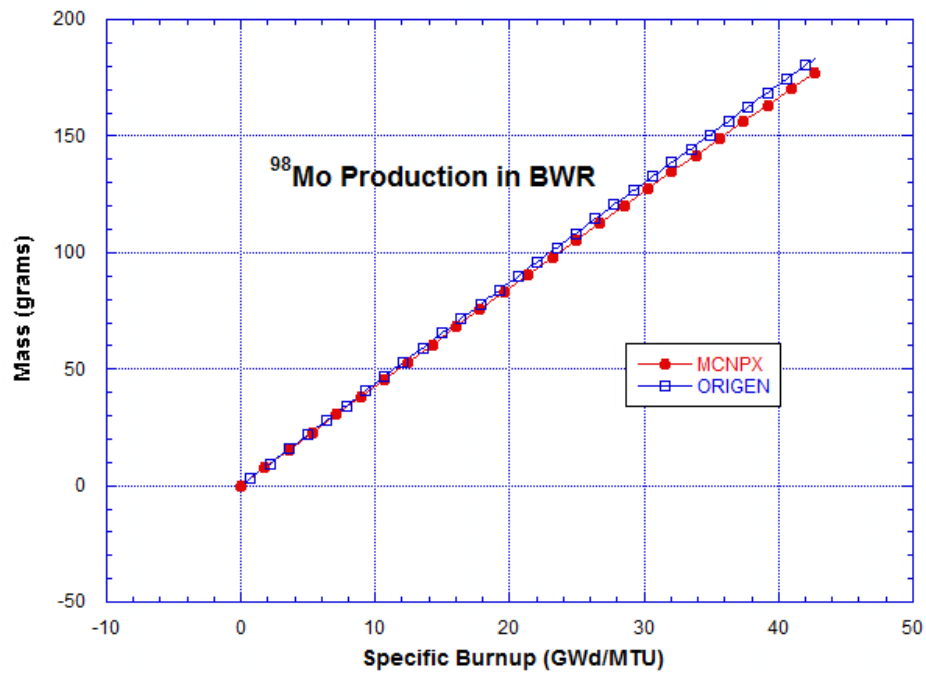


Figure 133: ⁹⁸Mo Production in GE 8x8-4 BWR Model

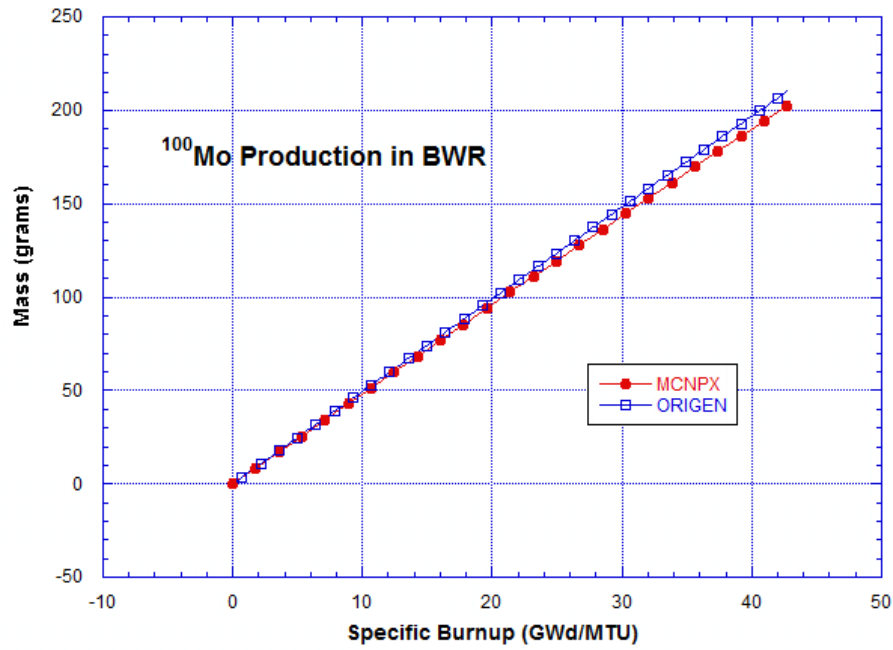


Figure 134: ¹⁰⁰Mo Production in GE 8x8-4 BWR Model

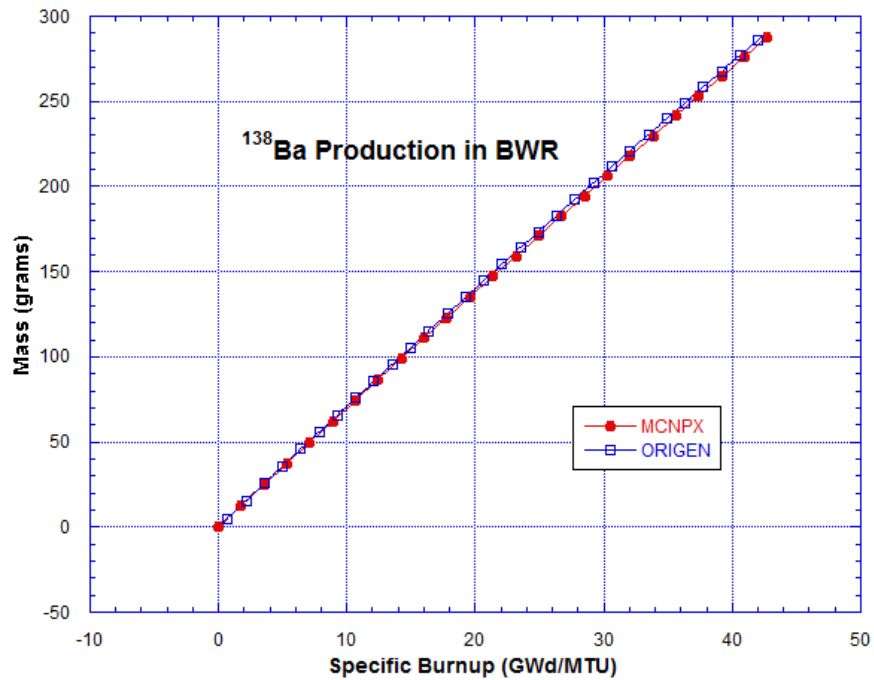


Figure 135: ¹³⁸Ba Production in GE 8x8-4 BWR Model

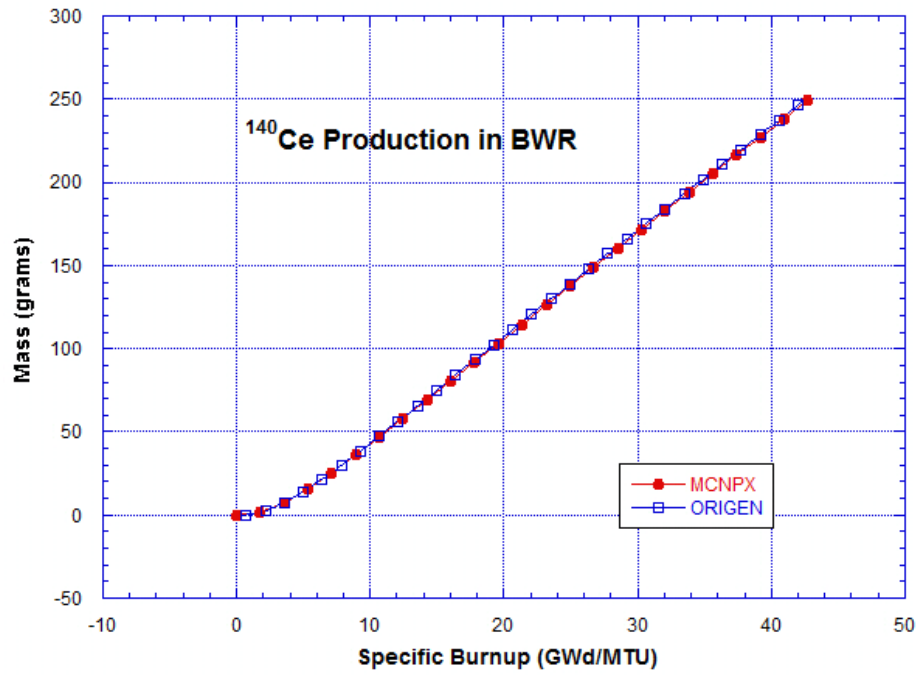


Figure 136: ¹⁴⁰Ce Production in GE 8x8-4 BWR Model

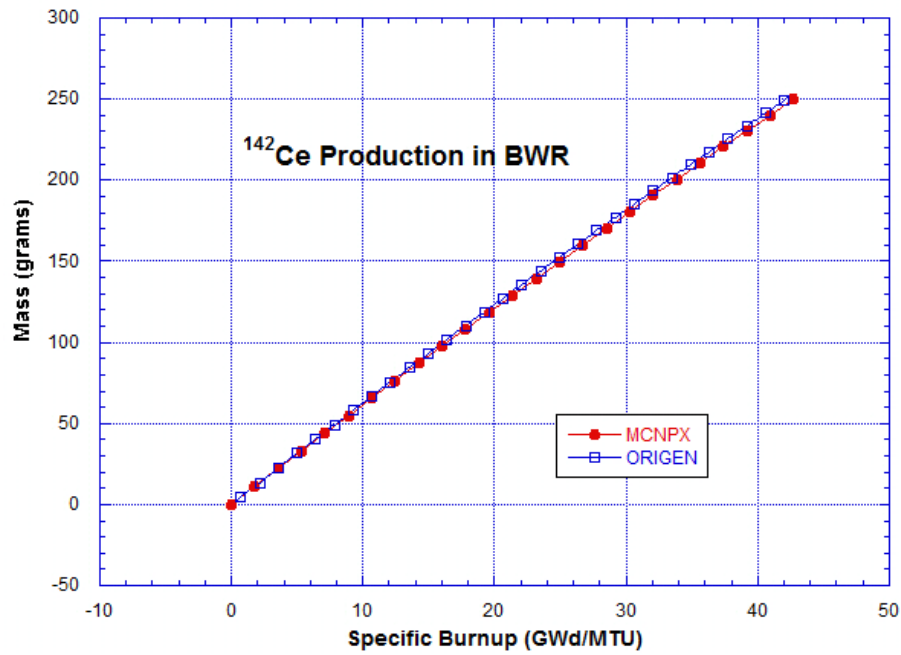


Figure 137: ¹⁴²Ce Production in GE 8x8-4 BWR Model

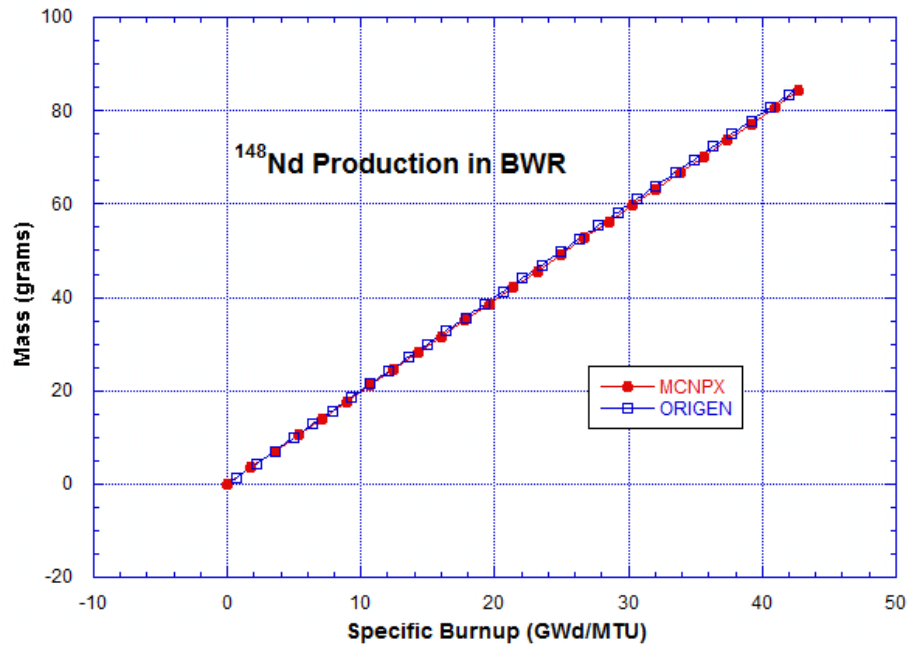


Figure 138: ¹⁴⁸Nd Production in GE 8x8-4 BWR Model

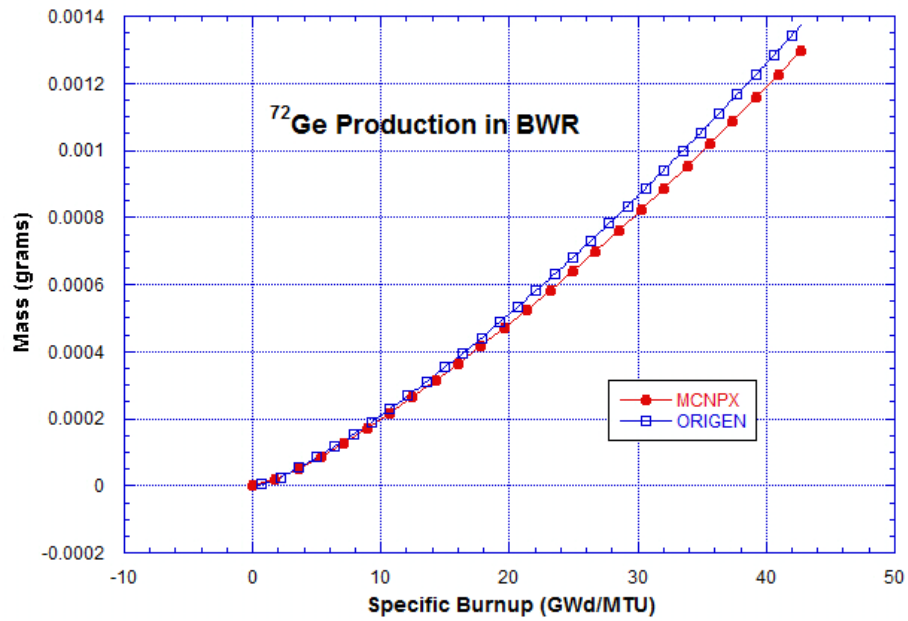


Figure 139: ⁷²Ge Production in GE 8x8-4 BWR Model

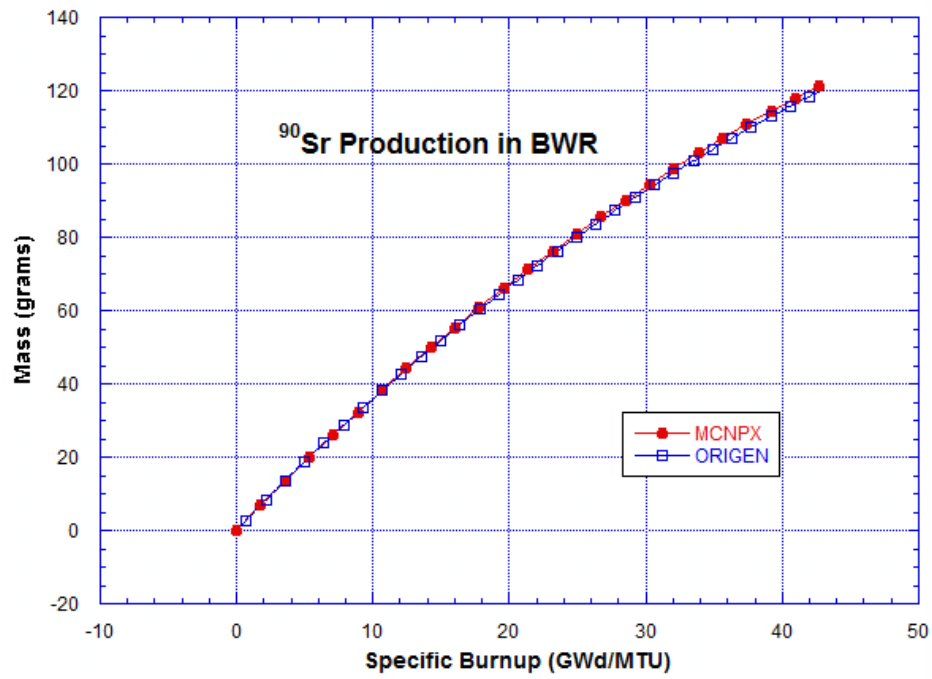


Figure 140: ⁹⁰Sr Production in GE 8x8-4 BWR Model

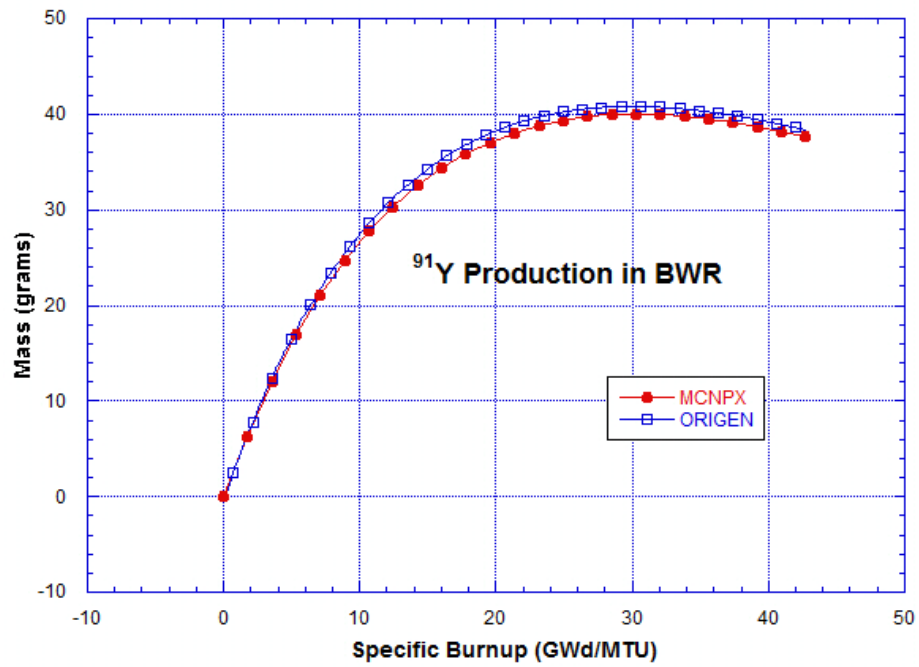


Figure 141: ⁹¹Y Production in GE 8x8-4 BWR Model

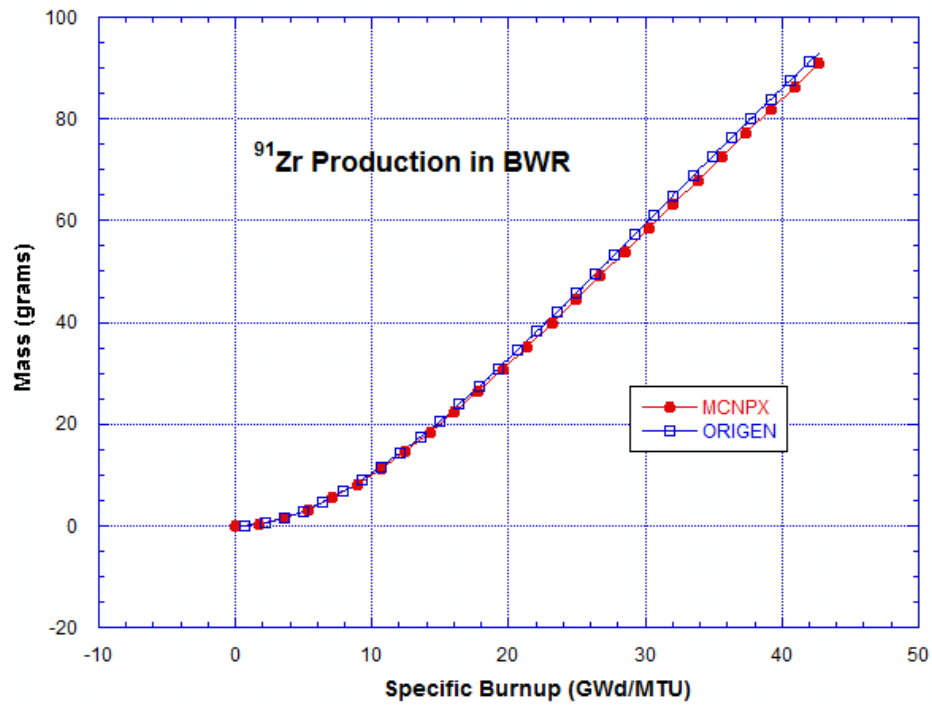


Figure 142: ⁹¹Zr Production in GE 8x8-4 BWR Model

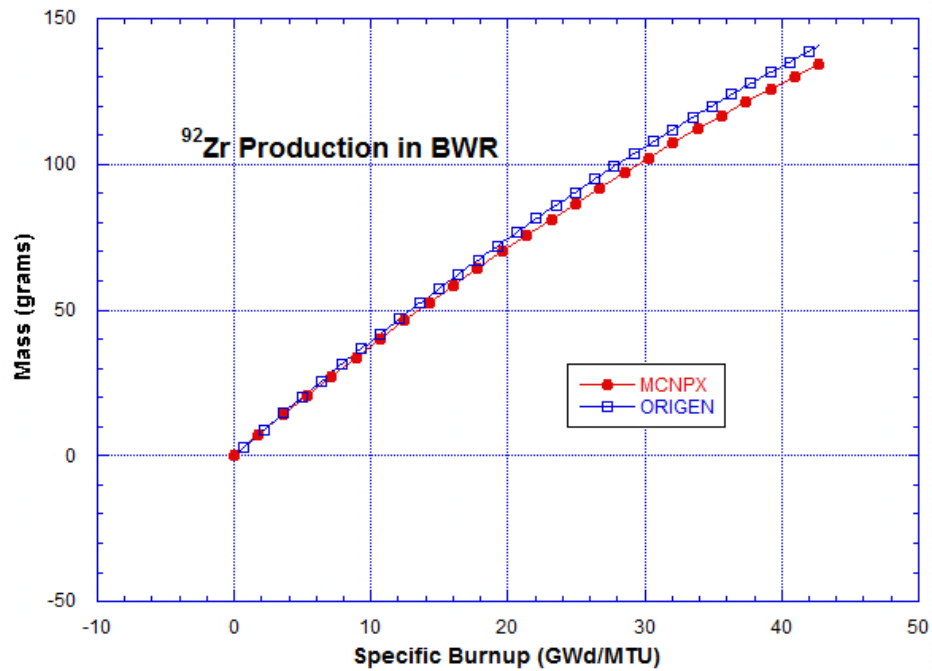


Figure 143: ⁹²Zr Production in GE 8x8-4 BWR Model

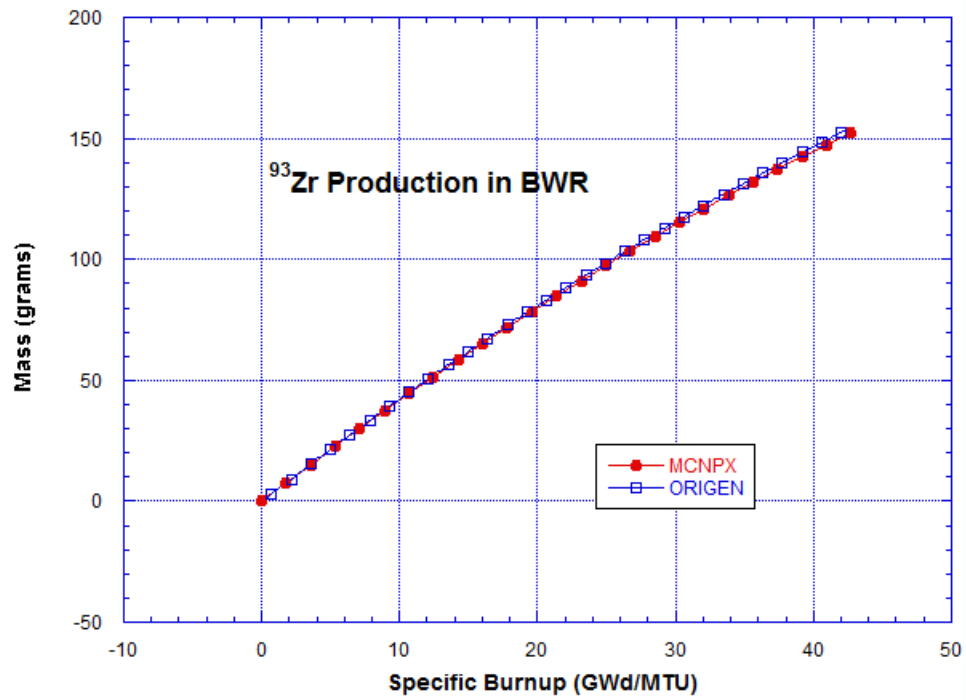


Figure 144: ⁹³Zr Production in GE 8x8-4 BWR Model

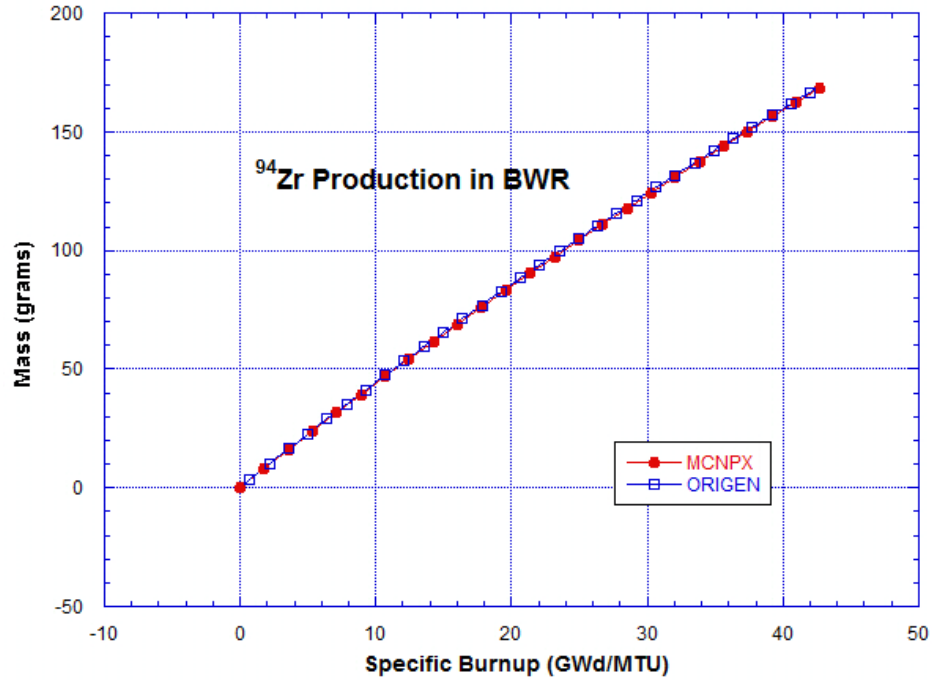


Figure 145: ⁹⁴Zr Production in GE 8x8-4 BWR Model

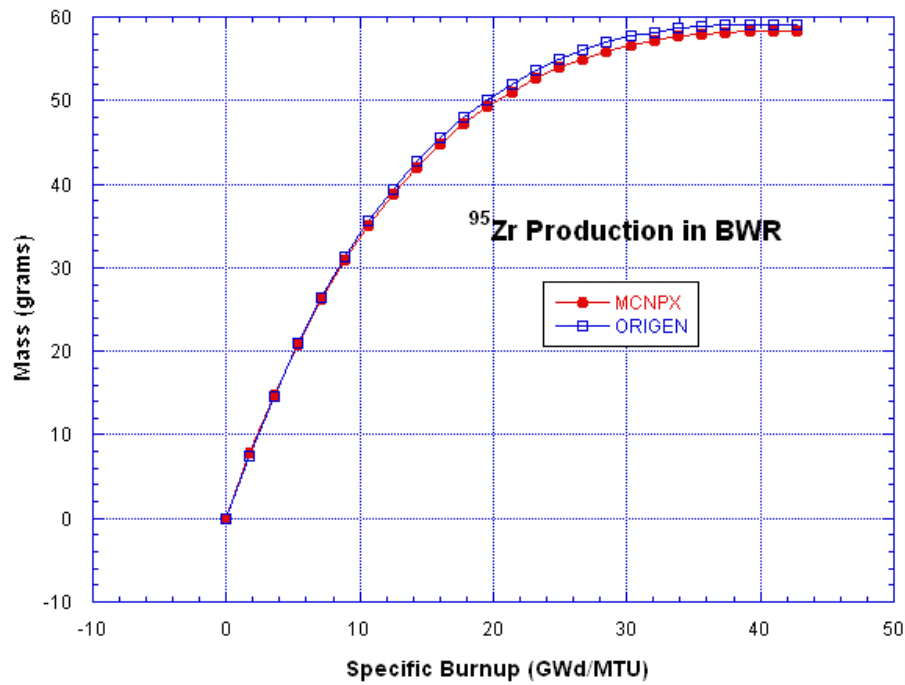


Figure 146: ⁹⁵Zr Production in GE 8x8-4 BWR Model

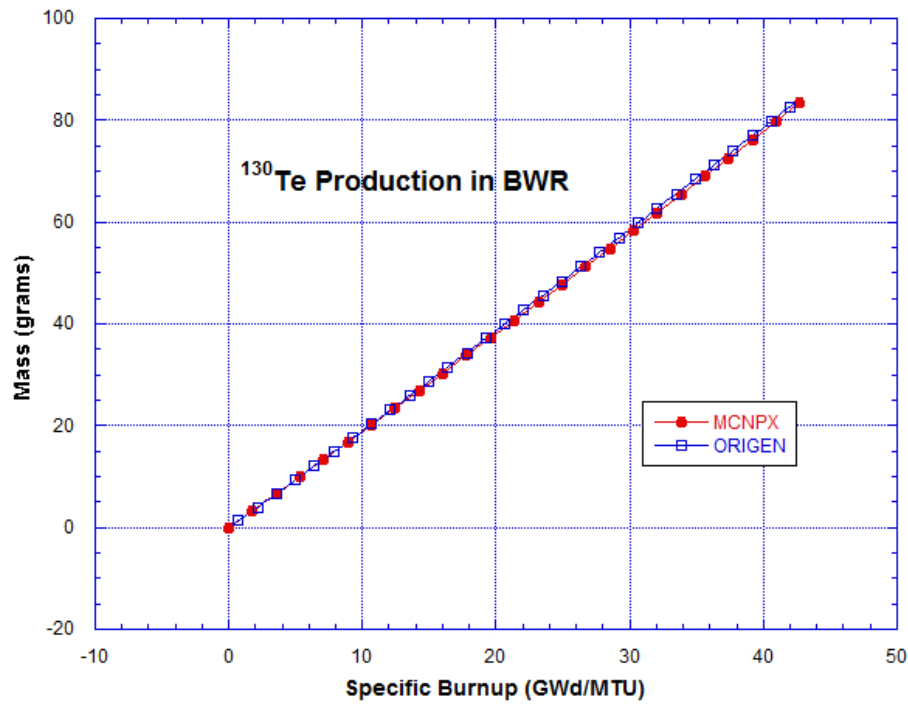


Figure 147: ¹³⁰Te Production in GE 8x8-4 BWR Model

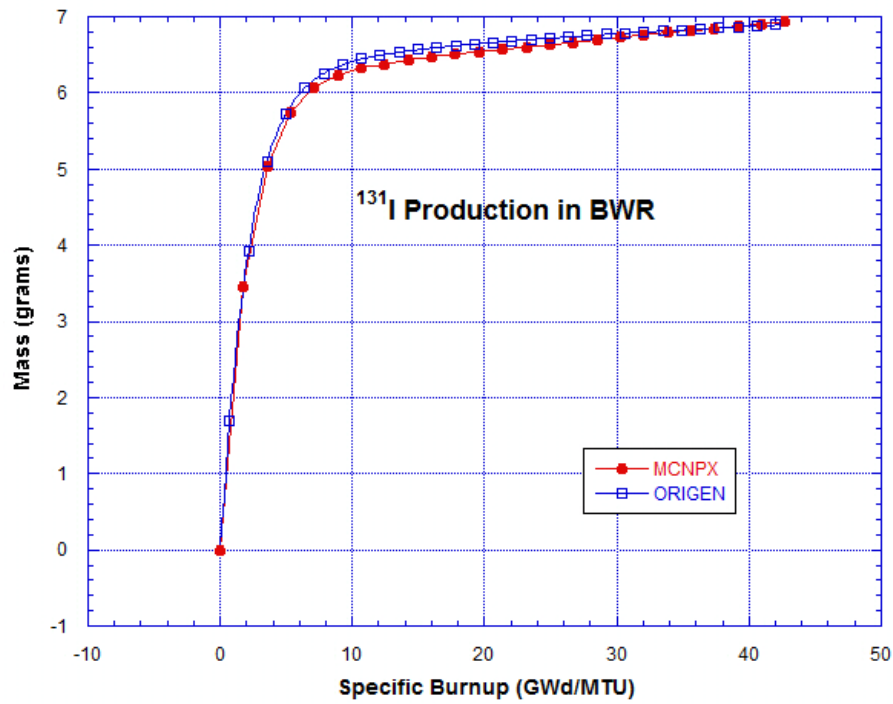


Figure 148: ¹³¹I Production in GE 8x8-4 BWR Model

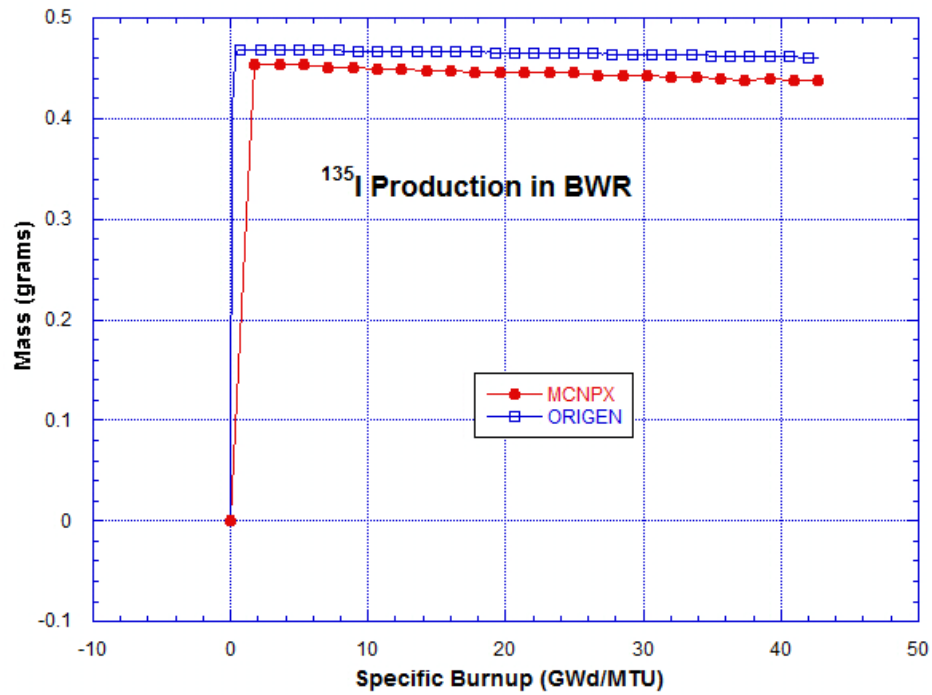


Figure 149: ¹³⁵I Production in GE 8x8-4 BWR Model

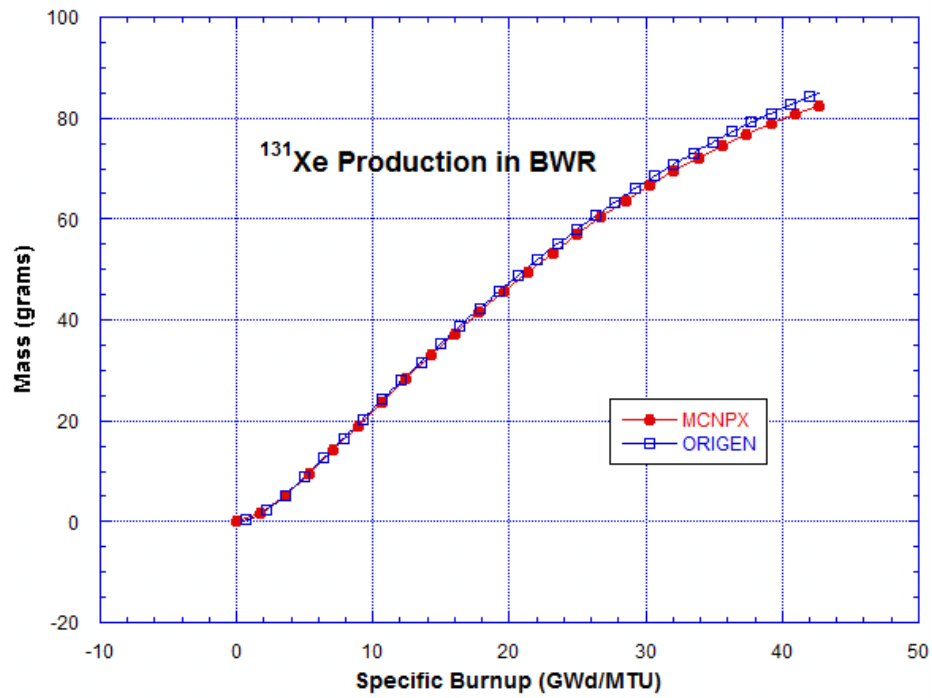


Figure 150: ¹³¹Xe Production in GE 8x8-4 BWR Model

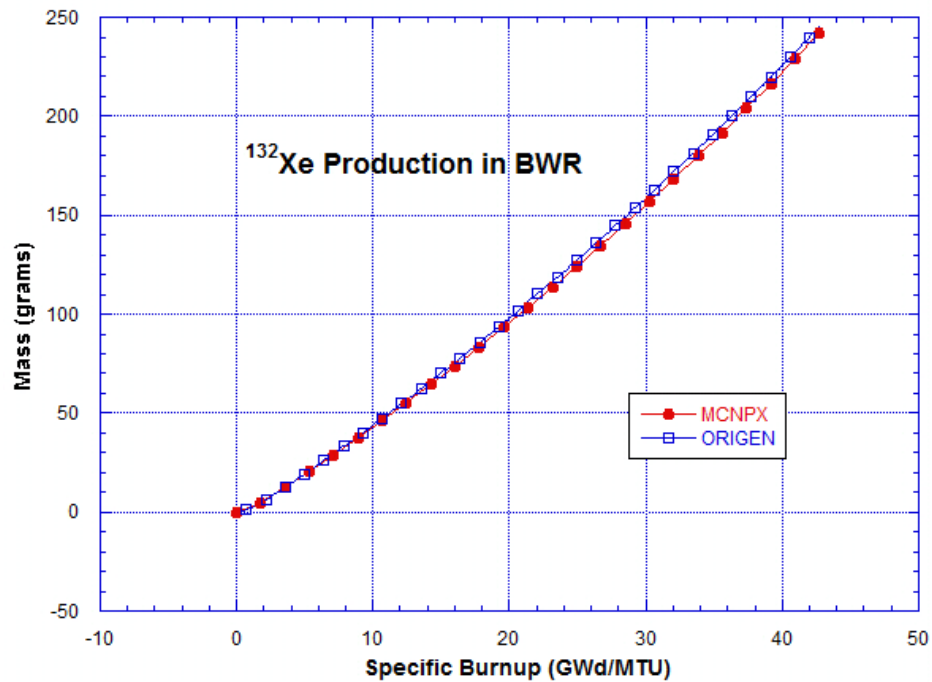


Figure 151: ¹³²Xe Production in GE 8x8-4 BWR Model

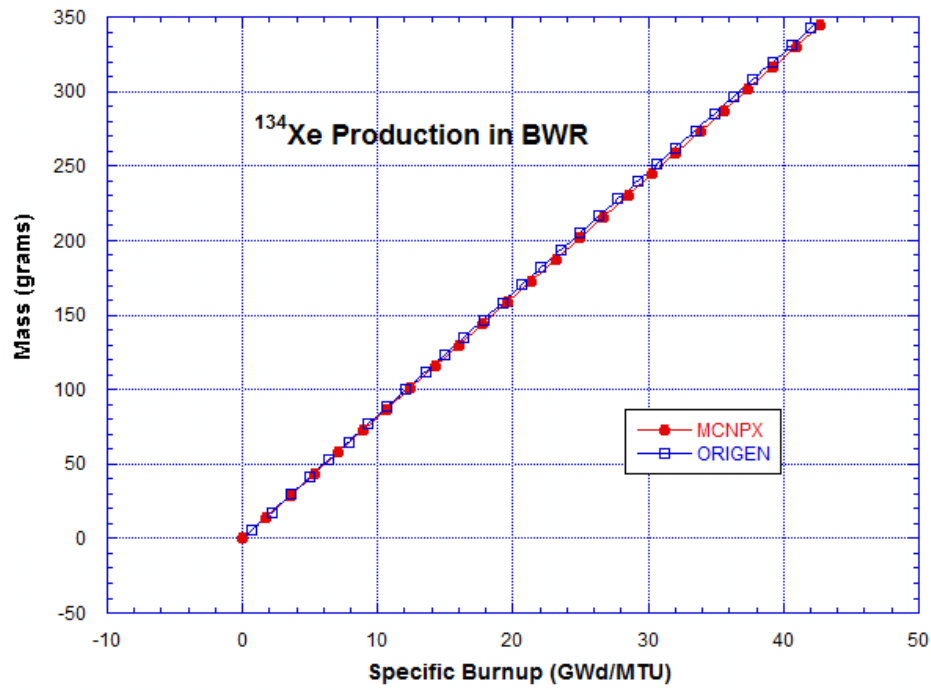


Figure 152: ¹³⁴Xe Production in GE 8x8-4 BWR Model

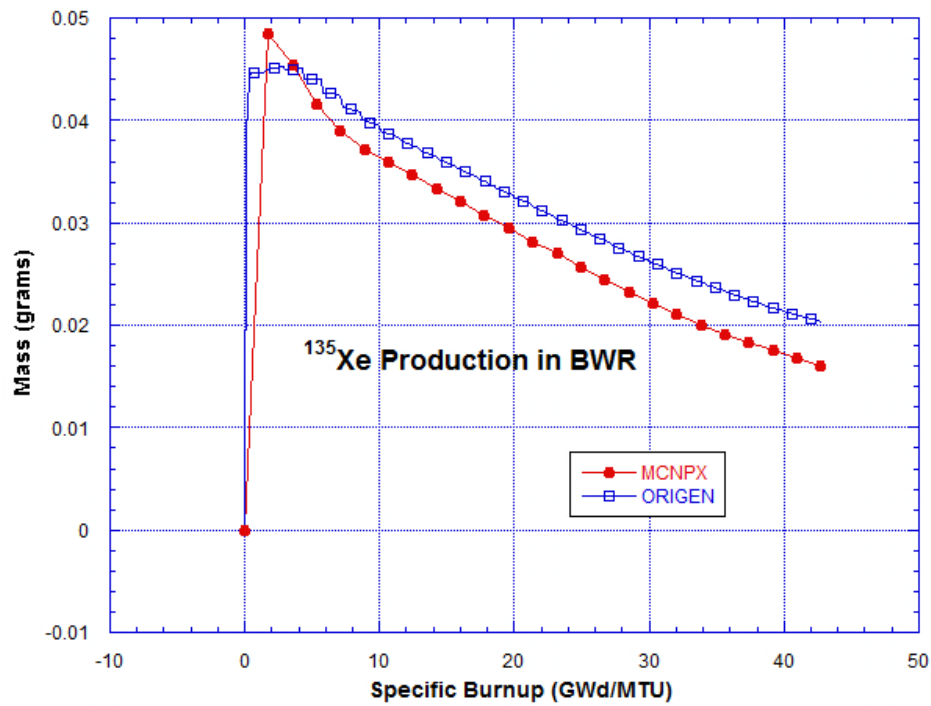


Figure 153: ¹³⁵Xe Production in GE 8x8-4 BWR Model

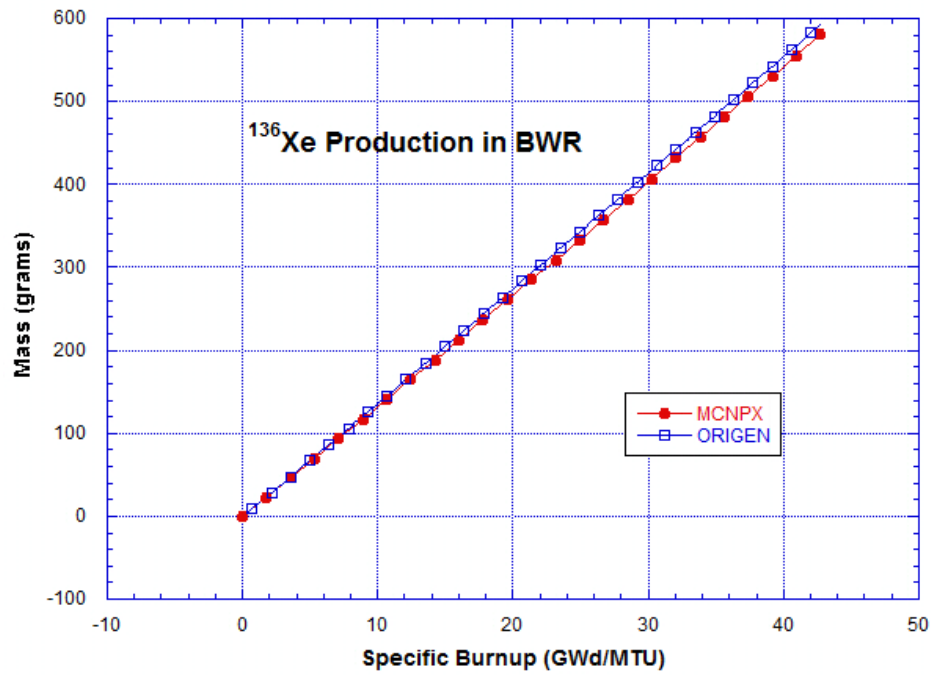


Figure 154: ¹³⁶Xe Production in GE 8x8-4 BWR Model

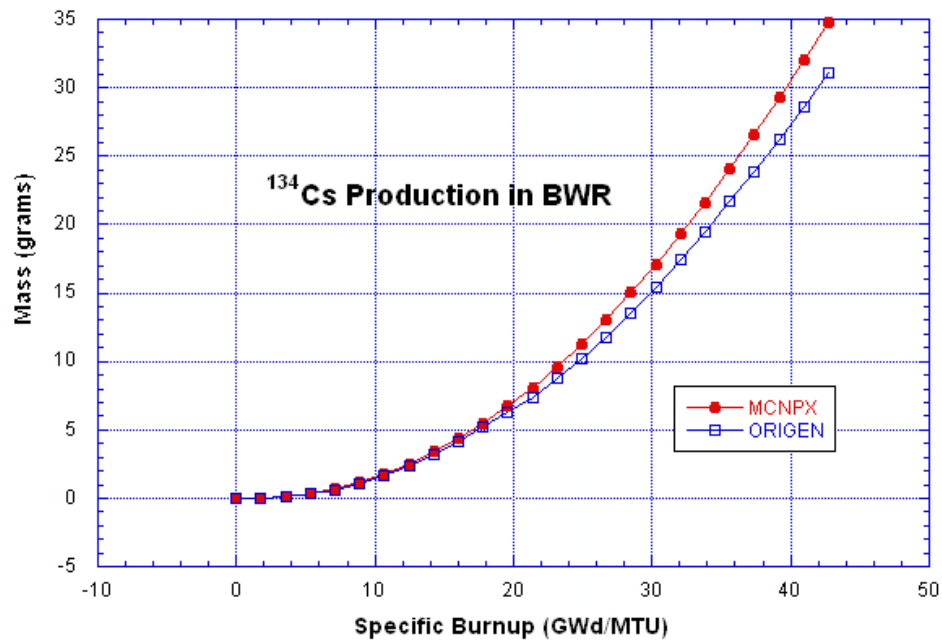


Figure 155: ¹³⁴Cs Production in GE 8x8-4 BWR Model

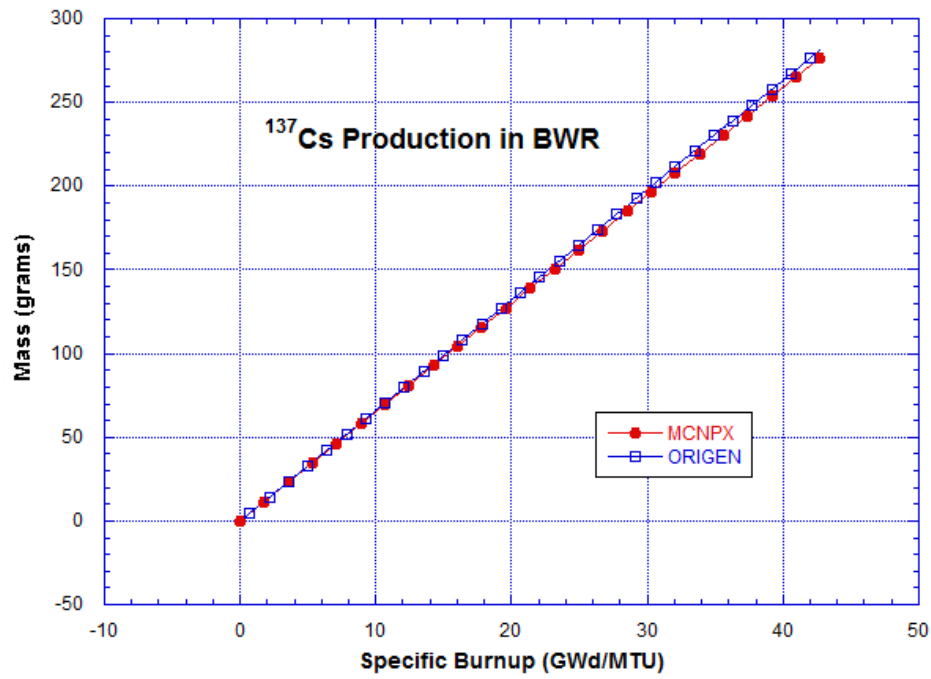


Figure 156: ¹³⁷Cs Production in GE 8x8-4 BWR Model

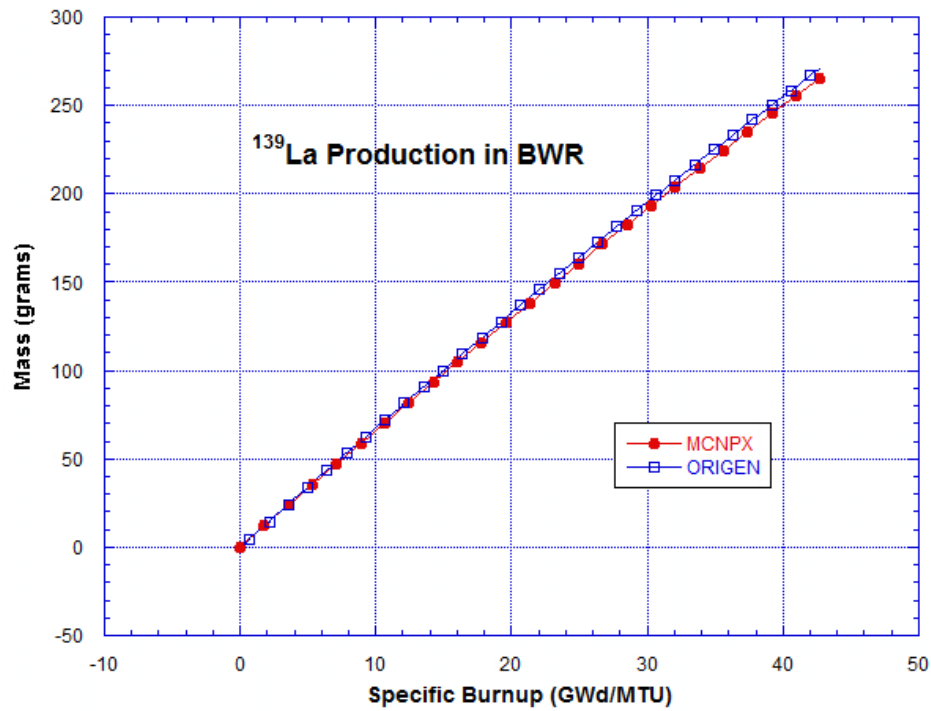


Figure 157: ¹³⁹La Production in GE 8x8-4 BWR Model

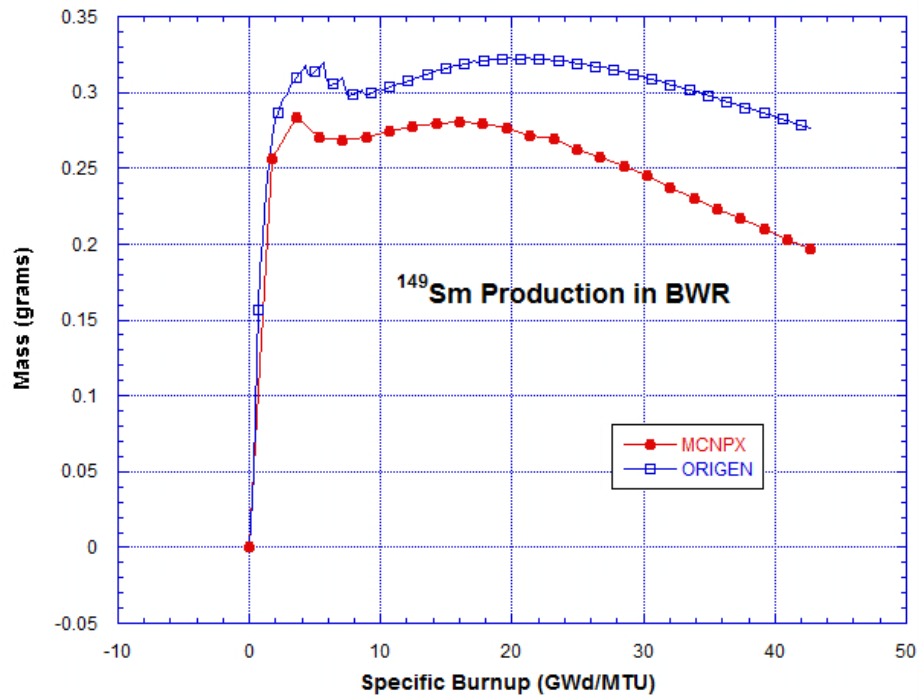


Figure 158: ¹⁴⁹Sm Production in GE 8x8-4 BWR Model

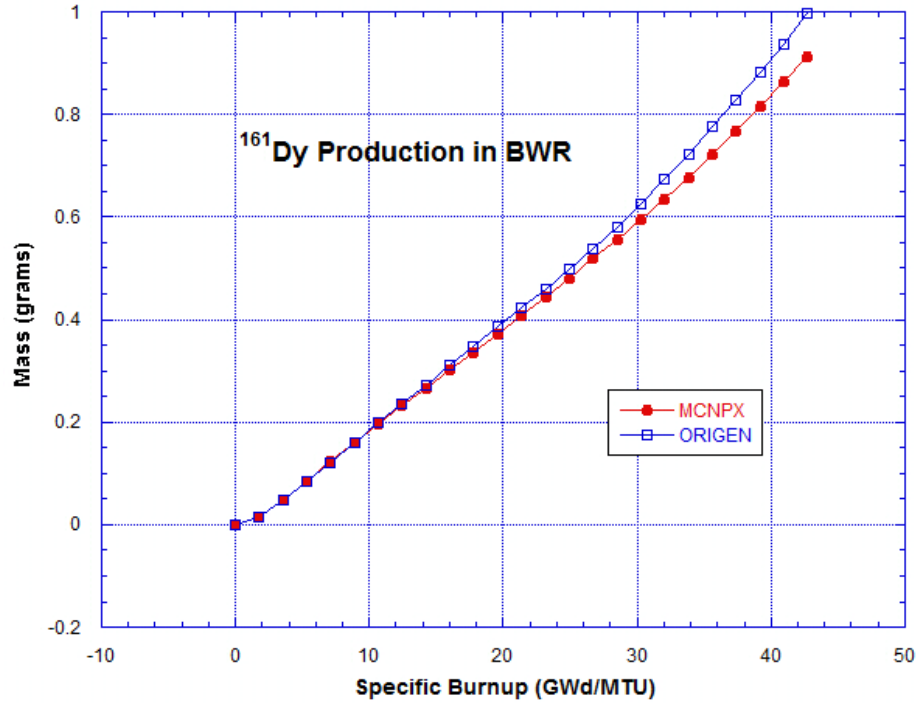


Figure 159: ¹⁶¹Dy Production in GE 8x8-4 BWR Model

Appendix E: PWR Plots of 46 Nuclides of Interest

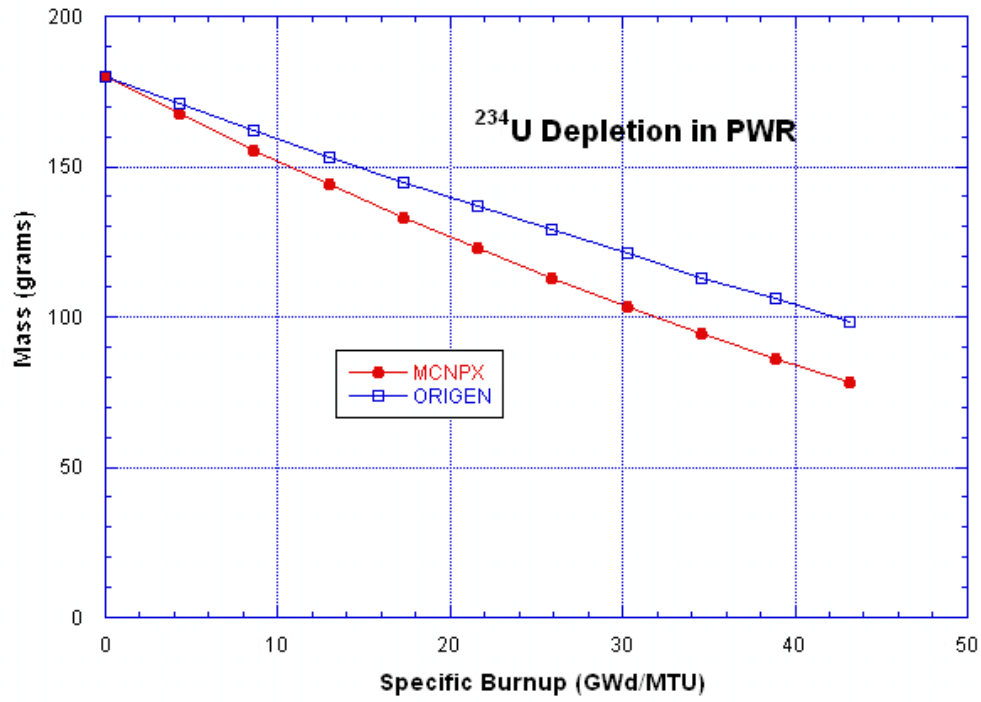


Figure 160: ²³⁴U Depletion in W 17x17 PWR Model

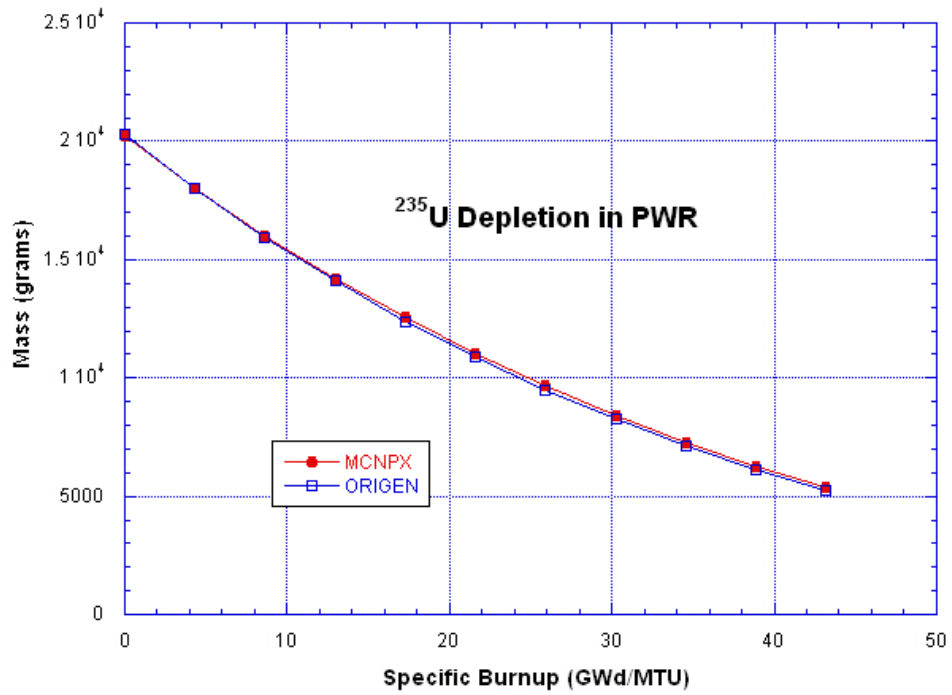


Figure 161: ²³⁵U Depletion in W 17x17 PWR Model

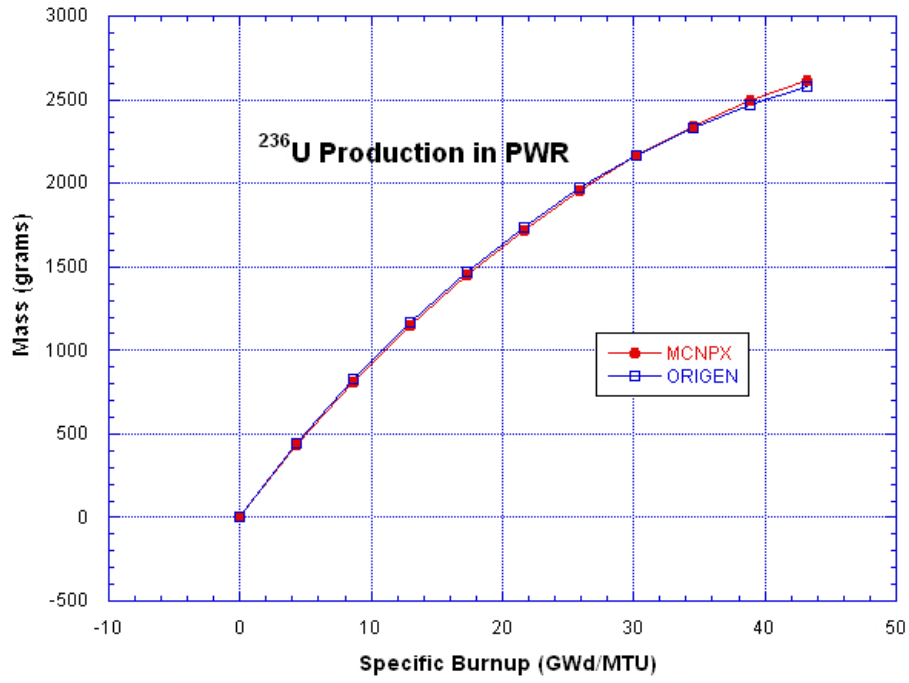


Figure 162: ²³⁶U Production in W 17x17 PWR Model

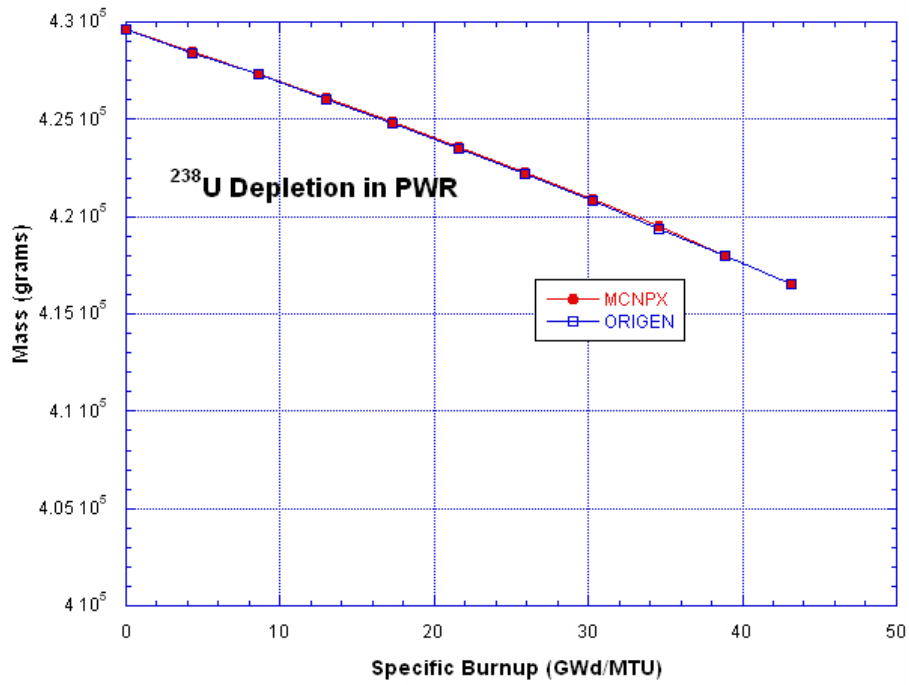


Figure 163: ²³⁸U Depletion in W 17x17 PWR Model

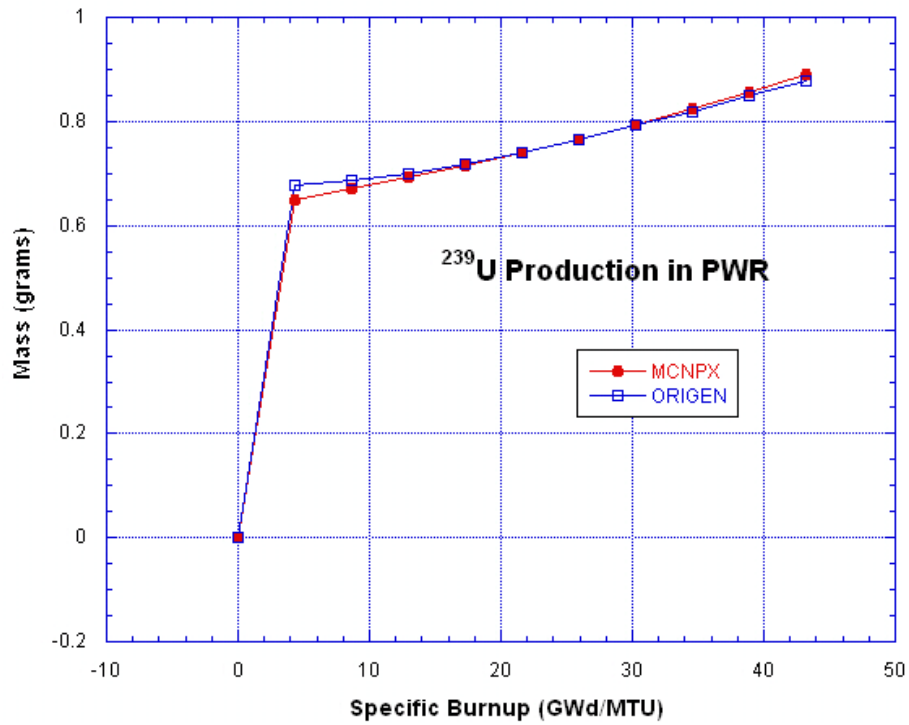


Figure 164: ²³⁹U Production in W 17x17 PWR Model

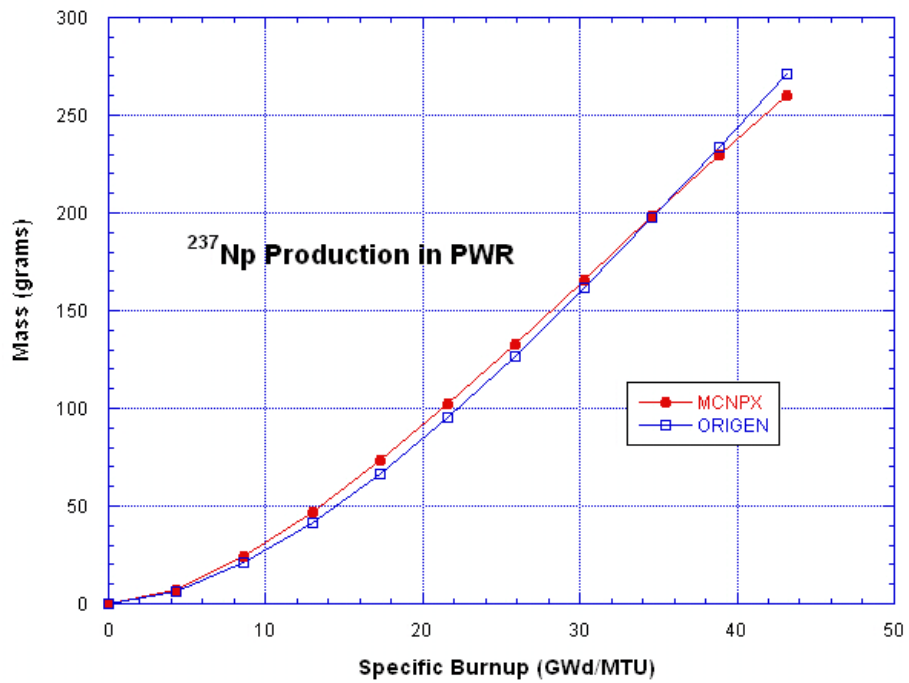


Figure 165: ²³⁷Np Production in W 17x17 PWR Model

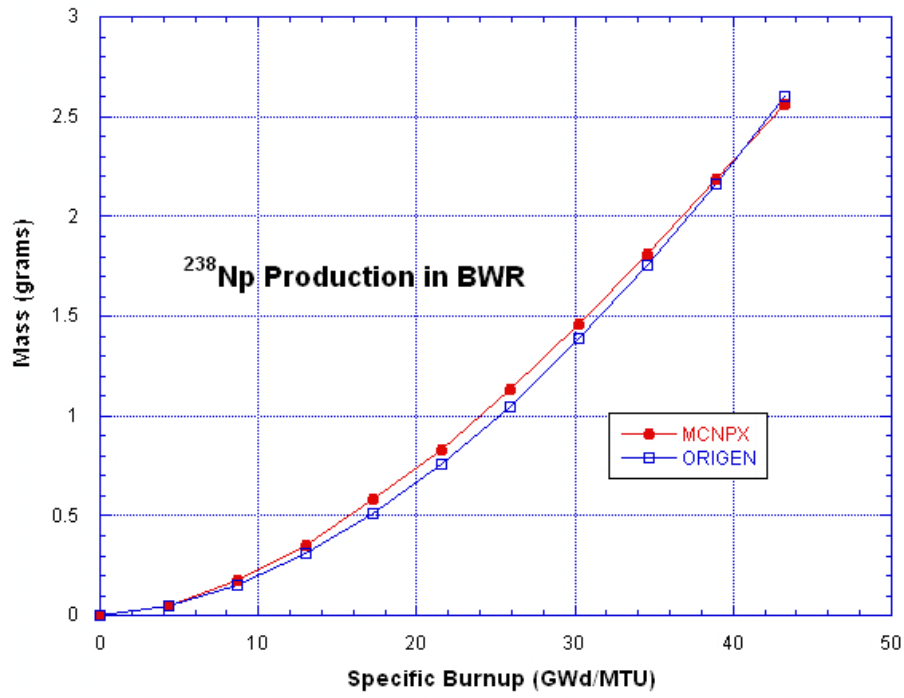


Figure 166: ²³⁸Np Production in W 17x17 PWR Model

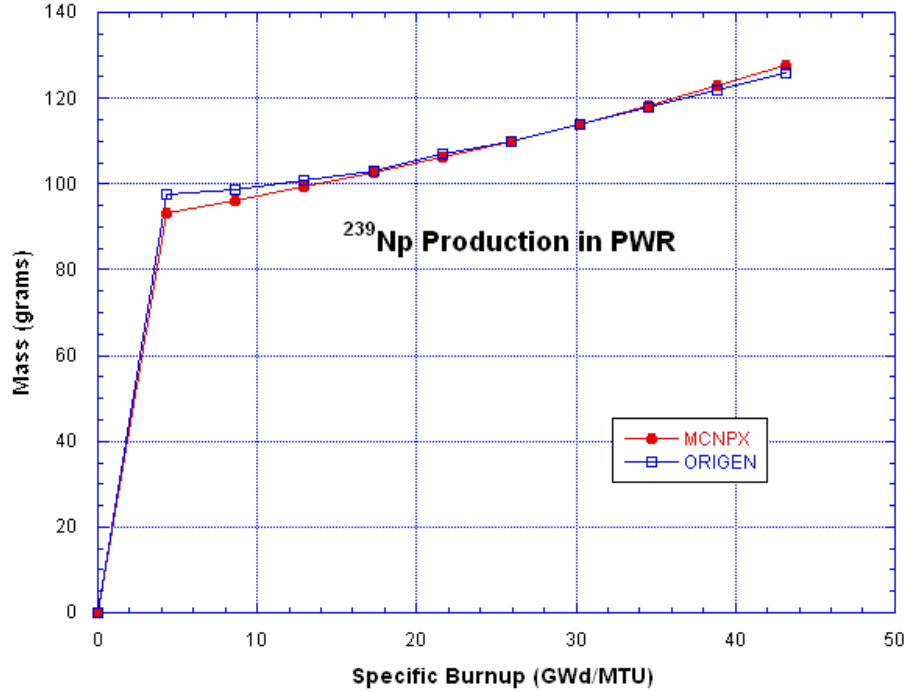


Figure 167: ²³⁹Np Production in W 17x17 PWR Model

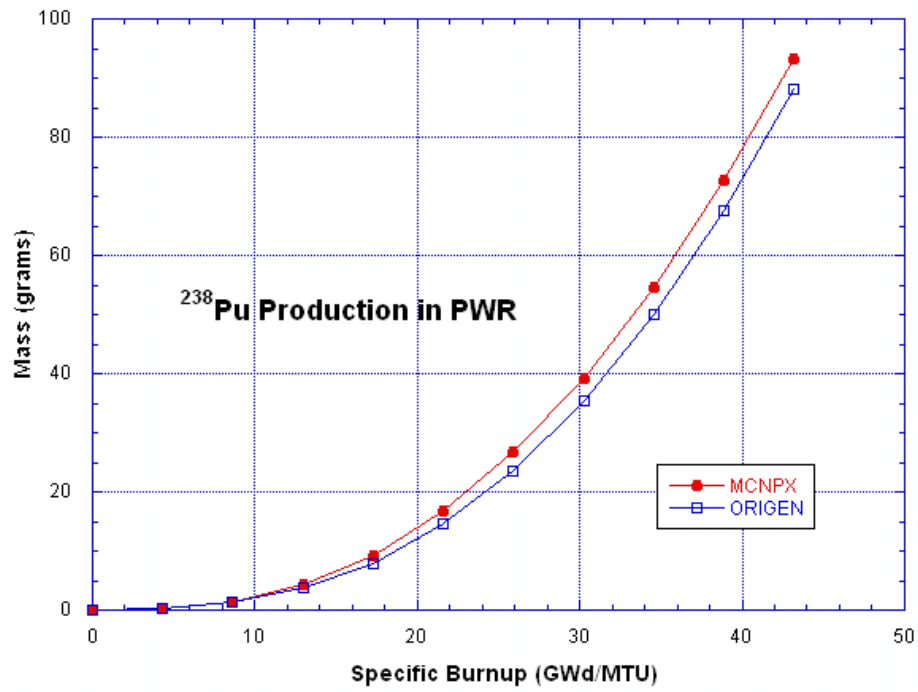


Figure 168: ²³⁸Pu Production in W 17x17 PWR Model

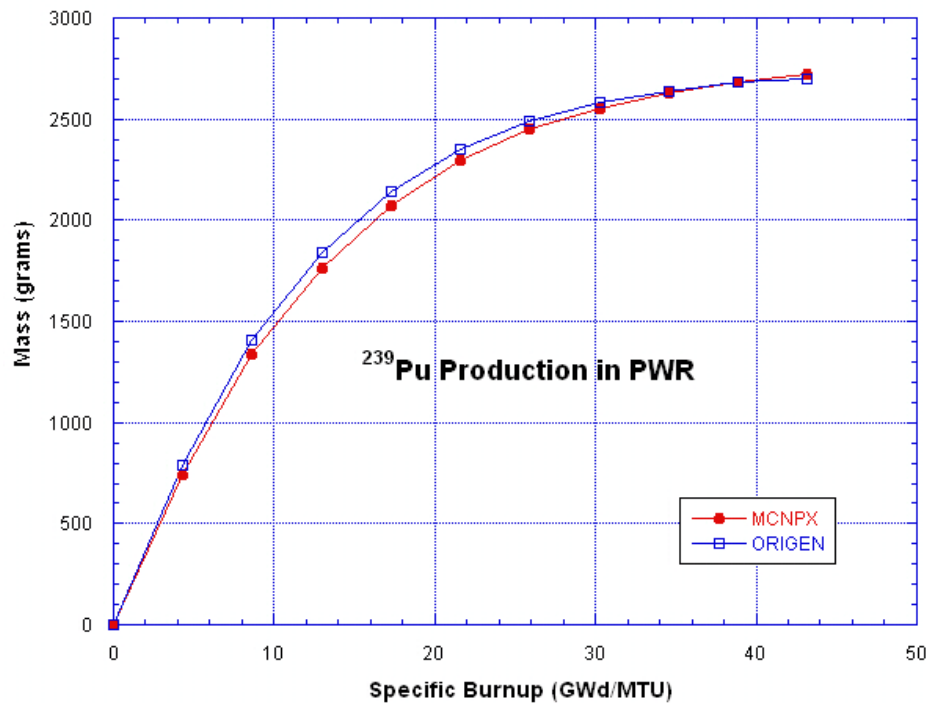


Figure 169: ²³⁹Pu Production in W 17x17 PWR Model

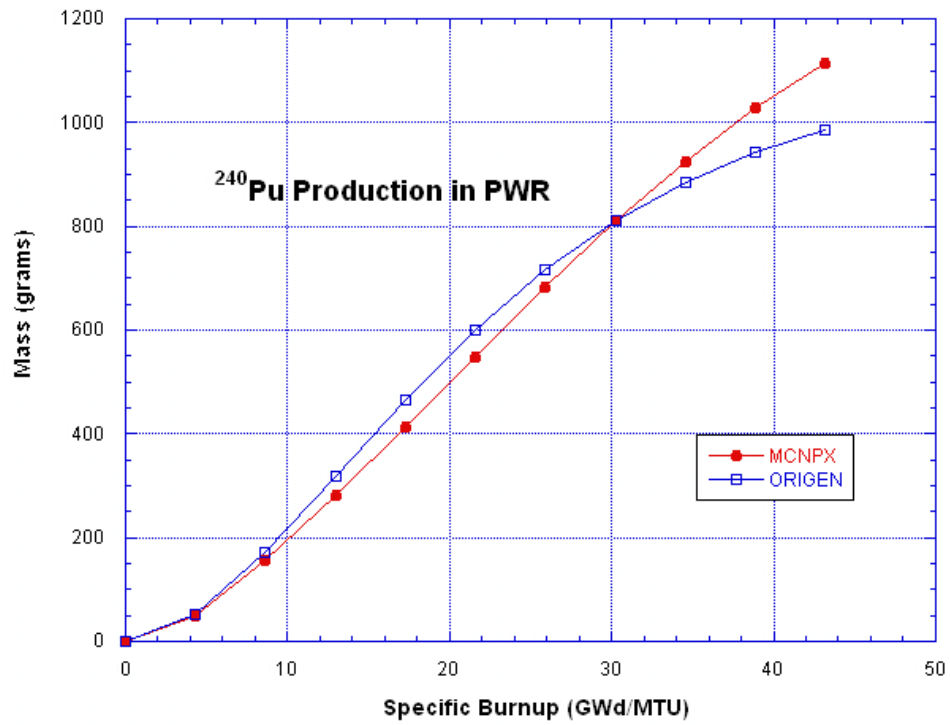


Figure 170: ²⁴⁰Pu Production in W 17x17 PWR Model

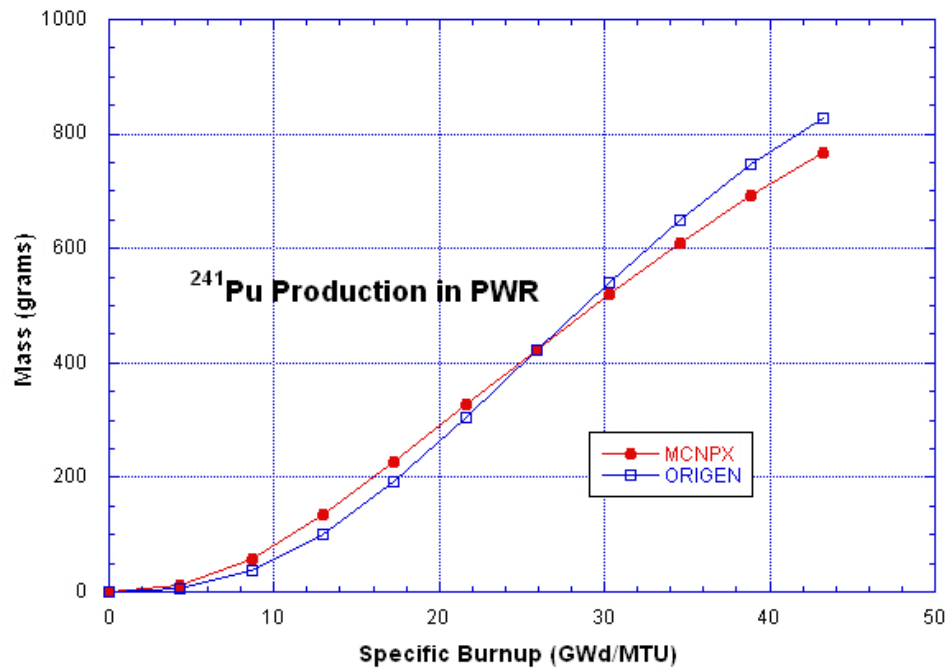


Figure 171: ²⁴¹Pu Production in W 17x17 PWR Model

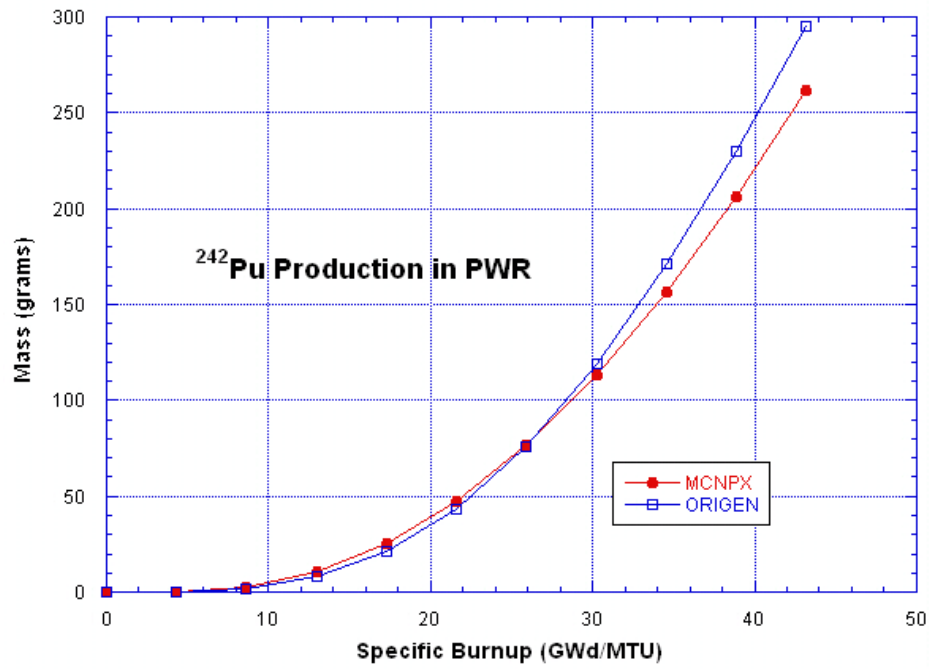


Figure 172: ²⁴²Pu Production in W 17x17 PWR Model

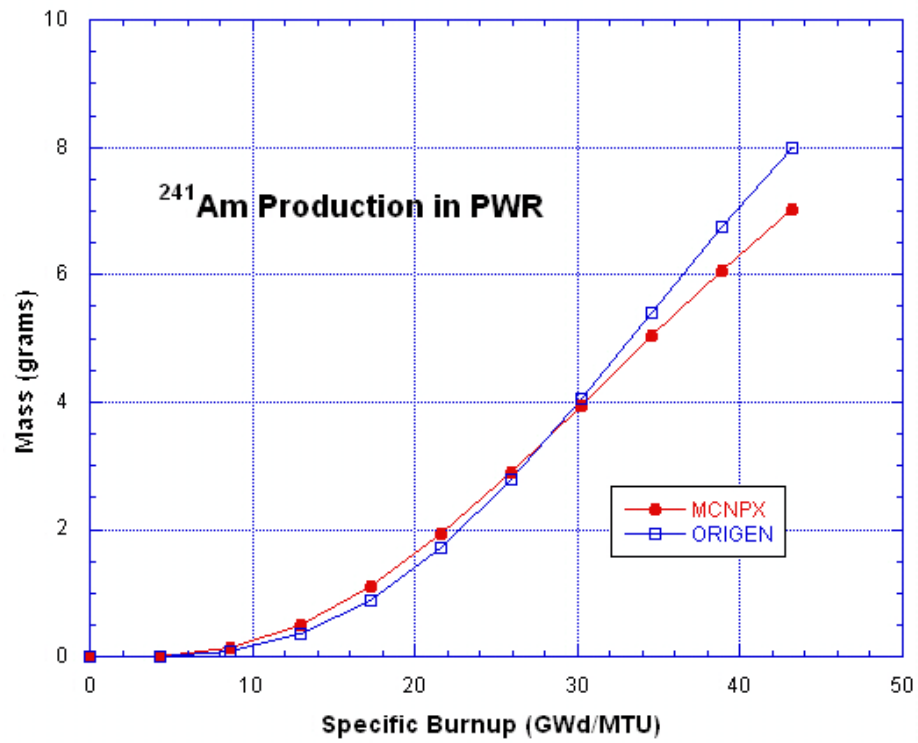


Figure 173: ²⁴¹Am Production in W 17x17 PWR Model

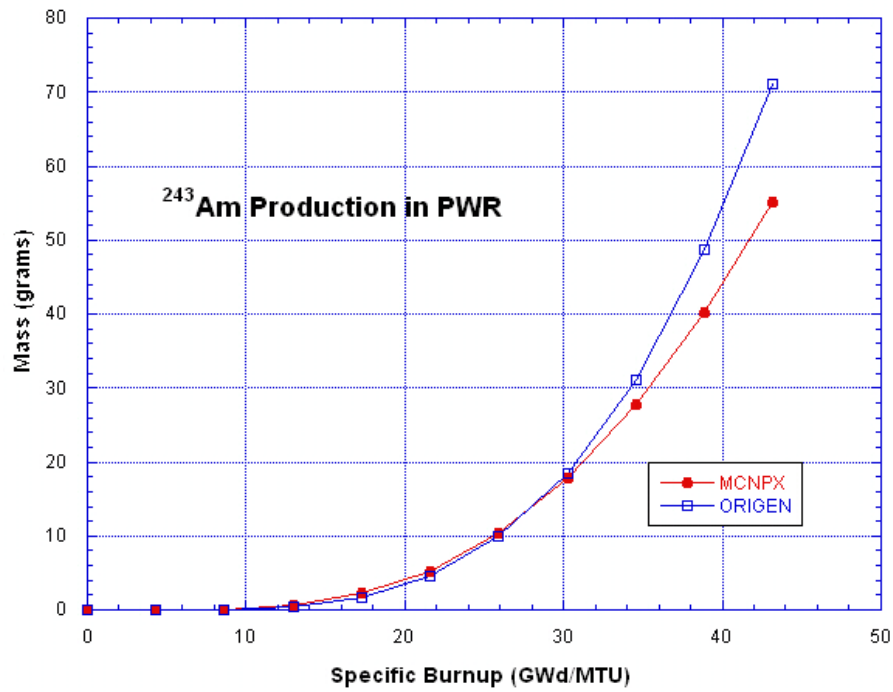


Figure 174: ²⁴³Am Production in W 17x17 PWR Model

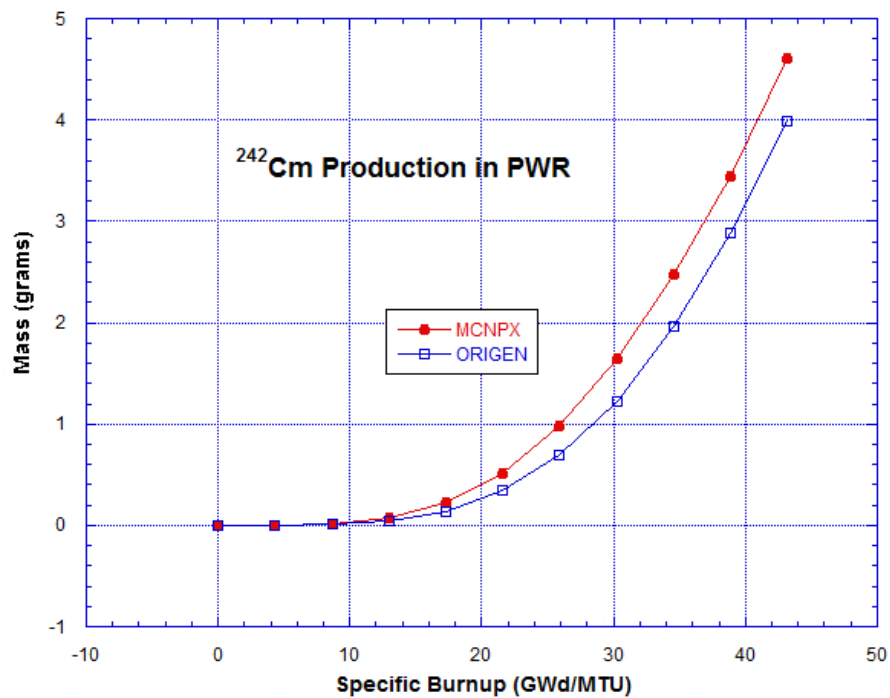


Figure 175: ²⁴²Cm Production in W 17x17 PWR Model

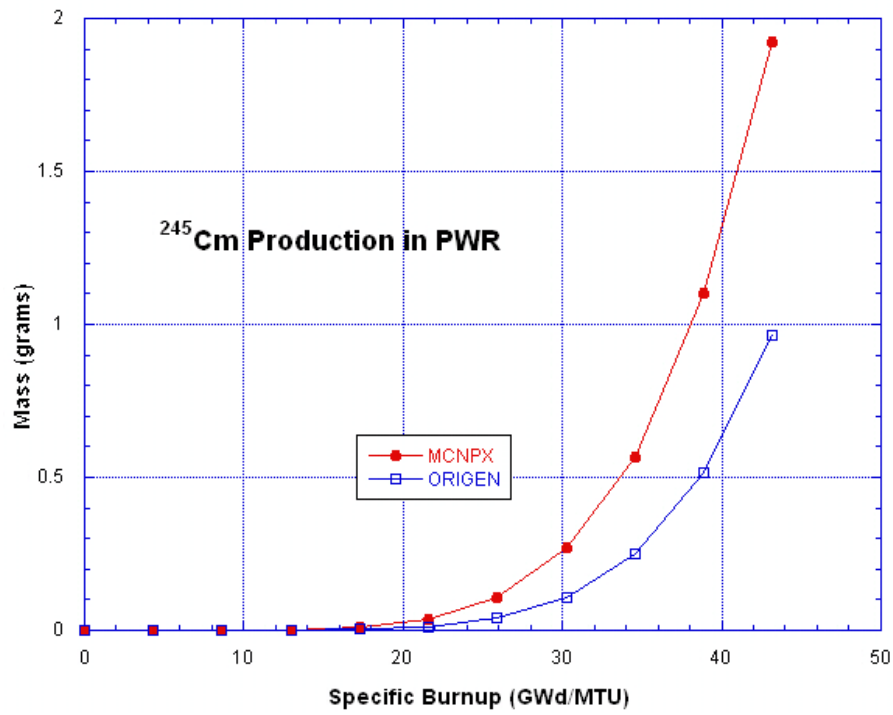


Figure 176: ²⁴⁵Cm Production in W 17x17 PWR Model

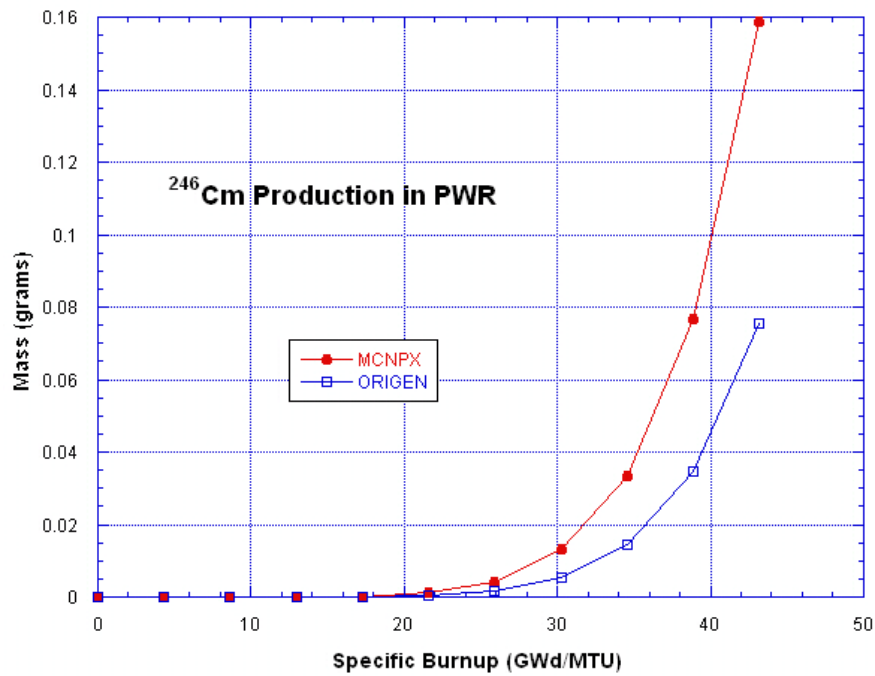


Figure 177: ²⁴⁶Cm Production in W 17x17 PWR Model

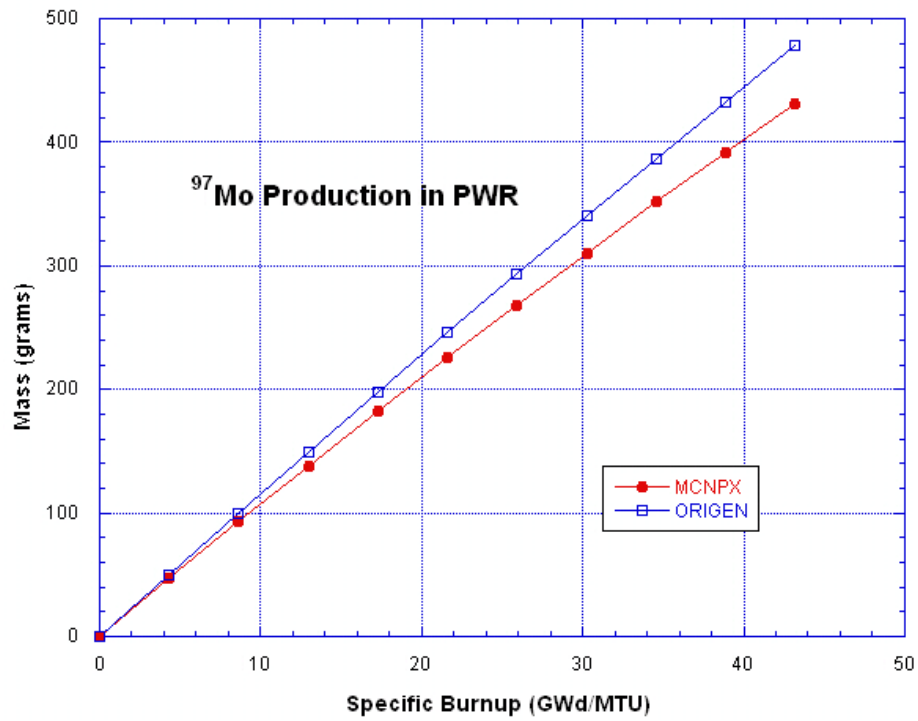


Figure 178: ⁹⁷Mo Production in W 17x17 PWR Model

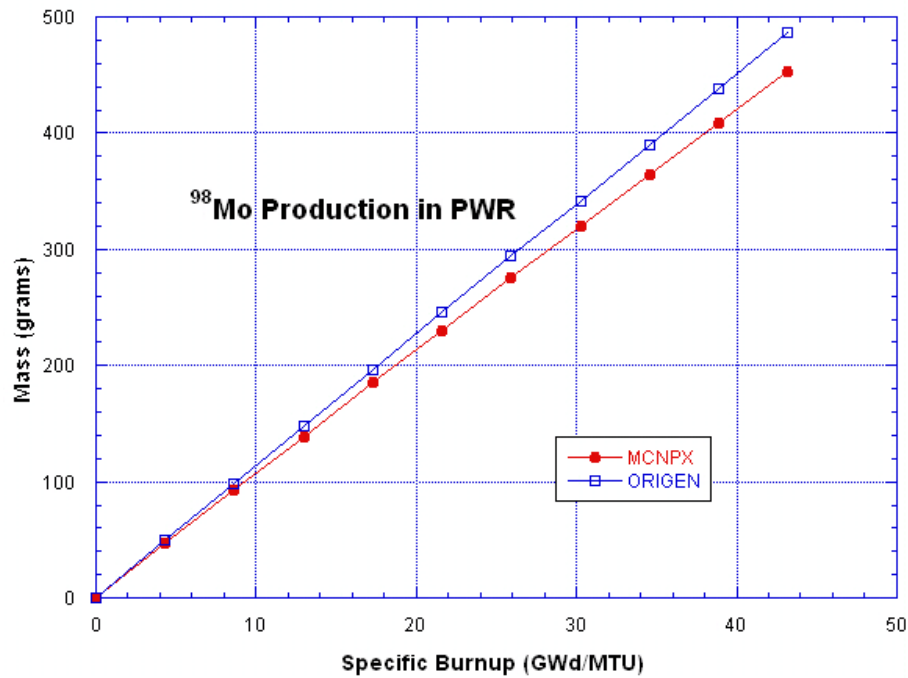


Figure 179: ⁹⁸Mo Production in W 17x17 PWR Model

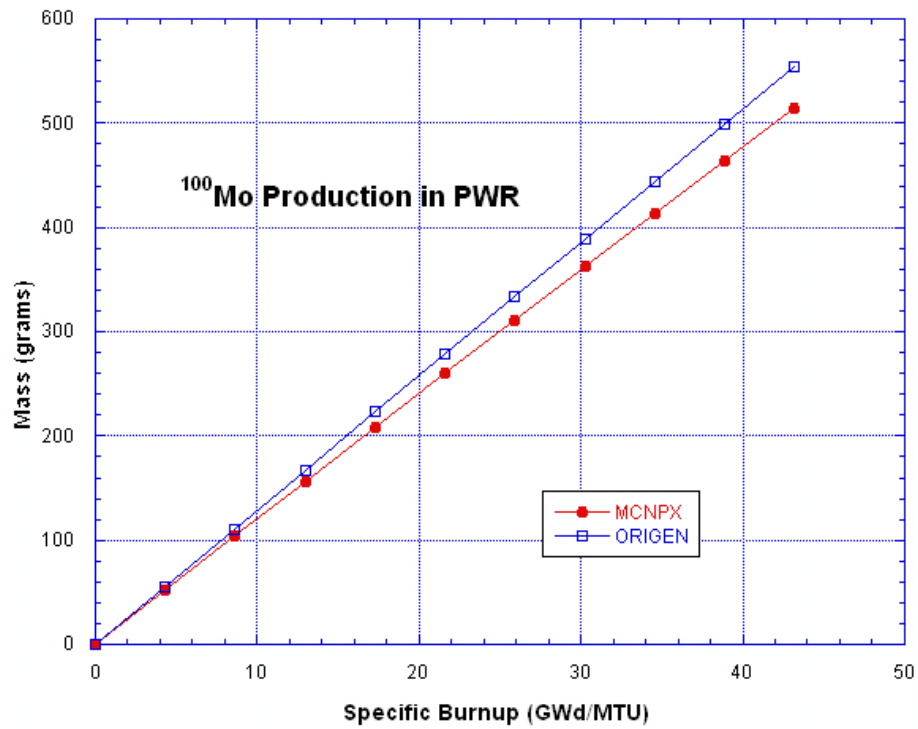


Figure 180: ¹⁰⁰Mo Production in W 17x17 PWR Model

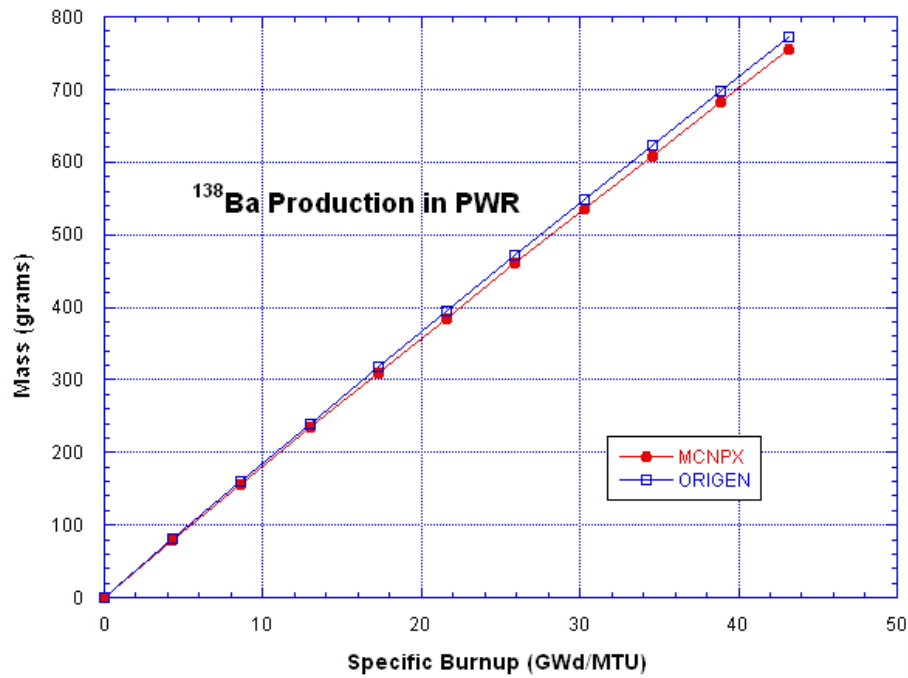


Figure 181: ¹³⁸Ba Production in W 17x17 PWR Model

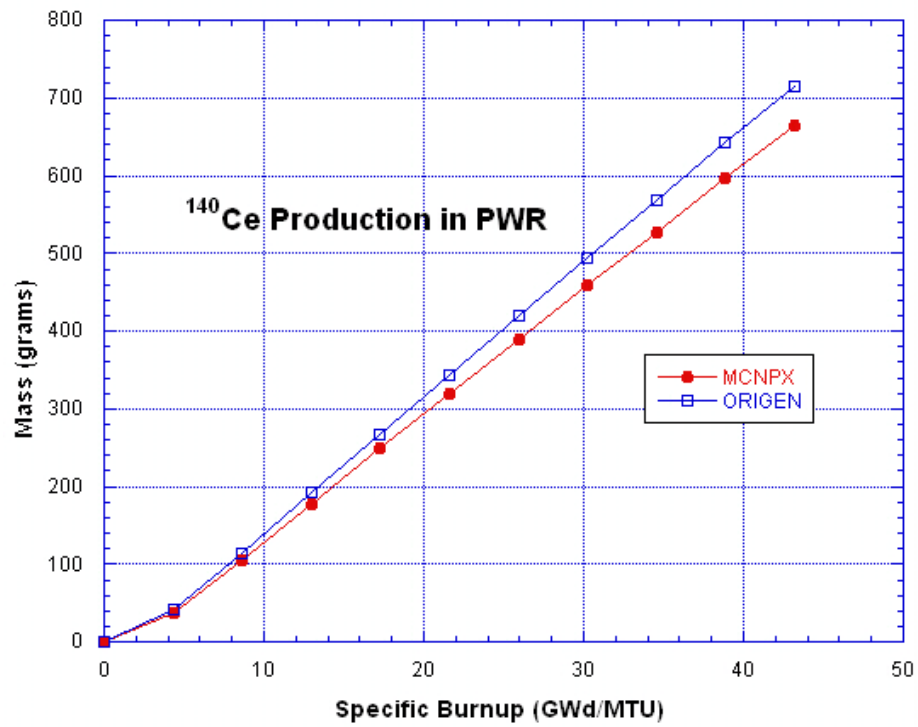


Figure 182: ¹⁴⁰Ce Production in W 17x17 PWR Model

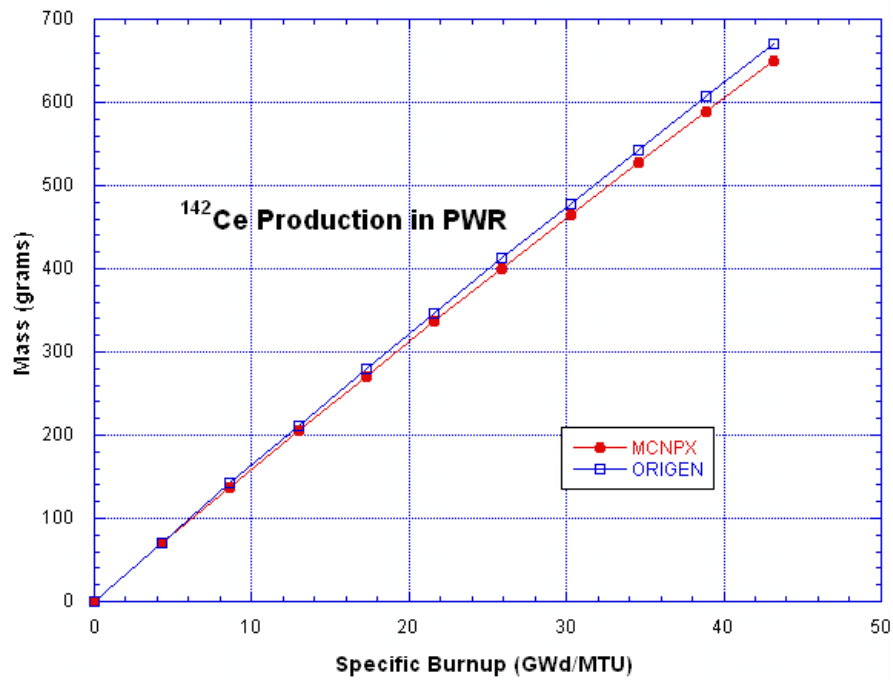


Figure 183: ¹⁴²Ce Production in W 17x17 PWR Model

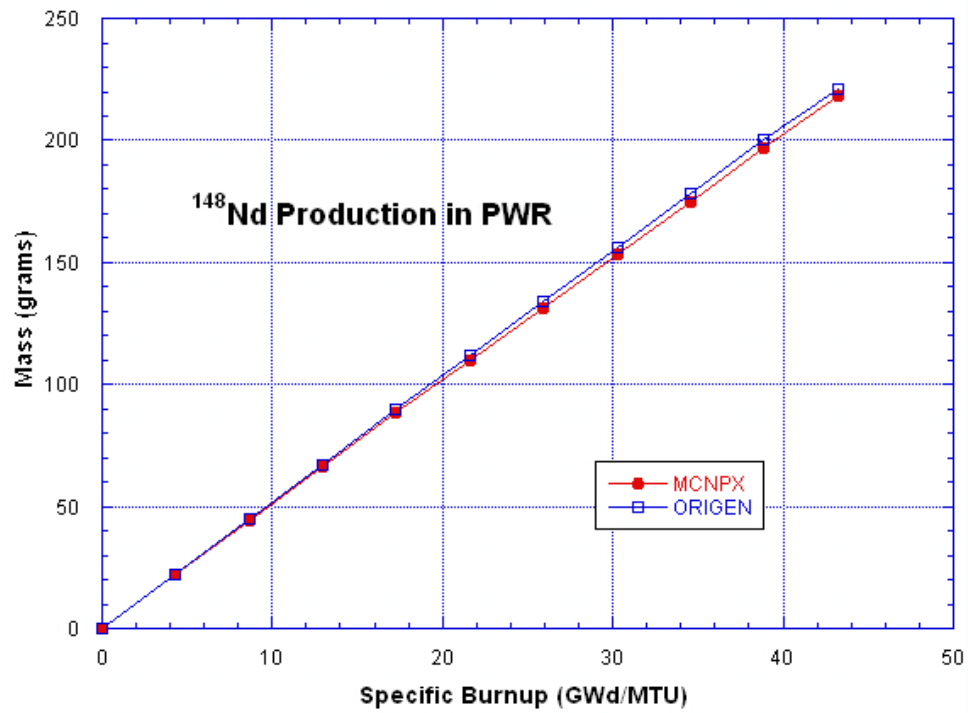


Figure 184: ¹⁴⁸Nd Production in W 17x17 PWR Model

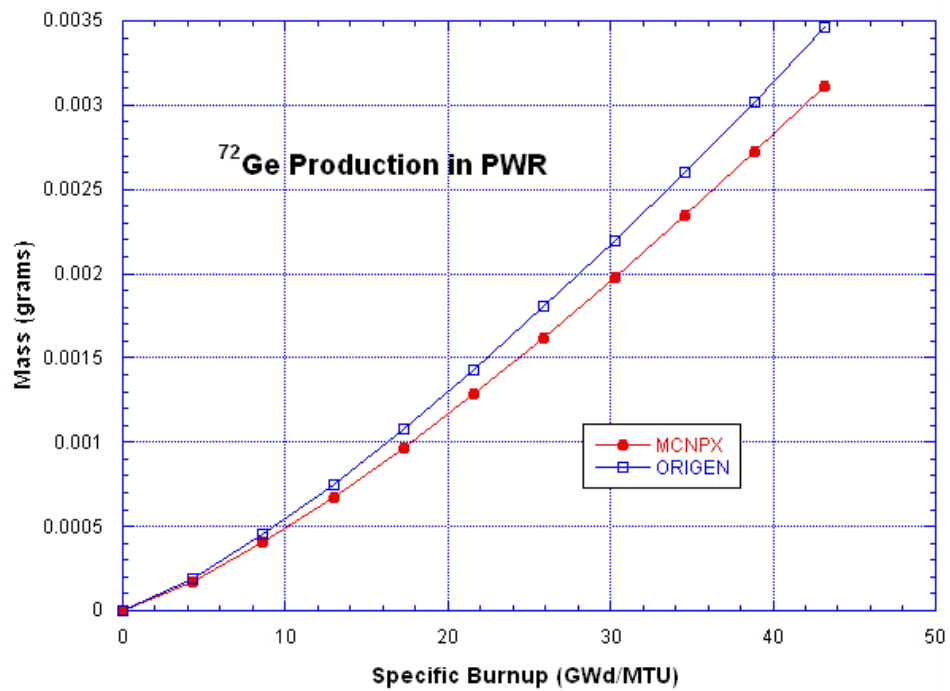


Figure 185: ⁷²Ge Production in W 17x17 PWR Model

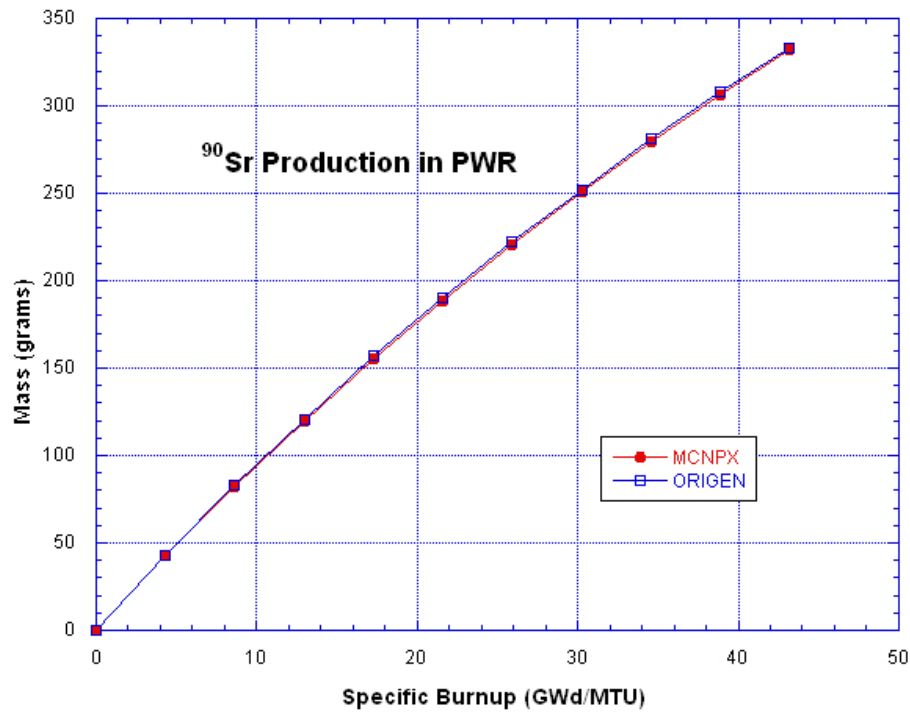


Figure 186: ⁹⁰Sr Production in W 17x17 PWR Model

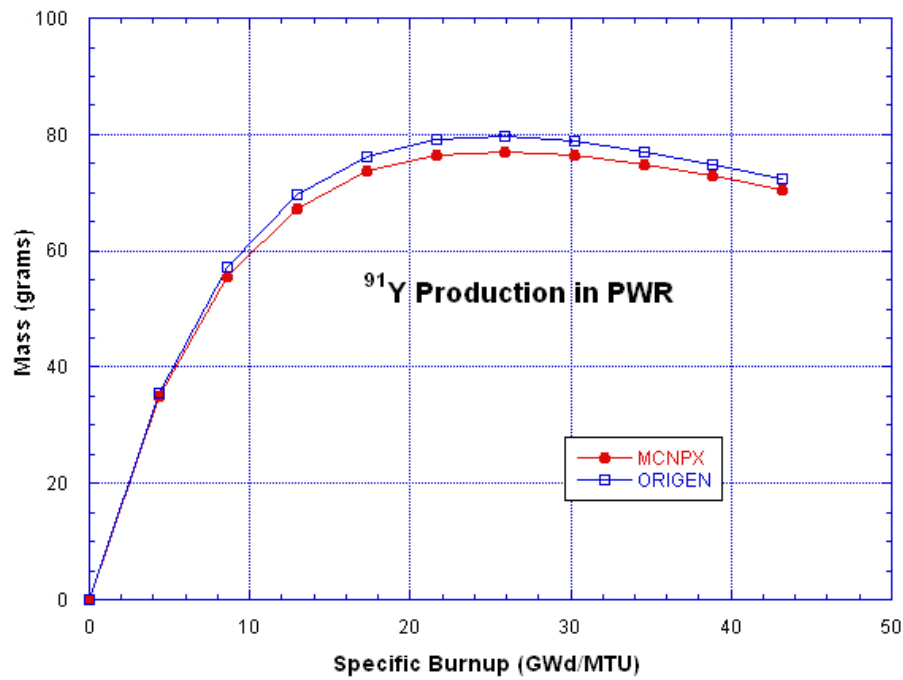


Figure 187: ⁹¹Y Production in W 17x17 PWR Model

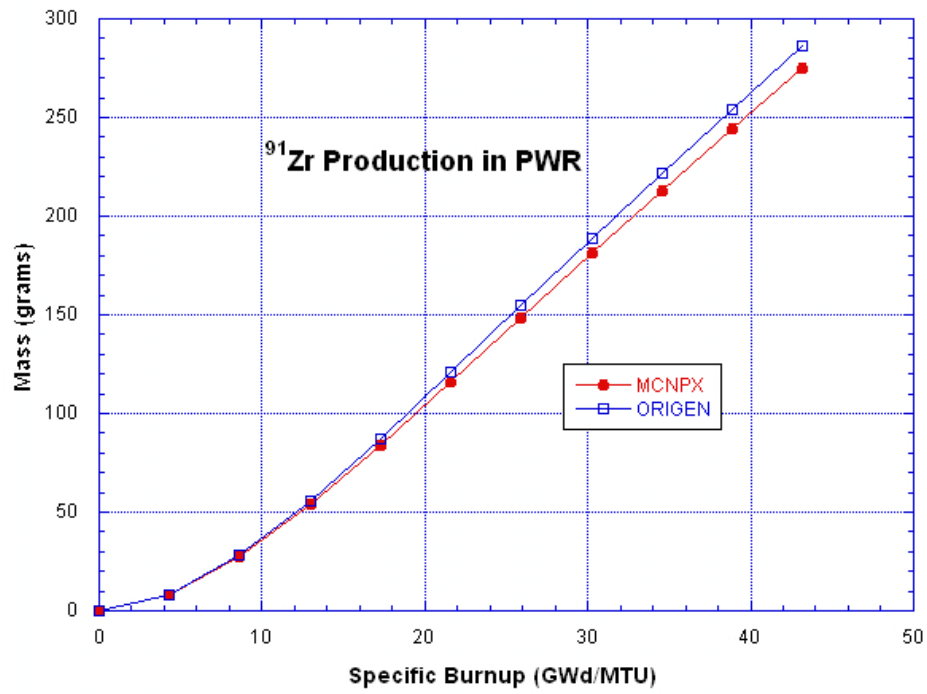


Figure 188: ⁹¹Zr Production in W 17x17 PWR Model

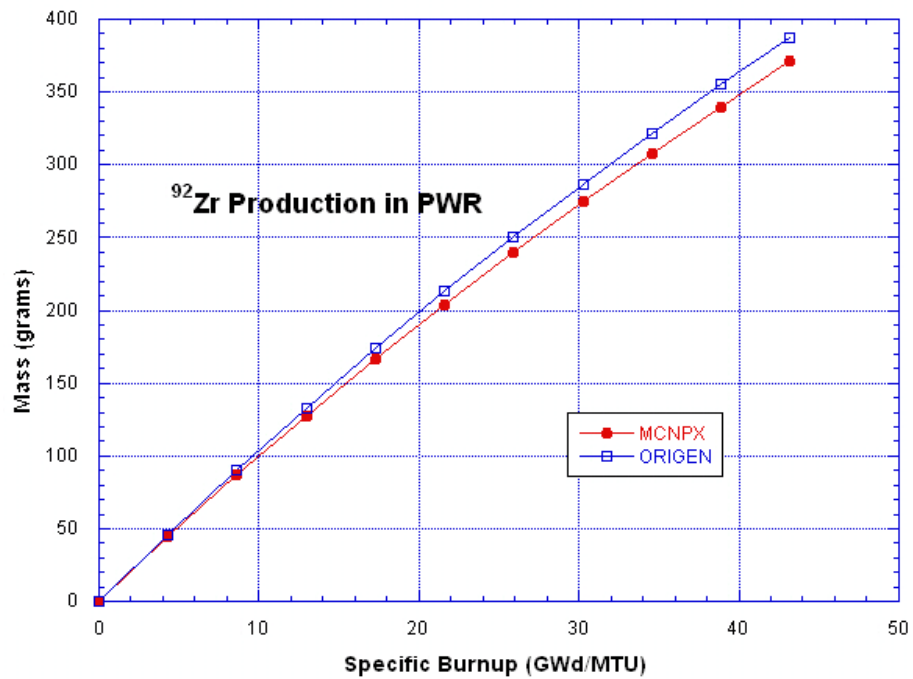


Figure 189: ⁹²Zr Production in W 17x17 PWR Model

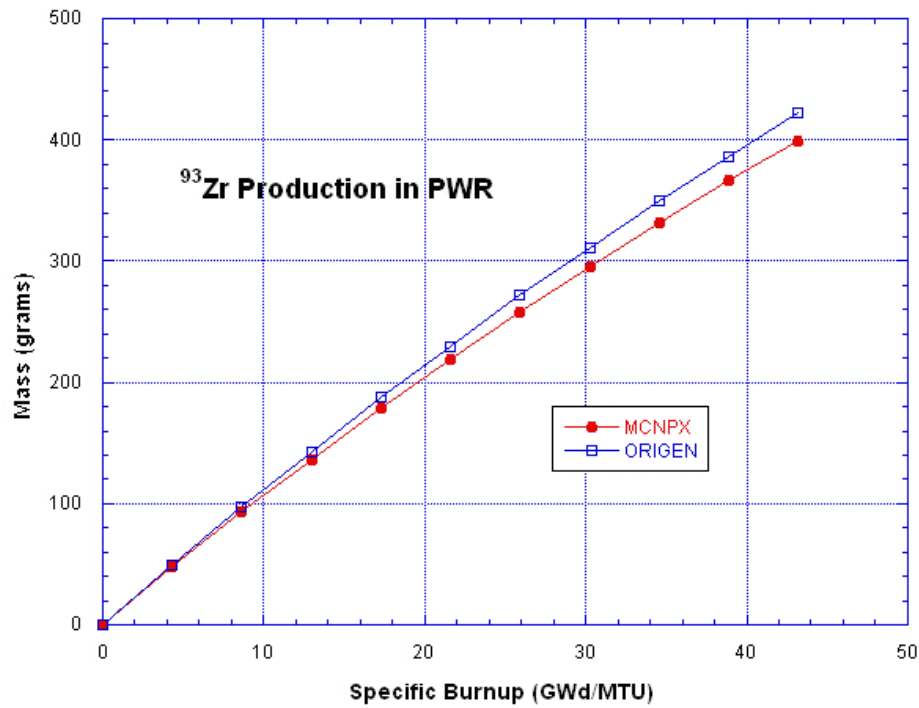


Figure 190: ⁹³Zr Production in W 17x17 PWR Model

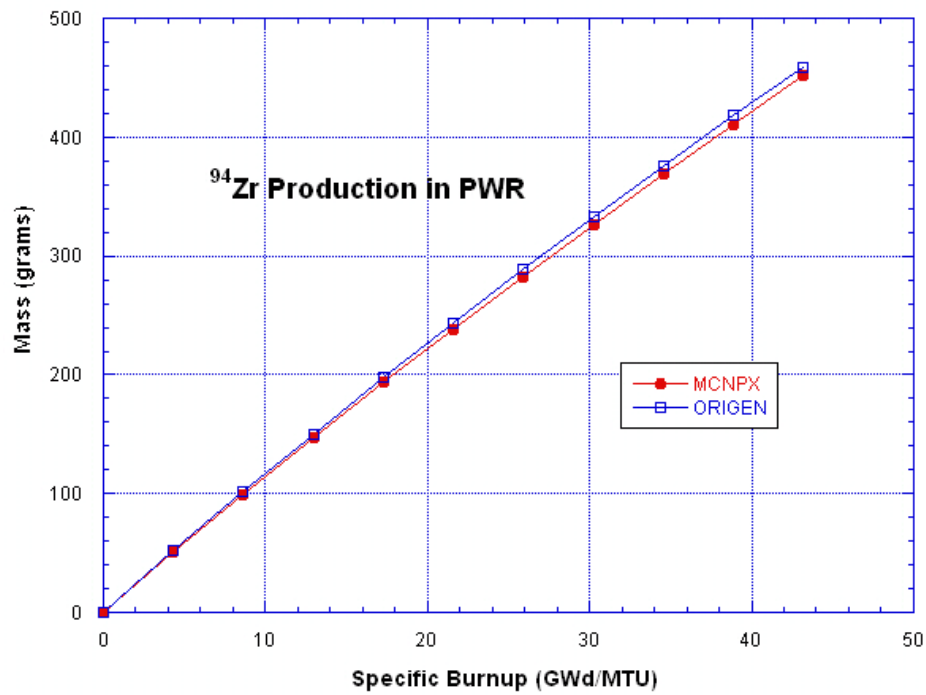


Figure 191: ⁹⁴Zr Production in W 17x17 PWR Model

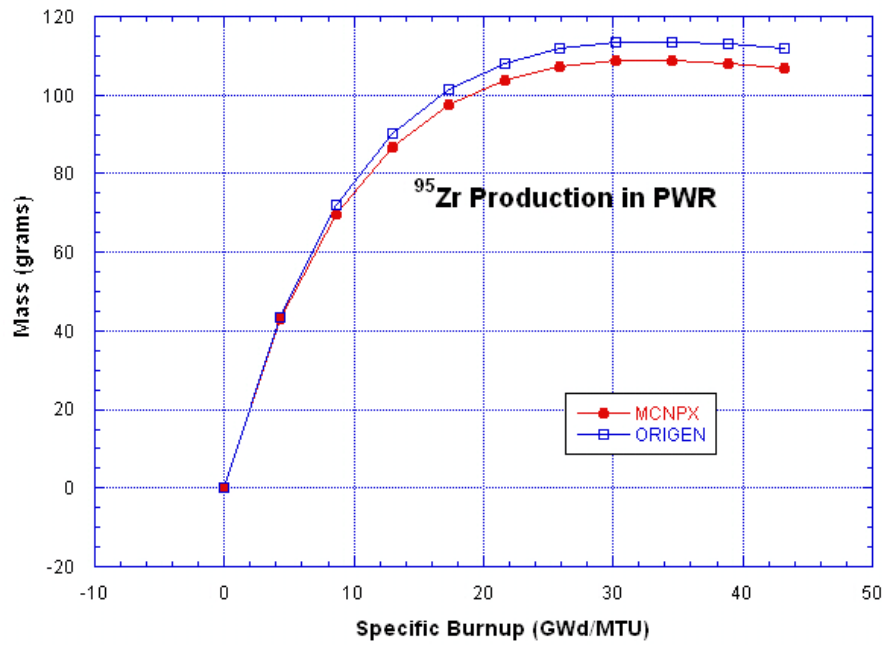


Figure 192: ⁹⁵Zr Production in W 17x17 PWR Model

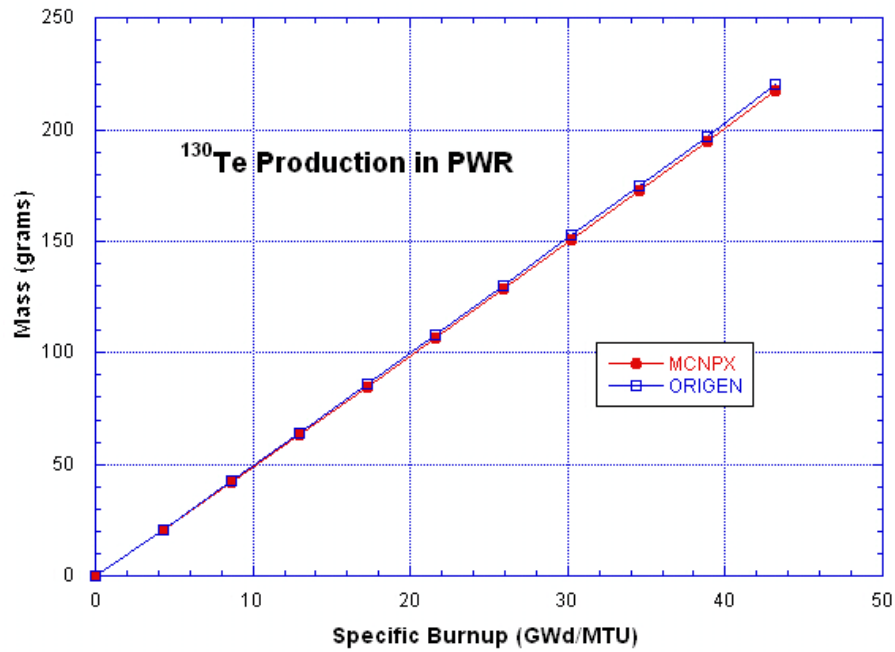


Figure 193: ¹³⁰Te Production in W 17x17 PWR Model

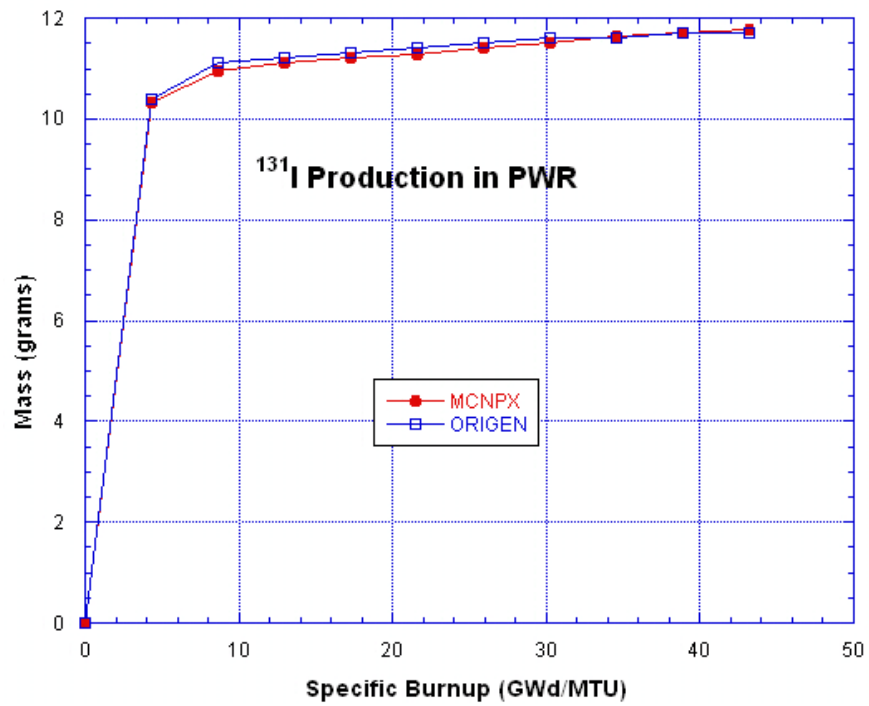


Figure 194: ^{131}I Production in W 17x17 PWR Model

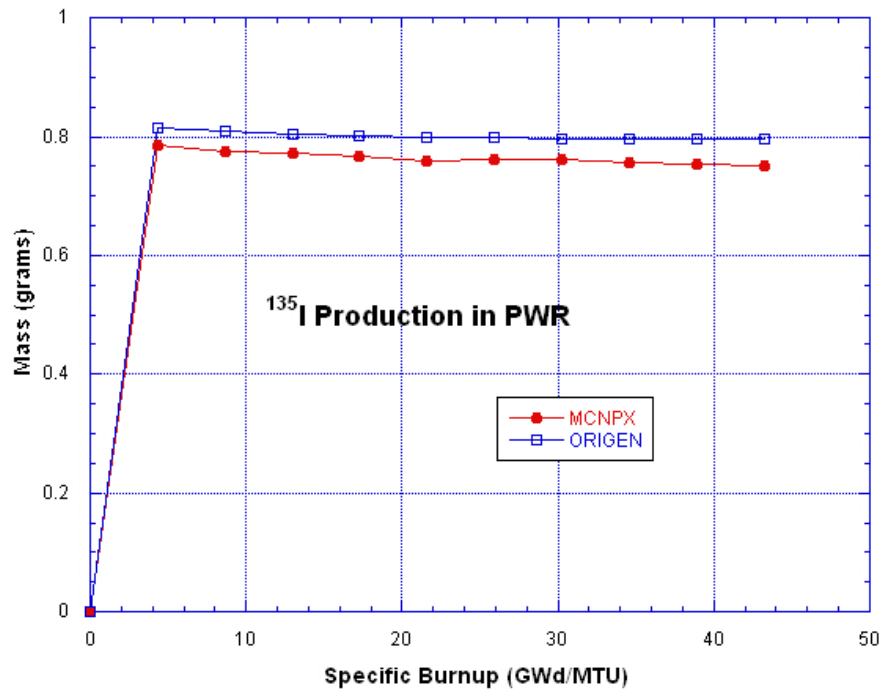


Figure 195: ^{135}I Production in W 17x17 PWR Model

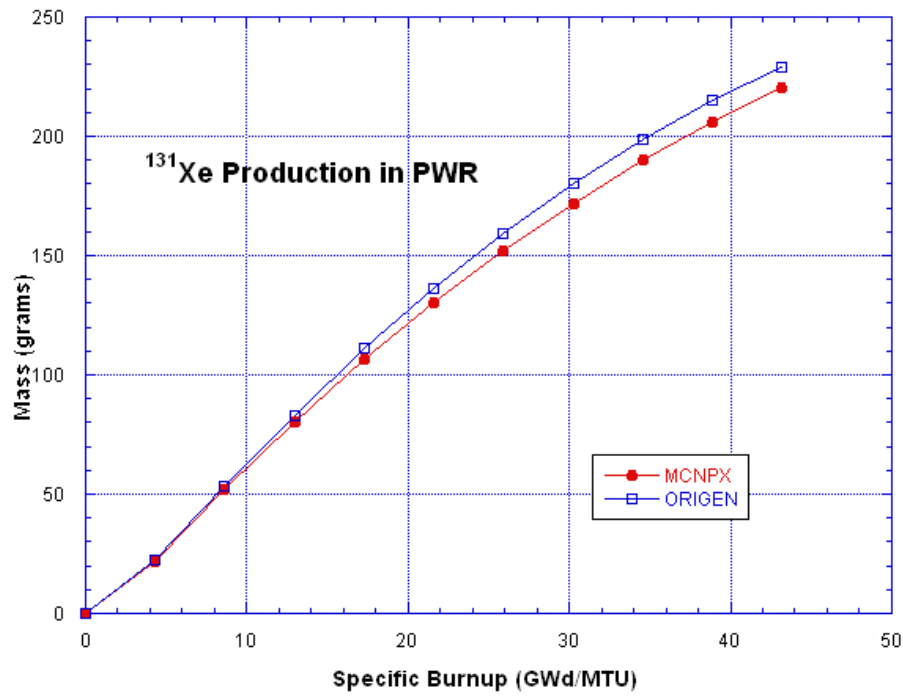


Figure 196: ¹³¹Xe Production in W 17x17 PWR Model

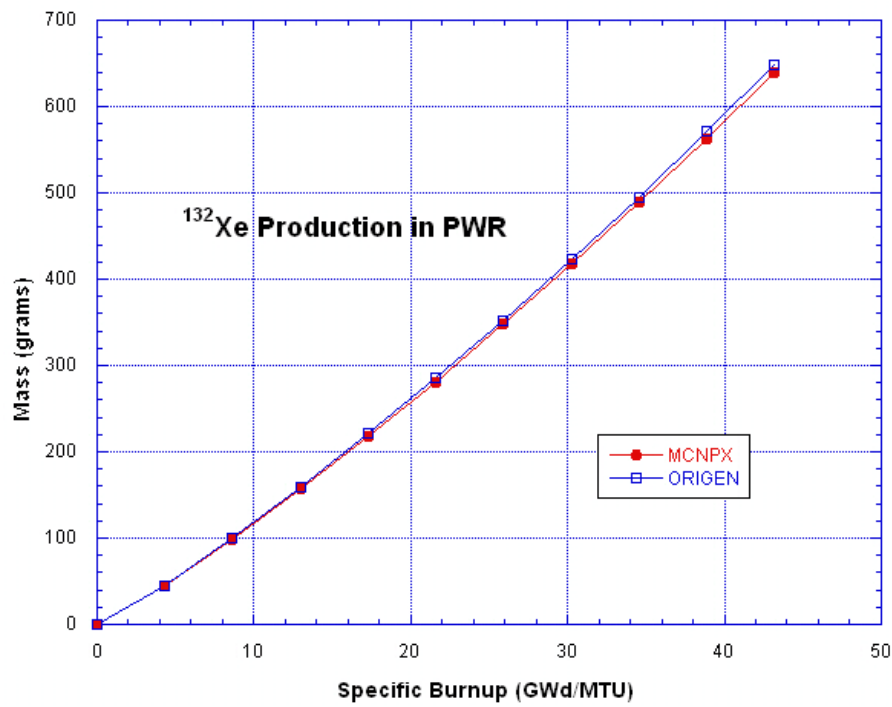


Figure 197: ¹³²Xe Production in W 17x17 PWR Model

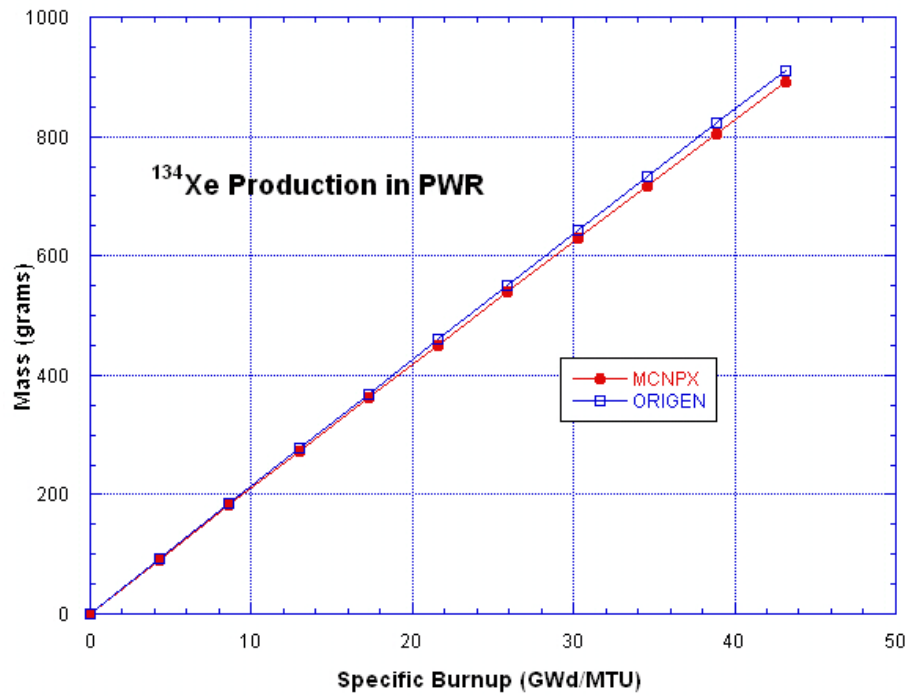


Figure 198: ¹³⁴Xe Production in W 17x17 PWR Model

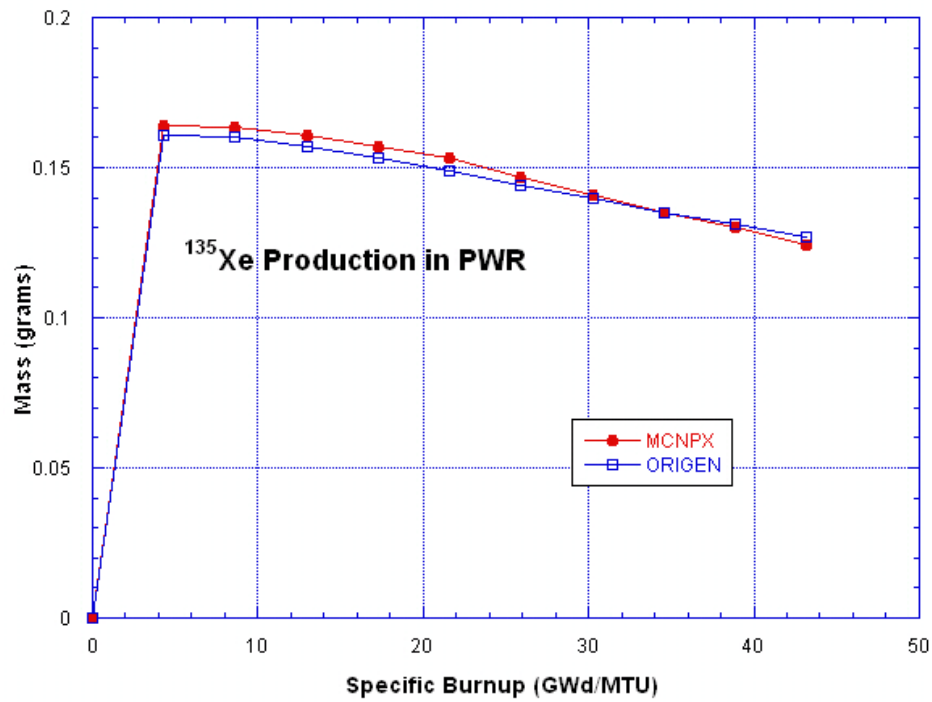


Figure 199: ¹³⁵Xe Production in W 17x17 PWR Model

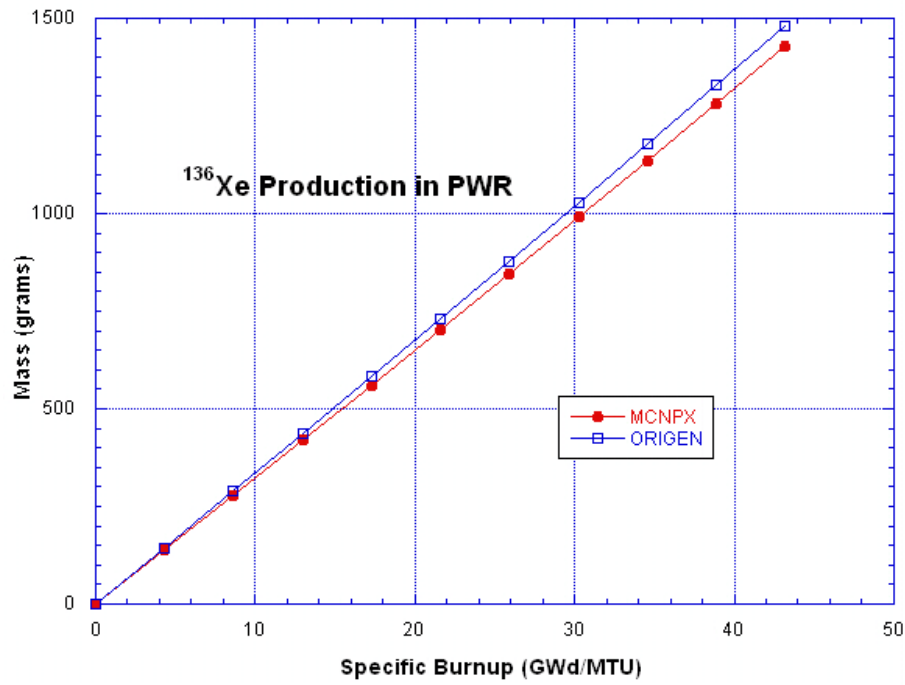


Figure 200: ¹³⁶Xe Production in W 17x17 PWR Model

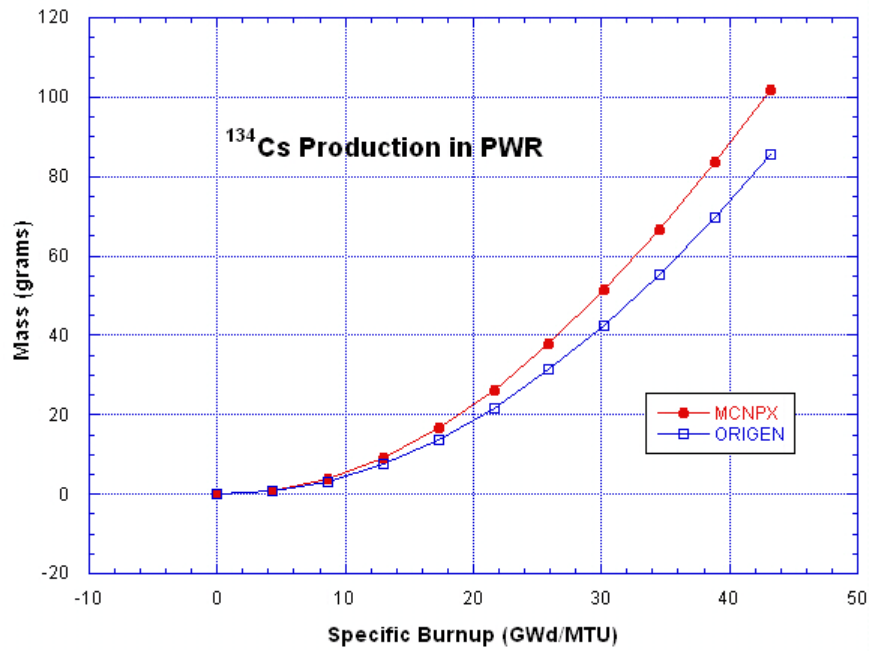


Figure 201: ¹³⁴Cs Production in W 17x17 PWR Model

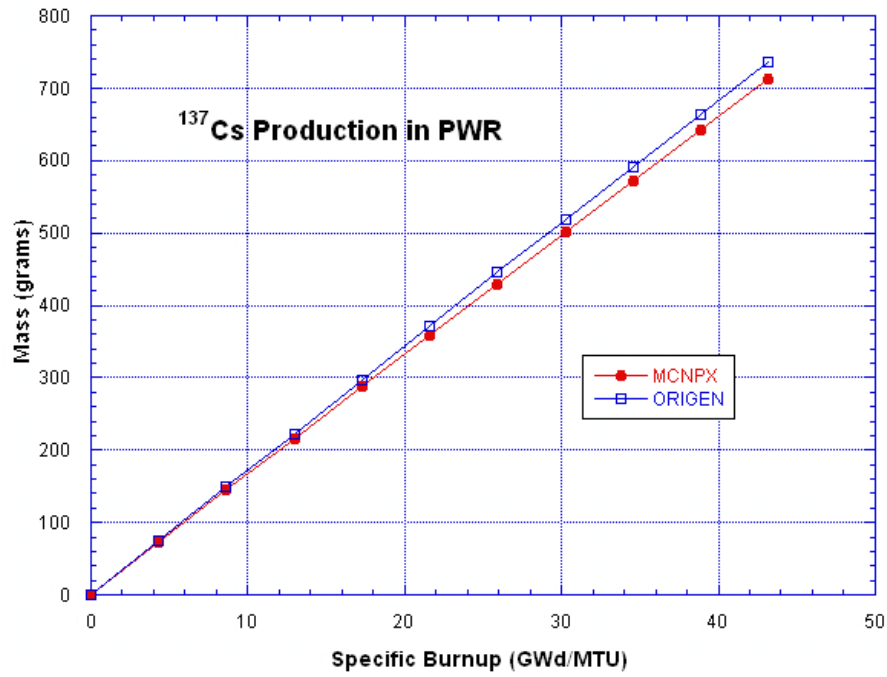


Figure 202: ¹³⁷Cs Production in W 17x17 PWR Model

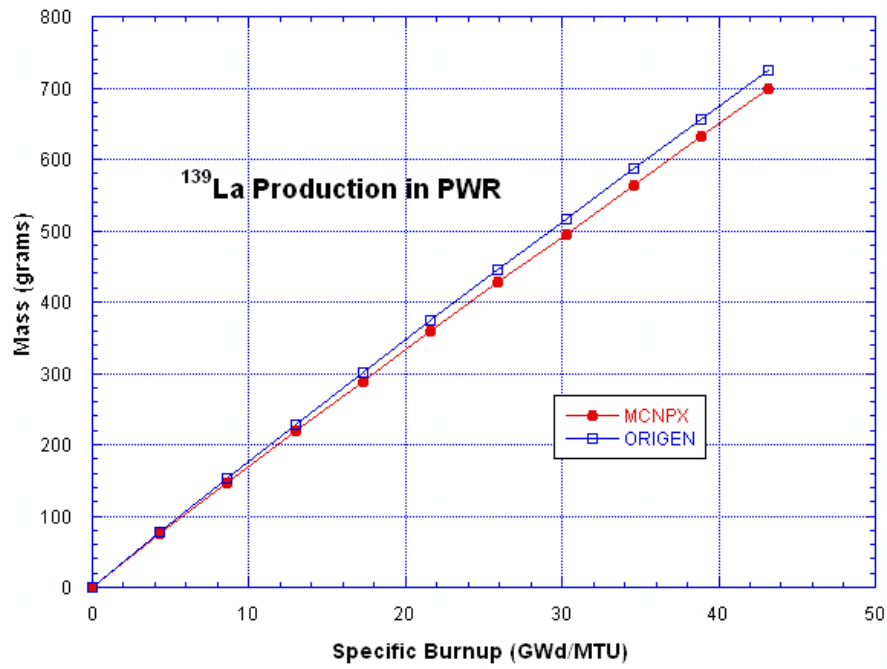


Figure 203: ¹³⁹La Production in W 17x17 PWR Model

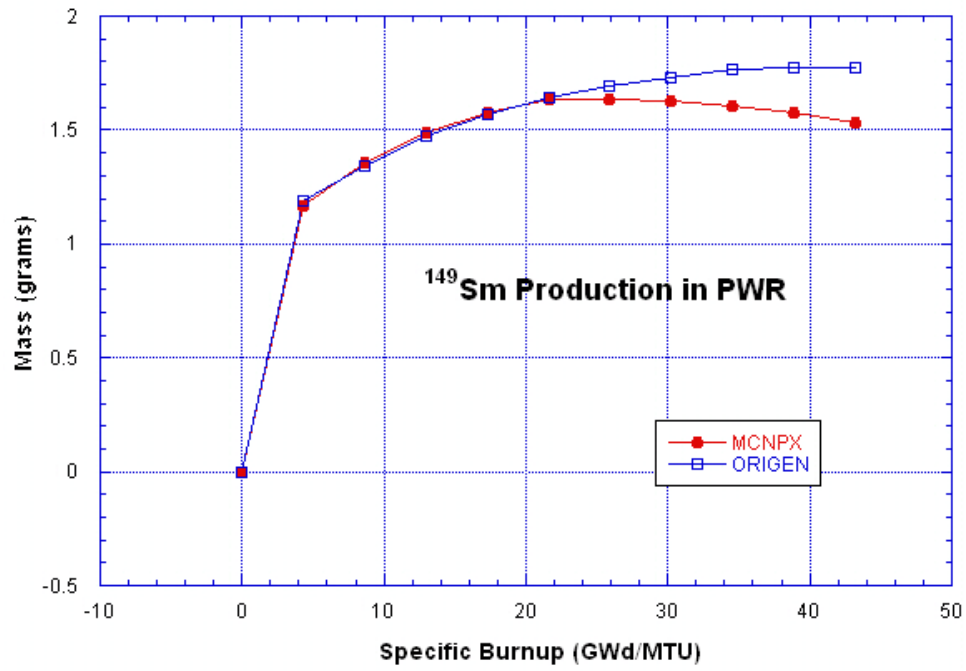


Figure 204: ¹⁴⁹Sm Production in W 17x17 PWR Model

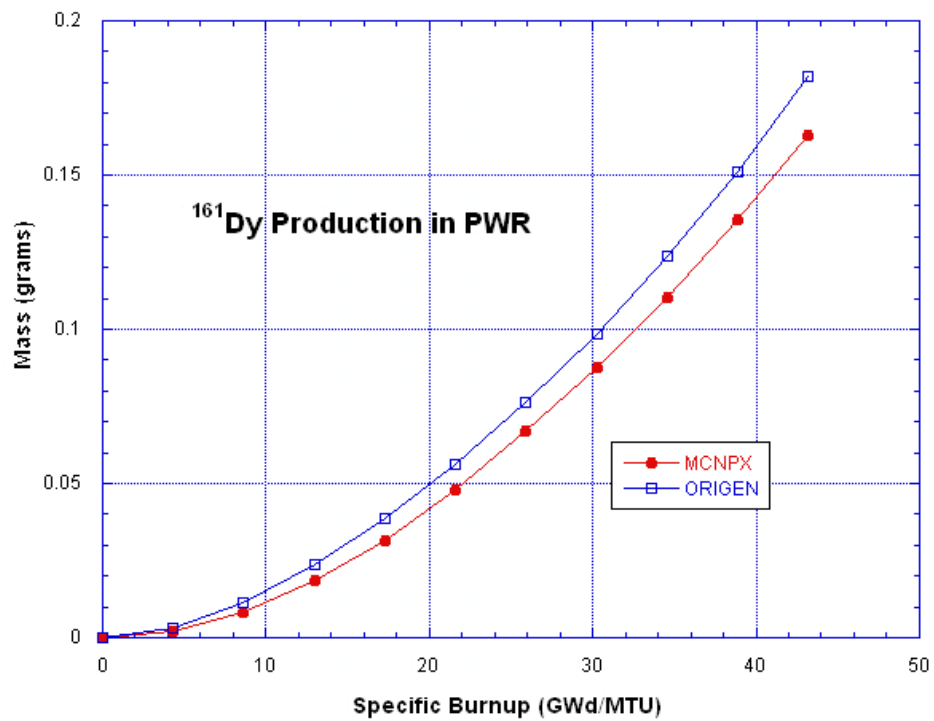


Figure 205: ¹⁶¹Dy Production in W 17x17 PWR Model

Appendix F: CANDU-37 Plots of 46 Nuclides of Interest

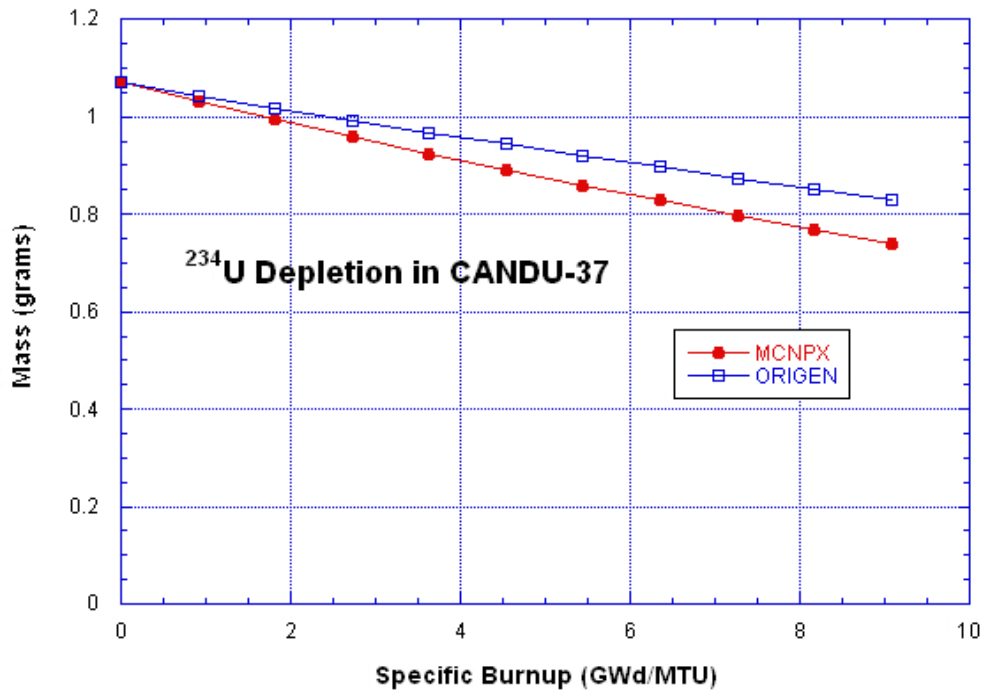


Figure 206: ²³⁴U Depletion in CANDU-37 Model

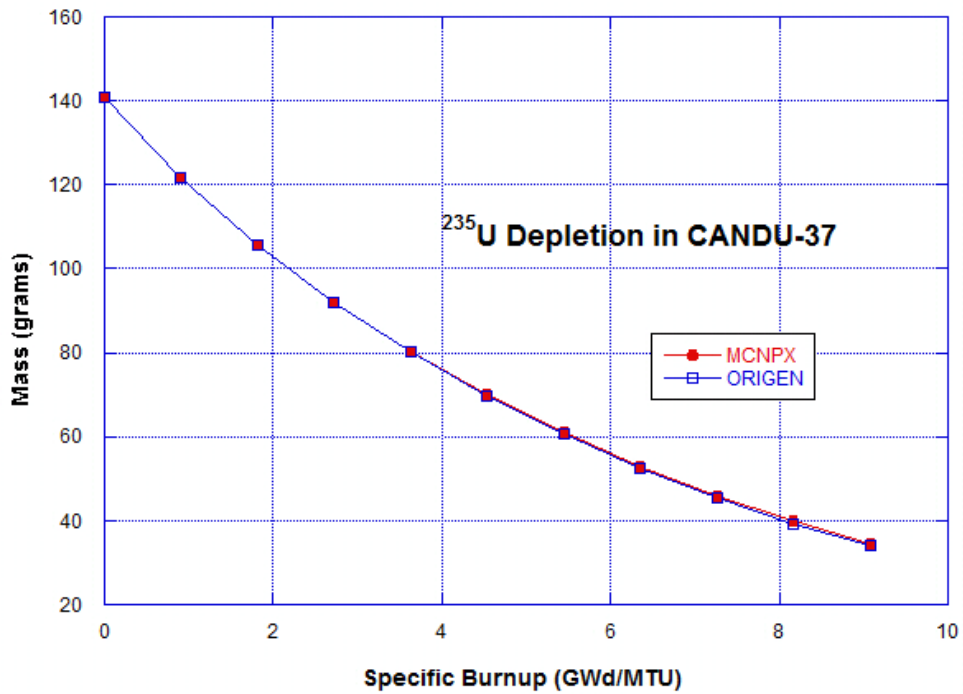


Figure 207: ²³⁵U Depletion in CANDU-37 Model

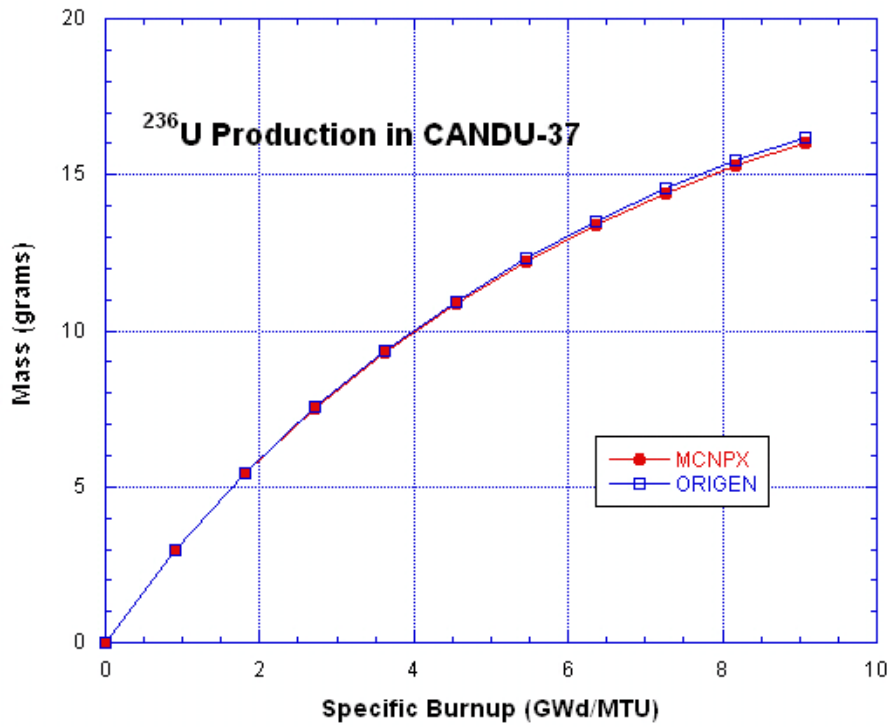


Figure 208: ^{236}U Production in CANDU-37 Model

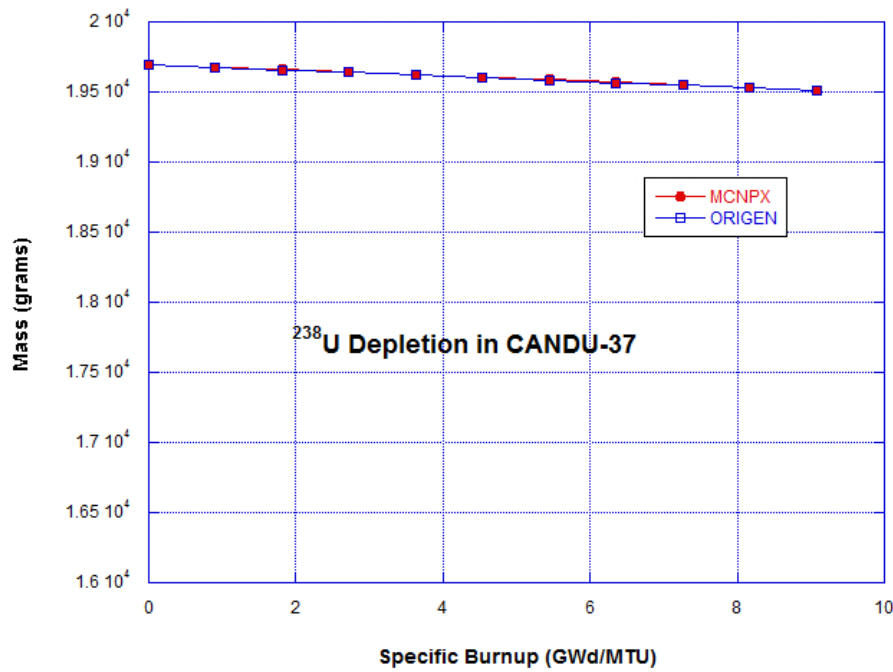


Figure 209: ^{238}U Depletion in CANDU-37 Model

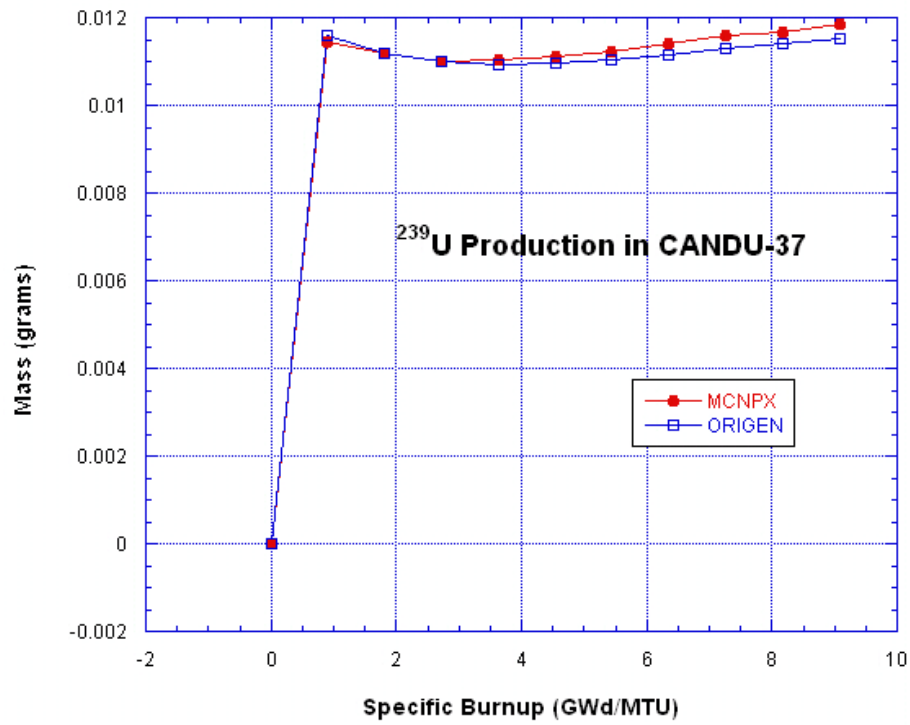


Figure 210: ²³⁹U Production in CANDU-37 Model

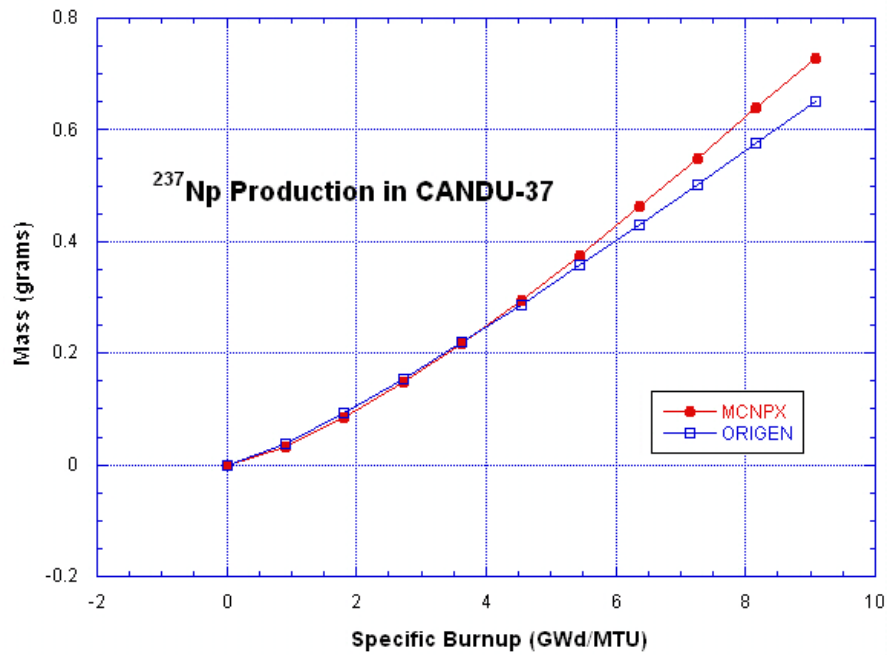


Figure 211: ²³⁷Np Production in CANDU-37 Model

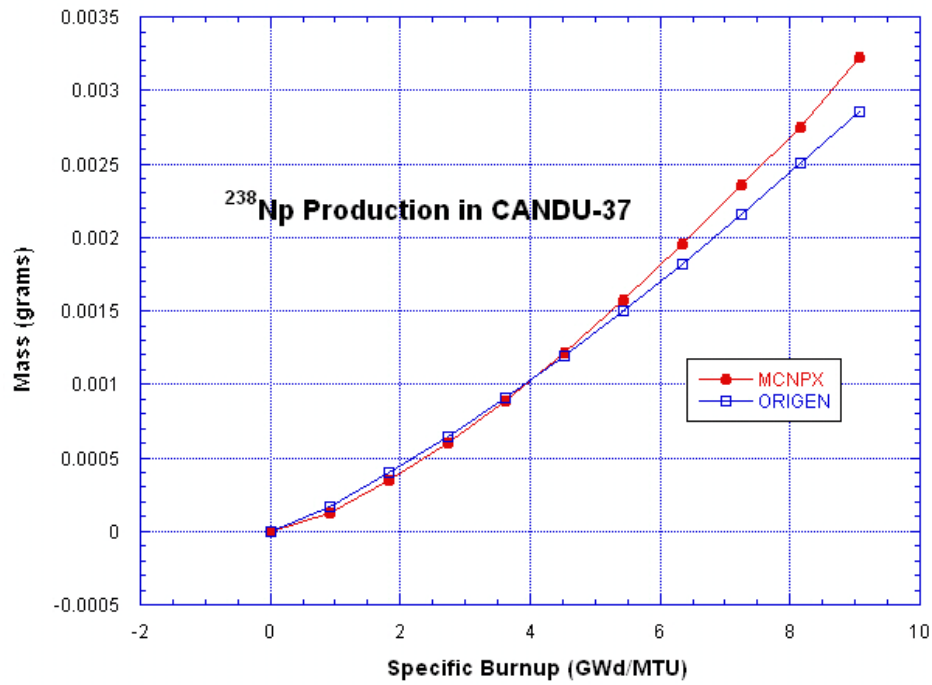


Figure 212: ²³⁸Np Production in CANDU-37 Model

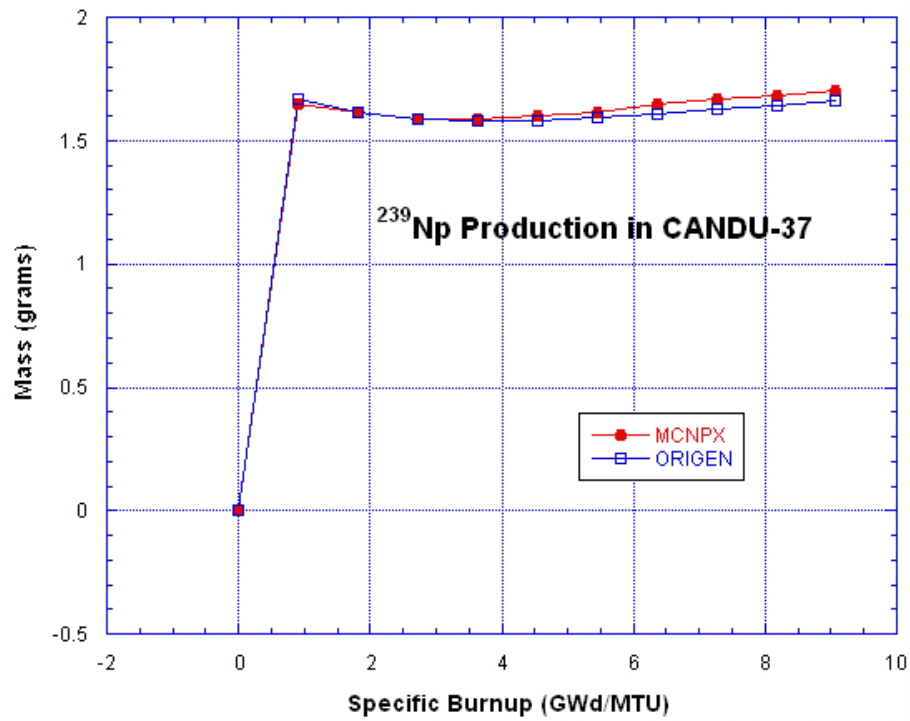


Figure 213: ²³⁹Np Production in CANDU-37 Model

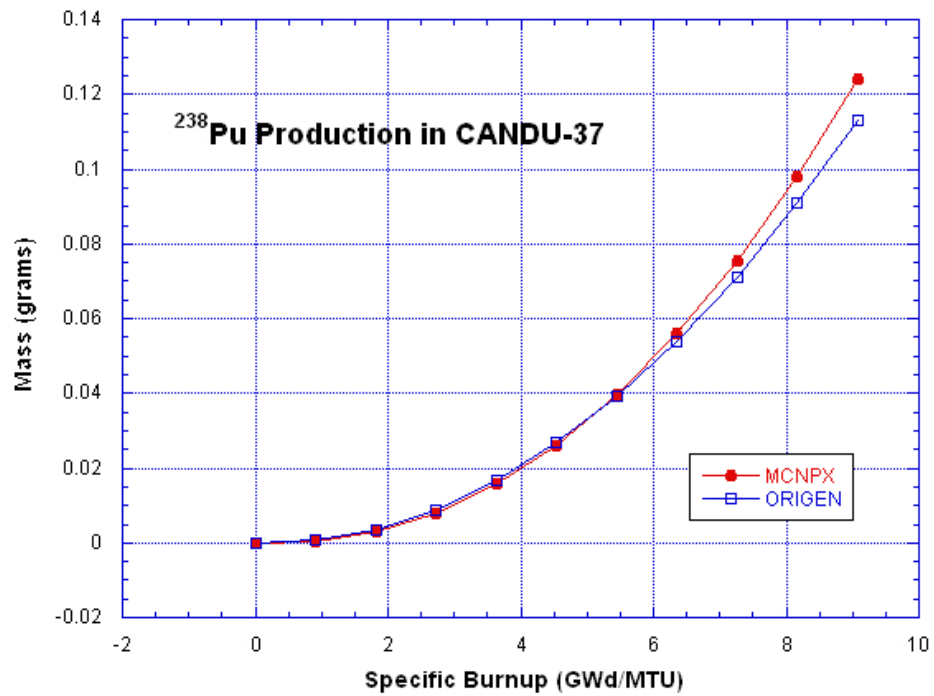


Figure 214: ²³⁸Pu Production in CANDU-37 Model

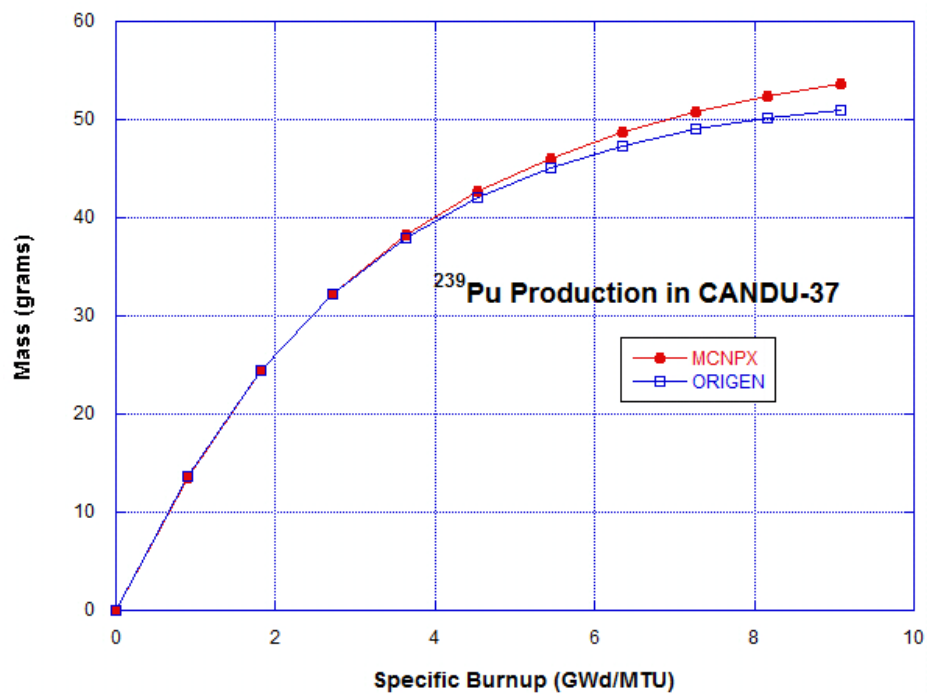


Figure 215: ²³⁹Pu Production in CANDU-37 Model

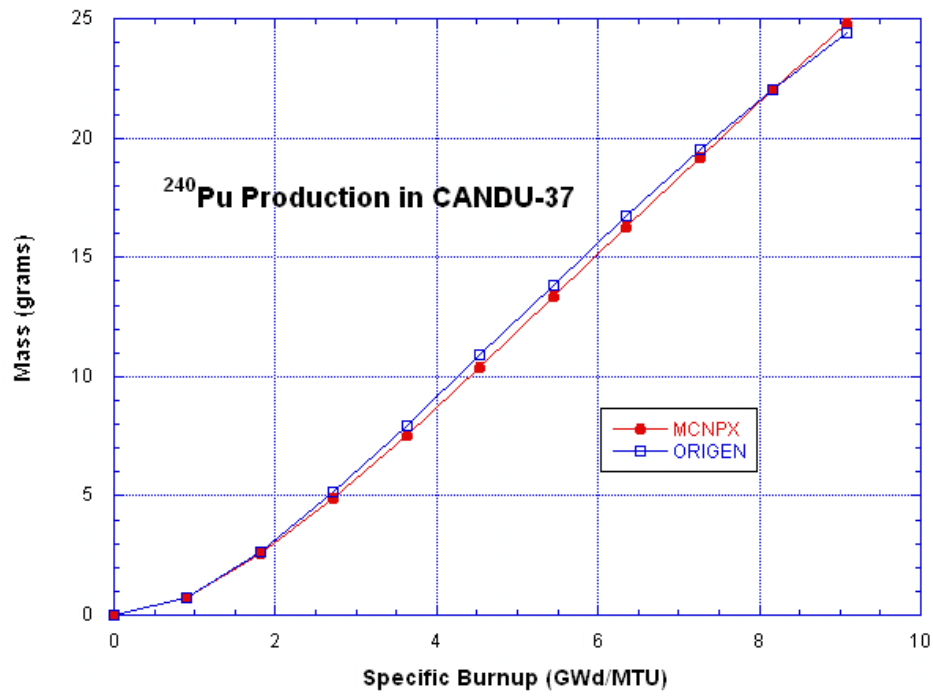


Figure 216: ²⁴⁰Pu Production in CANDU-37 Model

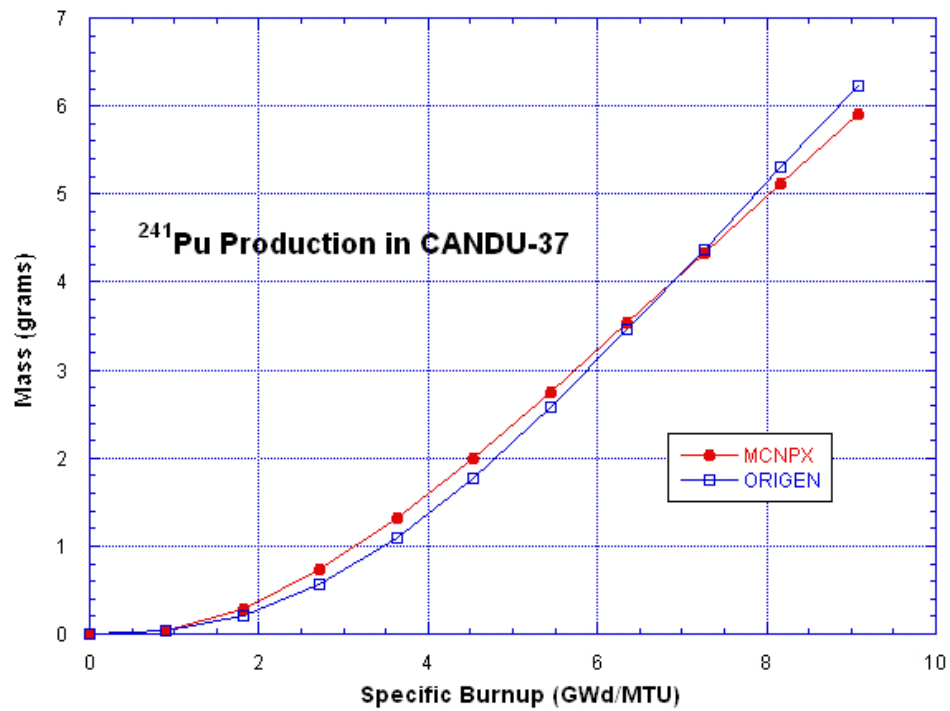


Figure 217: ²⁴¹Pu Production in CANDU-37 Model

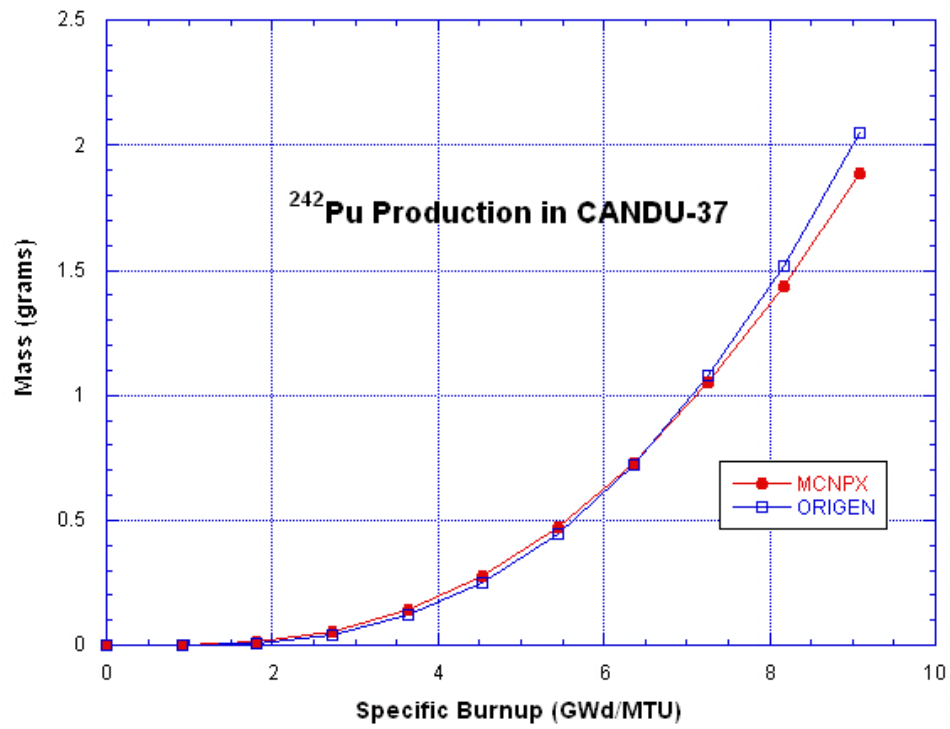


Figure 218: ²⁴²Pu Production in CANDU-37 Model

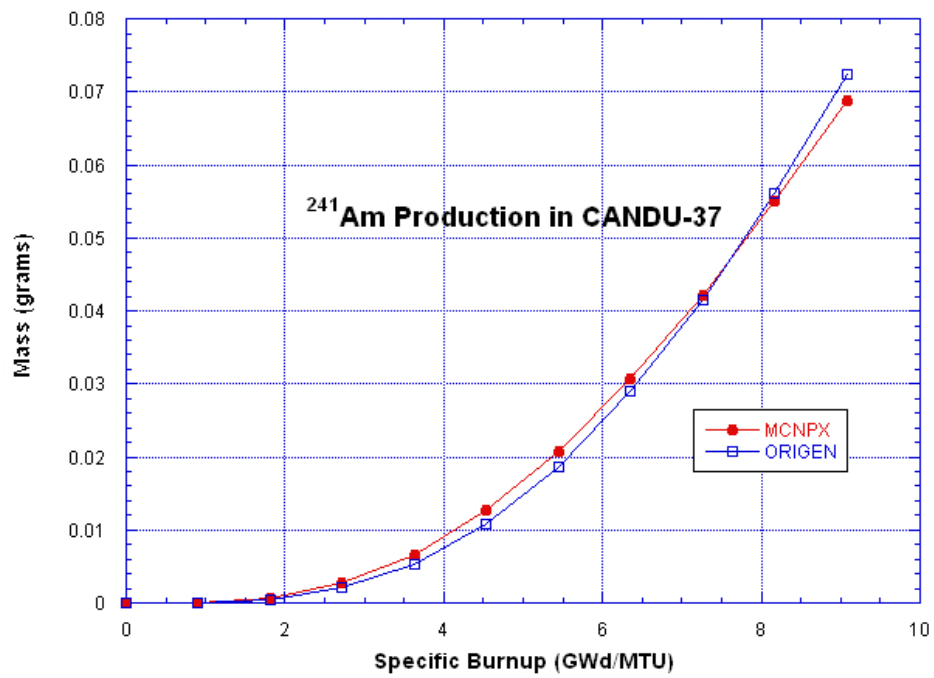


Figure 219: ²⁴¹Am Production in CANDU-37 Model

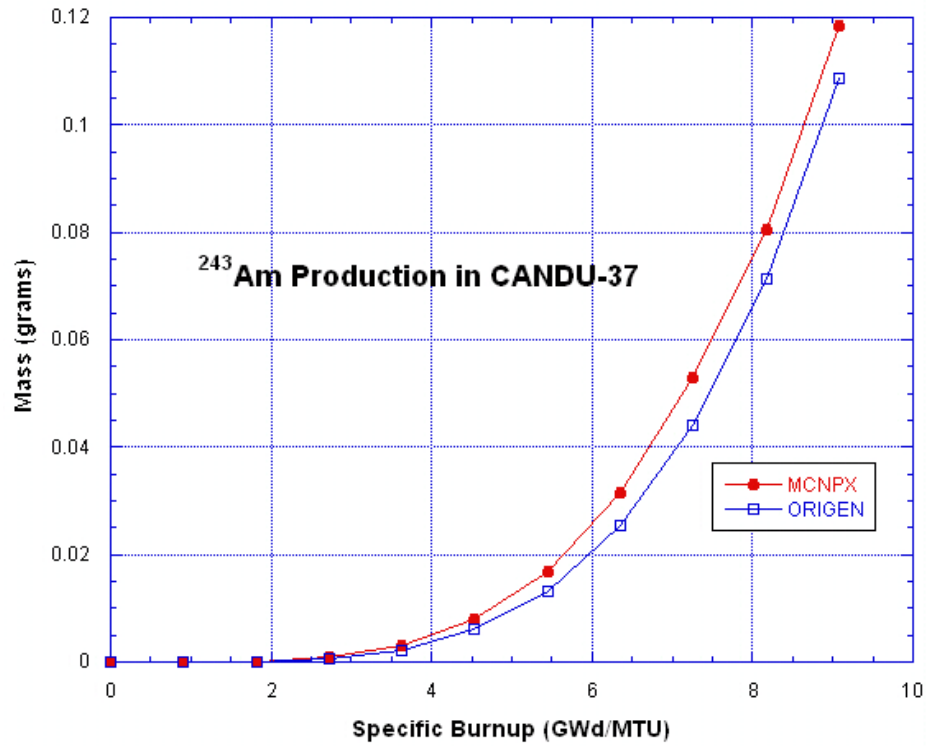


Figure 220: ²⁴³Am Production in CANDU-37 Model

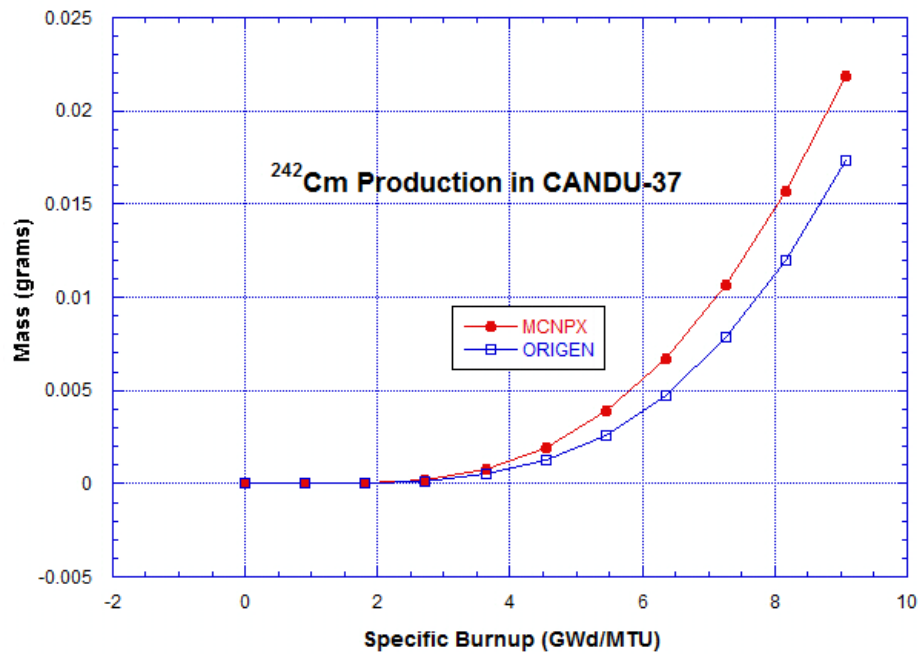


Figure 221: ²⁴²Cm Production in CANDU-37 Model

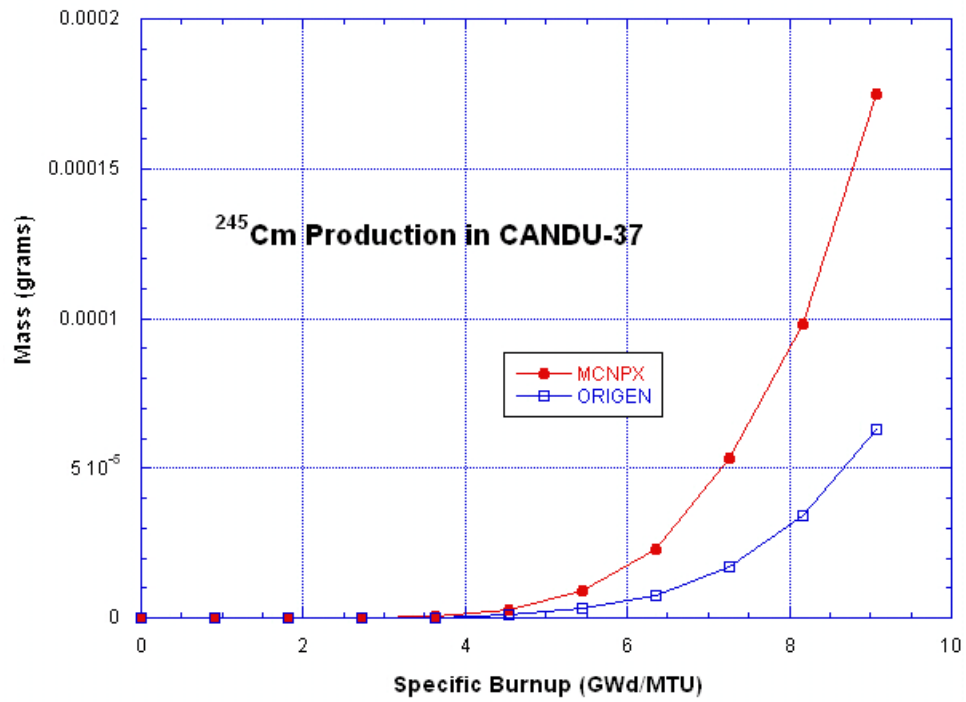


Figure 222: ²⁴⁵Cm Production in CANDU-37 Model

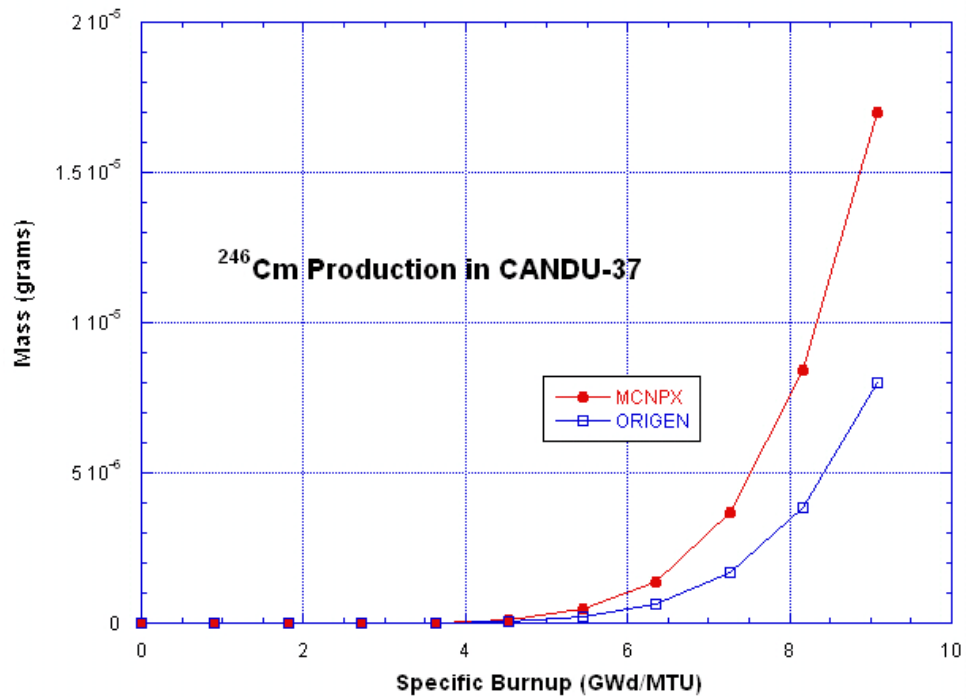


Figure 223: ²⁴⁶Cm Production in CANDU-37 Model

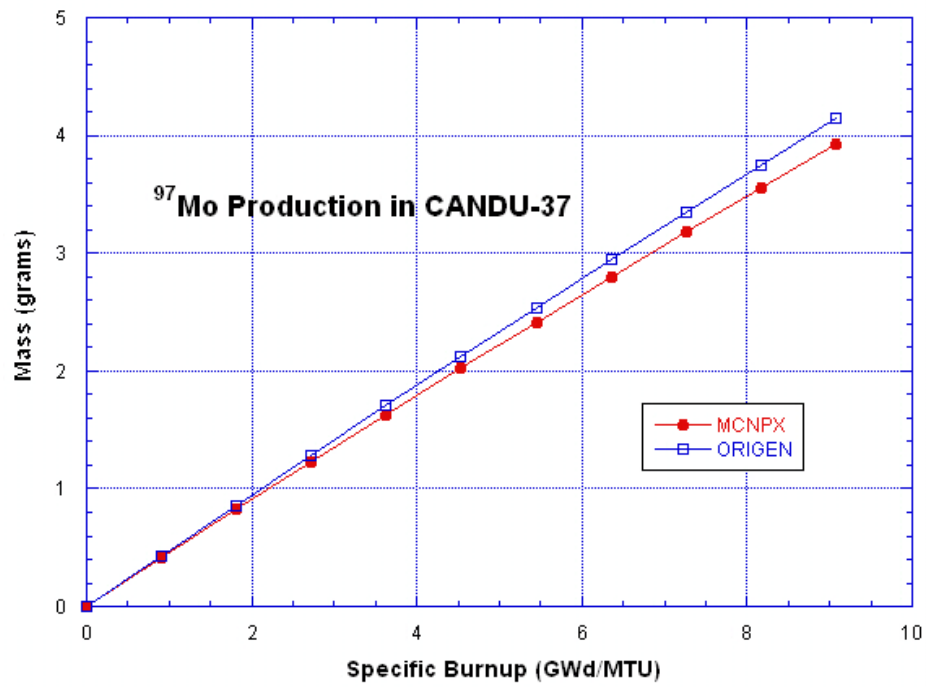


Figure 224: ⁹⁷Mo Production in CANDU-37 Model

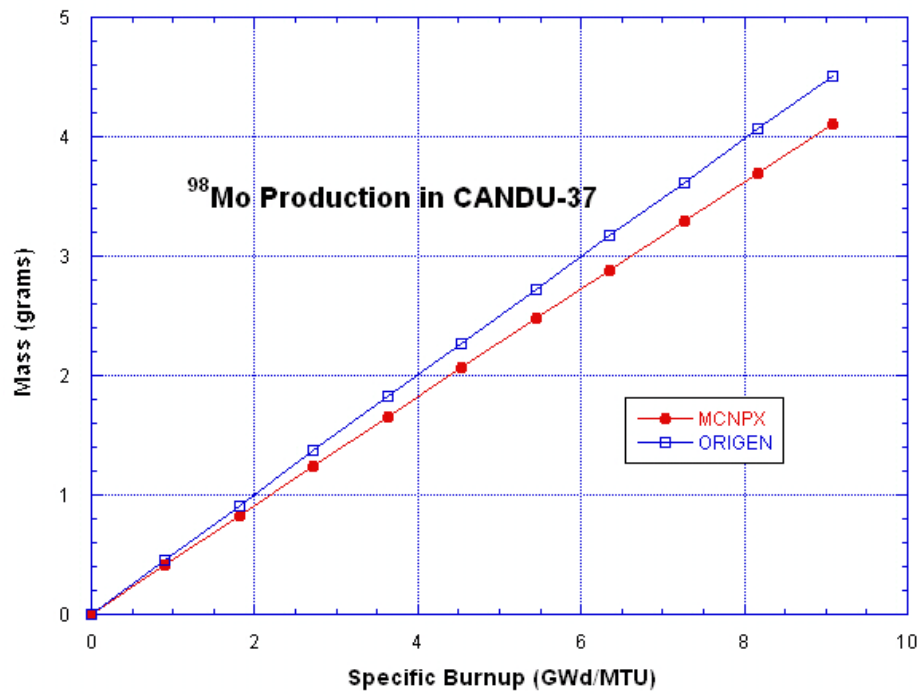


Figure 225: ⁹⁸Mo Production in CANDU-37 Model

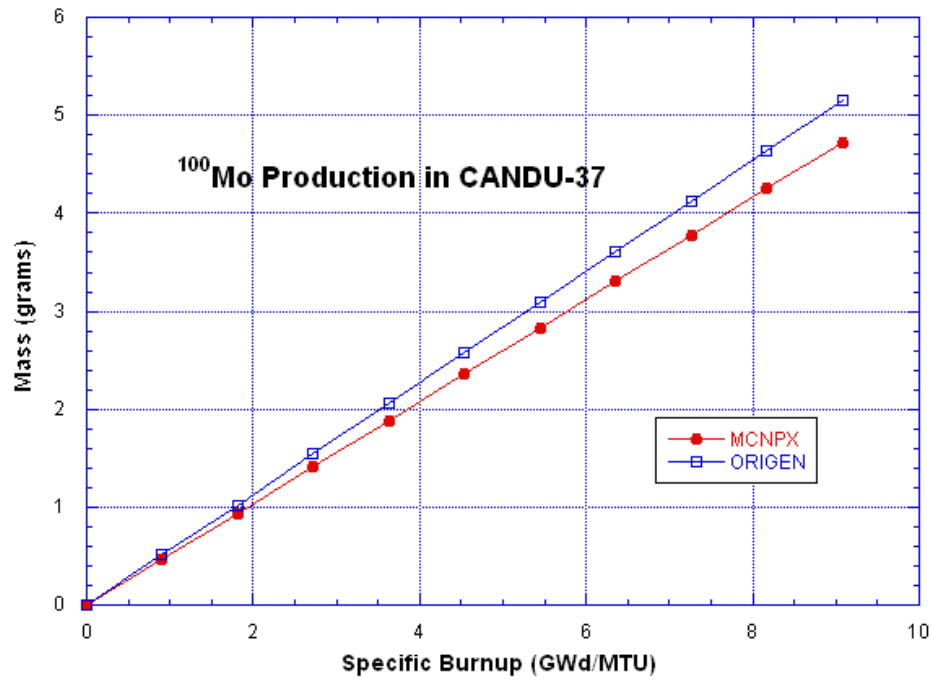


Figure 226: ¹⁰⁰Mo Production in CANDU-37 Model

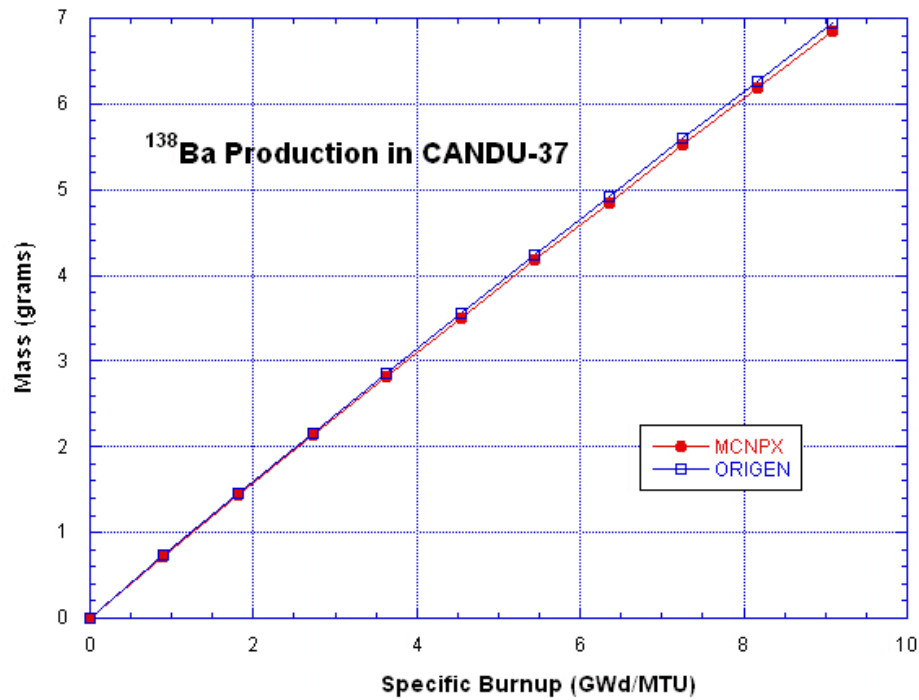


Figure 227: ¹³⁸Ba Production in CANDU-37 Model

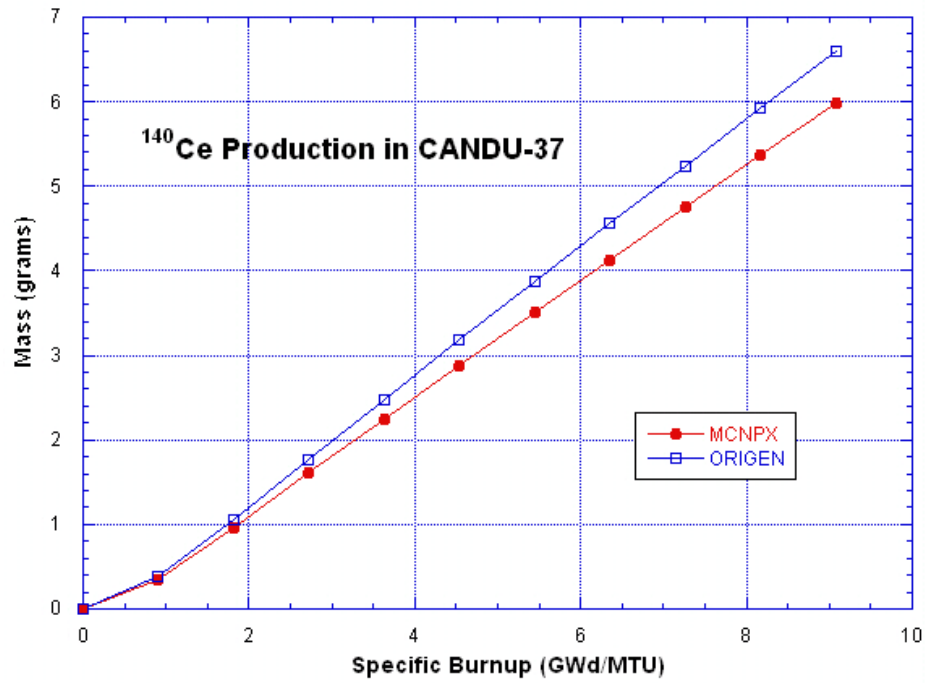


Figure 228: ¹⁴⁰Ce Production in CANDU-37 Model

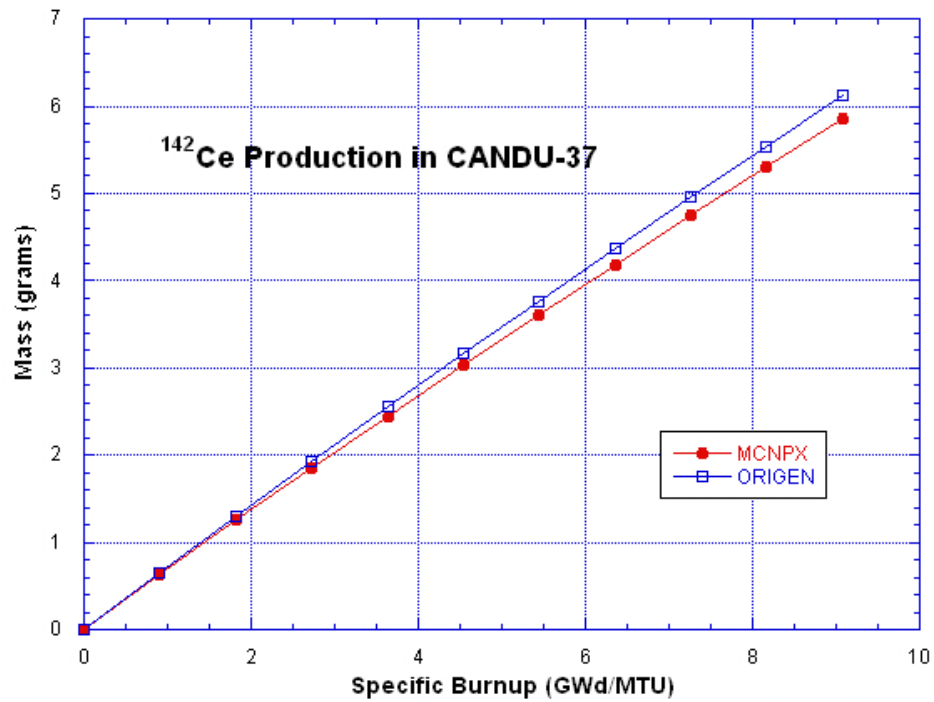


Figure 229: ¹⁴²Ce Production in CANDU-37 Model

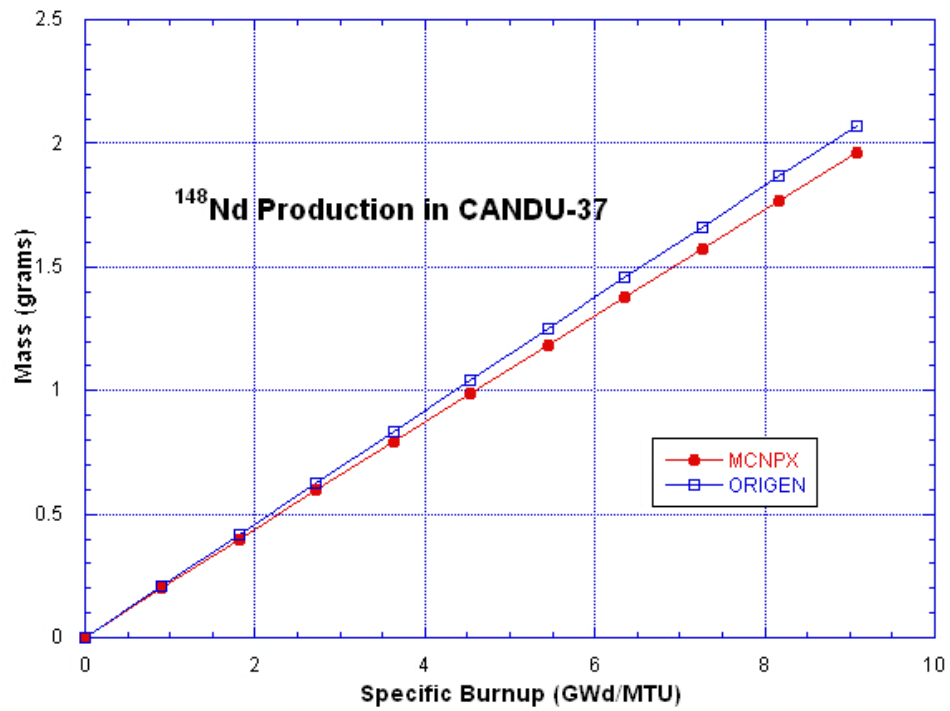


Figure 230: ¹⁴⁸Nd Production in CANDU-37 Model

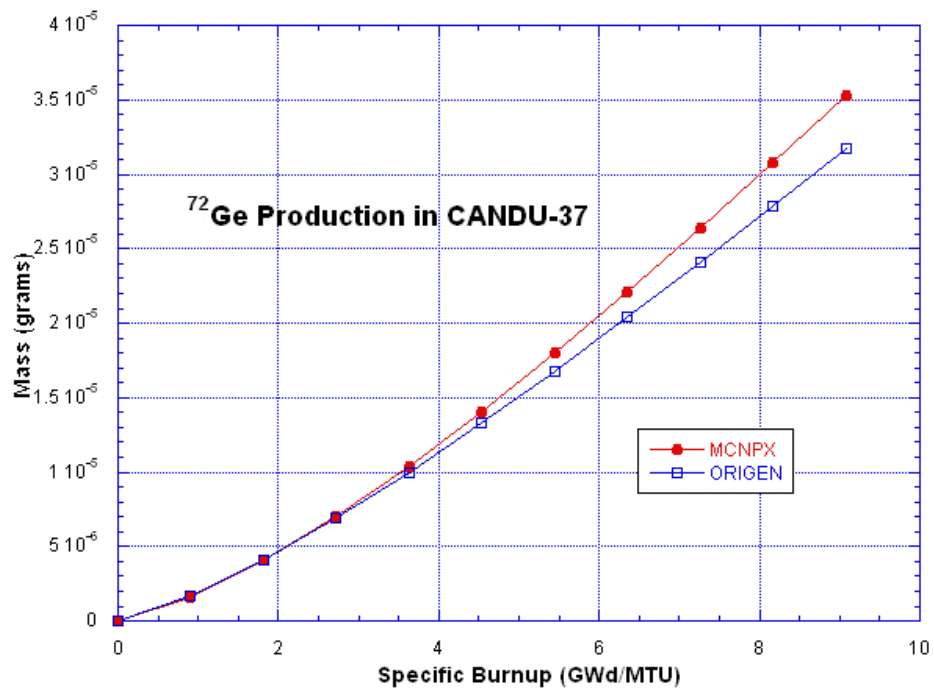


Figure 231: ⁷²Ge Production in CANDU-37 Model

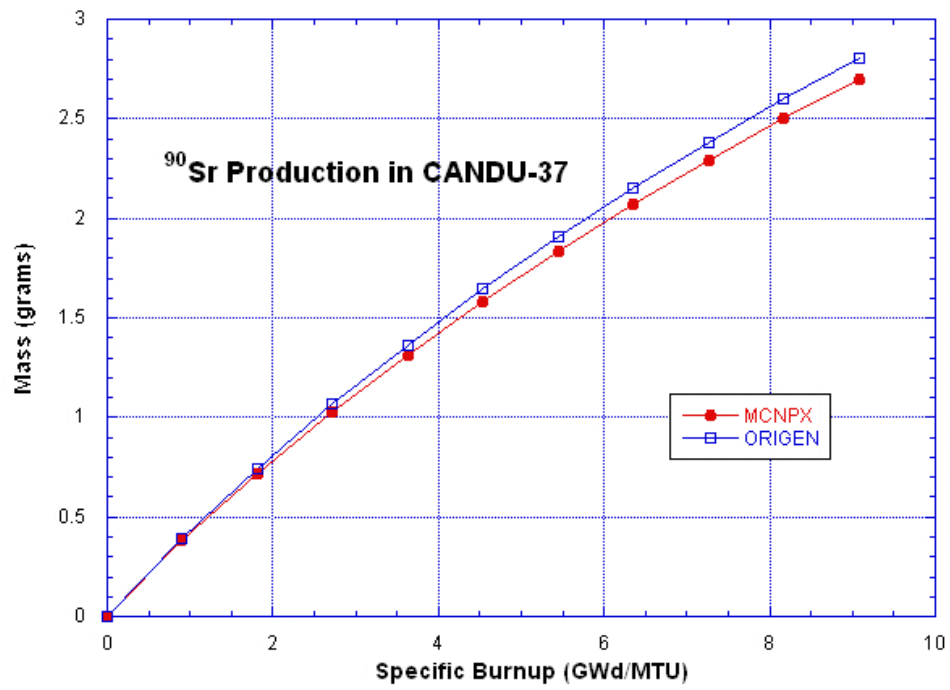


Figure 232: ⁹⁰Sr Production in CANDU-37 Model

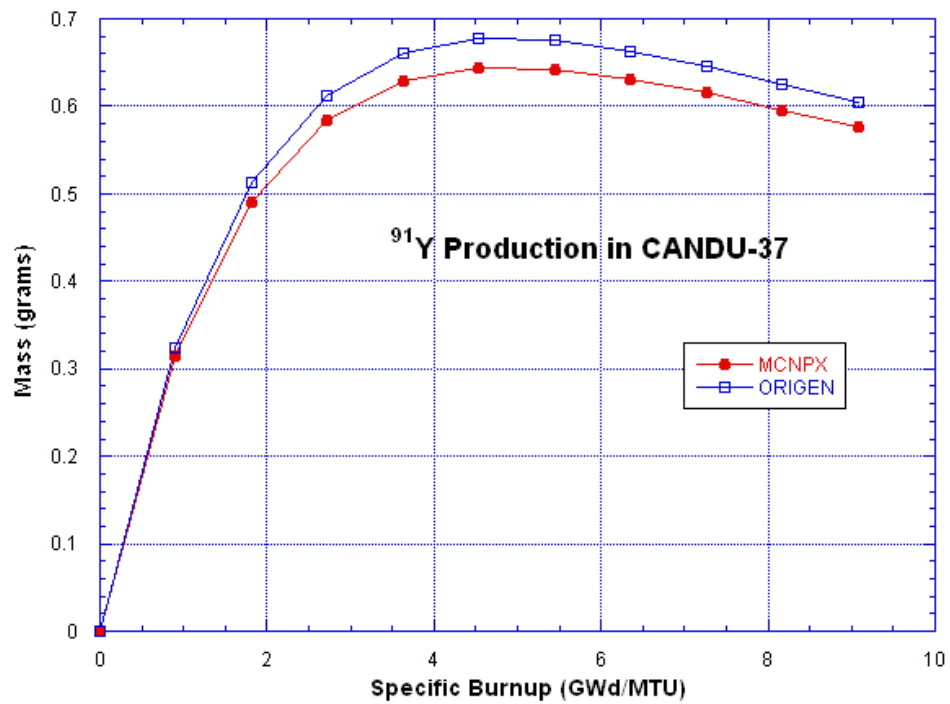


Figure 233: ⁹¹Y Production in CANDU-37 Model

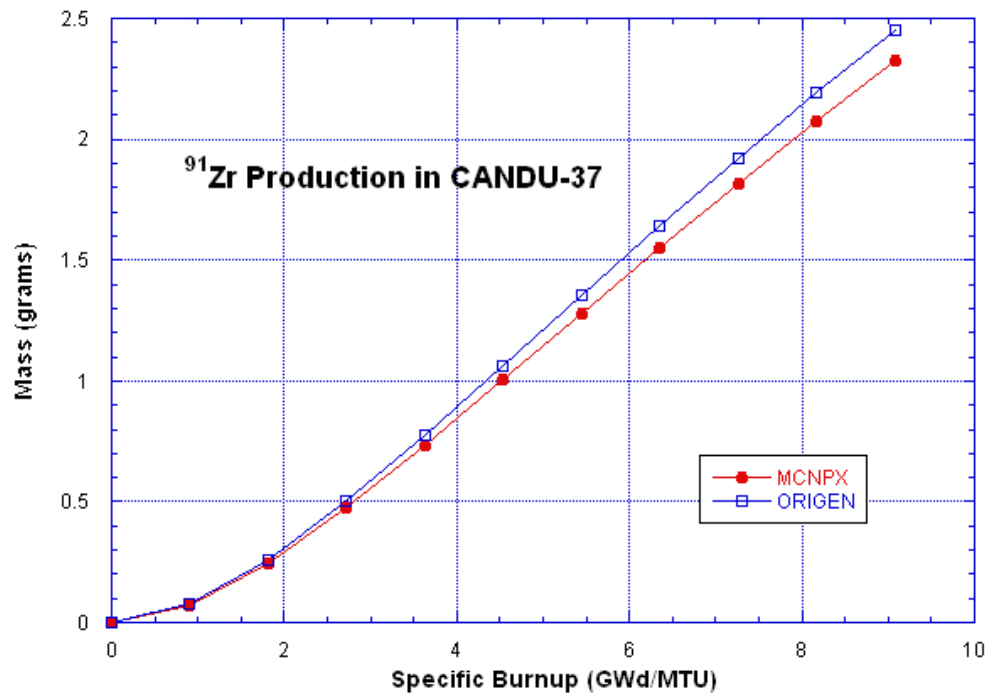


Figure 234: ⁹¹Zr Production in CANDU-37 Model

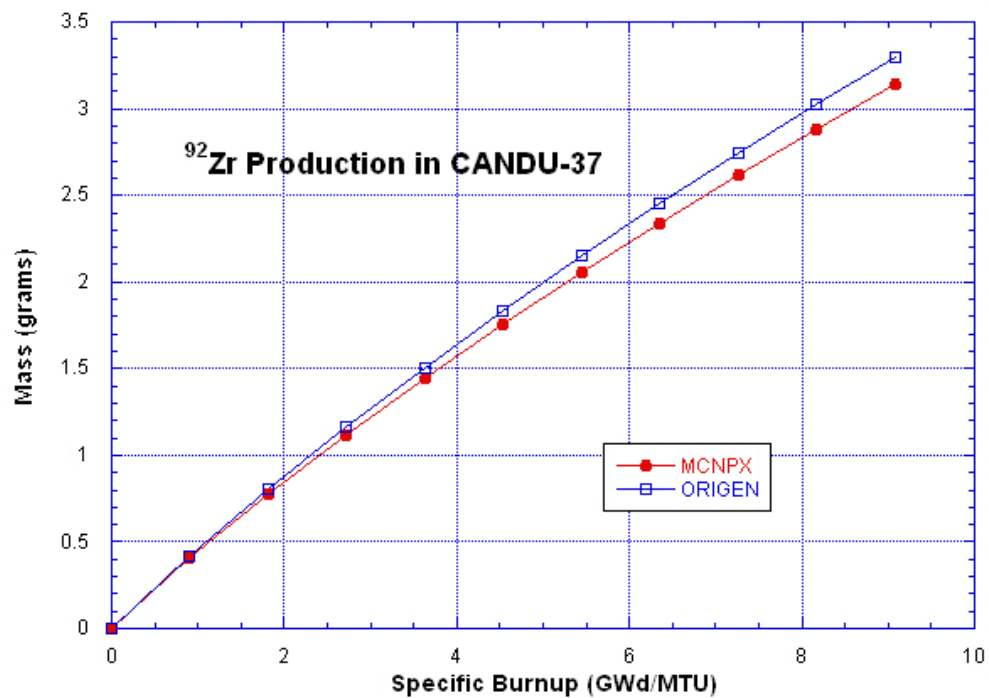


Figure 235: ⁹²Zr Production in CANDU-37 Model

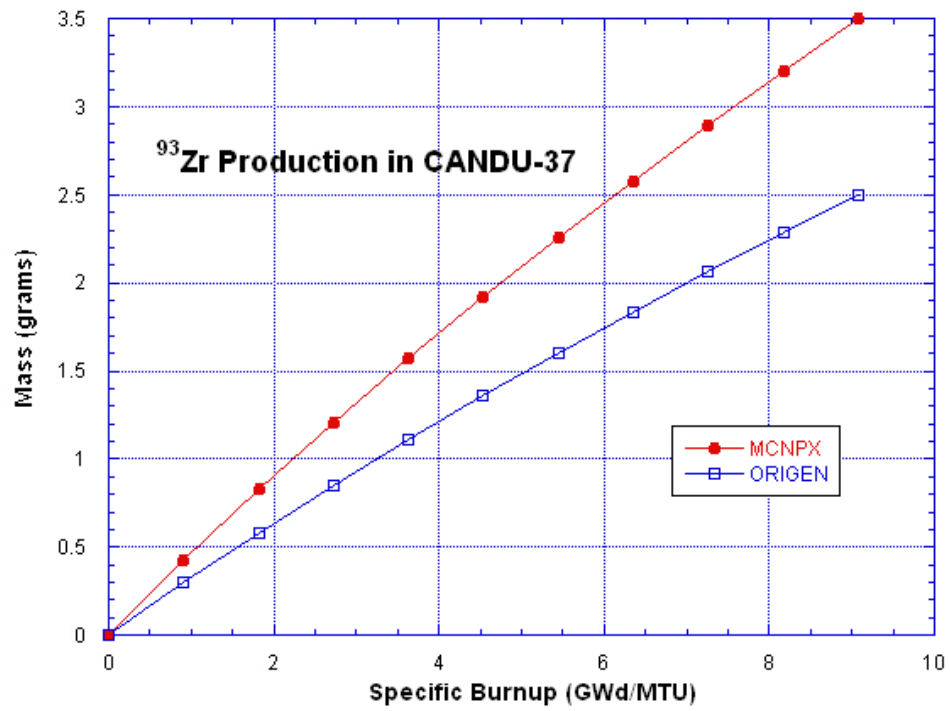


Figure 236: ⁹³Zr Production in CANDU-37 Model

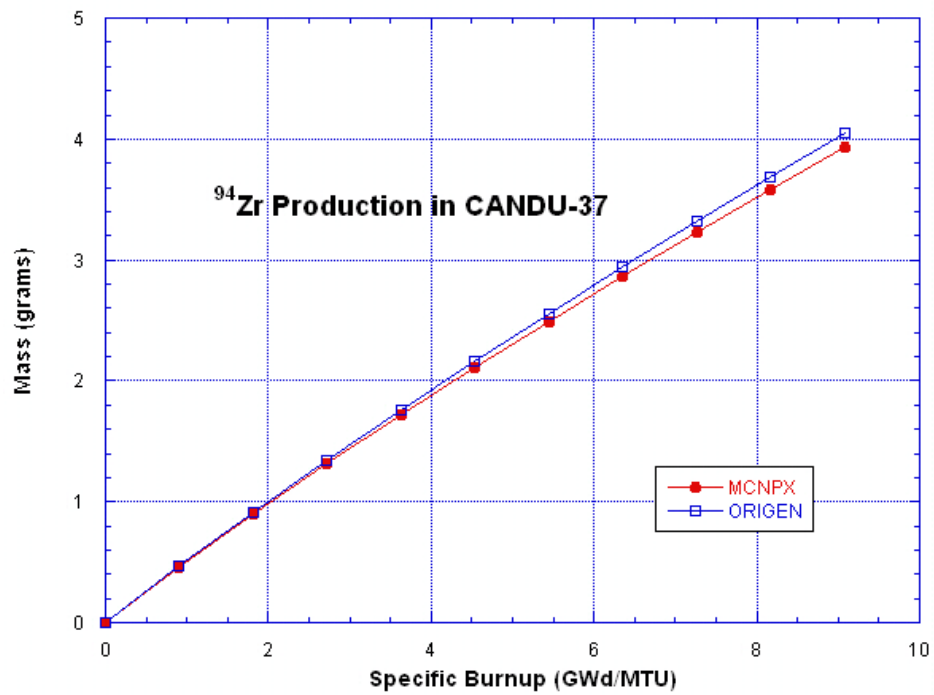


Figure 237: ⁹⁴Zr Production in CANDU-37 Model

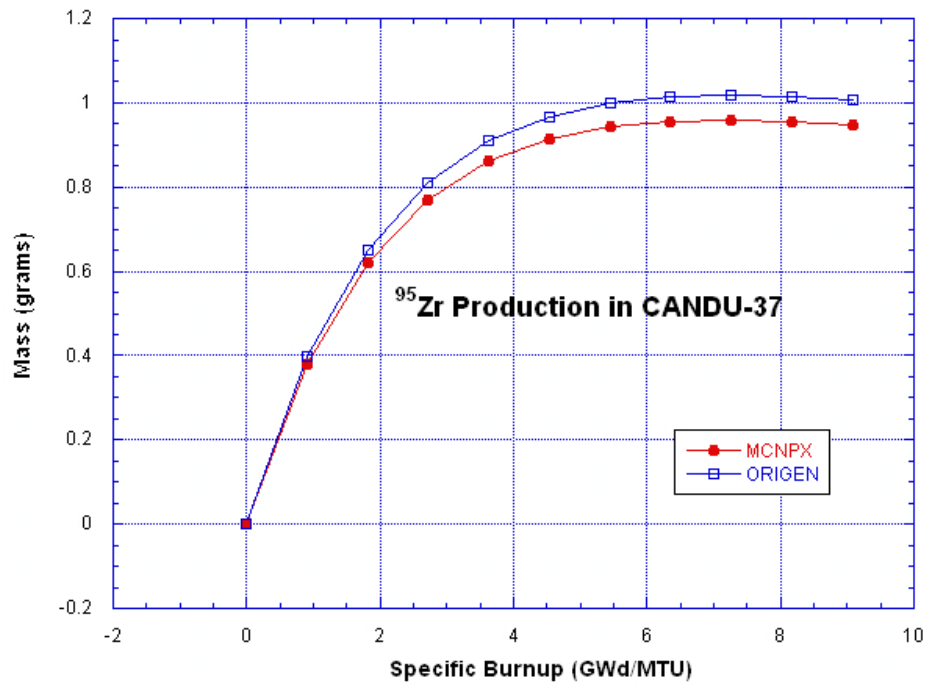


Figure 238: ⁹⁵Zr Production in CANDU-37 Model

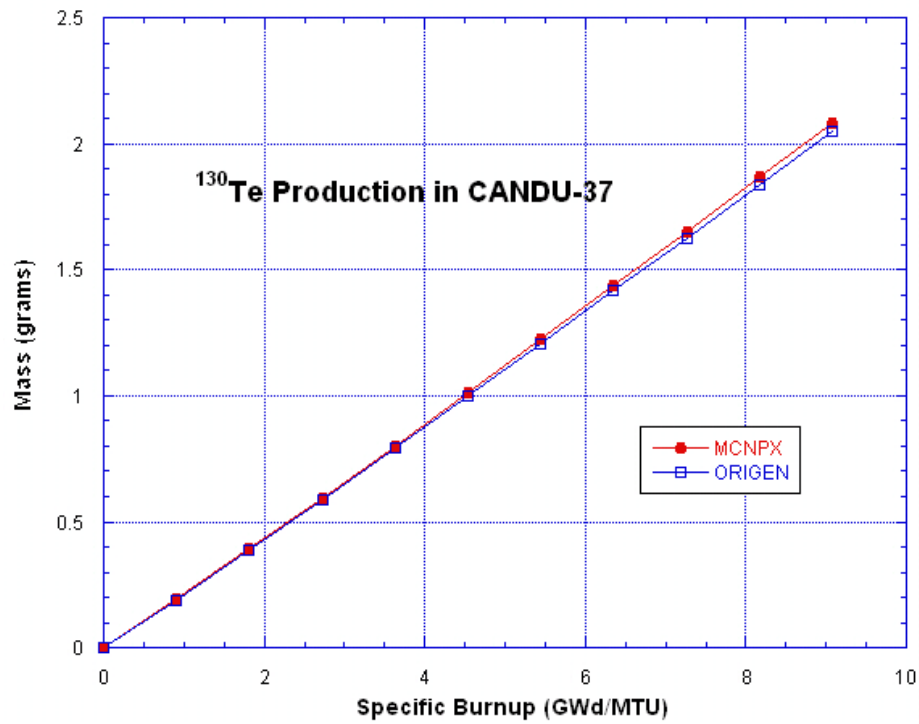


Figure 239: ¹³⁰Te Production in CANDU-37 Model

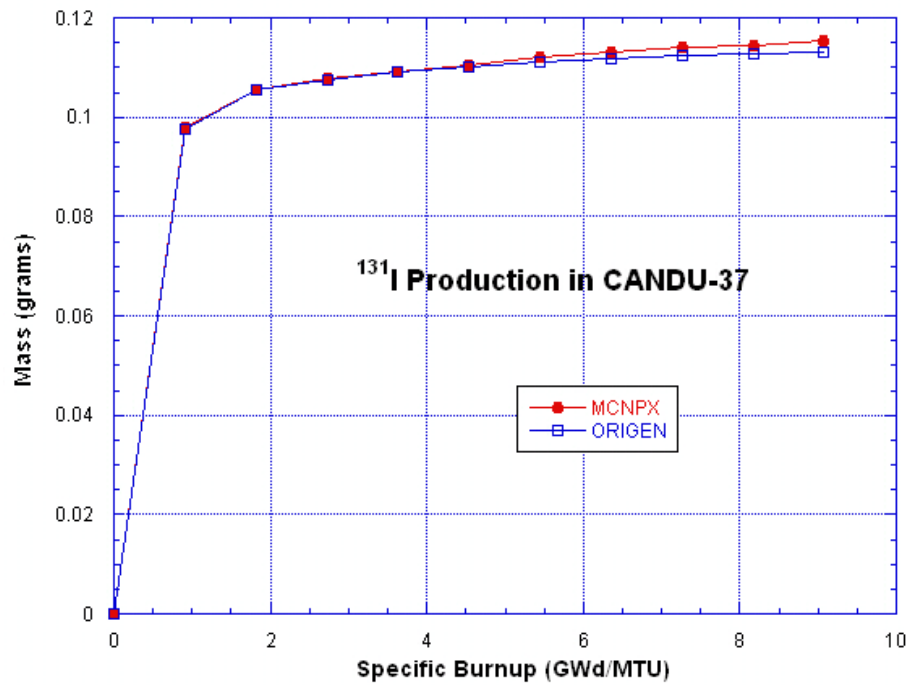


Figure 240: ¹³¹I Production in CANDU-37 Model

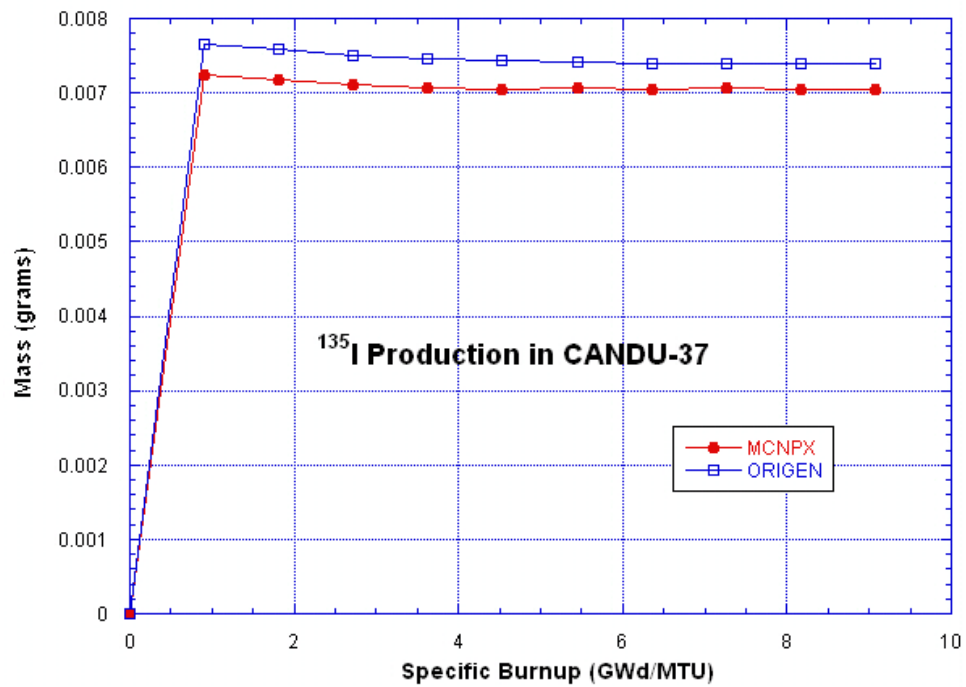


Figure 241: ¹³⁵I Production in CANDU-37 Model

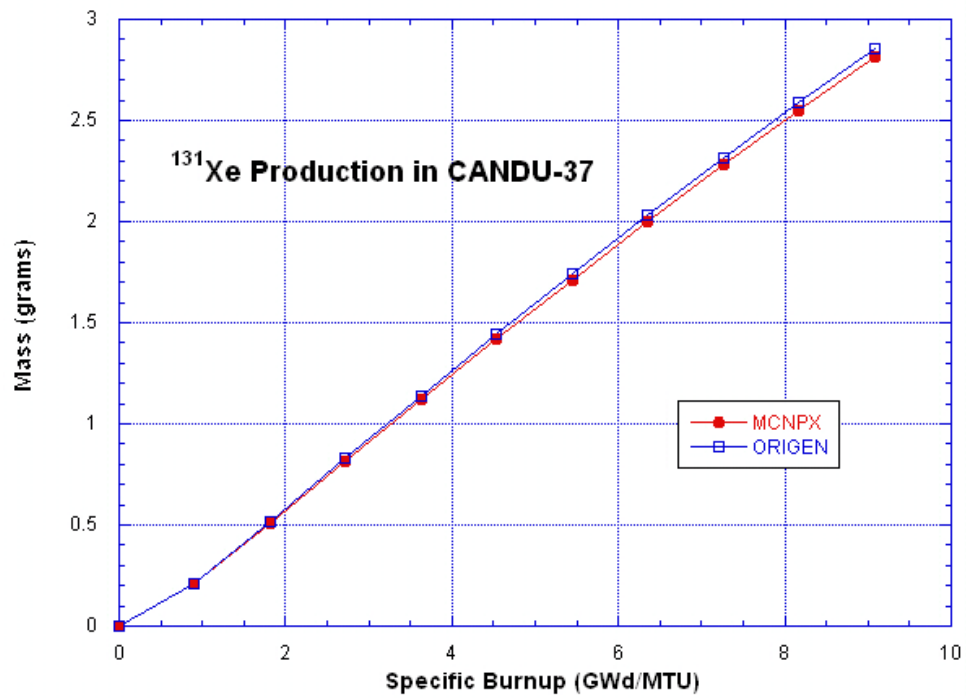


Figure 242: ¹³¹Xe Production in CANDU-37 Model

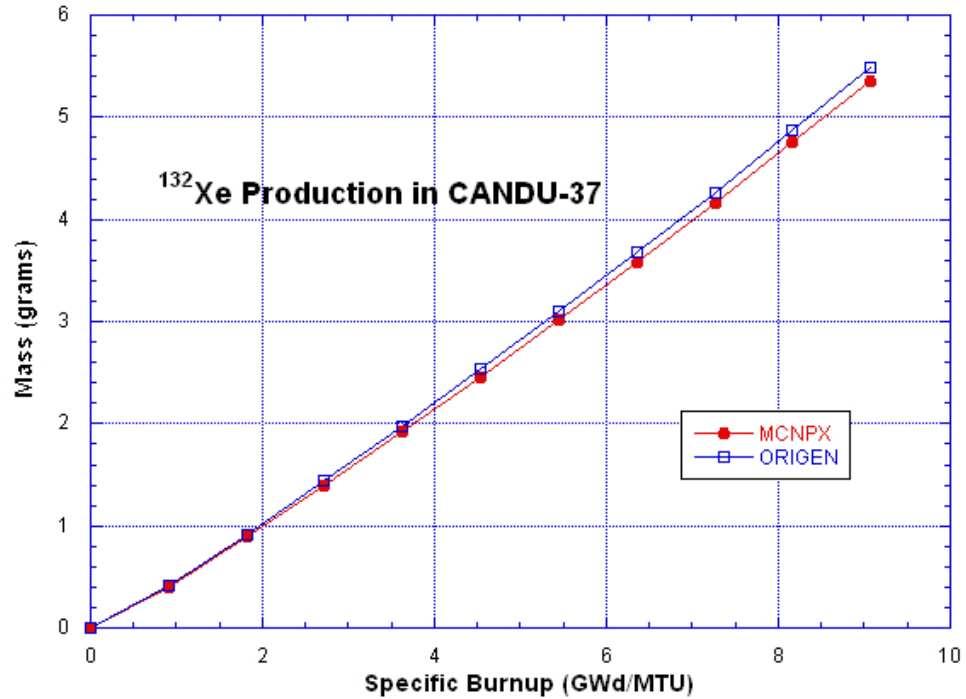


Figure 243: ¹³²Xe Production in CANDU-37 Model

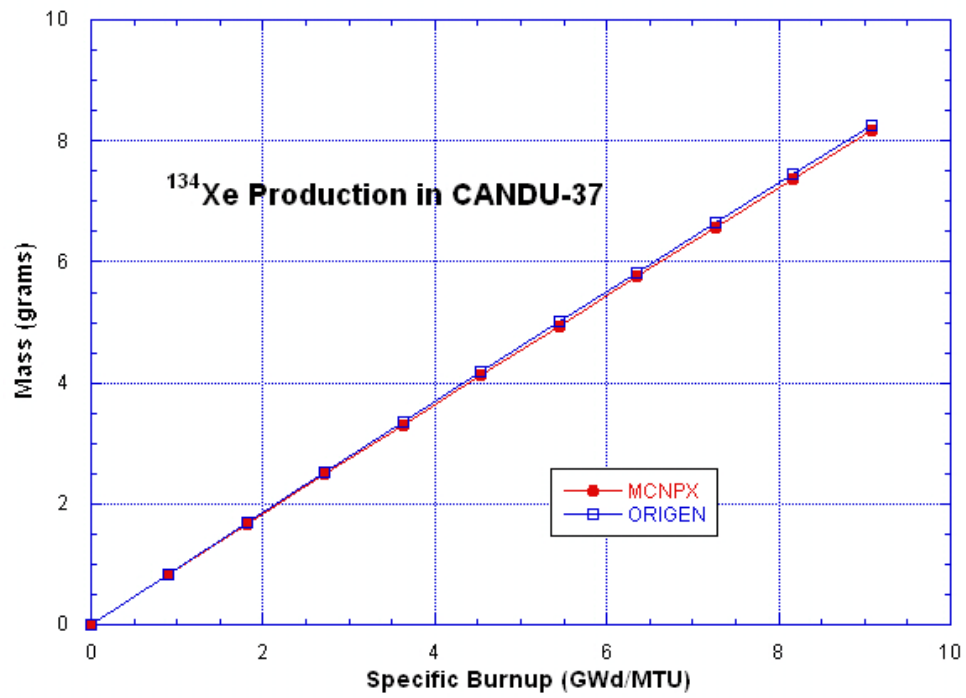


Figure 244: ¹³⁴Xe Production in CANDU-37 Model

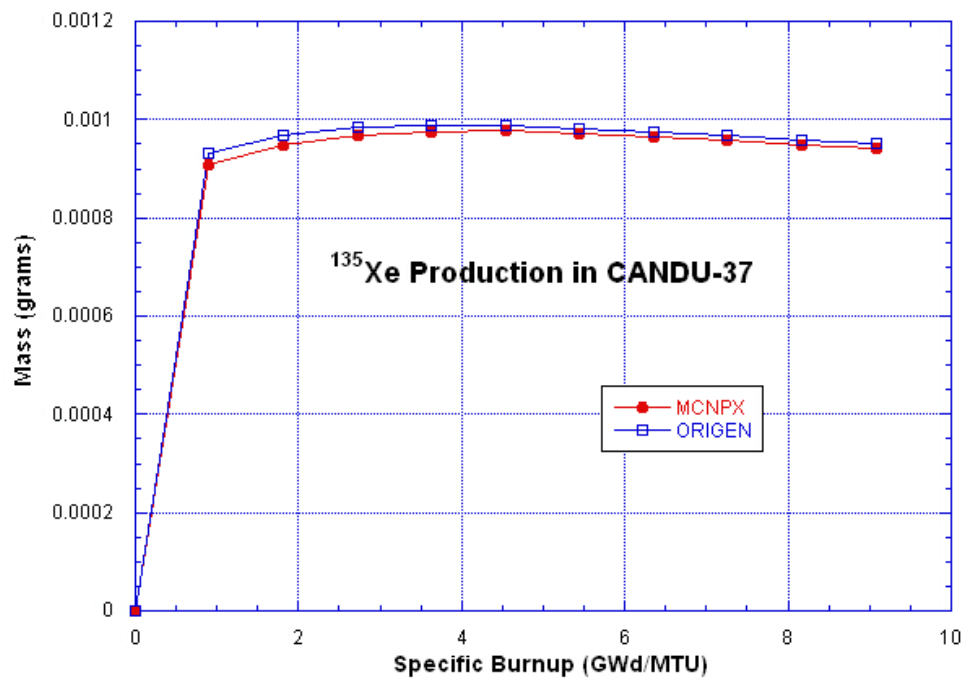


Figure 245: ¹³⁵Xe Production in CANDU-37 Model

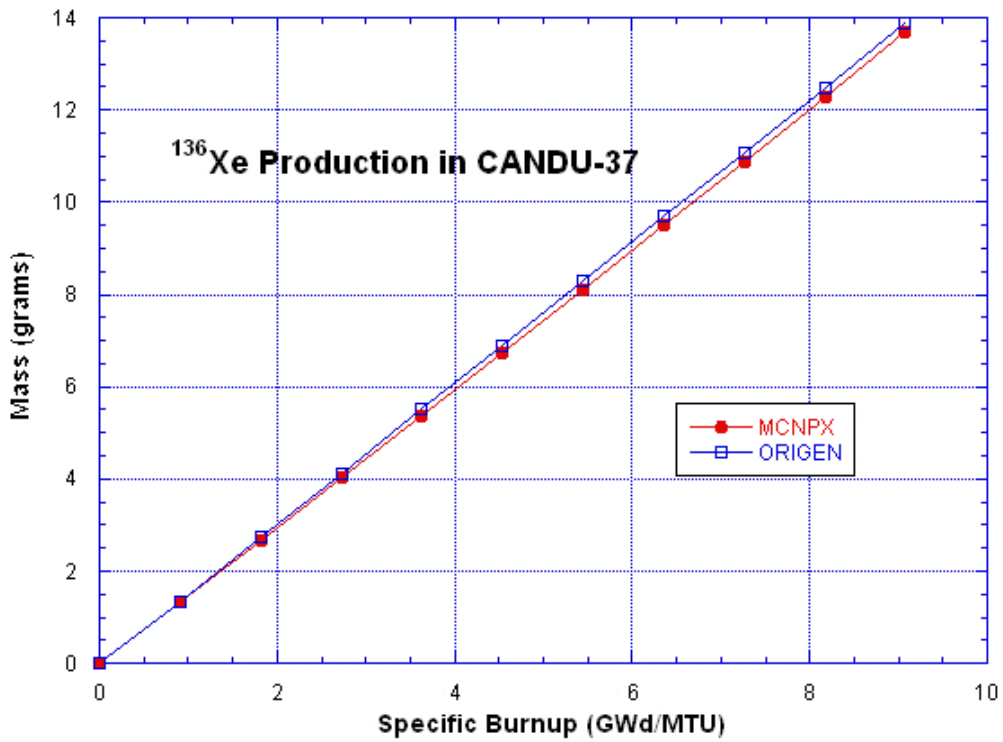


Figure 246: ¹³⁶Xe Production in CANDU-37 Model

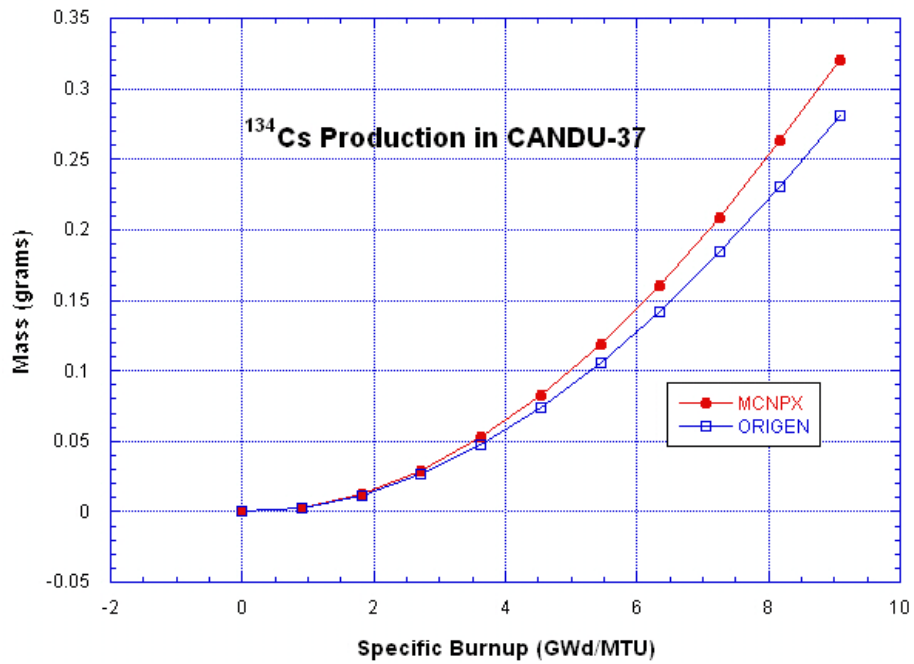


Figure 247: ¹³⁴Cs Production in CANDU-37 Model

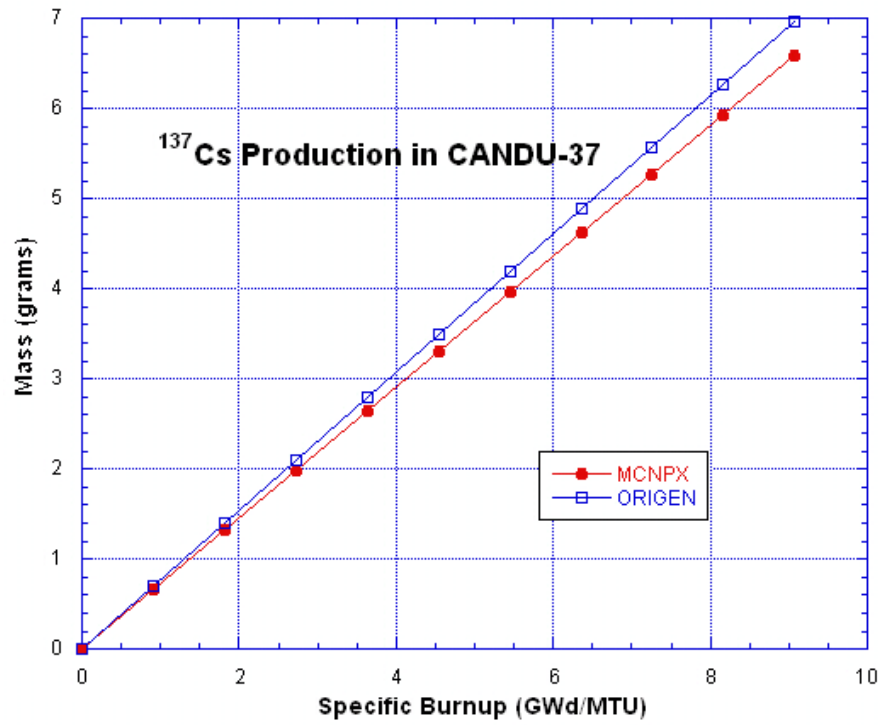


Figure 248: ¹³⁷Cs Production in CANDU-37 Model

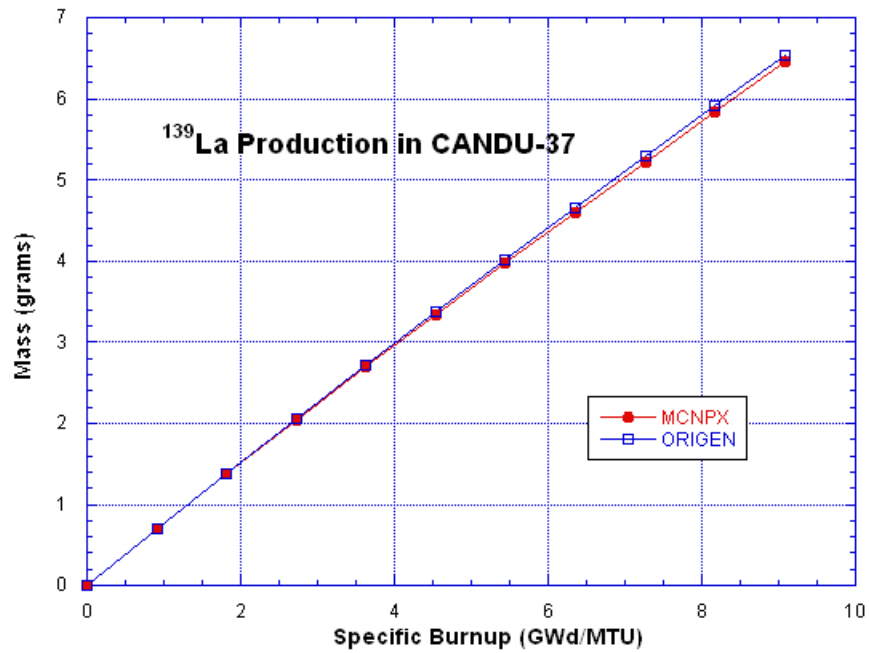


Figure 249: ¹³⁹La Production in CANDU-37 Model

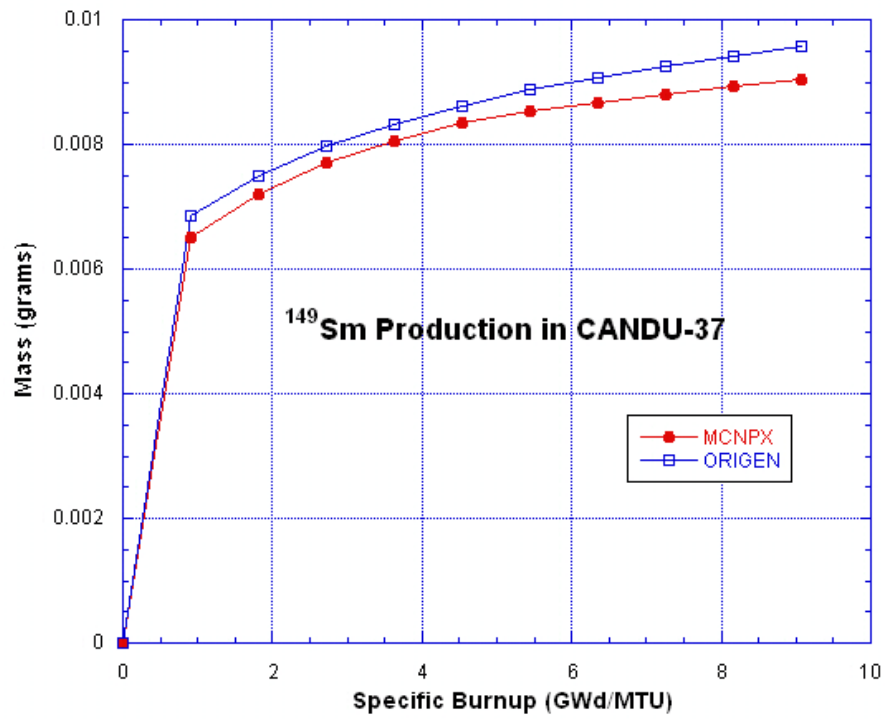


Figure 250: ¹⁴⁹Sm Production in CANDU-37 Model

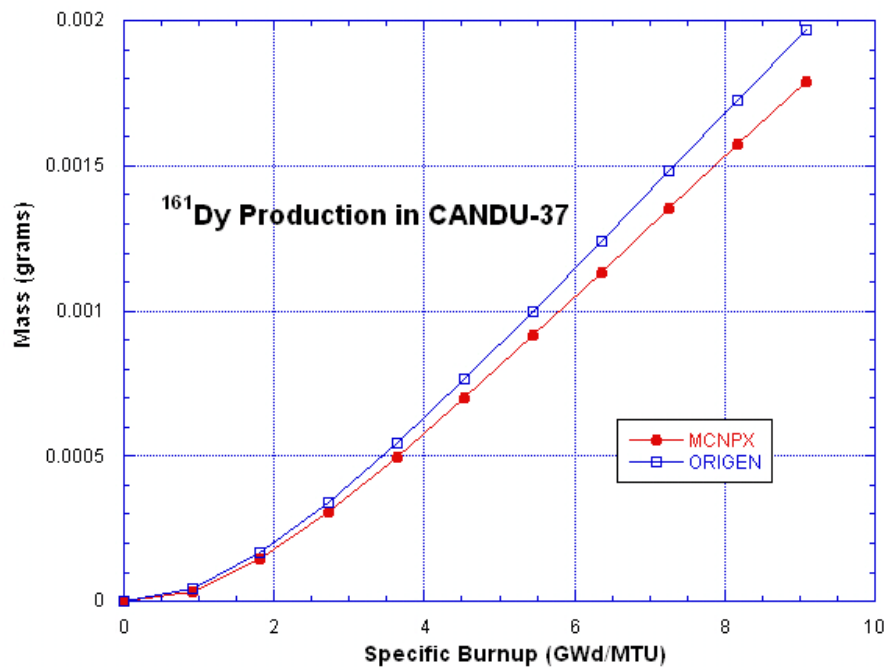


Figure 251: ¹⁶¹Dy Production in CANDU-37 Model

Appendix G: PWR Sensitivity Study Plots of 46 Nuclides of Interest

**PWR Sensitivity Study
Plots of 46 Nuclides of Interest
Rod Pitch Variation**

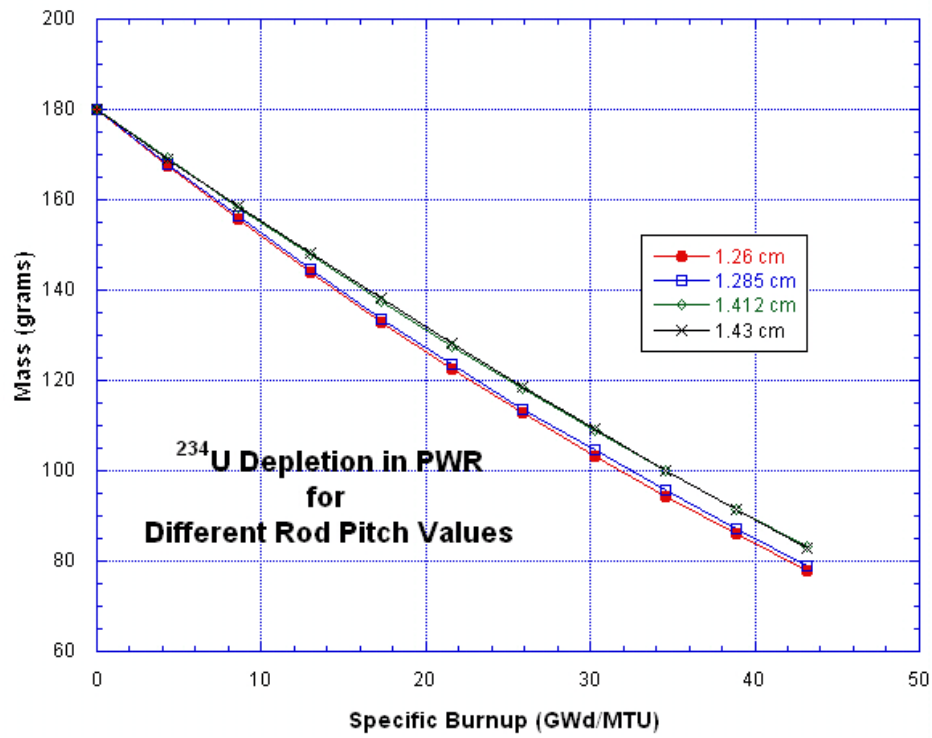


Figure 252: ²³⁴U Depletion in the PWR Model for Different Rod Pitch Values

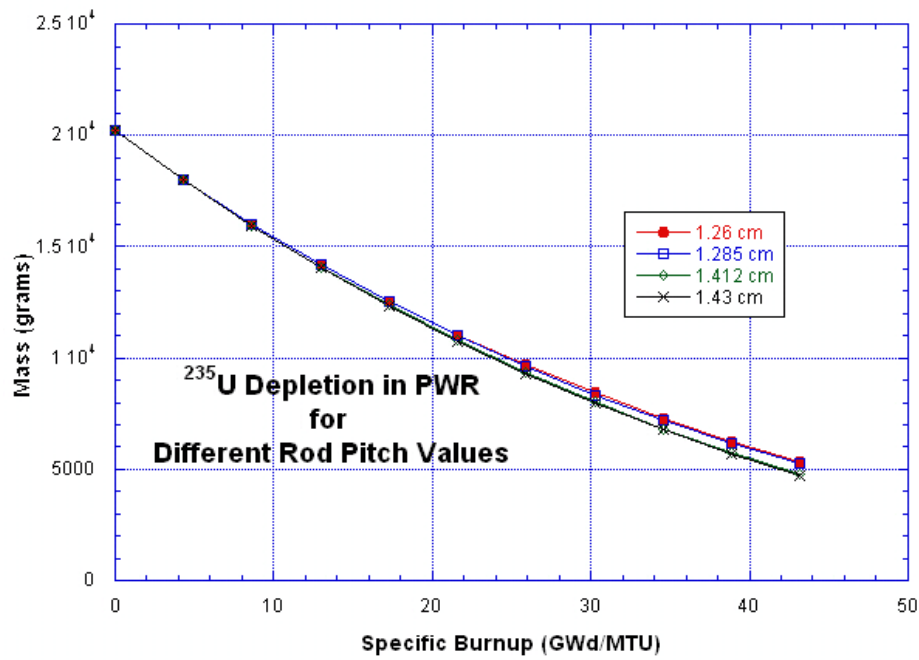


Figure 253: ²³⁵U Depletion in the PWR Model for Different Rod Pitch Values

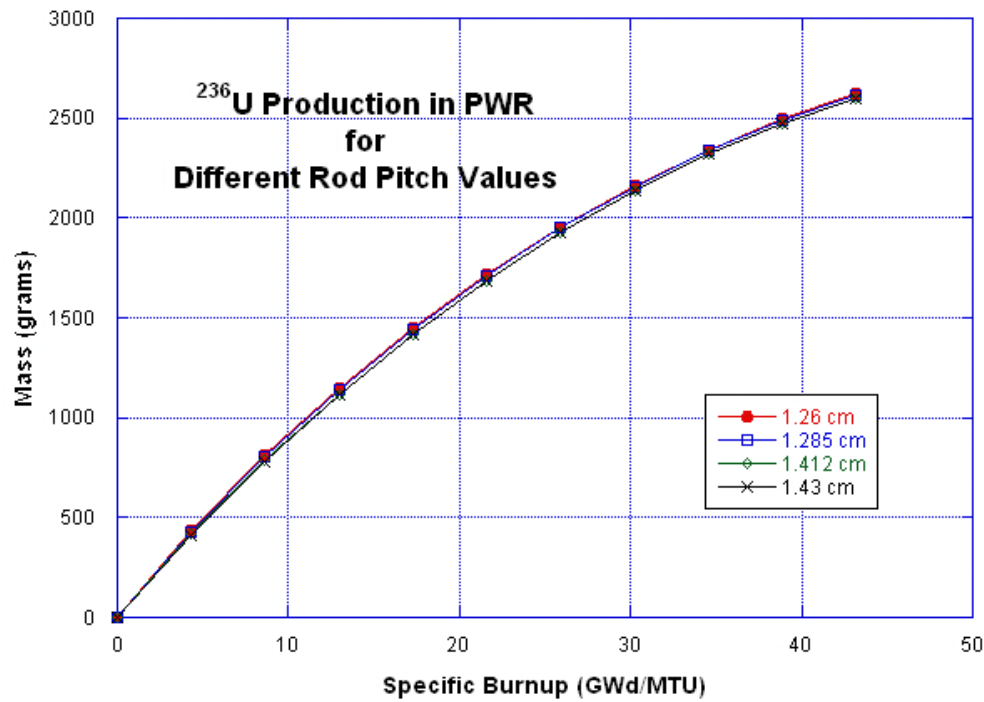


Figure 254: ^{236}U Production in the PWR Model for Different Rod Pitch Values

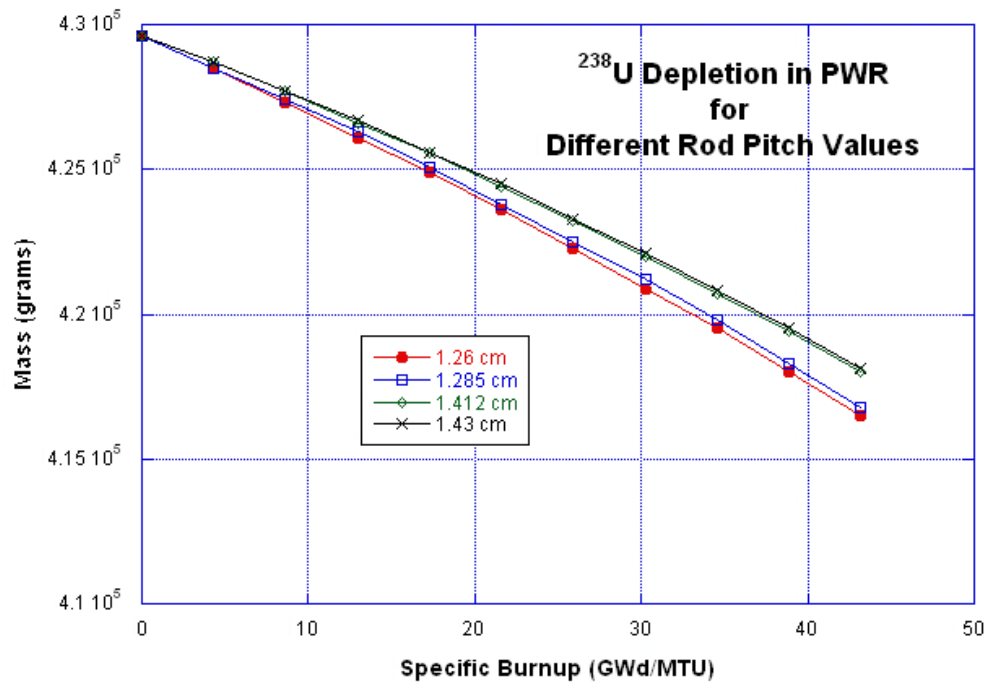


Figure 255: ^{238}U Depletion in the PWR Model for Different Rod Pitch Values

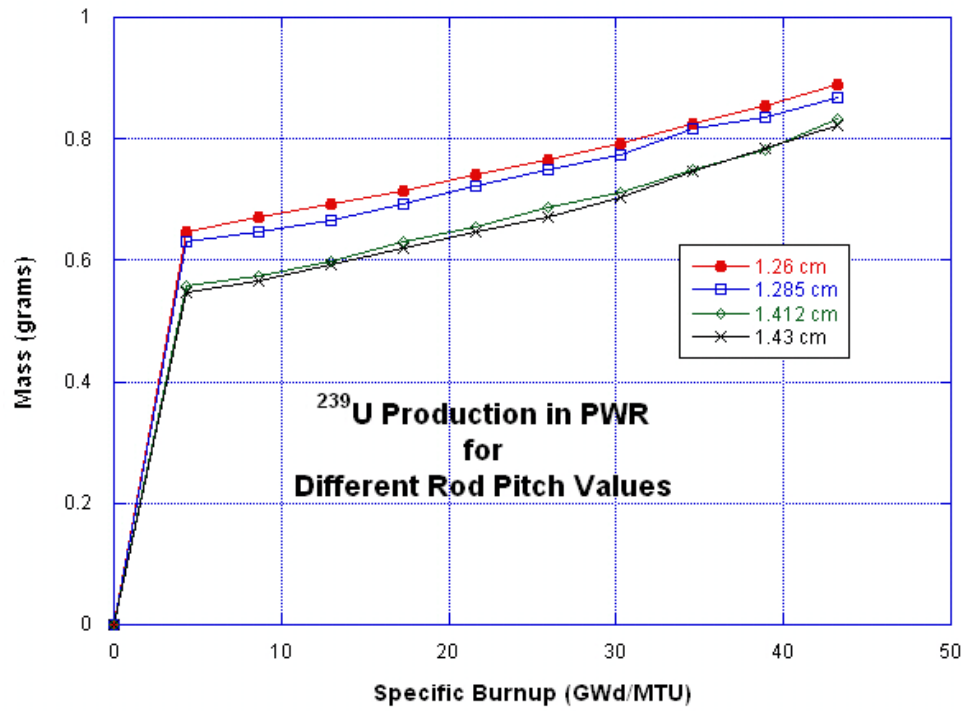


Figure 256: ²³⁹U Production in the PWR Model for Different Rod Pitch Values

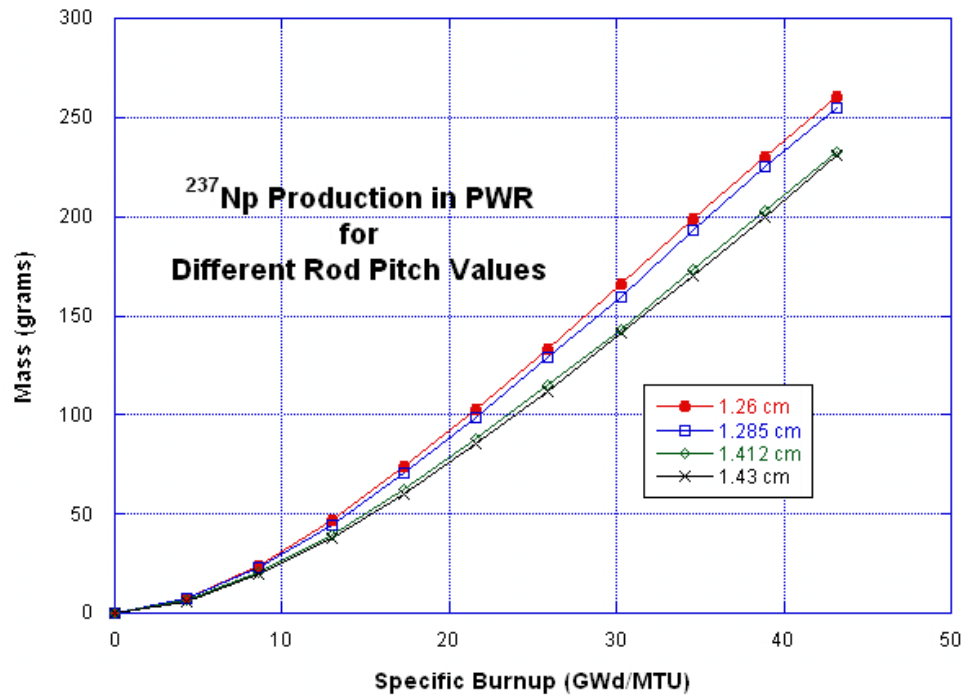


Figure 257: ²³⁷Np Production in the PWR Model for Different Rod Pitch Values

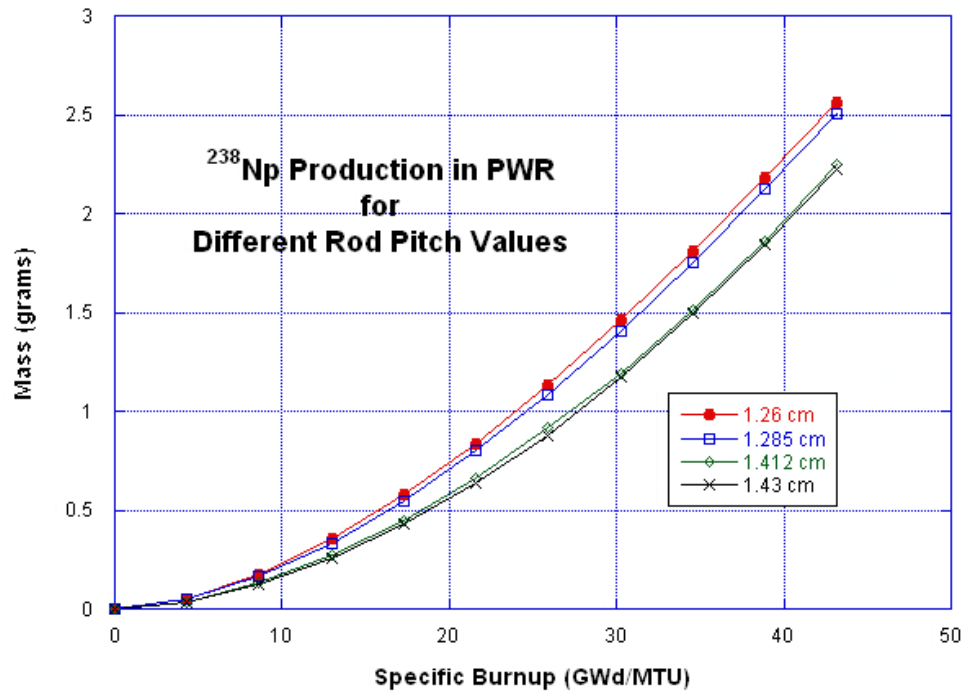


Figure 258: ²³⁸Np Production in the PWR Model for Different Rod Pitch Values

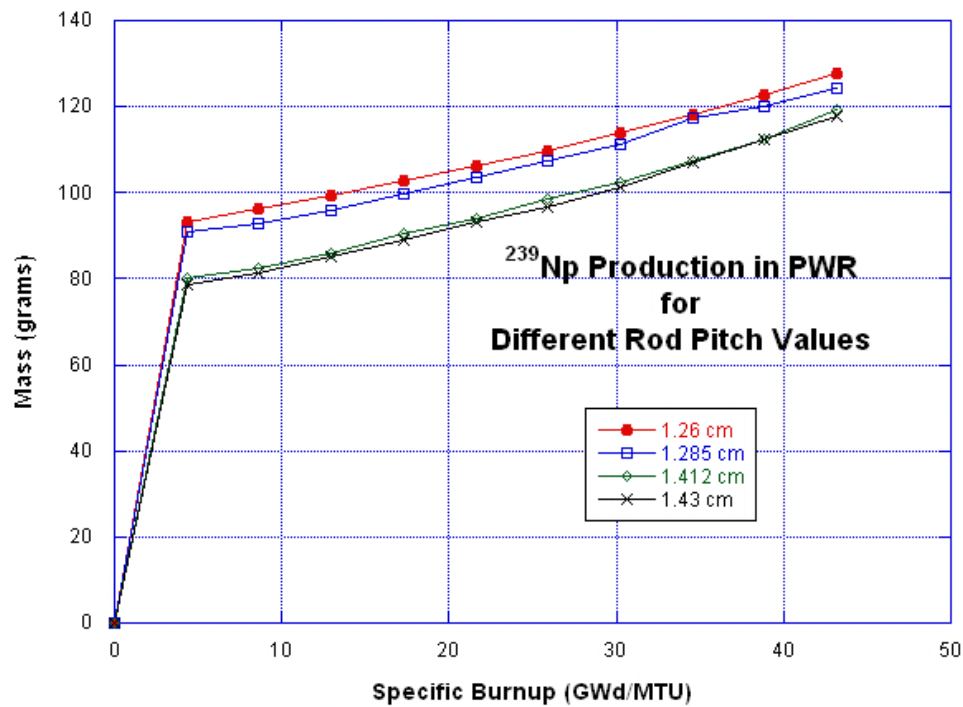


Figure 259: ²³⁹Np Production in the PWR Model for Different Rod Pitch Values

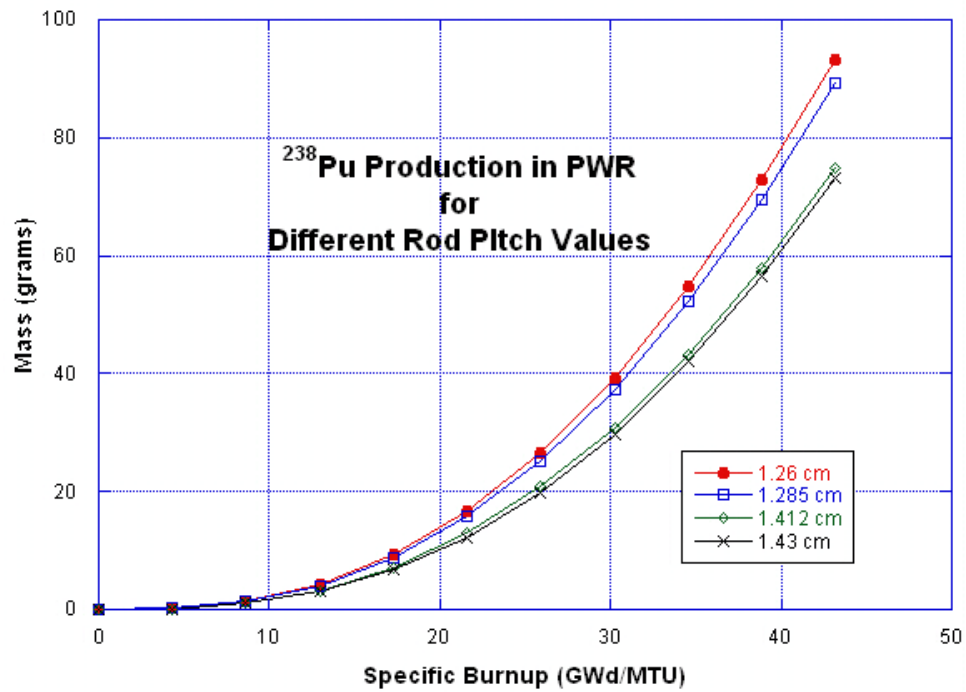


Figure 260: ²³⁸Pu Production in the PWR Model for Different Rod Pitch Values

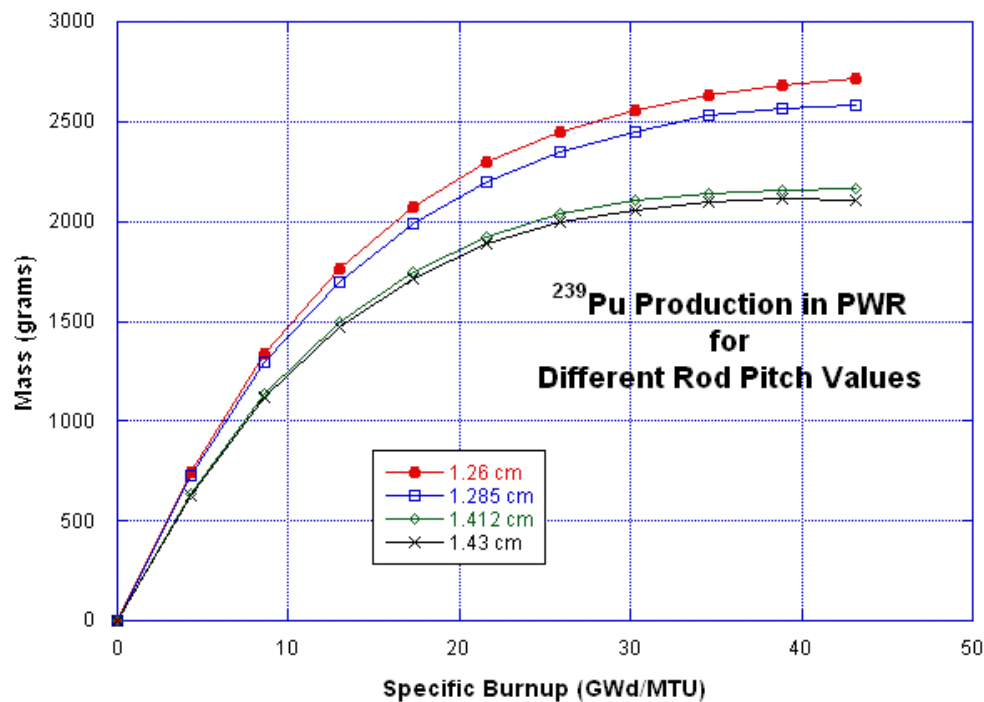


Figure 261: ²³⁹Pu Production in the PWR Model for Different Rod Pitch Values

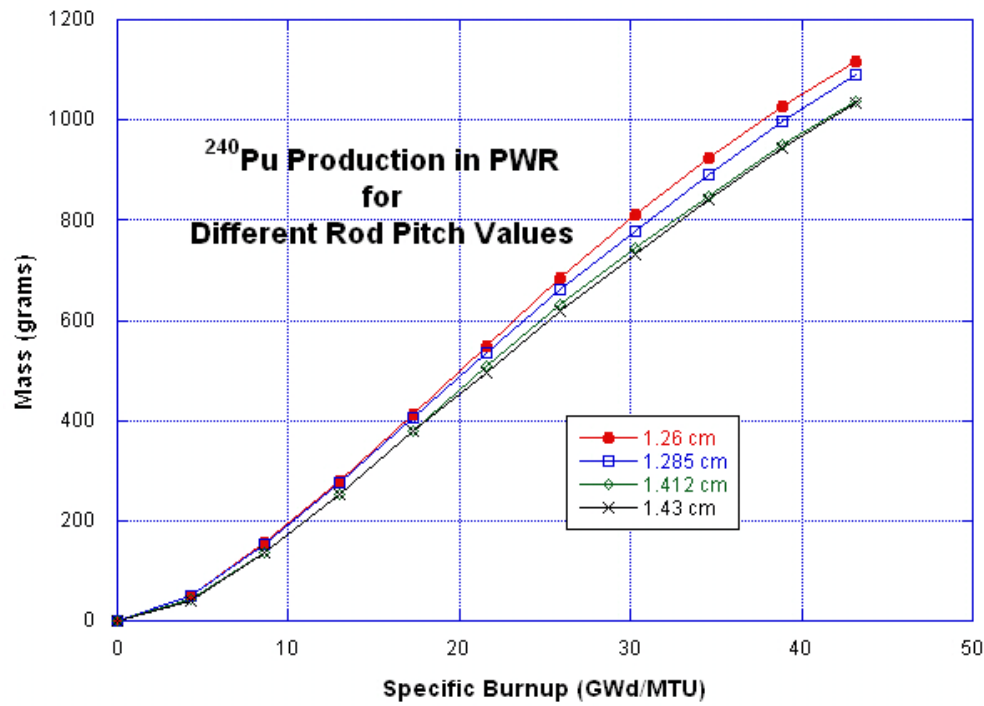


Figure 262: ²⁴⁰Pu Production in the PWR Model for Different Rod Pitch Values

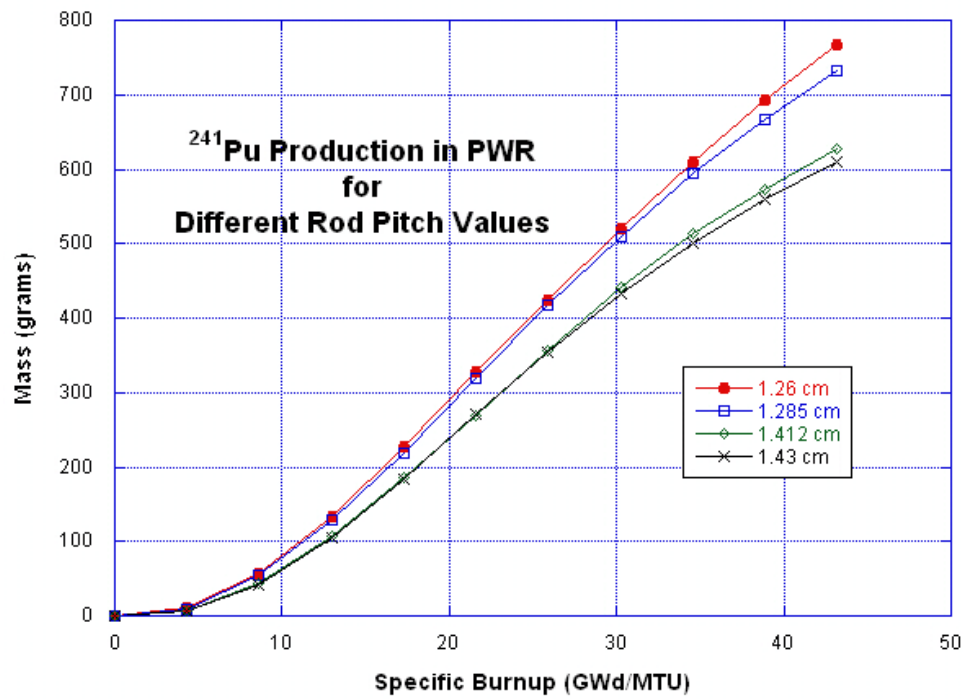


Figure 263: ²⁴¹Pu Production in the PWR Model for Different Rod Pitch Values

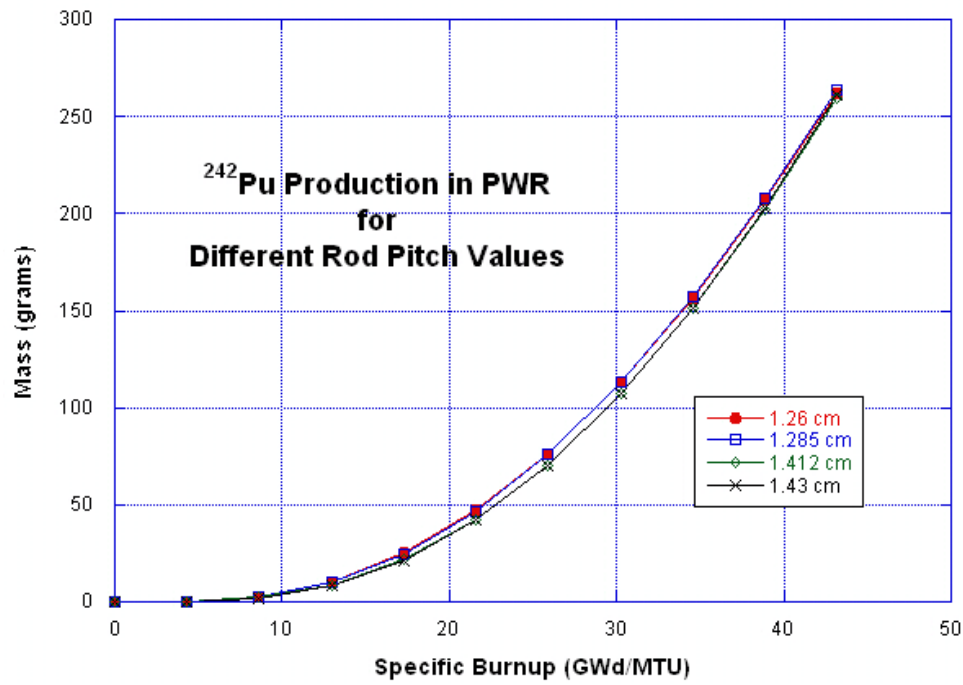


Figure 264: ²⁴²Pu Production in the PWR Model for Different Rod Pitch Values

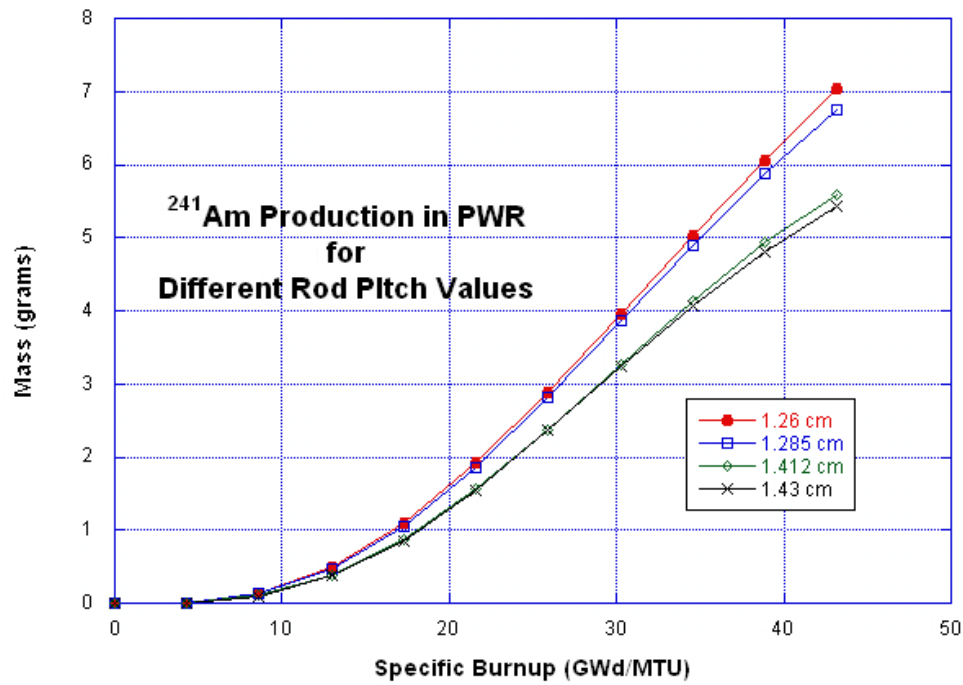


Figure 265: ²⁴¹Am Production in the PWR Model for Different Rod Pitch Values

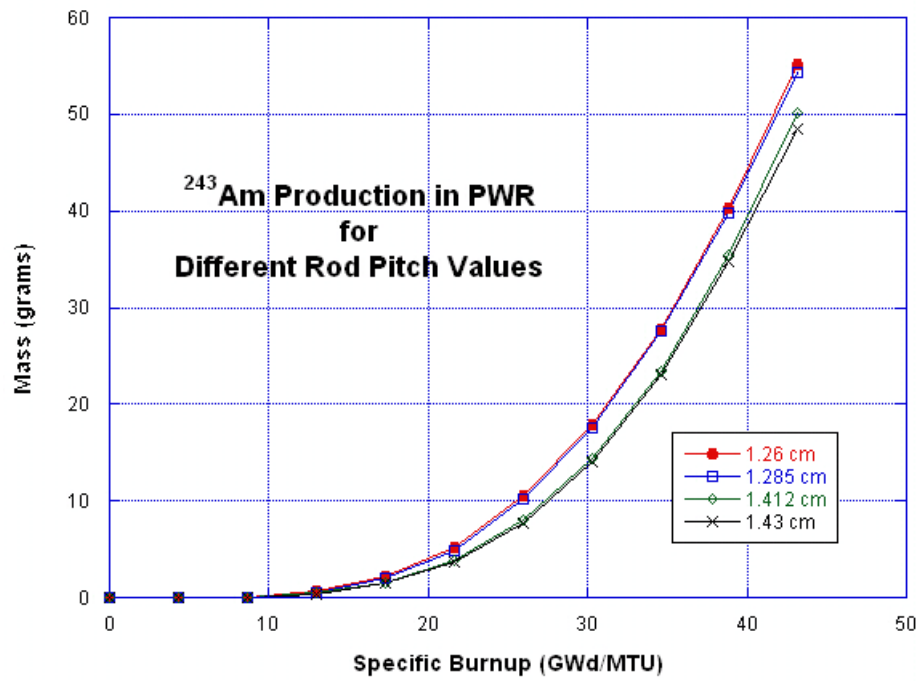


Figure 266: ²⁴³Am Production in the PWR Model for Different Rod Pitch Values

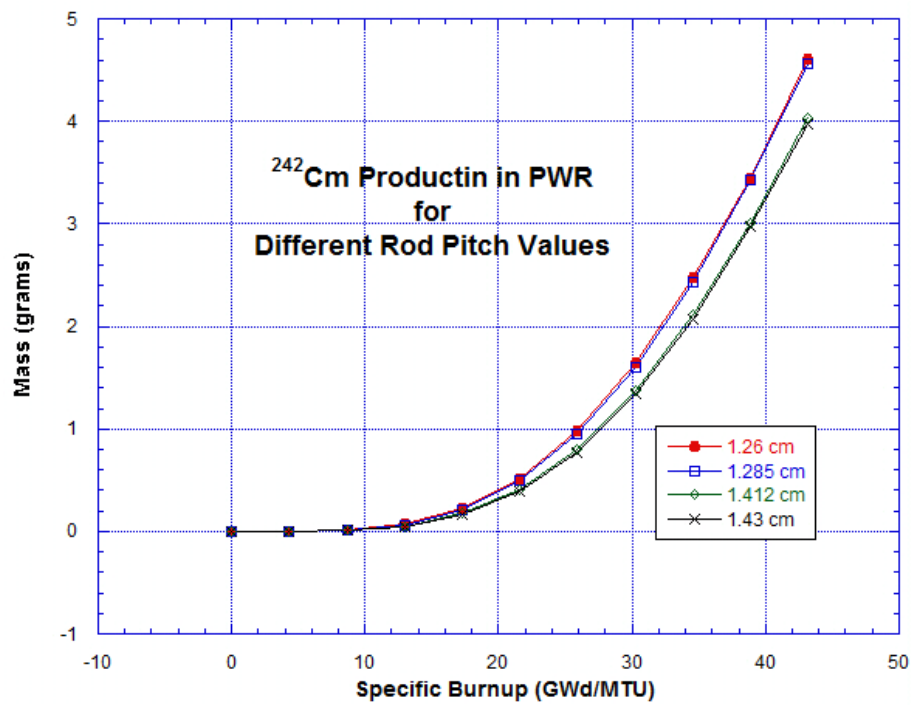


Figure 267: ²⁴²Cm Production in the PWR Model for Different Rod Pitch Values

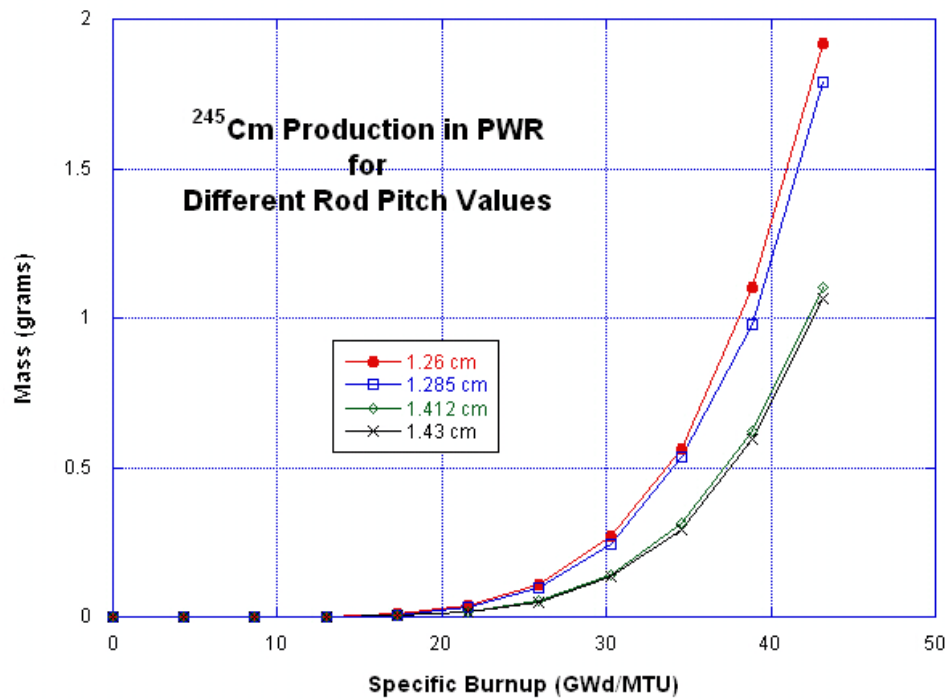


Figure 268: ²⁴⁵Cm Production in the PWR Model for Different Rod Pitch Values

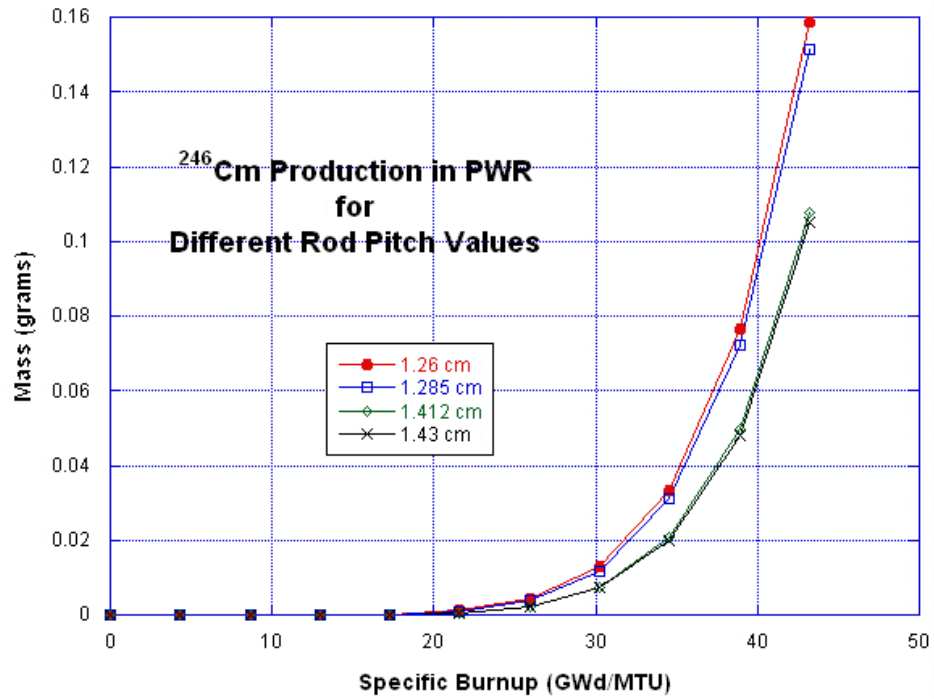


Figure 269: ²⁴⁶Cm Production in the PWR Model for Different Rod Pitch Values

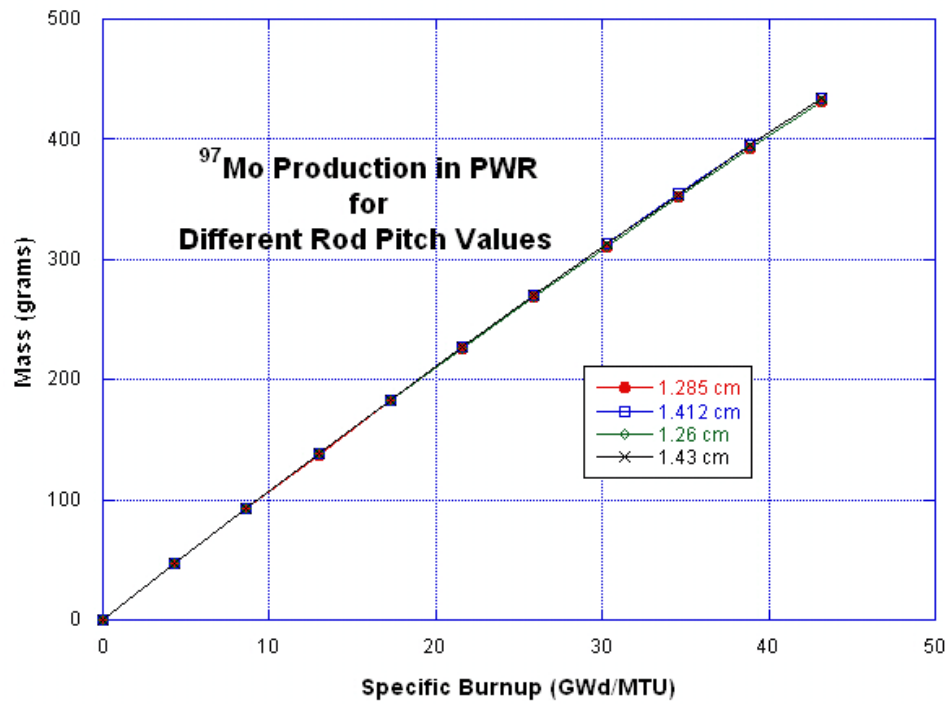


Figure 270: ⁹⁷Mo Production in the PWR Model for Different Rod Pitch Values

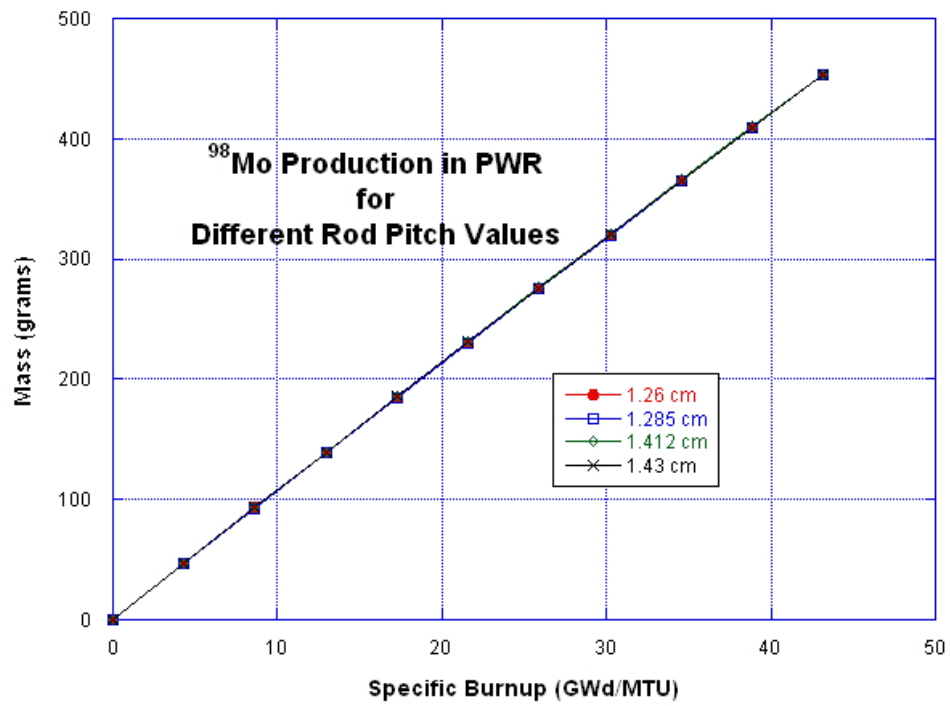


Figure 271: ⁹⁸Mo Production in the PWR Model for Different Rod Pitch Values

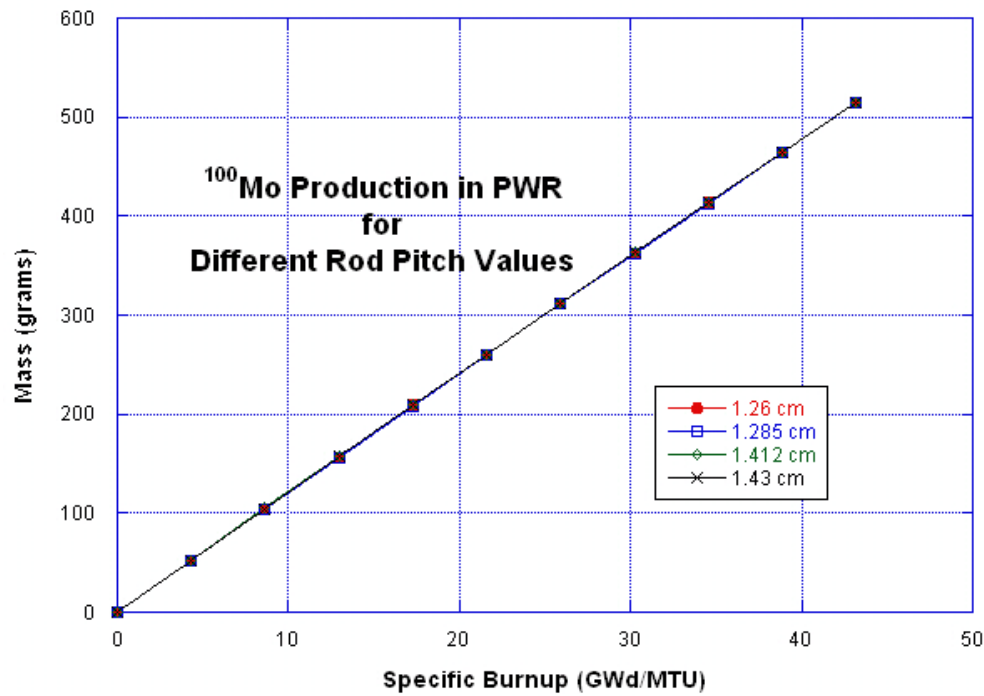


Figure 272: ¹⁰⁰Mo Production in the PWR Model for Different Rod Pitch Values

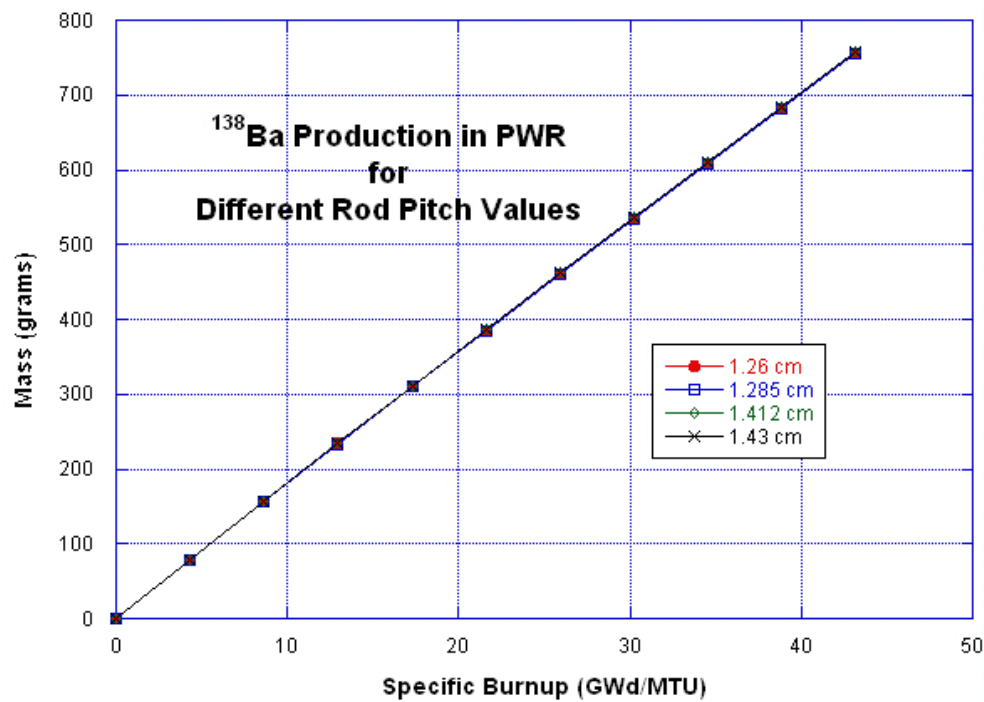


Figure 273: ¹³⁸Ba Production in the PWR Model for Different Rod Pitch Values

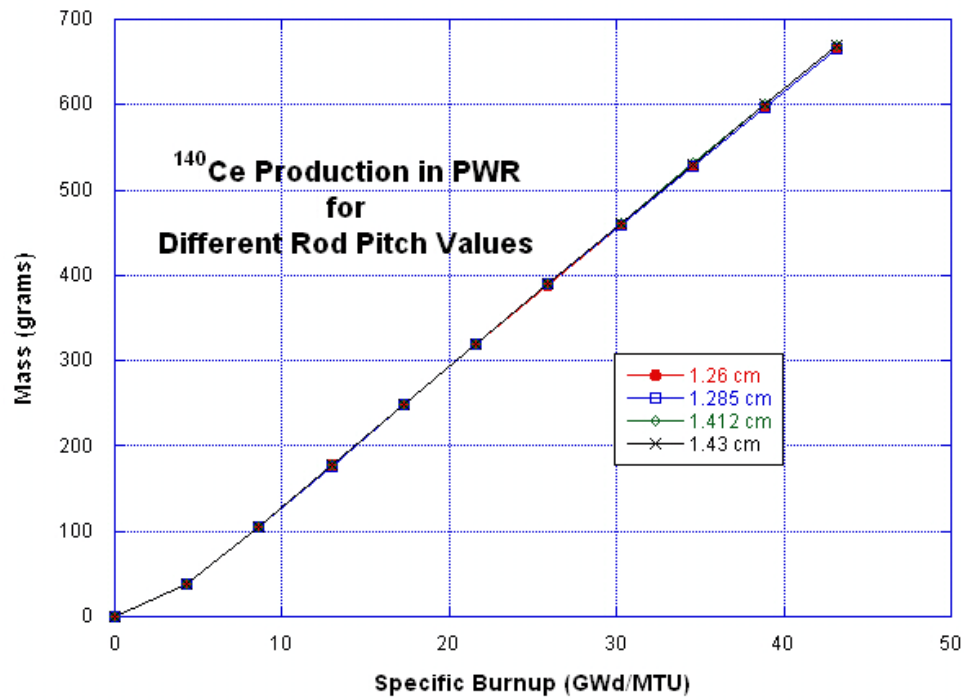


Figure 274: ¹⁴⁰Ce Production in the PWR Model for Different Rod Pitch Values

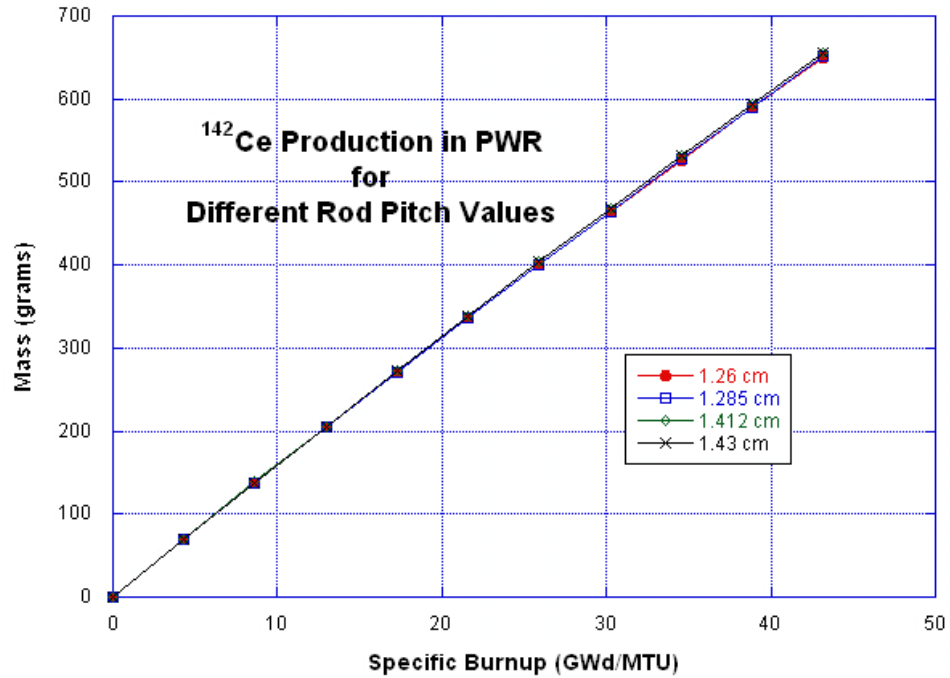


Figure 275: ¹⁴²Ce Production in the PWR Model for Different Rod Pitch Values

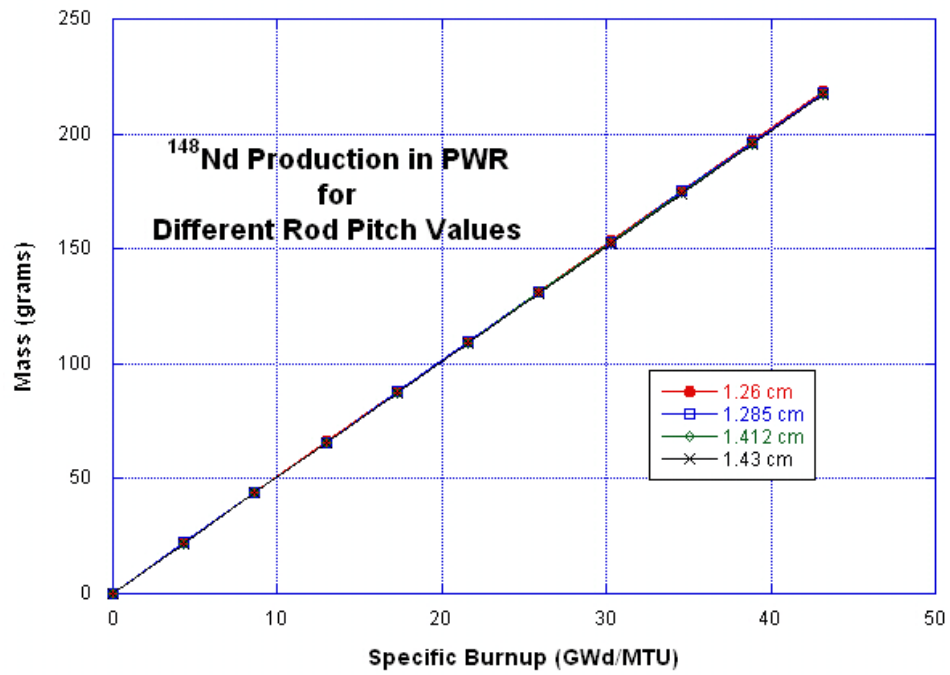


Figure 276: ¹⁴⁸Nd Production in the PWR Model for Different Rod Pitch Values

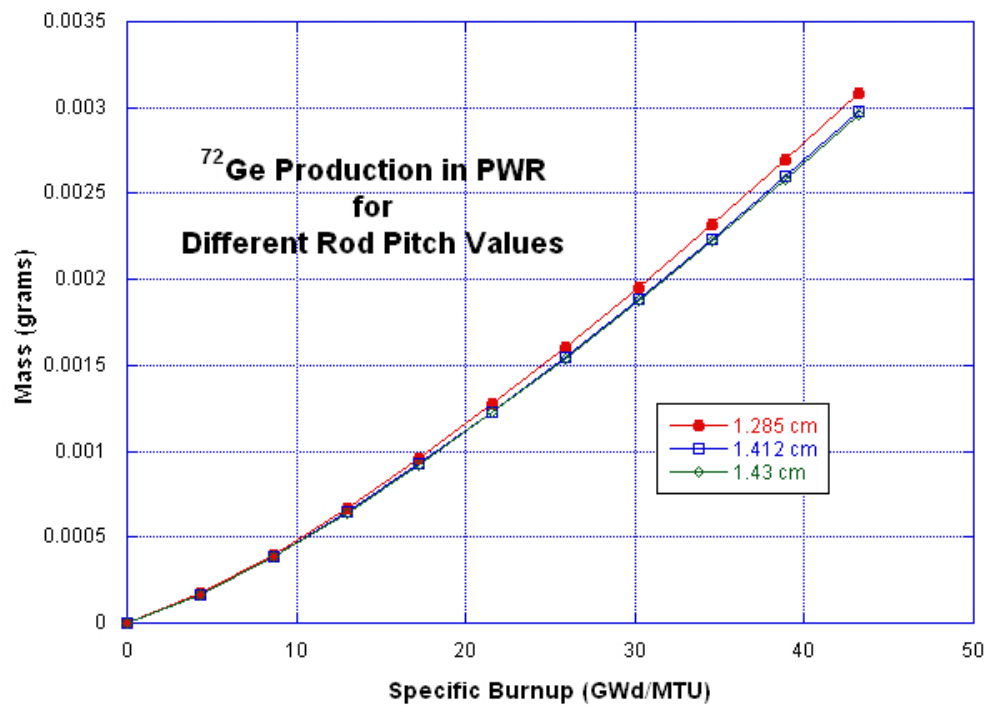


Figure 277: ⁷²Ge Production in the PWR Model for Different Rod Pitch Values

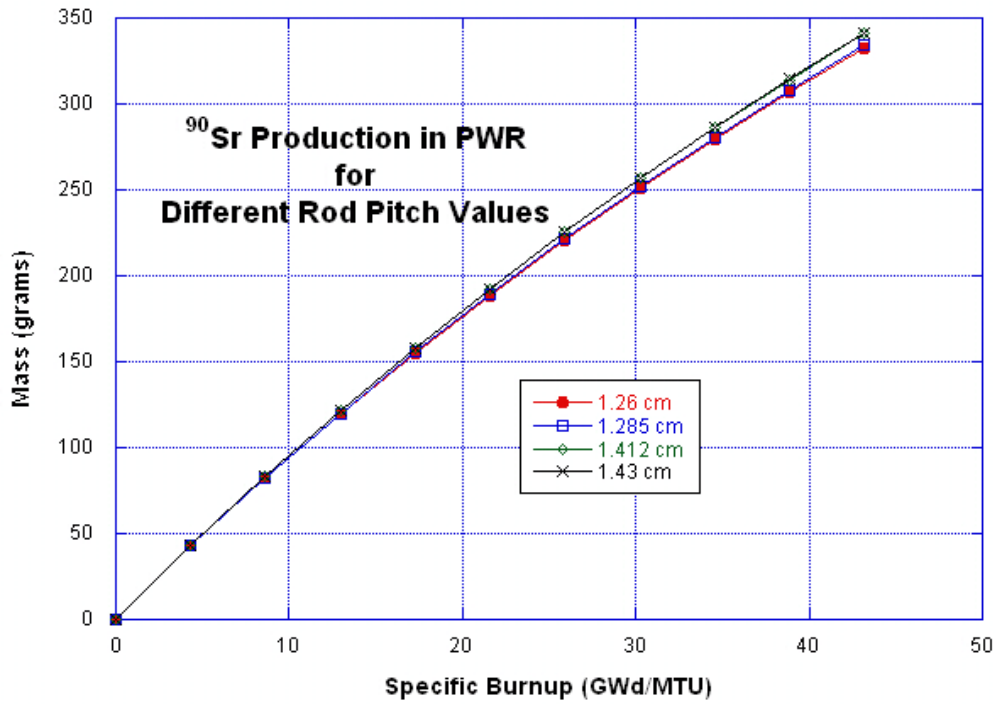


Figure 278: ⁹⁰Sr Production in the PWR Model for Different Rod Pitch Values

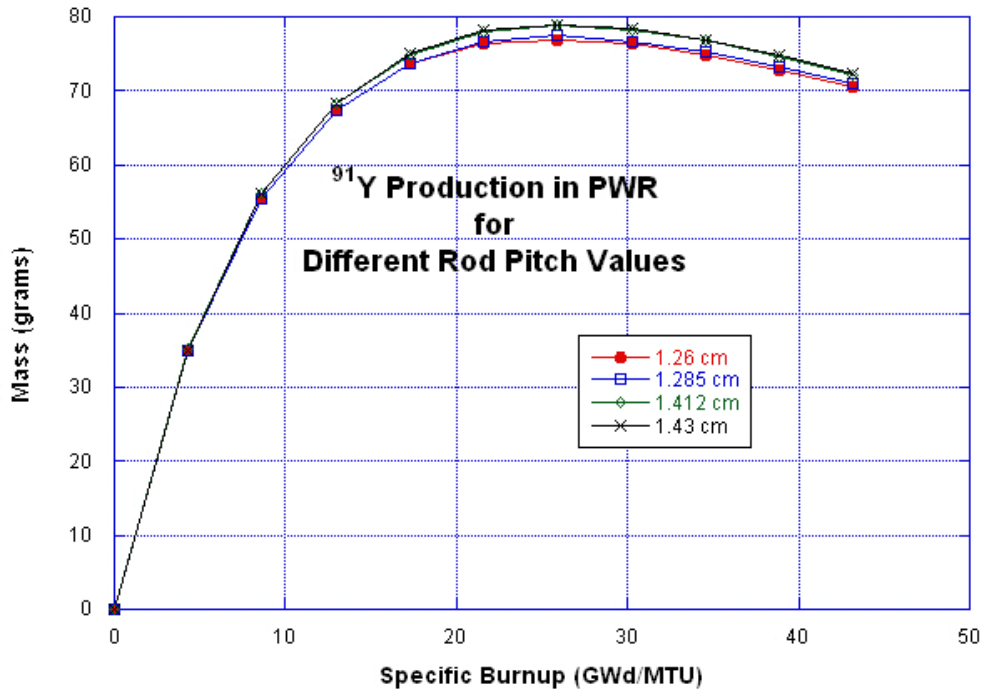


Figure 279: ⁹¹Y Production in the PWR Model for Different Rod Pitch Values

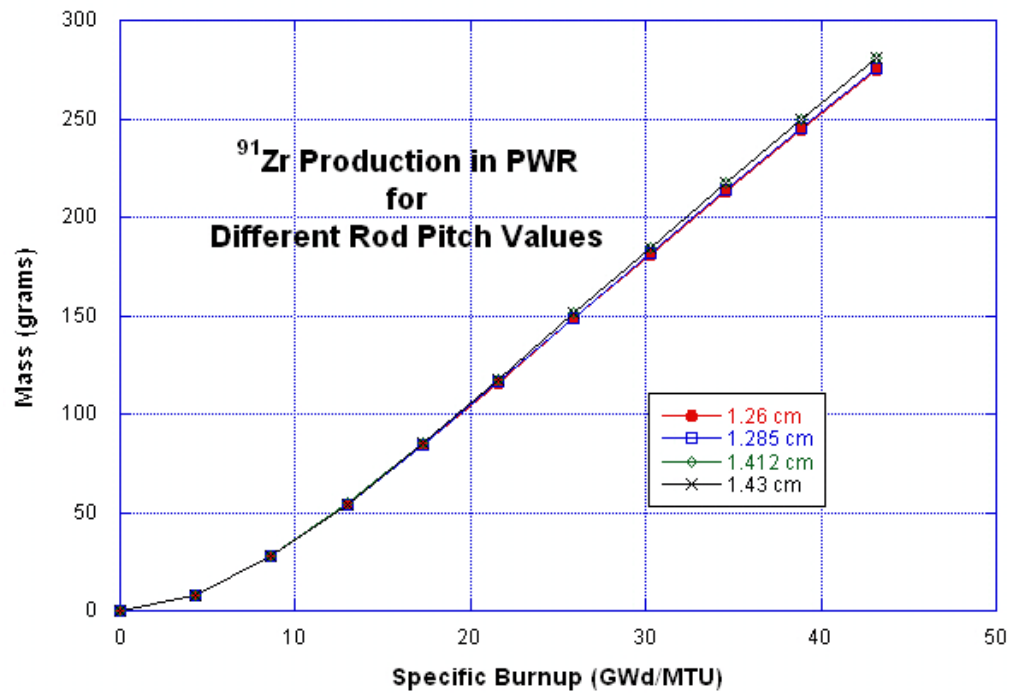


Figure 280: ⁹¹Zr Production in the PWR Model for Different Rod Pitch Values

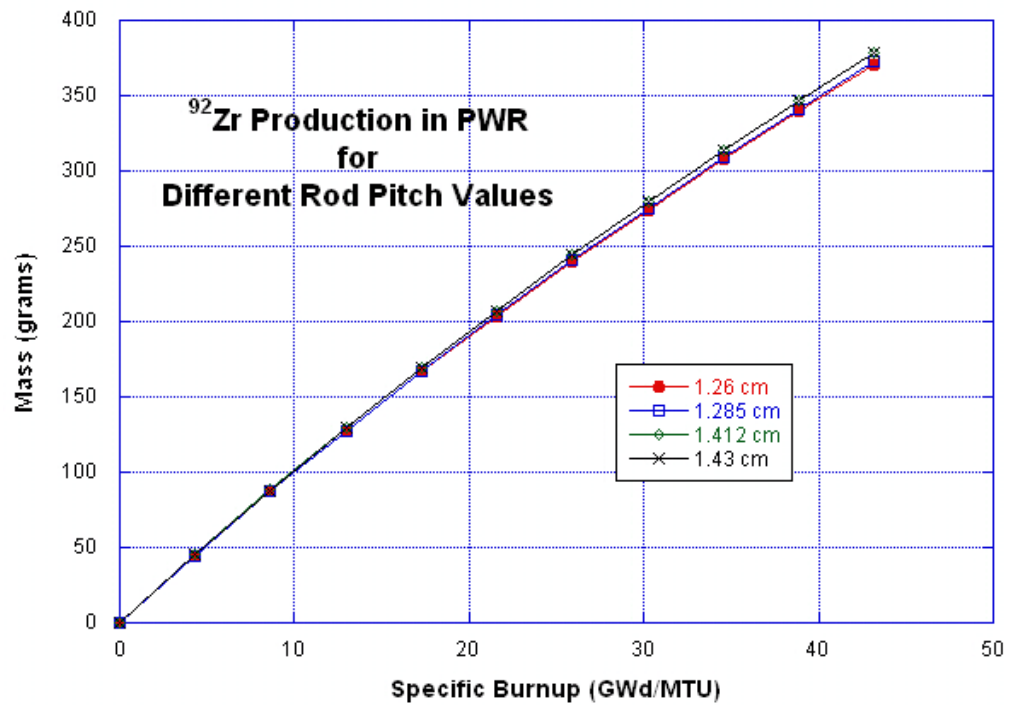


Figure 281: ⁹²Zr Production in the PWR Model for Different Rod Pitch Values

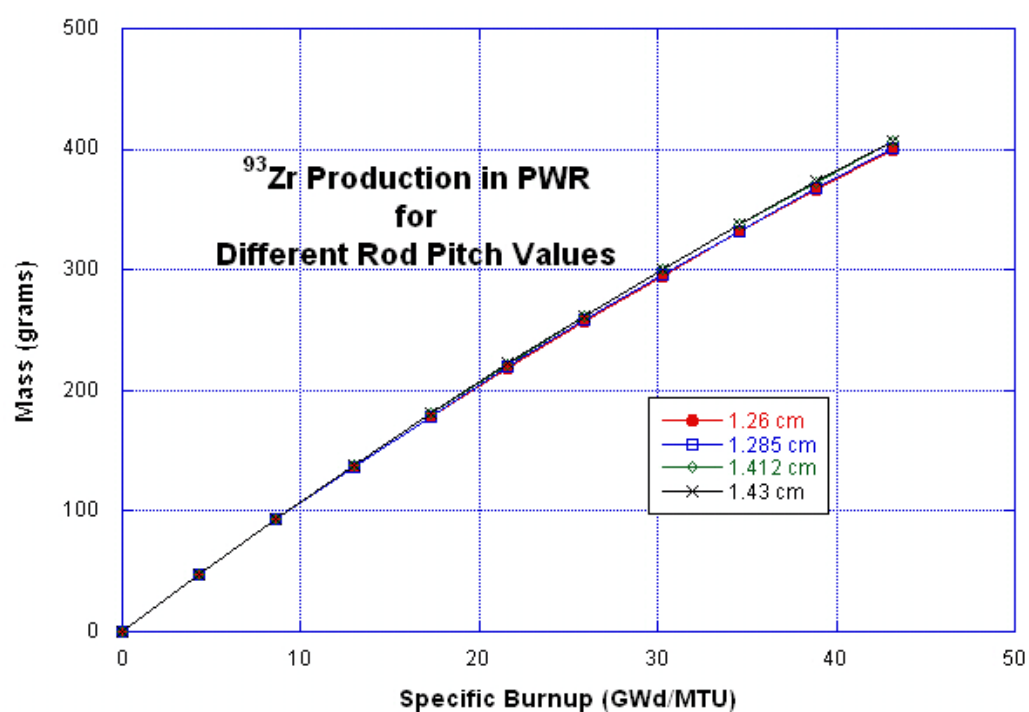


Figure 282: ⁹³Zr Production in the PWR Model for Different Rod Pitch Values

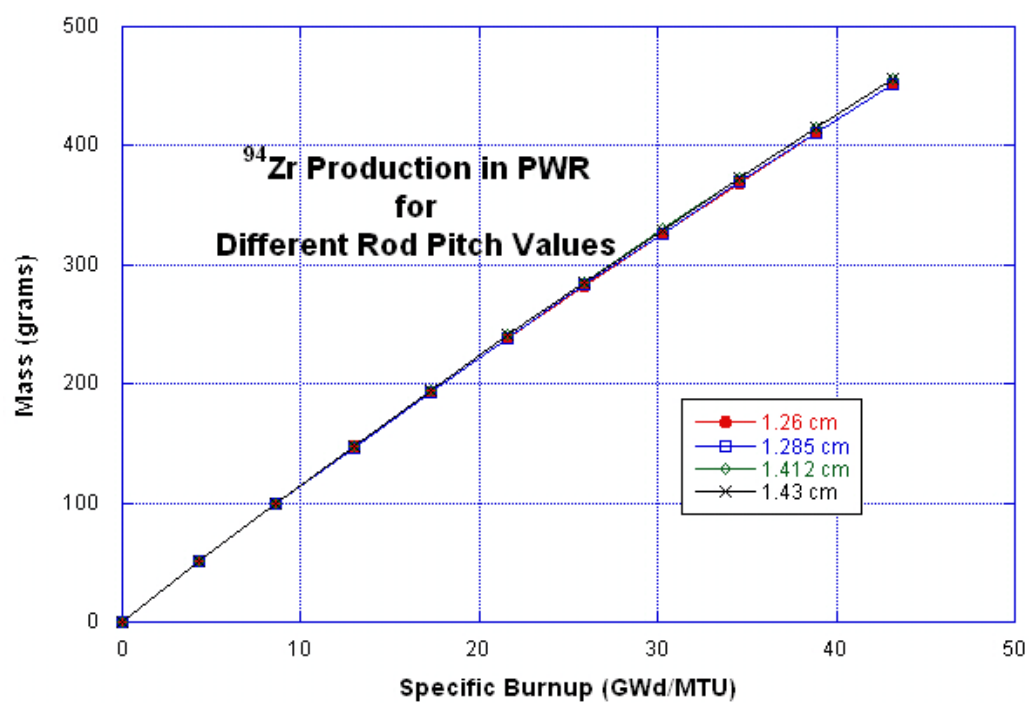


Figure 283: ⁹⁴Zr Production in the PWR Model for Different Rod Pitch Values

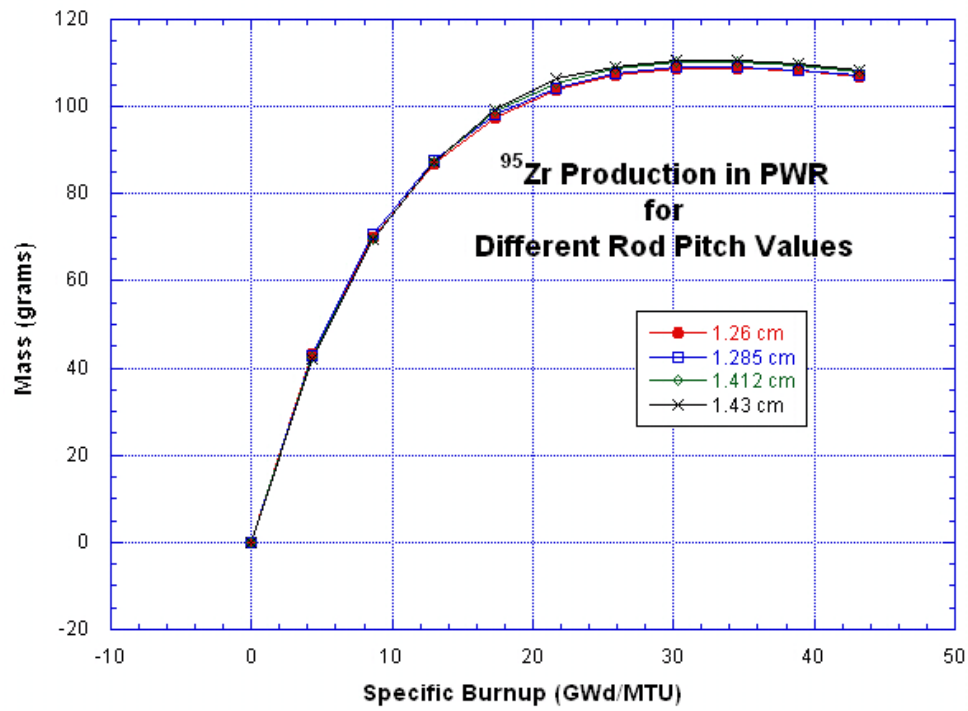


Figure 284 ⁹⁵Zr Production in the PWR Model for Different Rod Pitch Values

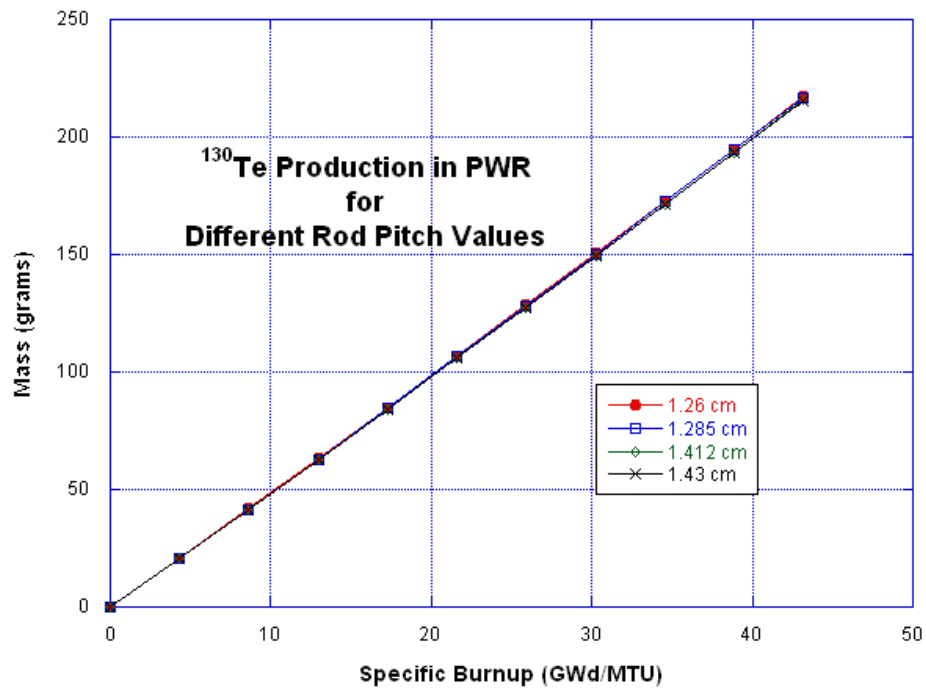


Figure 285: ¹³⁰Te Production in the PWR Model for Different Rod Pitch Values

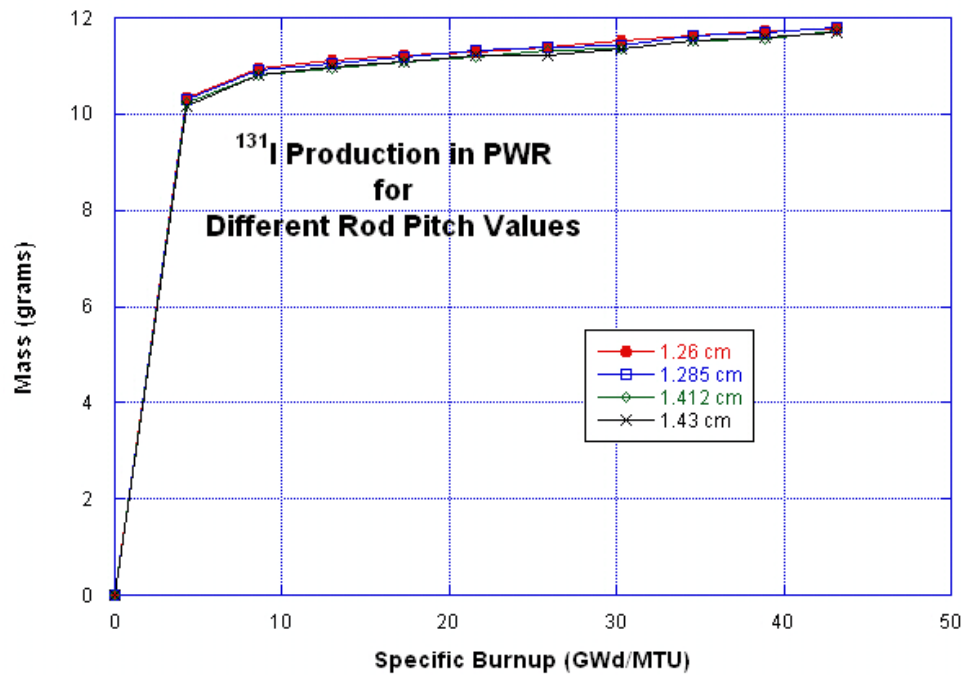


Figure 286: ¹³¹I Production in the PWR Model for Different Rod Pitch Values

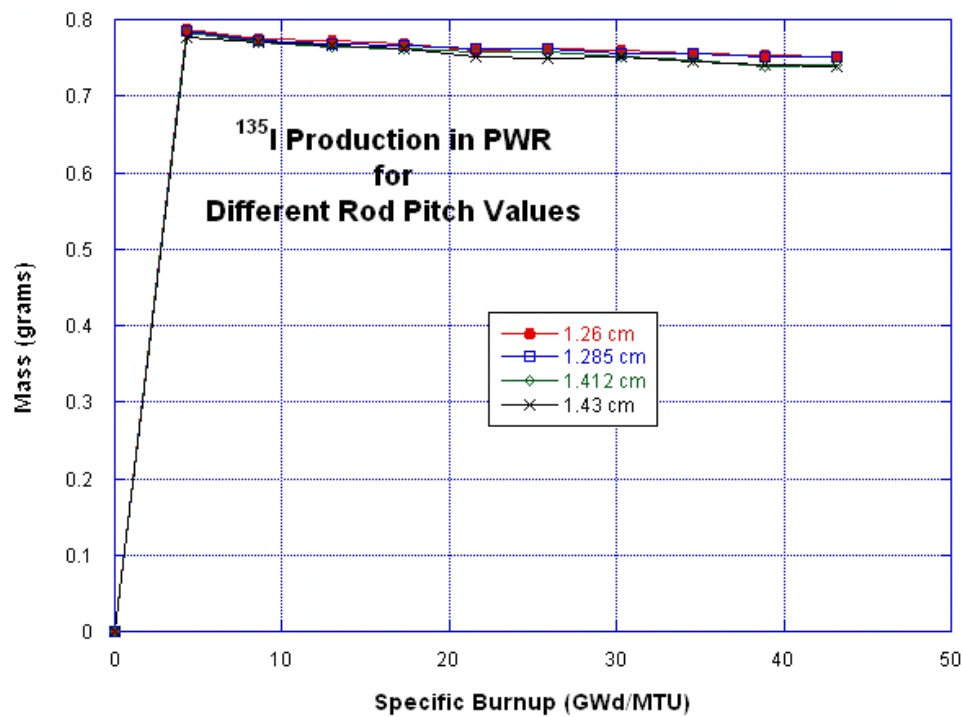


Figure 287: ¹³⁵I Production in the PWR Model for Different Rod Pitch Values

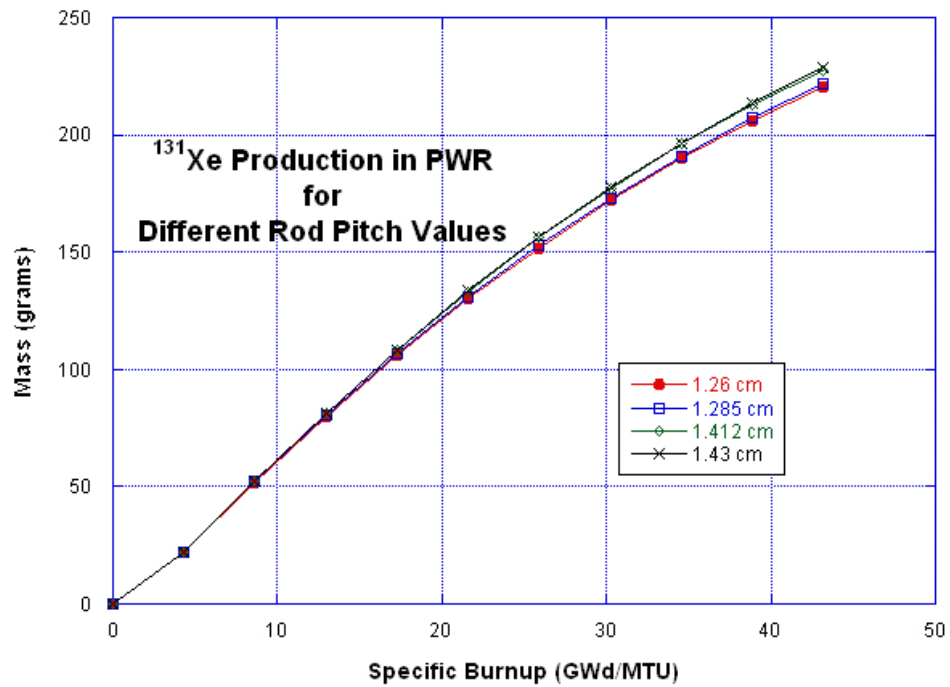


Figure 288: ¹³¹Xe Production in the PWR Model for Different Rod Pitch Values

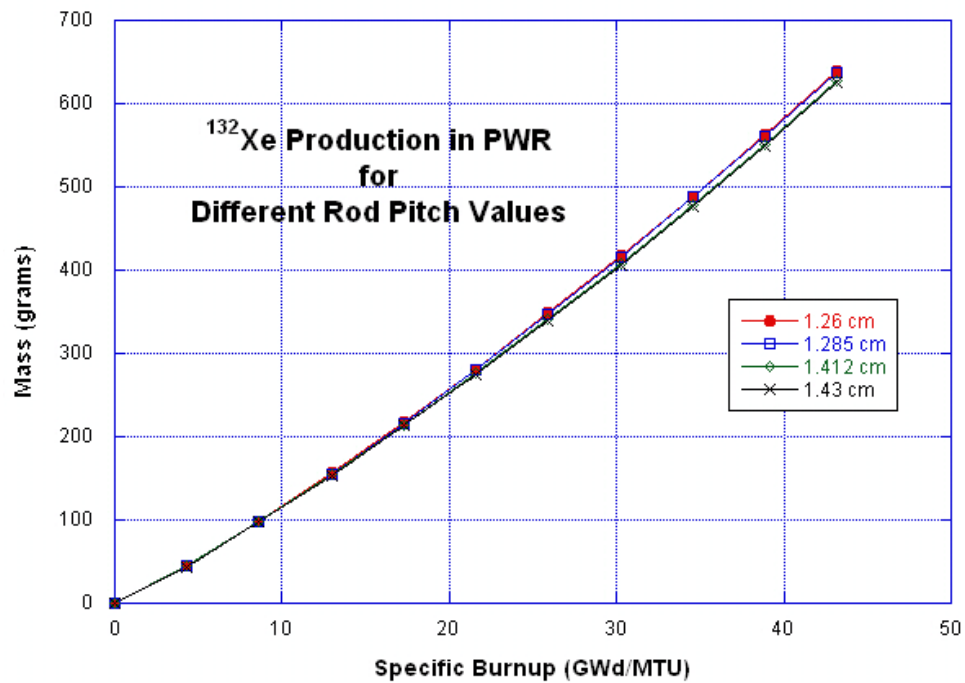


Figure 289: ¹³²Xe Production in the PWR Model for Different Rod Pitch Values

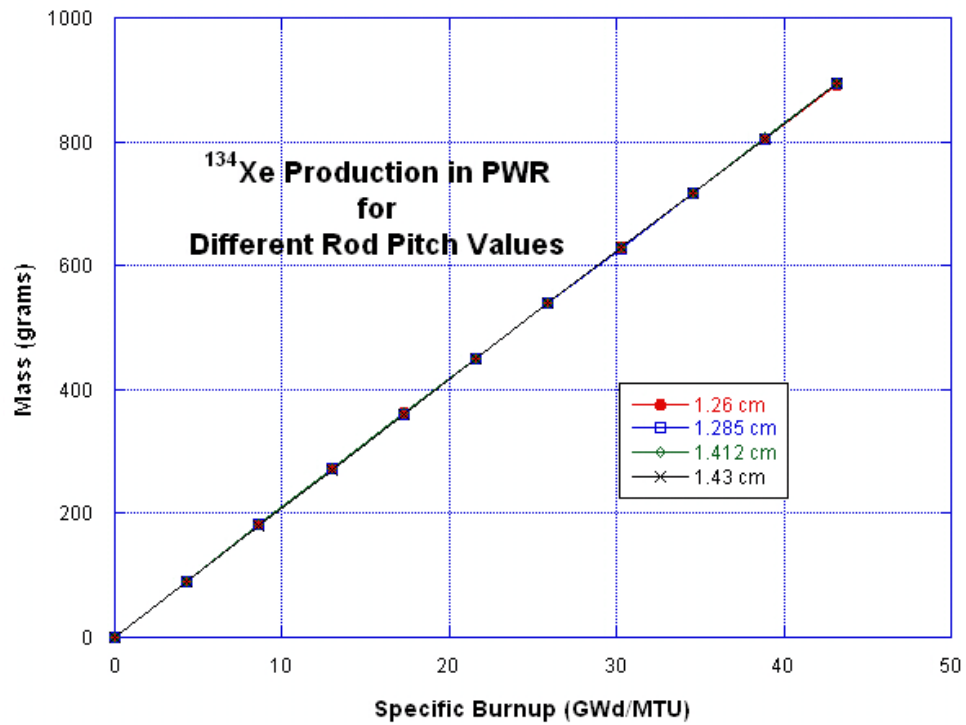


Figure 290: ¹³⁴Xe Production in the PWR Model for Different Rod Pitch Values

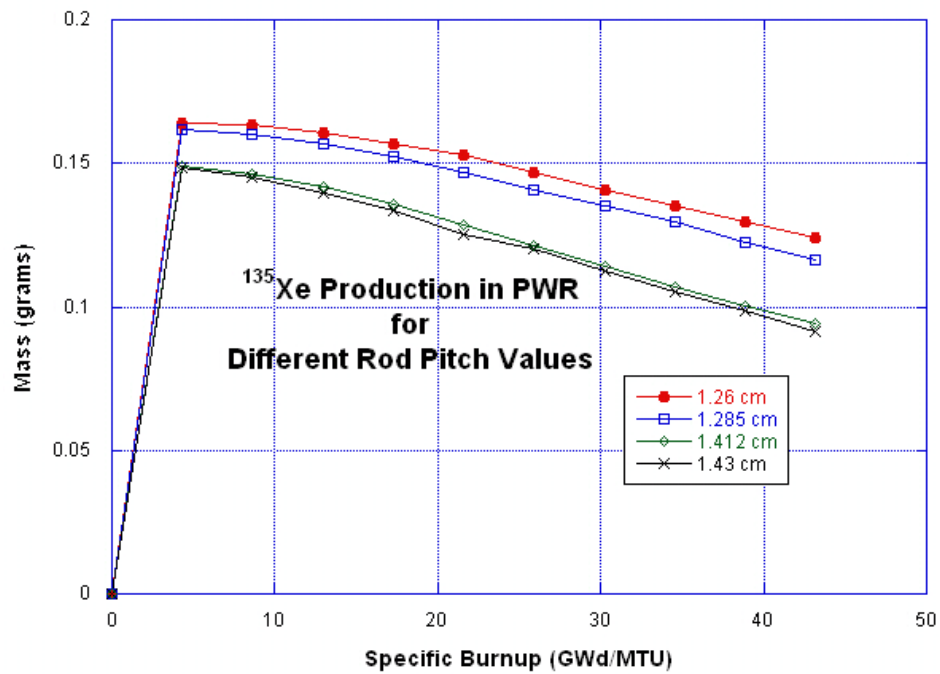


Figure 291: ¹³⁵Xe Production in the PWR Model for Different Rod Pitch Values

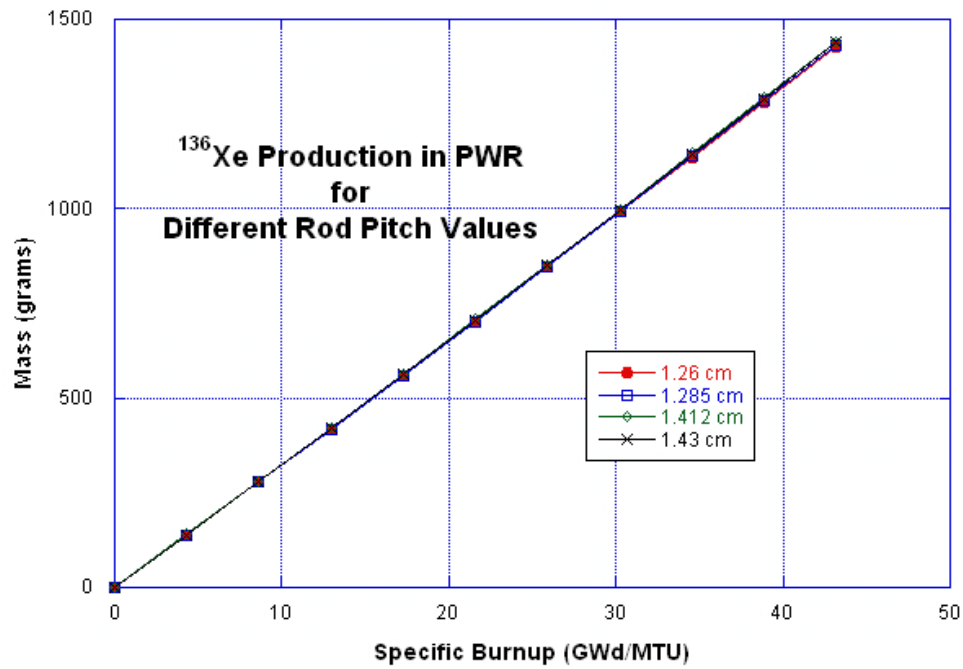


Figure 292: ¹³⁶Xe Production in the PWR Model for Different Rod Pitch Values

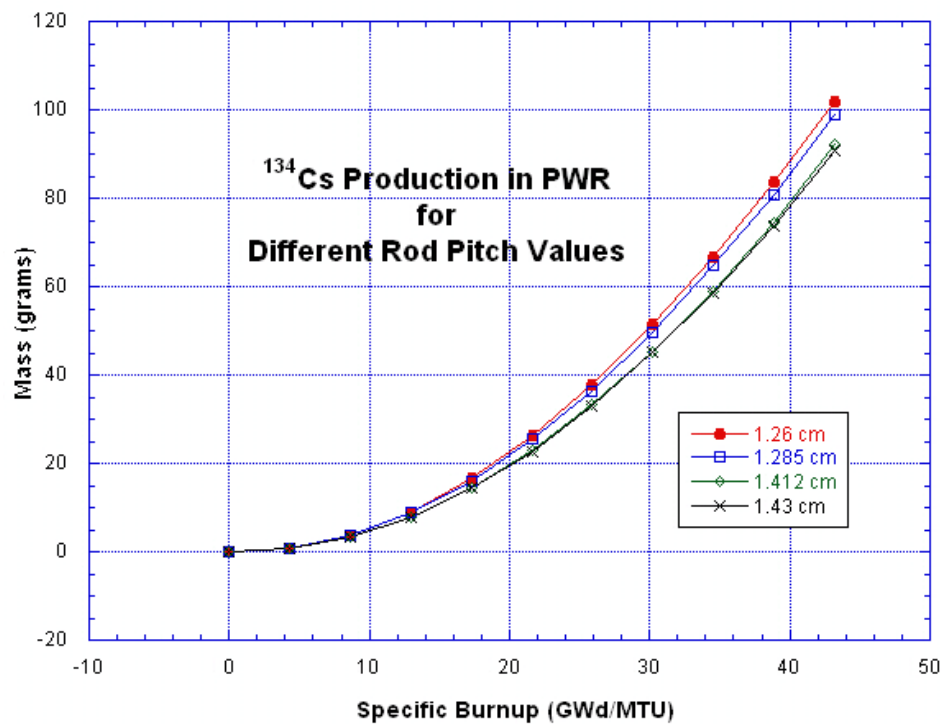


Figure 293: ¹³⁷Cs Production in the PWR Model for Different Rod Pitch Values

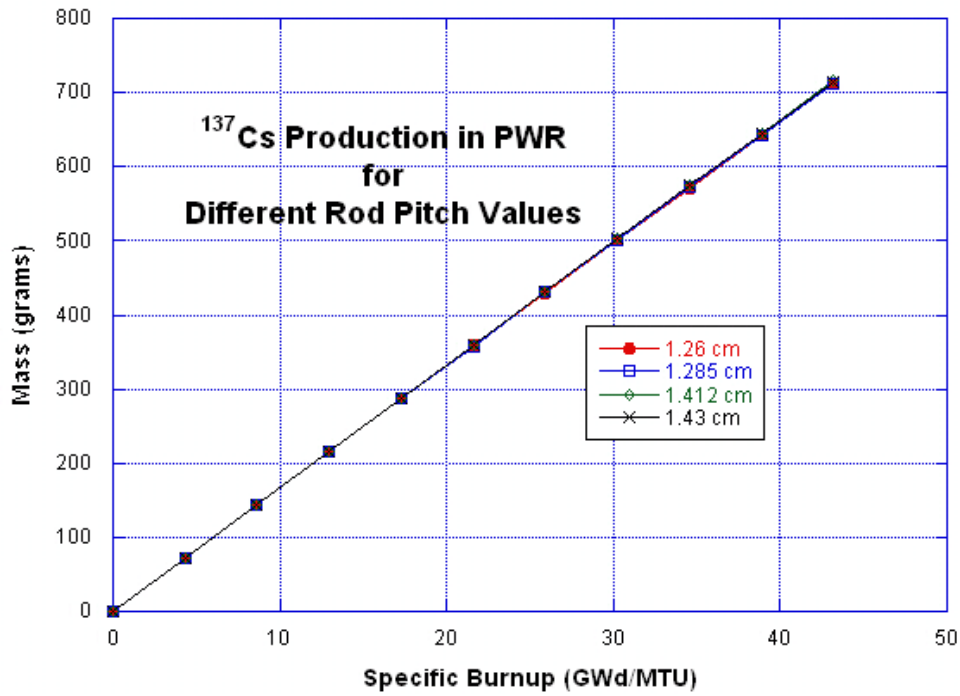


Figure 294: ¹³⁷Cs Production in the PWR Model for Different Rod Pitch Values

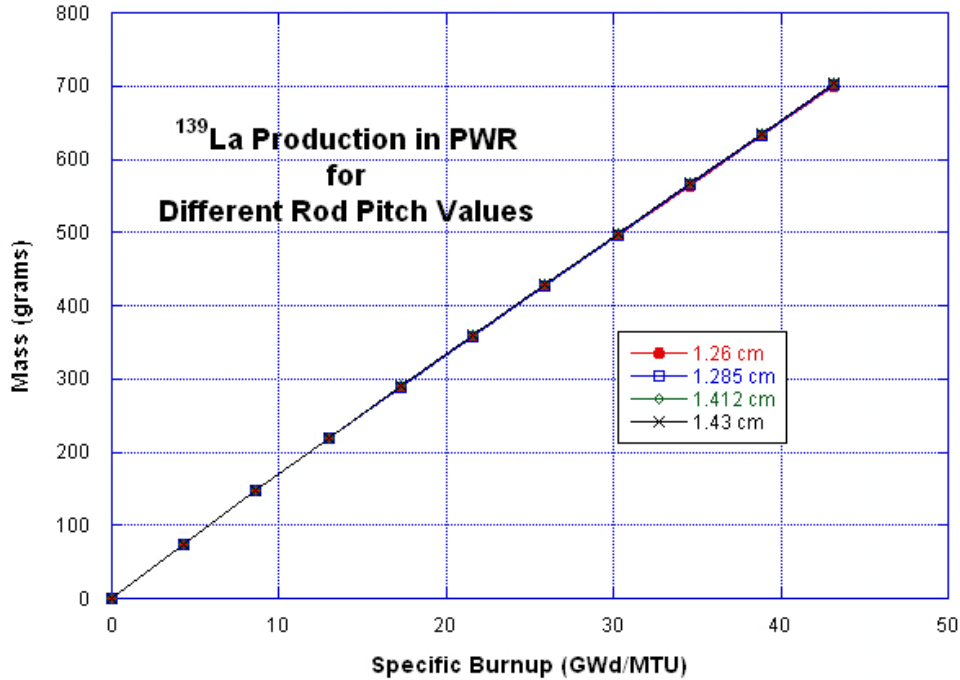


Figure 295: ¹³⁹La Production in the PWR Model for Different Rod Pitch Values

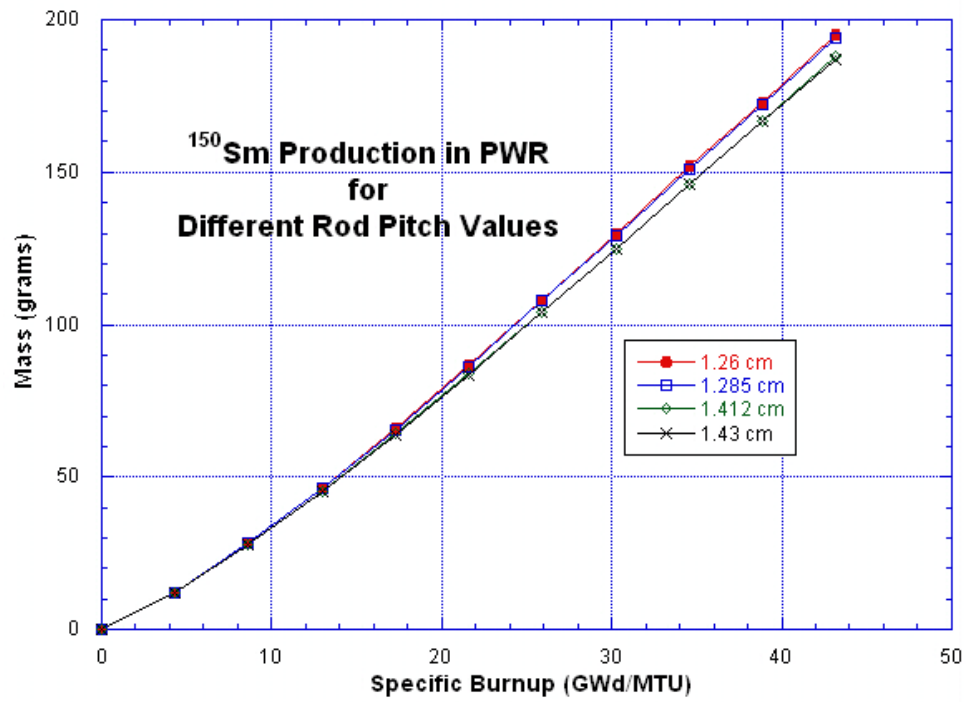


Figure 296: ¹⁵⁰Sm Production in the PWR Model for Different Rod Pitch Values

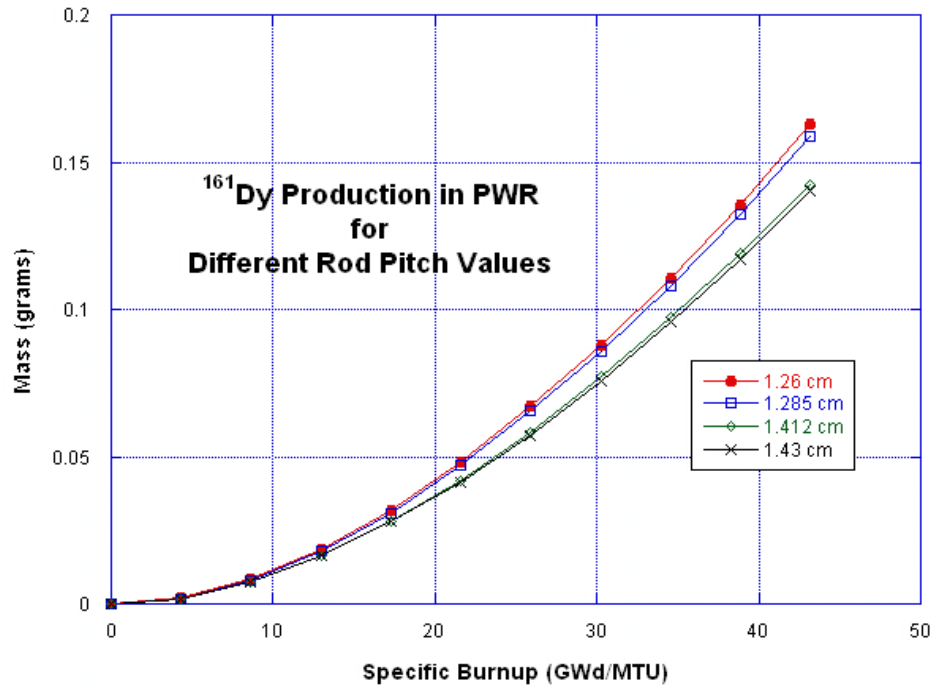


Figure 297: ¹⁶¹Dy Production in the PWR Model for Different Rod Pitch Values

**PWR Sensitivity Study
Plots of 46 Nuclides of Interest
Boron Concentration Variation**

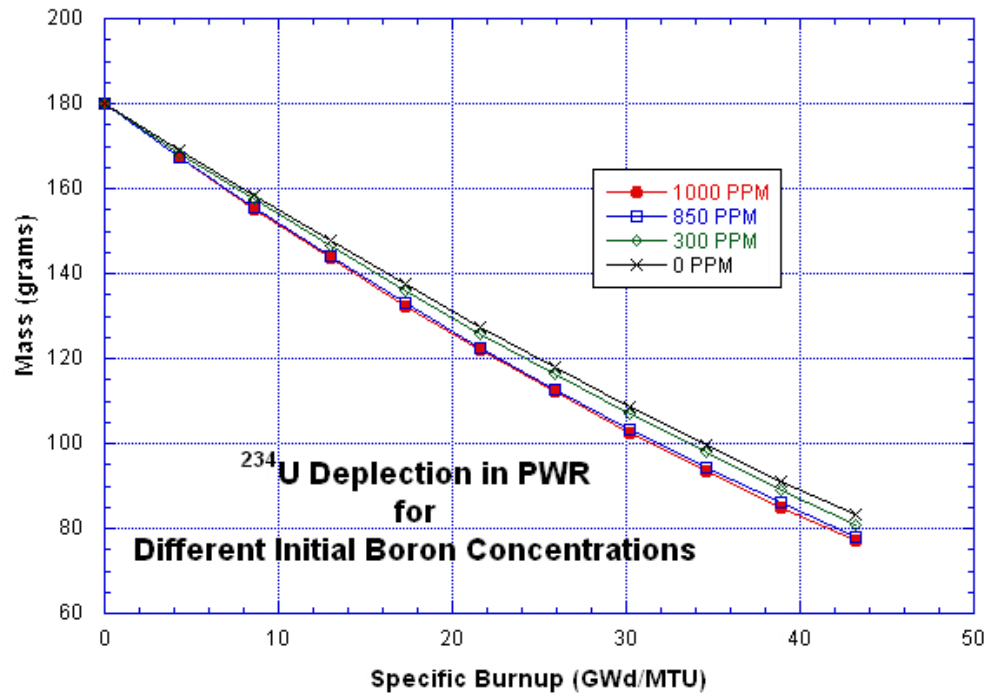


Figure 298: ²³⁴U Depletion in the PWR Model for Different Boron Concentrations

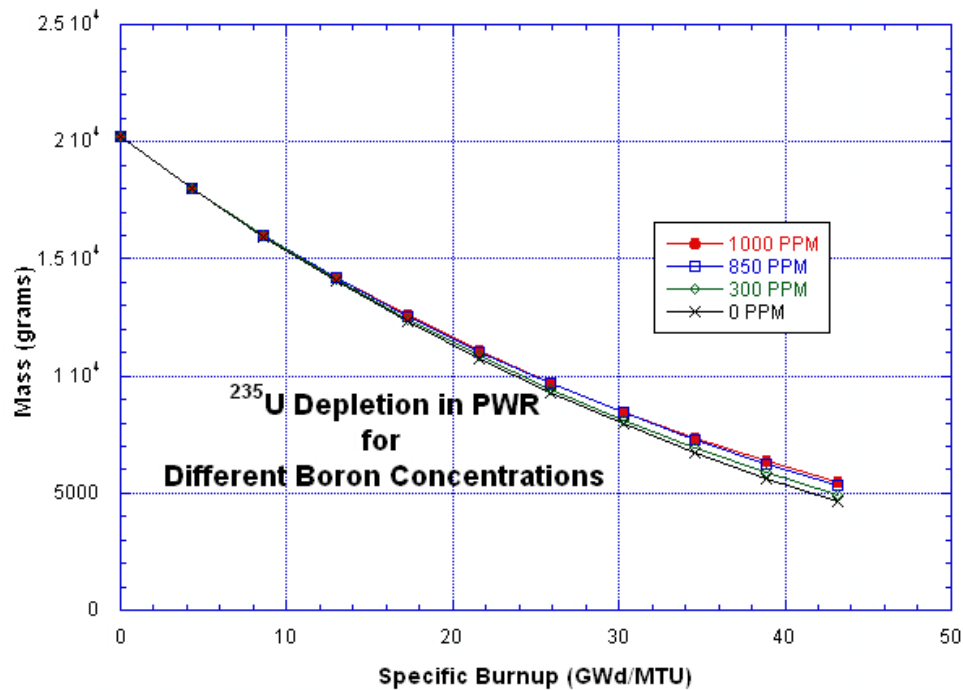


Figure 299: ²³⁵U Depletion in the PWR Model for Different Boron Concentrations

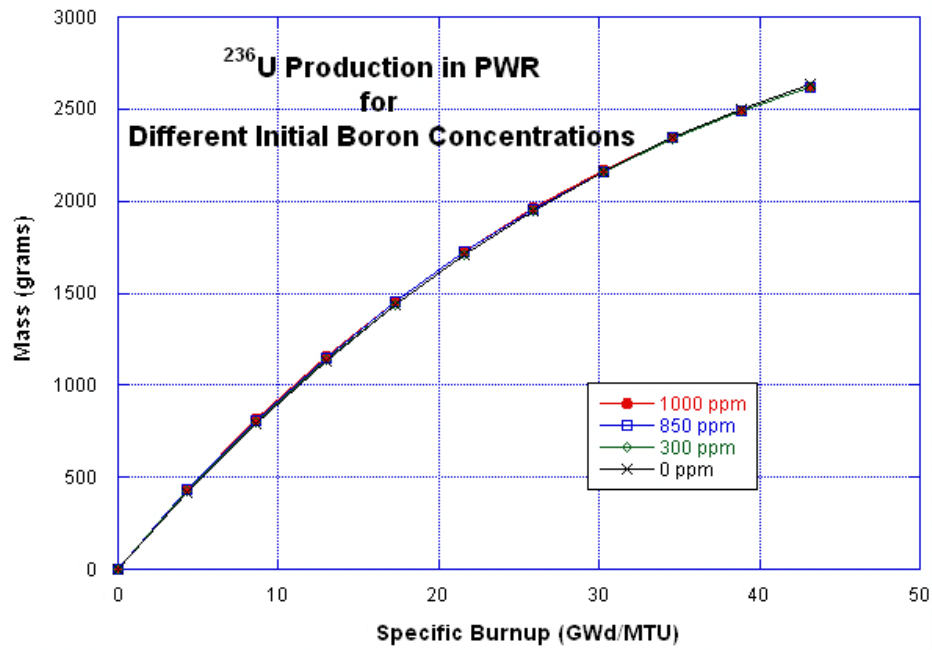


Figure 300: ²³⁶U Production in the PWR Model for Different Boron Concentrations

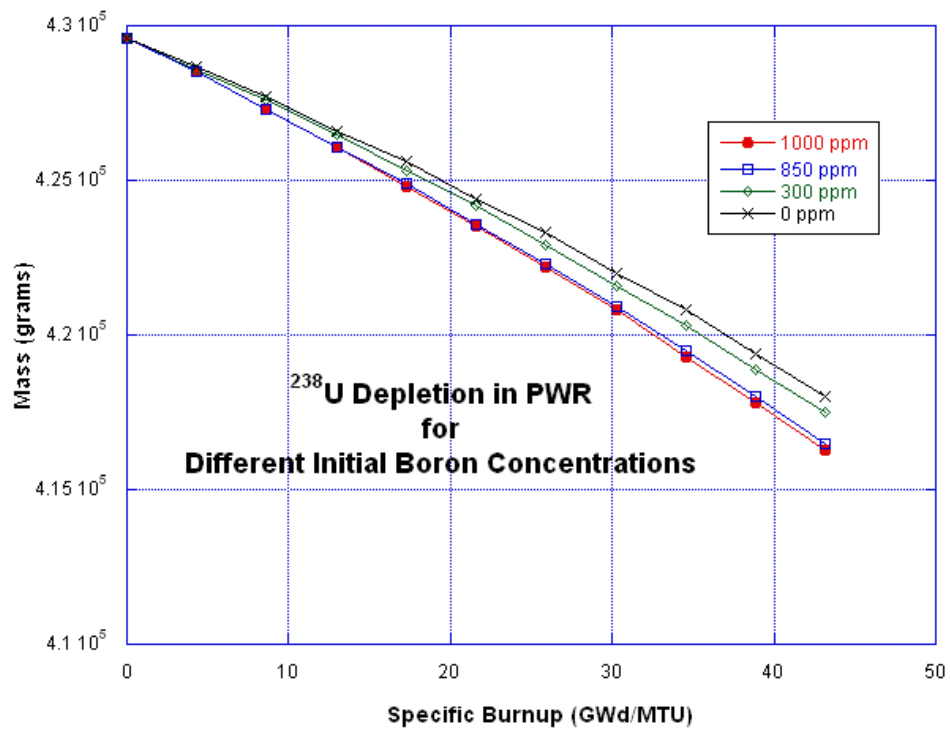


Figure 301: ²³⁸U Depletion in the PWR Model for Different Boron Concentrations

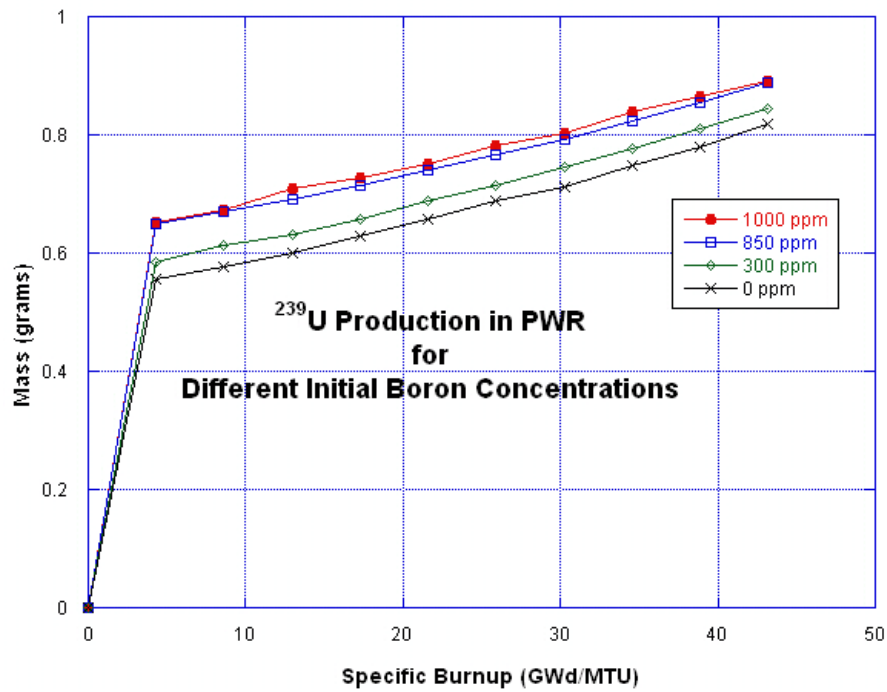


Figure 302: ^{239}U Production in the PWR Model for Different Boron Concentrations

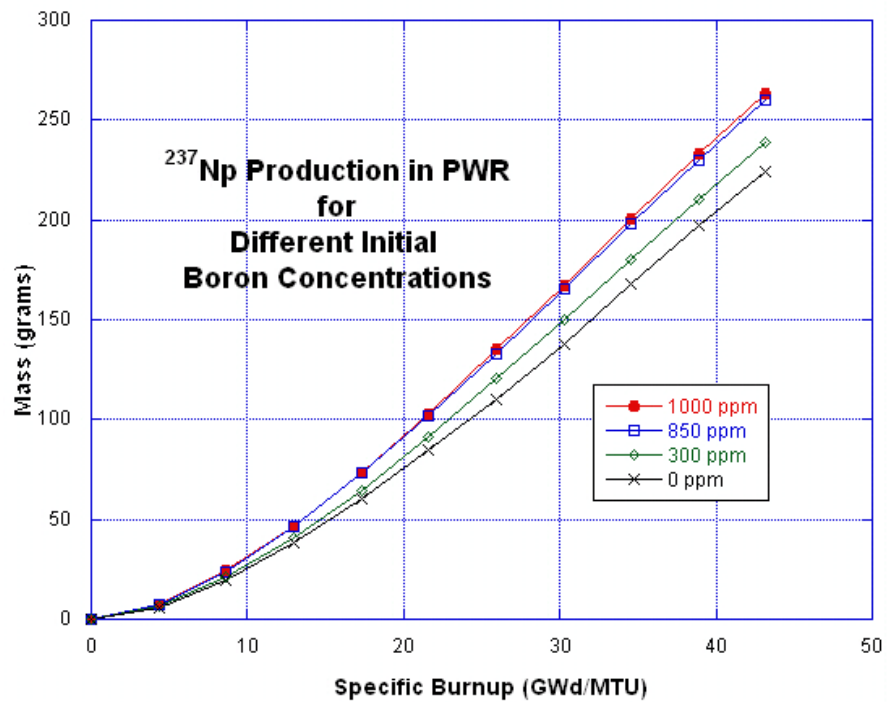


Figure 303: ^{237}Np Production in the PWR Model for Different Boron Concentrations

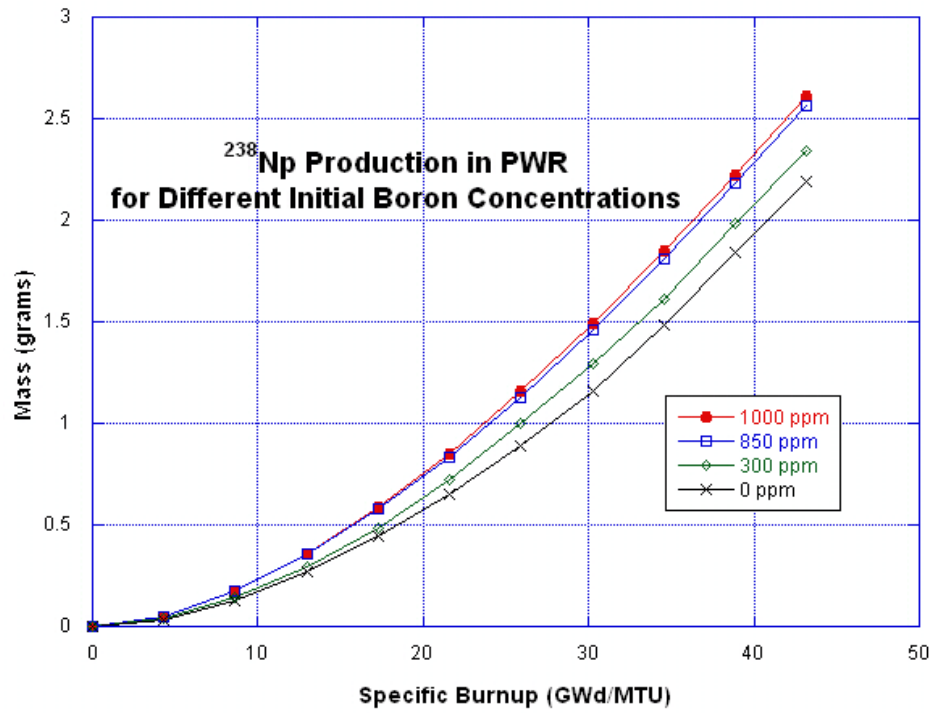


Figure 304: ²³⁸Np Production in the PWR Model for Different Boron Concentrations

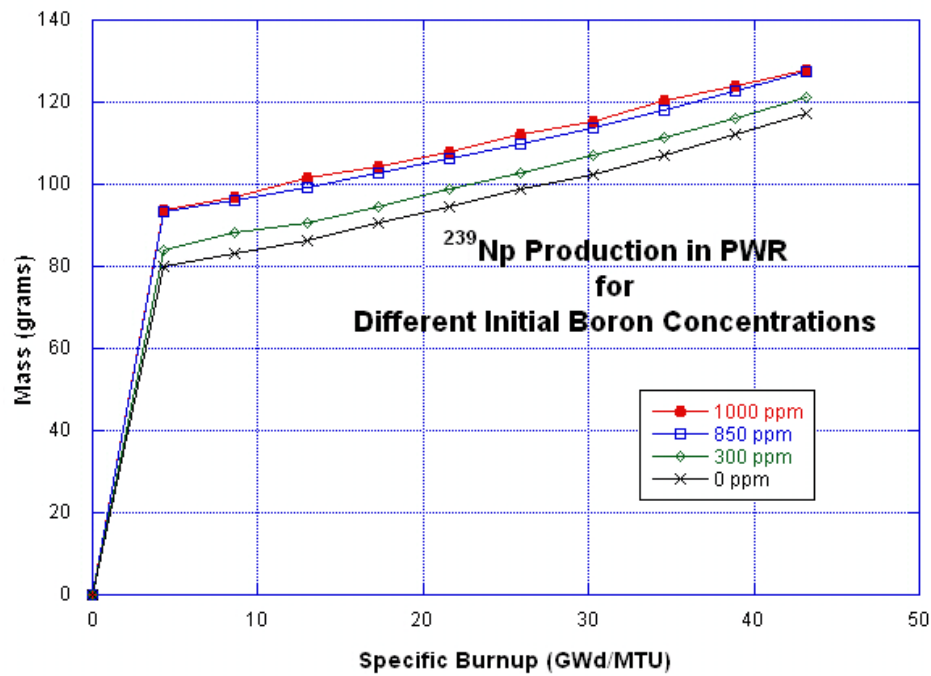


Figure 305: ²³⁹Np Production in the PWR Model for Different Boron Concentrations

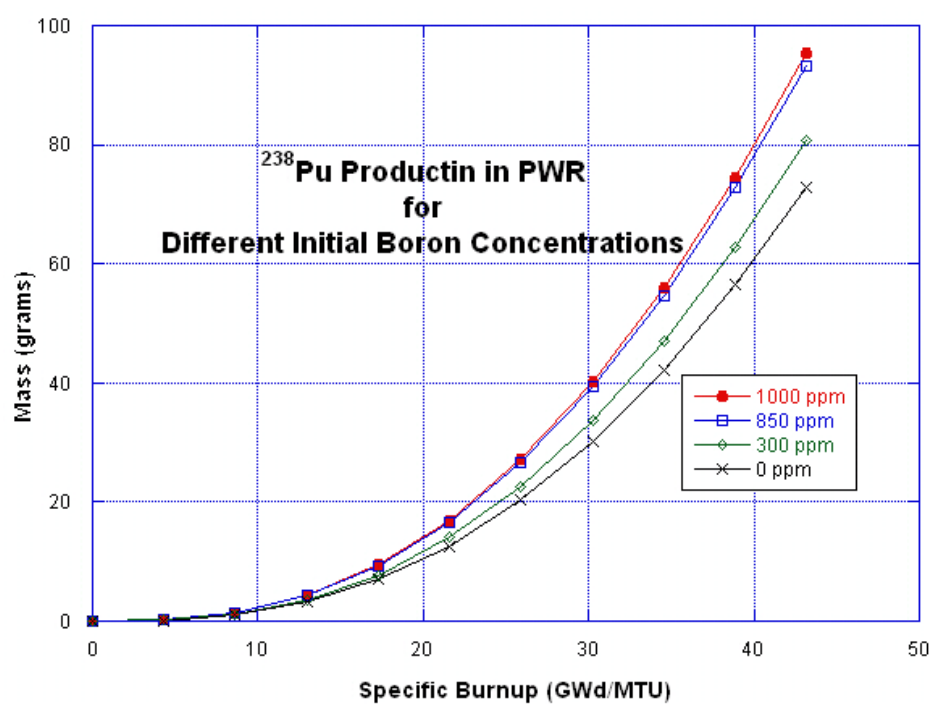


Figure 306: ²³⁸Pu Production in the PWR Model for Different Boron Concentrations

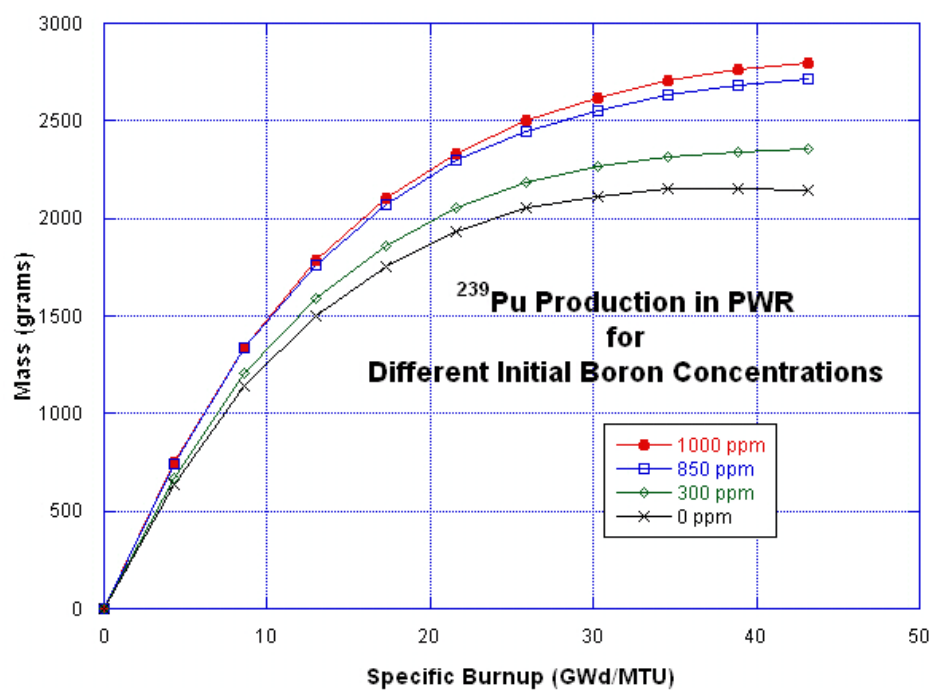


Figure 307: ²³⁹Pu Production in the PWR Model for Different Boron Concentrations

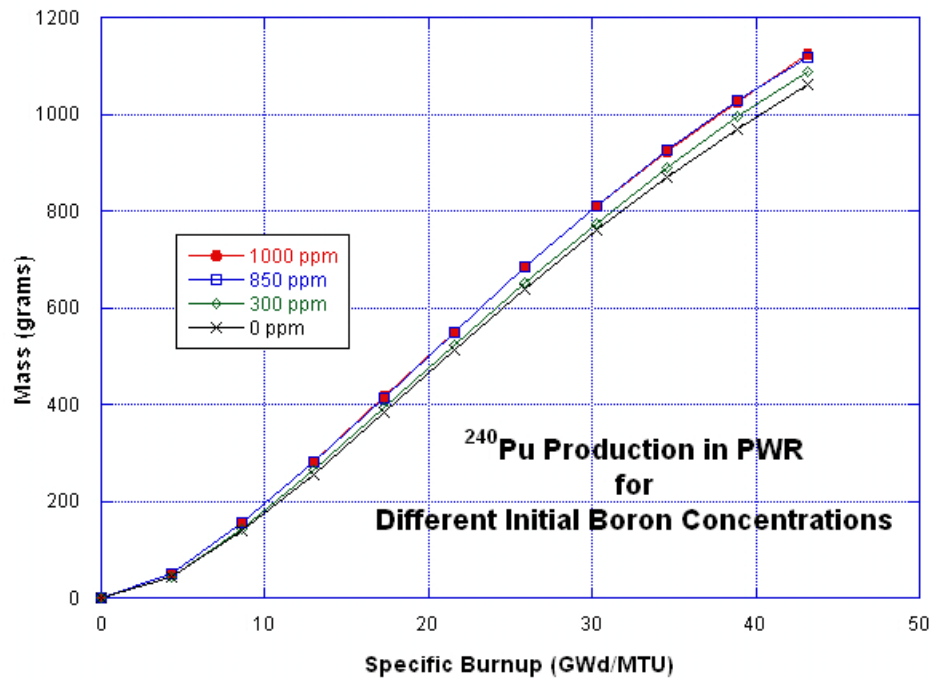


Figure 308: ²⁴⁰Pu Production in the PWR Model for Different Boron Concentrations

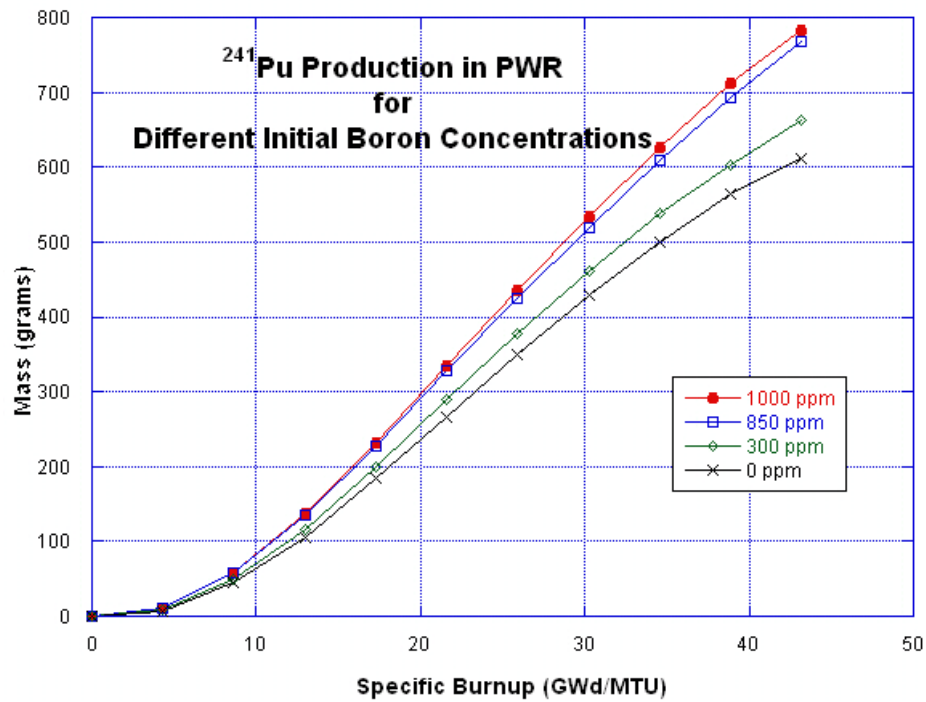


Figure 309: ²⁴¹Pu Production in the PWR Model for Different Boron Concentrations

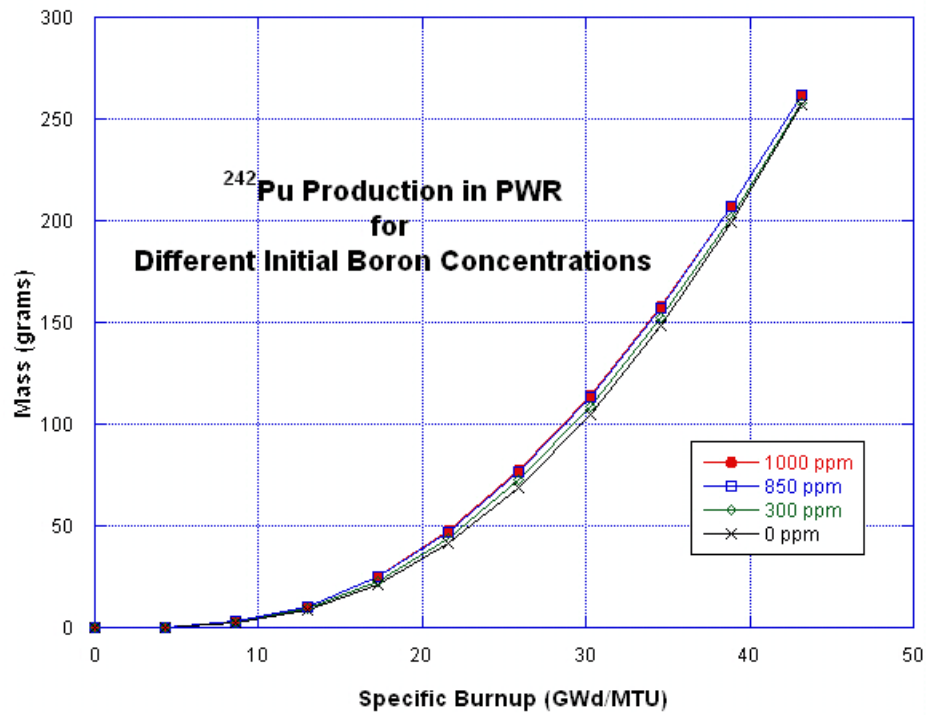


Figure 310: ²⁴²Pu Production in the PWR Model for Different Boron Concentrations

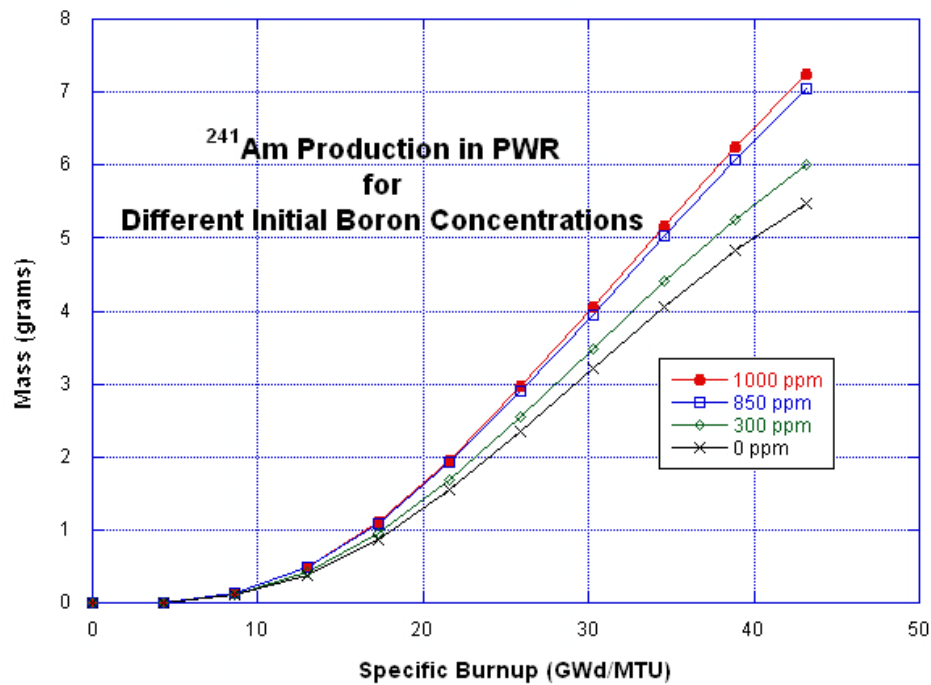


Figure 311: ²⁴¹Am Production in the PWR Model for Different Boron Concentrations

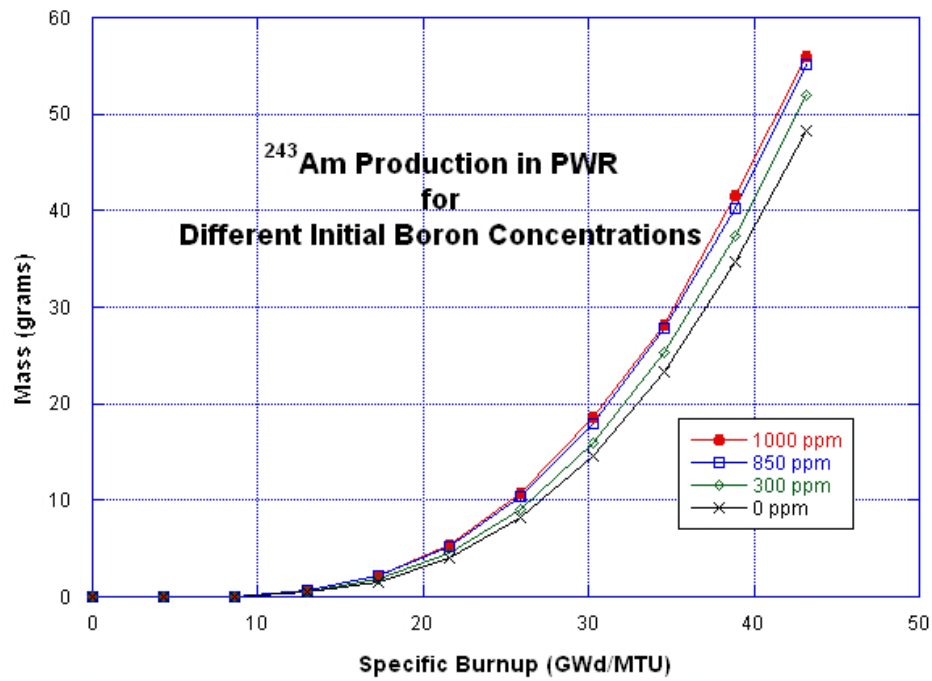


Figure 312: ²⁴³Am Production in the PWR Model for Different Boron Concentrations

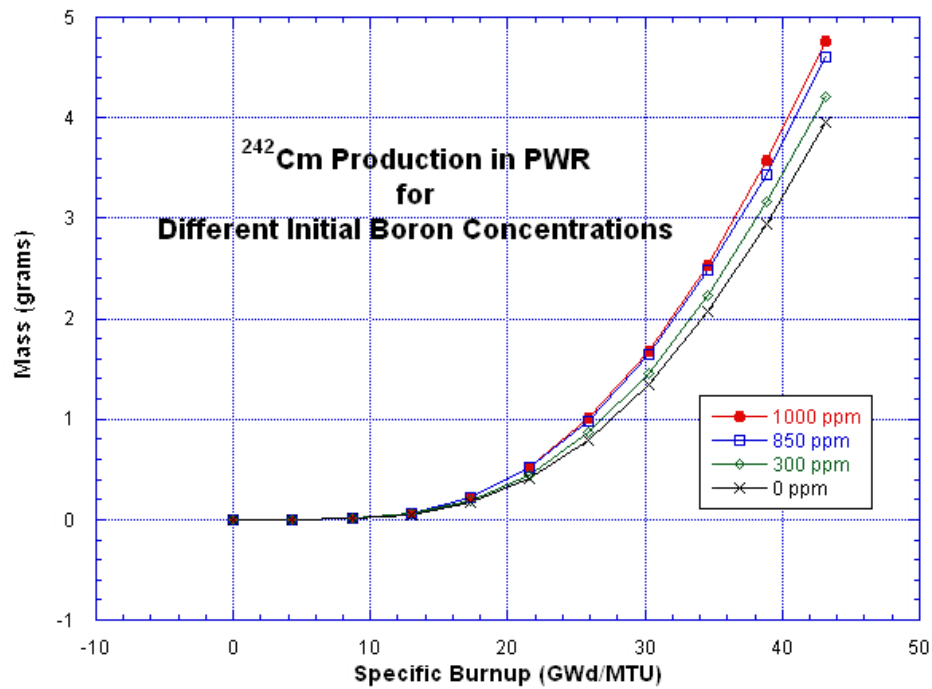


Figure 313: ²⁴²Cm Production in the PWR Model for Different Boron Concentrations

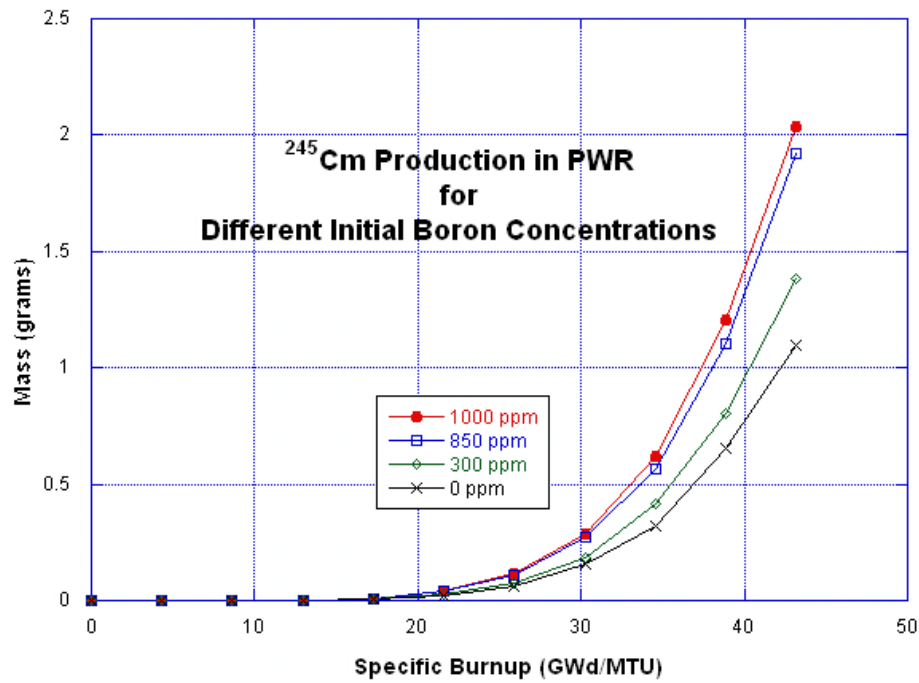


Figure 314: ²⁴⁵Cm Production in the PWR Model for Different Boron Concentrations

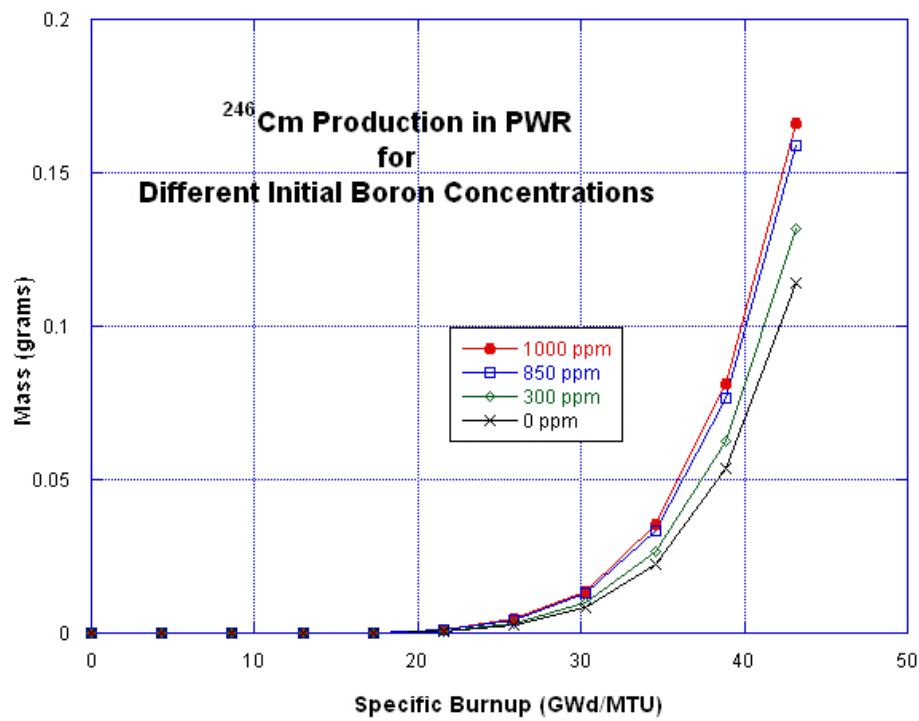


Figure 315: ²⁴⁶Cm Production in the PWR Model for Different Boron Concentrations

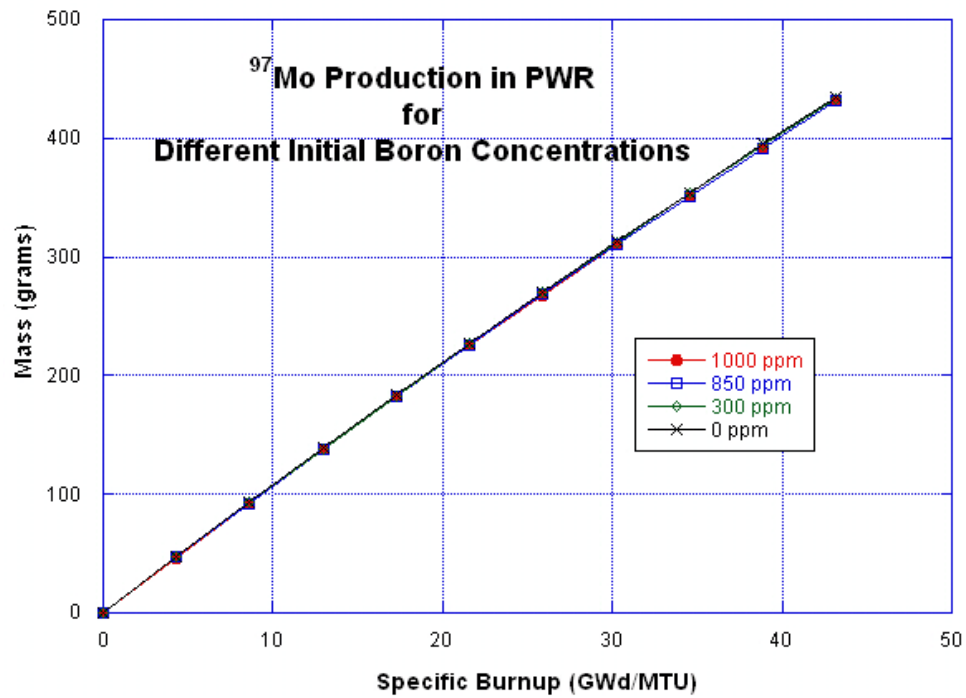


Figure 316: ⁹⁷Mo Production in the PWR Model for Different Boron Concentrations

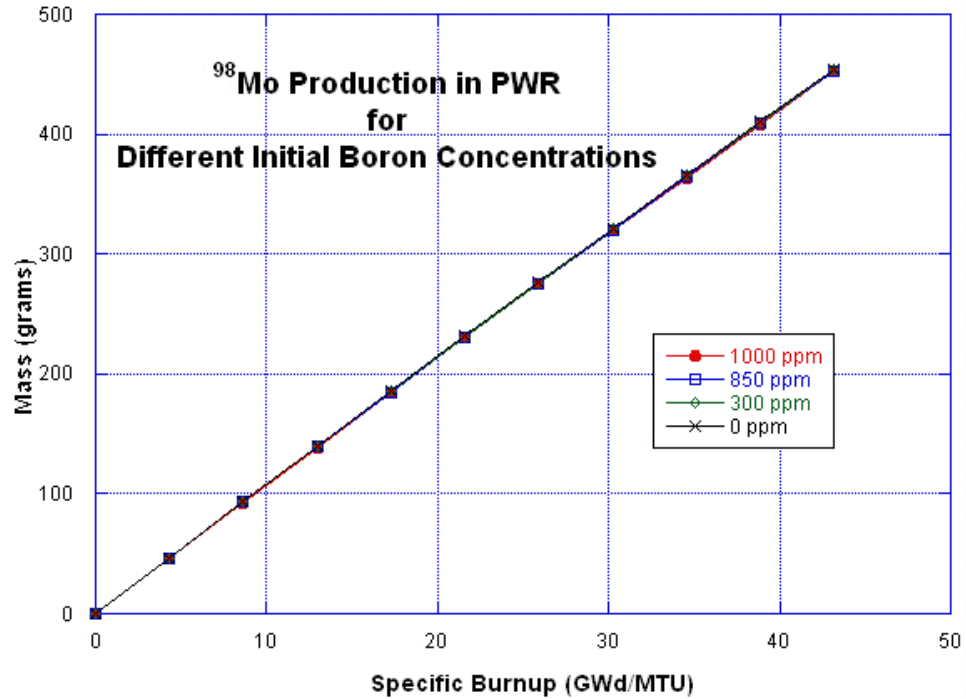


Figure 317: ⁹⁸Mo Production in the PWR Model for Different Boron Concentrations

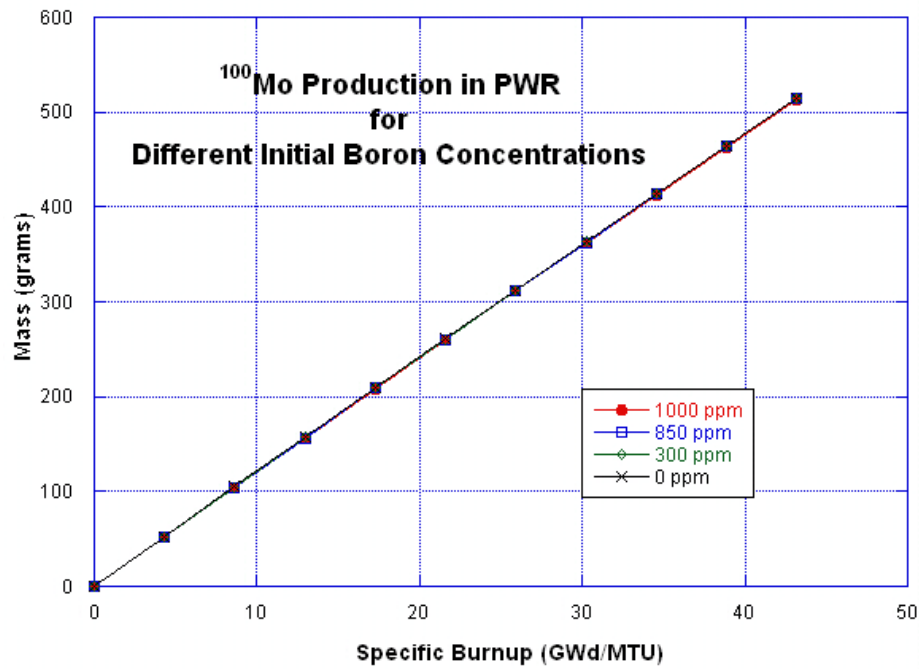


Figure 318: ¹⁰⁰Mo Production in the PWR Model for Different Boron Concentrations

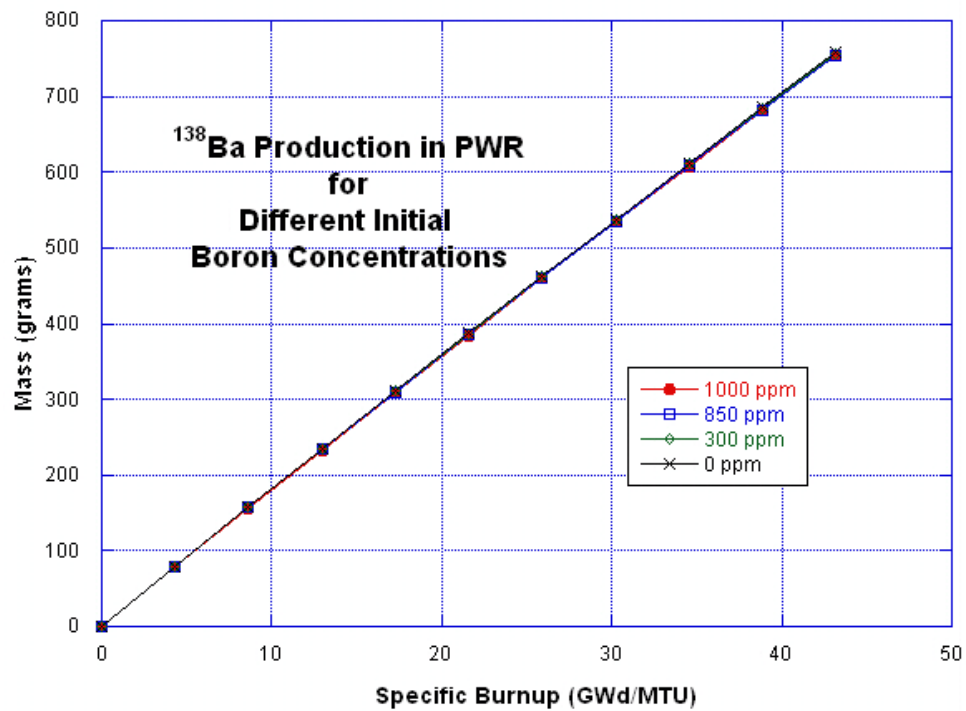


Figure 319: ¹³⁸Ba Production in the PWR Model for Different Boron Concentrations

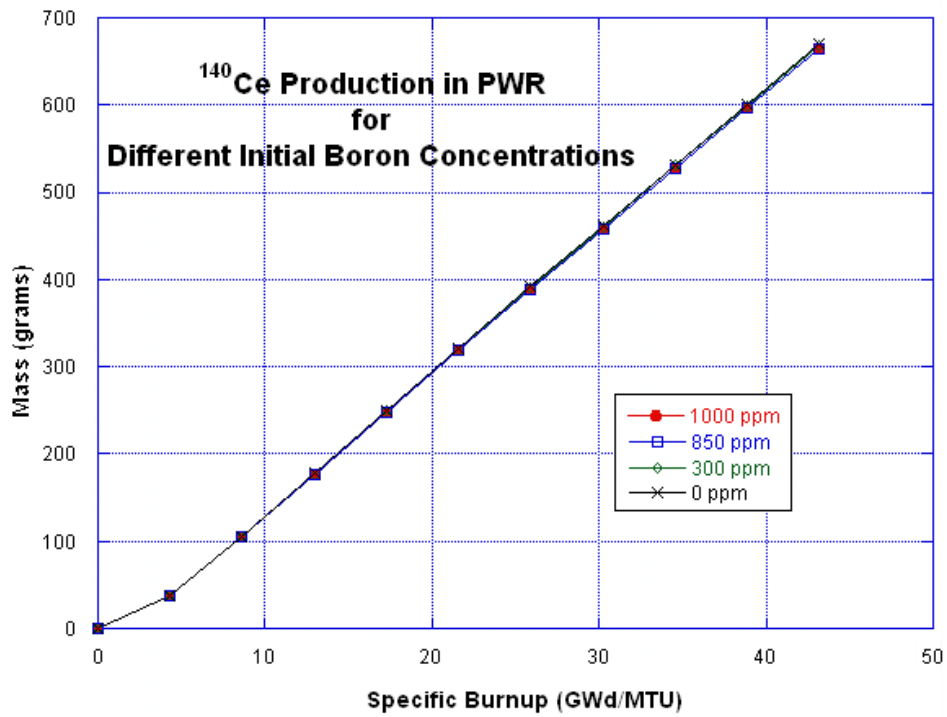


Figure 320: ¹⁴⁰Ce Production in the PWR Model for Different Boron Concentrations

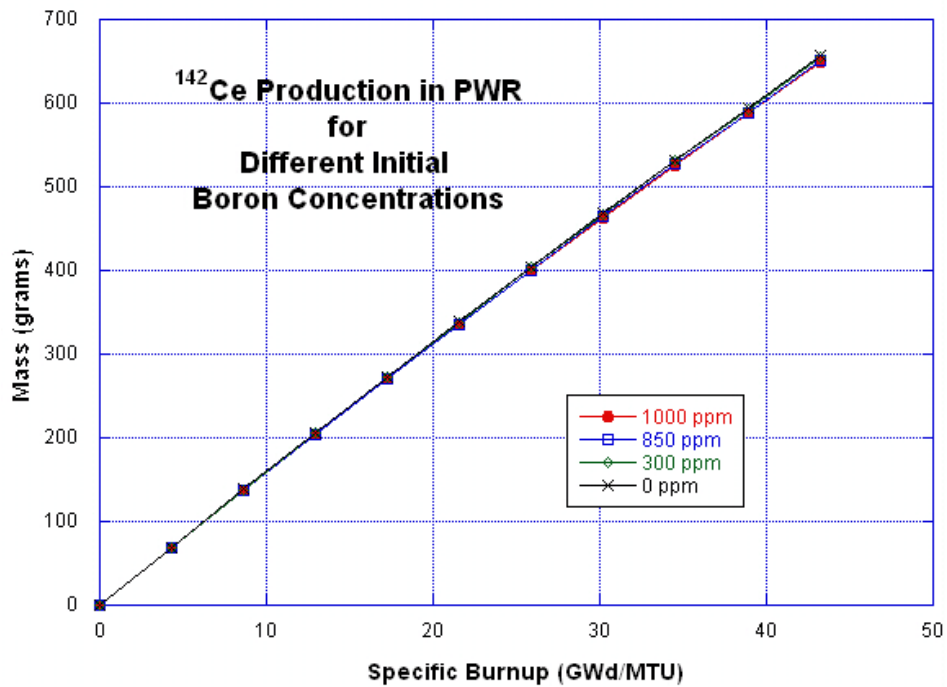


Figure 321: ¹⁴²Ce Production in the PWR Model for Different Boron Concentrations

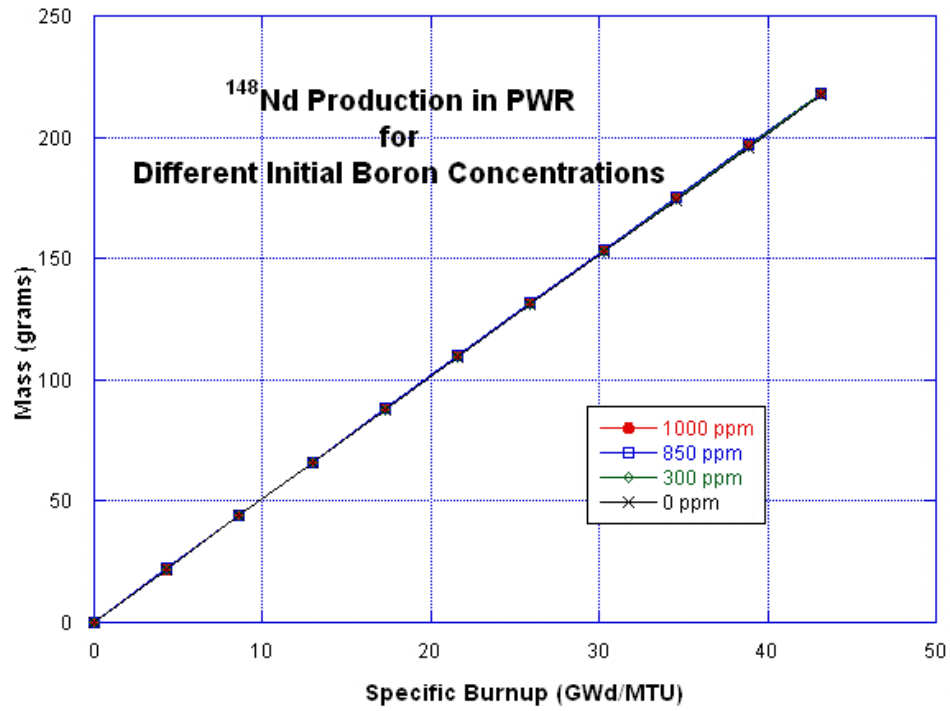


Figure 322: ¹⁴⁸Nd Production in the PWR Model for Different Boron Concentrations

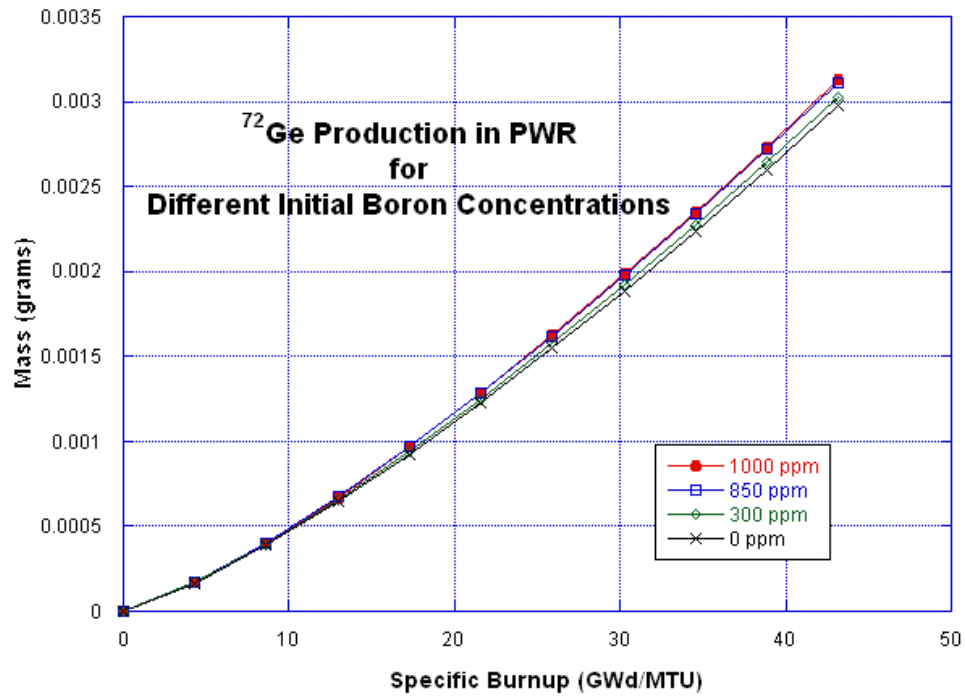


Figure 323: ⁷²Ge Production in the PWR Model for Different Boron Concentrations

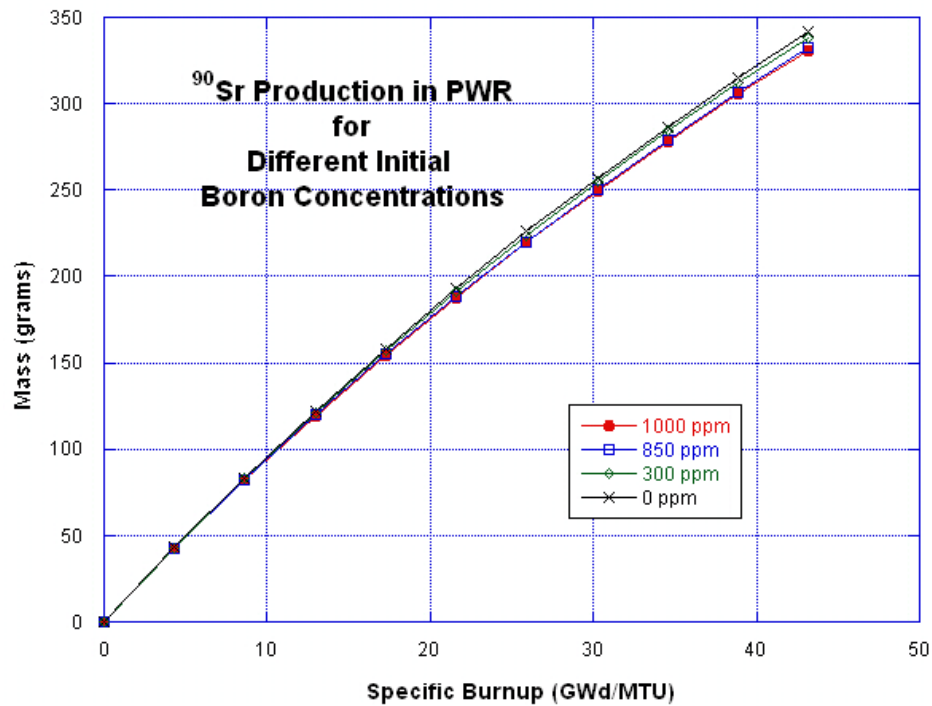


Figure 324: ⁹⁰Sr Production in the PWR Model for Different Boron Concentrations

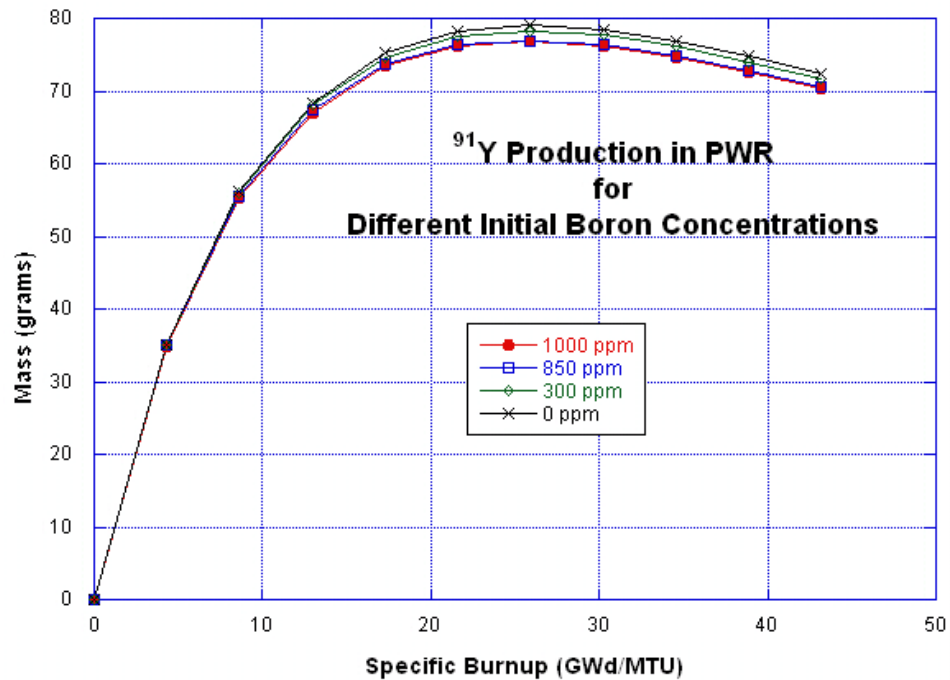


Figure 325: ⁹¹Y Production in the PWR Model for Different Boron Concentrations

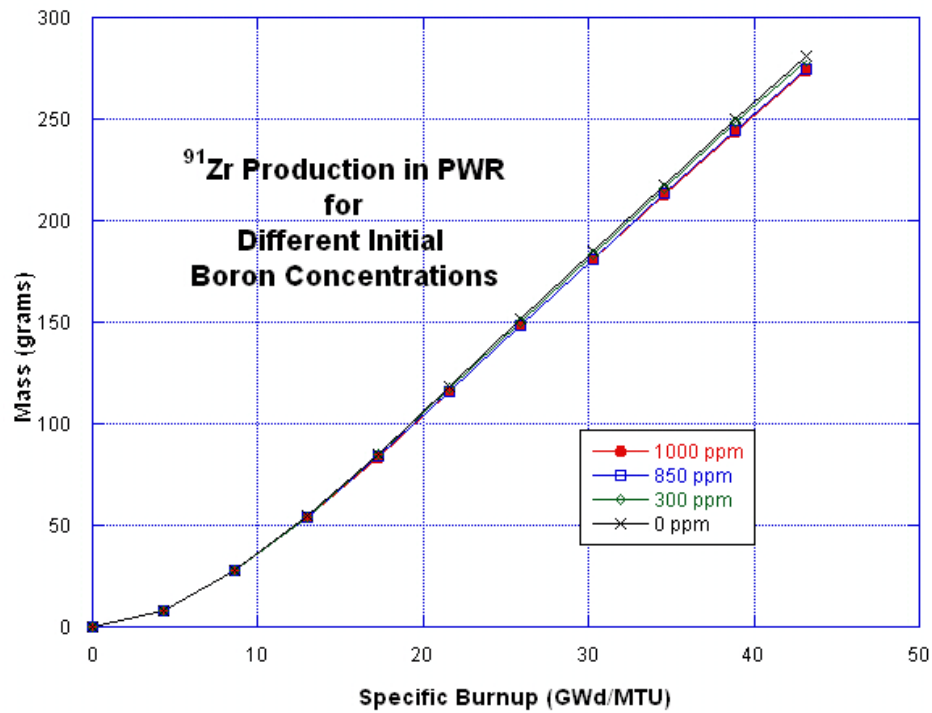


Figure 326: ⁹¹Zr Production in the PWR Model for Different Boron Concentrations

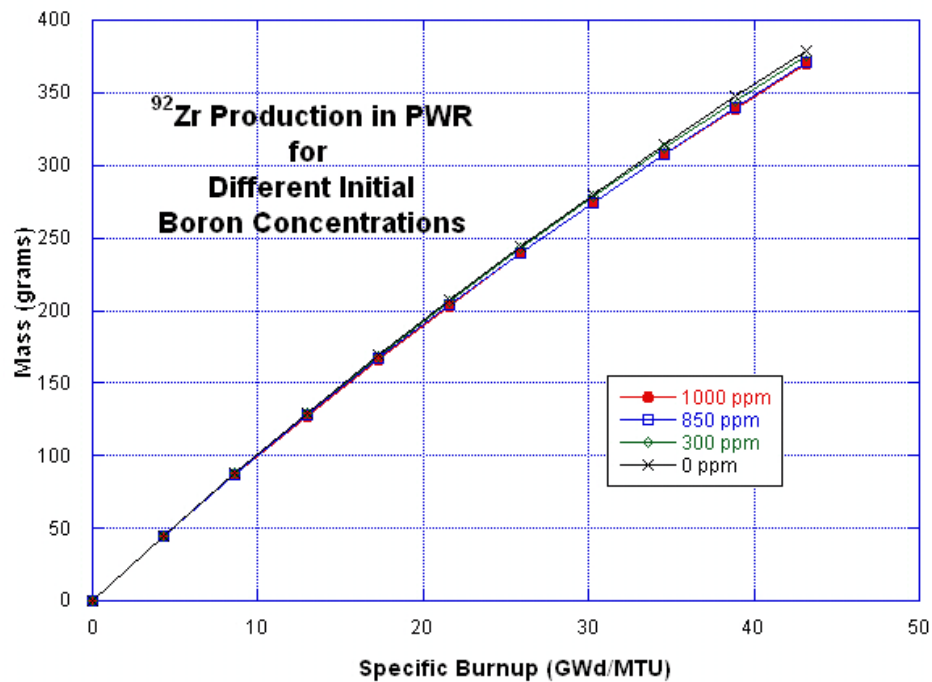


Figure 327: ⁹²Zr Production in the PWR Model for Different Boron Concentrations

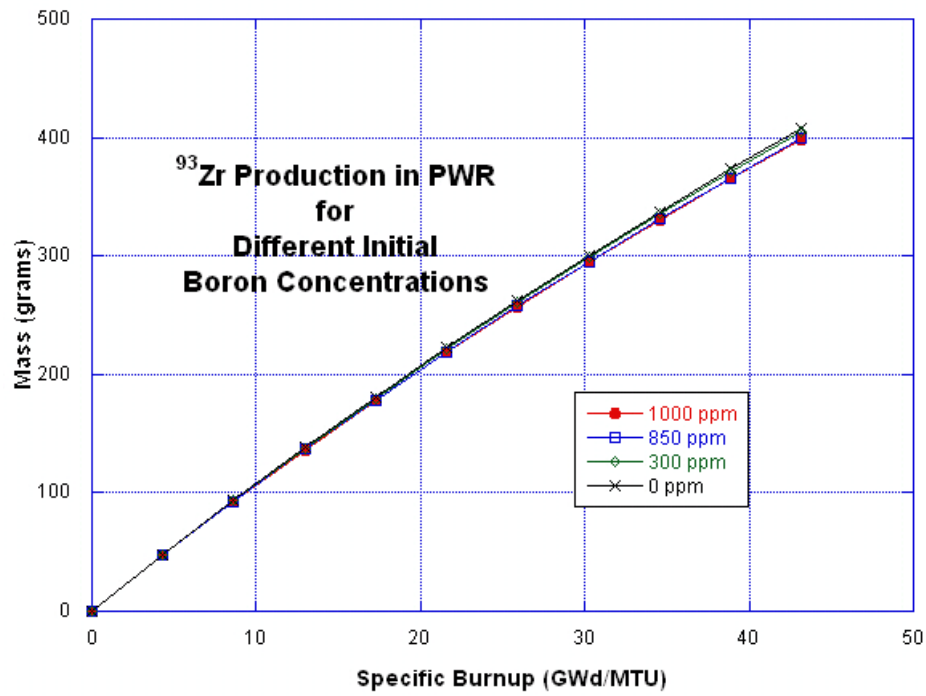


Figure 328: ⁹³Zr Production in the PWR Model for Different Boron Concentrations

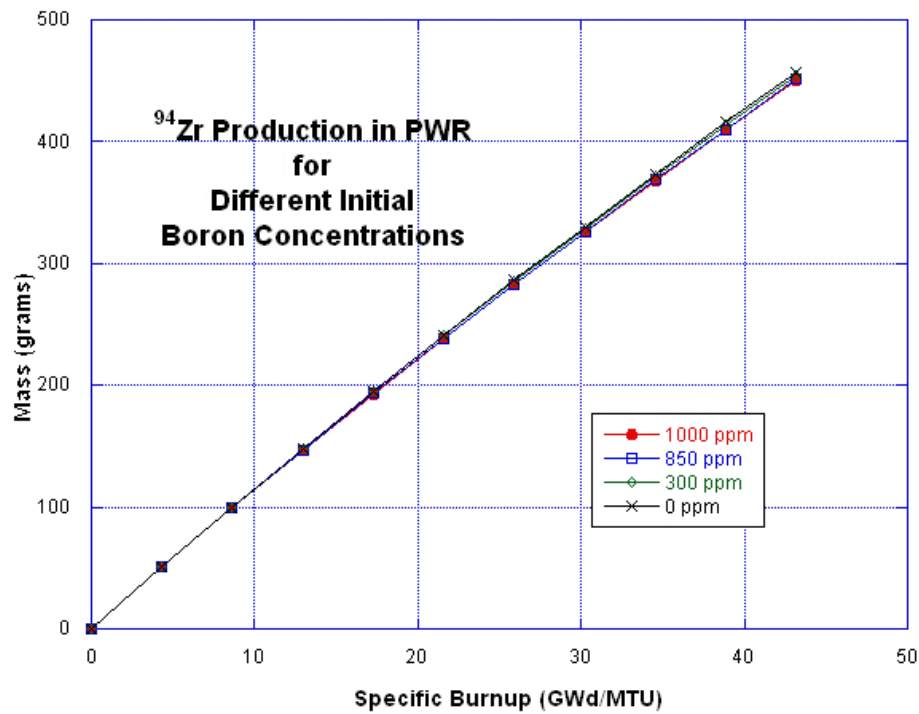


Figure 329: ⁹⁴Zr Production in the PWR Model for Different Boron Concentrations

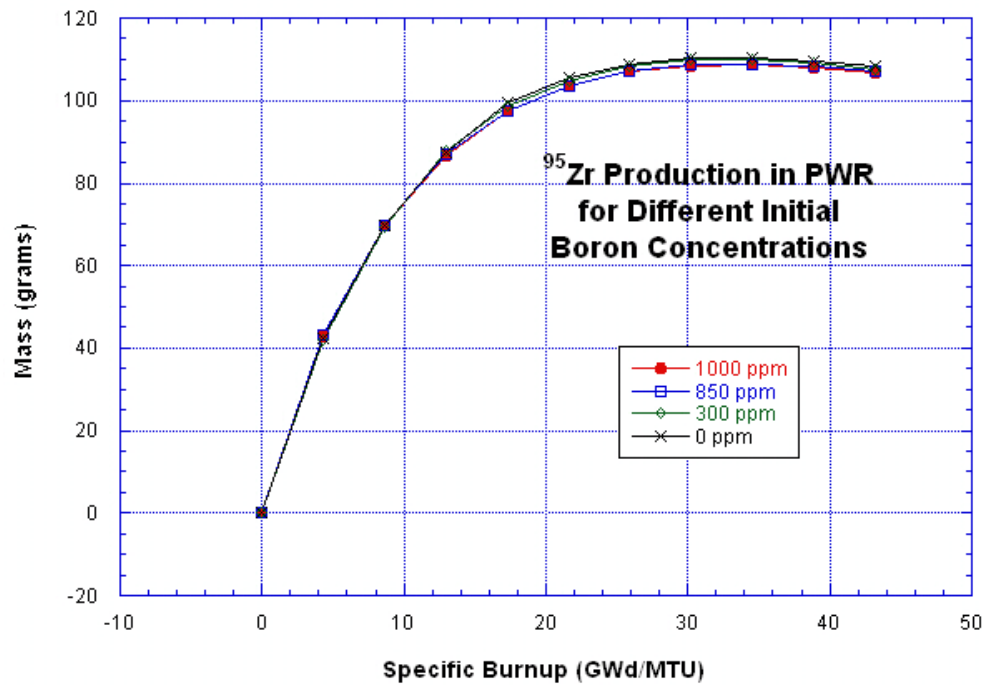


Figure 330: ⁹⁵Zr Production in the PWR Model for Different Boron Concentrations

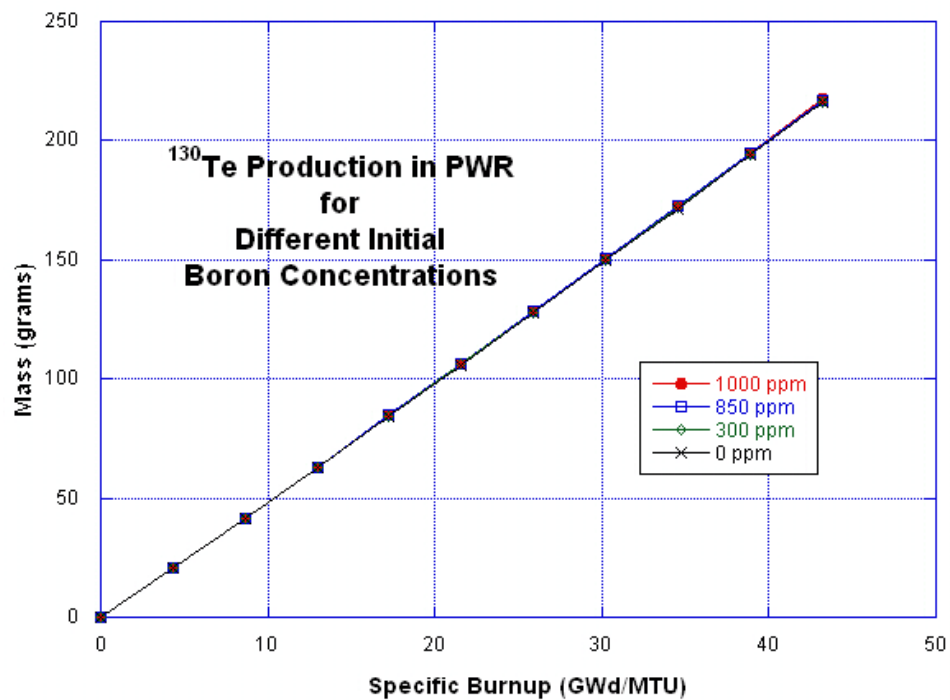


Figure 331: ¹³⁰Te Production in the PWR Model for Different Boron Concentrations

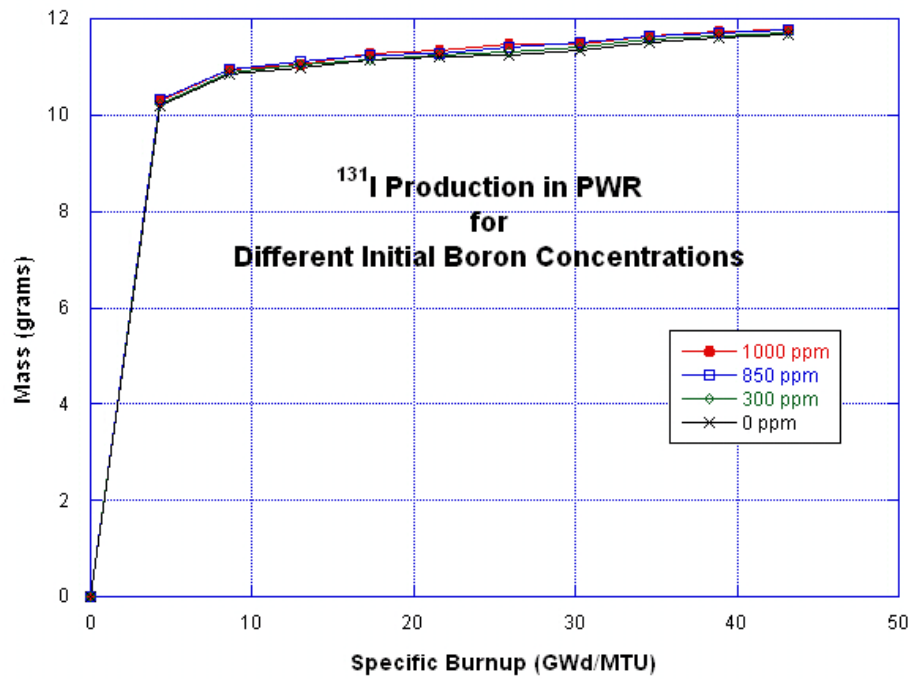


Figure 332: ¹³¹I Production in the PWR Model for Different Boron Concentrations

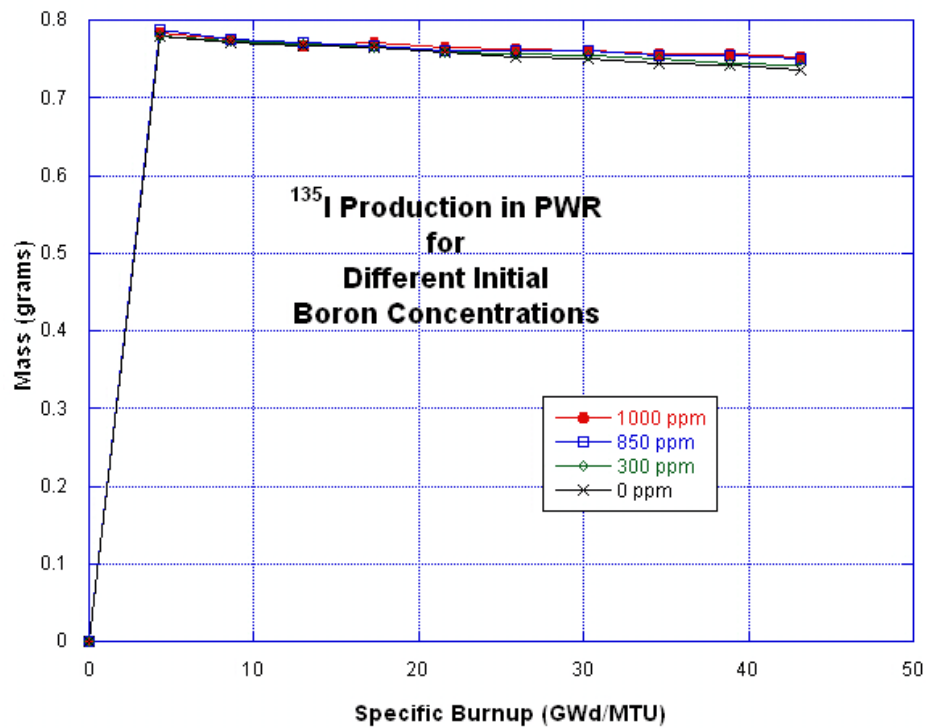


Figure 333: ¹³⁵I Production in the PWR Model for Different Boron Concentrations

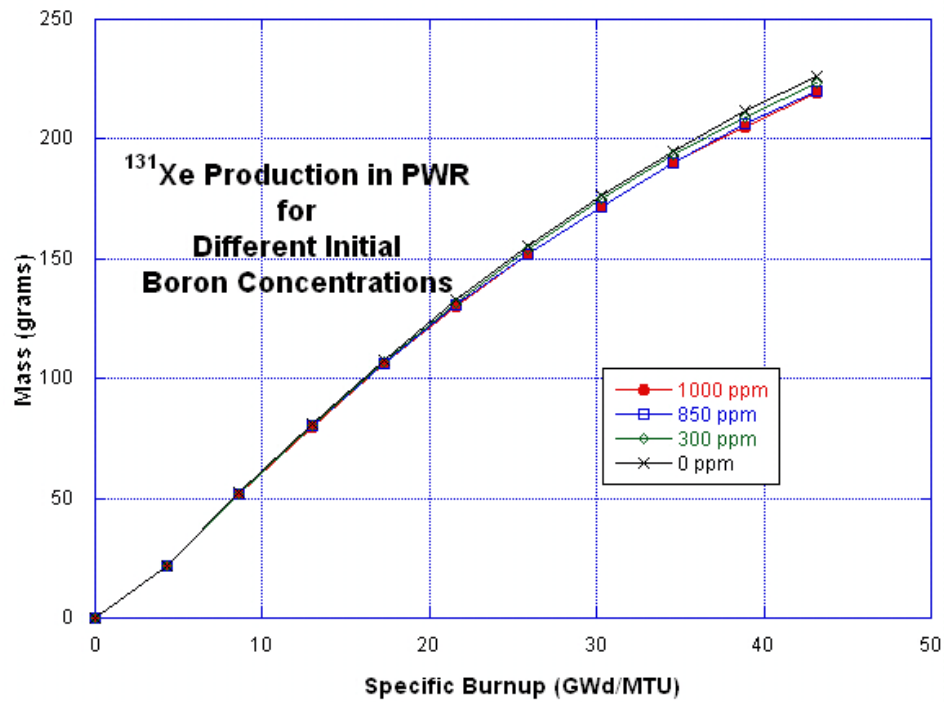


Figure 334: ¹³¹Xe Production in the PWR Model for Different Boron Concentrations

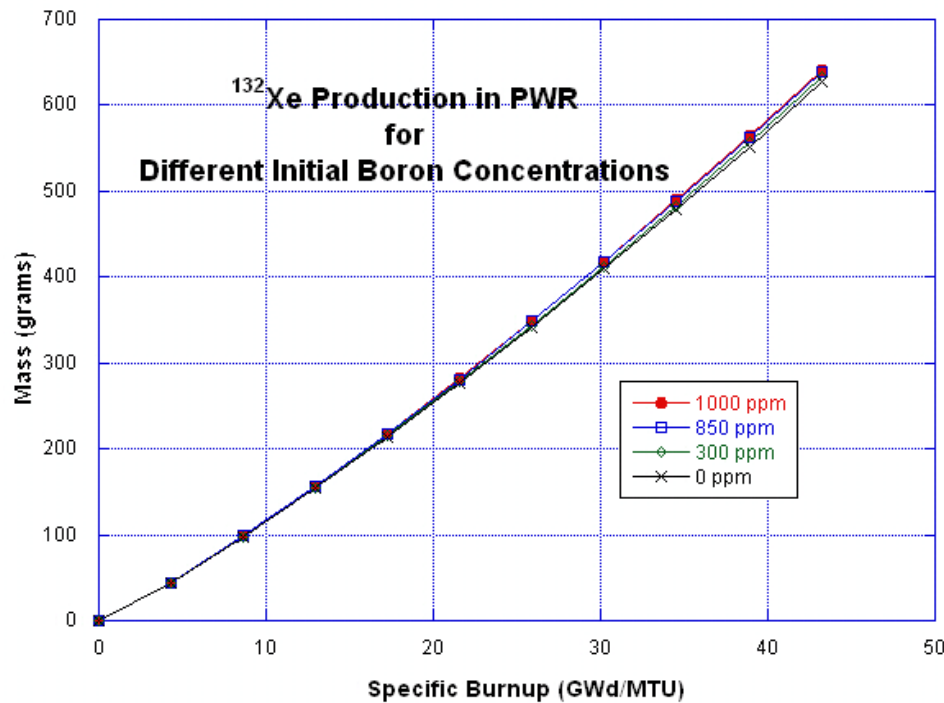


Figure 335: ¹³²Xe Production in the PWR Model for Different Boron Concentrations

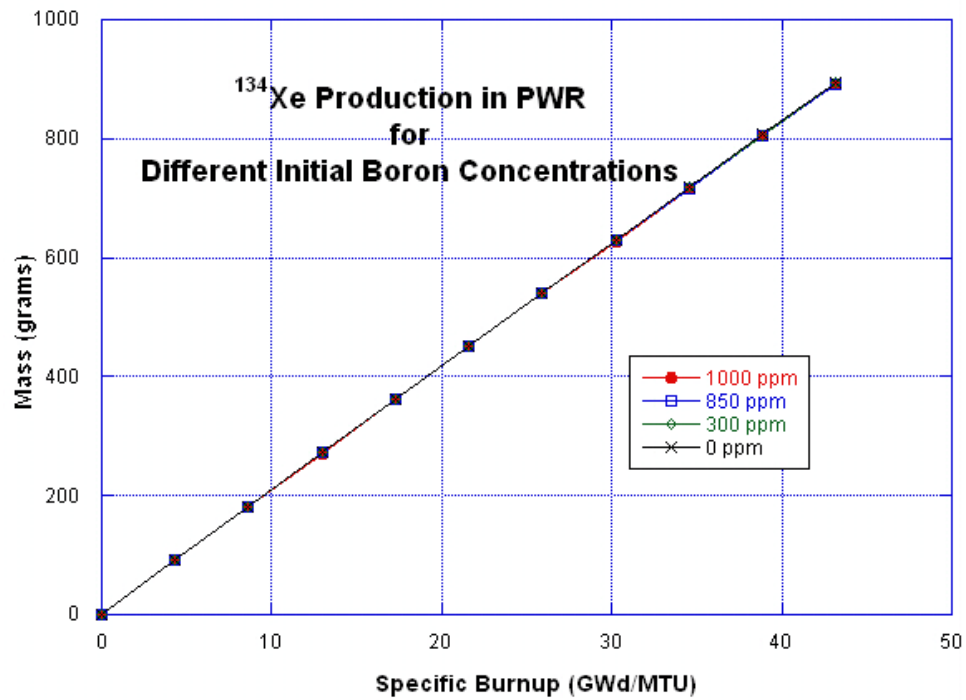


Figure 336: ¹³⁴Xe Production in the PWR Model for Different Boron Concentrations

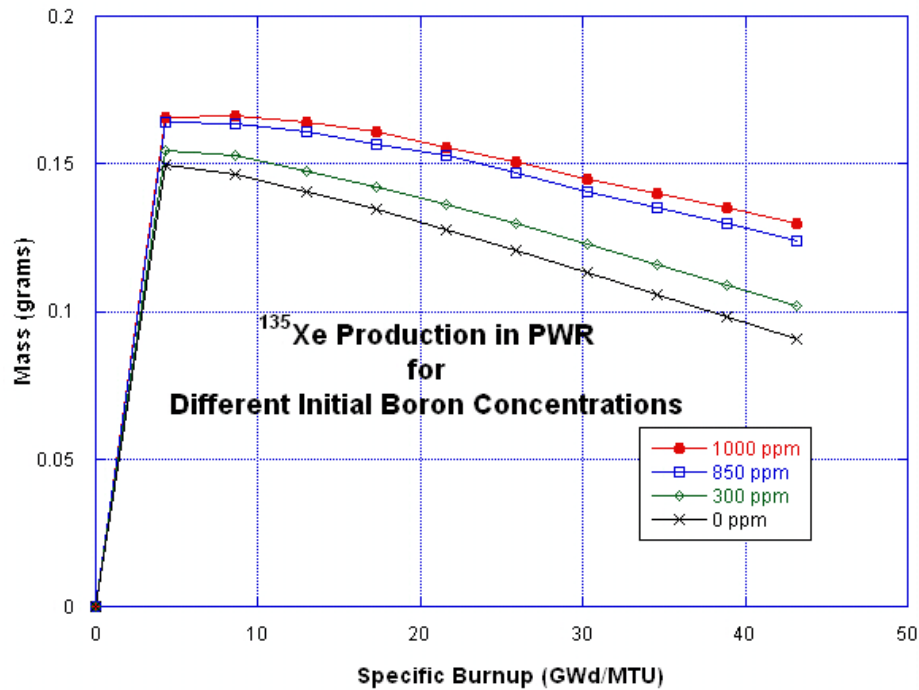


Figure 337: ¹³⁵Xe Production in the PWR Model for Different Boron Concentrations

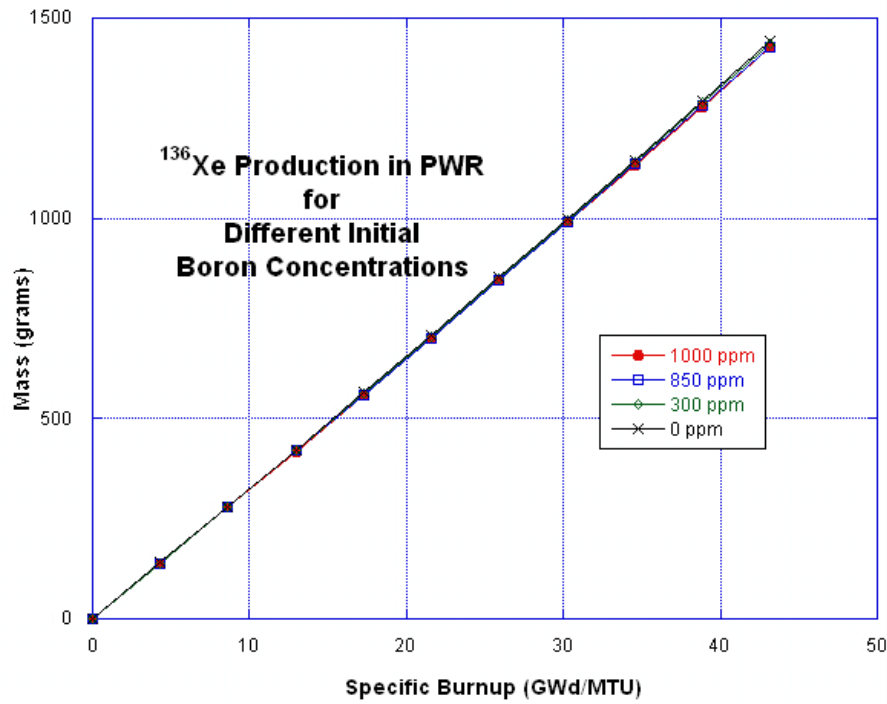


Figure 338: ¹³⁵Xe Production in the PWR Model for Different Boron Concentrations

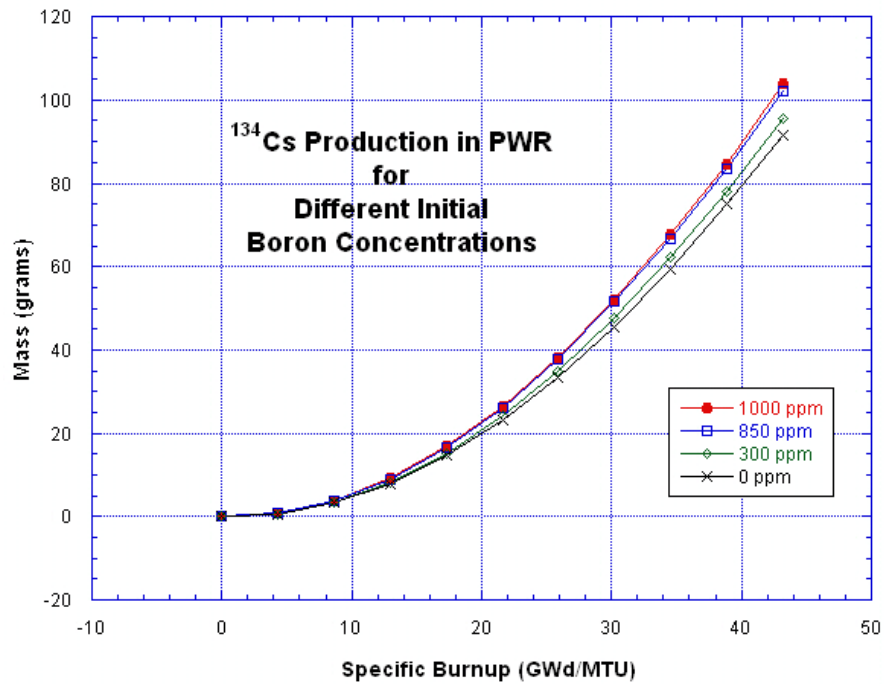


Figure 339: ¹³⁴Cs Production in the PWR Model for Different Boron Concentrations

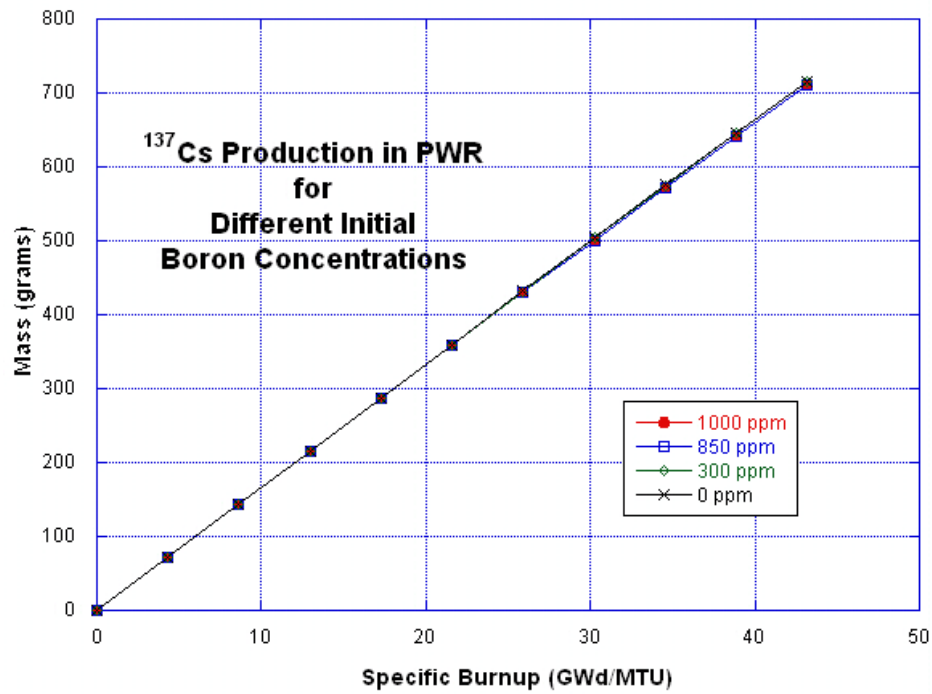


Figure 340: ¹³⁷Cs Production in the PWR Model for Different Boron Concentrations

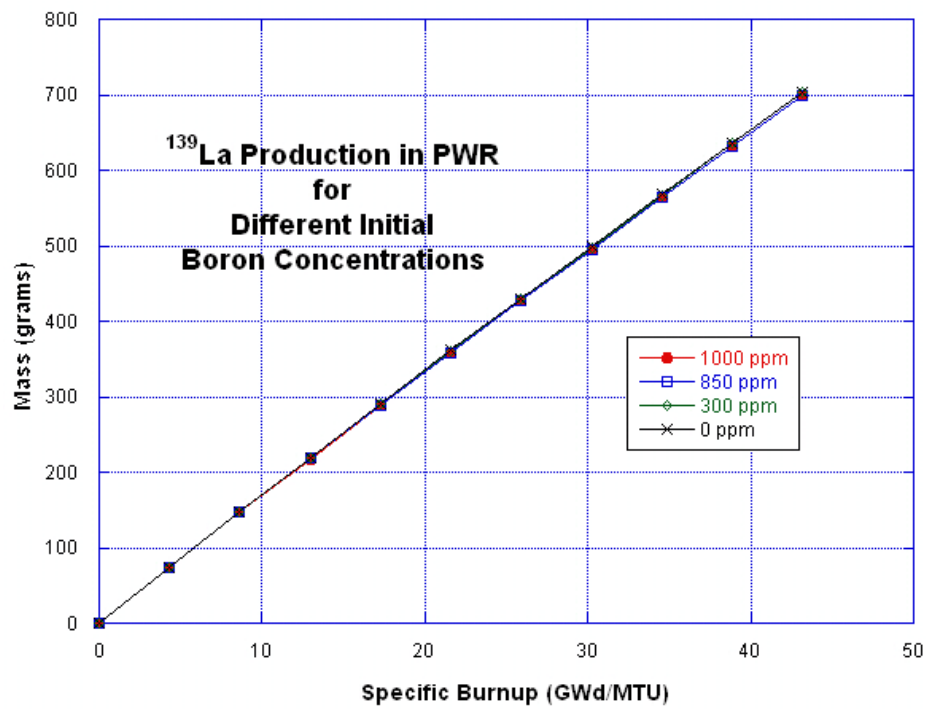


Figure 341: ¹³⁹La Production in the PWR Model for Different Boron Concentrations

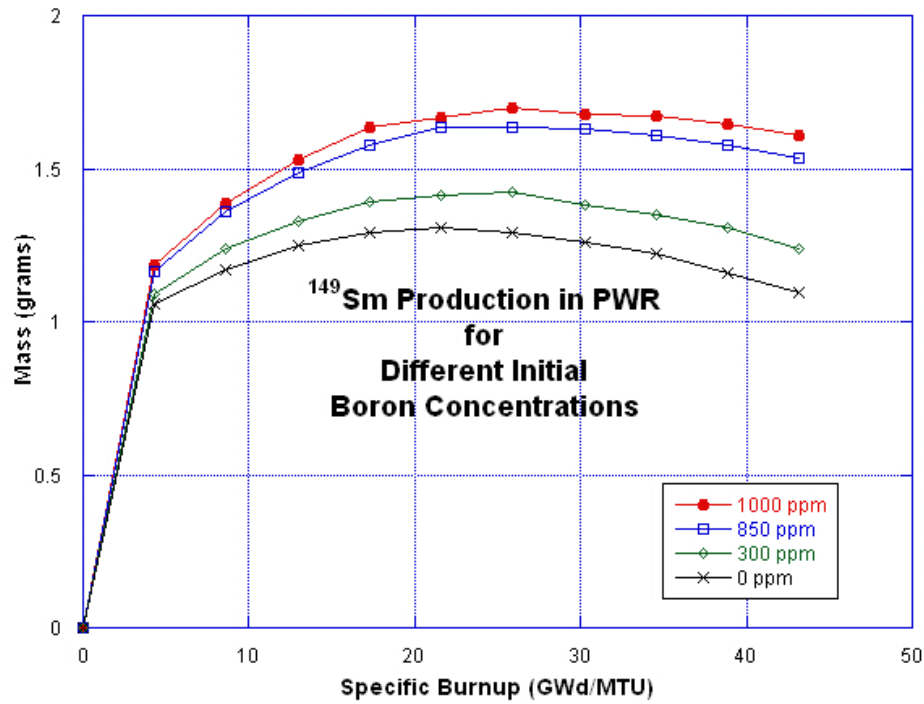


Figure 342: ¹⁴⁹Sm Production in the PWR Model for Different Boron Concentrations

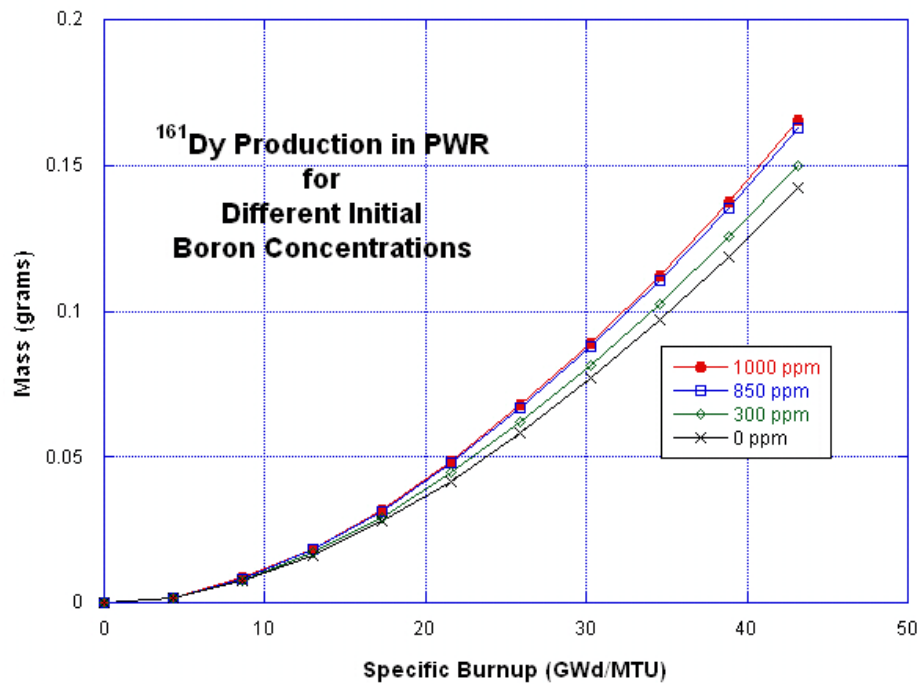


Figure 343: ¹⁶¹Dy Production in the PWR Model for Different Boron Concentrations

**PWR Sensitivity Study
Plots of 46 Nuclides of Interest
Cladding Thickness Variation**

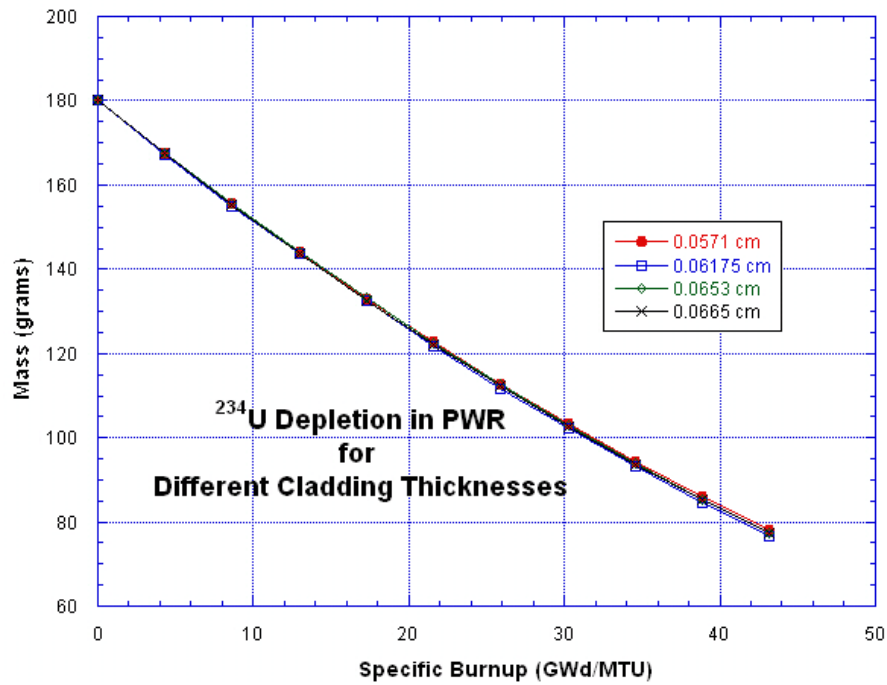


Figure 344: ²³⁴U Depletion in the PWR Model for Different Cladding Thicknesses

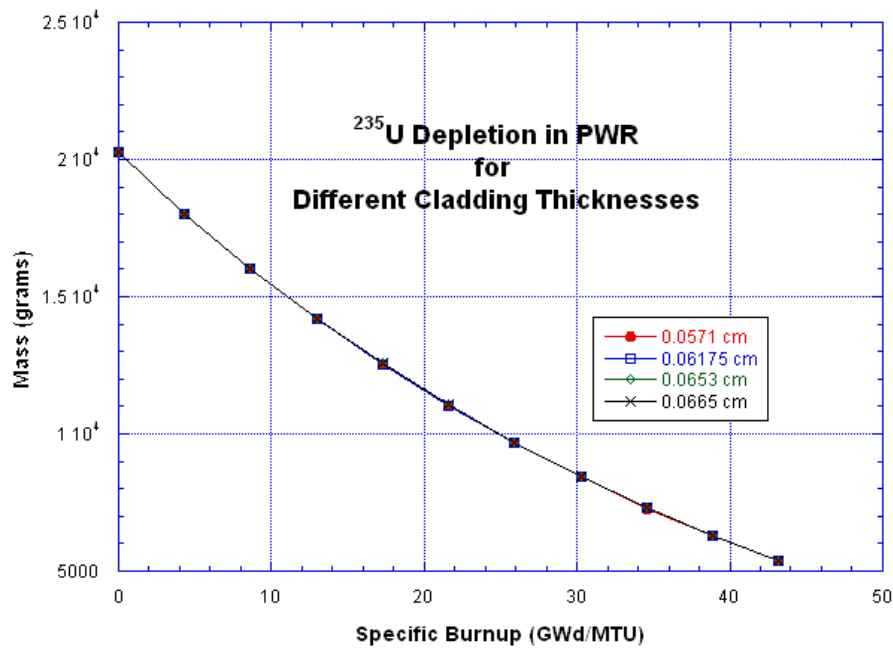


Figure 345: ²³⁵U Depletion in the PWR Model for Different Cladding Thicknesses

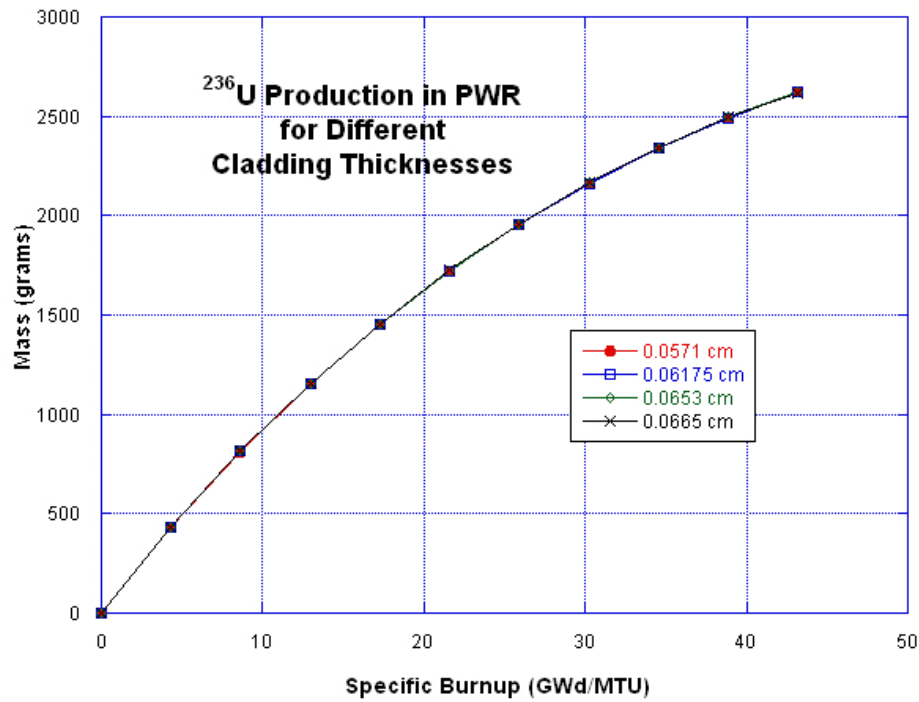


Figure 346: ²³⁶U Production in the PWR Model for Different Cladding Thicknesses

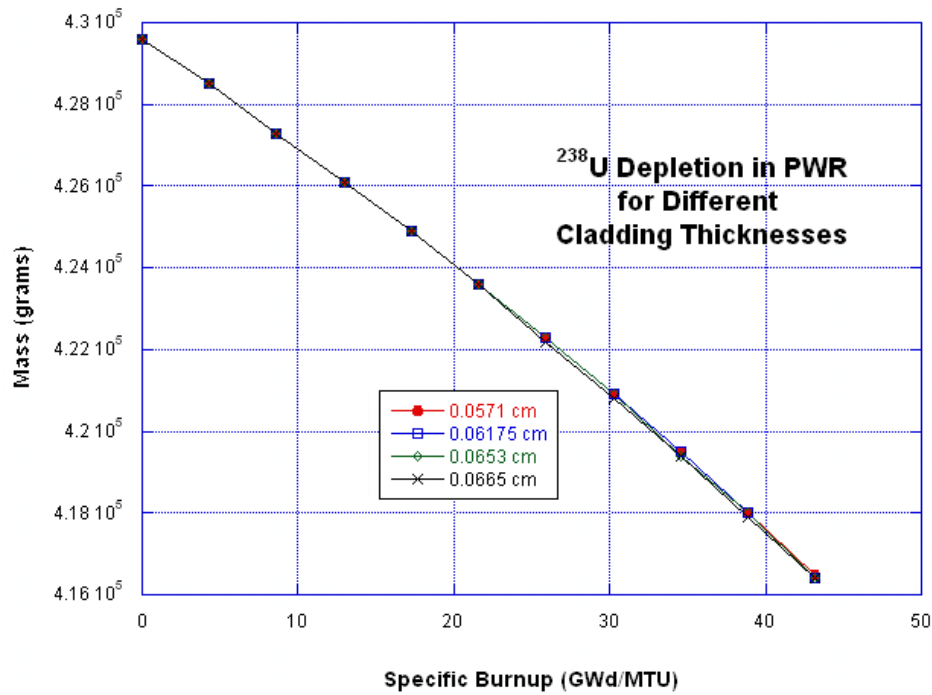


Figure 347: ²³⁸U Depletion in the PWR Model for Different Cladding Thicknesses

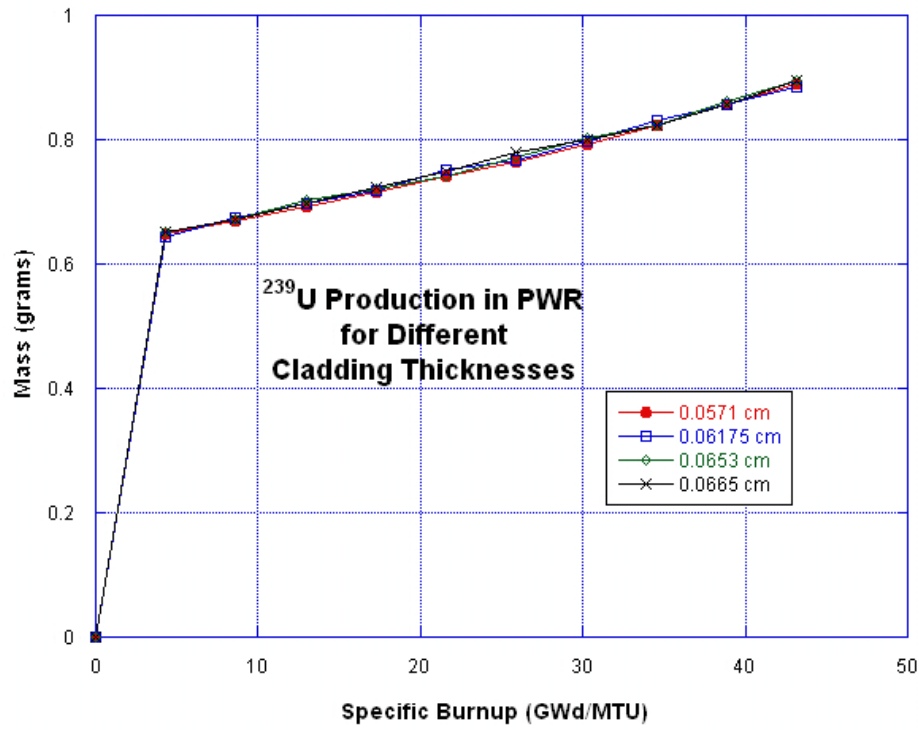


Figure 348: ²³⁹U Production in the PWR Model for Different Cladding Thicknesses

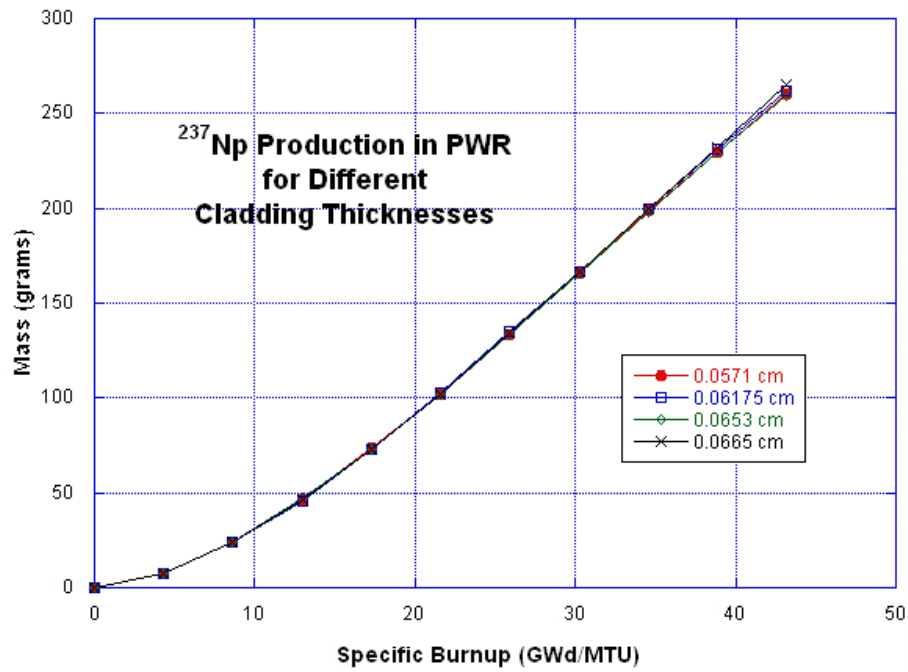


Figure 349: ²³⁷Np Production in the PWR Model for Different Cladding Thicknesses

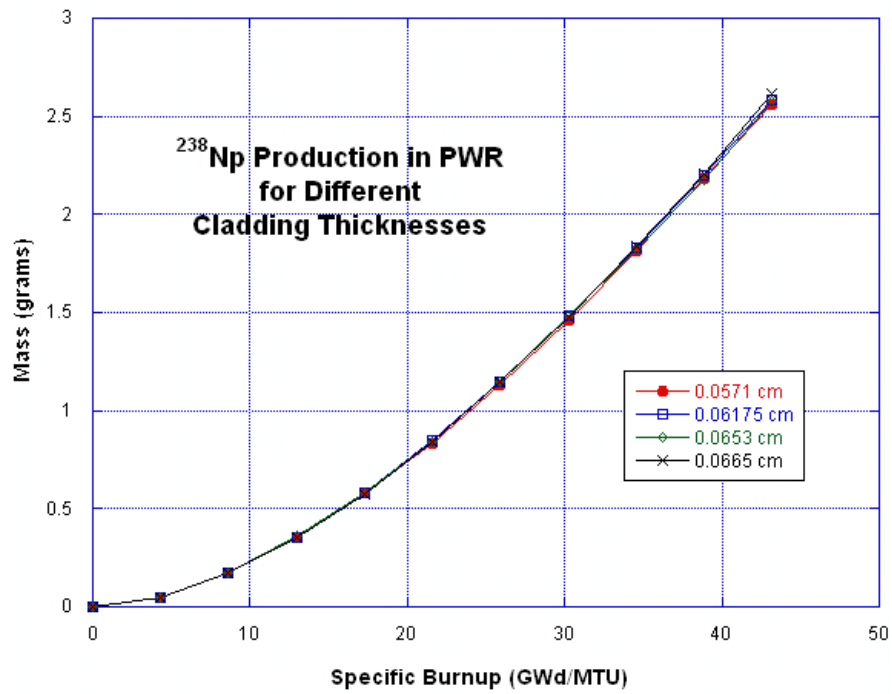


Figure 350: ^{236}U Production in the PWR Model for Different Cladding Thicknesses

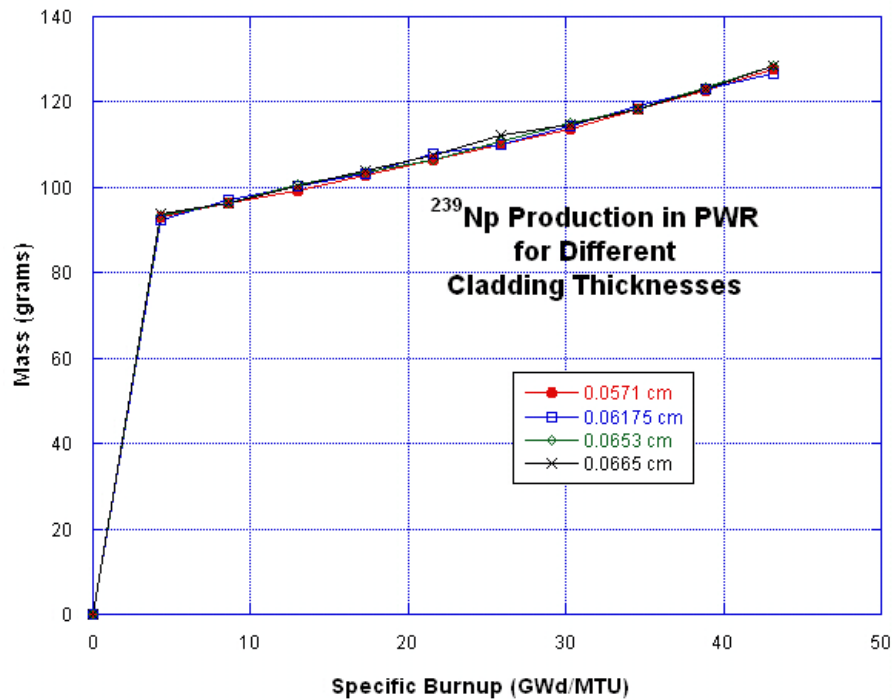


Figure 351: ^{236}U Production in the PWR Model for Different Cladding Thicknesses

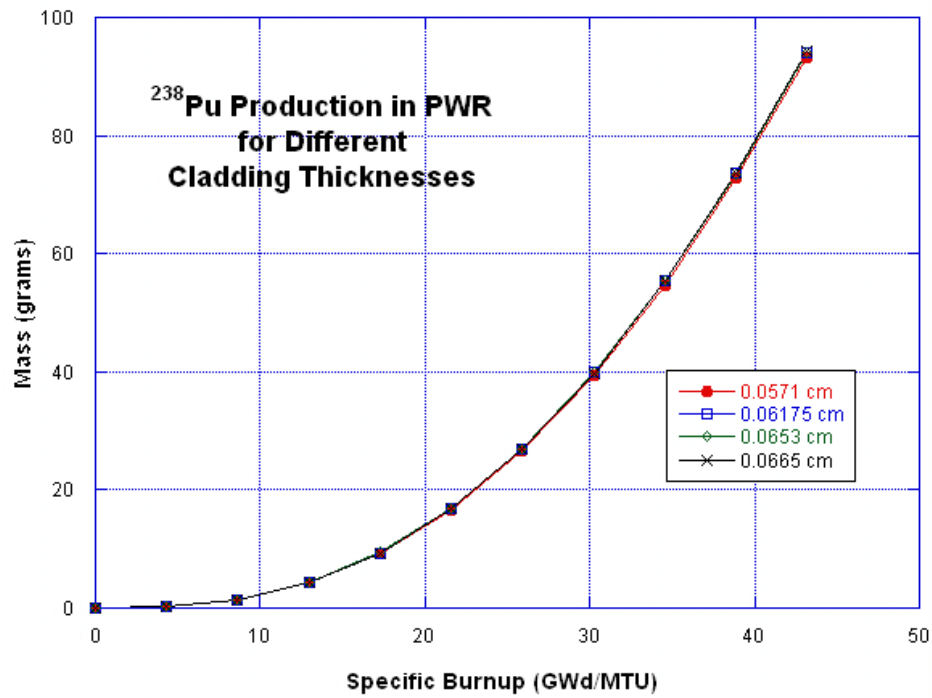


Figure 352: ²³⁸Pu Production in the PWR Model for Different Cladding Thicknesses

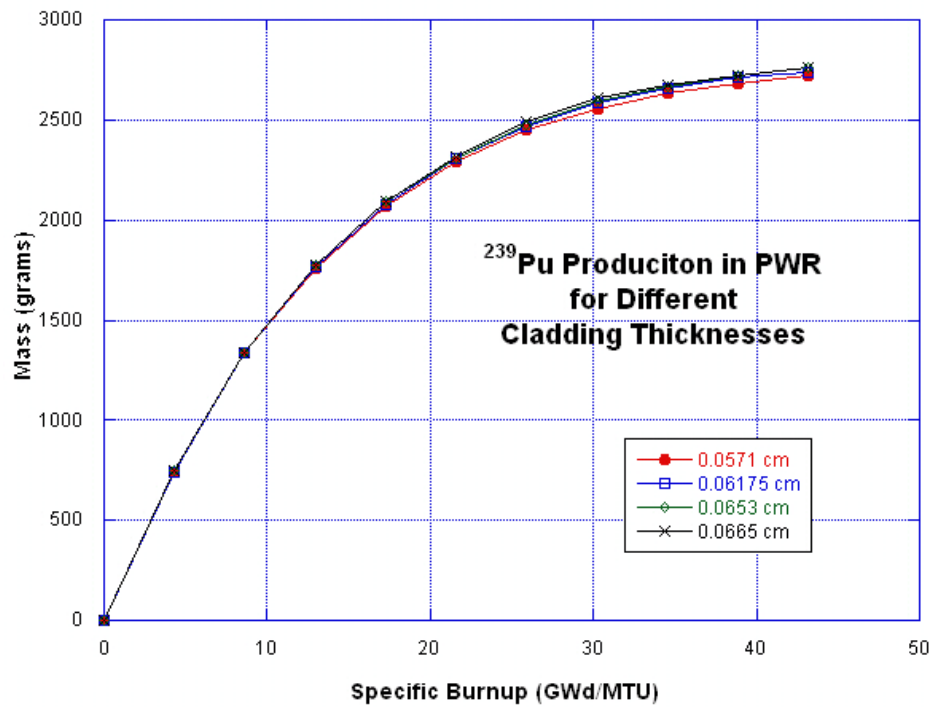


Figure 353: ²³⁹Pu Production in the PWR Model for Different Cladding Thicknesses

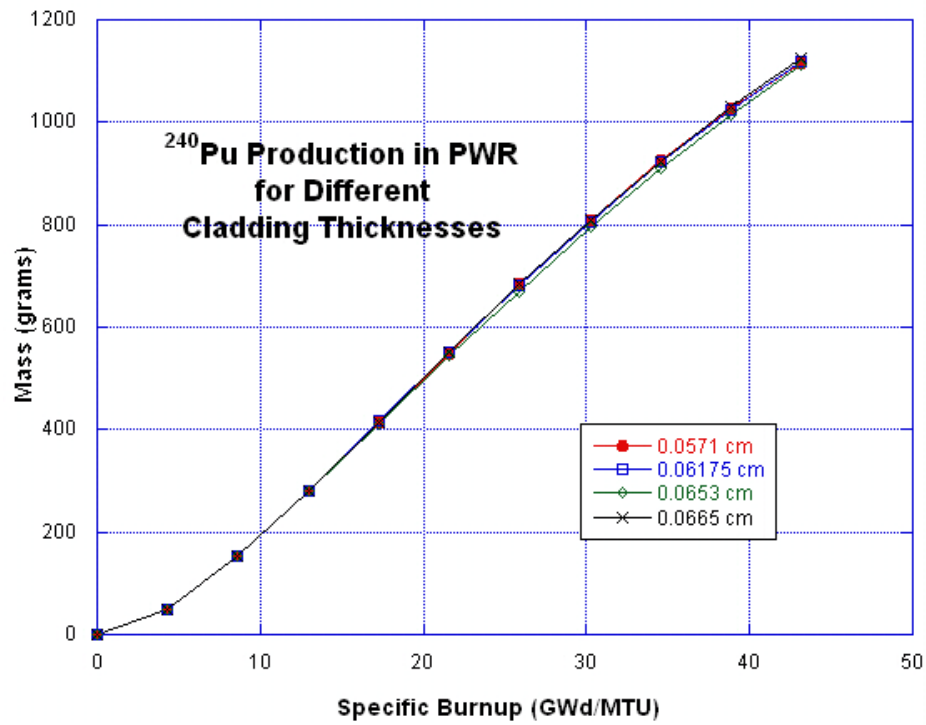


Figure 354: ²⁴⁰Pu Production in the PWR Model for Different Cladding Thicknesses

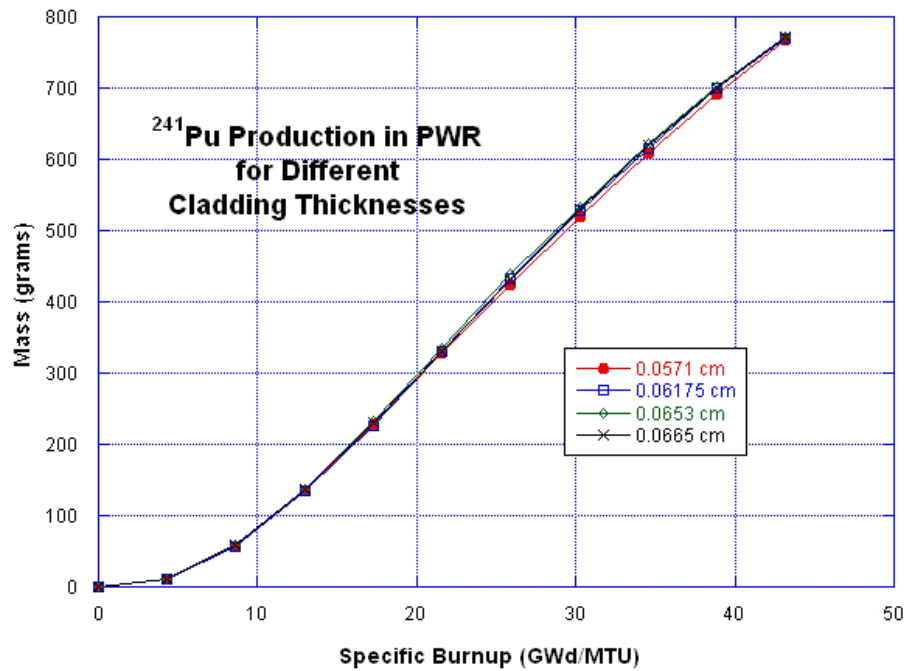


Figure 355: ²⁴¹Pu Production in the PWR Model for Different Cladding Thicknesses

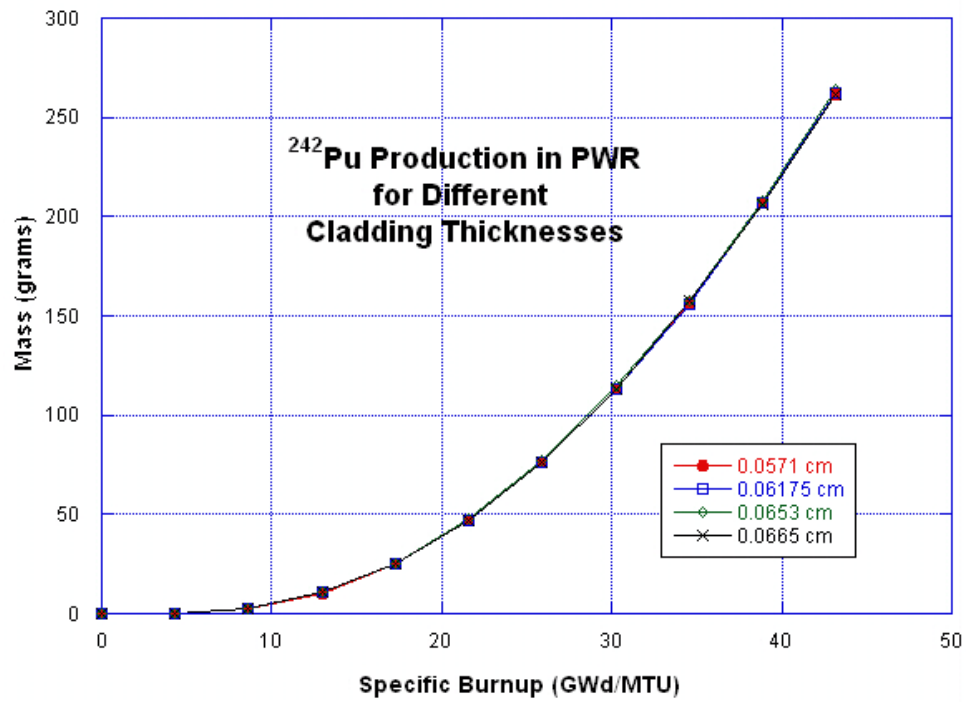


Figure 356: ²⁴²Pu Production in the PWR Model for Different Cladding Thicknesses

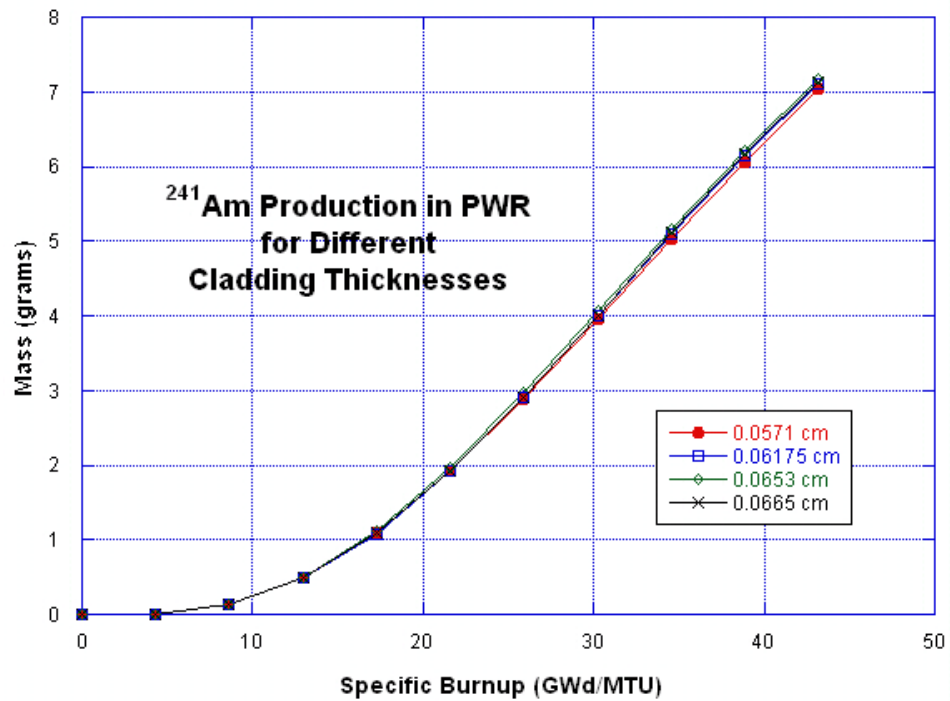


Figure 357: ²⁴¹Am Production in the PWR Model for Different Cladding Thicknesses

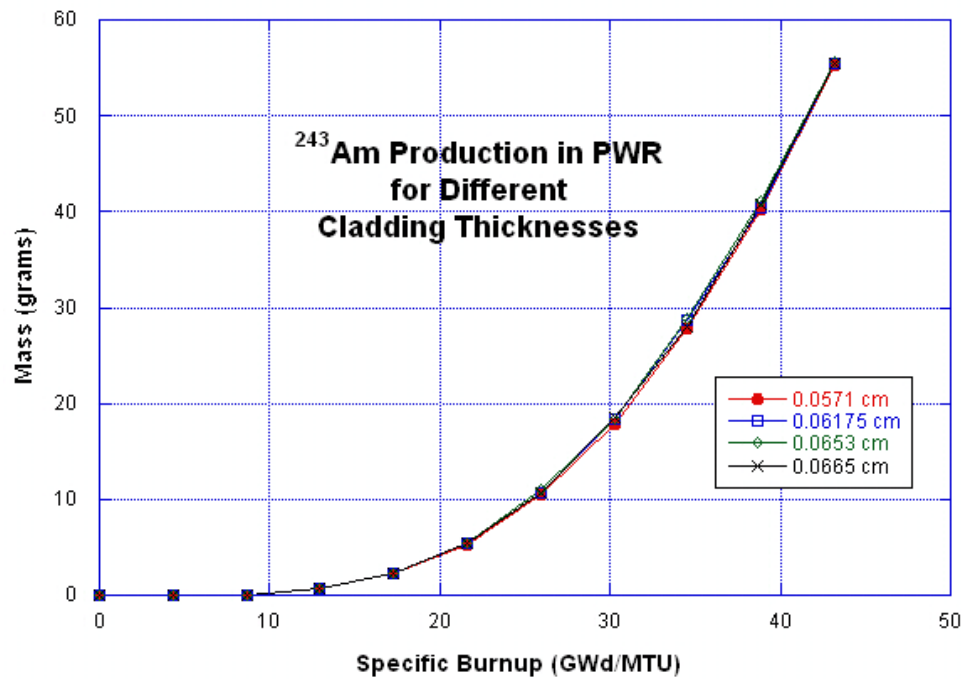


Figure 358: ²⁴³Am Production in the PWR Model for Different Cladding Thicknesses

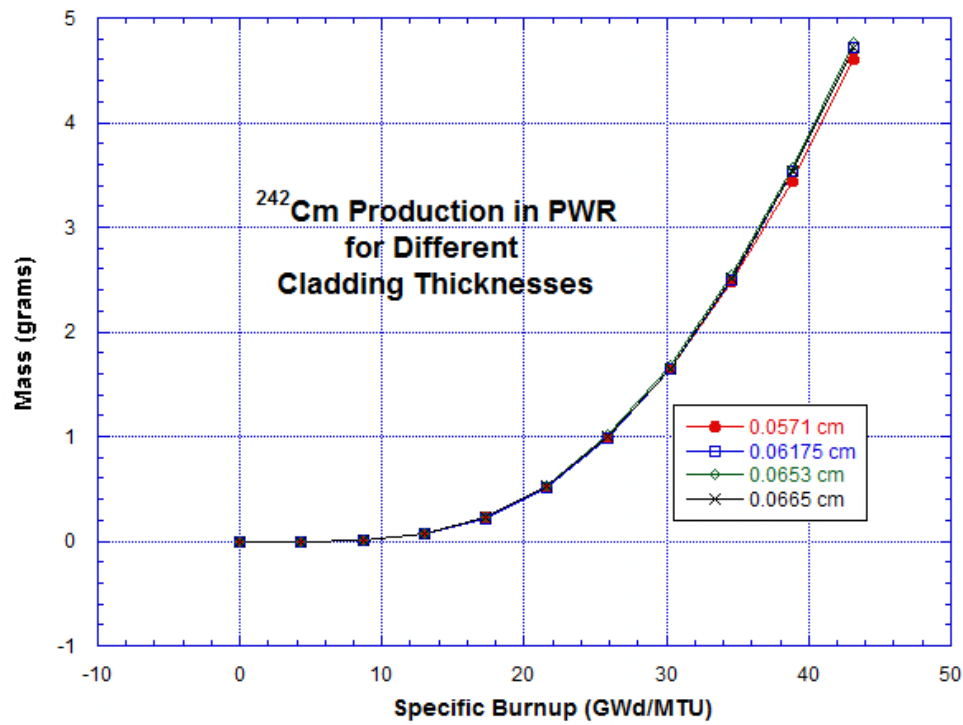


Figure 359: ²⁴²Cm Production in the PWR Model for Different Cladding Thicknesses

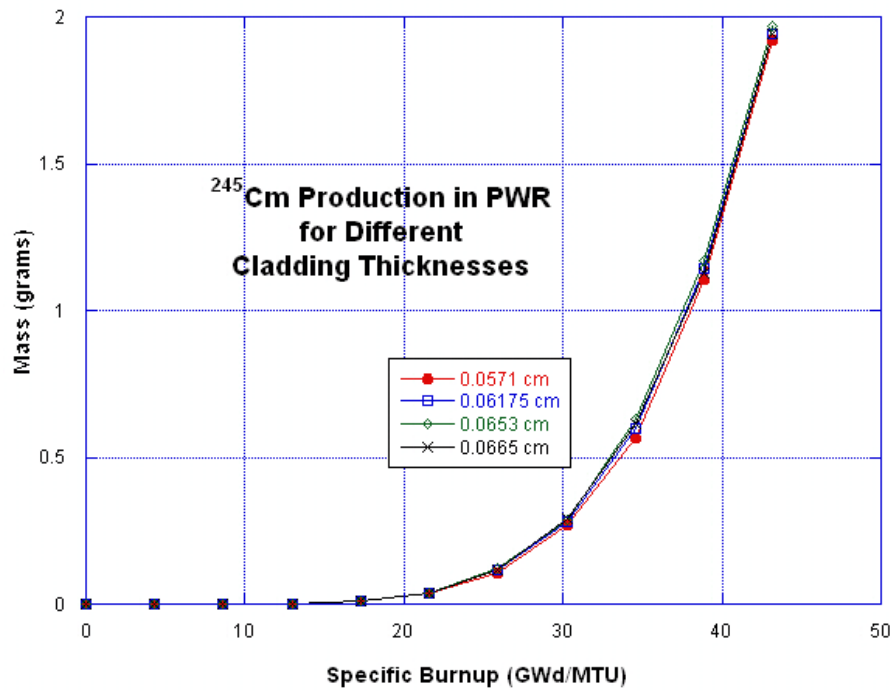


Figure 360: ²⁴⁵Cm Production in the PWR Model for Different Cladding Thicknesses

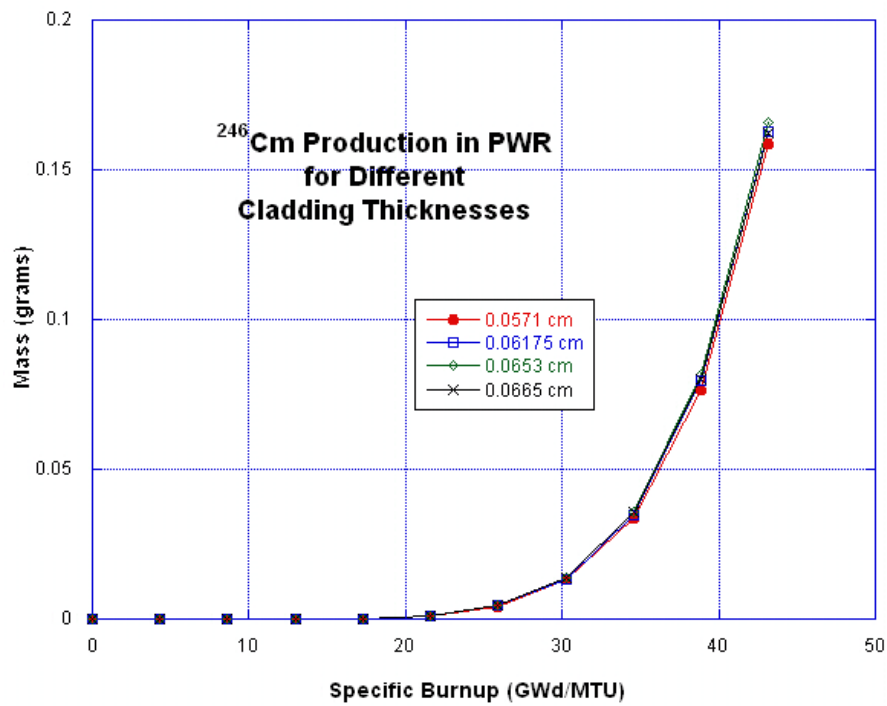


Figure 361: ²⁴⁶Cm Production in the PWR Model for Different Cladding Thicknesses

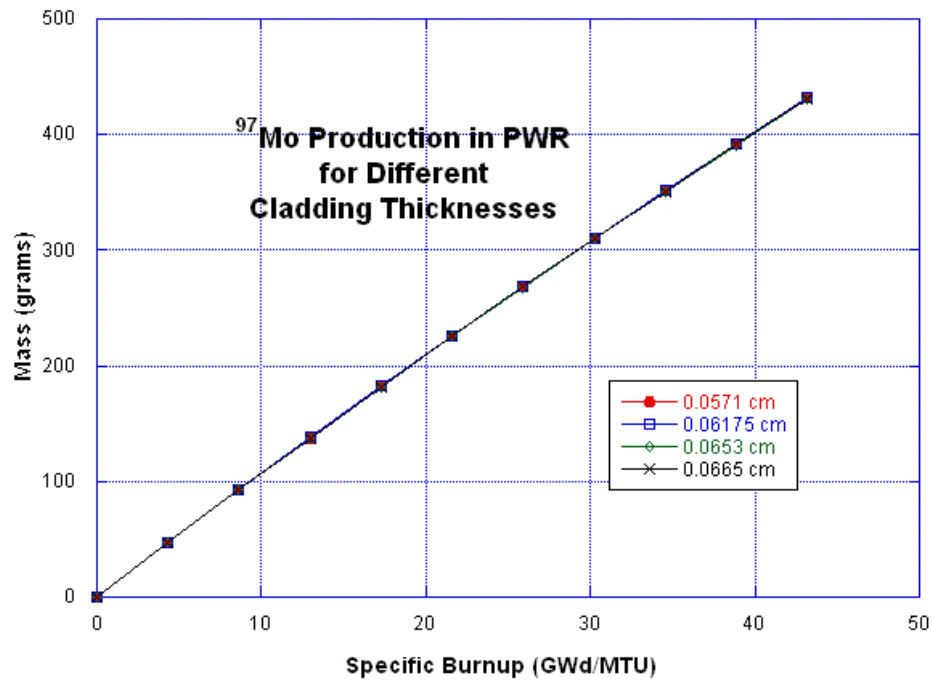


Figure 362: ⁹⁷Mo Production in the PWR Model for Different Cladding Thicknesses

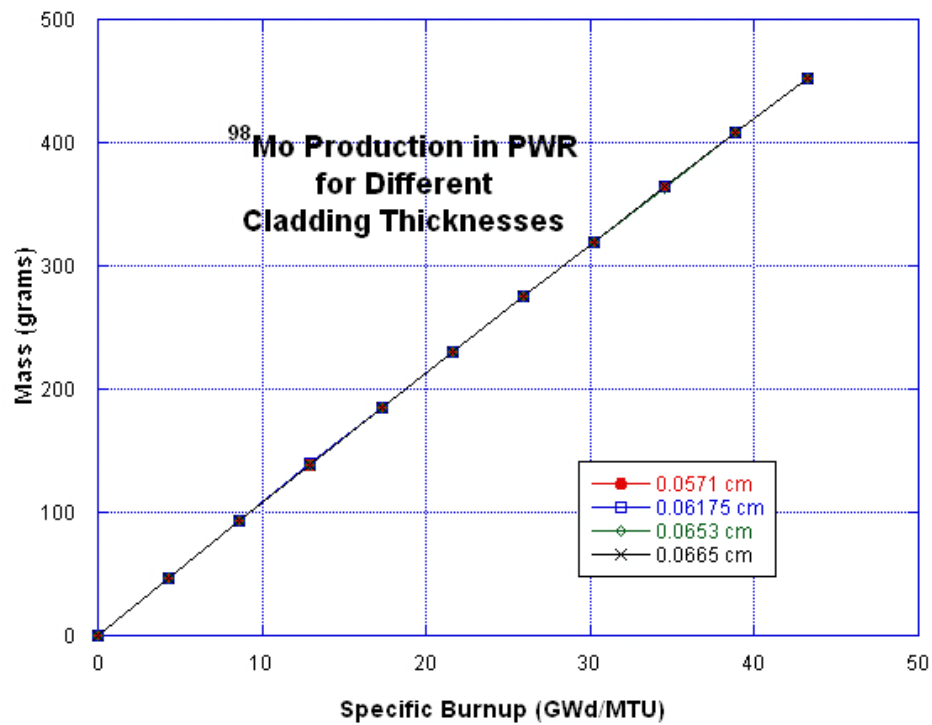


Figure 363: ⁹⁸Mo Production in the PWR Model for Different Cladding Thicknesses

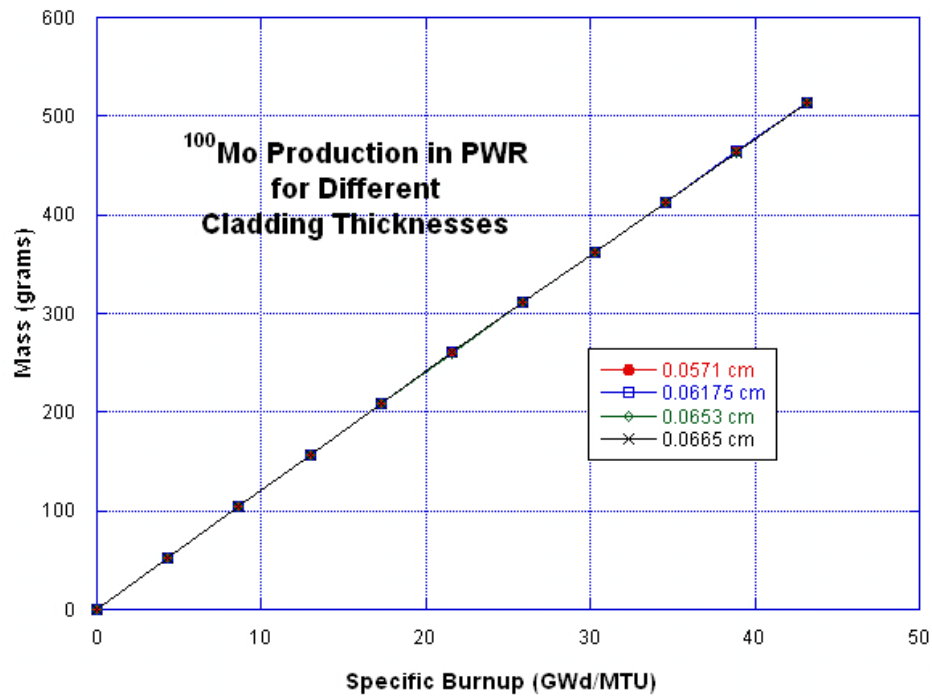


Figure 364: ¹⁰⁰Mo Production in the PWR Model for Different Cladding Thicknesses

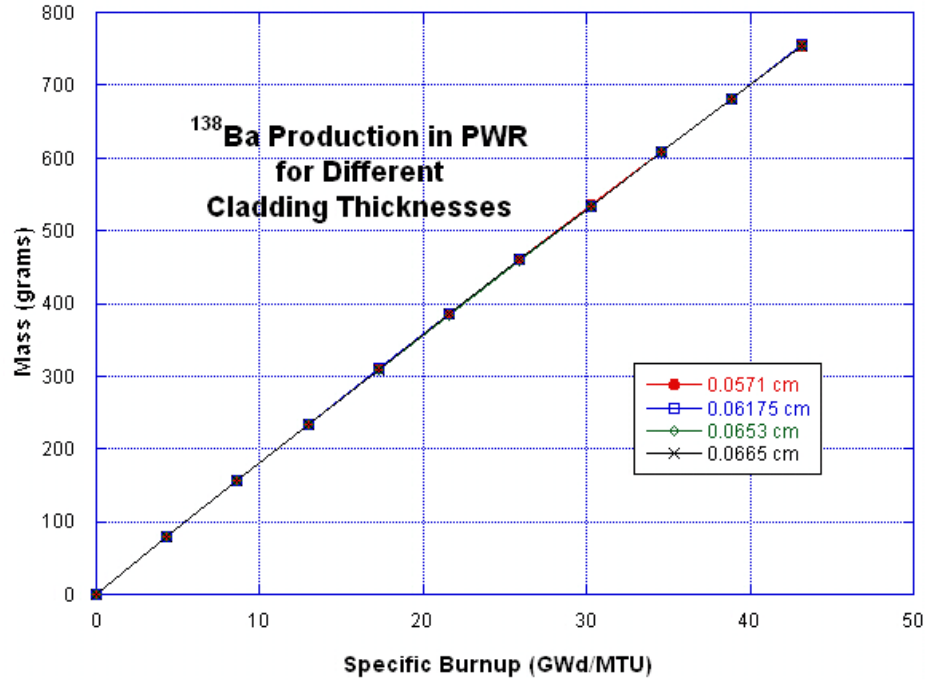


Figure 365: ¹³⁸Ba Production in the PWR Model for Different Cladding Thicknesses

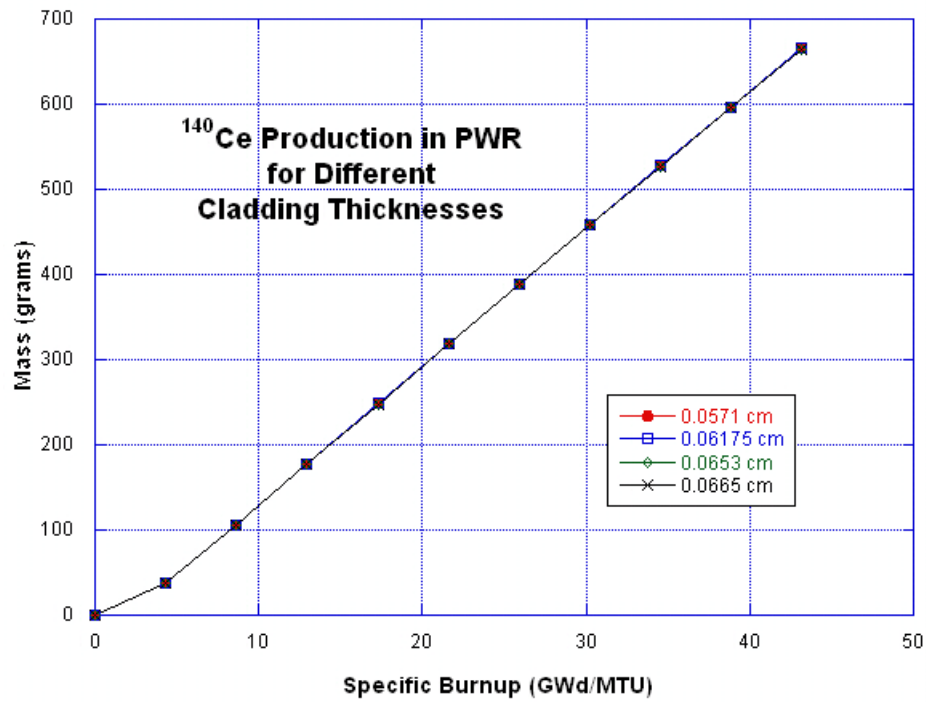


Figure 366: ¹⁴⁰Ce Production in the PWR Model for Different Cladding Thicknesses

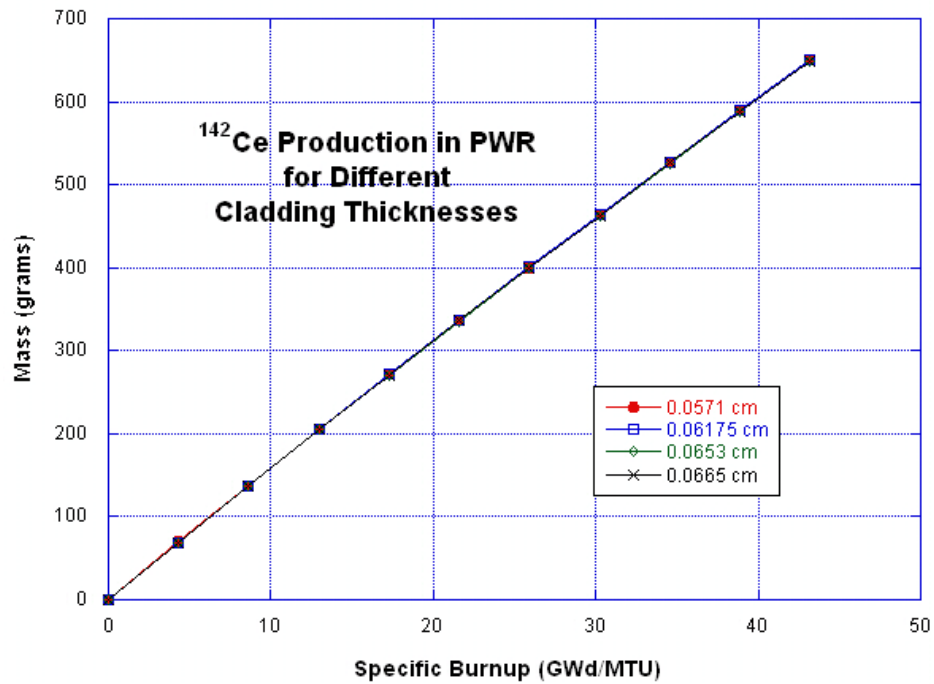


Figure 367: ¹⁴²Ce Production in the PWR Model for Different Cladding Thicknesses

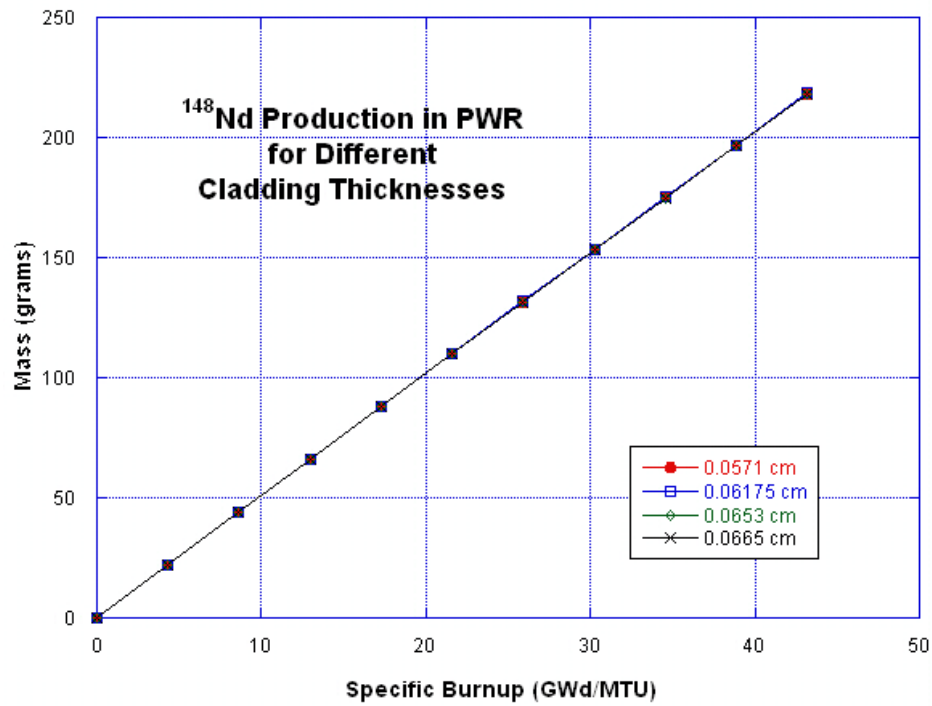


Figure 368: ¹⁴⁸Nd Production in the PWR Model for Different Cladding Thicknesses

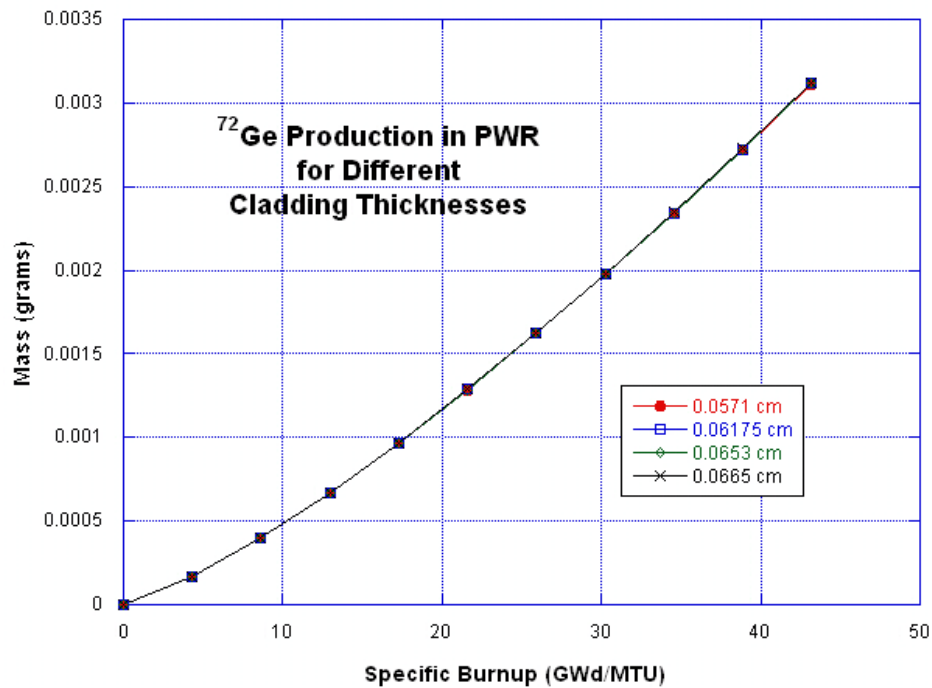


Figure 369: ⁷²Ge Production in the PWR Model for Different Cladding Thicknesses

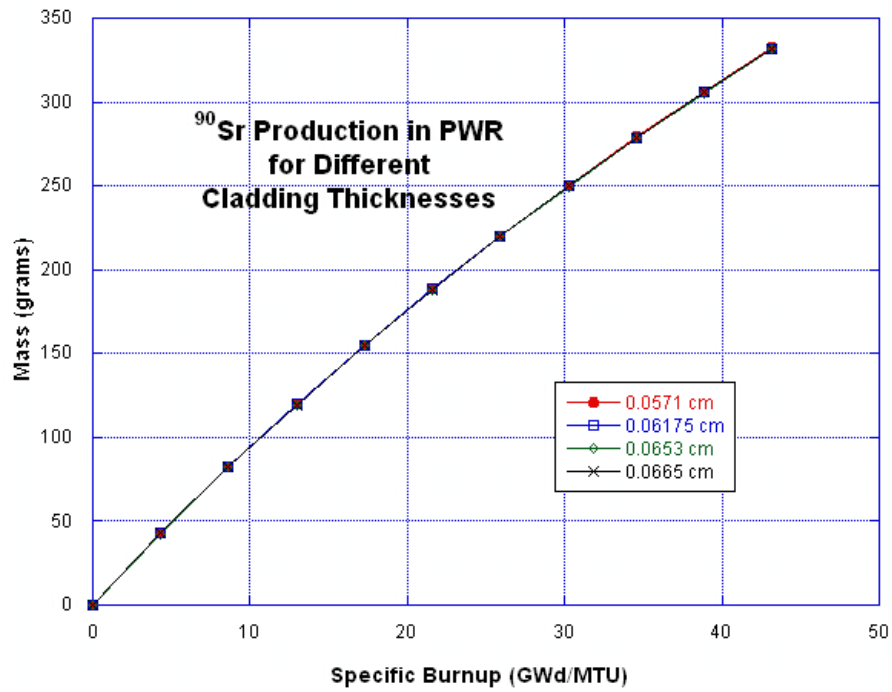


Figure 370: ⁹⁰Sr Production in the PWR Model for Different Cladding Thicknesses

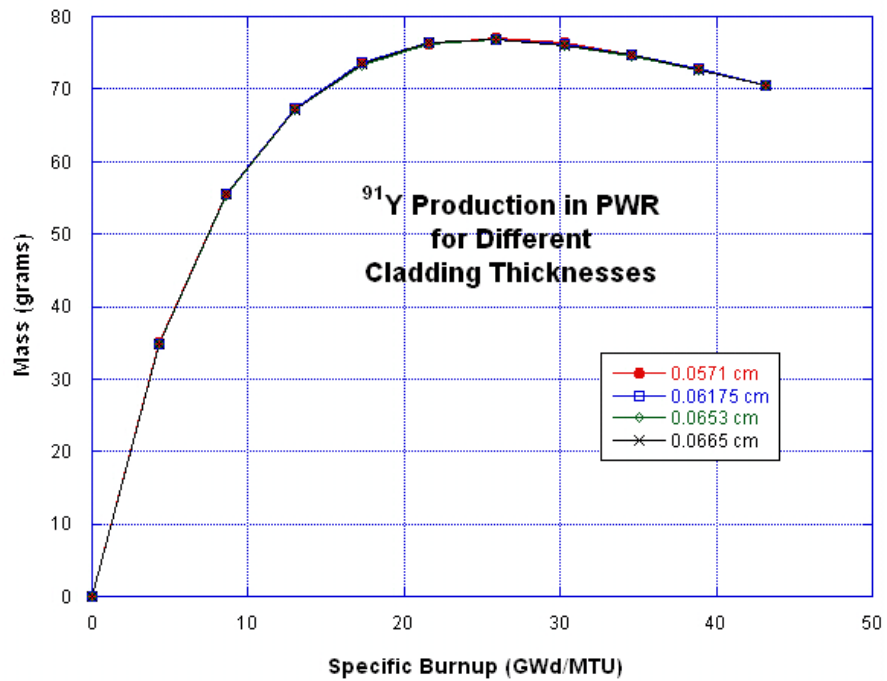


Figure 371: ⁹¹Y Production in the PWR Model for Different Cladding Thicknesses

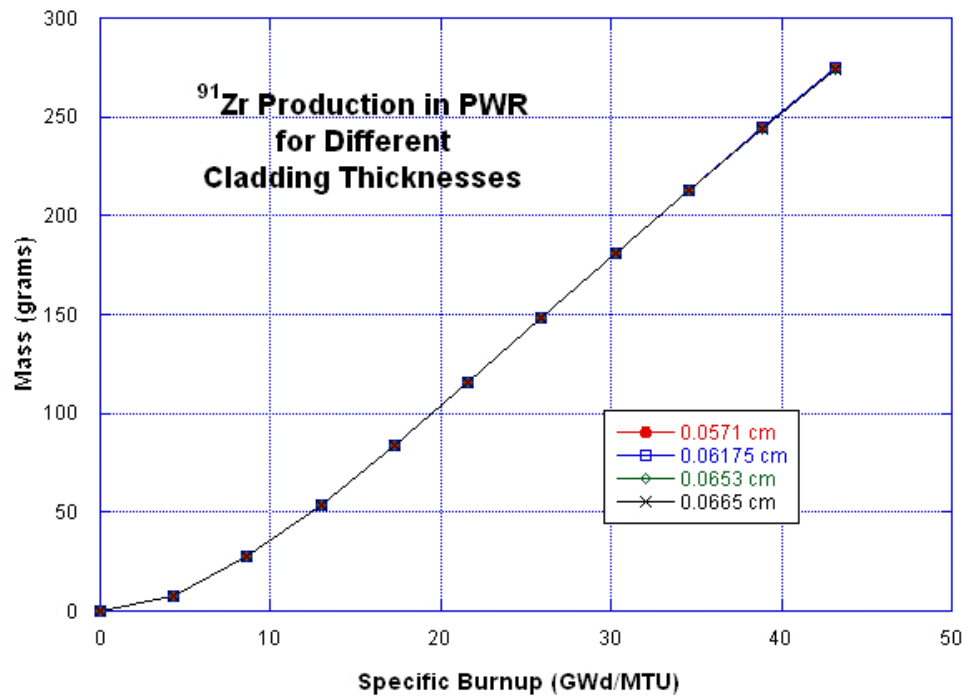


Figure 372: ⁹¹Zr Production in the PWR Model for Different Cladding Thicknesses

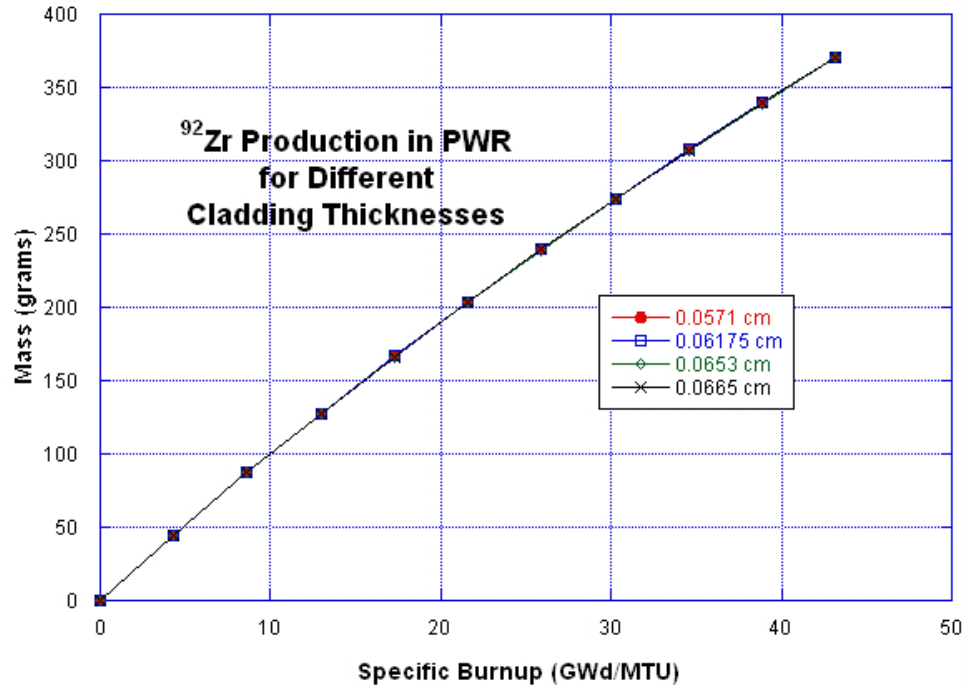


Figure 373: ⁹²Zr Production in the PWR Model for Different Cladding Thicknesses

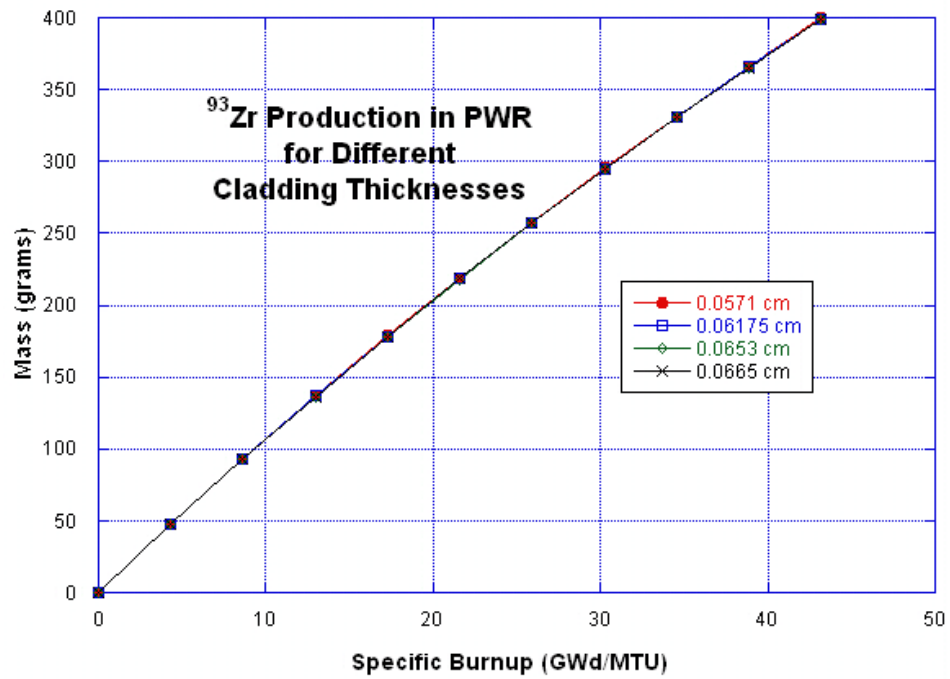


Figure 374: ⁹²Zr Production in the PWR Model for Different Cladding Thicknesses

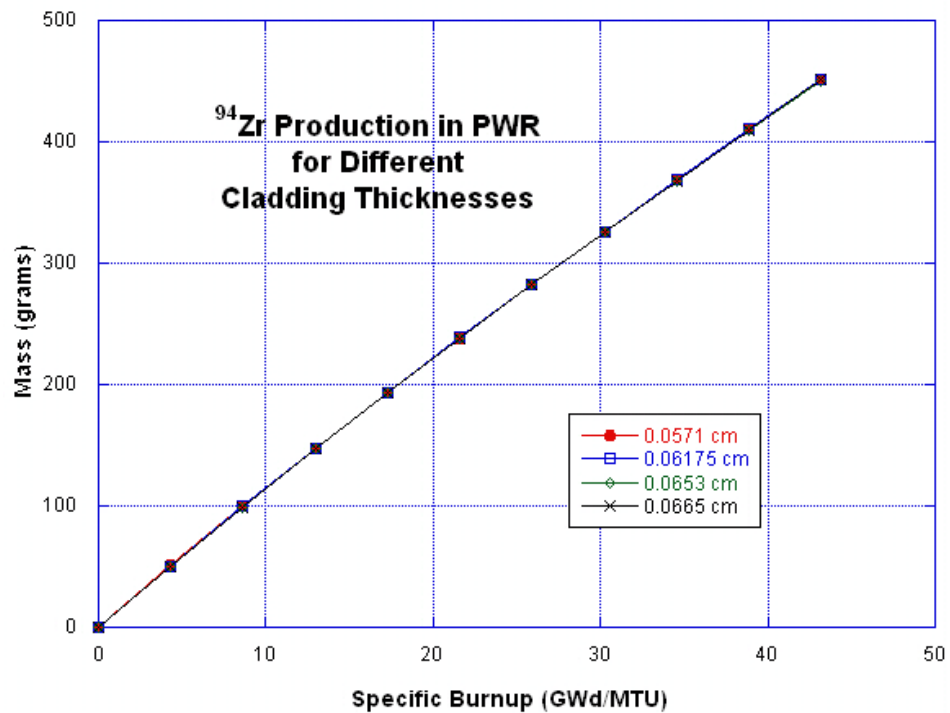


Figure 375: ⁹⁴Zr Production in the PWR Model for Different Cladding Thicknesses

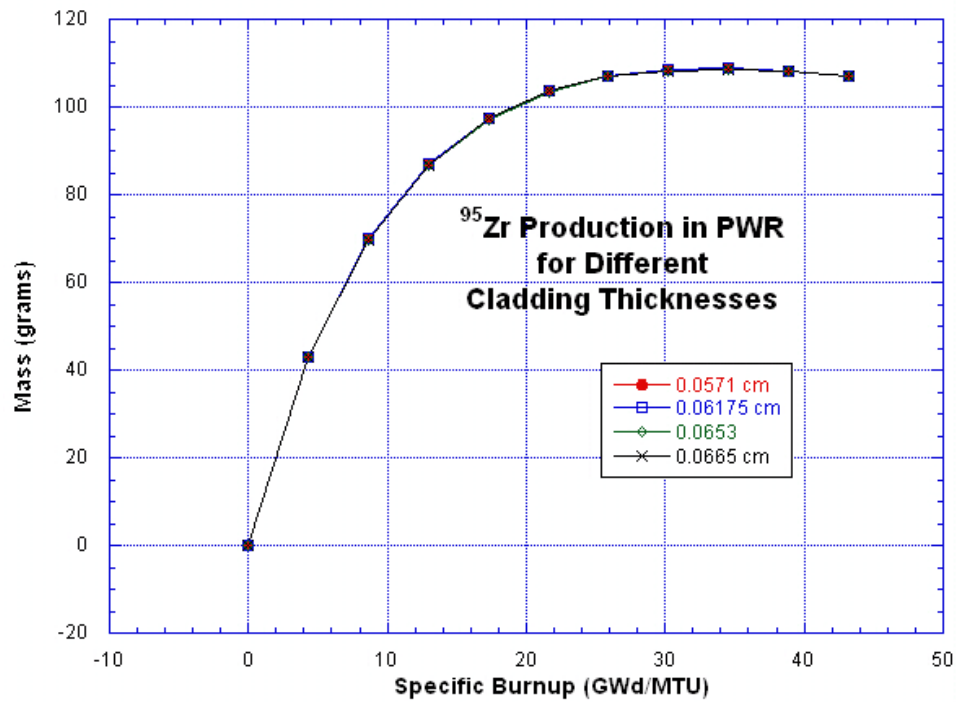


Figure 376: ⁹⁵Zr Production in the PWR Model for Different Cladding Thicknesses

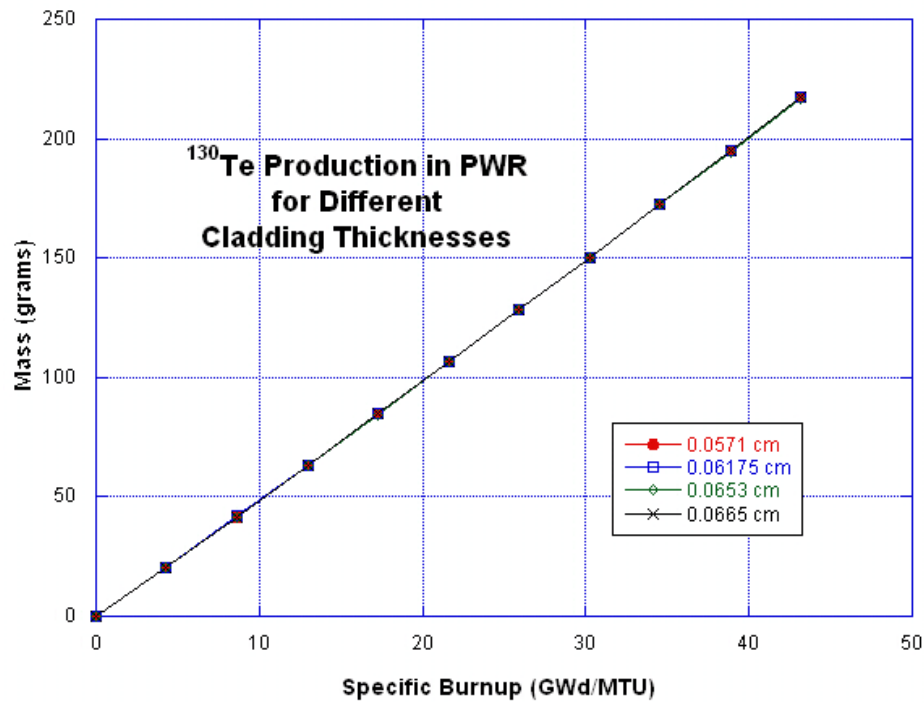


Figure 377: ¹³⁰Te Production in the PWR Model for Different Cladding Thicknesses

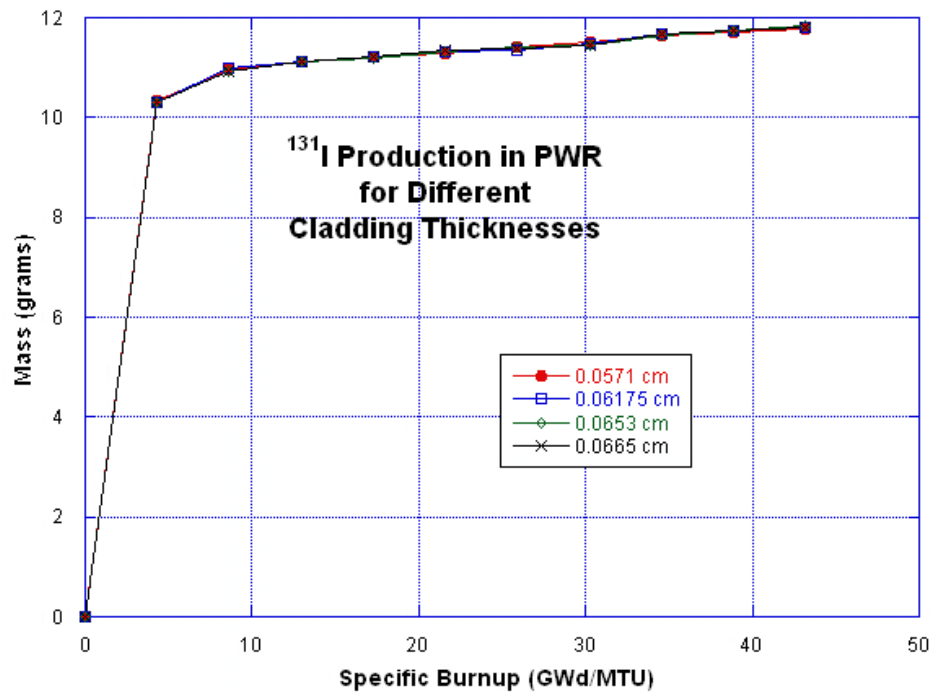


Figure 378: ¹³¹I Production in the PWR Model for Different Cladding Thicknesses

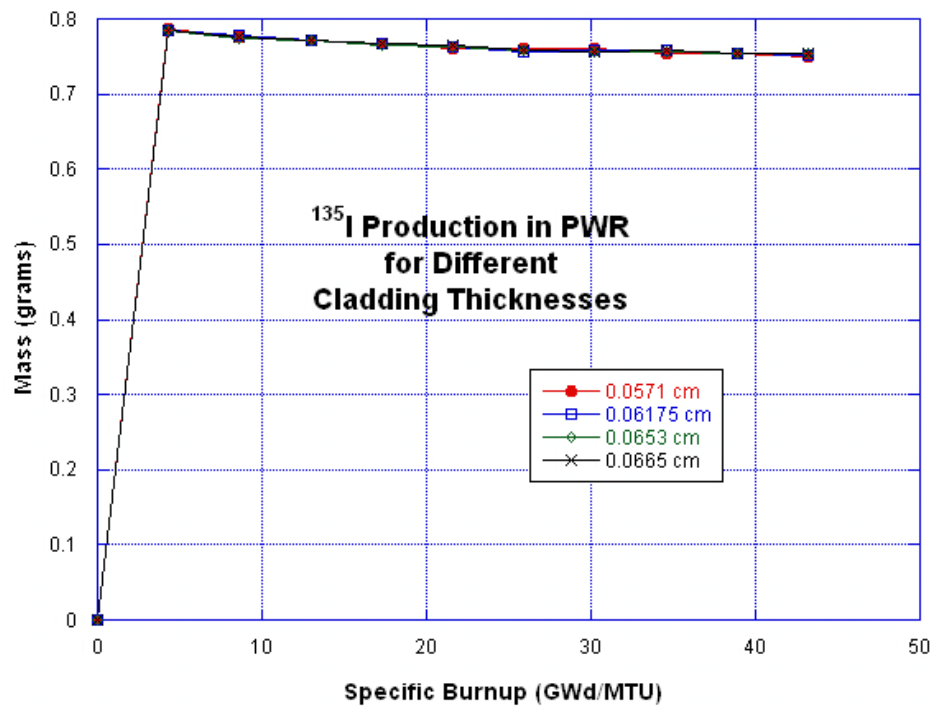


Figure 379: ¹³⁵I Production in the PWR Model for Different Cladding Thicknesses

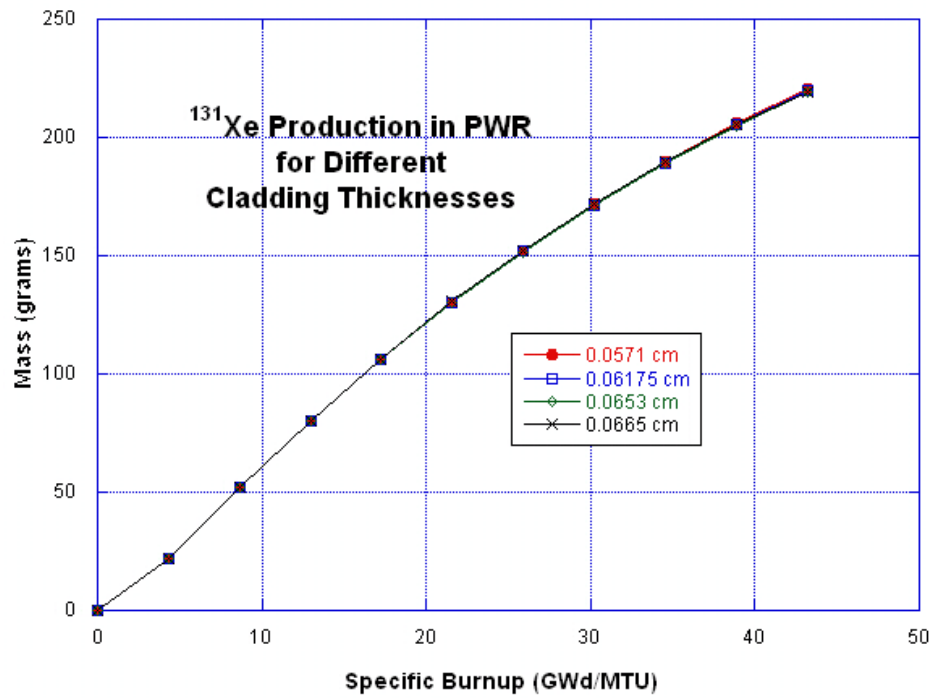


Figure 380: ¹³¹Xe Production in the PWR Model for Different Cladding Thicknesses

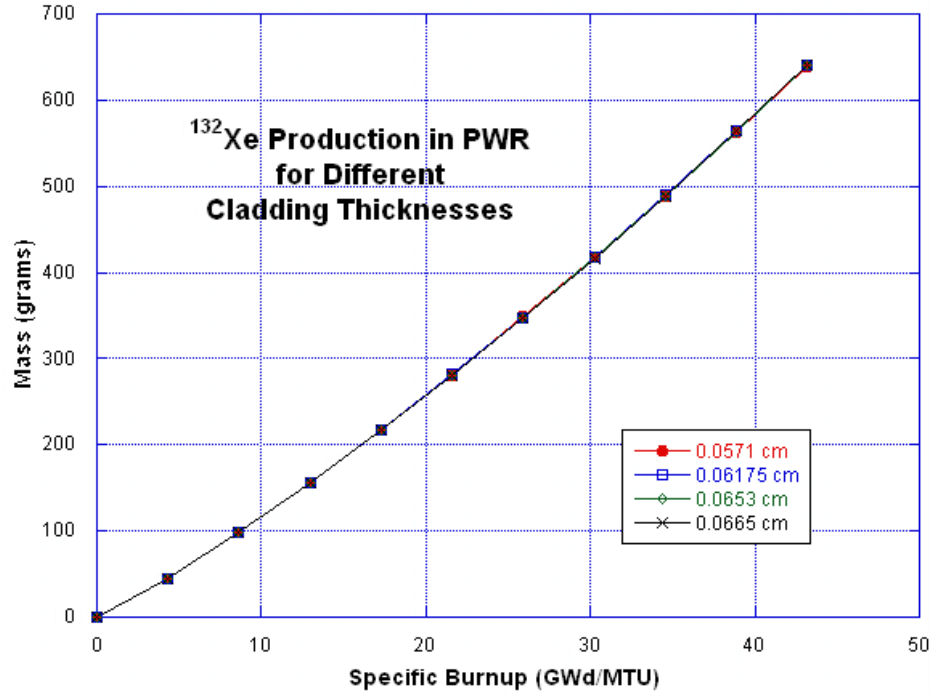


Figure 381: ¹³²Xe Production in the PWR Model for Different Cladding Thicknesses

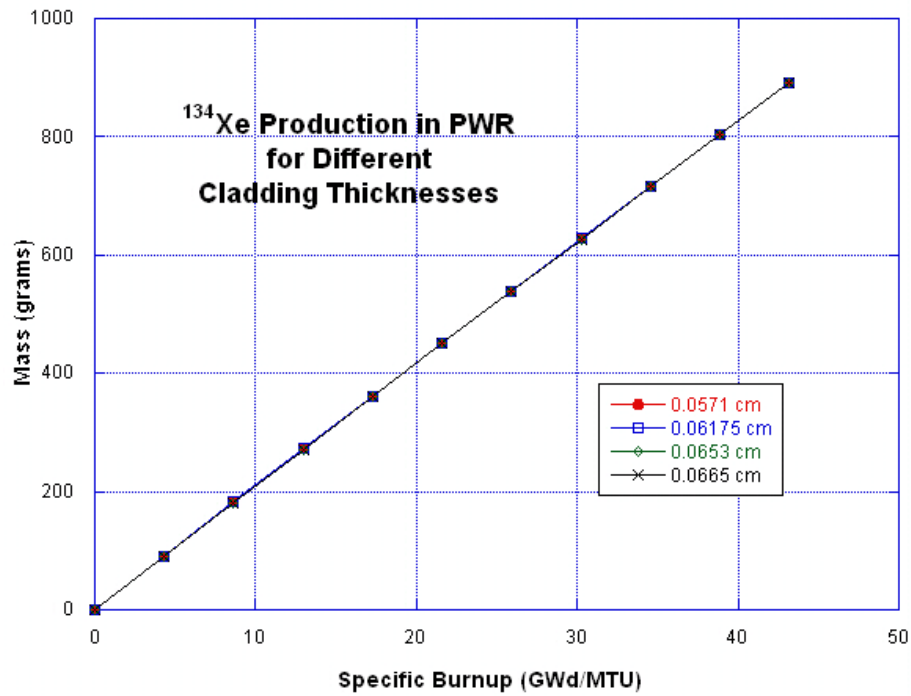


Figure 382: ¹³⁴Xe Production in the PWR Model for Different Cladding Thicknesses

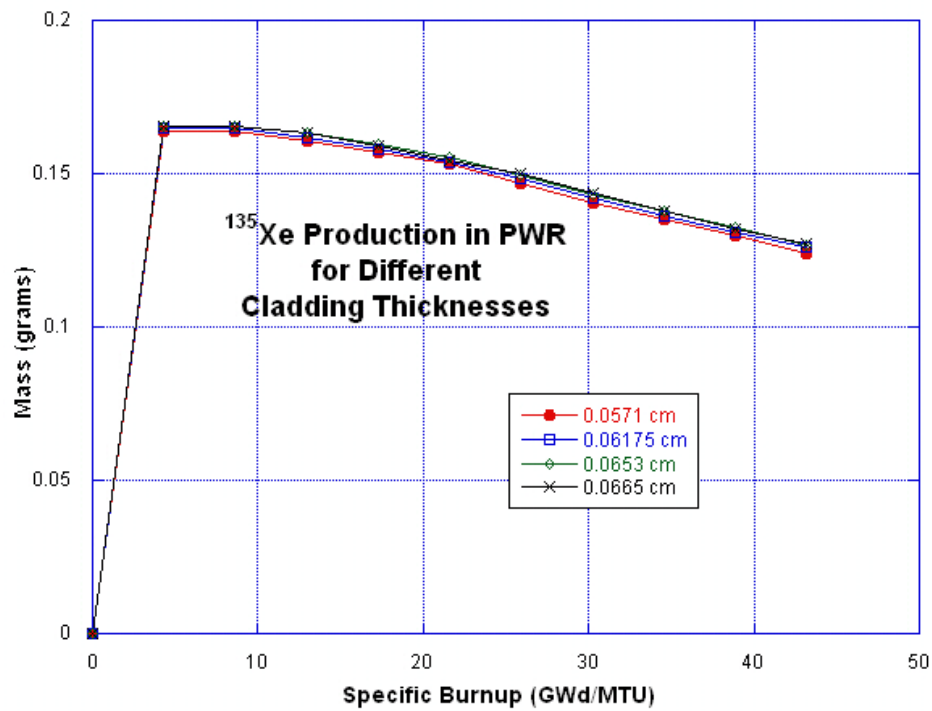


Figure 383: ¹³⁵Xe Production in the PWR Model for Different Cladding Thicknesses

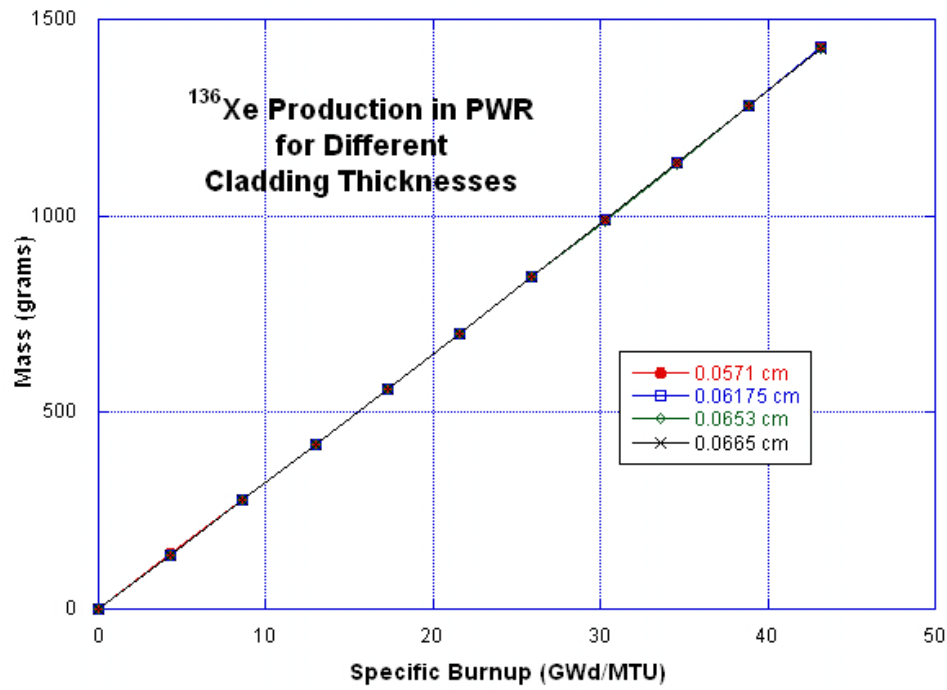


Figure 384: ^{136}Xe Production in the PWR Model for Different Cladding Thicknesses

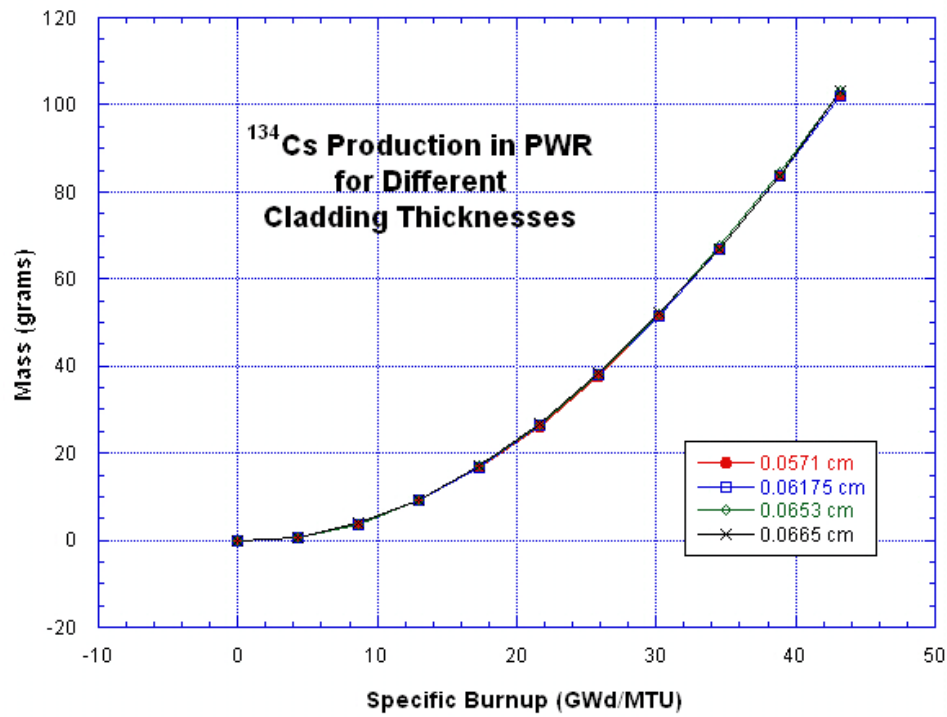


Figure 385: ^{134}Cs Production in the PWR Model for Different Cladding Thicknesses

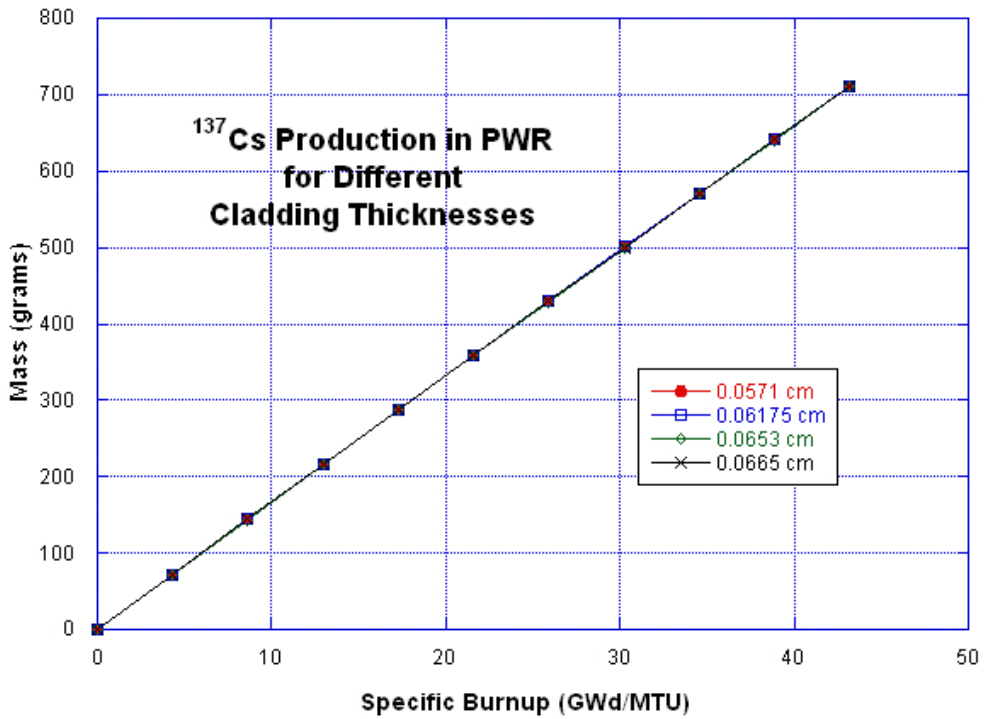


Figure 386: ¹³⁷Cs Production in the PWR Model for Different Cladding Thicknesses

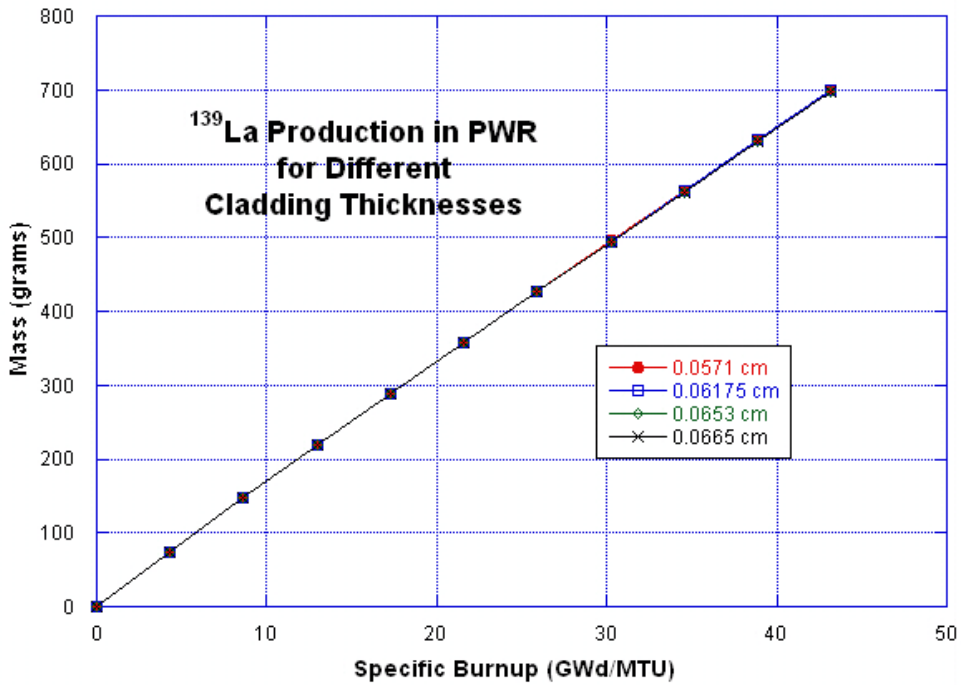


Figure 387: ¹³⁹La Production in the PWR Model for Different Cladding Thicknesses

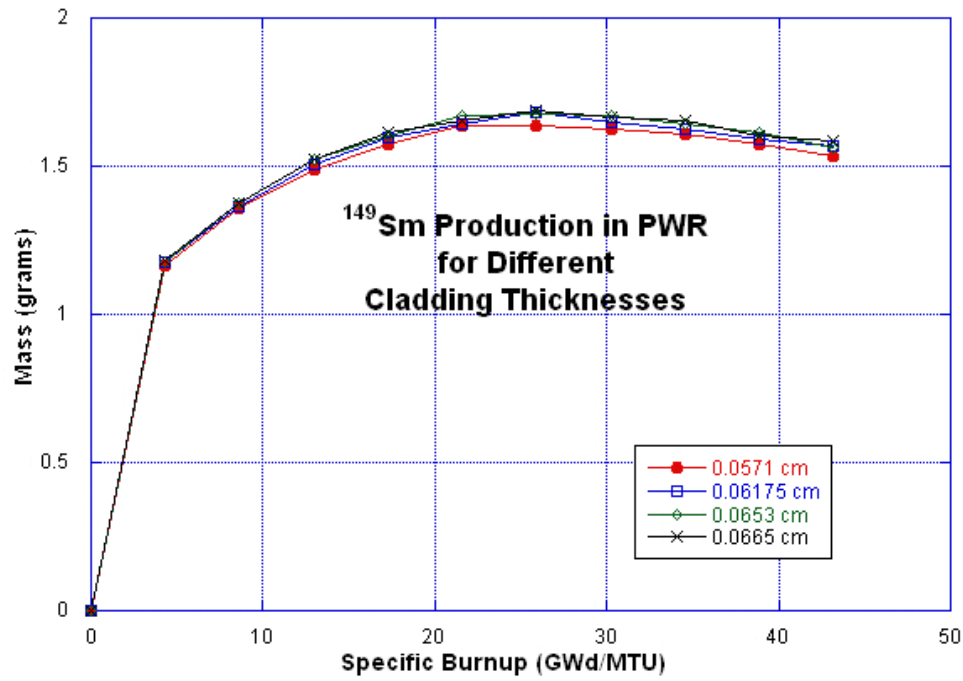


Figure 388: ¹⁴⁹Sm Production in the PWR Model for Different Cladding Thicknesses

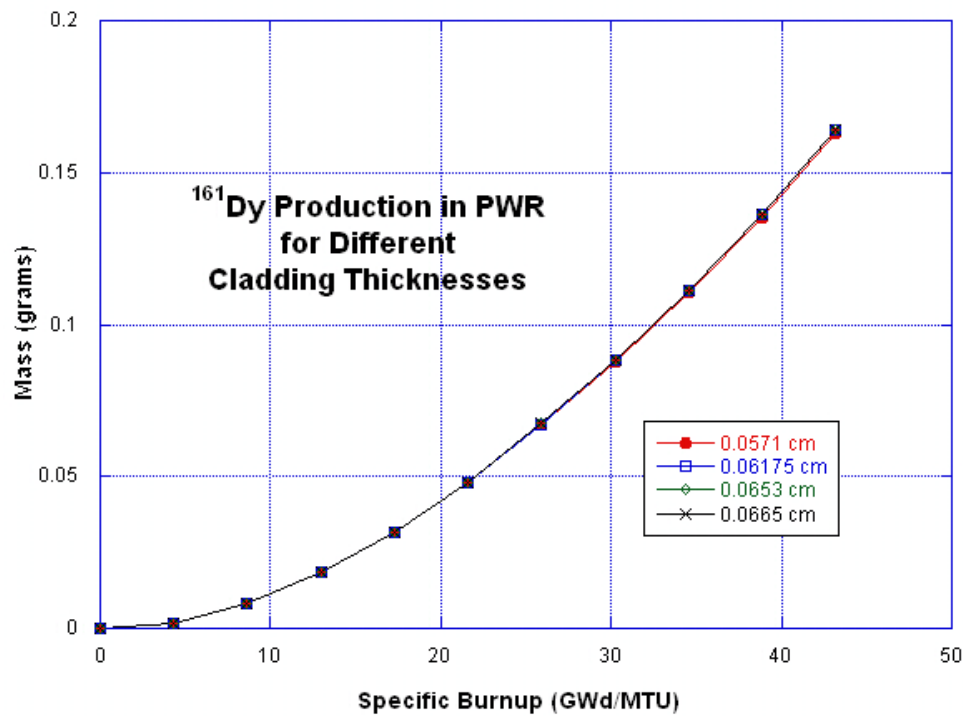


Figure 389: ¹⁶¹Dy Production in the PWR Model for Different Cladding Thicknesses

**PWR Sensitivity Study
Plots of 46 Nuclides of Interest
Water Density Variation**

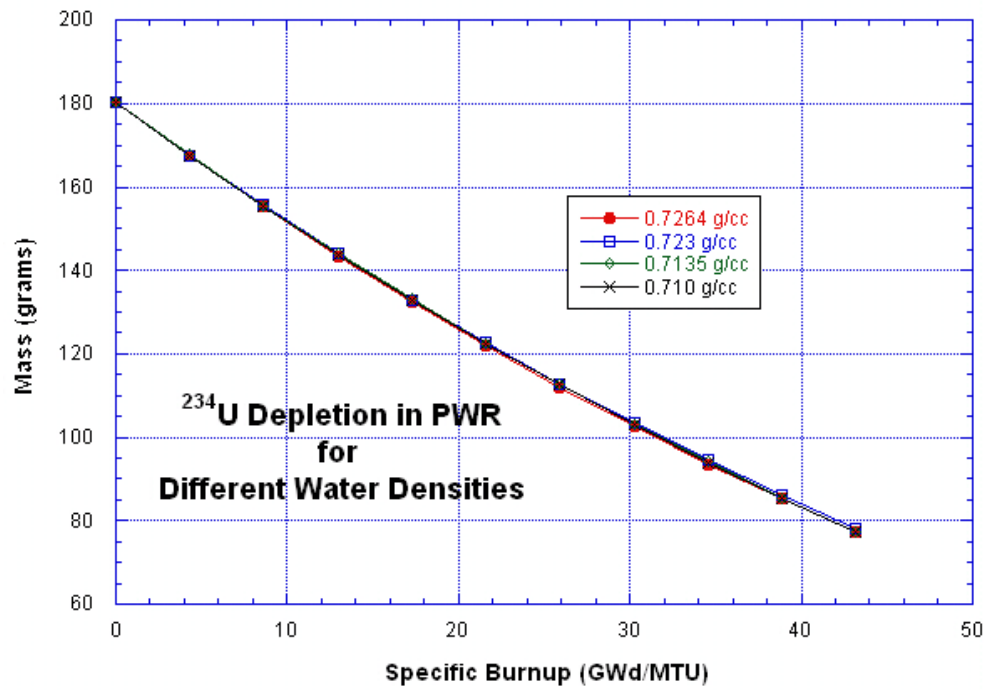


Figure 390: ²³⁴U Depletion in the PWR Model for Different Water Densities

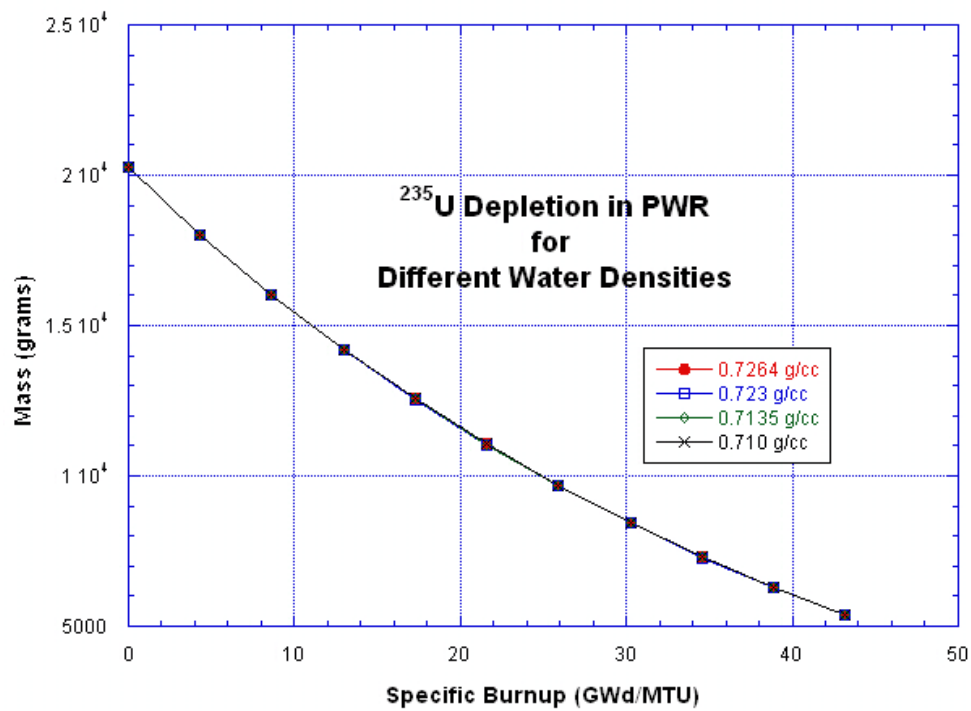


Figure 391: ²³⁵U Depletion in the PWR Model for Different Water Densities

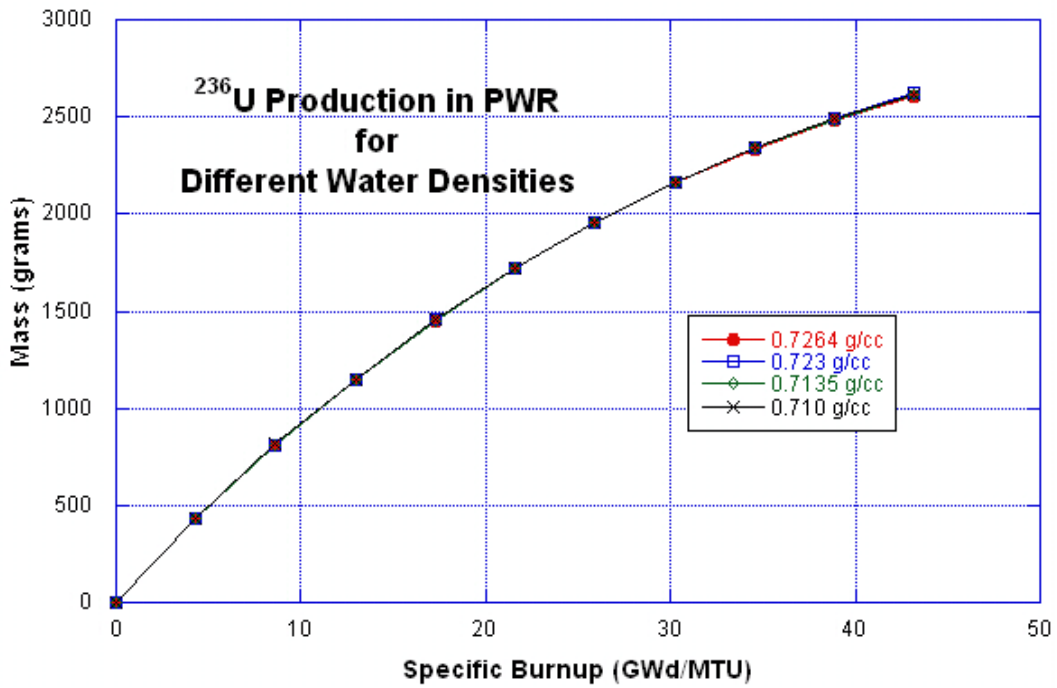


Figure 392: ²³⁶U Production in the PWR Model for Different Water Densities

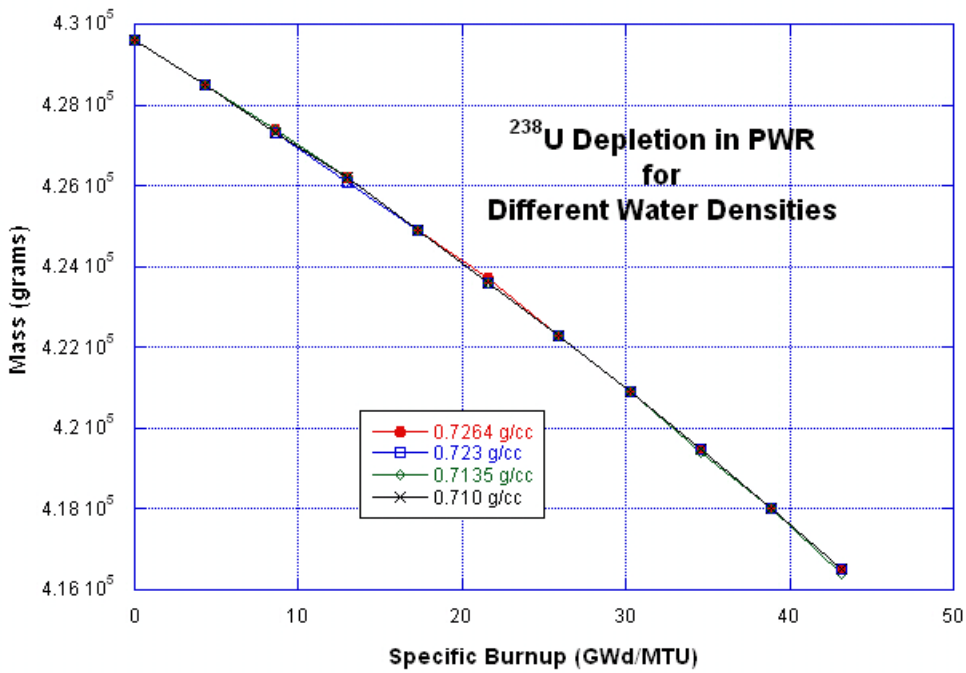


Figure 393: ²³⁸U Depletion in the PWR Model for Different Water Densities

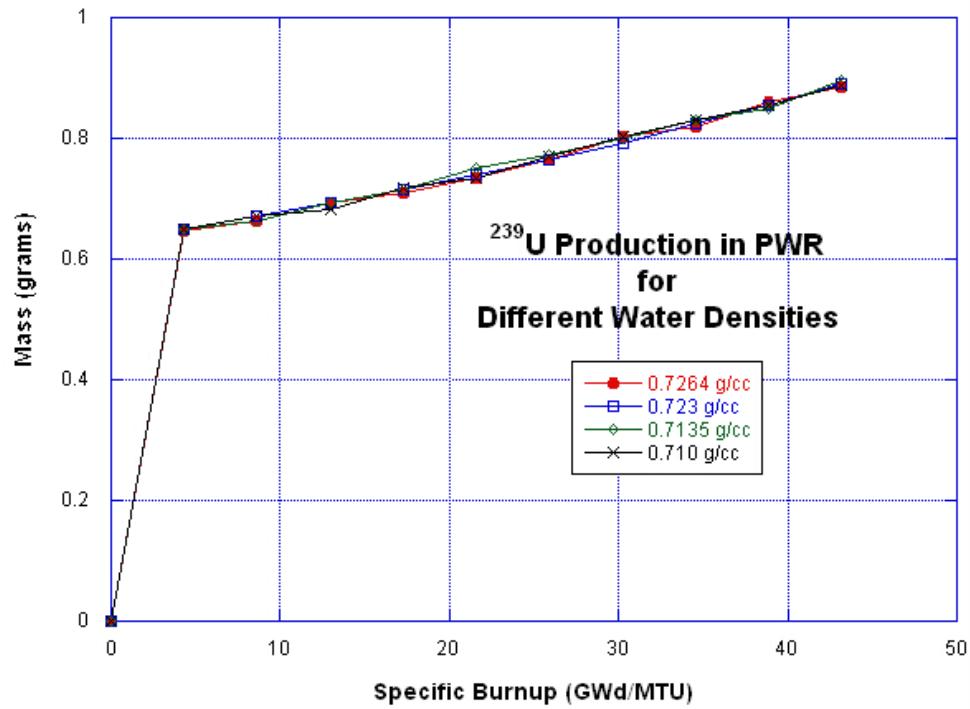


Figure 394: ²³⁹U Production in the PWR Model for Different Water Densities

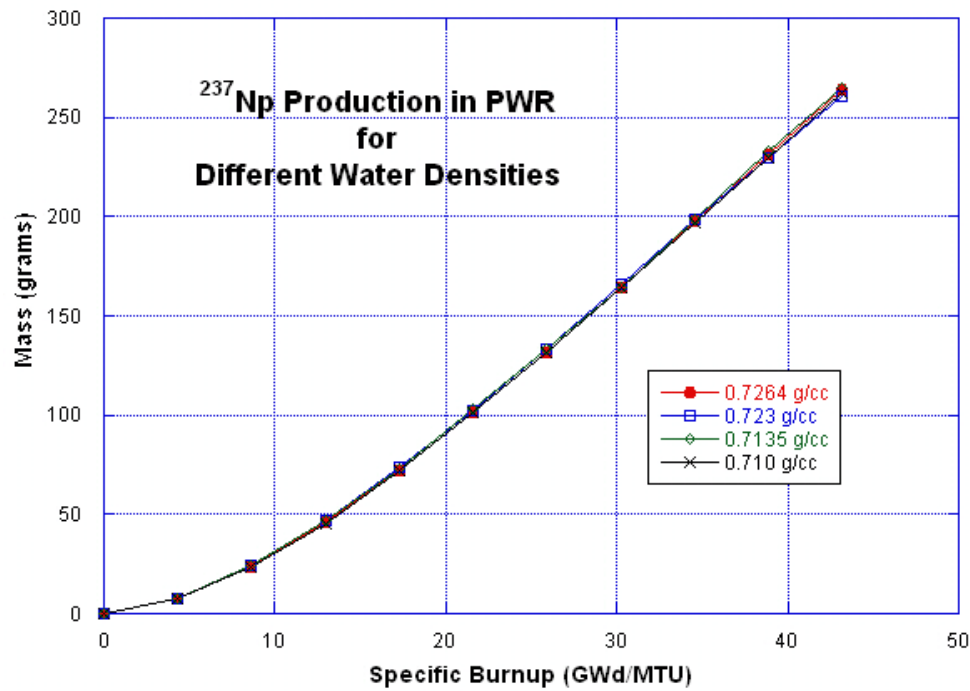


Figure 395: ²³⁷Np Production in the PWR Model for Different Water Densities

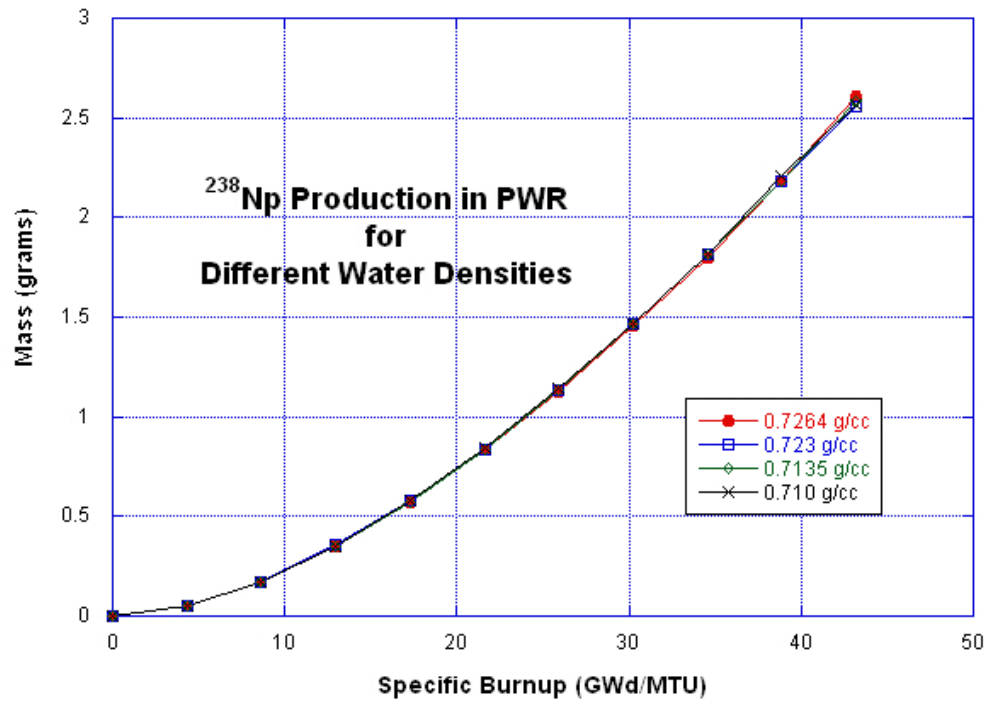


Figure 396: ²³⁸Np Production in the PWR Model for Different Water Densities

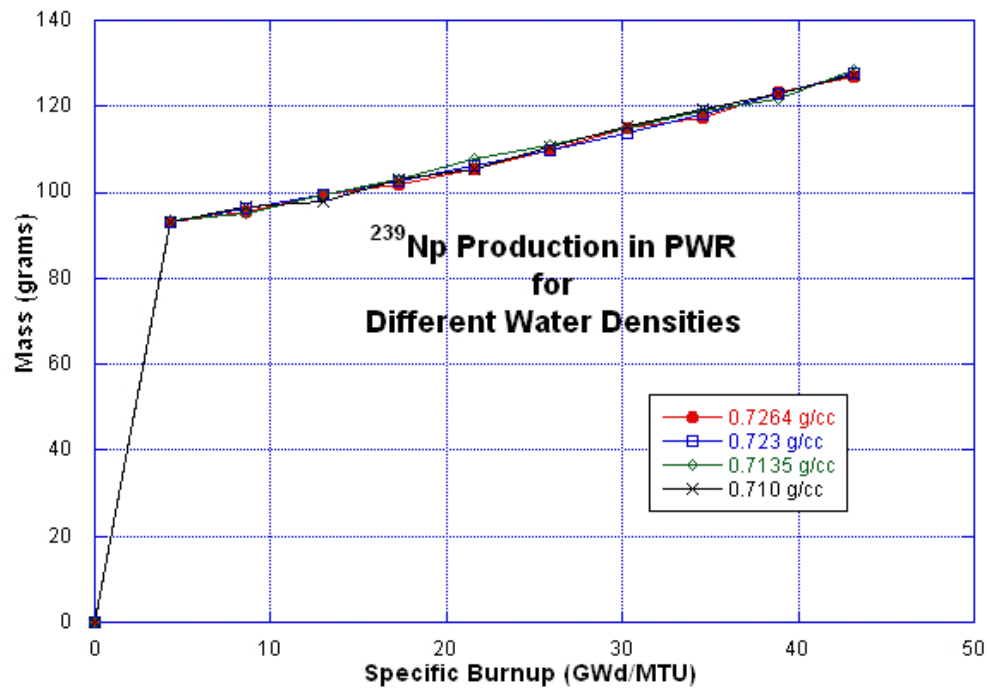


Figure 397: ²³⁹Np Production in the PWR Model for Different Water Densities

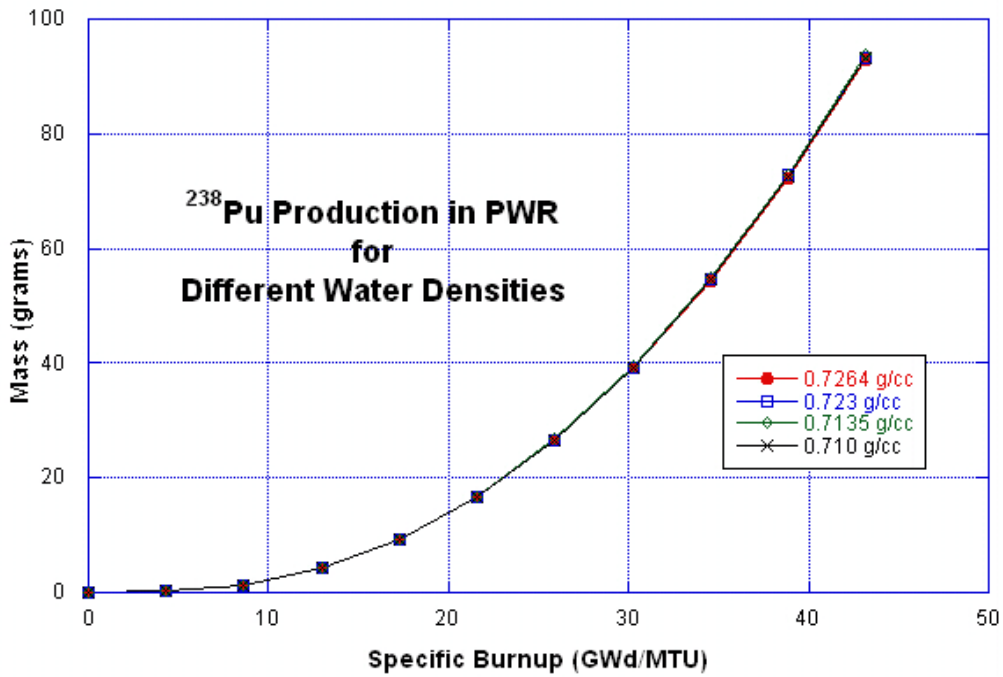


Figure 398: ²³⁸Pu Production in the PWR Model for Different Water Densities

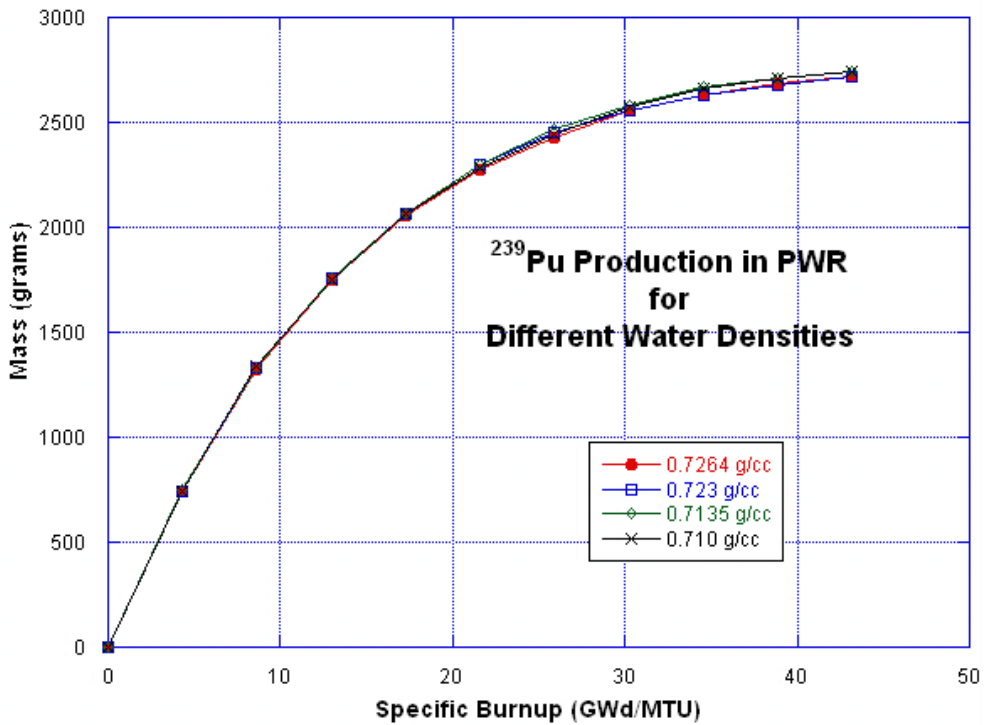


Figure 399: ²³⁹Pu Production in the PWR Model for Different Water Densities

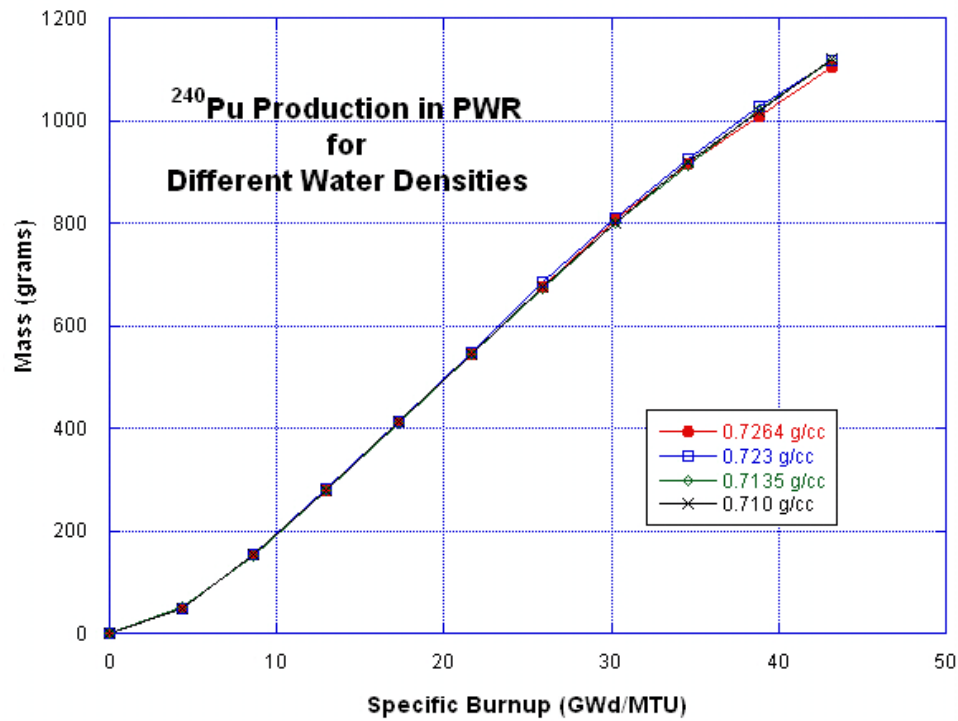


Figure 400: ²⁴⁰Pu Production in the PWR Model for Different Water Densities

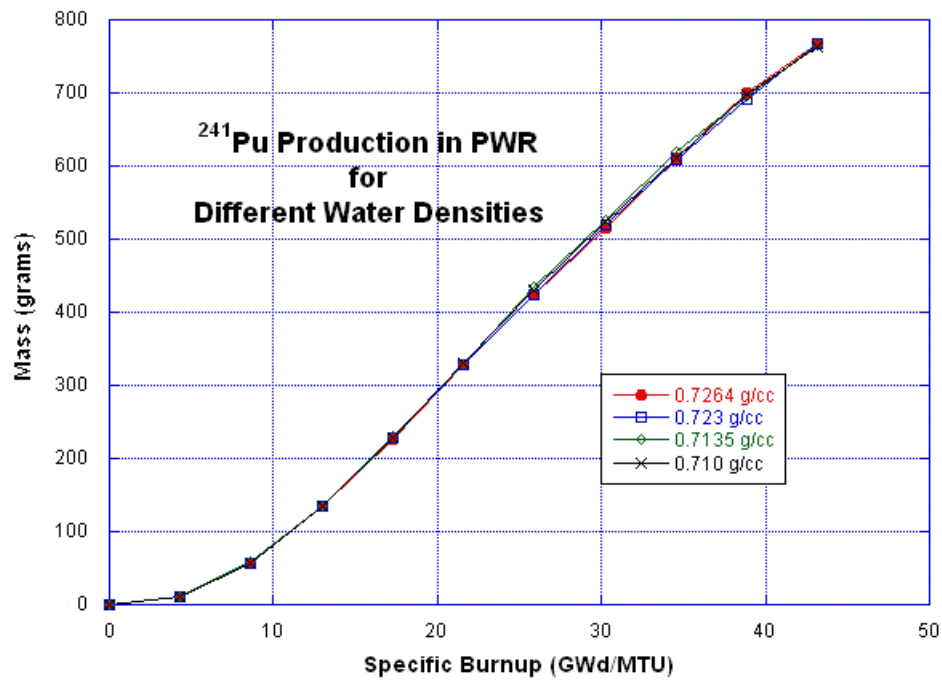


Figure 401: ²⁴¹Pu Production in the PWR Model for Different Water Densities

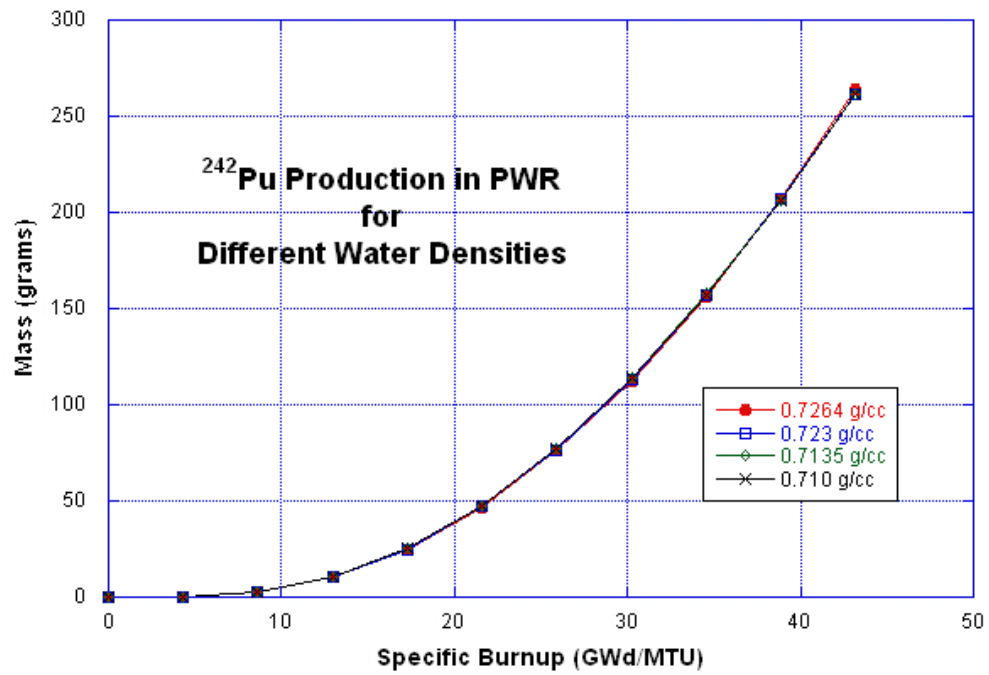


Figure 402: ²⁴²Pu Production in the PWR Model for Different Water Densities

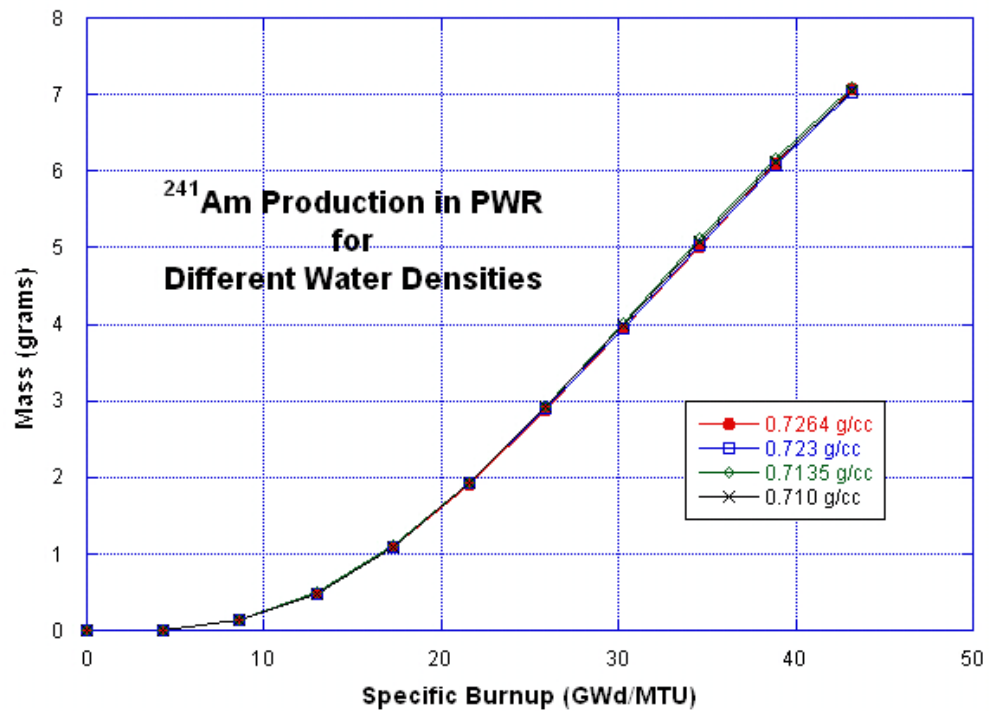


Figure 403: ²⁴¹Am Production in the PWR Model for Different Water Densities

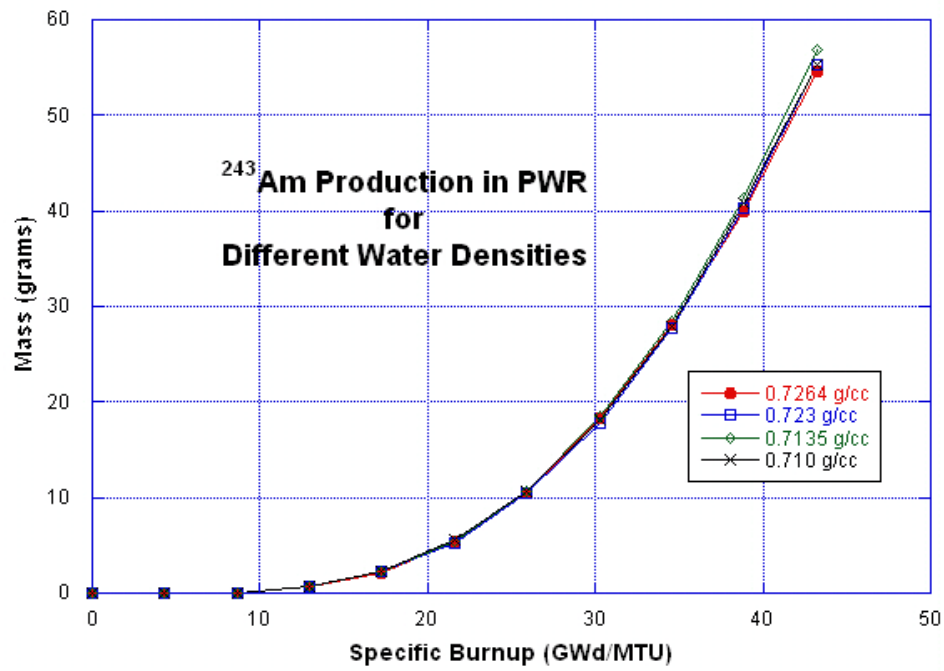


Figure 404: ²⁴³Am Production in the PWR Model for Different Water Densities

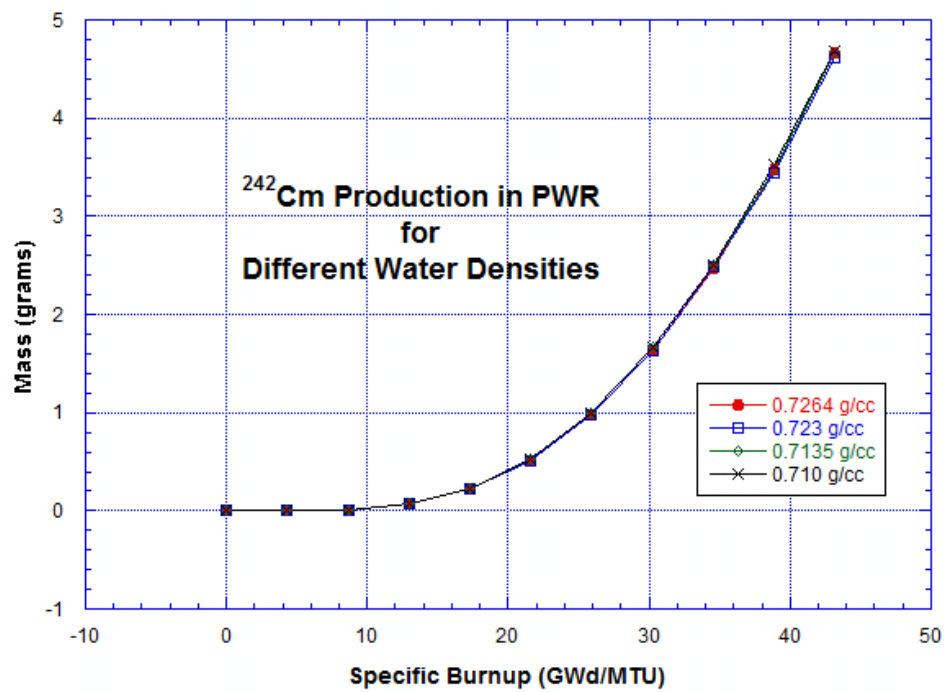


Figure 405: ²⁴²Cm Production in the PWR Model for Different Water Densities

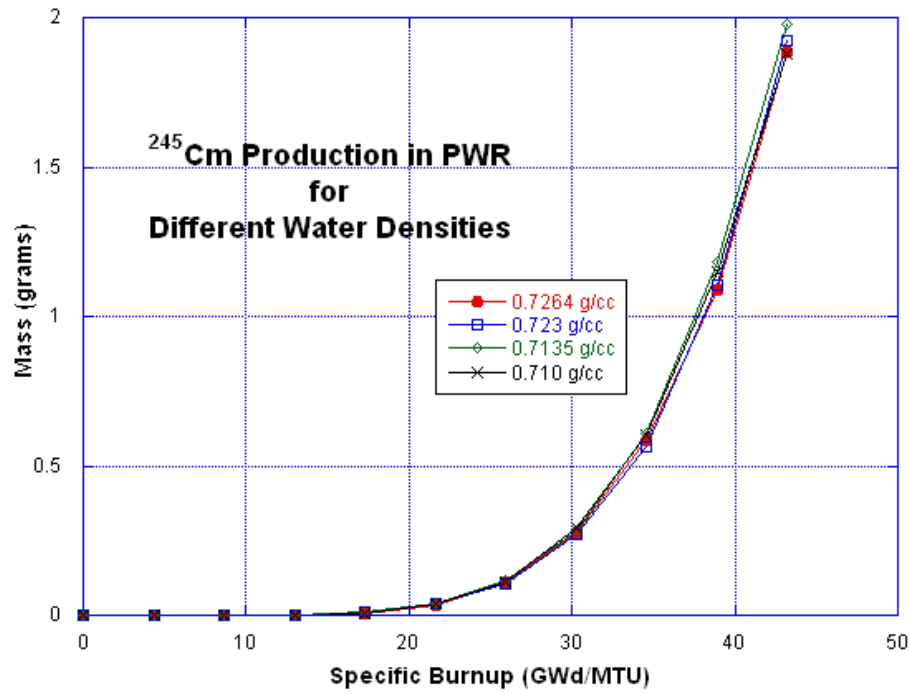


Figure 406: ²⁴⁵Cm Production in the PWR Model for Different Water Densities

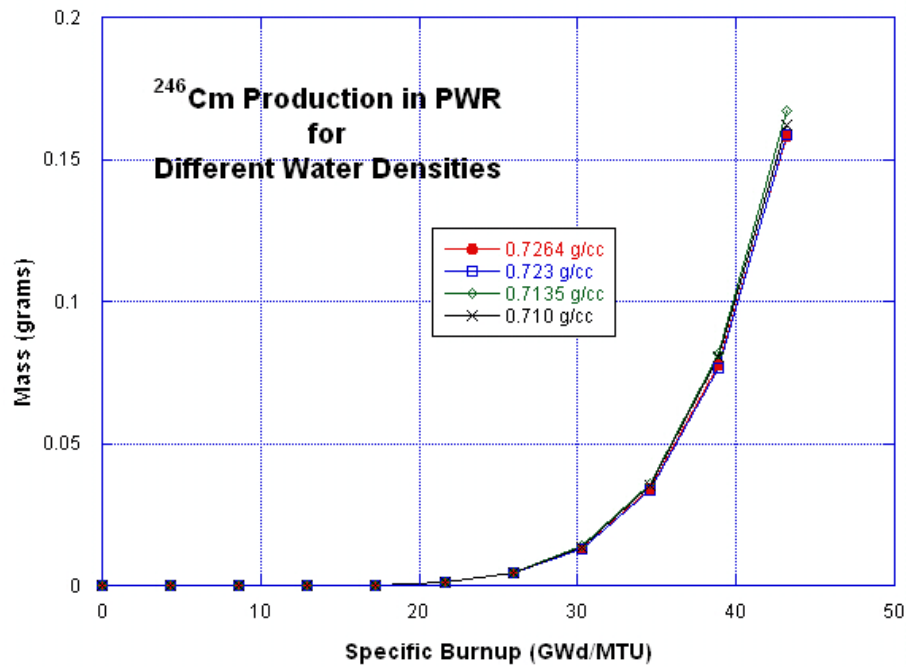


Figure 407: ²⁴⁶Cm Production in the PWR Model for Different Water Densities

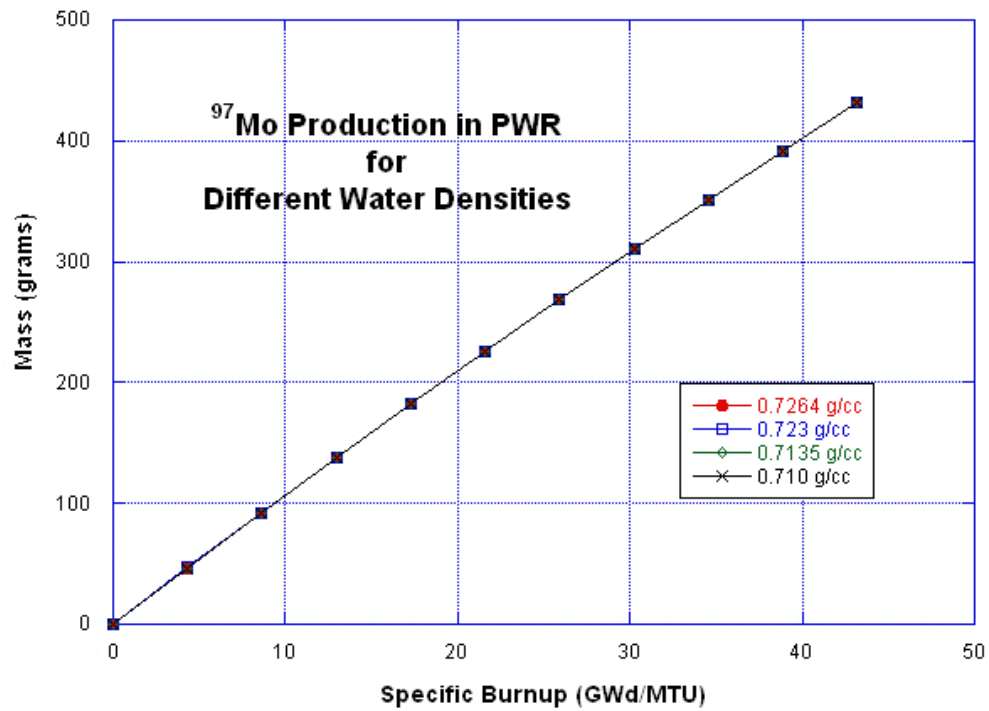


Figure 408: ⁹⁷Mo Production in the PWR Model for Different Water Densities

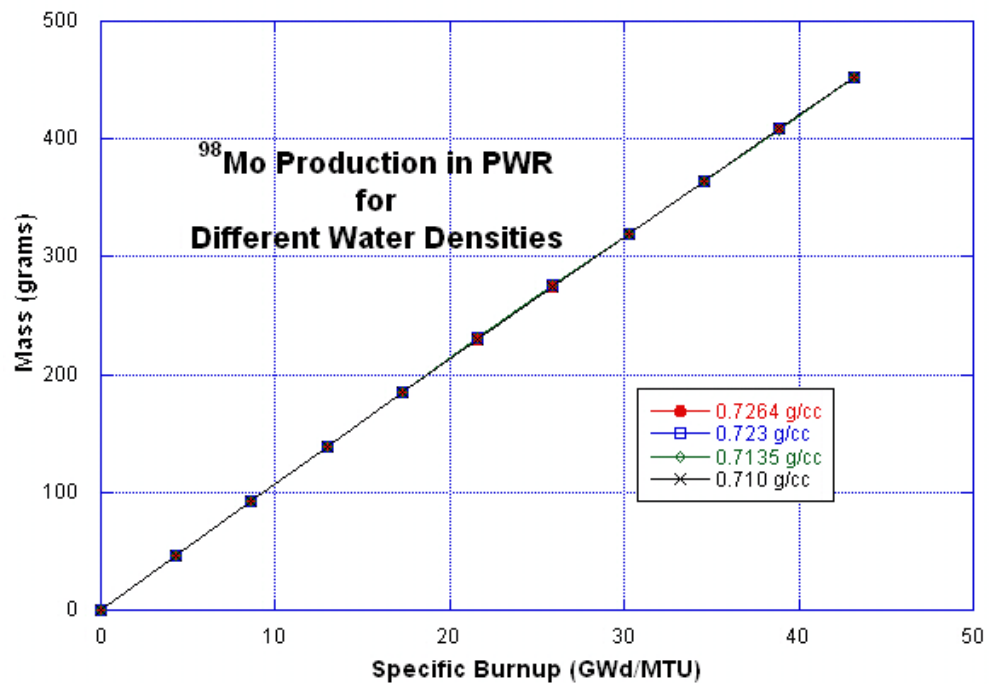


Figure 409: ⁹⁸Mo Production in the PWR Model for Different Water Densities

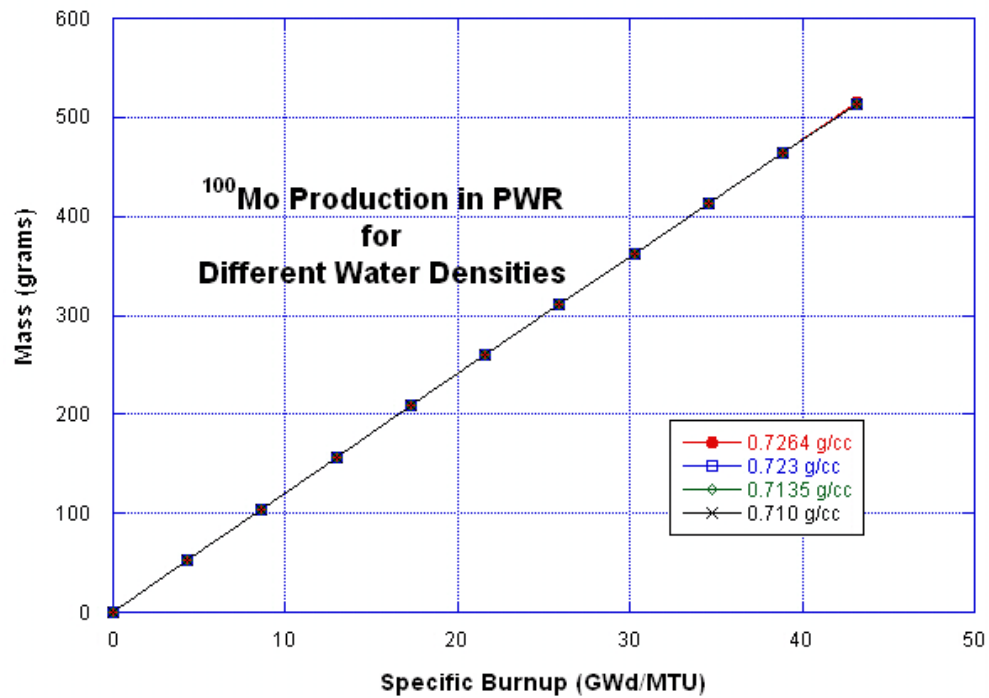


Figure 410: ¹⁰⁰Mo Production in the PWR Model for Different Water Densities

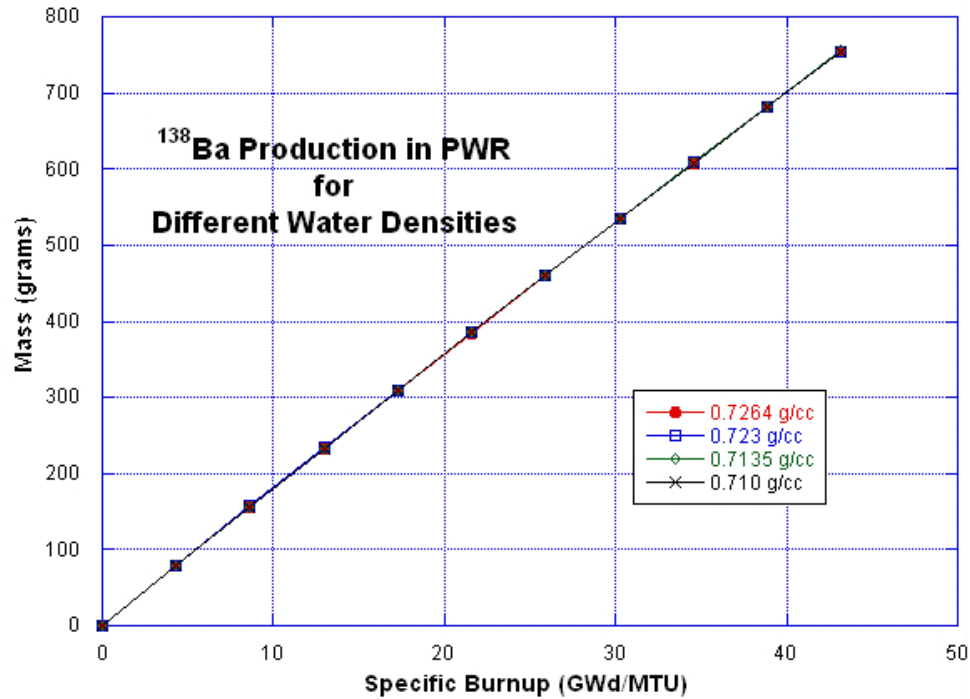


Figure 411: ¹³⁸Ba Production in the PWR Model for Different Water Densities

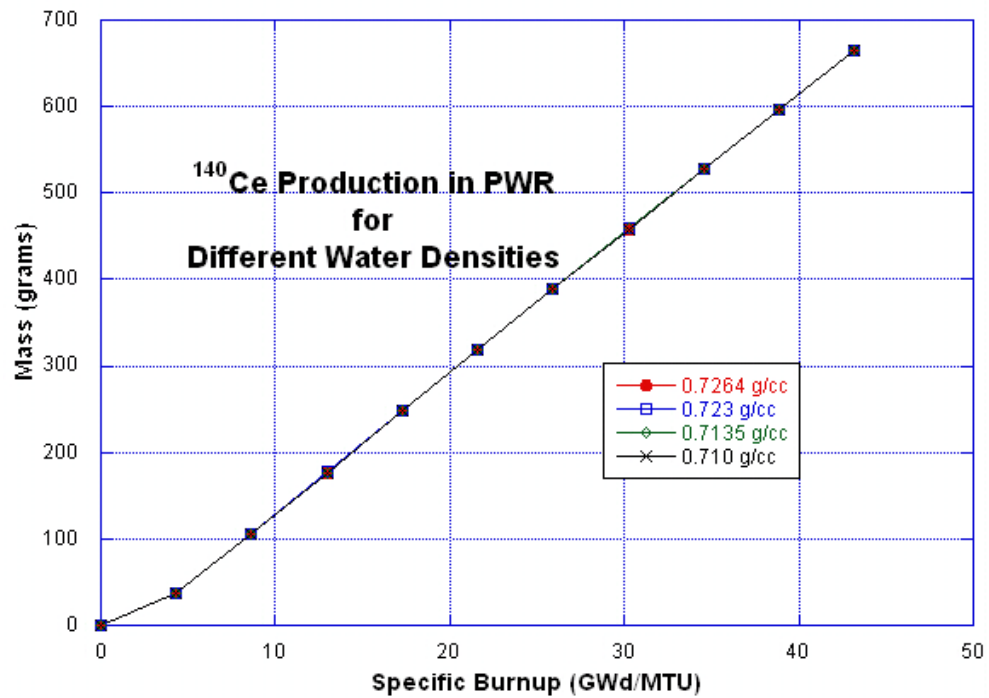


Figure 412: ¹⁴⁰Ce Production in the PWR Model for Different Water Densities

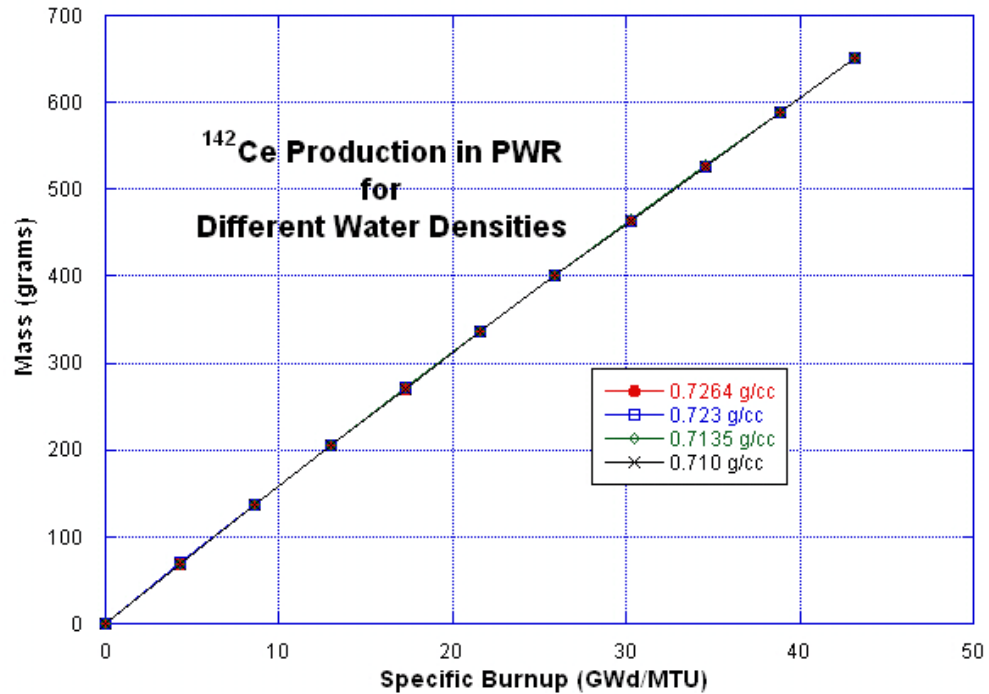


Figure 413: ¹⁴²Ce Production in the PWR Model for Different Water Densities

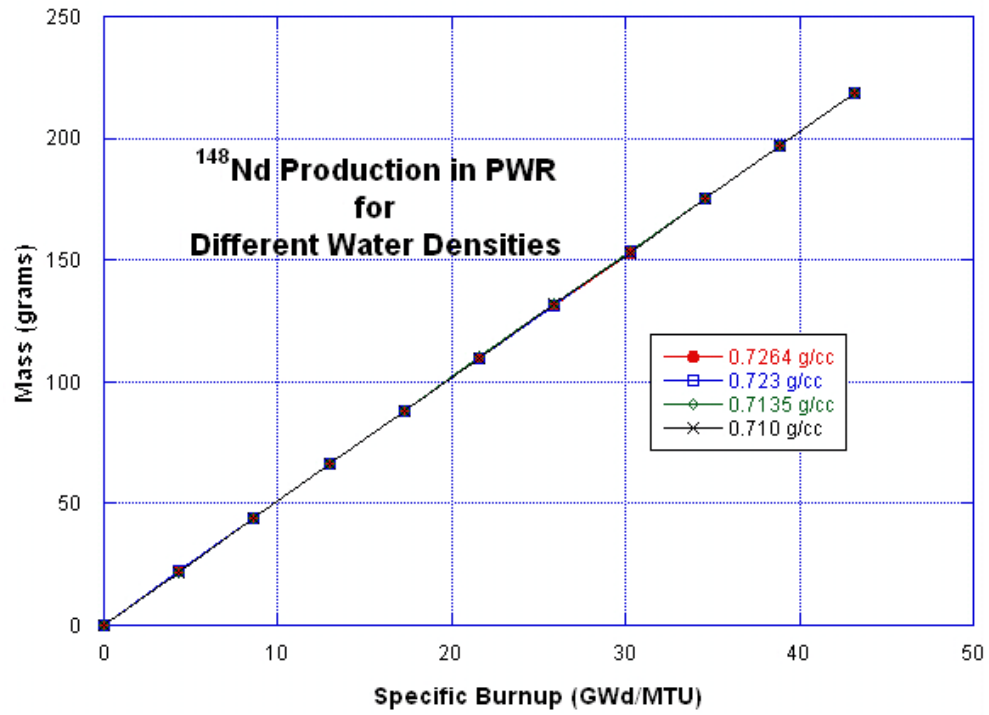


Figure 414: ¹⁴⁸Nd Production in the PWR Model for Different Water Densities

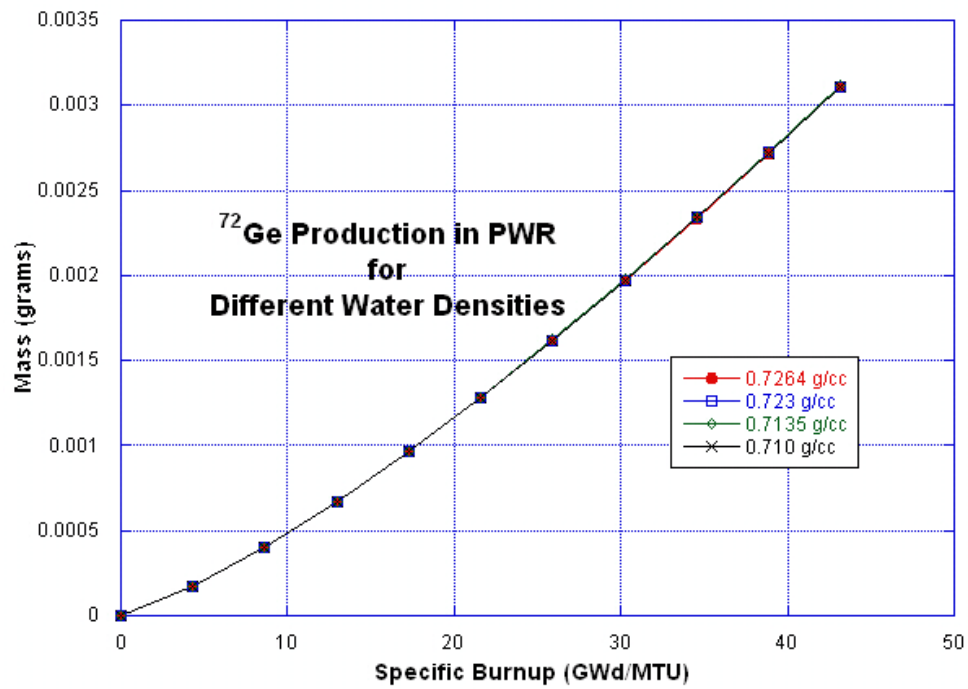


Figure 415: ⁷²Ge Production in the PWR Model for Different Water Densities

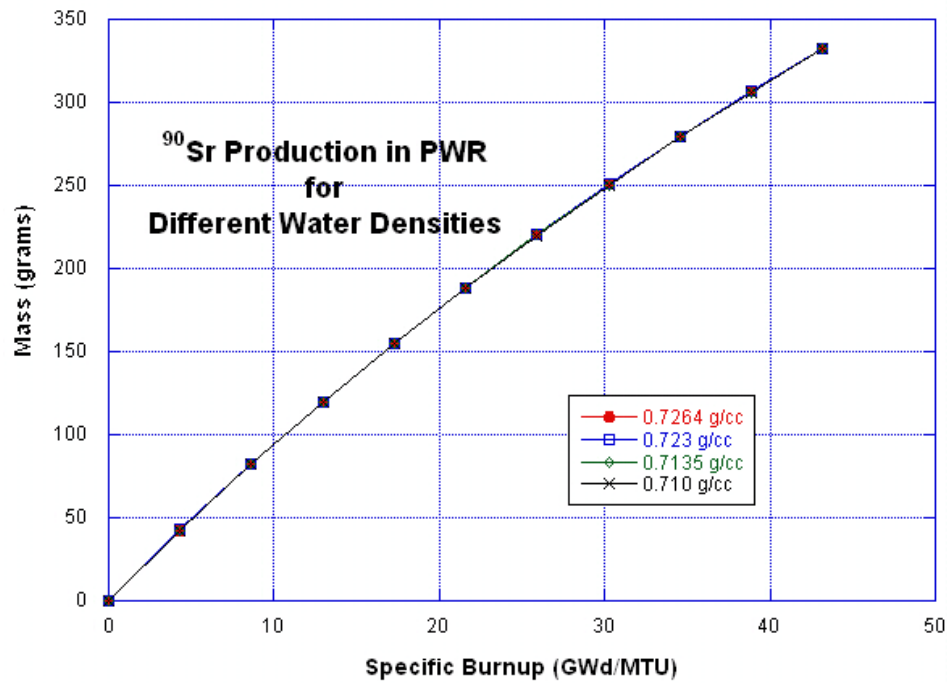


Figure 416: ⁹⁰Sr Production in the PWR Model for Different Water Densities

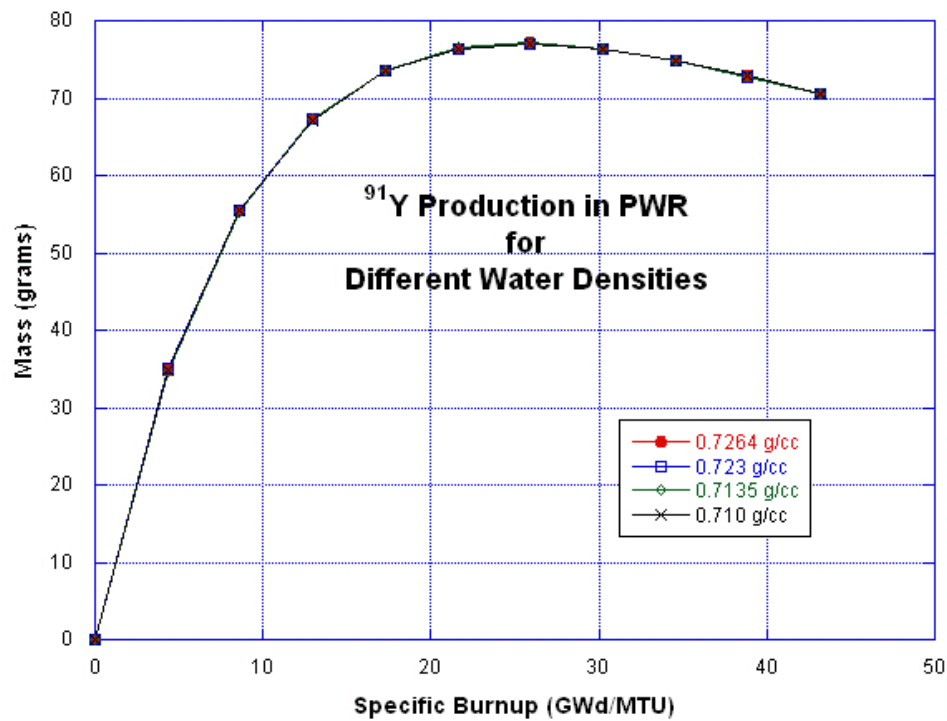


Figure 417: ⁹¹Y Production in the PWR Model for Different Water Densities

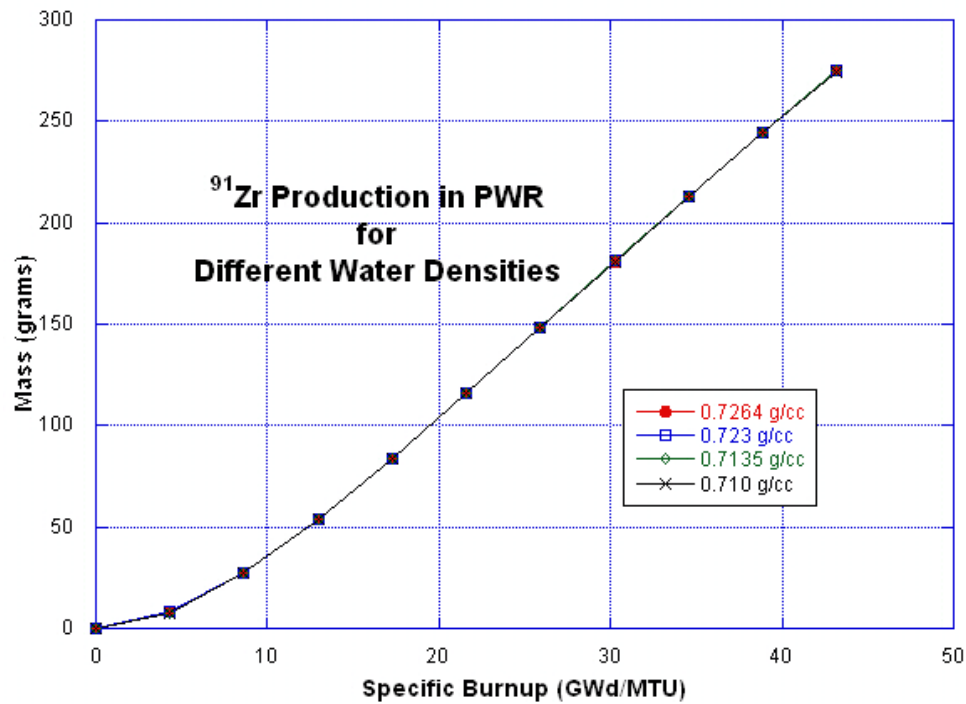


Figure 418: ⁹¹Zr Production in the PWR Model for Different Water Densities

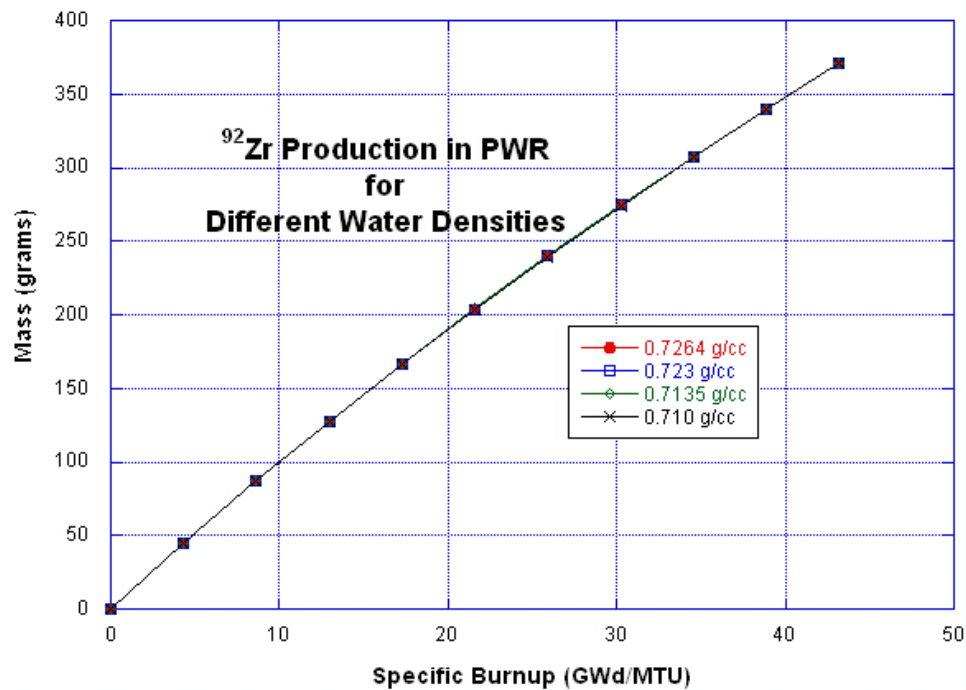


Figure 419: ⁹²Zr Production in the PWR Model for Different Water Densities

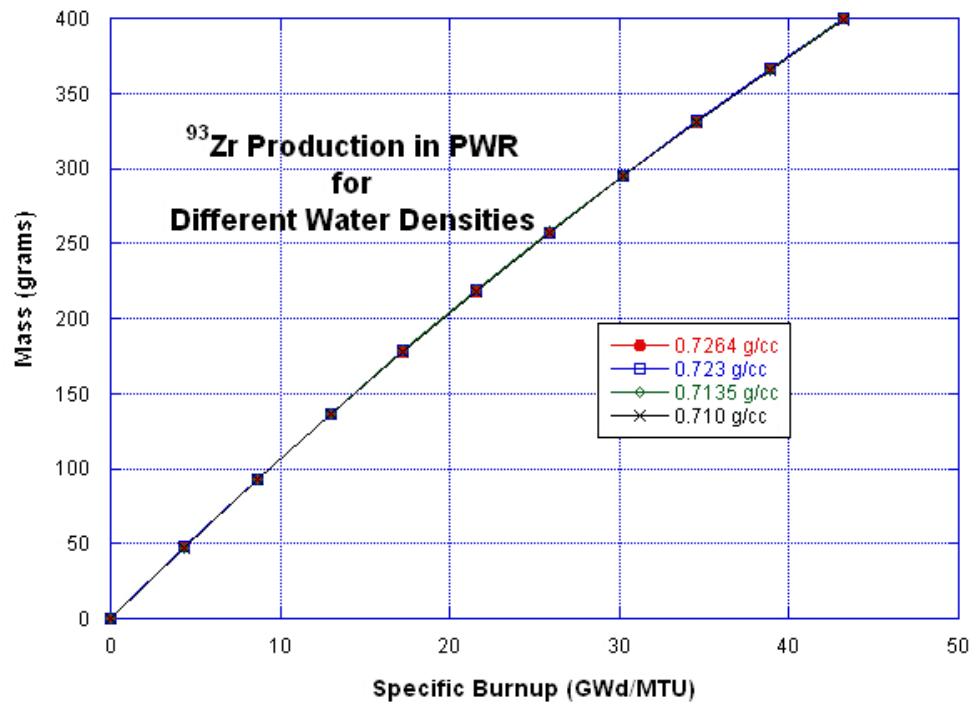


Figure 420: ⁹³Zr Production in the PWR Model for Different Water Densities

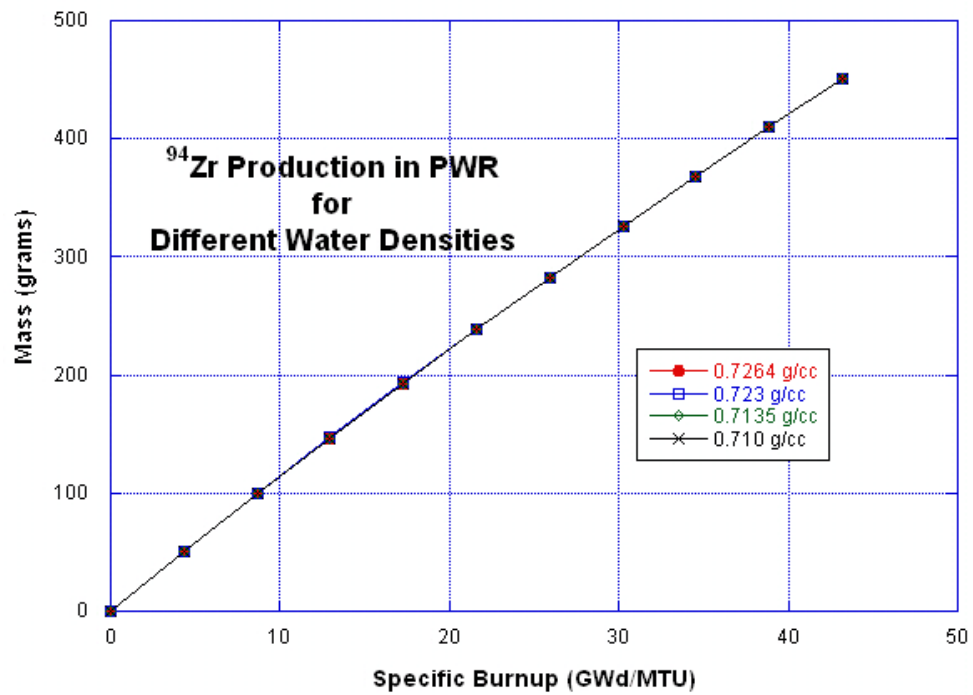


Figure 421: ⁹⁴Zr Production in the PWR Model for Different Water Densities

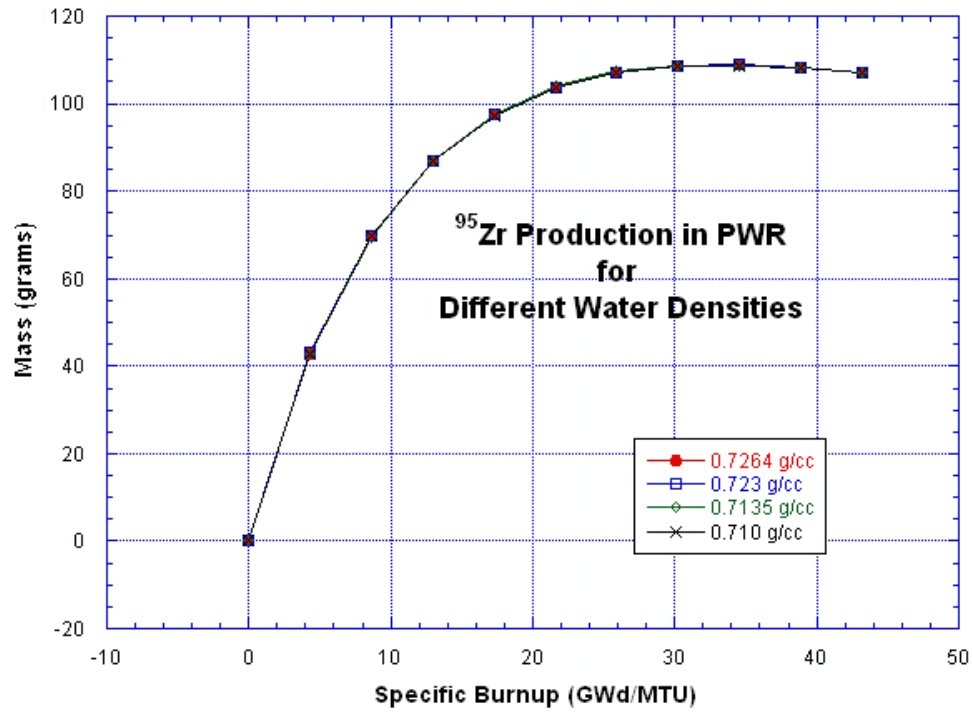


Figure 422: ⁹⁵Zr Production in the PWR Model for Different Water Densities

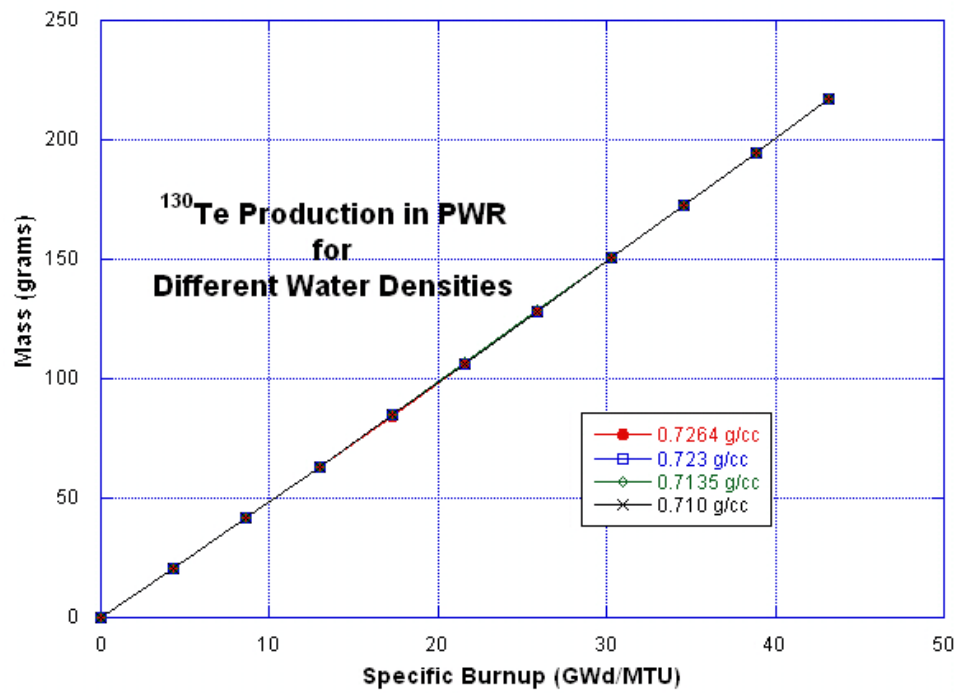


Figure 423: ¹³⁰Te Production in the PWR Model for Different Water Densities

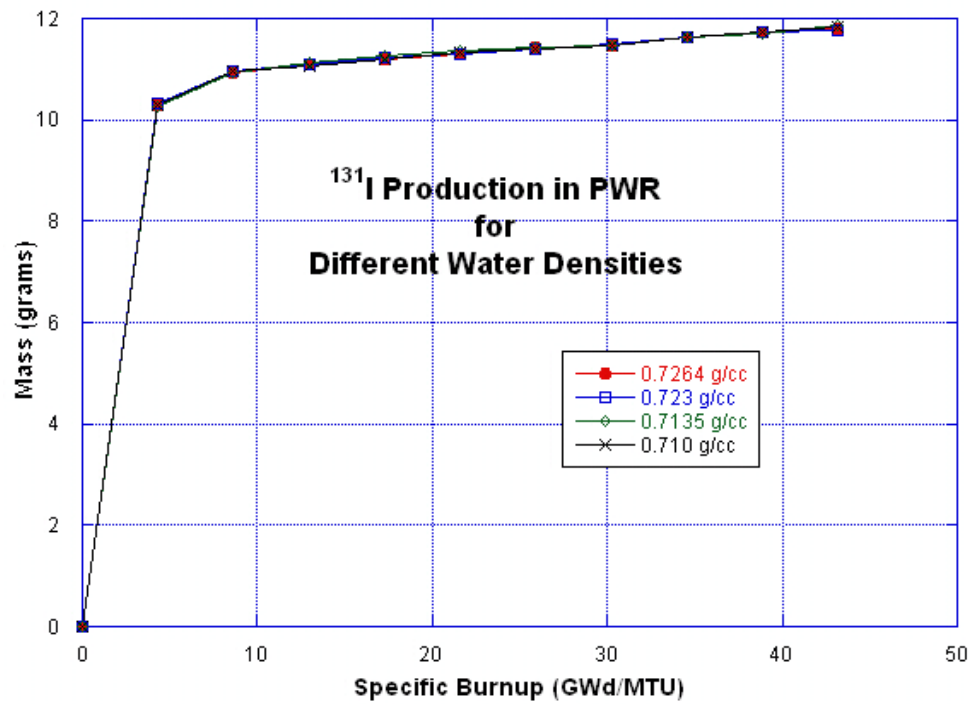


Figure 424: ¹³¹I Production in the PWR Model for Different Water Densities

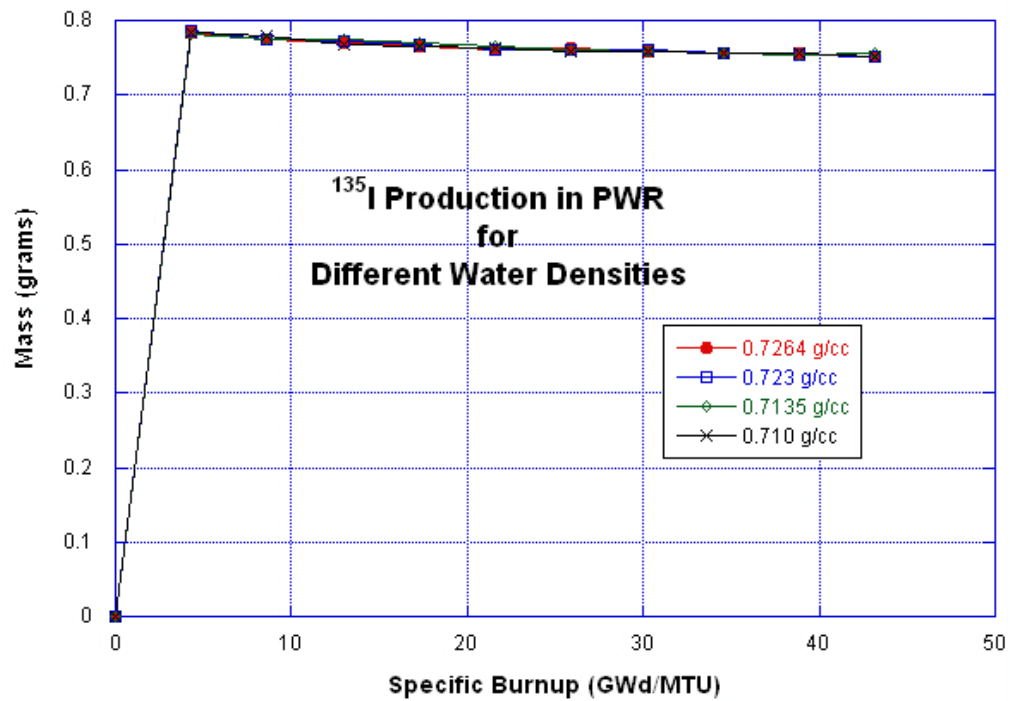


Figure 425: ¹³⁵I Production in the PWR Model for Different Water Densities

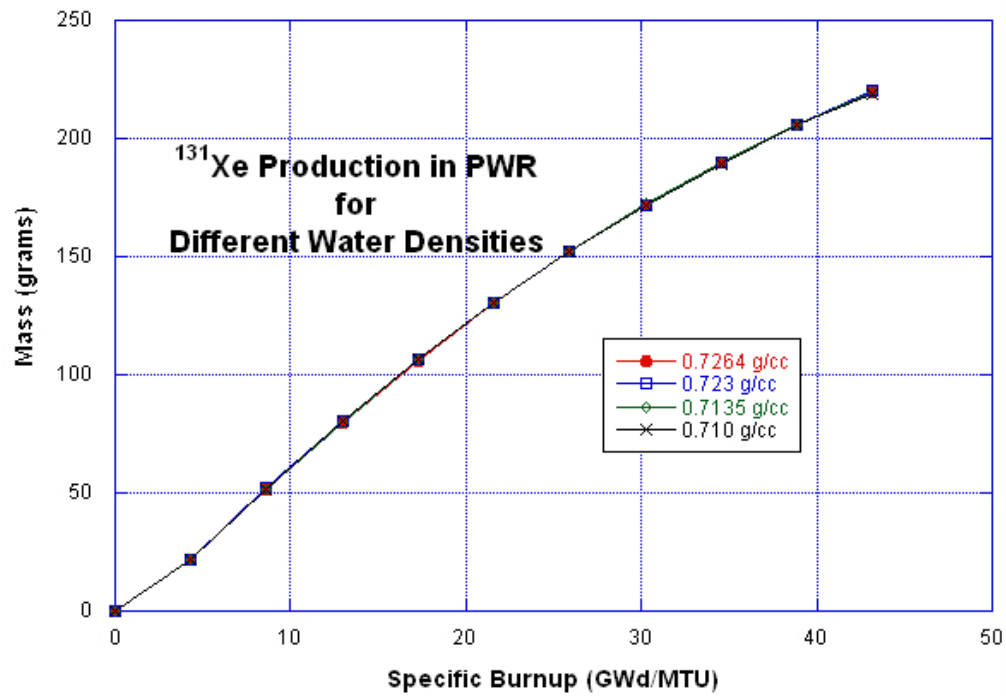


Figure 426: ¹³¹Xe Production in the PWR Model for Different Water Densities

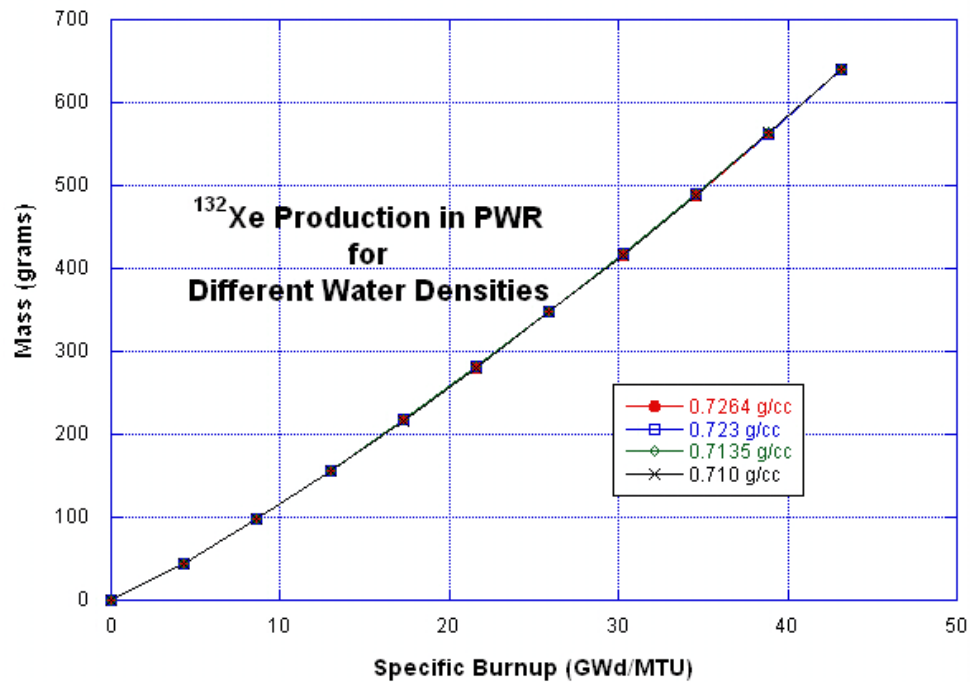


Figure 427: ¹³²Xe Production in the PWR Model for Different Water Densities

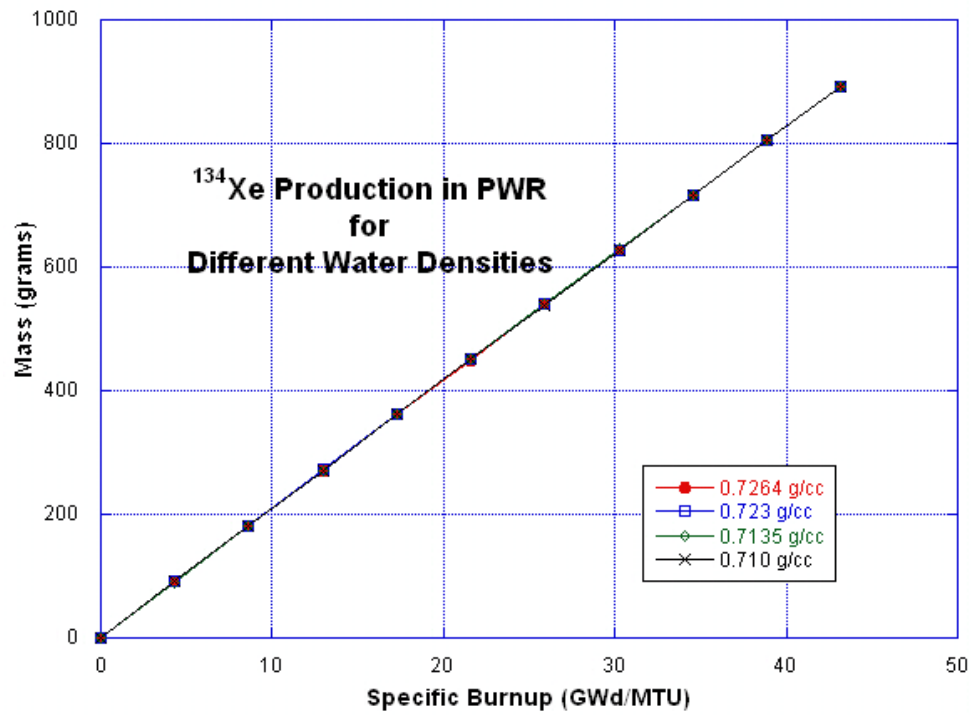


Figure 428: ^{134}Xe Production in the PWR Model for Different Water Densities

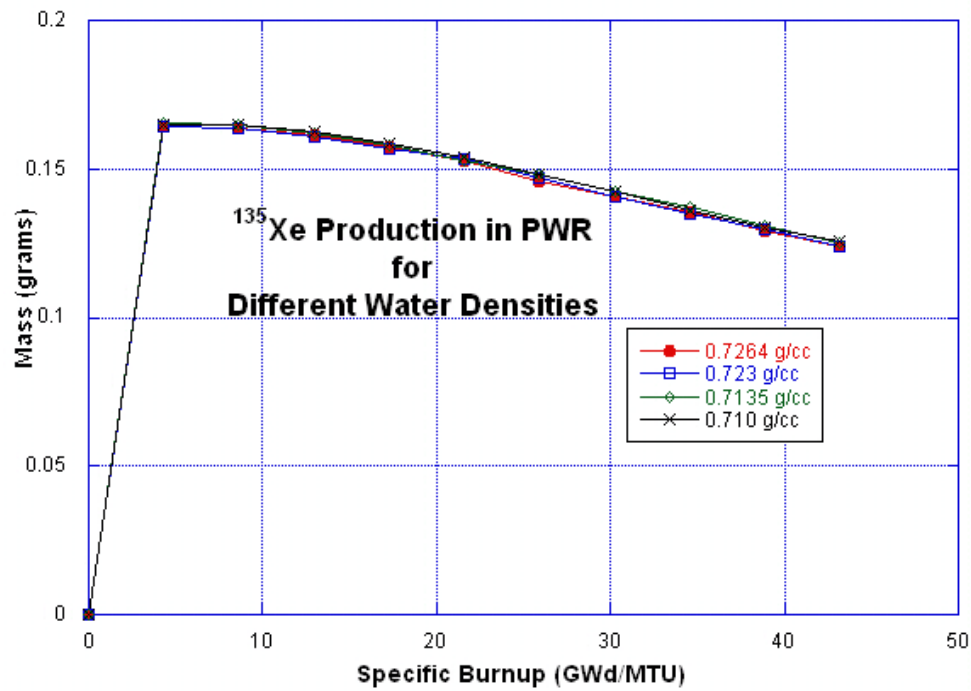


Figure 429: ^{135}Xe Production in the PWR Model for Different Water Densities

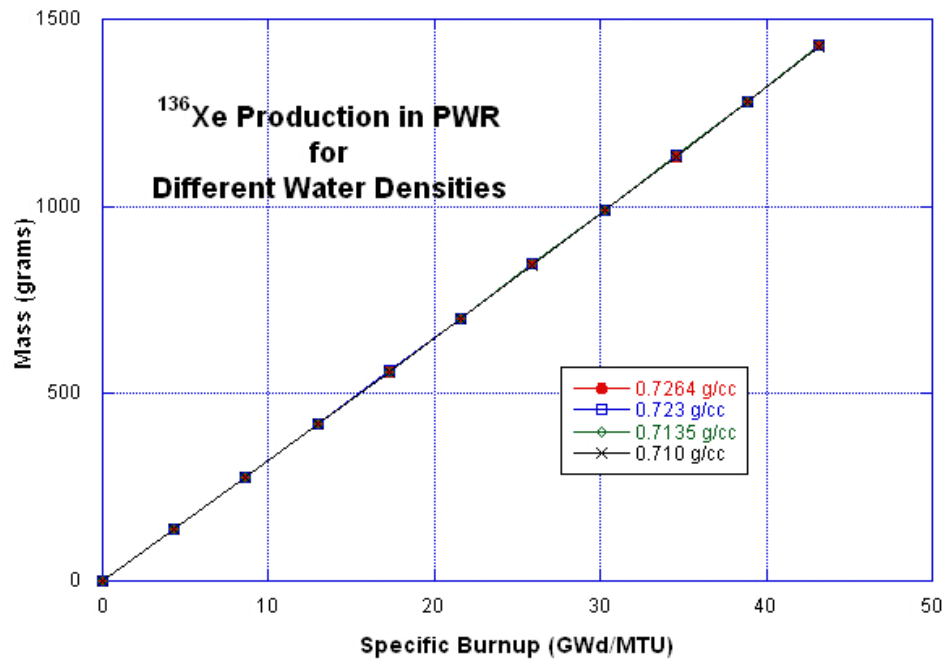


Figure 430: ^{136}Xe Production in the PWR Model for Different Water Densities

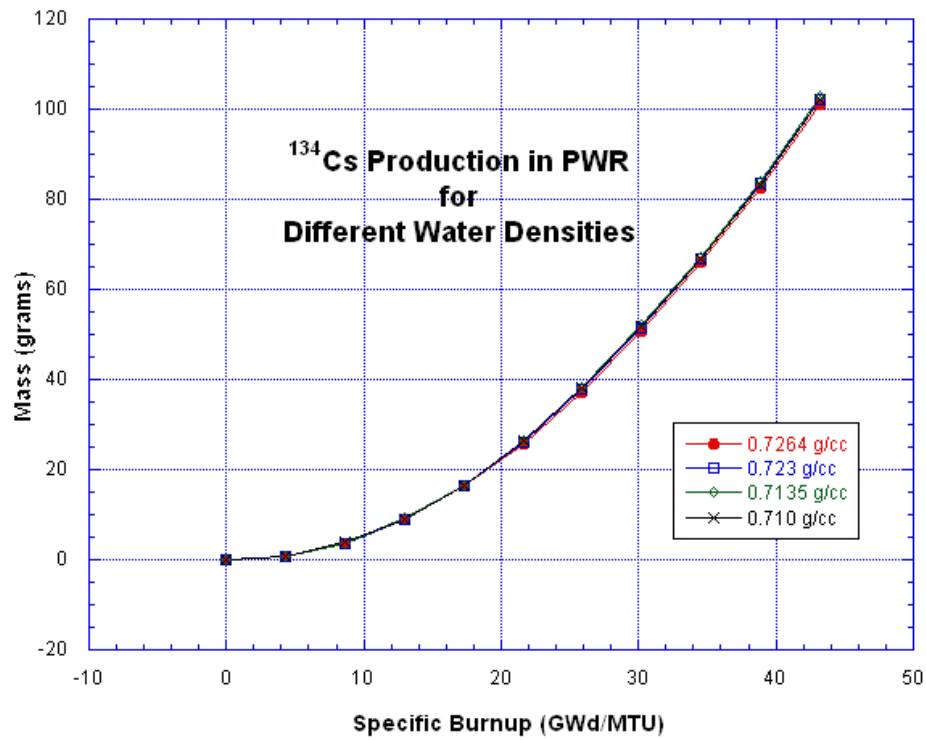


Figure 431: ^{134}Cs Production in the PWR Model for Different Water Densities

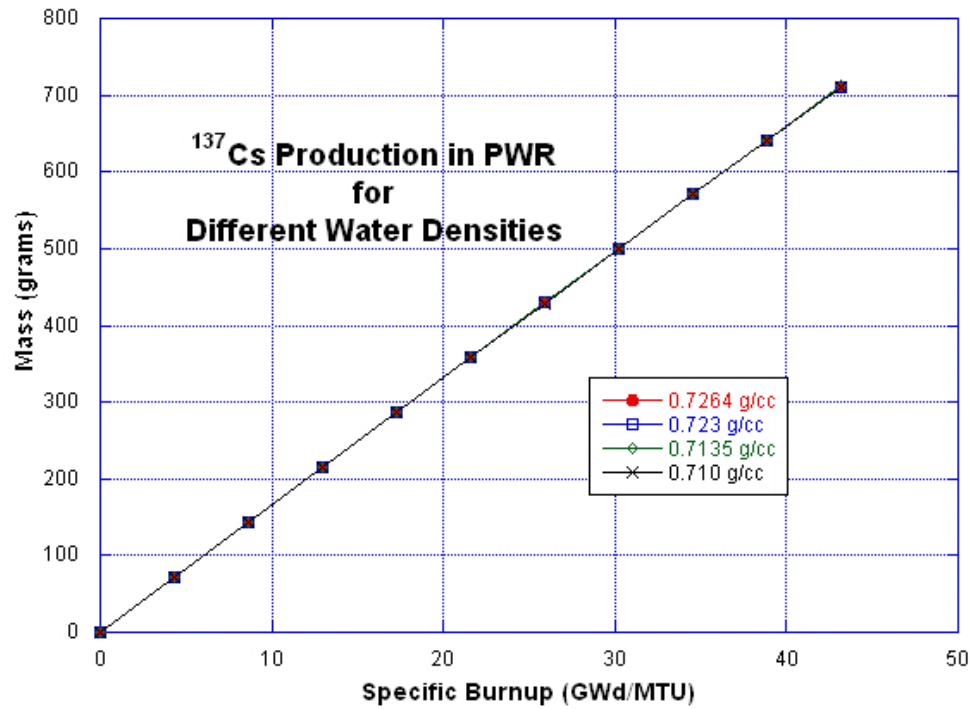


Figure 432: ¹³⁷Cs Production in the PWR Model for Different Water Densities

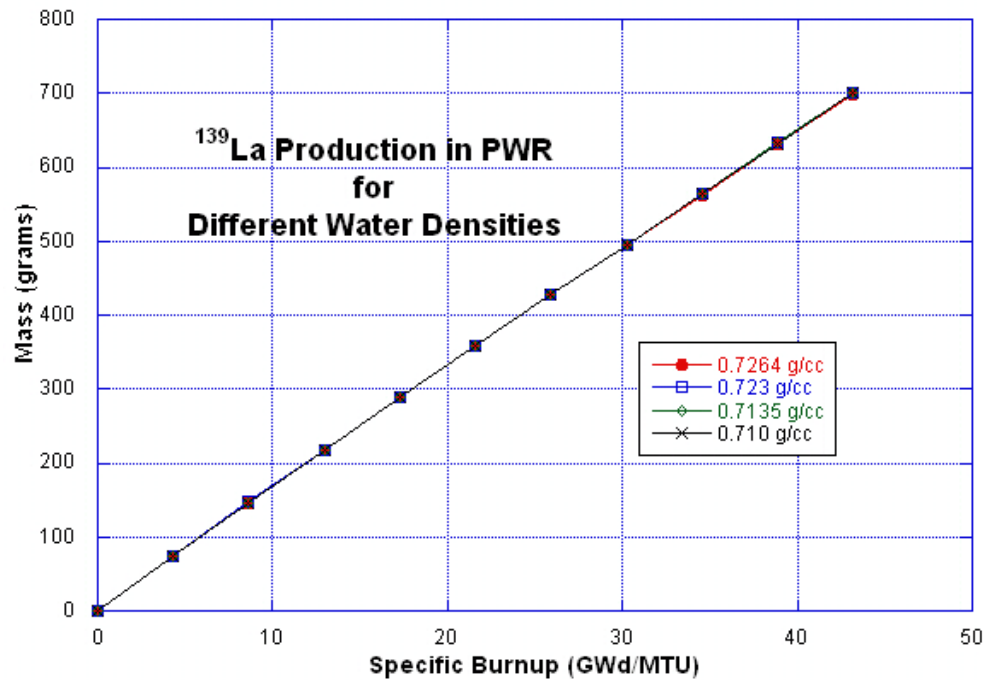


Figure 433: ¹³⁹La Production in the PWR Model for Different Water Densities

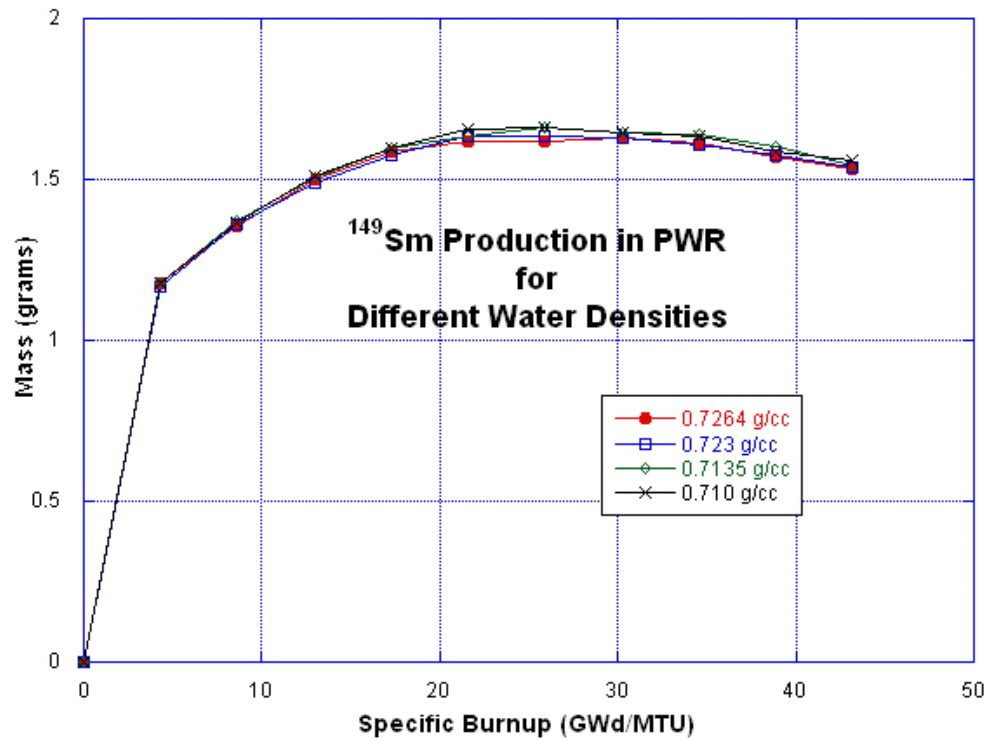


Figure 434: ¹⁴⁹Sm Production in the PWR Model for Different Water Densities

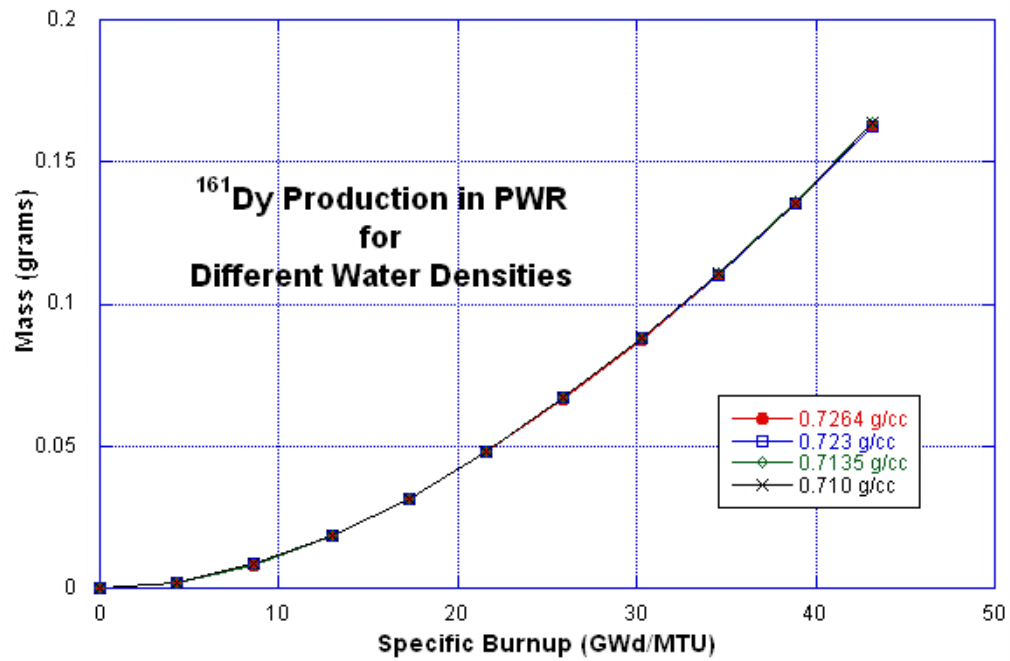


Figure 435: ¹⁶¹Dy Production in the PWR Model for Different Water Densities

**PWR Sensitivity Study
Plots of 46 Nuclides of Interest
Fuel Temperature Variation**

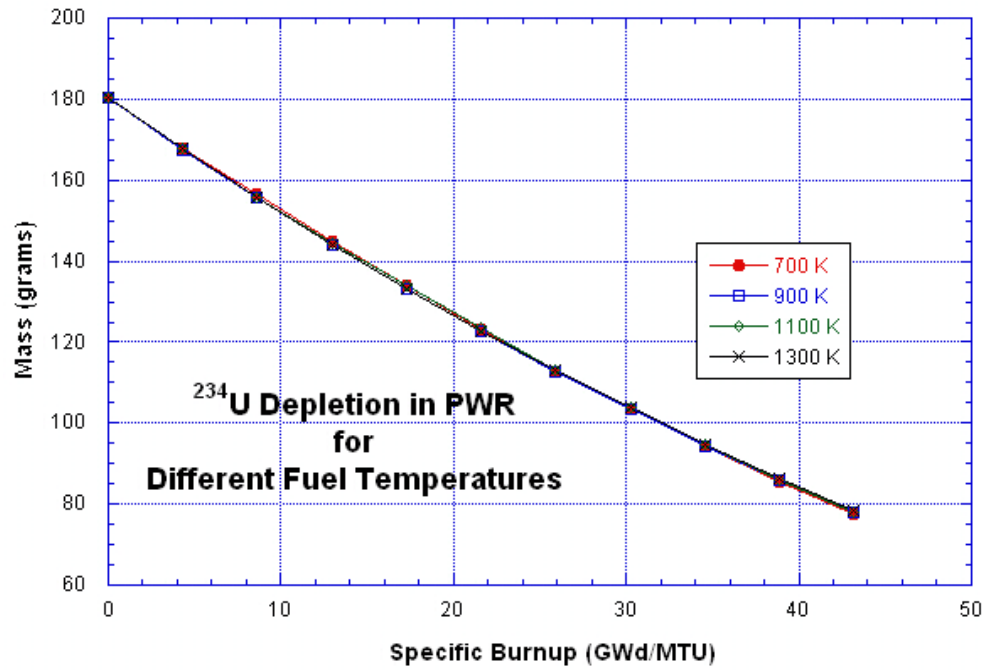


Figure 436: ²³⁴U Depletion in the PWR Model for Different Fuel Temperatures

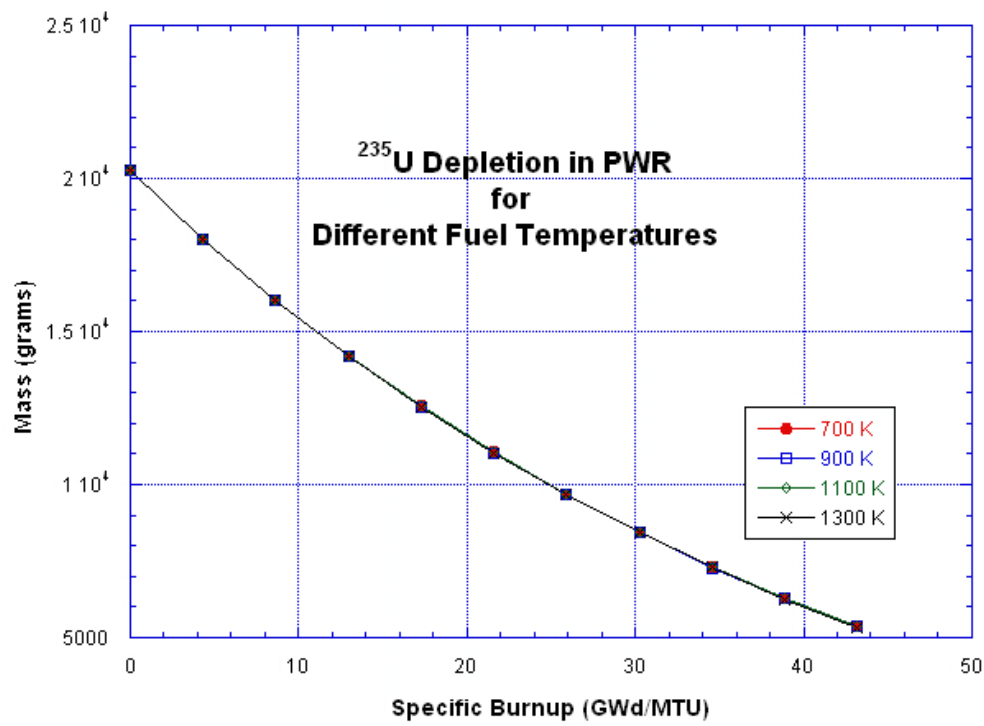


Figure 437: ²³⁵U Depletion in the PWR Model for Different Fuel Temperatures

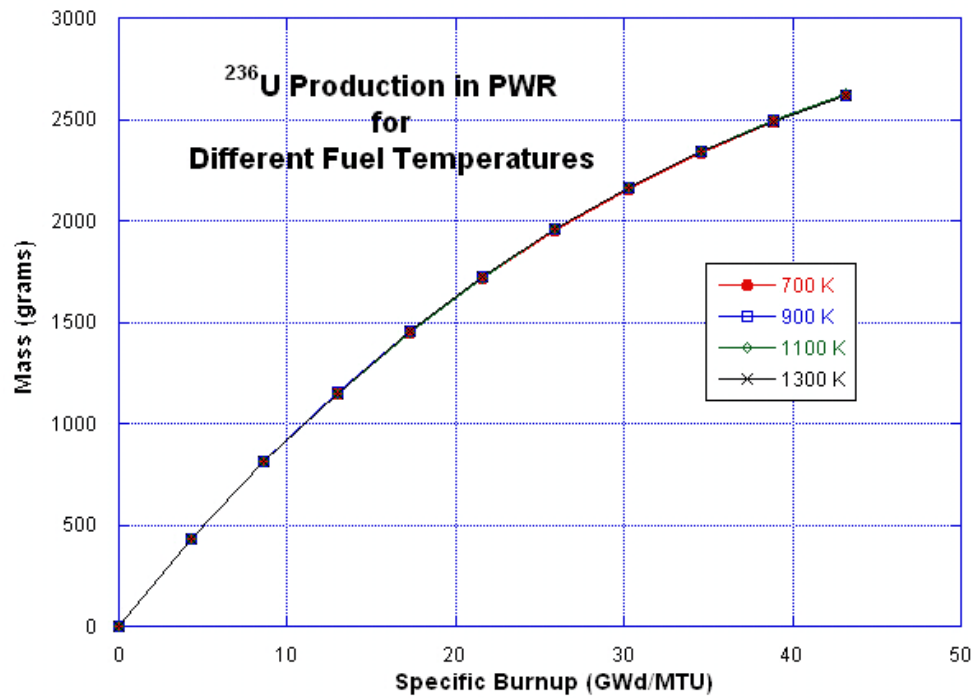


Figure 438: ²³⁶U Production in the PWR Model for Different Fuel Temperatures

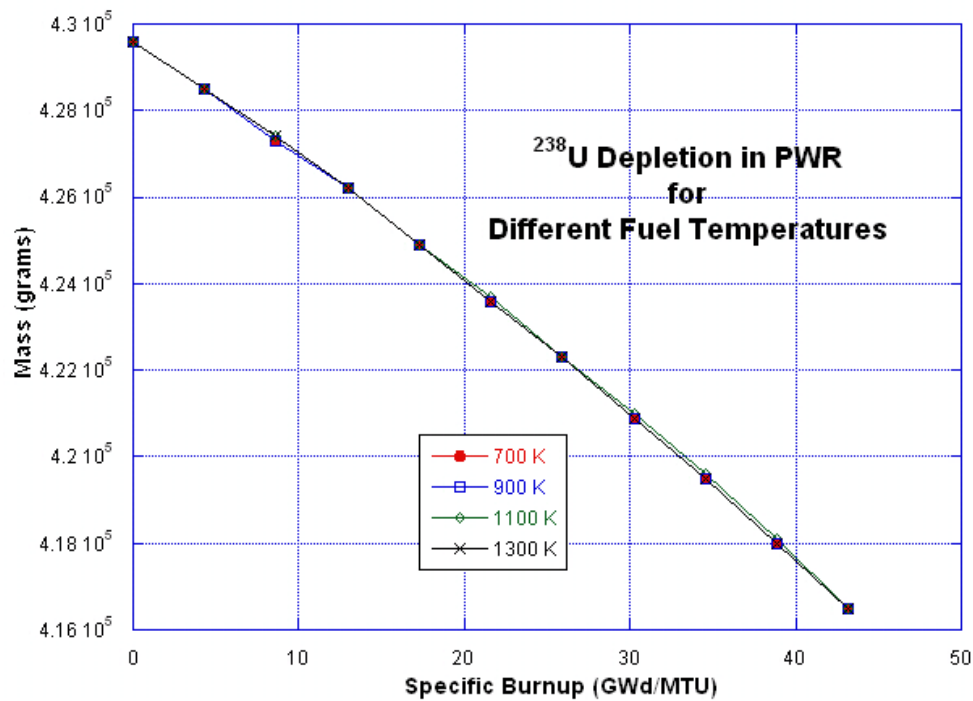


Figure 439: ²³⁸U Depletion in the PWR Model for Different Fuel Temperatures

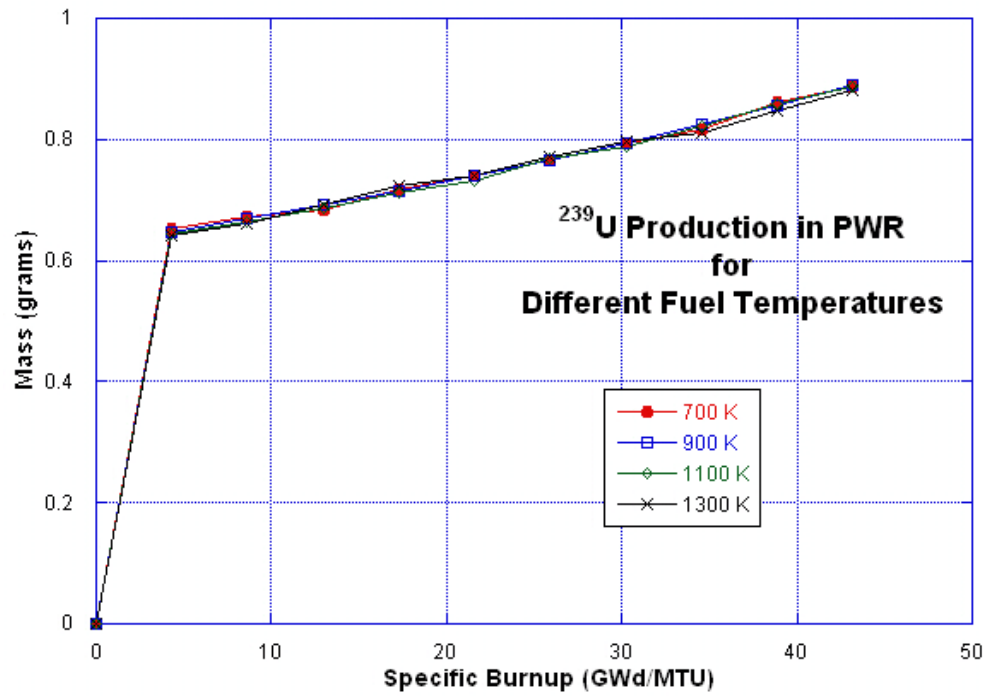


Figure 440: ²³⁹U Production in the PWR Model for Different Fuel Temperatures

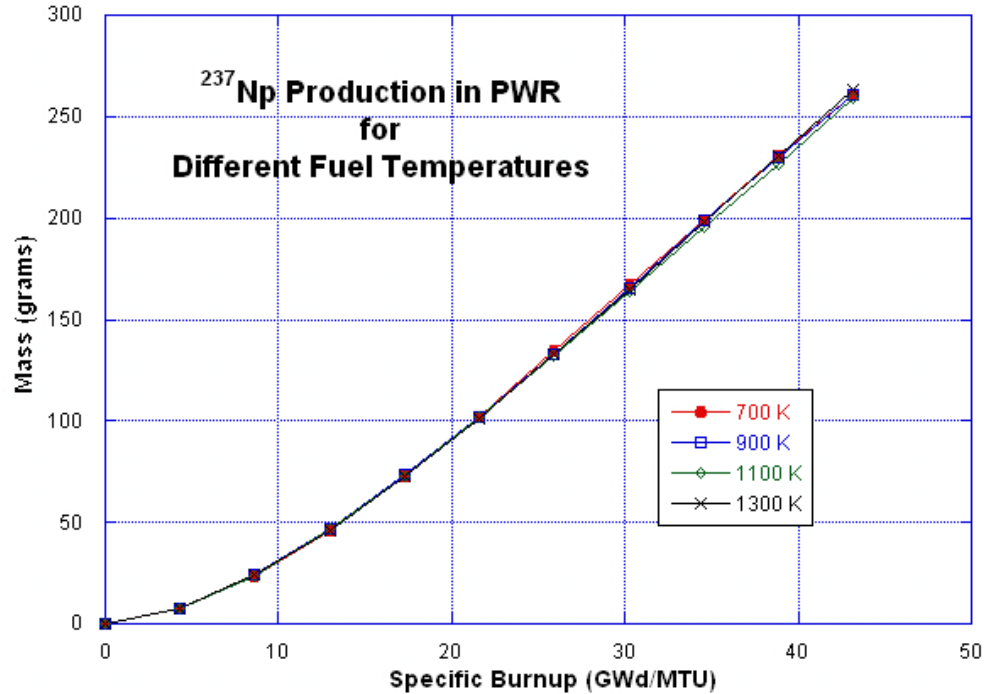


Figure 441: ²³⁷Np Production in the PWR Model for Different Fuel Temperatures

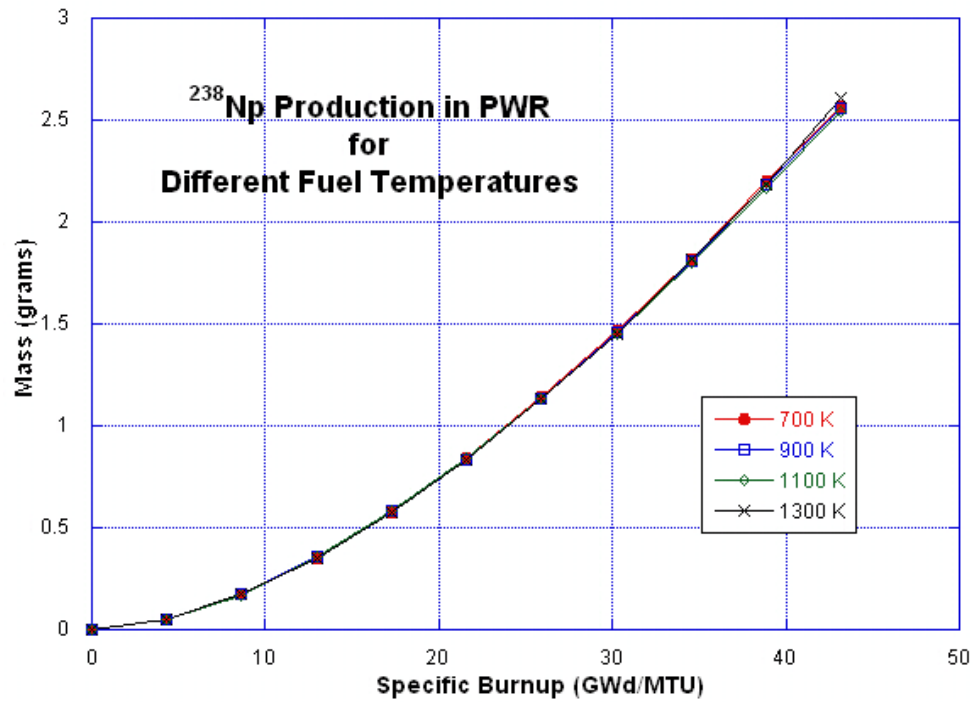


Figure 442: ²³⁸Np Production in the PWR Model for Different Fuel Temperatures

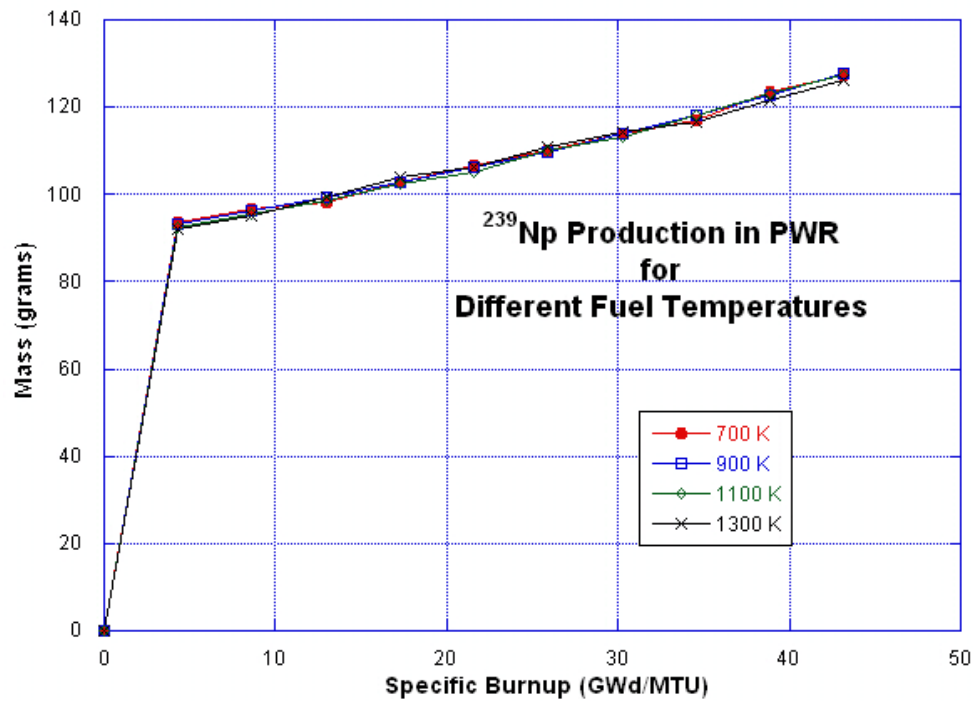


Figure 443: ²³⁹Np Production in the PWR Model for Different Fuel Temperatures

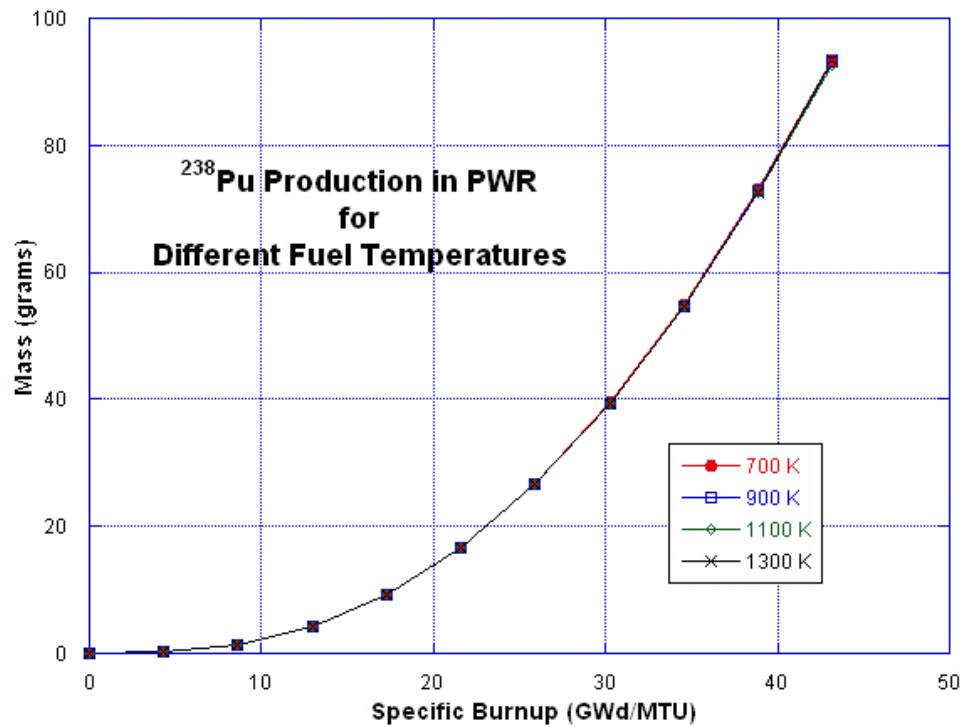


Figure 444: ²³⁸Pu Production in the PWR Model for Different Fuel Temperatures

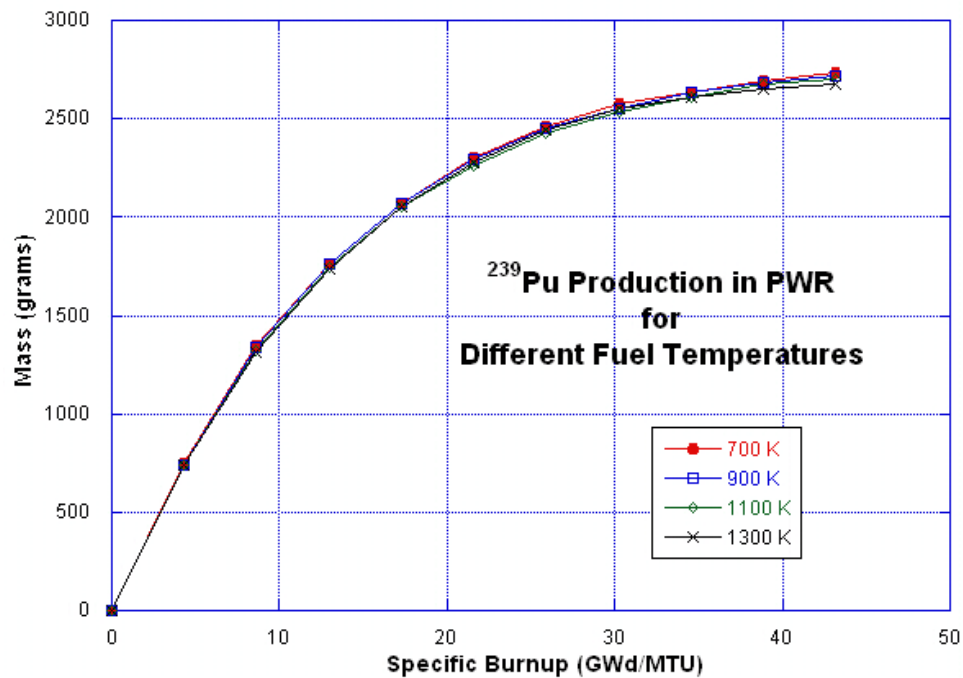


Figure 445: ²³⁹Pu Production in the PWR Model for Different Fuel Temperatures

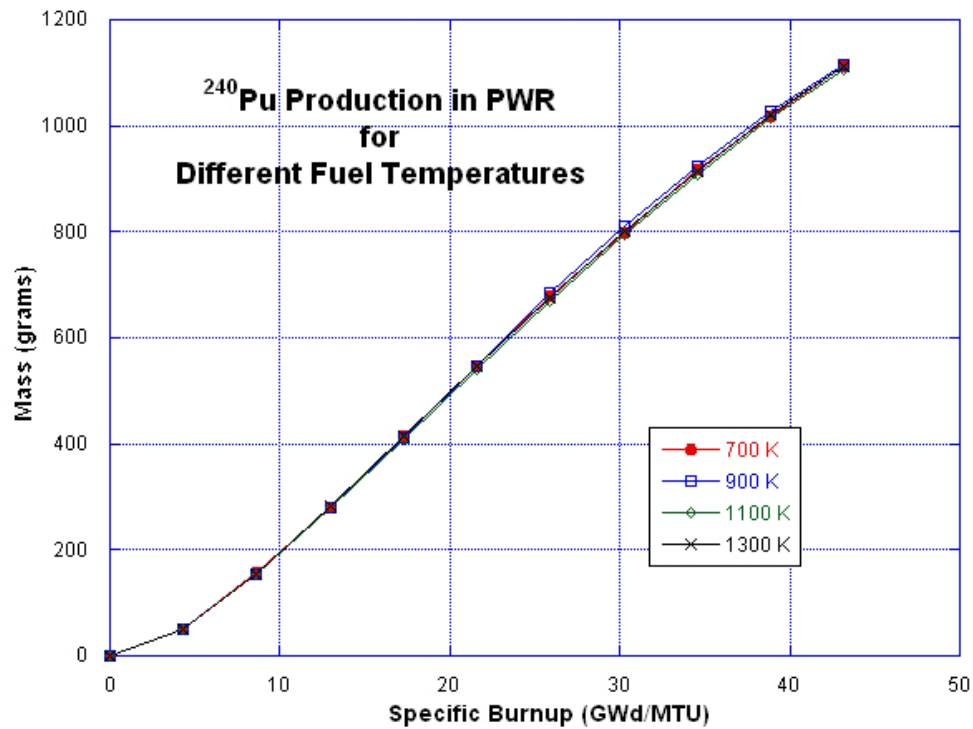


Figure 446: ²⁴⁰Pu Production in the PWR Model for Different Fuel Temperatures

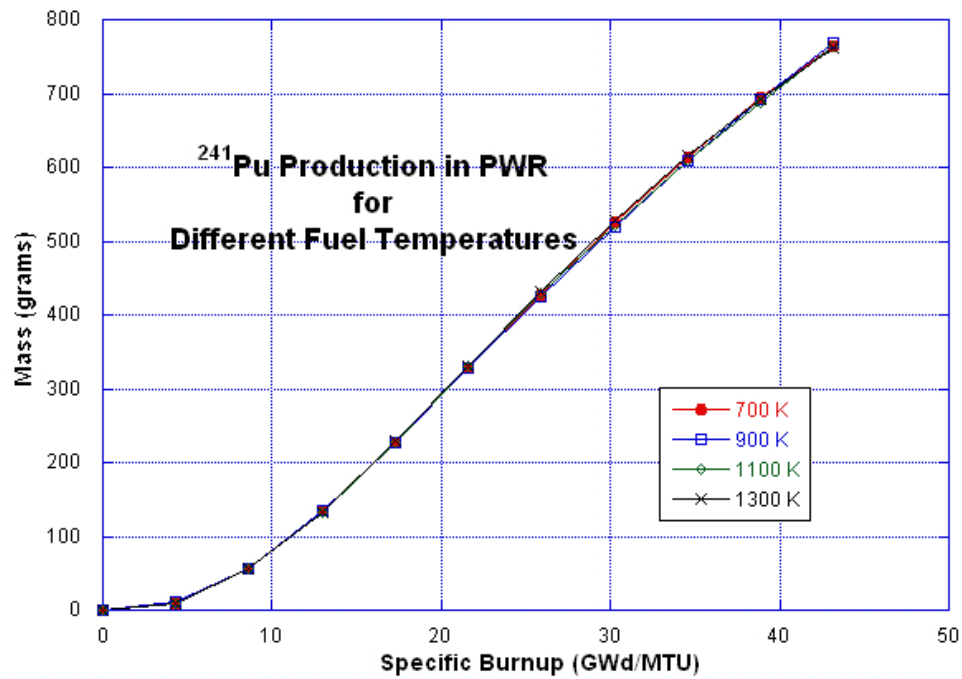


Figure 447: ²⁴¹Pu Production in the PWR Model for Different Fuel Temperatures

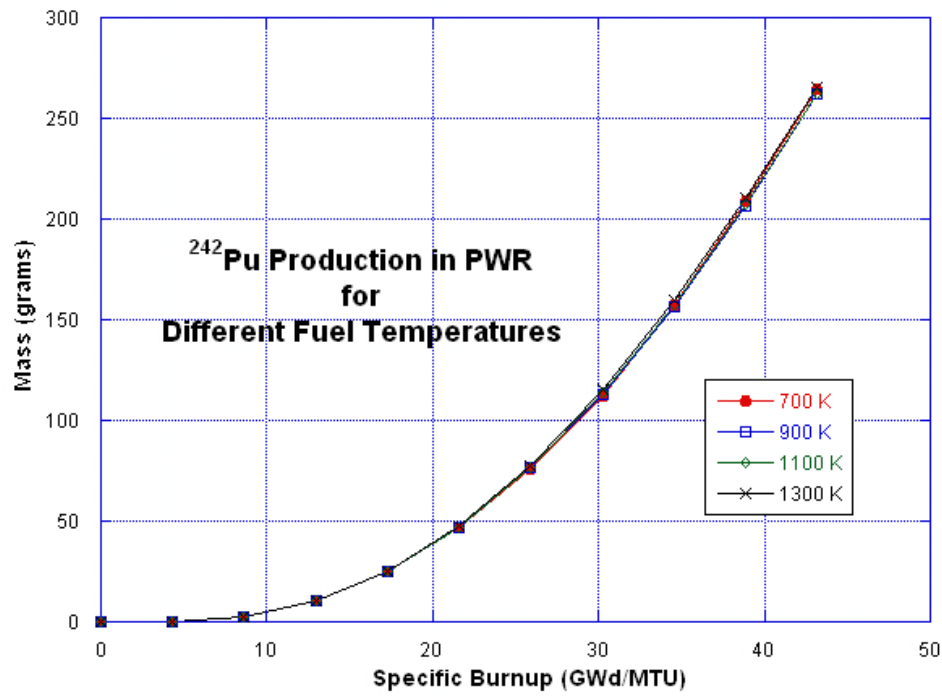


Figure 448: ²⁴²Pu Production in the PWR Model for Different Fuel Temperatures

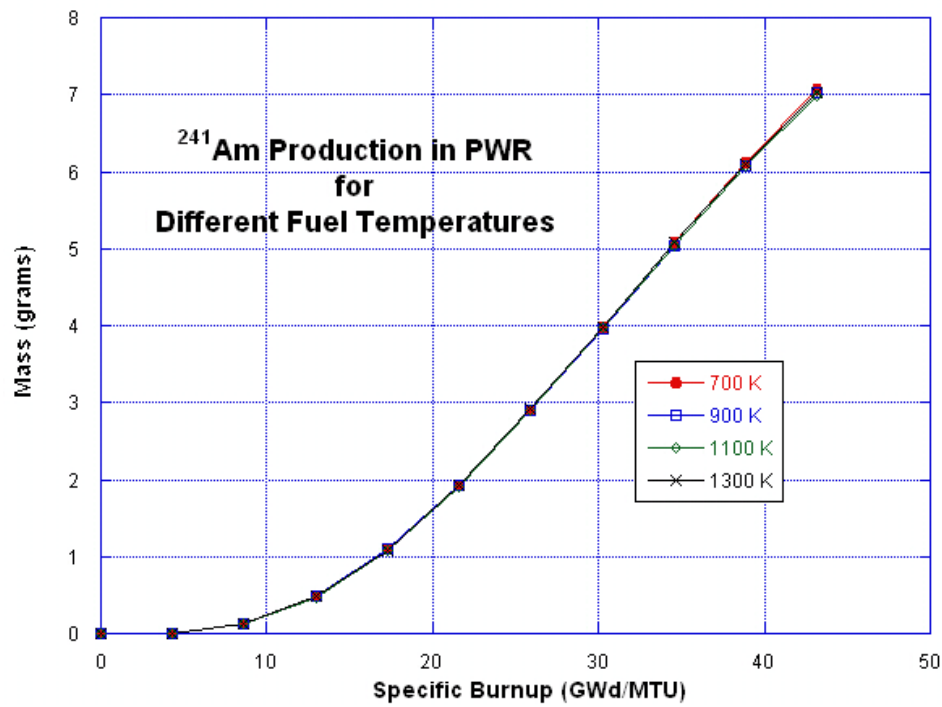


Figure 449: ²⁴¹Am Production in the PWR Model for Different Fuel Temperatures

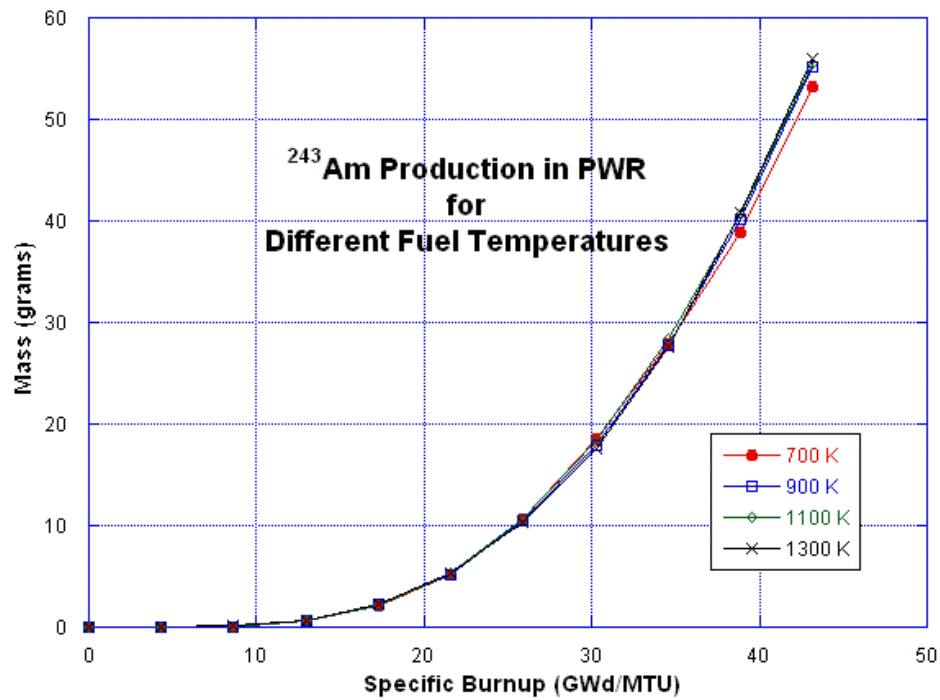


Figure 450: ²⁴³Am Production in the PWR Model for Different Fuel Temperatures

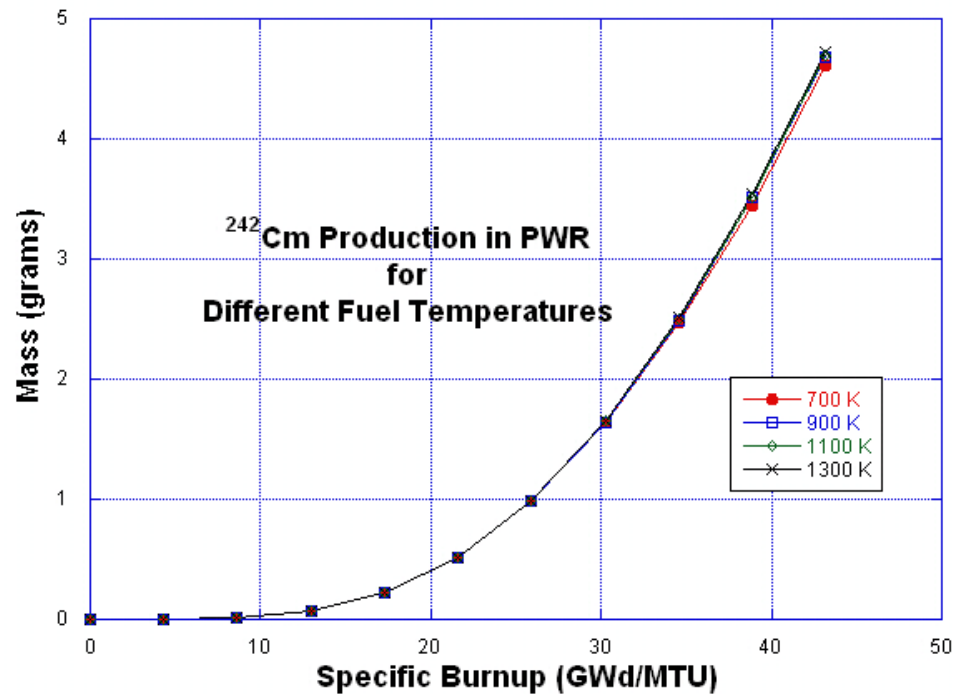


Figure 451: ²⁴²Cm Production in the PWR Model for Different Fuel Temperatures

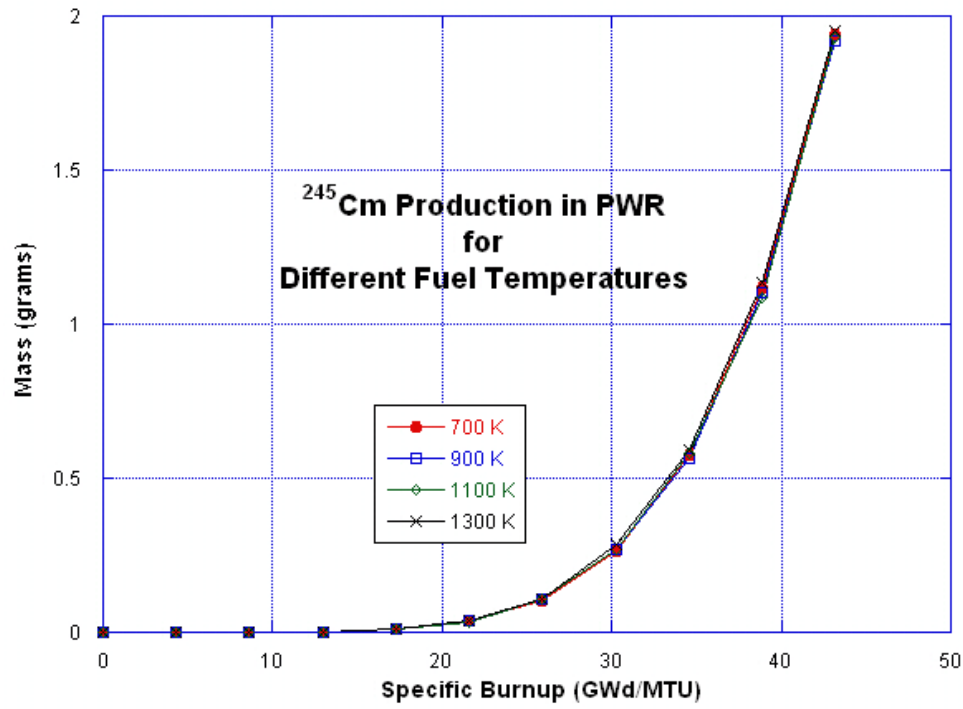


Figure 452: ²⁴⁵Cm Production in the PWR Model for Different Fuel Temperatures

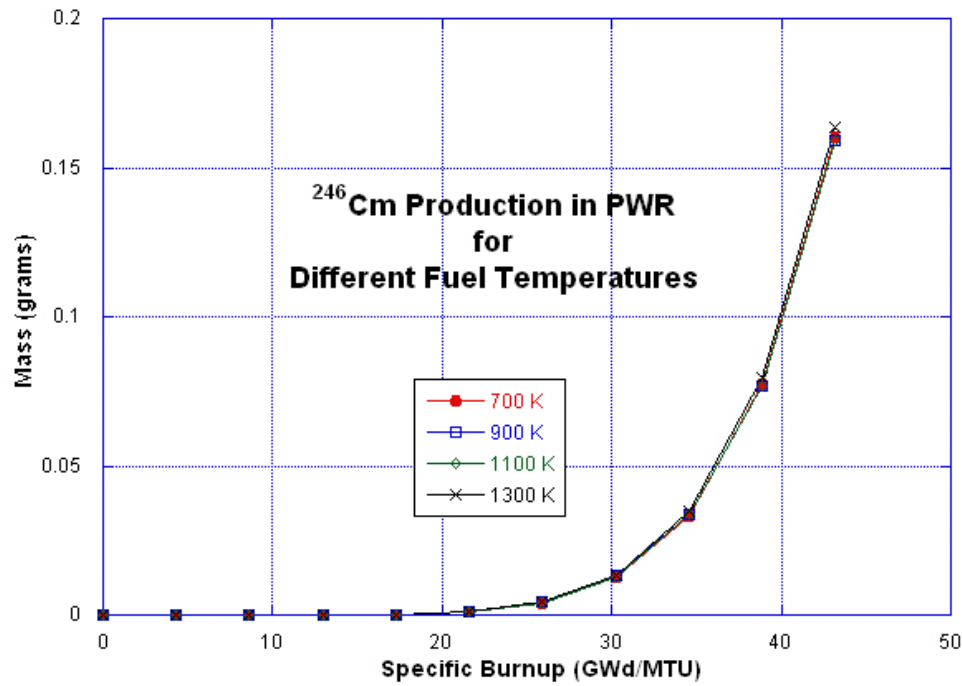


Figure 453: ²⁴⁶Cm Production in the PWR Model for Different Fuel Temperatures

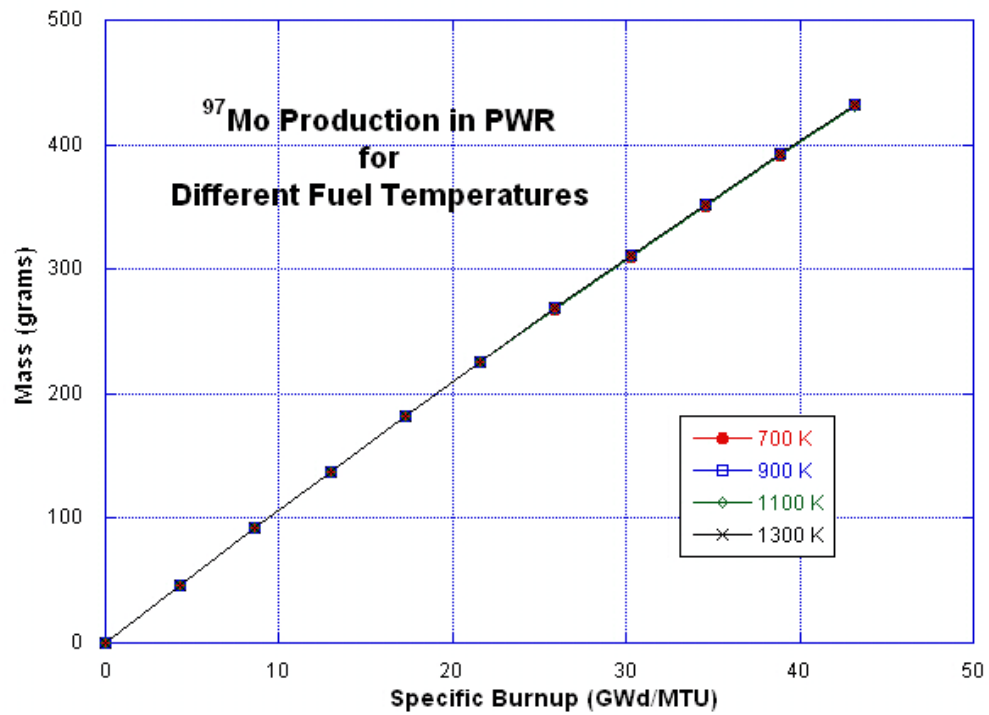


Figure 454: ⁹⁷Mo Production in the PWR Model for Different Fuel Temperatures

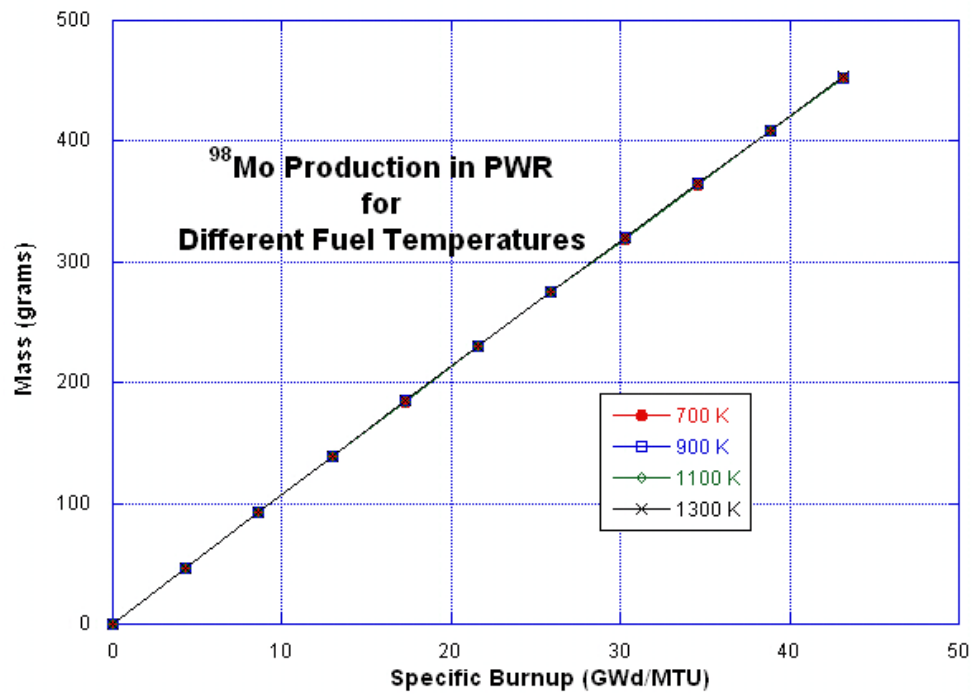


Figure 455: ⁹⁸Mo Production in the PWR Model for Different Fuel Temperatures

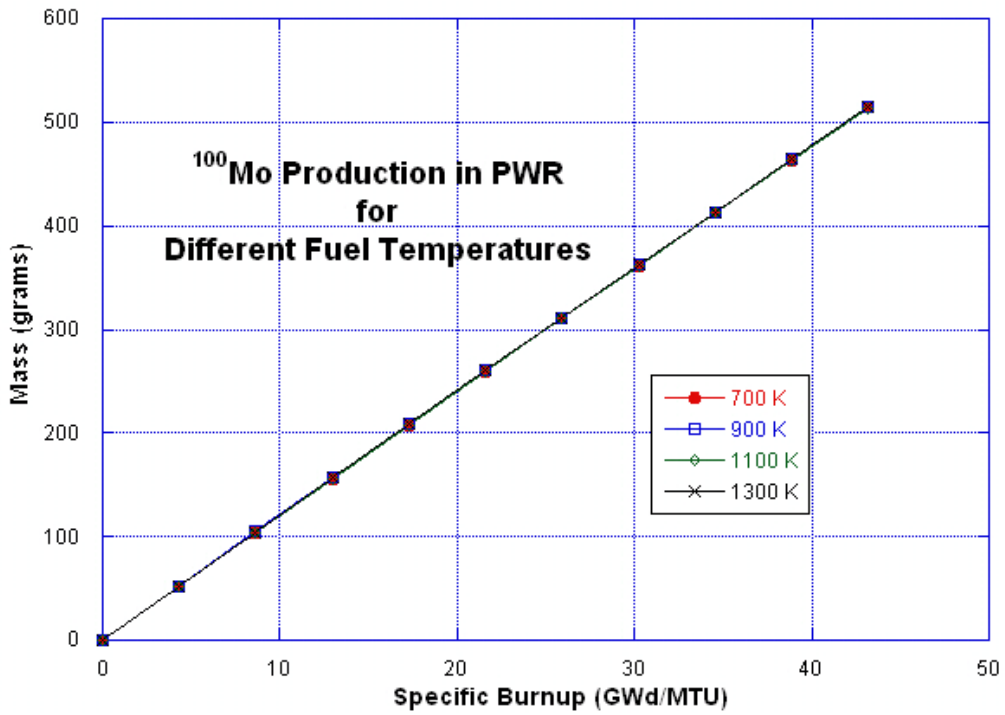


Figure 456: ¹⁰⁰Mo Production in the PWR Model for Different Fuel Temperatures

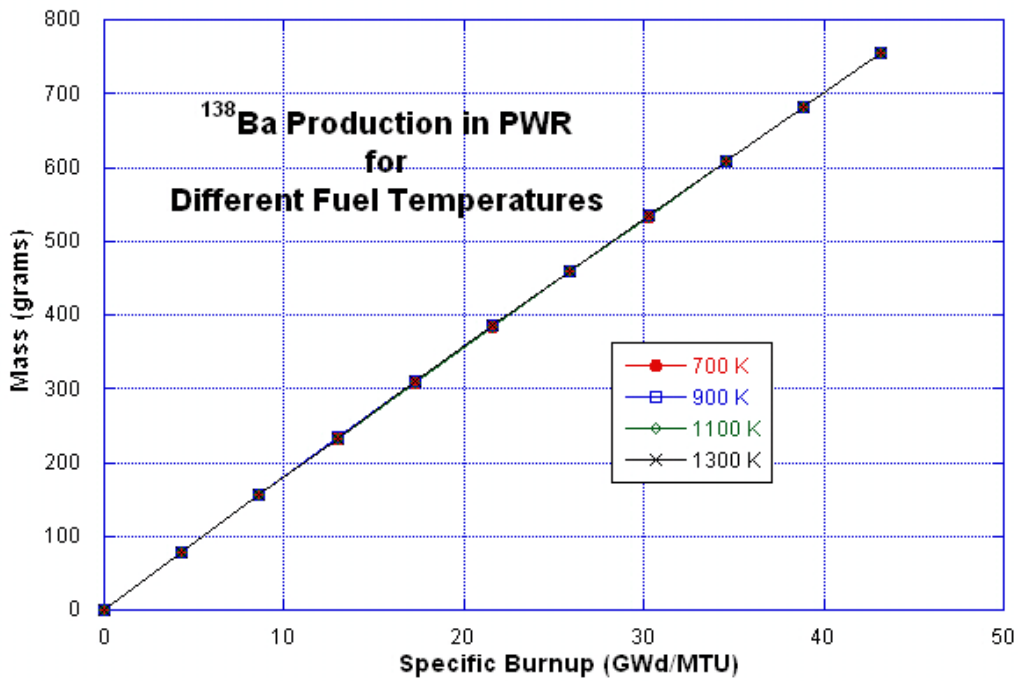


Figure 457: ¹³⁸Ba Production in the PWR Model for Different Fuel Temperatures

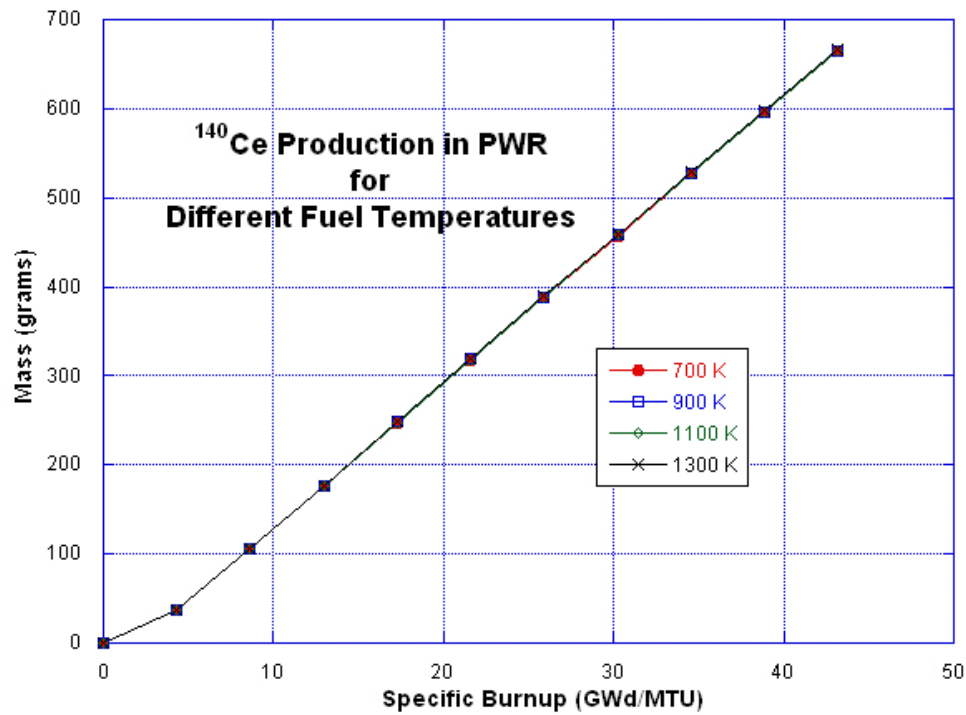


Figure 458: ¹⁴⁰Ce Production in the PWR Model for Different Fuel Temperatures

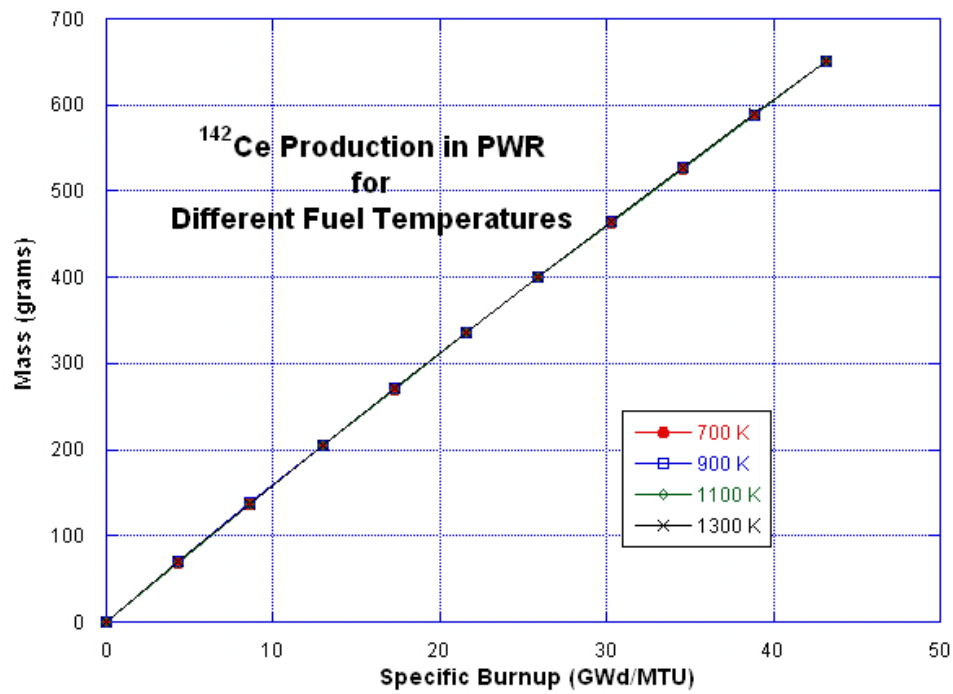


Figure 459: ¹⁴²Ce Production in the PWR Model for Different Fuel Temperatures

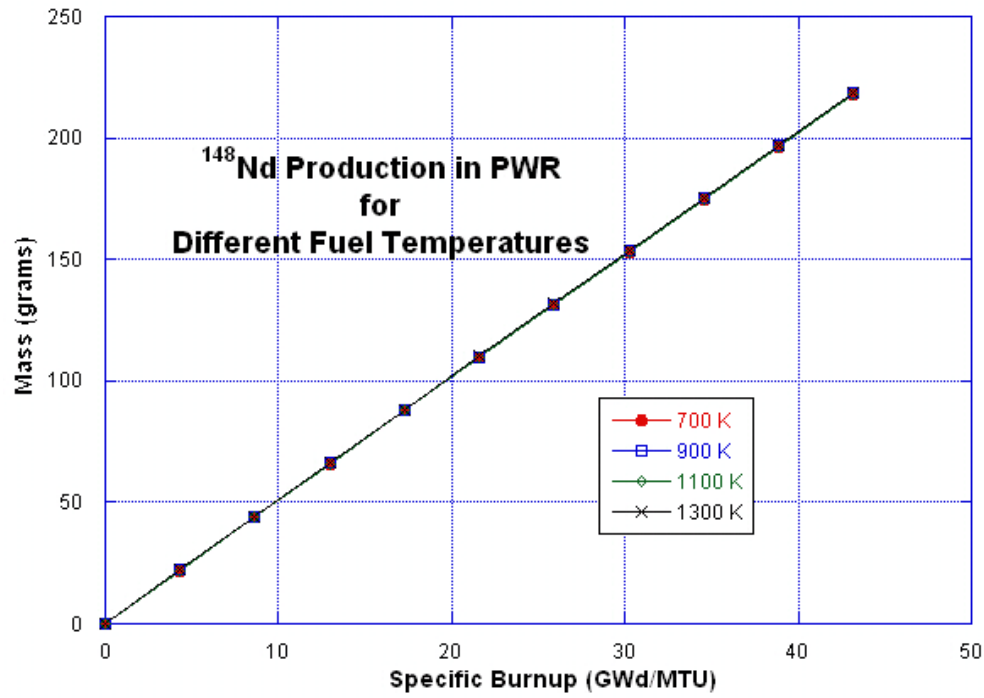


Figure 460: ¹⁴⁸Nd Production in the PWR Model for Different Fuel Temperatures

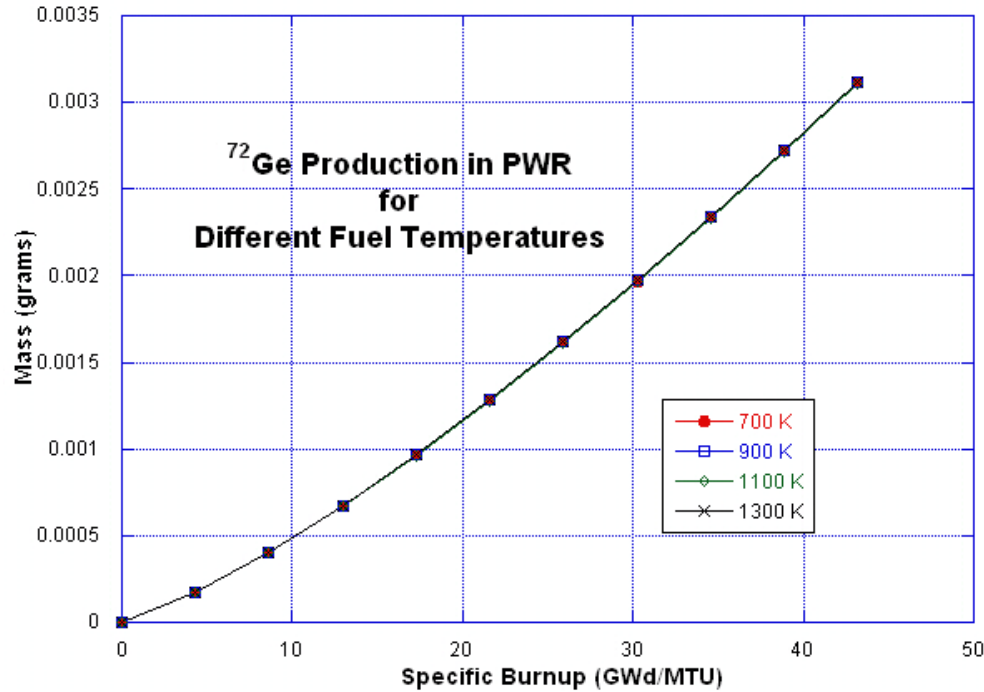


Figure 461: ⁷²Ge Production in the PWR Model for Different Fuel Temperatures

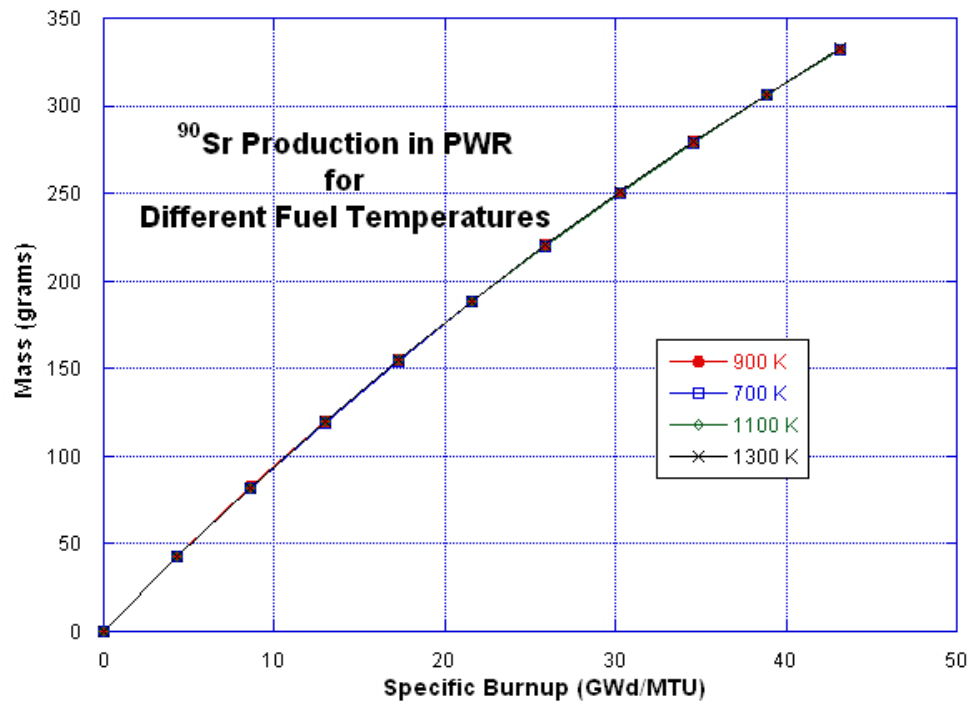


Figure 462: ⁹⁰Sr Production in the PWR Model for Different Fuel Temperatures

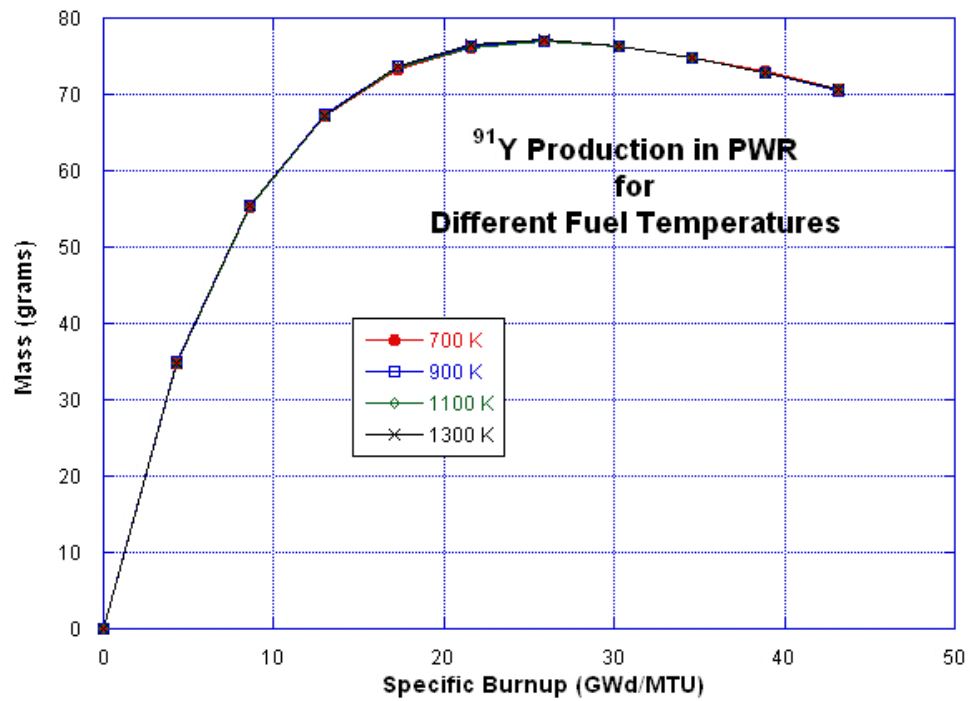


Figure 463: ⁹¹Y Production in the PWR Model for Different Fuel Temperatures

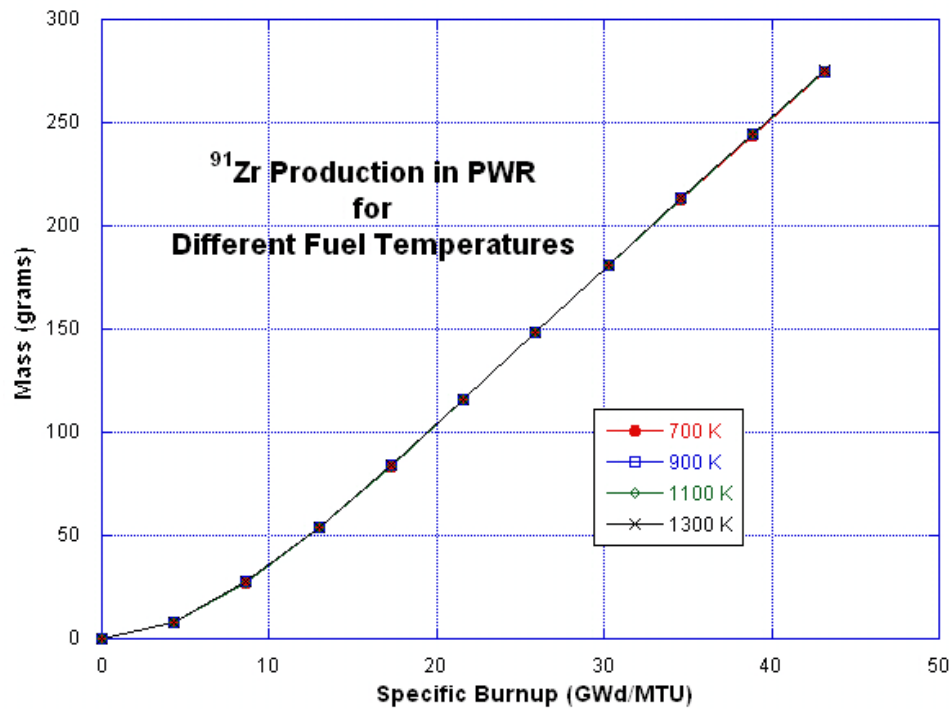


Figure 464: ⁹¹Zr Production in the PWR Model for Different Fuel Temperatures

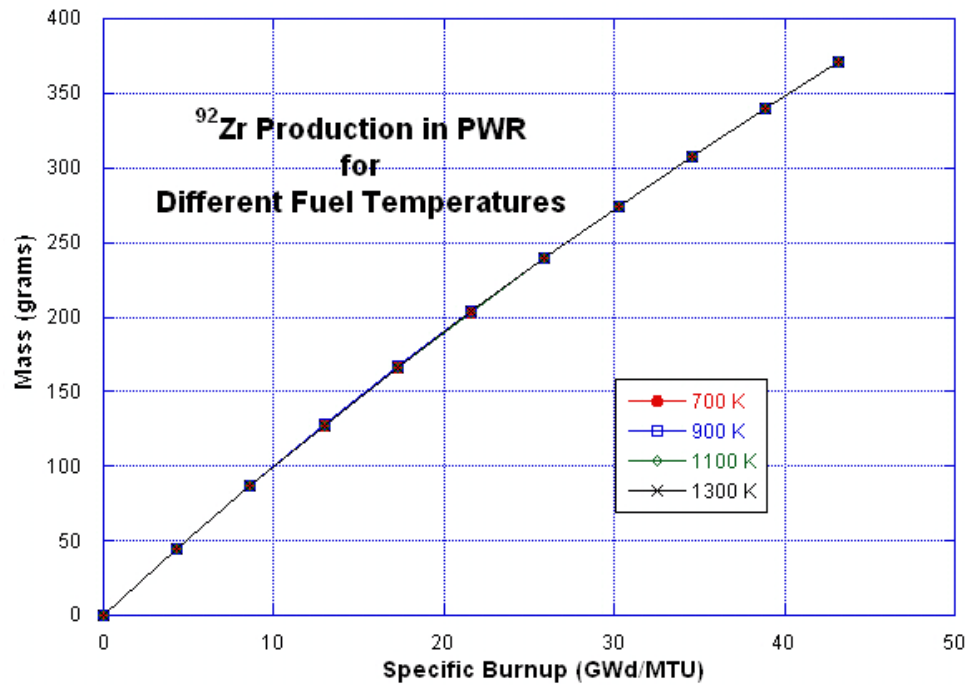


Figure 465: ⁹²Zr Production in the PWR Model for Different Fuel Temperatures

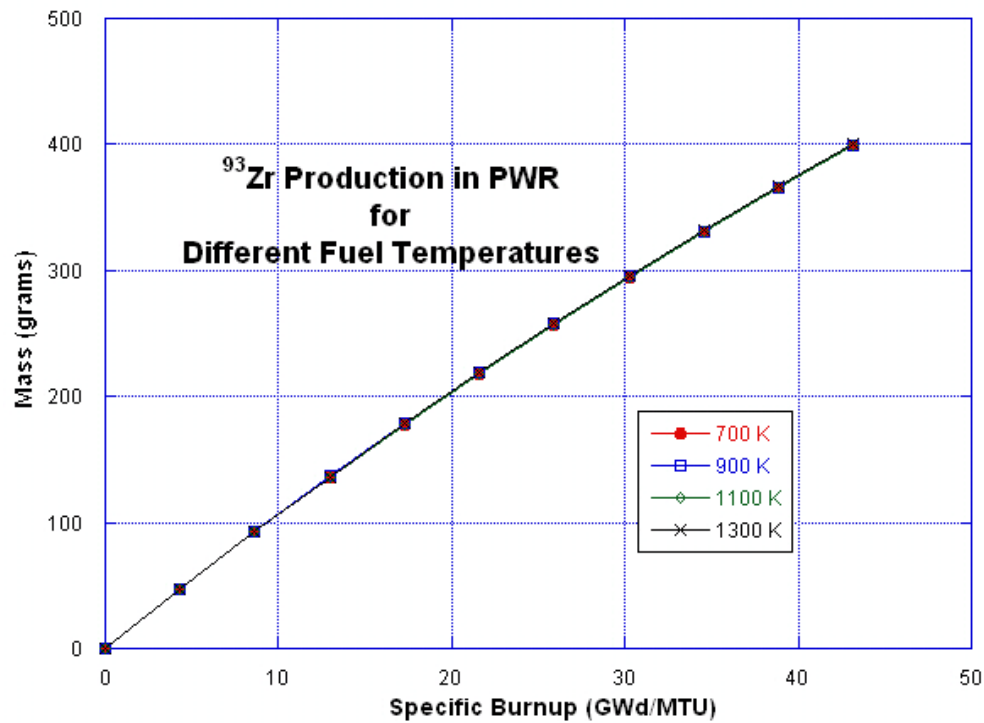


Figure 466: ⁹³Zr Production in the PWR Model for Different Fuel Temperatures

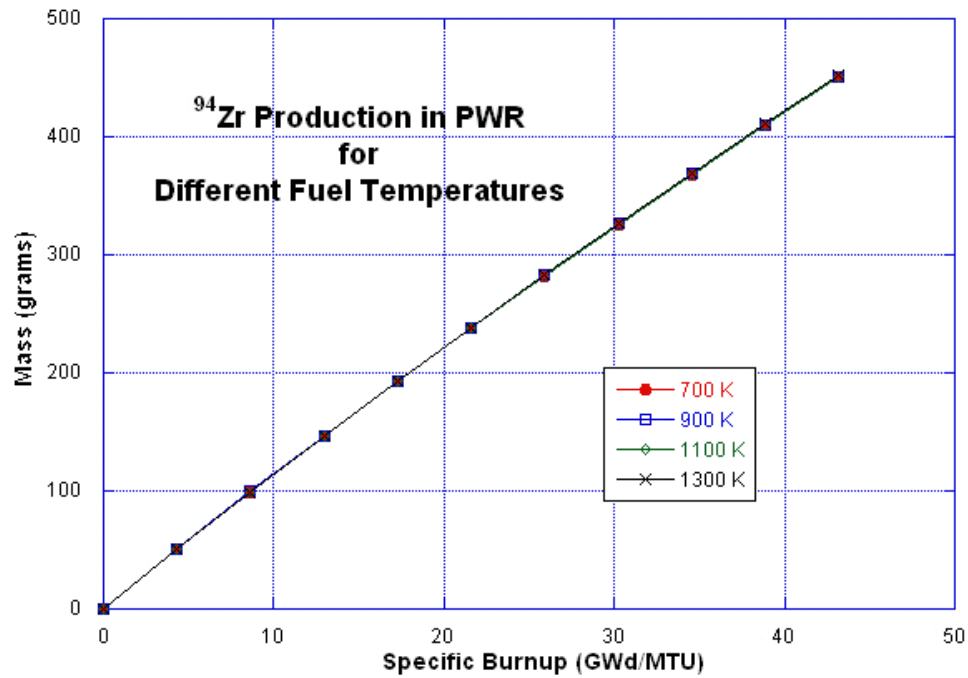


Figure 467: ⁹⁴Zr Production in the PWR Model for Different Fuel Temperatures

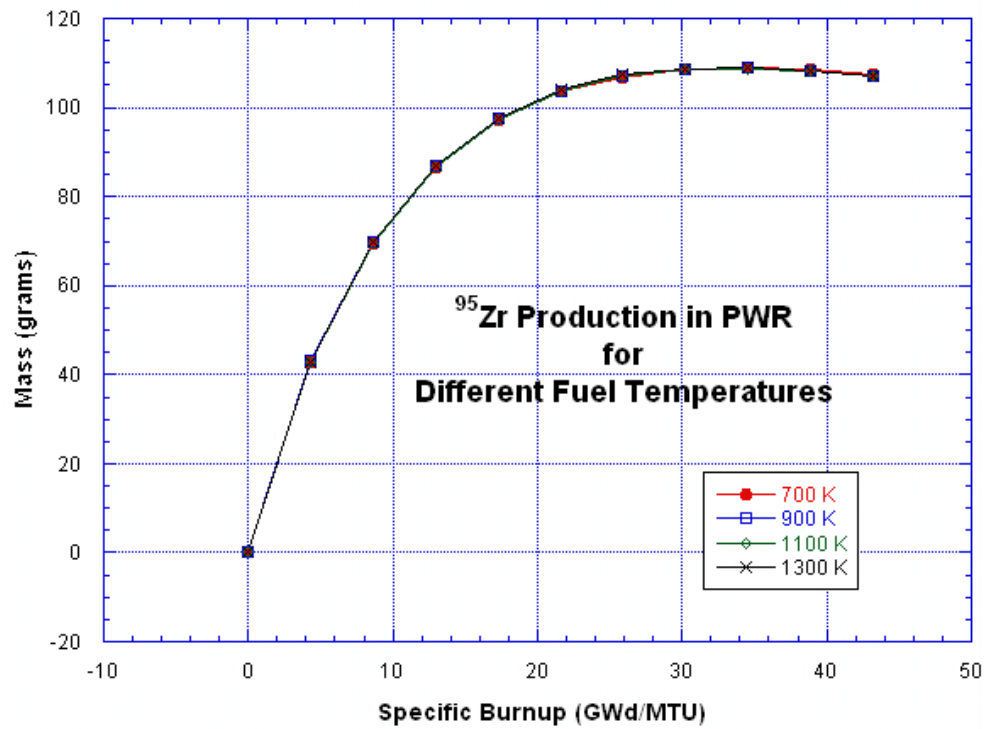


Figure 468: ⁹⁵Zr Production in the PWR Model for Different Fuel Temperatures

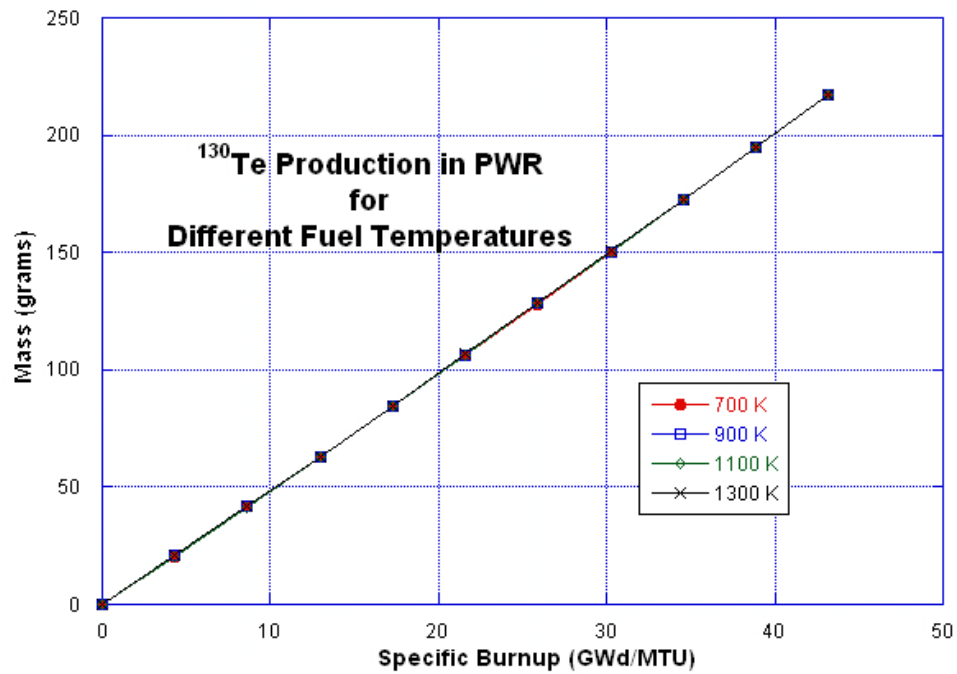


Figure 469: ¹³⁰Te Production in the PWR Model for Different Fuel Temperatures

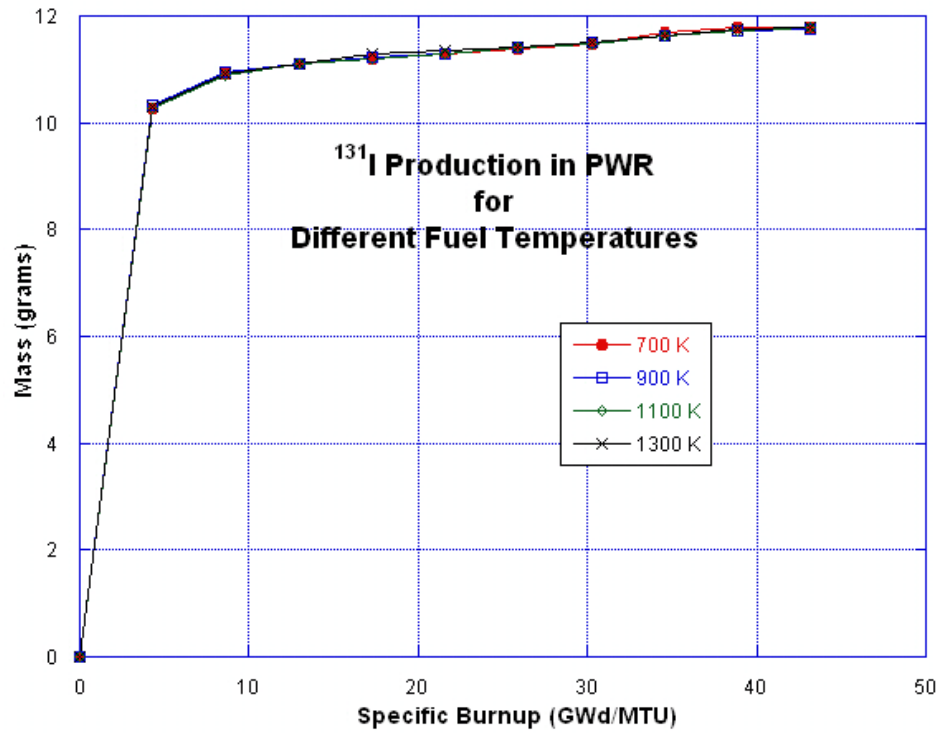


Figure 470: ¹³¹I Production in the PWR Model for Different Fuel Temperatures

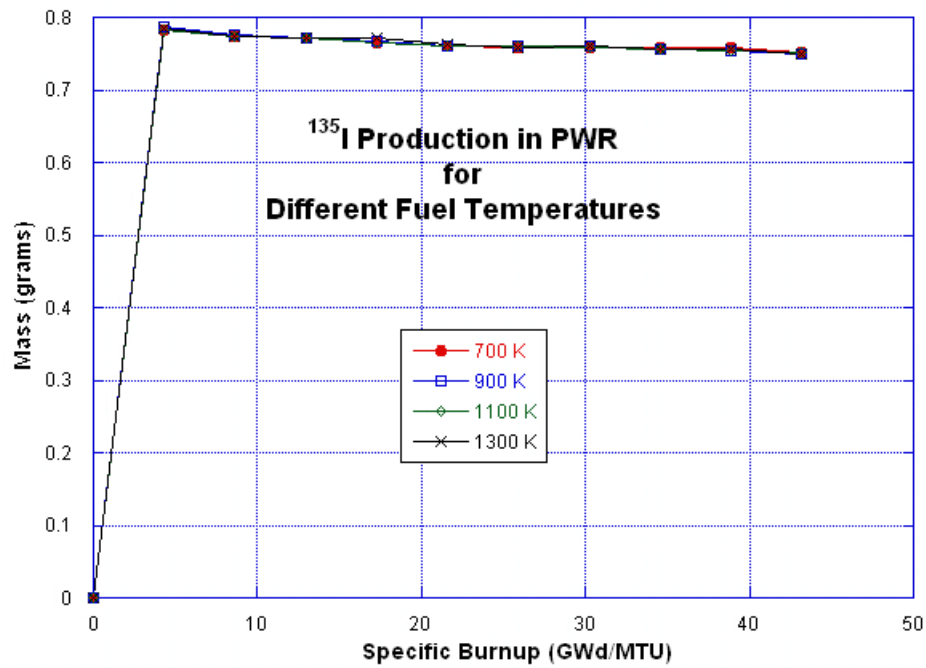


Figure 471: ¹³¹I Production in the PWR Model for Different Fuel Temperatures

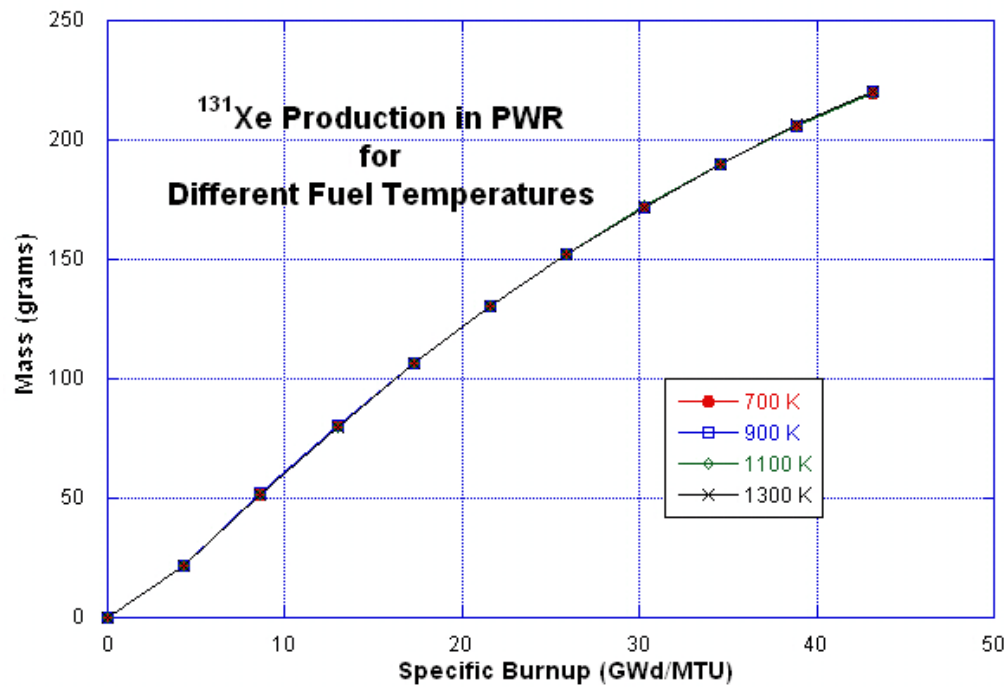


Figure 472: ¹³¹Xe Production in the PWR Model for Different Fuel Temperatures

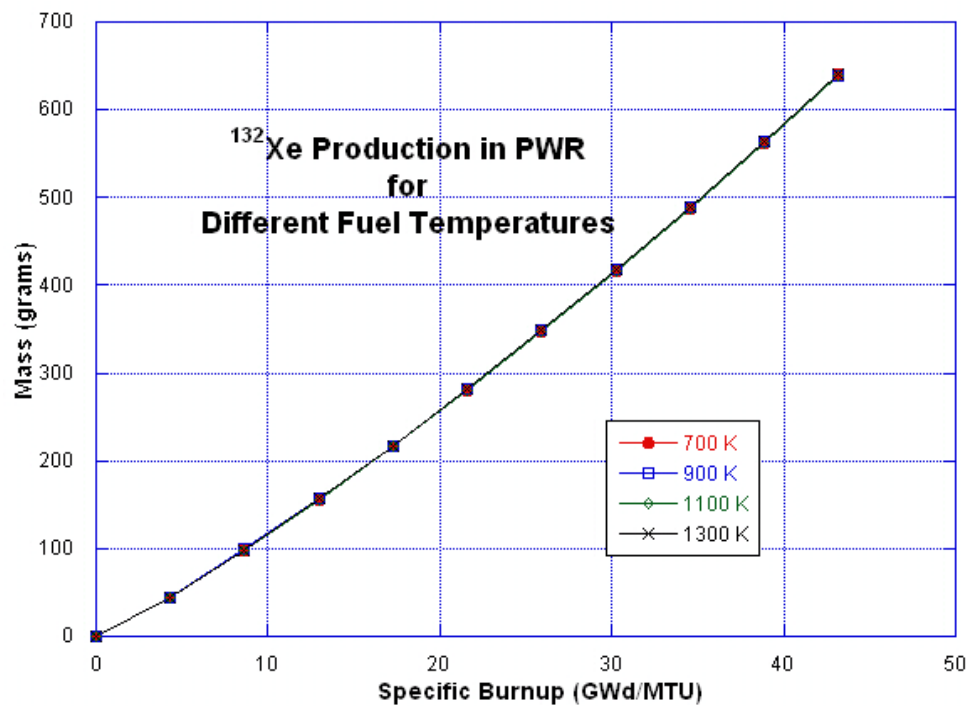


Figure 473: ¹³²Xe Production in the PWR Model for Different Fuel Temperatures

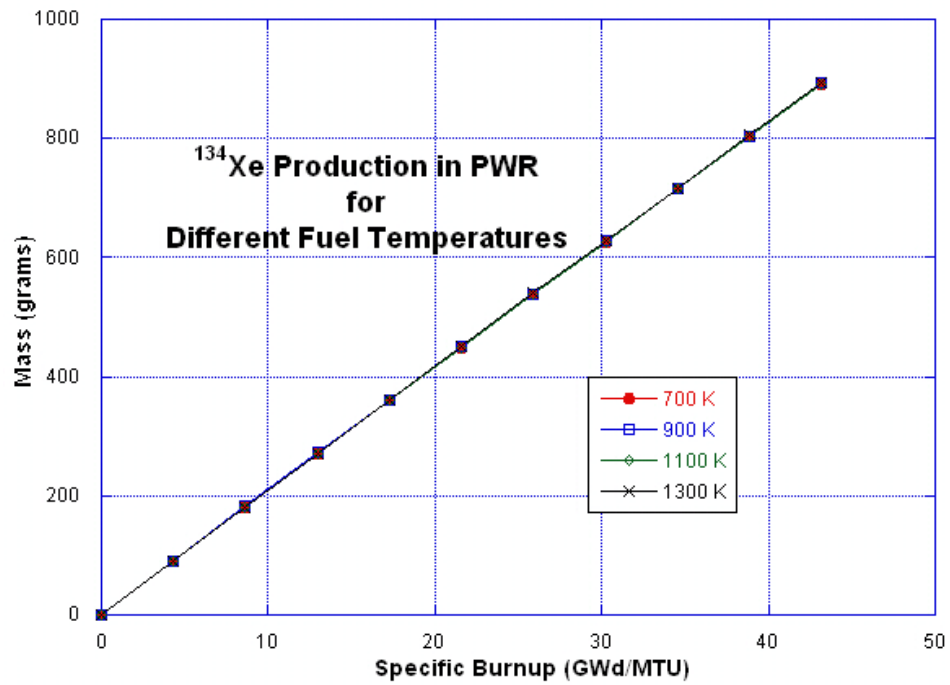


Figure 474: ¹³⁴Xe Production in the PWR Model for Different Fuel Temperatures

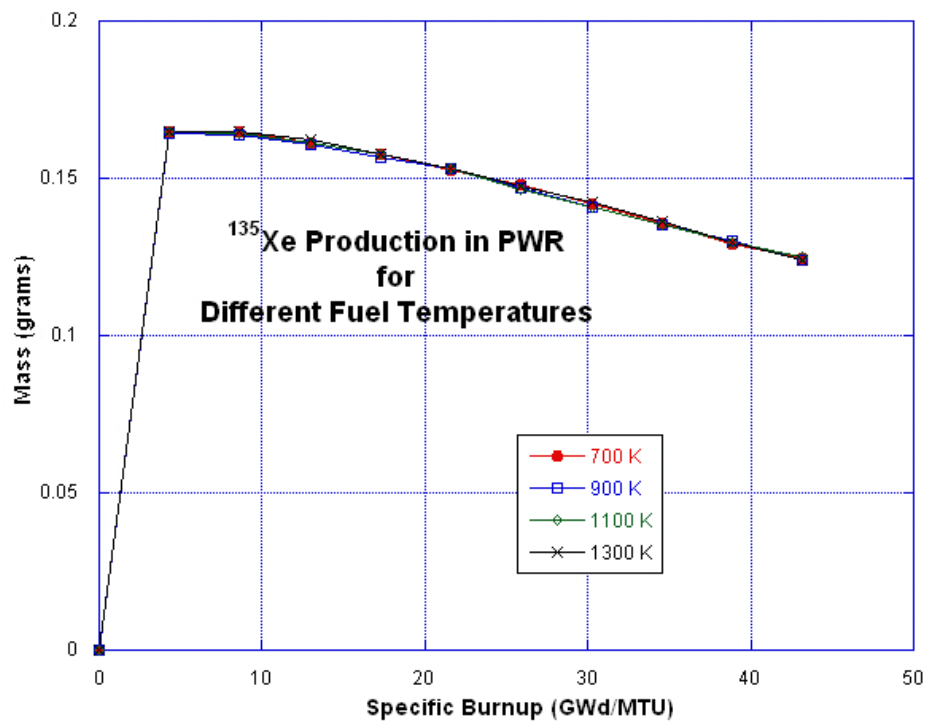


Figure 475: ¹³⁵Xe Production in the PWR Model for Different Fuel Temperatures

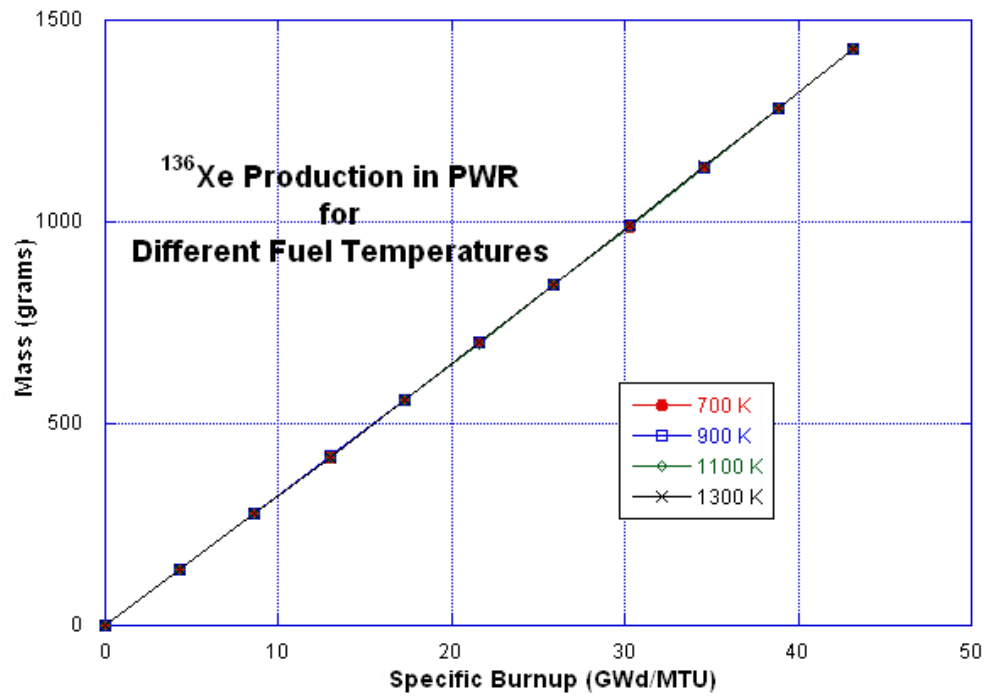


Figure 476: ¹³⁶Xe Production in the PWR Model for Different Fuel Temperatures

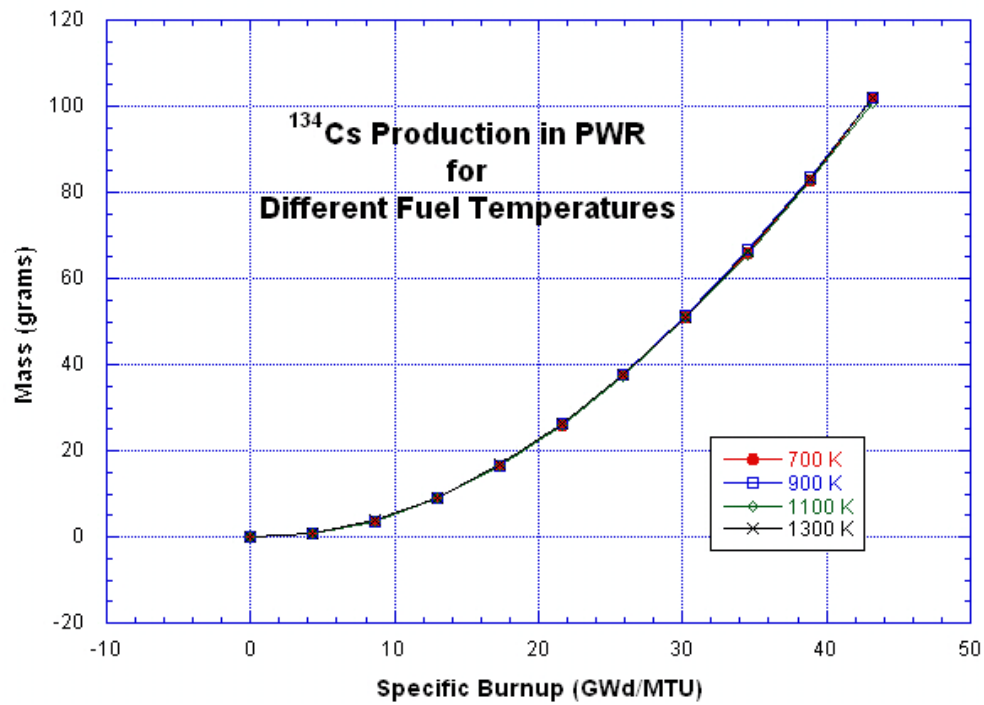


Figure 477: ¹³⁷Cs Production in the PWR Model for Different Fuel Temperatures

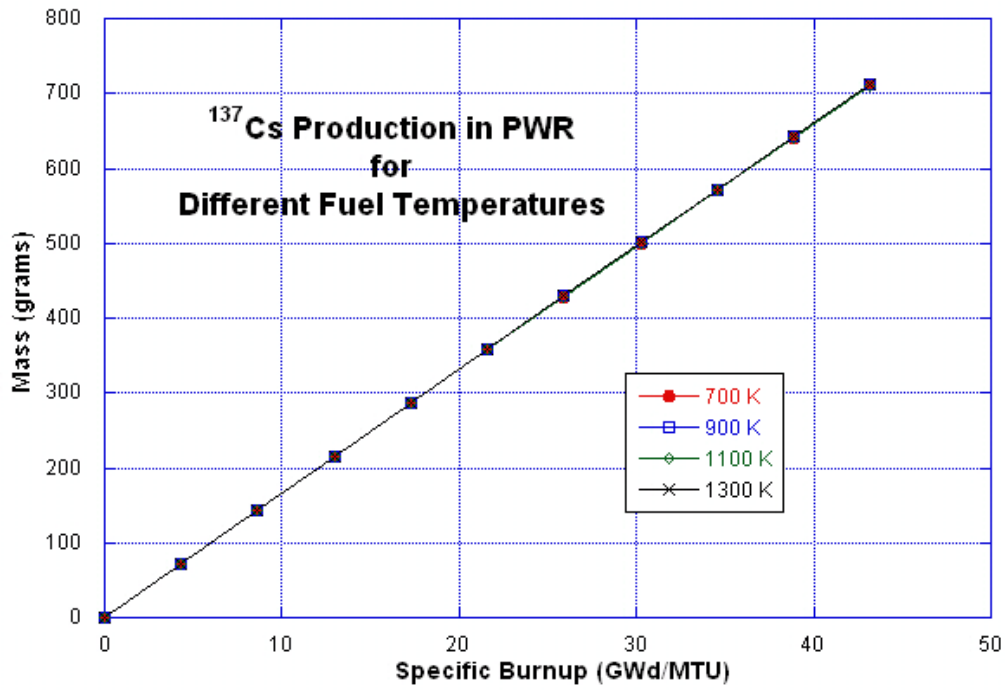


Figure 478: ¹³⁷Cs Production in the PWR Model for Different Fuel Temperatures

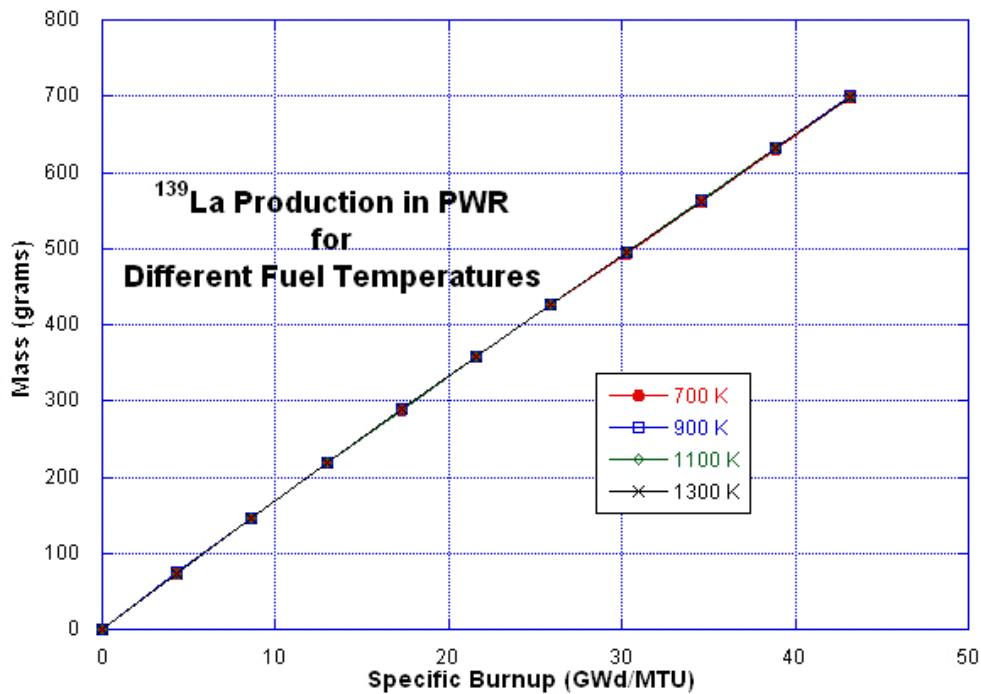


Figure 479: ¹³⁹La Production in the PWR Model for Different Fuel Temperatures

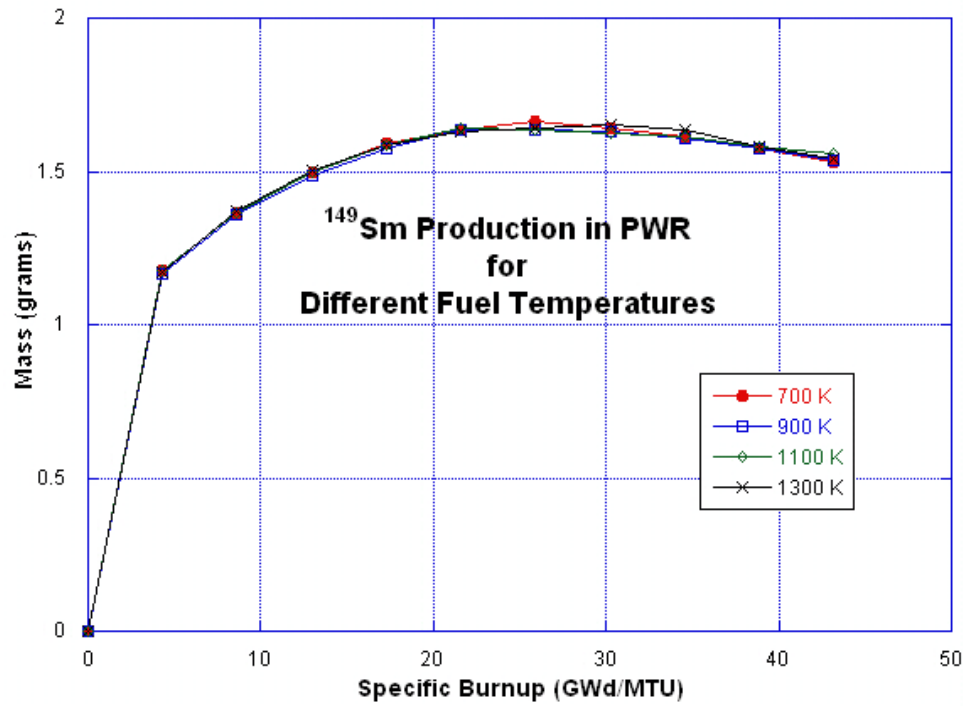


Figure 480: ¹⁴⁹Sm Production in the PWR Model for Different Fuel Temperatures

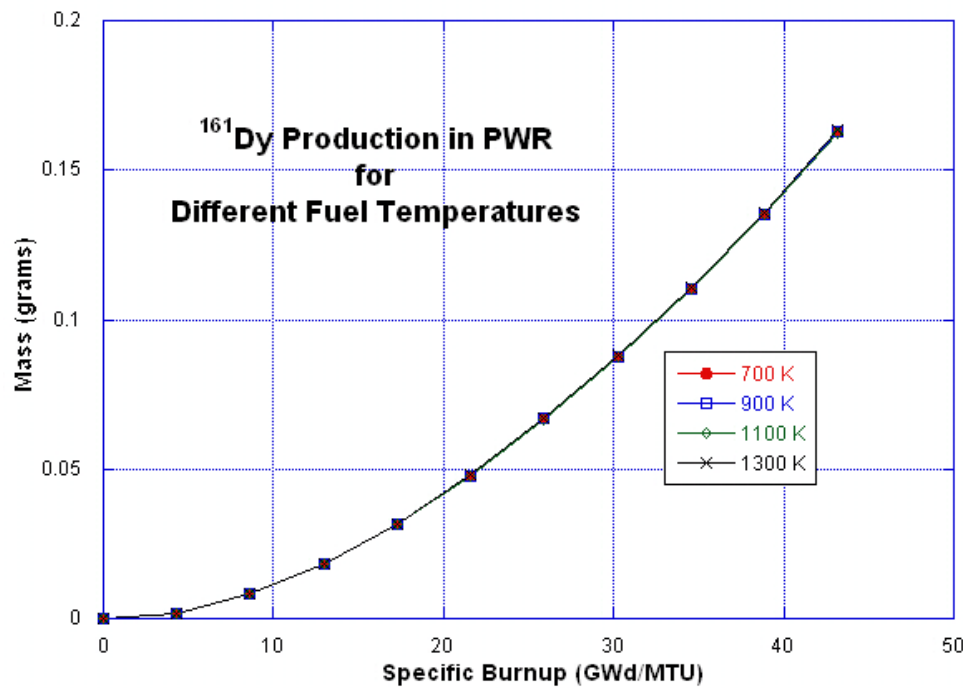


Figure 481: ¹⁶¹Dy Production in the PWR Model for Different Fuel Temperatures

Appendix H: ARP Cross Section Extraction Input and Output Files

```
=xseclist
g8_e20w07.arplib
10
26.71 28.49 30.27 32.05 33.83 35.6 37.39
39.17 40.95 42.73
b
n
4
922350 922380 942390 942410
end
        primary module access and input record ( Scale 5.1 driver )
```

module xseclist will be called at 23:16:00.670 on 12/29/2009.

```
g8_e20w07.arplib
10
26.71 28.49 30.27 32.05 33.83 35.6 37.39
39.17 40.95 42.73
b
n
4
922350 922380 942390 942410
```

module xseclist is finished. completion code 0. cpu time used
0.27 (seconds).

library name: g8_e20w07.arplib

no. of burnups: 10

burnups:

2.6710E+01	2.8490E+01	3.0270E+01	3.2050E+01
3.3830E+01			
3.5600E+01	3.7390E+01	3.9170E+01	4.0950E+01
4.2730E+01			

data (absorption (a), fission (f), or both (b)): b

list entire library (yes=y, no=n): n

no. of materials: 4

material identification:

922350 922380 942390 942410

***** absorption cross sections *****

----- light elements -----

----- end of light elements -----

----- actinides -----

material= 922350 (u235)

burnup	xsec
2.67100E+01	2.97483E+02
2.84900E+01	2.95549E+02
3.02700E+01	3.05397E+02
3.20500E+01	3.26814E+02
3.38300E+01	3.30516E+02
3.56000E+01	3.32712E+02
3.73900E+01	3.34772E+02
3.91700E+01	3.41859E+02
4.09500E+01	3.42889E+02
4.27300E+01	3.41851E+02

material= 922380 (u238)

burnup	xsec
2.67100E+01	3.92032E+00
2.84900E+01	3.98674E+00
3.02700E+01	3.90271E+00
3.20500E+01	3.72603E+00
3.38300E+01	3.70959E+00
3.56000E+01	3.69930E+00
3.73900E+01	3.68325E+00
3.91700E+01	3.60663E+00
4.09500E+01	3.61708E+00

4.27300E+01	3.65554E+00
-------------	-------------

material= 942390 (pu239)

burnup	xsec
2.67100E+01	9.39875E+02
2.84900E+01	9.58837E+02
3.02700E+01	9.48821E+02
3.20500E+01	9.53319E+02
3.38300E+01	9.50629E+02
3.56000E+01	9.48526E+02
3.73900E+01	9.47821E+02
3.91700E+01	9.51318E+02
4.09500E+01	9.52436E+02
4.27300E+01	9.51453E+02

material= 942410 (pu241)

burnup	xsec
2.67100E+01	8.90341E+02
2.84900E+01	9.62790E+02
3.02700E+01	9.54394E+02
3.20500E+01	9.65412E+02
3.38300E+01	9.67236E+02
3.56000E+01	9.68939E+02
3.73900E+01	9.71385E+02
3.91700E+01	9.83948E+02
4.09500E+01	9.86783E+02
4.27300E+01	9.85284E+02

----- end of actinides -----

----- fission products -----

----- end of fission products -----

***** end of absorption cross sections *****

***** fission cross sections *****

material= 922350 (u235)

burnup	xsec
2.67100E+01	2.46151E+02
2.84900E+01	2.44323E+02
3.02700E+01	2.53081E+02
3.20500E+01	2.72075E+02
3.38300E+01	2.75314E+02
3.56000E+01	2.77236E+02
3.73900E+01	2.79054E+02
3.91700E+01	2.85377E+02
4.09500E+01	2.86281E+02
4.27300E+01	2.85328E+02

material= 922380 (u238)

burnup	xsec
2.67100E+01	3.75639E-01
2.84900E+01	3.85609E-01

3.02700E+01	3.67978E-01
3.20500E+01	3.32672E-01
3.38300E+01	3.28766E-01
3.56000E+01	3.26301E-01
3.73900E+01	3.22974E-01
3.91700E+01	3.07992E-01
4.09500E+01	3.08753E-01
4.27300E+01	3.14736E-01

material= 942390 (pu239)

burnup	xsec
2.67100E+01	6.03329E+02
2.84900E+01	6.16111E+02
3.02700E+01	6.11885E+02
3.20500E+01	6.18888E+02
3.38300E+01	6.18128E+02
3.56000E+01	6.17442E+02
3.73900E+01	6.17562E+02
3.91700E+01	6.21568E+02
4.09500E+01	6.22656E+02
4.27300E+01	6.21931E+02

material= 942410 (pu241)

burnup	xsec
2.67100E+01	6.49950E+02
2.84900E+01	7.03425E+02
3.02700E+01	6.98058E+02
3.20500E+01	7.07042E+02
3.38300E+01	7.08626E+02
3.56000E+01	7.10049E+02
3.73900E+01	7.11983E+02
3.91700E+01	7.21578E+02
4.09500E+01	7.23742E+02
4.27300E+01	7.22636E+02

***** end of fission cross sections *****

References

1. Moody K. J. , Hutcheon I. D. , Grant P. M. , Nuclear Forensic Analysis, Taylor & Francis, New York, 2005.
2. M. R. Scott, *Nuclear Forensics: Attributing the Source of Spent Fuel Used in an RDD Event*, LA-14220-T, Los Alamos National Laboratory, June 2005.
3. S. M. Whitney, S. Biegalski, B. Buchholz, *Analyzing Nuclear Fuel Cycles from Isotopic Ratios of Waste Products Applicable to Measurement by Accelerator Mass Spectrometry*, Nuclear Science and Engineering, Volume 157, pp. 200-209, October 2007.
4. J. Weaver, S. R. F. Biegalski, B. A. Buchholz, *Assessment of Non-traditional Isotopic Ratios by Mass Spectrometry for Analysis of Nuclear Activities*, Journal of Radioanalytical and Nuclear Chemistry, July 2009.
5. *SCALE: A Modular Code System for Performing Standardized Computer Analyses for Licensing Evaluations*, ORNL/TM-2005/39, Version 5.1, Vols. I–III, November 2006. Available from Radiation Safety Information Computational Center at Oak Ridge National Laboratory as CCC-732.
6. *Criticality Calculations with MCNP: A Primer*, LA-12827-M, Los Alamos National Laboratory, August 1994.
7. *MCNPX, Version 26E*, LA-UR-07-6632, Los Alamos National Laboratory, November 17, 2007.
8. J.C. Wagner, M.D. DeHart, and B.L. Broadhead, ORNL/TM-1999/193, *Investigation of Burnup Credit Modeling Issues Associated with BWR Fuel*. October 2000.
9. *2007 World Nuclear Industry Handbook*, Nuclear Engineering International, 2007.
10. CANTEACH Image Library, Canteach.candu.org.
http://canteach.candu.org/image_index.html. (12 October 2009).
11. I.C. Gauld, K. A. Litwin, *Verification and Validation of the ORIGEN-S Code and Nuclear Data Libraries*, Atomic Energy of Canada Limited, RC-1429, August 1995.

12. Lamarsh, J. R., Baratta, A. J., Introduction to Nuclear Engineering, Third Edition, Prentice Hall, Upper Saddle River, New Jersey.
13. M.B. Chadwick, P. Oblozinsky, M. Herman et al., "ENDF/B-VII.0: Next Generation Evaluated Nuclear Data Library for Nuclear Science and Technology", Nuclear Data Sheets, vol. 107, pp. 2931-3060, 2006.
14. Neeb, K. H., The Radiochemistry of Nuclear Power Plants with Light Water Reactors, Walter de Gruyter, Berlin, New York, 1997.
15. R. E. MacFarlane, D. W. Muir, *The NJOY Nuclear Data Processing System*, Version 91, LA-12740-M, Los Alamos National Laboratory, October 1994.
16. Garland, Wm. J., "How and Why is CANDU Designed the Way It Is: Introduction", Revision 3, February 2003.
17. Brooks, Gord L., "A Short History of the CANDU Nuclear Power System", Revision 2, December 2002.
18. Germina Ilas, Ian C. Gauld, and Vince Jodoin, *LWR Cross Section Libraries for ORIGEN-ARP in SCALE 5.1*, Transactions of the American Nuclear Society 95, 706-708, Academic Press, 2006. C. Gauld, *SCALE-4 Analysis of LaSalle Unit 1 BWR Commercial Reactor Critical Configurations*, [ORNL/TM-1999/247](#), Lockheed Martin Energy Research Corp., Oak Ridge National Laboratory, March 2000.
19. J. C. Wagner and C. V. Parks, *Parametric Study of the Effect of Burnable Poison Rods for PWR Burnup Credit*, NUREG/CR-6761 (ORNL/TM-2000/373), U.S. Nuclear Regulatory Commission, Oak Ridge National Laboratory, March 2002.
20. G. M. O'Donnel, *A New Comparative Analysis of LWR Fuel Designs*, NUREG-1754, U.S. Nuclear Regulatory Commission, December 2001.
21. E. A. Schneider, M. R. Deinert, K. B. Cady, *A Computationally Simple Model for Determining the Time Dependent Spectral Neutron Flux in a Nuclear Reactor Core*, Journal of Nuclear Materials, April 2006.
22. O. W. Herman, S. M. Bowman, M. C. Brady, C. V. Parks, *Validation of the SCALE System for PWR Spent Fuel Isotopic Composition Analyses*, ORNL/TM-12667, Oak Ridge National Laboratory, March 1995.

23. L. C. Leal, O. W. Hermann, S. M. Bowman, C. V. Parks, *ARP: Automatic Rapid Process for the Generation of Problem-Dependent SAS2H/ORIGEN-S Cross-Section Libraries*, ORNL/TM-13584, Oak Ridge National Laboratory, April 1998.
24. Xiandeng Hou, Wen Chen, Yihua He, Bradley Jones, *Analytical Atomic Spectrometry for Nuclear Forensics*, *Applied Spectroscopy Reviews*, 40: 245-267, 2005.
25. S. R. Greene, *Reactor-Based Plutonium Disposition: Opportunities, Options, and Issues*, IAEA-SM-358/38.
26. I.C. Gauld, P Chare, R. C. Clarke, *Development of ORIGEN-ARP Methods and Data for LEU and MOX Safeguards Applications*, Paper Submitted to 44th Annual Institute of Nuclear Materials Management (INMM) Annual Meeting, July 13-17, 2003.
27. Foderaro, Anthony, *Elements of Neutron Interaction Theory*, The MIT Press, Cambridge, Massachusetts and London, England, 1971.
28. Cochran, Robert G. and Tsoulfanidis, Nicholas, *The Nuclear Fuel Cycle: Analysis and Management*, Second Edition, American Nuclear Society, La Grange Park, Illinois, USA, 1999.
29. Foster, Arthur R and Wright, Jr., Robert L., *Basic Nuclear Engineering*, Fourth Edition, Allyn and Bacon, Inc., Boston, London, Sydney, Toronto, 1983.
30. *MCNPX–User’s Manual, Version 2.6.0*, LA-CP-07-1473, Los Alamos National Laboratory, April 2008.
31. M. L. Fensin, S. J. Tobin, N. P. Sandoval, M. T. Swinhoe, S. J. Thompson, *A Monte Carlo Linked Depletion Spent Fuel Library for Assessing Varied Nondestructive Assay Techniques for Nuclear Safeguards*, American Nuclear Society Topical Meeting, *Advances in Nuclear Fuel Management IV*, 2009.
32. M. L. Fensin, J. S. Hendricks, S. Anghaie, *The Enhancements and Testing for the MCNPX 2.6.0 Depletion Capability*, *Nuclear Technology*, Volume 170, April 2010.

Vita

Angela Sue Chambers was born in Portsmouth, Ohio, the daughter of John and Janet Brown. She received the degree of Bachelor of Science from The Ohio State University in May 1994. She received her Master of Science degree, also from The Ohio State University, in December 1996. From 1996 to 1998, she was employed by Battelle Memorial Institute. From 1998 to 2009, she was employed as a technical staff member and engineer by the Los Alamos National Laboratory. From 2009 until present, she is employed as a nuclear explosive safety engineer by the National Nuclear Security Administration. She currently serves as a Lieutenant Commander in the United States Navy Reserve. In January 2001, she entered the Graduate School at The University of Texas at Austin.

Permanent address: 3211 Bowie Street, Amarillo, Texas 79109

This dissertation was typed by the author.